Supercritical Fluids as Solvents and Reaction Media

by Gerd H. Brunner

- ISBN: 0444515747
- Publisher: Elsevier Science & Technology Books
- Pub. Date: July 2004

PREFACE

Supercritical fluids are gaseous compounds or mixtures of compounds with properties in between of a typical gas and of a typical liquid. These properties can be smoothly changed by varying the pressure. The effect is that supercritical fluids behave either like a gas or a liquid, depending on the values of thermodynamic properties (p,V,T). This tuning of properties, and other advantageous properties of supercritical fluids like a very low viscosity, led to innovative technologies.

More than 100 plants of production size are now in operation worldwide in the areas of process and production technology, environmental applications, and particle engineering. New processes are under research and development in various fields, including downstream processing in biotechnical processes and enzymatic catalysis.

Actually, processes applying supercritical fluids are in operation for a long time and for huge amounts of substances. Examples are supercritical paraffins in mineral oil processing (e.g. the ROSE-process) and high pressure polymerization of ethylene to poly-ethylene. These important processes make use of the advantageous properties of supercritical fluids in singular cases. Application of these properties in processing technology has often been proposed since Hannay and Hogarth in 1879 first observed these phenomena. Yet these activities remained isolated. Only since about 1970, when Zosel proposed a great variety of processes with supercritical fluids, the topic began to be treated more systematically. In the 70ies of the 20th century it developed into a rapidly growing field of research, development, and technical application. All fields of process technology involving solvents are now under close investigation, and new applications will emerge soon.

The scientific community may now comprise about 1500 researchers with about 500 researchers having chosen supercritical fluids as their main area of interest. World conferences on supercritical fluids, like the 6th International Symposium on Supercritical Fluids, April 2003 in Versailles, France, attract about 450 participants with about 350 scientific contributions.

German scientific institutes and German industry still play an important role in the field of supercritical fluids and its application as sustainable and environmental benign technology. Knowledge and production plants have been created and exported. The perspective of this technology is bright, provided that research and development is continued on an appropriate scale.

Therefore, the “Deutsche Forschungsgemeinschaft, DFG”, (the German National Council For Science) launched a research program on “Supercritical fluids as solvents and reaction media” on the initiative of the “GVC-Fachausschuß Hochdruckverfahrenstechnik” (i.e. the German working party on High Pressure Chemical Engineering of the Society of Chemical Engineers), and after a proposal of

Prof. Dr. G. Brunner, Technische Universität Hamburg-Harburg,
Prof. Dr. Buback, Universität Göttingen,
Prof. Dr. H. Lentz, Universität-GHS Siegen,
Prof. Dr. G. Luft, Technische Universität Darmstadt,
Prof. Dr. G.M. Schneider, Ruhr-Universität Bochum,
Prof. Dr. O. Tiltscher , Technische Universität München.

The cooperation between pure and applied scientists, as had been the case within the working group "Hochdruckverfahrenstechnik" for a long time, made it probable to achieve substantial results within the limited time of the program of 6 years.

The goal was to achieve the scientific and engineering fundamentals for new innovative processes using supercritical fluids. Further applications of supercritical fluids should be made accessible. Research should concentrate on further investigation of physical and chemical properties of supercritical fluids, transport properties, separation processes (summarized under the term "extraction"), chemical reactions in and with supercritical fluids, making use of the tunable properties of supercritical fluids for engineering of particles and materials, and to further develop mechanical compounds for processing plants.

The book contains results of most of the projects. The table of contents lists the contributions. They speak for themselves and are therefore not additionally commented here. Further results of projects sponsored within this program are published in various scientific journals.

The content of this book provides an overview on the research activities in this field in Germany. Many of the groups involved have additional research activities in similar areas. Therefore, this book is by no means a report on all the activities in the field of supercritical fluids in Germany from 1996 to 2002. Nevertheless, the research program "Supercritical fluids as solvents and reaction media" provided an immensely valuable platform for exchange of knowledge and experience. More than 50 young researchers were involved contributing with their expertise, their new ideas, and the motivation of youth. Cooperation between the research groups was intensified during the research program. It will carry on, since there are still many things to be found out and to be developed in the field of supercritical fluids.

Hamburg, June 2003 G. Brunner

Table of Contents

1	Phase equilibrium, solubility	1
1.1	Experimental determination of phase equilibria and comprehensive examination of the predictive capabilities of group contribution equations of state with a view to the synthesis of supercritical extraction processes	3
1.2	Influence of additional components on the solvent power of supercritical ethylene	39
1.3	High pressure phase equilibria of copolymer solutions - experiments and correlation	61
1.4	Fluid phase equilibria of binary mixtures with supercritical solvents with in-situ concentration measurements by Raman spectroscopy	85
1.5	High-pressure solubility measurement of solids in near- and supercritical fluids	121
1.6	Phase behaviour of organic solid solutes and supercritical fluids with respect to particle formation processes	147
1.7	Supercritical carbon dioxide as solvent for organic compounds present in aqueous salt solutions	163
1.8	Correlation and prediction of high-pressure phase equilibria and related	185

	thermodynamic properties of simple fluid mixtures	
1.9	Development of simplified equation of state for molecular fluids and their applications for the investigation of supercritical chain molecule solutions and mixtures	211
1.10	Correlation of the solubility of low-volatile organic compounds in near- and supercritical fluids based on an accurate equation of state	241
1.11	Thermo- and fluiddynamic aspects of the hydrogenation of triglycerides and esters in presence of supercritical fluids	269
1.12	Perturbed-chain-SAFT : development of a new equation of state for simple, associating, multipolar and polymeric compounds	295
1.13	Extractability of As-chelates and solubility of different Rh, Pd-chelates is supercritical fluid CO[subscript 2]	323
2	Properties	341
2.1	P,T-dependence of molecular mobility in supercritical fluids studied by high pressure NMR	343
2.2	Interfacial phenomena in countercurrent and spray processing using supercritical fluids	363
3	Formulation	379
3.1	Synthesis of silica aerogels and their application as drug delivery system	381
3.2	Investigation and modelling of the gas-antisolvent process	429
3.3	Formation of nanoscale drugs by rapid expansion of supercritical	449

	solutions (RESS): - experimental and theoretical investigations -	
4	Extraction	463
4.1	Separation efficiency and axial mixing in packed high pressure extraction columns	465
4.2	Separation of organic compounds from aqueous solutions by means of supercritical carbon dioxide	489
4.3	Supercritical SO[subscript 2] for preparation of sulfur dioxide complexes and for recovery of precious metals from used catalysts	523
5	Reactions	531
5.1	Polymerizations in supercritical carbon dioxide : surfactants, micelle formation, and heterophase polymerization	533
5.2	The kinetics of the early stage of dispersion polymerization in supercritical CO[subscript 2]	559
5.3	Rate coefficients of free-radical polymerization in homogeneous fluid mixtures with carbon dioxide	573
5.4	Ammonia as reagent or reaction medium for polymers	593
5.5	Inorganic materials (metals, ceramics, glasses) under the influence of reactants in supercritical aqueous solutions as well as chemical reactions (partial oxidations, hydrolysis, dehydrations) under the influence of inorganic materials in supercritical aqueous solutions	

Supercritical Fluids as Solvents and Reaction Media
G. Brunner (editor)

Chapter 1.1.

Experimental determination of phase equilibria and comprehensive examination of the predictive capabilities of group contribution equations of state with a view to the synthesis of supercritical extraction processes

H. Gardeler and J. Gmehling*

University of Oldenburg, Department of Industrial Chemistry,
P.O. Box 2503, D-26111 Oldenburg, Germany
* Corresponding author. E-mail: gmehling@tech.chem.uni-oldenburg.de;
Tel: ++49 (0)441 798 3831; Fax: ++49 (0)441 798 3330.

ABSTRACT

Isothermal vapor-liquid equilibrium data for eight asymmetric binary systems were measured. Furthermore enthalpy data are presented for the three systems carbon dioxide with dodecane, ethylene with 1-decanol at 318K in a pressure range from 45 to 140 bar. While for the VLE measurements a static apparatus equipped with on-line sampler-injectors, for the measurement of the enthalpy data an isothermal flow calorimeter was used. Furthermore a comprehensive model comparison was performed to check the quality of the prediction obtained with several group contribution equations of state.

1. INTRODUCTION

For the synthesis and design of extraction processes with supercritical fluids a reliable knowledge of the solubility of the high boiling compound in the selected supercritical fluid with or without co-solvent, and its variation with temperature and pressure is required. Apart from direct experimental data, only reliable predictive equations of state can provide this information.

The data measured in this work belong to the experimental part of a systematic study. The objective of this study is to define rules, recommendations, and limitations for thermodynamic approaches for calculating the phase equilibrium behavior for supercritical fluid extraction processes. Simple cubic equations of state are suitable models for correlating the phase equilibria in a large temperature and pressure range [1-3]. But their

applicability for a reliable estimation of the small solubility of high boiling substances in supercritical fluids as function of temperature and pressure, and the influence of co-solvents on the solubility is not analyzed and reviewed until now.

The experimental VLE data were obtained using a thermostated pressure cell equipped with two on-line samplers [4]. Using this technique very small samples can be withdrawn from the equilibrated vapor and the liquid phase, and transferred directly into the carrier gas stream for gas chromatographic analysis. For the determination of the enthalpy data an isothermal flow calorimeter (Hart Scientific) was used.

Although several VLE (vapor-liquid equilibrium) and gas solubility data are available for the selected systems ethane + decane [5-8], propane + dodecane [9-11], carbon dioxide + dodecane [9, 12-17], and ethylene + 1-decanol [18], only a limited number of them provide the required information about the vapor phase composition [5, 18]. The system ethane + decane was selected as a test system to compare our results with those published by Reamer and Sage [5]. Only heats of mixing data [19] and LLE (liquid-liquid equilibrium) data [20-22] are available for the system ethane + 1-decanol. No data were published for the system propane + 1-decanol. SLE (solid-liquid equilibrium) data are available for the systems ethane + decane [23] and propane + dodecane [24].

2. EXPERIMENTAL

2.1. Materials

All liquids used for the measurements were dried over molecular sieve 4A. Furthermore the solvents were distilled and degassed as described by Fischer and Gmehling [25]. In order to remove impurities a distillation column equipped with 2 m laboratory packing (Sulzer DX) was used. The water content was checked by Karl Fischer titration and found to be lower than 35 ppm. Final purities have been checked by gas chromatography. The gases have been used as supplied without any further purification. Table 1 lists the suppliers and the final purity of the chemicals.

2.2. Apparatus and procedure

For the measurements a static apparatus as shown in Fig. 1 was used. It can be applied in a pressure range up to 25 MPa and at temperatures from 20 to 200°C. The apparatus consists of an equilibrium cell with a magnetically driven stirrer. It is mounted in a thermostated air bath and equipped with two borosilicate windows for visual observation. This is in particular important at higher pressures, because it allows to check whether the mixture is already in the supercritical state, and to observe the formation of additional phases, which

might occur at certain conditions. The pressure inside the cell is measured with a pressure transmitter (model 891.20.501, WIKA), which is regularly calibrated with a dead weight balance pressure gauge (model 21000, D&H). The temperature is monitored using a Pt 100 thermometer (1560, Hart Scientific) using a probe mounted inside the stainless steel body of the equilibrium cell. The compounds are charged into the equilibrium cell using piston injectors (2200-801, Ruska), or a thermostated pressure vessel.

The equilibrium cell is equipped with two on-line samplers, one at the bottom and one at the top of the cell, which allow to withdraw very small samples (e.g. < 0.1 µl) directly from the liquid and the vapor phase after equilibration. The samplers are controlled pneumatically. Due to the very small sample size the equilibrium inside the cell is not disturbed. Fig. 2 shows a schematic view of the micro samplers. The samples are injected and vaporized directly into the carrier gas stream of the gas chromatograph (6890, Hewlett Packard) equipped with a TCD. To avoid condensation and adsorption of the high boiling components the samplers and all the lines for the gas stream are superheated. The injector of the gas chromatograph was modified in a way, that an additional inert gas stream can be added to the carrier gas stream at the top of the injector, which was used in a splitless mode together with packed columns to ensure that the entire sample is transferred. For each data point a minimum of 10 to 15 samples were taken from both phases.

To obtain the compositions from the chromatograms, for each compound the response factor (chromatographic signal as function of the injected amount) was determined by injection of different known amounts of the pure gases or liquids with the help of an autosampler (A200S, Carlo Erba Instruments). While

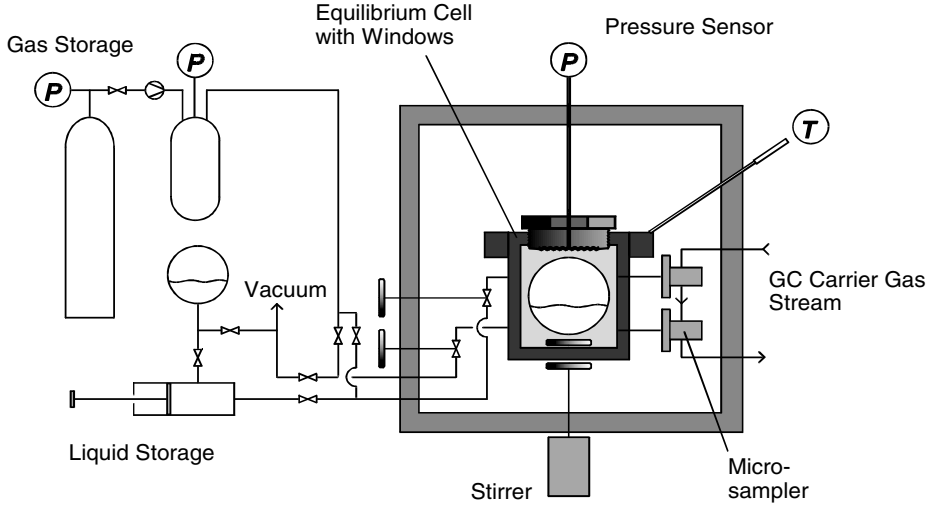

Fig.1. Static Apparatus with sampling devices for phase analysis.

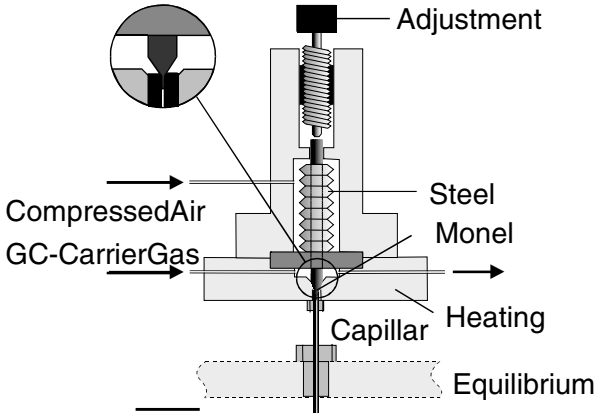

Fig.2. Pneumatic controlled sampling device for micro samples.

for gases gas-tight syringes with a volume of maximum 250 µl were used the liquids were injected as pure substance, or diluted in solvents using 1 µl syringes.

The experimental uncertainties of the apparatus are estimated as follows:
$\sigma(T/\mathrm{K}) = 0.05$, $\sigma(P/\mathrm{MPa}) = 0.005 + 0.0005\cdot(P/\mathrm{MPa})$.

The uncertainty of the liquid phase mole fraction x_i is equal to the uncertainty of the vapor phase mole fraction y_i and depends on the concentration range considered:

$\sigma(x_i) = 0.005 + 0.005\cdot x_i$ in the range of $x_i > 0.1$,
$\sigma(x_i) = 0.002 + 0.01\cdot x_i$ in the range of $x_i > 0.01$,
$\sigma(x_i) = 0.05\cdot x_i$ in the range of $x_i < 0.01$.

For the measurement of enthalpy effects an isothermal flow calorimeter shown in Fig. 3 was used. The apparatus was described previously [26]. The apparatus consist of two thermostated and computer driven HPLC-pumps, which allow to provide a flow of constant composition through a thermostated calorimeter cell equipped with a pulsed heater and a Peltier cooler. The Peltier cooler is working at constant power, providing a constant heat loss from the calorimeter cell, which is compensated by the pulsed heater. The required frequency is influenced by any endothermal and exothermal heat effects that occur in the mixing tube of the calorimeter cell. The heat effects can be determined from the frequency change between the baseline and the actual measurement. A back-pressure controller serves to keep the pressure at a constant and precisely known level.

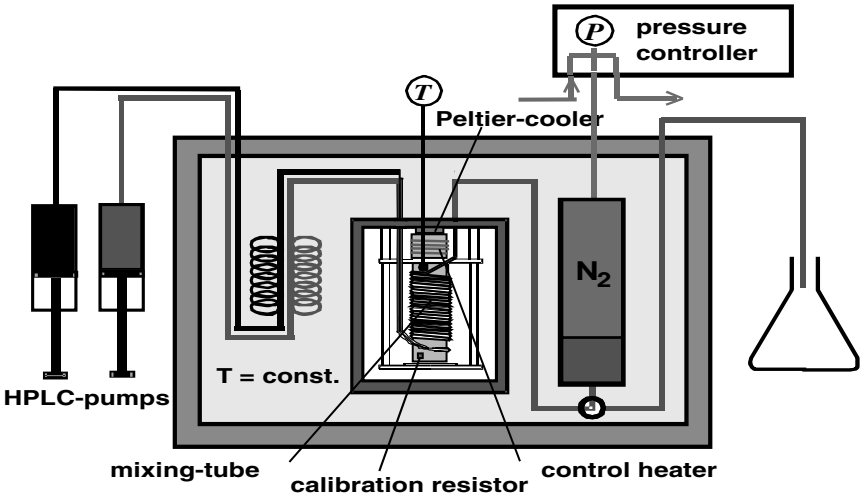

Fig.3. Isothermal flow calorimeter with pneumatic nitrogen backpressure control.

2.3. Results

The experimental VLE data are listed in Tables 2 to 14 and shown graphically in Fig. 4 to 12. The group contribution equation of state PSRK [27] was used to predict the VLE behavior and to compare the predicted with the experimental values. While the continuous lines in Fig. 4 – 10 show the predicted results, the symbols represent the experimental data. Due to the low concentration of the high boiling component in the gas phase, the data for the systems propane + 1-decanol (Fig. 6), ethane + 1-decanol (Fig. 7), ethylene + 1-decanol (Fig. 8), and carbon dioxide + dodecane (Fig. 9) are shown in a logarithmic concentration scale. In case of measurements at temperatures much higher (more than 100 K) than the critical temperature of the supercritical fluid, the solubility change of the high boiling compounds with pressure is not very large, as can be seen from the data for the systems ethane + decane, propane + dodecane, propane + 1-decanol, or ethane + 1-decanol. But at temperatures near the critical temperature (up to ca. 30 K above) of the supercritical fluid, the solubility change with pressure exceeds a factor of 100, what is used in supercritical extraction processes, as can be seen from the data for the systems ethylene + 1-decanol, and carbon dioxide + dodecane.

2.3.1. System ethane + decane

This system was chosen as a test system, since Reamer and Sage [5] published reliable complete VLE data. Our results are in good agreement with the literature data at both temperatures 411 K (Fig. 4) and 444 K (Fig. 5). The system belongs to Type I according to the classification of van Konynenburg and Scott [28]. The PSRK model predicts slightly higher pressures of the

boiling point curve and the critical point and slightly larger solubilities of decane in ethane. Better results are obtained with the VTPR model as discussed later.

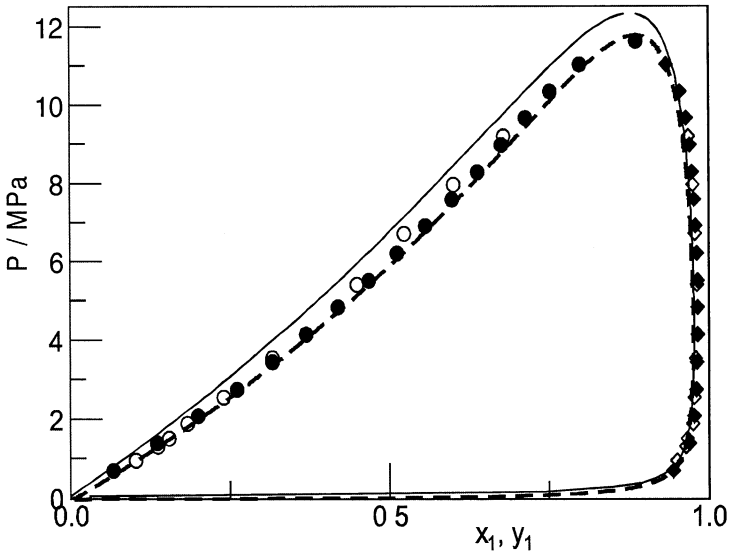

Fig.4. Experimental (this work (o,◊); literature data [5] (•,♦)) and calculated (PSRK (—) VTPR(---))*P-x-y* data for the system ethane (1) + decane (2) at 410.95 K.

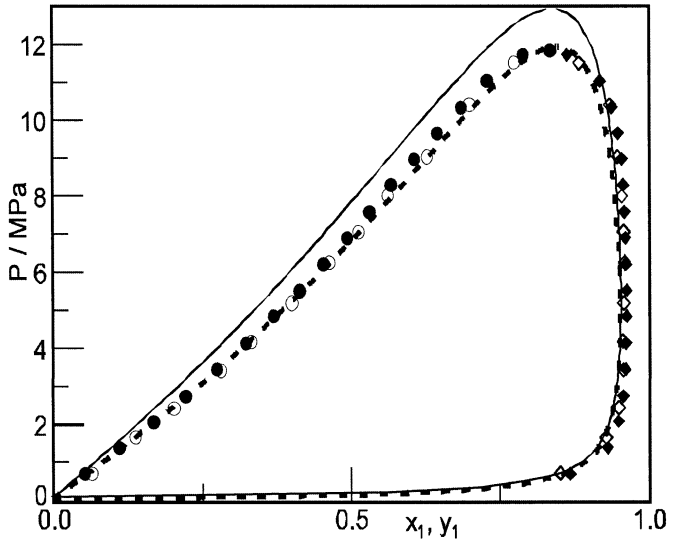

Fig.5. Experimental (this work (o,◊); literature data [5] (•,♦)) and calculated (PSRK (—) VTPR(---))*P-x-y* data for the system ethane (1) + decane (2) at 444.25 K.

2.3.2. System propane + dodecane

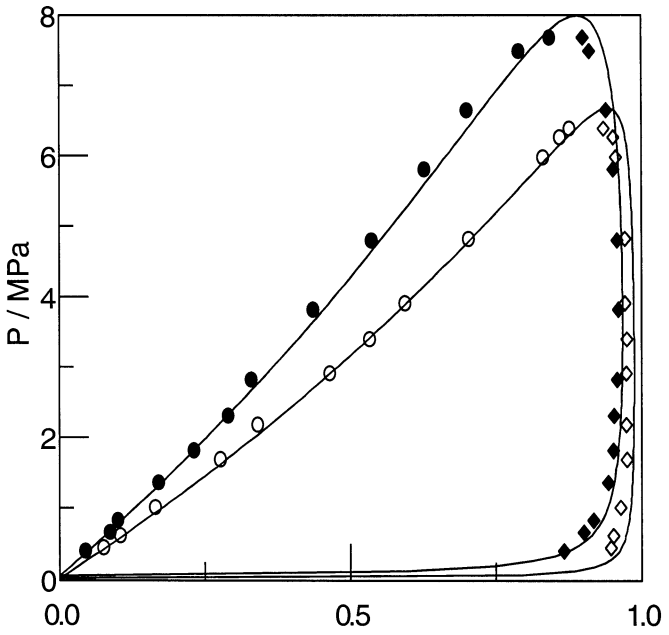

Fig.6. Experimental (this work at 419.15 K (o,◊) and at 457.65 K (•,♦)) and calculated (PSRK (—)) *P-x-y* data for the system propane (1) + dodecane (2).

This system is also of Type I. The predicted results of the PSRK model perfectly agree with the boiling point curve, as can be seen in Fig. 6. But the experimental solubilities of dodecane in propane are larger than the predicted one at both temperatures, 419 and 458 K.

2.3.3. System propane + 1-decanol

Since the solubility of 1-decanol in propane is quite small, the phase diagram is also shown in logarithmic form in Fig. 7. At 408 and 448 K the system seems to be similar to the systems ethane + decane and propane + decane, but in fact it is known [29] that the system is of type III, IV, or V according to the classification of van Konynenburg and Scott. The PSRK model predicts a slightly higher pressure of the boiling point curve and a slightly larger solubility of 1-decanol in propane.

2.3.4. System ethane + 1-decanol

This system also belongs to type III, IV, or V. The corresponding VLLE behavior has been observed experimentally [20-22] between 298 and 303 K. The phase equilibrium behavior is at least predicted qualitatively correct with

PSRK. In Fig. 8 it can be seen that the boiling point curve predicted with PSRK provides lower pressures and larger solubilities of 1-decanol in ethane than observed experimentally.

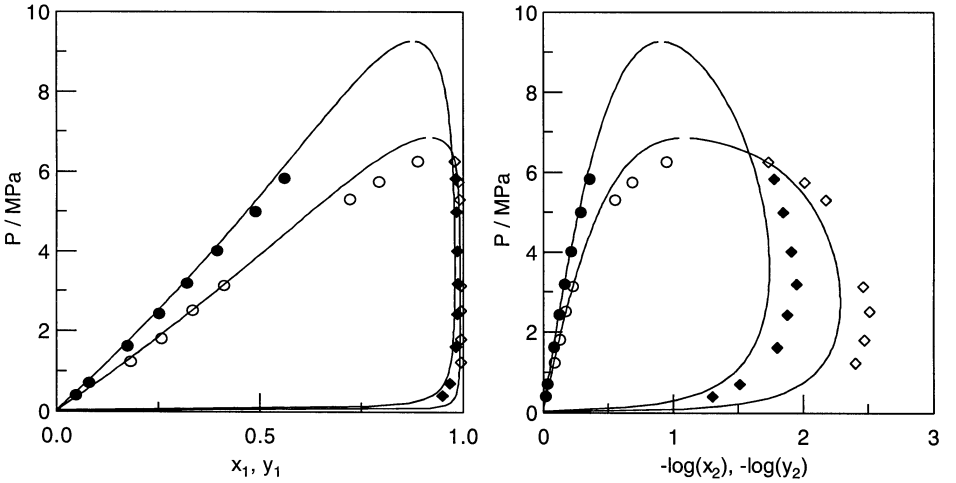

Fig.7. Experimental (this work at 408.15 K (o,◊) and at 448.15 K (•,♦)) and calculated (PSRK (—)) *P-x-y* data for the system propane (1) + 1-decanol (2).

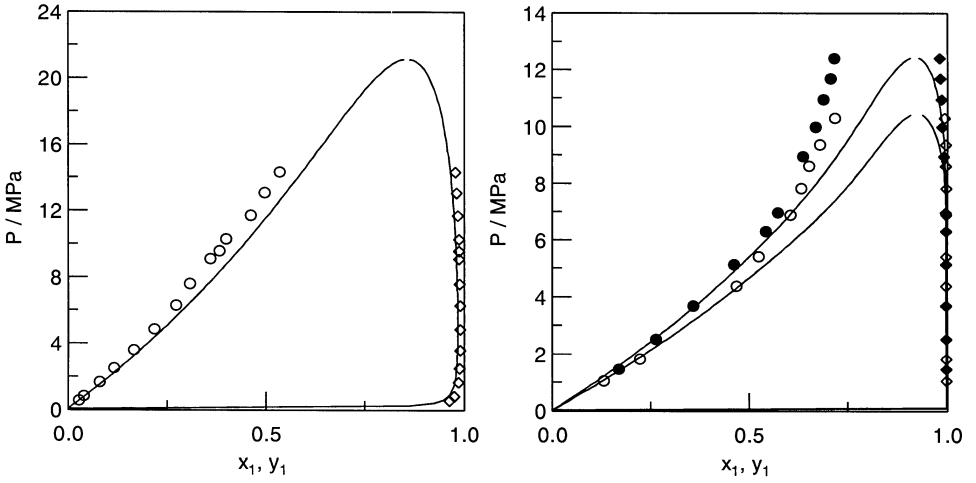

Fig.8. Experimental (this work at 448.15 K (O,◊)) and calculated (PSRK (—)) *P-x-y* data for the system ethane (1) + 1-decanol (2).

Fig.9. Experimental (this work at 308.15 K (o,◊) and at 318.15 K (•,♦)) and calculated (PSRK (—)) *P-x-y* data for the system ethylene (1) + 1-decanol (2).

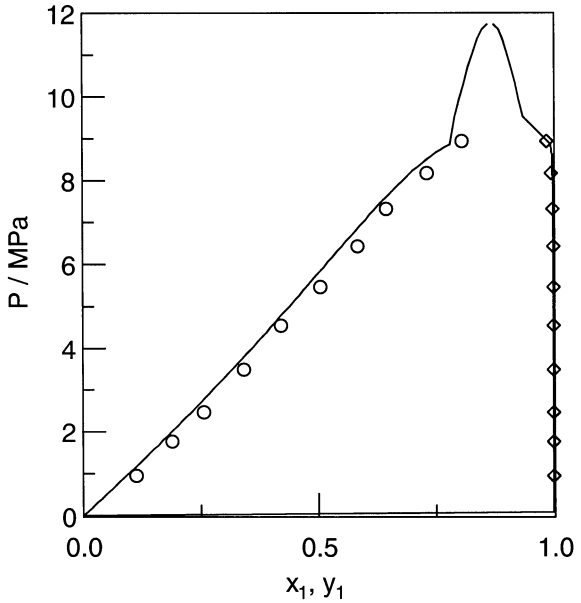

Fig.10. Experimental (this work at 318.15 K (o,◊)) and calculated (PSRK (—)) *P-x-y* data for the system carbon dioxide (1) + dodecane (2).

2.3.5. System ethylene + 1-decanol

The behavior and class of this system is similar to the ethane + 1-decanol system. The prediction of the VLE data at 308 and 318 K shown in Fig. 9 differs from the experimental data especially at high pressure. Probably the critical pressure is very much underestimated.

2.3.6. System carbon dioxide + dodecane

For this system it is not clear until now whether it belongs to type II or III or IV. Schneider discussed the critical behavior for different CO_2 – alkane systems [29]. The predicted results using PSRK are in good agreement with the experimental data measured at 318.15K, as shown in Fig. 10.

2.3.7. System carbon dioxide + 1-decanol

For this system experimental *P-x-y* data have been measured at 322.05 K and 357.25 K. The experimental data are shown in Fig. 12 together with the predicted data using the PSRK model. While the agreement at 357.25 K is quite satisfactory at the lower temperature the predicted solubility of 1-decanol in the supercritical gas phase is about a factor of ten to high.

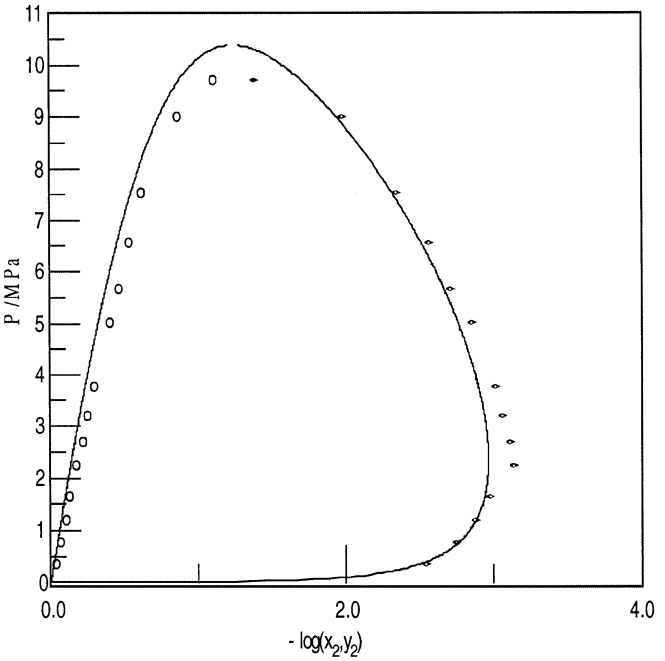

Fig.11. Experimental (this work at 358.55 K (o,◊) and calculated (PSRK (—) *P-x-y* data for the system ethane (1) + dodecane (2).

2.3.8. System ethane + dodecane

For this system experimental *P-x-y* data have been measured at 358.55 K. The experimental data are shown in Fig. 11 together with the predicted data using the PSRK model. As can be seen the agreement between the experimental and calculated data is very good.

The experimental enthalpy data are listed in the Tables 18 to 20 and selected data are shown graphically in Fig. 13 and 14.

2.3.9. System ethylene + 1-decanol

For this system the enthalpy effects at 318.15K three pressures (at 81, 121 and 146 bar) and have been measured. The results are shown graphically in Fig. 13 together with polynomial interpolation of the data. From the intersection of the polynomials in the homogeneous region and a straight line in the two-phase region the composition at the boiling point can be obtained. In Fig. 13 the enthalpy data are shown together with the experimental *P-x* data for this system measured in this project. As can be seen a very good agreement for the boiling point curve is obtained for the two independent methods. Unfortunately the procedure is not accurate enough for the determination of dew point data. Due to the very small solubility of the high boiling component in the vapor phase a determination of these data was not possible by flow calorimetry.

2.3.10. System carbon dioxide + dodecane

For this system seven isobars at 318.15K and pressures between 65 and 140 bar are shown in Fig. 14 together with the predicted data using the PSRK group contribution equation of state. Although these data have not been used to fit the model parameters the pressure dependency of the enthalpy effects is described quite well.

2.3.11. System carbon dioxide + 1-decanol

For this system six isobars at 318.15 K and pressures between 90 and 140 bar have been measured. The data are listed in Table 16.

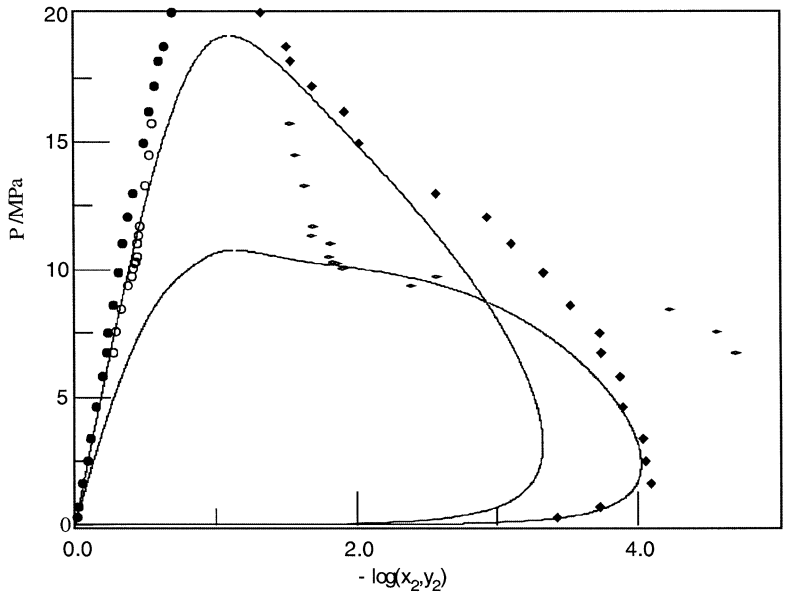

Fig.12. Experimental (this work at 322.05 K (o,◊) and 357.25K(●,◆)) and calculated (PSRK (—)) *P-x-y* data for the system carbon dioxide (1) + 1-decanol (2).

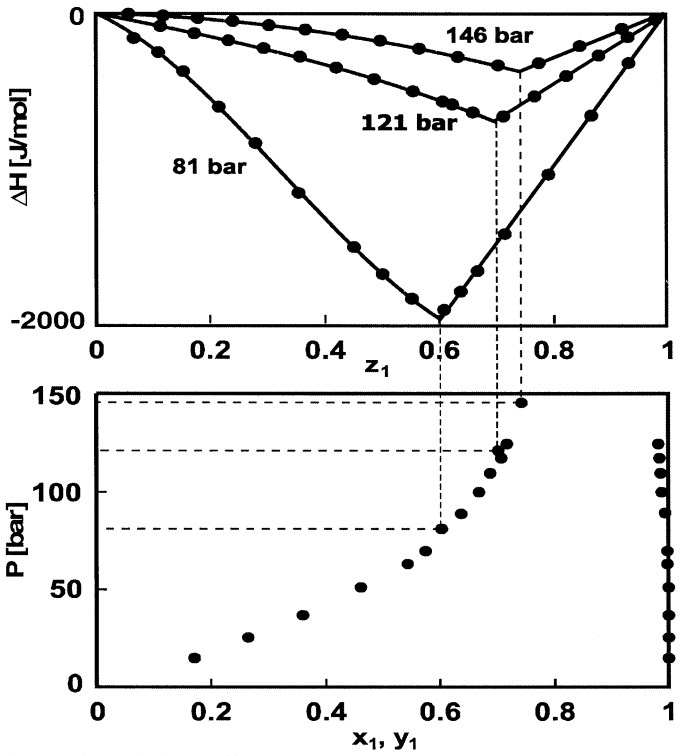

Fig.13. Experimental enthalpy effects and VLE data for the system ethylene (1) + 1-decanol at 318.15 K (●) together with a polynomial fit (—) of the enthalpy data.

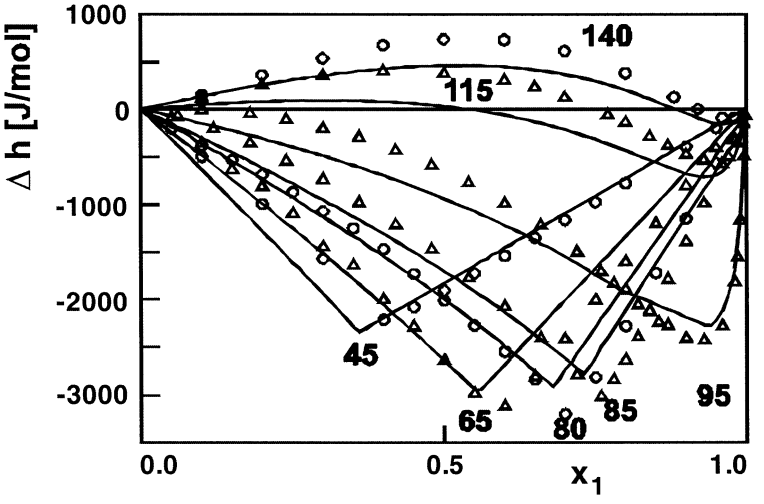

Fig.14. Experimental enthalpy data for the system carbon dioxide (1) + dodecane at 318.15 K (different pressures from 45 to 140 bar) together with data predicted using PSRK (—).

3. MODEL COMPARISON

Most important for the synthesis and design of extraction processes with supercritical fluids is a reliable knowledge of the phase equilibrium behavior, which can be calculated with the help of equations of state (EOS). Of particular importance is a reliable description of the solubility of the high boiling compound in the considered supercritical fluid as function of temperature and pressure. For process development it would be most desirable to use predictive thermodynamic models, e.g. group contribution equations of state, since this would allow to perform predictions for a large variety of process alternatives already during the process design step.

To check the quality of the different group contribution equations of state a comprehensive model comparison was performed.

3.1. Thermodynamic fundamentals

Depending on the state (liquid or solid) of the considered high boiling compound different expressions were used to calculate the phase equilibrium behavior:

$T > T_m$: $$x_i \varphi_i^L = y_i \varphi_i^V \tag{1}$$

$T < T_m$: $$f_2^{os} = P_2^s \exp \frac{v_2^s \left(P - P_2^s\right)}{RT} = y_2 \varphi_2^V P \tag{2}$$

In both cases a reliable description of the vapor pressure of the high boiling liquid resp. solid is of particular importance. While in the first case the vapor pressure is taken into account by the α-function used, in the second case the vapor pressure of the solid is required. Additionally for the calculation of the Poynting-factor the molar volume of the solid has to be known. In most cases the vapor pressure at the chosen temperatures are quite small and special techniques are required for the measurement. But the vapor pressure of the solid phase can also be derived from the values of the liquid using the following simplified equation, which can be derived by a thermodynamic cycle (Gmehling, and Kolbe 1992) [30]:

$$\ln P_2^s(solid) \approx \ln P_2^s(liquid) - \frac{\Delta h_{m,2}}{RT}\left(1 - \frac{T}{T_m}\right) \tag{3}$$

This means that similar to the solubility of solids in liquid solvents the standard fugacity (vapor pressure) has a great influence on the solubility of the

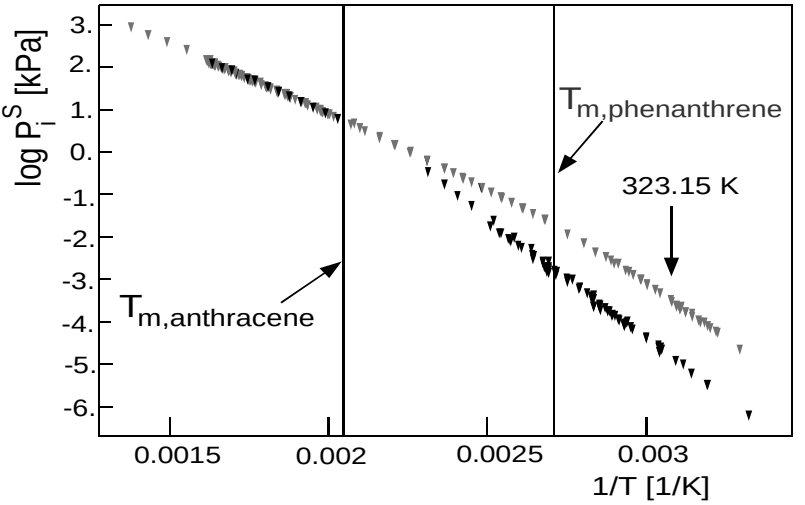

Fig. 15. Vapor pressure of anthracene and phenanthrene as function of the inverse temperature.

high boiling compound in the supercritical fluid, so that even similar chemical compounds can show very different solubilities in the supercritical fluid.

In Fig. 15 the vapor pressures of anthracene and phenanthrene are shown as function of the inverse temperature. As can be seen because of the different melting points T_m and heats of fusion Δh_m for these similar compounds, at around 50 °C the vapor pressure (standard fugacity) of phenanthrene is appr. 20 times larger than the values for anthracene. Following Eq. (2) this of course will directly influence the solubility in the supercritical fluid as can be seen in Fig 28.

Additionally the standard fugacity is influenced by the Poynting-factor which only depends on the molar volume of the solid and the pressure difference $P - P_2^s$, whereby it is assumed that the molar volume v_2 is constant in the whole pressure range covered, whereby it has to be mentioned that already the accuracy of the densities published for solid organic compounds at atmospheric pressure are often questionable.

Qualitatively the contributions of the Poynting-factor and the fugacity coefficient in the vapor phase φ_2^V on the solubility of phenanthrene in carbon dioxide are shown in Fig. 16. While the Poynting-factor increases the solubility by a factor of approximately 20 at around 400 bar, the main influence is caused by the reality in the vapor phase, i.e. φ_2^V.

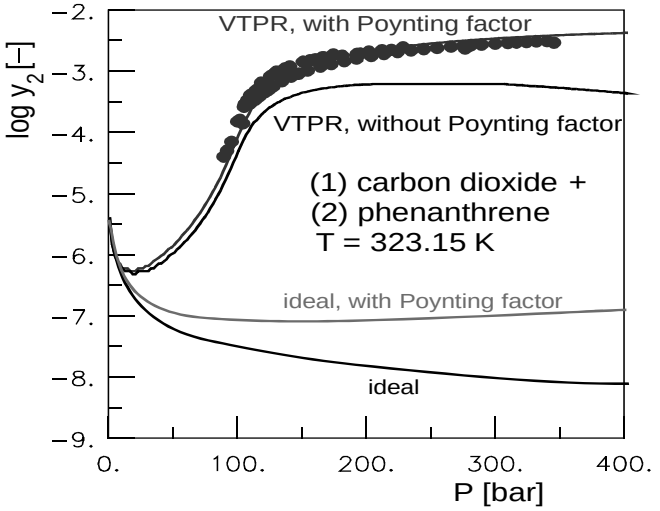

Fig. 16. Contribution of the different parts of equation 2 to the solubility of solid phenanthrene in carbon dioxide at 323.15 K.

3.2. Data base and equations of state used for the model comparison

For the model comparison the relative and absolute deviations between experimental and calculated vapor phase compositions of the high boiling compound (2) were evaluated according to Eq. (4) and (5).

$$\Delta y_2 = y_{2,calc} - y_{2,exp} \tag{4}$$

$$\Delta y_{2,rel} = \Delta y_2 / y_{2,exp} \quad \text{when} \quad \Delta y_2 \text{ is positive} \tag{5a}$$

$$\Delta y_{2,rel} = \Delta y_2 / y_{2,calc} \quad \text{when} \quad \Delta y_2 \text{ is negative} \tag{5b}$$

The use of Eq. (5a) and (5b) for the relative deviations provides a more consistent way to take into account positive and negative deviations, e.g. for $y_{2,exp} = 0.01$ a calculated value of $y_{2,calc} = 0.02$ or $y_{2,calc} = 0.005$ in both cases lead to a relative deviation of 100 %.

For the model comparison the vapor-liquid equilibria of low boiling substances stored in the Dortmund Data Bank (20 700 isotherms or isobars) were used. But only binary isothermal data sets were considered for which the following three conditions were fulfilled:

- The reduced temperature of the supercritical fluid is lower than 1.2.
- The reduced temperature of the subcritical component is above 0.4.
- Experimental vapor phase composition data are available.

Furthermore, it had to be checked by the melting temperature, if Eq. (1) or (2) had to applied for the prediction. The first two conditions were selected to ensure that the selected experimental data fulfill the conditions, which are representative for extraction processes with supercritical fluids. The solubility data in the vapor phase are required to judge the quality of the solubility prediction. Because of their importance for supercritical extraction, systems with CO_2, C_2H_4, C_2H_6 were studied in more detail. For these gases and liquid high boilers more than 1000 data sets have been considered for the model comparison.

The group contribution equations of state used for the model comparison were built from the following equations of state, alpha functions, mixing rules for the parameters a and b of the EOS.

The following EOS types were used:

Soave-Redlich-Kwong [31, 32]:

$$P = \frac{RT}{v-b} - \frac{a(T)}{v(v+b)} \tag{6}$$

Peng-Robinson [32]:

$$P = \frac{RT}{v-b} - \frac{a(T)}{v(v+b)+b(v-b)} \tag{7}$$

Volume translated Peng-Robinson[34-36]:

$$P = \frac{RT}{v+c-b} - \frac{a(T)}{(v+c)(v+c+b)+b(v+c-b)} \tag{8}$$

In combination with the following alpha functions:

Mathias-Copeman [37]

$$\alpha(T) = (1+m\cdot\sqrt{T_r}))^2 \qquad \text{with} \tag{9}$$

$$m = c_1 + c_2\cdot(1-\sqrt{T_r}) + c_3\cdot(1-\sqrt{T_r})^2 \tag{10}$$

Melham, Saini and Goodwin [38]

$$\alpha(T) = \exp\left(c_1 \left(1 - \sqrt{T_r}\right) \cdot c_2 \left(1 - \sqrt{T_r}\right)^2 \right) \tag{11}$$

Twu-Bluck-Cunningham-Coon [39]

$$\alpha(T) = T_r^{c_3 \cdot (c_2 - 1)} \cdot \exp\left(c_1 - \left(1 - T_r^{c_2 \cdot c_3}\right)\right) \tag{12}$$

As mixing rules for the parameter b besides the classical linear mixing rule Eq. (13) the mixing rule proposed by Chen [40] Eq. (14) where used.

$$b = \sum_i x_i \cdot b_i \tag{13}$$

$$b = \sum_i x_i \cdot x_j \cdot b_{ij} \quad \text{with} \quad b_{ij}^{3/4} = \left(b_i^{3/4} + b_j^{3/4}\right)/2 \tag{14}$$

For the attractive parameter a the following g^E-mixing rules were considered:
PSRK [41]:

$$\frac{a}{bRT} = \sum_i x_i \cdot \frac{a_{ii}}{b_i RT} + \frac{1}{A}\left(\frac{g^E}{RT} + \sum_i x_i \ln \frac{b}{b_i} \right) \quad \text{with } A = -0.64663 \tag{15}$$

Chen [40]:

$$\frac{a}{b} = \sum_i x_i \cdot \frac{a_{ii}}{b_i} + \frac{g^{E,residual}}{A} \qquad \text{with } A = -0.53087 \tag{16}$$

For each combination first the required parameters for the alpha function were fitted for the 145 compounds considered to describe the vapor pressures in the temperature range from T_r = 0.4 to T_r = 1 with the required accuracy, whereby "quasi-experimental" vapor pressures calculated using DIPPR parameters were used.

Since for most combinations, with the exception of the PSRK model the required group interaction parameters are not available for the different model combinations the groups and group interaction parameters from the original PSRK model had to be used. This means that for all models except for original PSRK the results can be further improved.

3.3. Results

For all data sets of the selected data base the vapor-liquid equilibrium behavior was calculated using the different group contribution equation of state and for each data point the difference between calculated and experimental solubility $y_{2,calc}$ was determined using Eq. (4). Depending on the results the relative deviations were calculated using Eq. (5a) resp. Eq. (5b).

Then the relative deviations were averaged over the whole database for each combination used, whereby relative mean deviations around ca. 400% were obtained. Because of the high deviations obtained a careful graphical examination of all data sets were performed. As a result of the examination in total 46 data sets with questionable data sets, data sets with very scattering data and data sets with constant vapor phase mole fraction (often the lowest detectable concentration) were excluded.

The results for the remaining data base (in total 960 data sets with 7300 data points) are summarized in Fig. 17. As can be seen for the various group contribution equations of state still deviations between 80 and 120 % are obtained.

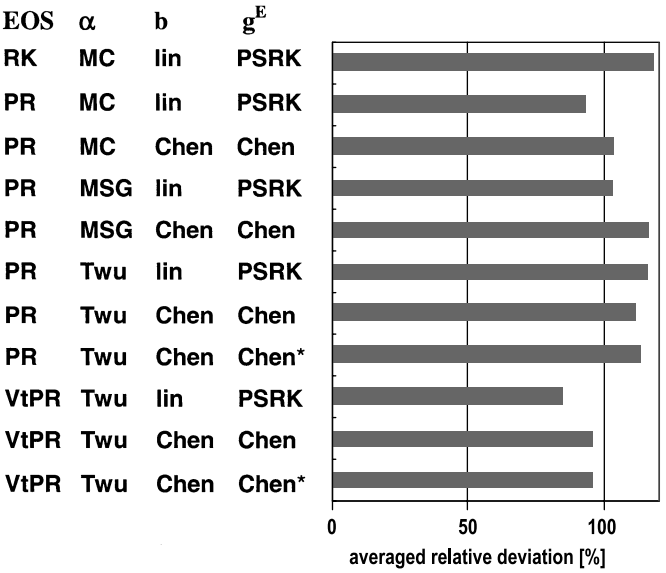

Fig 17. Averaged relative deviations for different combinations of group contribution EOS
EOS-Type: **PR**: Peng Robinson, **VtPT**: volume translated Peng Robinson
α-Function: **MC**: Mathias Copeman, **MSG**: Melham Saini Goodwin, **Twu**: Twu Bluck Cunningham Coon;
g^E-Mixing rule: **PSRK**: PSRK mixing rule, **Chen**: mixing rule proposed by Chen
b-mixing rule: **lin**: linear mixing rule, **Chen**: mixing rule proposed by Chen
*: modified g^E-parameter matrix used (single parameters optimized).

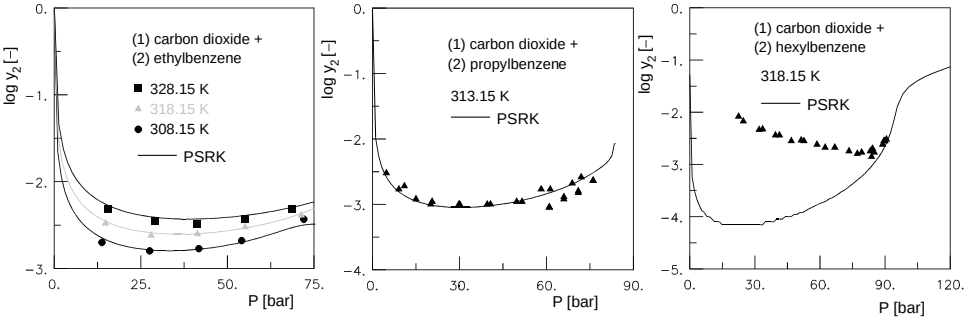

Fig. 18. Comparison of the predicted and experimental results for CO_2-alkylbenzene systems. CO_2-ethylbenzene [43], CO_2-propylbenzene [44],[45], CO_2-hexylbenzene [42].

The relatively high deviations for the whole resp. reduced data base are mainly caused by the poor quality of the experimental solubility data for the high boiling component and not by the model used. This is demonstrated in Fig. 18 – 20. In Fig. 18 the experimental and predicted results for the PSRK model are shown for alkylbenzenes with carbon dioxide in the temperature range from 308 – 328 K. While very good agreement is observed for the systems with ethylbenzene and propylbenzene, the predictions are in total disagreement with the experimental findings for the system with hexylbenzene (up to 12000 % relative deviation following Eq. (5b)). From these results it has to be concluded that the experimental data reported by Lansangan [42] must be wrong, since the results with the other alkylbenzenes are satisfying.

In Fig. 19 experimental and predicted solubilities of hexadecane in carbon dioxide in the temperature range from 308 to 333 K are given. While good agreement for the different temperatures is achieved with the experimental data of three authors, very poor agreement is observed with the data from the Kobayashi group. Depending on the temperature these data sets show averaged relative deviations from 3000 % to 27000% on the left side and between 60% to 450 % on the right side.

As a further example in Fig. 20 the experimental data of different authors for the system CO_2-1-octanol at 313 K are shown together with the predicted results using the PSRK model. As can be seen satisfying agreement is observed. But nevertheless the relative deviations for this system are approximately 100%. In particular the poor experimental data of Scheidgen [50] are responsible for the large relative deviation obtained. Without this data set the mean relative deviation would be reduced dramatically. All these examples (Fig. 18 – 20) undoubtedly indicate that the high relative deviations obtained with the various group contribution equations of state are mainly caused by experimental uncertainties of the small solubilities of the high boiling compound investigated.

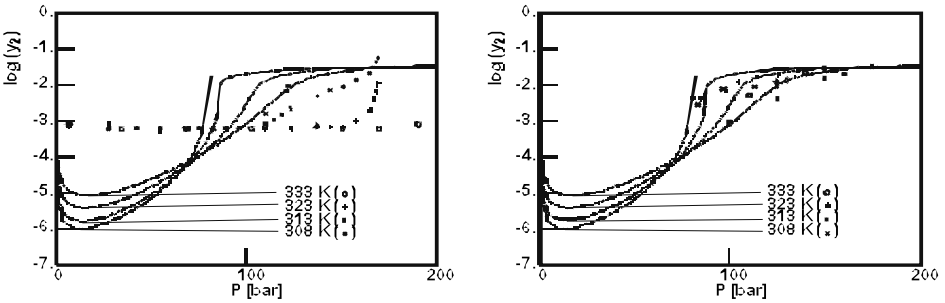

Fig. 19. Experimental data and PSRK predictions (—) for the system carbon dioxide with hexadecane at different temperatures (left side: all experimental data from Charoensombut-Amon T., Martin R. J., Kobayashi R. [46], right side: (+) D'Souza, Patrick J. R., Teja A. S.: [47], (o),( ) De Haan A.B. [48], (×) Eustaquio-Rincon R., Trejo A.[49].

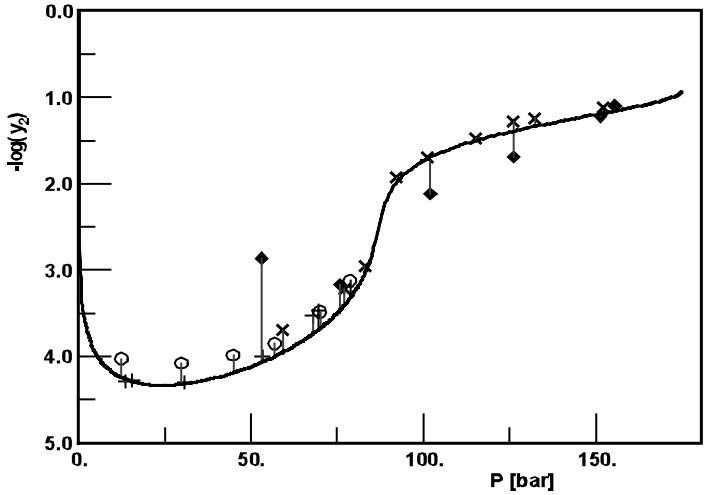

Fig. 20. Experimental and predicted (PSRK) mole fraction y_2 in the vapor phase as function of pressure for the system carbon dioxide(1)-1-octanol(2) at 313.0 K, (♦) Scheidgen [50], (+) Schlichting [51], (o) Gregorowicz et al. [52],(×) Chrisochoou et al. [53].

In Fig. 21 as an additional example the experimental and predicted data (PSRK) for the system CO_2-benzene at 313 K are shown. On the first glance the predicted results in form of an isothermal $P,x(y)$-diagram seems to be in excellent agreement with the experimental data measured by three different groups. But when the vapor phase composition is shown in logarithmic form, the scatter of the experimental data measured by different authors become obvious. Although the prediction seems to be perfect the relative mean deviation to the experimental data is still approximately 15%

A more detailed evaluation of the results as function of the molecular weight of the high boiling component e.g. for the PSRK model showed that the relative deviations increase with increasing molecular weight. The results are

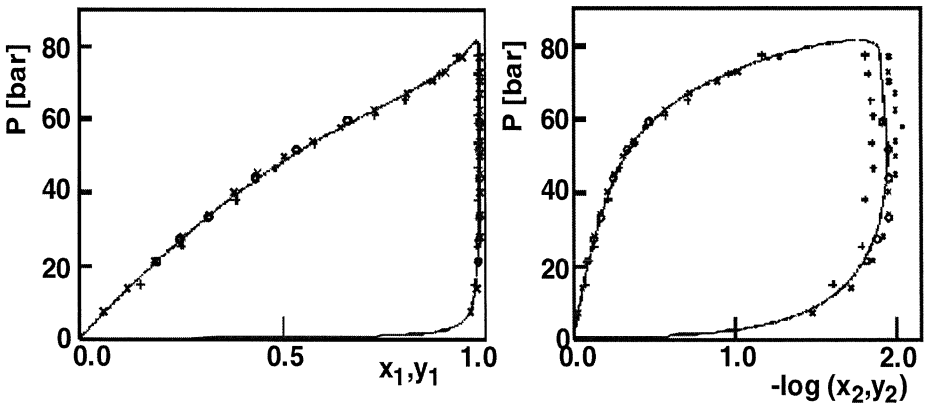

Fig. 21. Experimental and predicted (PSRK) mole fraction y_2 in the vapor phase as function of pressure for the system carbon dioxide(1)-benzene(2) at 313.0 K, + Ohgaki and Katayama [54], × Gupta et al. [55], o Kim et al. [56].

not surprising, since it is well known that the various group contribution equations of state show problems for strong asymmetric systems. But in the meantime these problems were solved with the help of an empirical modification, resp. improved mixing rules [34].

For the systems ethane + octacosane at 300 °C and for the system ethylene + diphenylmethane at 65°C the results for PSRK and VTPR are shown in Fig. 22 and Fig. 23. It can be seen that essential improvements in the description of the vapor phase composition can be achieved with the volume translated Peng-Robinson equation of state [33] together with the alpha function proposed by Twu, Bluck, Coon and Cunningham. Similar improvements are e.g. also obtained for the system ethane-decane measured in our laboratory, as shown already in Fig. 4 and 5.

The high relative deviations obtained for a large data base may indicate, that a group contribution equation of state can not be applied successfully to predict the solubility of a high boiling substance in the supercritical fluids. However, to a great part the high relative deviations are caused by the poor quality of the published solubility data. As already shown in Fig. 18-23 for reliable experimental data in most cases satisfying agreement is obtained with the predicted results using group contribution equations of state.

This means that already the existing group contribution equations of state are suitable tools for the selection of the most suitable supercritical fluid and operating conditions for extraction processes with supercritical fluids. With the development of improved mixing rules the results can still be improved. In the next Figures satisfying results for different systems are presented. Fig. 24 shows e.g. that the influence of different gases (CO_2, ethylene, ethane) on the vapor-liquid equilibrium behavior of n-heptane is described correctly.

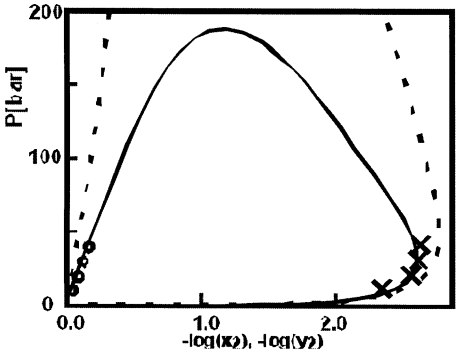

Fig. 22. Experimental and predicted vapor-liquid equilibrium for the system ethane + octacosane at 573 K; o,×: exp. data,(—)VTPR,(--)PSRK.

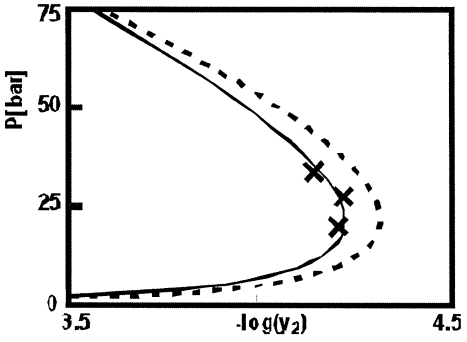

Fig.23. Experimental and predicted vapor-liquid equilibrium for the system ethylene + diphenylmethane at 338 K ×: exp. data, (—) VTPR, (--) PSRK

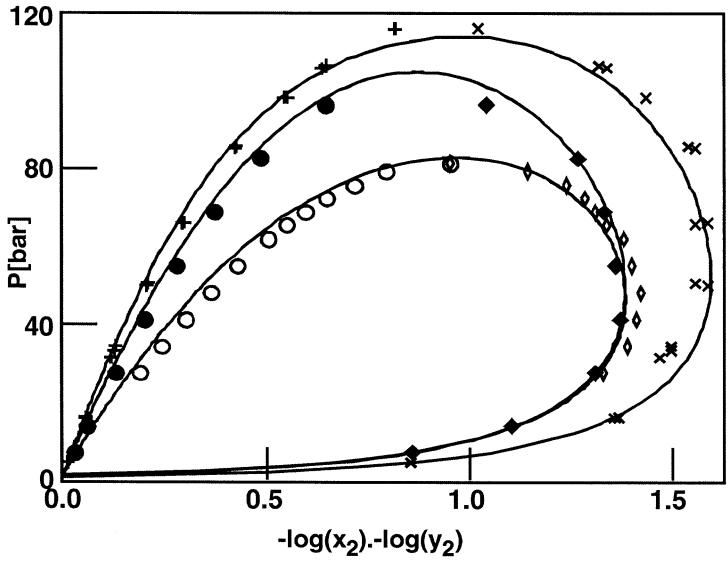

Fig. 24. Vapor-liquid equilibria of n-heptane (2) in carbon dioxide (+,×) at 352.59 K; in ethylene (●,◆) at 366.48 K and in ethane (○,◇) at 366.48 K, (—)VTPR.

In Fig. 25 typical VTPR results are shown for the system CO_2-Diphenylmethane. As can be seen nearly perfect agreement is obtained.

In Fig. 26 - 28 the solubilities of different high boiling components (naphthalene, phenanthrene, anthracene) in CO_2 respectively ethylene are shown. Since these are solid compounds, Eq. (2) was used for the prediction, whereby

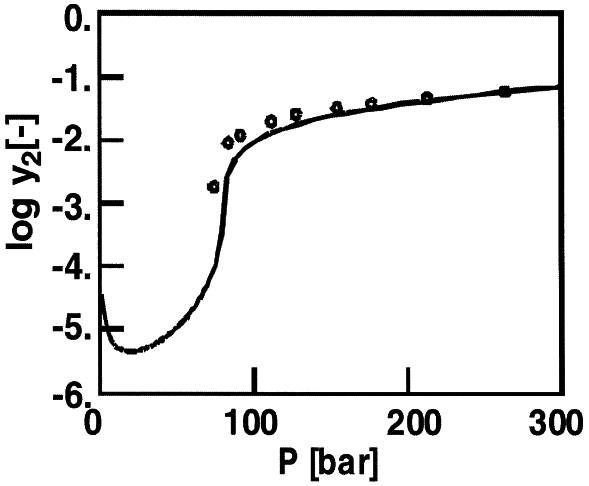

Fig. 25. Experimental and predicted results of VTPR for the system CO_2-diphenylmethane at 308.15 K.

the fugacity coefficients in the vapor phase were either calculated using the VTPR or the PSRK equation of state. As can be seen in all cases very good agreement between the predicted and experimental data is achieved. Even the well known positive effect of the co-solvent methanol on the solubility of naphthalene in carbon dioxide (see Fig. 27) is predicted. Unfortunately this effect is only mentioned qualitatively in literature, so that a quantitative comparison is not possible.

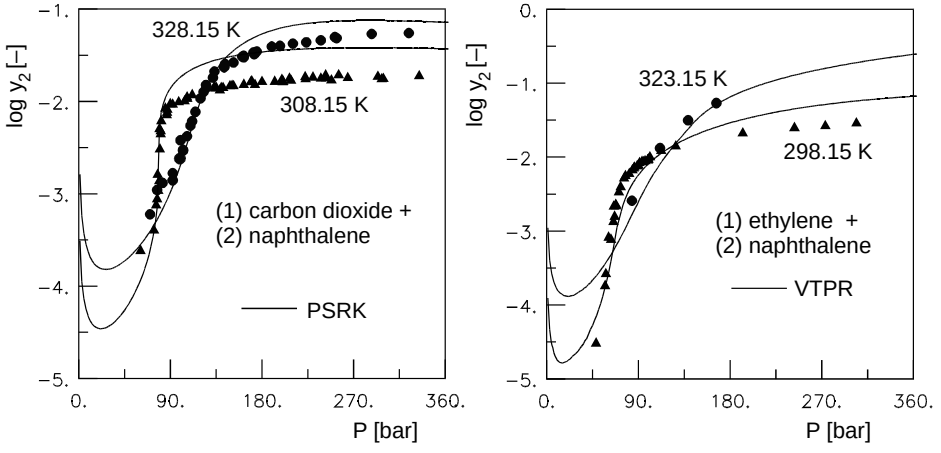

Fig. 26. Experimental and predicted solubilities of solid naphthalene in supercritical carbon dioxide and ethylene, respectively.

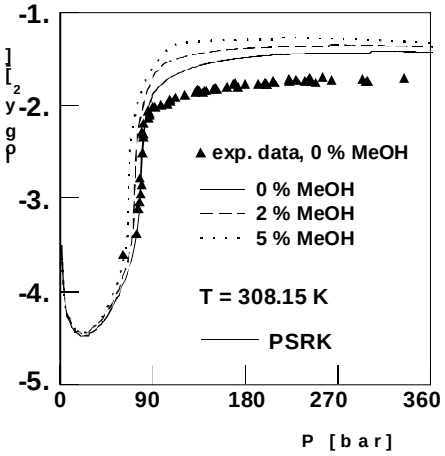

Fig. 27. Predicted Influence of the Co-Solvent methanol (0 – 5 Mol%) on the solubility of naphthalene in carbon dioxide at 308.15 K.

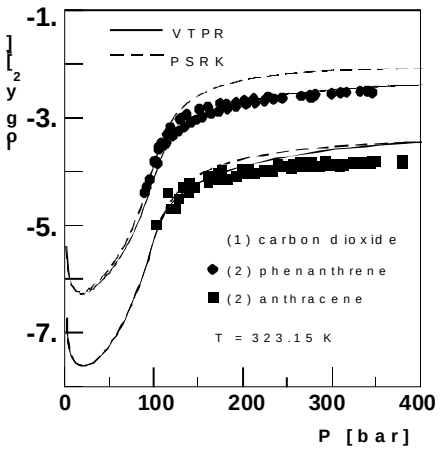

Fig. 28. Experimental and predicted solubility (PSRK, VTPT) of phenantrene and anthracene in carbon dioxide at 323.15 K.

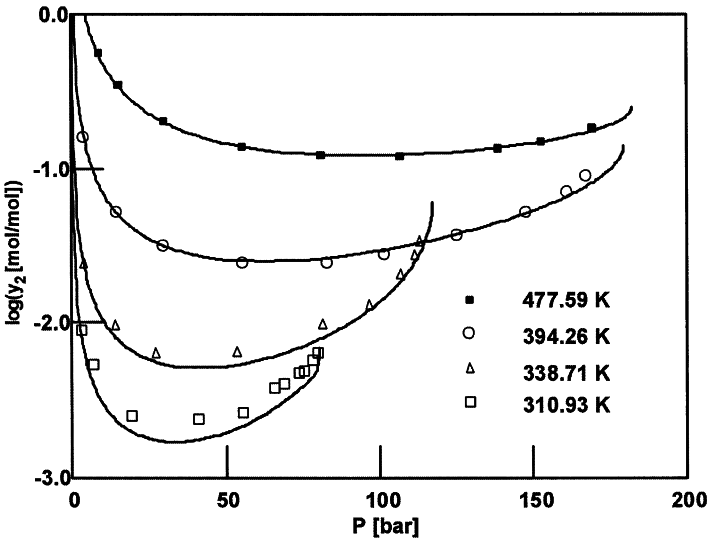

Fig. 29. Experimental and predicted solubility (VTPR) of m-xylene in carbon dioxide in the temperature range between 310 – 477 K.

Rainwater [57] studied already 1991 the quality of high-pressure VLE data. At the end he recommended 129 binary systems. Unfortunately he investigated systems like CO-methane, CO_2-H_2S, etc. and did not concentrate on VLE data of interest for supercritical extraction. But one of the recommended systems is m-xylene-CO_2. Therefore also this system was

investigated. Not only with the PSRK but also the VTPR a very agreement with the experimental finding was obtained as shown in Fig. 29 for VTPR.

4. CONCLUSION

A static analytical apparatus for the measurement of high pressure VLE data of asymmetric systems was developed and it was shown that the new equipment equipped with a micro-sampler can be applied for the reliable determination of the solubility of the high boiling compound in the supercritical fluid in a wide temperature and pressure range. In total fourteen isothermal complete VLE data sets were measured for eight different binary systems. The results of the test system ethane + decane are in agreement with published data.

In addition an isothermal flow calorimeter with reliable pressure control was applied to measure the enthalpy effects at different pressures. The enthalpy data allowed to determine the bubble point lines for asymmetric systems and are in agreement with the VLE data measured. All new experimental data were compared with the results predicted with the PSRK group contribution equation of state.

With the help of the high pressure VLE data stored in the Dortmund Data Bank a comprehensive model comparison was performed for given conditions ($T_{r,\,SCF} < 1.2$, $T_{r,2} > 0.4$). Although the relative deviations obtained for the different group contribution equations of state is relatively high, the main part of the deviations is caused by the questionable solubilities of the high boiling compound reported by different research groups. With the PSRK and the VTPR EOS a method is available where the influence of different supercritical fluids on the solubility of different high boiling components is described satisfactory. Also the influence of co-solvents on the solubility is described at least qualitatively.

This means, that group contribution equations of state are suitable thermodynamic models for the synthesis of extraction processes with supercritical fluids. Still existing weaknesses for the very asymmetric systems can be greatly reduced using improved mixing rules. For a comprehensive model comparison it would be helpful to have more reliable solubility data for the different supercritical fluids and high boiling compounds. Perhaps sophisticated experimental techniques (gas stripping or more reliable dew point techniques) can help to provide systematically more reliable solubility data.

5. EXPERIMENTAL RESULTS

Table 1
Suppliers and Purities of the Chemicals

Component	Supplier	Final Purity
Decane	Sigma Aldrich	99.9 %
Dodecane	Sigma Aldrich	99.9 %
1-Decanol	Sigma Aldrich	99.9 %
Carbon Dioxide	A. Lübke KG	99.995
Ethane	Messer Griesheim	99.95
Ethylene	Messer Griesheim	99.95
Propane	Messer Griesheim	99.5

Table 2
Experimental *P-x-y* Data for the System Ethane (1) + Decane (2) at 410.95 K

x_1	y_1	*P*/MPa	x_1	y_1	*P*/MPa
0.1024	0.95079	0.947	0.3166	0.98071	3.543
0.1368	0.96476	1.295	0.4490	0.98240	5.418
0.1547	0.96772	1.497	0.5232	0.97898	6.702
0.1832	0.97605	1.876	0.6008	0.97628	7.960
0.2400	0.97799	2.552	0.6795	0.96964	9.175

Table 3
Experimental *P-x-y* Data for the System Ethane (1) + Decane (2) at 444.25 K

x_1	y_1	*P*/MPa	x_1	y_1	*P*/MPa
0.0649	0.85098	0.704	0.4636	0.95929	6.254
0.1382	0.92902	1.663	0.5127	0.95855	7.069
0.2018	0.94987	2.434	0.5619	0.95544	7.988
0.2807	0.95736	3.432	0.6273	0.94894	9.020
0.3313	0.95592	4.180	0.6989	0.93477	10.388
0.3998	0.95798	5.195	0.7744	0.88402	11.498

Table 4
Experimental *P-x-y* Data for the System Propane (1) + Dodecane (2) at 419.15 K

x_1	y_1	*P*/MPa	x_1	y_1	*P*/MPa
0.0755	0.94865	0.453	0.5334	0.97598	3.397
0.1048	0.95308	0.622	0.5938	0.97276	3.907
0.1642	0.96513	1.011	0.7033	0.97255	4.820
0.2766	0.97601	1.694	0.8322	0.95778	5.975
0.3403	0.97512	2.185	0.8609	0.95338	6.255

Table 5
Experimental *P-x-y* Data for the System Propane (1) + Dodecane (2) at 457.65 K

x_1	y_1	*P*/MPa	x_1	y_1	*P*/MPa
0.0451	0.86820	0.406	0.4361	0.96134	3.813
0.0872	0.90189	0.663	0.5363	0.95919	4.792
0.0999	0.91889	0.830	0.6278	0.95279	5.799
0.1698	0.94423	1.367	0.7008	0.94045	6.640
0.2306	0.95299	1.825	0.7899	0.91217	7.487
0.2901	0.95408	2.309	0.8436	0.90126	7.682
0.3293	0.96007	2.815			

Table 6
Experimental *P-x-y* Data for the System Propane (1) + 1-Decanol (2) at 408.15 K

x_1	y_1	*P*/MPa	x_1	y_1	*P*/MPa
0.1817	0.99607	1.223	0.7220	0.99336	5.295
0.2573	0.99662	1.800	0.7943	0.99027	5.735
0.3345	0.99695	2.502	0.8889	0.98141	6.251
0.4118	0.99655	3.124			

Table 7
Experimental *P-x-y* Data for the System Propane (1) + 1-Decanol (2) at 448.15 K

x_1	y_1	*P*/MPa	x_1	y_1	*P*/MPa
0.0475	0.95012	0.395	0.3209	0.98885	3.180
0.0797	0.96945	0.698	0.3950	0.98767	4.013
0.1738	0.98415	1.613	0.4895	0.98571	4.989
0.2520	0.98673	2.423	0.5615	0.98330	5.819

Table 8
Experimental *P-x-y* Data for the System Ethane (1) + 1-Decanol (2) at 448.15 K

x_1	y_1	*P*/MPa	x_1	y_1	*P*/MPa
0.0275	0.96483	0.538	0.3077	0.99081	7.565
0.0406	0.97584	0.810	0.3595	0.98892	9.056
0.0803	0.98671	1.658	0.3828	0.98908	9.556
0.1166	0.99023	2.506	0.3992	0.98816	10.250
0.1660	0.99173	3.589	0.4615	0.98584	11.700
0.2185	0.99216	4.844	0.4963	0.98267	13.050
0.2731	0.99230	6.284	0.5350	0.98013	14.320

Table 9
Experimental *P-x-y* Data for the System Ethylene (1) + 1-Decanol (2) at 308.15 K

x_1	y_1	*P*/MPa	x_1	y_1	*P*/MPa
0.1309	0.99998	1.035	0.6319	0.99927	7.808
0.2233	0.99999	1.818	0.6522	0.99830	8.615
0.4682	0.99998	4.388	0.6790	0.99789	9.358
0.5241	0.99988	5.410	0.7173	0.99525	10.306
0.6045	0.99958	6.872			

Table 10
Experimental *P-x-y* Data for the System Ethylene (1) + 1-Decanol (2) at 318.15 K

x_1	y_1	*P*/MPa	x_1	y_1	*P*/MPa
0.1702	0.99999	1.465	0.6372	0.99366	8.944
0.2637	0.99999	2.520	0.6686	0.98875	9.972
0.3585	0.99998	3.690	0.6884	0.98684	10.960
0.4617	0.99980	5.130	0.7070	0.98433	11.690
0.5430	0.99861	6.303	0.7160	0.98288	12.400
0.5737	0.99753	6.953			

Table 11
Experimental *P-x-y* Data for the System CO_2 (1) + Dodecane (2) at 318.15 K

x_1	y_1	*P*/MPa	x_1	y_1	*P*/MPa
0.1140	0.99993	0.950	0.5051	0.99983	5.463
0.1902	0.99996	1.767	0.5831	0.99944	6.423
0.2571	0.99996	2.465	0.6453	0.99716	7.305
0.3410	0.99994	3.473	0.7320	0.99490	8.156
0.4208	0.99991	4.528	0.8052	0.98512	8.935

Table 12
Experimental *P-x-y* Data for the System CO_2 (1) + 1-Decanol (2) at 422.05 K

x_1	y_1	*P*/MPa	x_1	y_1	*P*/MPa
0.4673		6.7260	0.6368	0.984349	10.5045
0.4898		7.5670	0.6441	0.984464	11.0380
0.5295		8.4350	0.6503	0.979142	11.3540
0.5803		9.4093	0.6582	0.979514	11.7200
0.6110		9.7280	0.6830	0.976348	13.3140
0.6166	0.987366	10.0580	0.7034	0.972699	14.5200
0.6246	0.986146	10.2670	0.7191	0.969864	15.7395
0.6337	0.985073	10.3390			

Table 13
Experimental *P-x-y* Data for the System CO_2 (1) + 1-Decanol (2) at 357.25 K

x_1	y_1	*P*/MPa	x_1	y_1	*P*/MPa
0.02566	0.999629	0.3020	0.50847	0.999538	9.9090
0.04949	0.999817	0.6750	0.54706	0.999213	11.0190
0.11112	0.999920	1.6210	0.58500	0.998819	12.0790
0.18565	0.999912	2.5000	0.61606	0.997308	13.0170
0.22431	0.999909	3.4020	0.67944	0.990562	14.9960
0.29035	0.999872	4.6250	0.70561	0.987790	16.2130
0.36201	0.999866	5.8340	0.73164	0.979559	17.1920
0.39979	0.999818	6.7530	0.74825	0.971020	18.1590
0.42147	0.999815	7.5160	0.76674	0.968579	18.7240
0.46025	0.999698	8.5960	0.79612	0.953079	20.1200

Table 14
Experimental *P-x-y* Data for the System Ethylene (1) + Dodecane (2) at 358.55 K

x_1	y_1	*P*/MPa	x_1	y_1	*P*/MPa
0.0709	0.997158	0.3669	0.4899	0.999039	3.7620
0.1398	0.998220	0.7710	0.6031	0.998603	5.0160
0.2056	0.998685	1.2090	0.6554	0.998055	5.6830
0.256	0.998957	1.6420	0.7037	0.997277	6.5790
0.3264	0.999278	2.2480	0.7572	0.99548	7.5470
0.3925	0.999242	2.6900	0.8616	0.989398	8.9970
0.4324	0.999131	3.2175	0.9215	0.958409	9.7170

Table 15
Experimental Enthalpy Data for the System Carbon Dioxide (1) + Dodecane (2) at 318.15 K

x_1	*Δh[J/mol]*	x_1	*Δh[J/mol]*	x_1	*Δh[J/mol]*
40 bar					
0.0999	-465.2	0.4998	-1774.4	0.7498	-908.2
0.1999	-924.9	0.5498	-1605.1	0.7999	-723.0
0.2998	-1462.7	0.5998	-1433.0	0.8999	-363.8
0.3998	-2060.1	0.6498	-1258.0	0.95	-183.3
0.4498	-1935.4	0.6998	-1083.1		
65 bar					
0.05	-80.0	0.3498	-1526.0	0.6498	-2614.7
0.0999	-335.0	0.3998	-1868.4	0.7498	-1873.1
0.1499	-595.5	0.4498	-2129.0	0.7999	-1497.2
0.1999	-759.3	0.4998	-2455.6	0.8499	-1121.2
0.2498	-1021.7	0.5498	-2777.5	0.8999	-749.0
0.2998	-1348.3	0.5998	-2898.5	0.95	-376.8

Table 15 (continued)
Experimental Enthalpy Data for the System Carbon Dioxide(1) + Dodecane (2) at 318.15 K

x_1	Δh[J/mol]	x_1	Δh[J/mol]	x_1	Δh[J/mol]
80 bar					
0.05	-186.1	0.3998	-1369.7	0.6998	-2974.8
0.0999	-352.7	0.4498	-1610.7	0.7498	-2616.5
0.1499	-495.0	0.4998	-1872.2	0.7999	-2121.5
0.1999	-640.2	0.5498	-2114.1	0.8499	-1600.4
0.2498	-809.5	0.5998	-2367.2	0.8999	-1068.2
0.2998	-996.6	0.6498	-2637.0	0.95	-529.5
85 bar					
0.06	-69.8	0.5398	-1652.6	0.8399	-1978.2
0.1199	-191.7	0.5998	-1933.6	0.8699	-1664.7
0.1799	-332.2	0.6598	-2239.7	0.8999	-1299.9
0.2399	-509.9	0.7198	-2596.1	0.9299	-922.1
0.2998	-691.4	0.7599	-2808.2	0.96	-543.4
0.3598	-913.7	0.7799	-2646.3	0.98	-299.6
0.4198	-1129.6	0.7999	-2449.1		
0.4798	-1373.4	0.8199	-2229.5		
90 bar					
0.05	-35.4	0.4498	-914.7	0.8499	-2422.1
0.0999	-110.7	0.4998	-1093.3	0.8599	-2323.4
0.1499	-190.8	0.5498	-1287.8	0.8999	-1775.4
0.1999	-271.7	0.5998	-1491.6	0.94	-1187.3
0.2498	-383.4	0.6498	-1726.1	0.95	-1022.6
0.2998	-496.0	0.6998	-1975.4	0.96	-879.3
0.3498	-621.6	0.7498	-2249.0	0.98	-568.5
0.3998	-758.4	0.7999	-2526.3		
95 bar					
0.0999	-9.3	0.6598	-1131.5	0.8699	-2117.8
0.2399	-101.4	0.7198	-1398.5	0.8999	-2245.3
0.2998	-189.8	0.7599	-1591.1	0.9299	-2262.0
0.3598	-275.4	0.7799	-1709.3	0.96	-2127.1
0.4198	-406.6	0.7999	-1769.8	0.98	-1700.0
0.4798	-552.7	0.8199	-1915.9	0.985	-1444.1
0.5398	-721.1	0.8399	-1985.7	0.99	-1093.3
105 bar					
0.0999	64.2	0.6998	-219.6	0.995	-260.5
0.1999	153.5	0.7999	-530.4	0.998	-156.3
0.2998	214.9	0.8699	-764.9		
0.3998	219.6	0.9299	-894.2		
0.4998	153.5	0.97	-780.7		

Table 15 (continued)
Experimental Enthalpy Data for the System Carbon Dioxide(1) + Dodecane (2) at 318.15 K

x_1	Δh[J/mol]	x_1	Δh[J/mol]	x_1	Δh[J/mol]
115 bar					
0.0999	106.1	0.6498	213.1	0.8999	-443.8
0.1999	234.5	0.6998	116.3	0.9299	-499.7
0.2998	325.7	0.7699	-56.8	0.97	-461.5
0.3998	374.1	0.7999	-130.3	0.985	-334.0
0.4998	349.9	0.8399	-268.0	0.995	-145.2
0.5998	284.7	0.8699	-353.6	0.998	-62.3
125 bar					
0.0999	123.8	0.5998	501.5	0.95	-259.6
0.1999	314.5	0.6998	361.0	0.97	-246.6
0.2998	428.0	0.7999	118.2	0.99	-135.9
0.3998	522.9	0.8499	-33.5		
0.4998	550.9	0.8999	-181.4		
140 bar					
0.0999	141.4	0.4998	688.6	0.8799	120.0
0.1999	335.9	0.5998	683.9	0.9199	1.9
0.2998	502.5	0.6998	574.1	0.96	-83.7
0.3998	631.8	0.7999	355.4	0.98	-85.6

Table 16
Experimental Enthalpy Data for Carbon Dioxide (1) + 1-Decanol (2) at 318.15 K

x_1	Δh[J/mol]	x_1	Δh[J/mol]	x_1	Δh[J/mol]
90 bar					
0.0701	-112.6	0.4002	-870.9	0.6502	-1339.0
0.1401	-249.4	0.4502	-1005.9	0.7202	-1085.9
0.2101	-369.4	0.5002	-1185.4	0.7901	-827.2
0.2802	-531.3	0.5502	-1403.2	0.8601	-573.2
0.3502	-723.0	0.6002	-1507.4	0.9301	-322.0
100 bar					
0.0701	2.8	0.4002	-134.0	0.6502	-561.1
0.1401	7.4	0.4502	-201.9	0.7202	-541.5
0.2101	-22.3	0.5002	-282.9	0.7901	-518.3
0.2802	-53.0	0.5502	-376.8	0.8601	-499.7
0.3502	-92.1	0.6002	-503.4		
105bar					
0.1452	56.8	0.4606	66.1	0.7286	-252.2
0.2172	87.5	0.5107	17.7	0.7970	-282.9
0.2887	110.7	0.5606	-48.4	0.8651	-322.0
0.3598	107.9	0.6102	-133.1	0.9327	-355.4
0.4103	94.9	0.6597	-221.5		

Table 16 (continued)
Experimen tal Enthalpy Data for Carbon Dioxide (1) + 1- Decanol (2) at 318.15 K

x_1	Δh[J/mol]	x_1	Δh[J/mol]	x_1	Δh[J/mol]
	67.0	0.4606	225.2	0.797	-129.3
0.2172	146.1	0.5606	154.5	0.9327	-256.8
0.2581	183.3	0.6102	85.6	0.9616	-285.7
0.2887	201.0	0.6399	31.6	0.9904	-315.4
0.3598	228.0	0.6597	-1.9	0.9952	-195.4
0.4103	237.3	0.7286	-65.1	0.9981	-81.0
120 bar					
0.1458	170.3	0.6113	358.2	0.9809	-199.1
0.218	249.4	0.6607	286.6	0.9905	-162.8
0.2897	311.7	0.7295	186.1	0.9924	-139.6
0.3609	366.6	0.7978	81.9	0.9952	-94.9
0.4115	392.7	0.8656	-19.5	0.9981	-40.9
0.4618	418.7	0.933	-118.2	0.9990	-18.6
0.5119	420.6	0.9426	-143.3		
0.5617	399.2	0.9618	-174.0		
140 bar					
0.0737	99.6	0.5140	660.6	0.9336	59.6
0.1469	218.7	0.5639	675.5	0.9526	25.1
0.2195	329.4	0.6134	655.1	0.9716	-14.0
0.2915	442.9	0.6627	604.8	0.9905	-33.5
0.3629	536.9	0.7312	485.7	0.9953	-21.4
0.4136	591.8	0.7992	343.4	0.9981	-8.4
0.4639	641.1	0.8666	199.1		-1339.0

Table 17
Experimental Enthalpy Data for the System Ethylene (1) + 1-Decanol (2) at 318.15 K and 81 bar

x_1	Δh[J/mol]	x_1	Δh[J/mol]	x_1	Δh[J/mol]
81 bar					
0.0670	-148.9	0.4522	-1393.9	0.7173	-1312.9
0.1098	-232.6	0.5023	-1554.9	0.7941	-956.5
0.1534	-346.1	0.5533	-1701.9	0.8698	-606.7
0.2158	-555.5	0.6102	-1767.9	0.9353	-295.0
0.2798	-771.4	0.6396	-1659.1		
0.3550	-1068.2	0.6689	-1536.2		
121 bar					
0.1137	-78.2	0.4884	-390.8	0.7699	-493.2
0.1729	-119.1	0.5565	-463.4	0.8258	-373.1
0.2326	-161.9	0.6083	-522.9	0.8827	-250.3

Table 17 (continued)
Experimental Enthalpy Data for the System Ethylene (1) + 1-Decanol (2) at 318.15 K and 81 bar

x_1	Δh[J/mol]	x_1	Δh[J/mol]	x_1	Δh[J/mol]
0.2946	-207.5	0.6252	-541.5	0.9339	-139.6
0.3580	-258.7	0.6612	-587.1	0.9821	-37.2
0.4219	-322.9	0.7150	-611.3		
146 bar					
0.0581	-5.6	0.3680	-96.8	0.7057	-308.9
0.1182	-15.8	0.4325	-126.5	0.7775	-295.9
0.1792	-29.8	0.4992	-162.8	0.8495	-193.5
0.2404	-46.5	0.5671	-210.3	0.9240	-90.3
0.3037	-70.7	0.6353	-260.5		

REFERENCES

[1] Orbey, H.; Sandler, S.I., A Comparison of Various Cubic Equation of State Mixing Rules for the Simultaneous Description of Excess Enthalpies and Vapor-Liquid Equilibria. *Fluid Phase Equilib.* 1996, *121*, 67-83.

[2] Orbey, H.; Sandler, S.I., On the combination of equation of state and excess free energy models. *Fluid Phase Equilib.* 1995, *11*, 53-70.

[3] Orbey, H.; Sandler, S.I., Analysis of Excess Free Energy Based Equations of State Models. *AIChE J.* 1996, *42*, 2327-2334.

[4] Guilbot, P.; Valtz, A.; Legendre, H.; Richon, D., Rapid On-line Sampler-Injector: A Reliable Tool for HAT-HP Sampling and on-line GC Analysis. *Analysis* 2000, *28*, 426–431.

[5] Reamer, H.H.; Sage B.H., Phase Equilibria in Hydrocarbon Systems. Volumetric and Phase Behavior of the Ethane – n-Decane System. *J. Chem. Eng. Data* 1962, *7*, 161-168.

[6] Reamer, H.H.; Lower, J.H.; Sage, B.H., Diffusion Coefficients in Hydrocarbon Systems. The Ethane-n-Decane System in the Liquid Phase. *J. Chem. Eng. Data* 1964, *9*, 54-59.

[7] Bufkin, B.A.; Robinson, R.L.; Estrera, S.S.; Luks, K.D., Solubility of Ethane in n-Decane at Pressures to 8.2 MPa and Temperatures from 278 to 411 K. *J. Chem. Eng. Data* 1986, *31*, 421-423.

[8] Singh, H.; Lucien, F.P.; Foster, N.R., Critical Properties for Binary Mixtures of Ethane Containing Low Concentrations of n-Alkane. *J. Chem. Eng. Data* 2000, *45*, 131-135.

[9] Hayduk, W.; Walter, E.B.; Simpson P., Solubility of Propane and Carbon Dioxide in Heptane, Dodecane, and Hexadecane. *J. Chem. Eng. Data* 1972, *17*, 5 9-61.

[10] Gonzales, R.; Murrieta-Guevera, F.; Parra, O.; Trejo, A. Solubility of Propane and Butane in Mixtures of n-Alkanes. *Fluid Phase Equilib.* 1987, *34*, 69-81.

[11] Sciamanna, S.F.; Lynn, S., Solubility of Hydrogen Sulfide, Sulfur Dioxide, Carbon Dioxide, Propane, and n-Butane in Poly (glycol ethers). *Ind. Eng. Chem. Res.* 1988, *27*, 492-499.

[12] King, M.B.; Al-Najjar, H., The Solubilities of Carbon Dioxide, Hydrogen Sulphide, and Propane in Some Normal Alkane Solvents. *Chem. Eng. Sci.* 1977, *32*, 1241-1246.

[13] Makranczy, J.; Megyery-Balog, K.; Rusz, L.; Patyi L., Solubility of Gases in Normal Alkanes. *Hung. J. Ind. Chem.* 1976, *4*, 269-280.

[14] Henni, A.; Jaffer, S.; Mather, A.E., Solubility of N_2O and CO_2 in n-Dodecane. *Can. J.*

Chem. Eng. 1996, *74*, 554-557.
[15] Stewart, W.C.; Nielsen, R.F., Phase Equilibria for Mixtures of Carbon Dioxide and Several Normal Saturated Hydrocarbons. *Bull. Miner. Ind. Exp. St. (Pennsylvania State Univ.)* 1953, *62*, 19-29.
[16] Schneider G., Druckeinfluß auf die Entmischung flüssiger Systeme. IV. Entmischung flüssiger n-Alkan-CO_2-Systeme bis –60 °C und 1500 bar. Messungen zum Problem der sog. "Entmischung in der Gasphase". *Ber. Bunsen-Ges. Phys. Chem.* 1966, *70*, 10-16.
[17] Hottovy, J.D.; Luks, K.D.; Kohn, J.P., Three-Phase Liquid-Liquid-Vapor Equilib. Behavior of Certain Binary CO_2-n-Paraffin Systems. *J. Chem. Eng. Data* 1981, *26*, 256-258.
[18] Todd, D.B.; Elgin, J.C., Phase Equilib. in Systems with Ethylene Above Its Critical Temperature. *AIChE J.* 1955, *1*, 20-27.
[19] McFall, T.A.; Post, M.E.; Christensen, J.J.; Izatt, R.M., The Excess Enthalpies of Eight (Ethane + Alcohol) Mixtures at 298.15 K. *J. Chem. Thermodyn.* 1981, *13*, 441-446.
[15] Lam, D.H.; Jangkamolkulchai, A.; Luks, K.D., Liquid-Liquid-Vapor Phase Equilibrium Behavior of Certain Binary Ethane + n-Alkanol Mixtures. *Fluid Phase Equilib.* 1990, *59*, 263-277.
[16] Lam, D.H.; Luks, K.D. Multiphase Equilibrium Behaviour of the Mixture Ethane + Methanol + 1-Decanol. *J. Chem. Eng. Data* 1991, *36*, 307-311.
[17] Patton, C.L.; Luks, K.D. Multiphase Equilibrium Behavior of the Mixture Ethane + 1-Decanol + n-Docosane. *Fluid Phase Equilib.* 1993, *85*, 181-190.
[18] Kohn, J.P.; Luks, K.D.; Liu, P.H. Three-Phase Solid-Liquid-Vapor Equilib. of Binary-n-Alkane Systems (Ethane-n-Octane, Ethane-n-Decane, Ethane-n-Dodecane). *J. Chem. Eng. Data* 1976, *21*, 360-362.
[19] Tiffin, D.L.; Kohn, J.P.; Luks, K.D., Three-Phase Solid-Liquid-Vapor Equilibrium of the Binary Hydrocarbon Systems Ethane-2-Methylnaphthalene, Ethane-Naphthalene, Propane-n-Decane, and Propane-n-Dodecane. *J. Chem. Eng. Data* 1979, *24*, 98-100.
[20] Lam, D.H.; Jangkamolkulchai, A.; Luks, K.D. Liquid-Liquid-Vapor Phase Equilibrium Behavior of Certain Binary Ethane + n-Alkanol Mixtures. *Fluid Phase Equilib.* 1990, *59*, 263-277.
[21] Lam, D.H.; Luks, K.D. Multiphase Equilibrium Behaviour of the Mixture Ethane + Methanol + 1-Decanol. *J. Chem. Eng. Data* 1991, *36*, 307-311.
[22] Patton, C.L.; Luks, K.D. Multiphase Equilibrium Behavior of the Mixture Ethane + 1-Decanol + n-Docosane. *Fluid Phase Equilib.* 1993, *85*, 181-190.
[23] Kohn, J.P.; Luks, K.D.; Liu, P.H., Three-Phase Solid-Liquid-Vapor Equilibria of Binary-n-Alkane Systems (Ethane-n-Octane, Ethane-n-Decane, Ethane-n-Dodecane). *J. Chem. Eng. Data* 1976, *21*, 360-362.
[24] Tiffin, D.L.; Kohn, J.P.; Luks, K.D., Three-Phase Solid-Liquid-Vapor Equilibria of the Binary Hydrocarbon Systems Ethane-2-Methylnaphthalene, Ethane-Naphthalene, Propane-n-Decane, and Propane-n-Dodecane. *J. Chem. Eng. Data* 1979, *24*, 98-100.
[25] Fischer, K.; Gmehling J. P-x and γ^{∞} Data for the Different Binary Butanol-Water Systems at 50°C. *J. Chem. Eng. Data* 1994, *39*, 309-315.
[26] Gmehling, J. Excess Enthalpies for 1,1,1-Trimethylchloroethane with Alkanes, Ketones, and Esters *J. Chem. Eng. Data*1993, *38,* 143-146.
[27] Horstmann, S.; Fischer, K.; Gmehling, J. PSRK Group Contribution Equation of State: Revision and Extension III. *Fluid Phase Equilib.* 2000, *167*, 173-186.
[28] van Konynenburg, P.H.; Scott, R.L., Critical Lines and Phase Equilibria in Binary van der Waals Mixtures *Phils. Trans. R. Soc. London Ser. A* 1980, *298*, 495-540.
[29] Schneider, G.M. High-pressure Phase Diagrams and Critical Properties of Fluid Mixtures *Chemical Thermodynamics*, Specialist Periodical Reports. McGlashan, M.L. (Editor), Vol. 2, 105-146, Chemical Society, London, 1978.

[30] Gmehling, J., Kolbe, B., Thermodynamik, Zweite überarbeite Auflage, VCH-Verlagsgesellschaft, Weinheim 1992.

[31] Redlich, O., Kwong, J. N. S., On the Thermodynamics of Solutions. V. An Equation of State. Fugacities of Gaseous Solutions. *Chem. Rev.* 1949, 233–244.

[32] Soave, G., Equilibrium Constants from a Modified Redlich Kwong Equation of State. *Chem. Eng. Sci.* 1972 1197 – 1203.

[33] Peng, D.-Y., Robinson, D. B. A new Two-Parameter Equation of State *Ind. Eng. Chem. Fundam.* 1976, 59-64.

[34] Ahlers, J.; Gmehling, J. Development of an Universal Group Contribution Equation of State I. Prediction of Liquid Densities for Pure Compounds with a Volume Translated Peng-Robinson Equation of State. *Fluid Phase Equilib.* 2001, 191, 177-188.

[35] Ahlers, J.; Gmehling, J., Development of an Universal Group Contribution Equation of State II. Prediction of Vapor-Liquid Equilibria for Asymmetric Systems. *Ind. Eng. Chem. Res.* 2002, 41, 3489-3498.

[36] Ahlers, J.; Gmehling, J., Development of an Universal Group Contribution Equation of State: III. Prediction of Vapor-Liquid Equilibria, Excess Enthalpies and Activity Coefficients at Infinite Dilution with the VTPR model. *Ind. Eng. Chem. Res.* 2002, 41, 5890-5899.

[37] Mathias, P. M., Copeman, T.W., Extension of the Peng Robinson Equation of State to Complex Mixtures: Evaluation of the Various Forms of the Local Composition Concept. *Fluid Phase Equilib.* 1983, 13, 91-108.

[38] Melhem, G. A., Saini R., Goodwin B.M., A Modified Peng Robinson Equation of State *Fluid Phase Equilib.* 1989 47, 189-237.

[39] Twu, C.H., Bluck, D., Cunningham, J. D., Coon, J. E., A Equation of State with a new Alpha Function and a new Mixing Rule *Fluid Phase Equilib.* 1991, 69, 33-50.

[40] J. Chen, K. Fischer, J., Gmehling, Modification of PSRK Mixing Rules and Results for Vapor-Liquid Equilibria, Enthalpy of Mixing and Activity Coefficients at Infinite Dilution *Fluid Phase Equilib.* 2002, 200, 411-429.

[41] Fischer K., Gmehling J., Further Development, Status and Result of the PSRK Method for the Prediction of Vapor-Liquid Equilibria and Gas Solubilities (corrected version) *FluidPhaseEquilib.* 1996, 121, 185-206.

[42] Lansangan R.M., Jangkamolkulchai A., Luks K.D., "Binary Vapor-Liquid Equilibria Behavior in the Vicinity of Liquid-Liquid-Vapor Loci", *Fluid Phase Equilib. 1987*, 36, p 49-66.

[43] Tan C.-S., Yarn S.-J., Hsu J.-H., Vapor-Liquid Equilibria for the Systems Carbon Dioxide-Ethylbenzene and Carbon Dioxide Styrene, *J.Chem.Eng.Data, 1991*,36, 23-25.

[44] Renon H., Laugier S., Schwarzentruber J., Richon D., "New Determinations of High Pressure Vapor-Liquid Equilibria in Binary Systems Containing n-Propylbenzene with Nitrogen or Carbon Dioxide Consistent with the Prausnitz-Keeler Test", Fluid Phase Equilib., *1989* 51, p. 285-298.

[45] Bamberger A., Maurer G., "High-Pressure Vapor-Liquid Equilibria in Binary Mixtures of Carbon Dioxide and Aromatic Hydrocarbons: Experimental Data and Correlations for CO_2 + Acetophenone, CO_2 + 1-Chloronaphthalene, CO_2 +Methylbenzoate and CO_2 + n-Propylbenzene", *J .Supercrit. Fluids, 1994*,7, p115-127.

[46] Charoensombut-Amon T., Martin R. J., Kobayashi R., Application of a Generalized Multiproperty Apparatus to Measure Phase Equilibrium and Vapor Phase Densities of Supercritical Carbon Dioxide in n-Hexadecane Systems up to 26 MPa, *Fluid Phase Equilib.*1986, 3,89-104.

[47] D'Souza, Patrick J. R., Teja A. S., High Pressure Phase Equilibria in the Carbon Dioxide - n-Hexadecane and Carbon Dioxide - Water Systems, *Can. J. Chem. Eng,*1988,66,319-323.

[48] De Haan A.B., Supercritical Fluid Extraction of Liquid Hydrocarbon Mixtures, Thesis, 1991, 129-138.

[49] Eustaquio-Rincon R., Trejo A., Solubility of n-octadecane in supercritical carbon dioxide at 310, 313, 333, and 353 K, in the range 10-20 MPa, *Fluid Phase Equilib.* 2001, 231-239.

[50] Scheidgen A., Fluidphasengleichgewichte binärer und ternärer Kohlendioxidmischungen mit schwerflüchtigen organischen Substanzen bis 100 MPa Cosolvency effect, Miscibility windows und Löcher in der kritischen Fläche, *Thesis*, 1997,1-272.

[51] Schlichting H., Experimentelle Bestimmung und Korrelierung der Löslichkeit verschiedener Lösungsmittel in Hochdruckgasen, *Thesis*, 1991.

[52] Gregorowicz J.; Chylinski K. On the Solubility of Chain Alcohols in Supercritical Carbon Dioxide. *Pol.J.Chem.* 1998, 72, 877 – 885.

[53] Chrisochoou A.A., Schaber K., Stephan K., Phase Equilibria with Supercritical Carbon Dioxide for the Enzymatic Production of an Enantiopure Pyrethroid Component. Part 1. Binary Systems, *J.Chem.Eng.Data*, 1997,42(3), 551-557.

[54] Ohgaki K., Katayama T., Isothermal Vapor-Liquid Equilibrium Data for Binary Systems Containing Carbon Dioxide at High Pressures: Methanol-Carbon Dioxide, n-Hexane-Carbon Dioxide, and Benzene-Carbon Dioxide Systems, *J.Chem.Eng.Data*, 1976, 21(1), 53-55.

[55] Gupta M.K., Li Y.-H., Hulsey B.J., Robinson R.L., Phase Equilibrium for Carbon Dioxide-Benzene at 313.2, 353.2, and 393.2 K, *J.Chem.Eng.Data*, 1982,27(1), 55-57.

[56] Kim C.-H., Vimalchand P., Donohue M.D., Vapor-Liquid Equilibria for Binary Mixtures of Carbon Dioxide with Benzene, Toluene and para-Xylene, *Fluid Phase Equilib.* 1986, 3, 299 – 311.

[57] Rainwater in Supercritical Fluid Technology: Reviews in Modern Theory and Applications, T.J: Bruno and J.F. Ely (Eds), CRC Press, Boca Raton, FL, *1991* . 57-162.

Supercritical Fluids as Solvents and Reaction Media
G. Brunner (editor)

Chapter 1.2.

Influence of additional components on the solvent power of supercritical ethylene

H. Dörr, M. Kinzl, G. Luft and O. Ruhl

Department of Chemical Engineering and Macromolecular Science, Darmstadt University of Technology, Petersenstraße 20, D-64287 Darmstadt, Germany

1. INTRODUCTION

Highly compressed supercritical ethylene is known as a good solvent for organic compounds. Several industrial production and separation processes, such as the high-pressure polymerization of ethylene and its copolymerization with various co-monomers, take advantage of the solubility of polymers and copolymers in this medium. In the polymerization reactor the resulting polymers should be completely dissolved in the supercritical monomers. In the high pressure separator after the reactor the polymer must be separated from the un-reacted monomers by decreasing the pressure. It is general experience that a lower pressure in the separator improves the separation but results in a higher energy for the re-compression of the un-reacted monomer to the operation pressure of the reactor to which it is recycled [1].

Whereas the influence of co-monomers like vinyl acetate, acrylic acid, acrylic acid esters or 1-olefins on the phase behaviour of (co)polymer/ethylene systems has been investigated in detail [2-10], only few studies on the influence of inert compounds, which can be entrained into and build up during the process or can be added to the reaction mixture, exist [11, 12].

For this reason the effect of nitrogen, carbon dioxide, helium and alkanes like methane, ethane, propane and n-butane on the cloud point pressures and the composition of phases of mixtures with poly(ethylene-co-vinyl acetate) copolymers (EVA) or poly(ethylene-co-1-hexene) and the monomers was investigated as a function of temperature, pressure and composition of the mixtures. The results of the measurements were compared to simulations by means of the Statistical Associating Fluid Theory (SAFT).

2. EXPERIMENTAL

2.1. Apparatus

Two view cells, a smaller and a larger one, developed in Darmstadt were available. The smaller one (Fig.1) was used to measure the cloud point pressures. It has a volume of 50 ml and is designed for a maximum pressure of 250 MPa and a temperature of 513 K [13]. For the optical observation two windows (13, 15) made of synthetic sapphire are arranged one opposite the other. One of which is used to illuminate the interior of the autoclave. The pressure can be varied in a range of up to 80 MPa without feeding or removing material by a metal bellows (7, 8) which position is measured by a transducer (3). For this purpose the bellows is connected to a pump operated by a pressure controller.

First the polymer is placed in the autoclave together with an inhibitor (2,6-di-tert-butyl-4-methyl-phenol). After evacuation, the co-monomer is sucked into the autoclave from a burette. Finally ethylene and the inert compound are fed from storage vessels. While heating to the pre-set temperature the apparatus is shaken to mix the components. Three plates are arranged around the metal bellows to support the mixing.

After homogenization, the pressure is reduced stepwise by means of the bellows, while the phase state is observed visually. The phase separation is indicated by cloudiness. The procedure was repeated at different temperatures to measure the cloud point curve. The reproducibility of the measurement was better than 3%.

In order to determine the composition of the phases, experiments were performed in a larger autoclave of 750 ml, operated at pressures up to 250 MPa

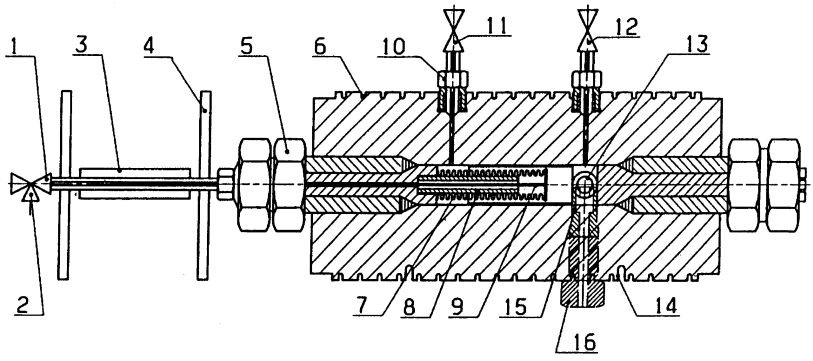

Fig. 1. High-pressure autoclave for the measurement of cloud-point pressures; 1 needle valve; 2 hydraulic oil inlet; 3 position transducer; 4 heat shield; 5 nut; 6 groove; 7,8 metal bellows; 9 metal stick; 10 cone to cone connection; 11 monomer and comonomer inlet; 12 inert compound inlet; 13,15 window; 14 groove for thermocouple; 16 high-pressure screwing.

and temperatures to 525 K. As the smaller autoclave it was equipped with sapphire windows for visual observation of the phase behaviour and a metal bellows to adjust the pressure and to maintain it constant during sampling [8].

For sampling the autoclave was brought in a vertical position after mixing and adjustment of pressure and temperature. The samples from the dense phase were taken at the bottom through a needle valve and from the light phase through the valve arranged at the top. The samples were collected in glass vials which were cooled by liquid nitrogen. The concentration of the polymer was determined gravimetrically. The gases were analysed by gas chromatography.

The arrangement of the view cells is presented in Fig. 2. As an example the auxiliary equipment of the larger cell is shown. On one side the cell is connected to storage vessels (3) and (4). The monomer is taken from bombs (1) and compressed into the storage vessels from which it is metered into the cell. On the other side the pressure control device is joined to the metal bellows. It consists of a pressure controller (PC) which operates the control valve (9), a high pressure pump (5), a storage vessel (6) and a buffer (8) for the hydraulic medium.

The experiments to evaluate the cloud point pressures and the composition of phases were performed in a range of 393 to 493 K and 5 to 220 MPa. The concentration of the copolymer was always 15 wt% and that of the inert component was increased up to 15 wt%. The mass ratio of co-monomer to the monomer was varied between 0 and 3.

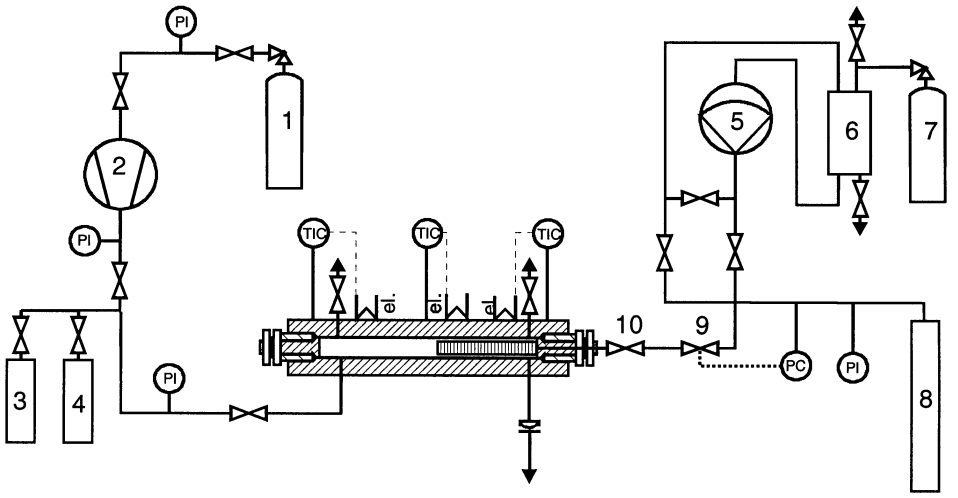

Fig. 2. Experimental setup; 1 bomb for monomer; 2 membrane compressor; 3,4 storage vessels; 5 high pressure pump; 6,8 storage vessel and buffer for hydraulic medium, 7 nitrogen supply; 9 control valve; 10 valve.

Table 1
Data of the copolymers

Copolymer	Comonomer	Incorporated comonomer wt%	M_N g/mol	M_W g/mol	Polydispersity
EVA 1	Vinyl acetate	27	64 000	319 000	4.98
EVA 2	Vinyl acetate	27	130 000	379 000	2.92
EVA 3	Vinyl acetate	26.5	80 000	289 000	3.73
EVA 4	Vinyl acetate	27	30 000	91 000	3.03
EH 1	1-Hexene	16	73 000	151 000	2.07
EH 2	1-Hexene	16	159 000	407 000	2.56

2.2. Materials

The copolymers were analyzed by GPC (gel permeation chromatography) and NMR (nuclear magnetic resonance). The data are collected in Table 1. The low ratio of weight average molecular weight (M_W) to number average molecular weight (M_N), the so-called polydispersity, of the EH-copolymers is typical for resins manufactured with metallocene catalysts.

The purities of ethylene, co-monomers, inerts, and the inhibitor are listed in Table 2 together with the supplier.

Table 2
Data of comonomers and inerts

Substance	Purity	Supplier
Ethylene	99.995	Linde
Vinyl acetate	99	Acros
1-Hexene	97	Acros
Methane	99.5	Linde
Ethane	99.95	Linde
Propane	99.5	Linde
n-Butane	99.5	Linde
Nitrogen	99.996	Linde
Carbon dioxide	99.995	Linde
Helium	99.996	Linde
2,6-di-tert-4-methyl-phenol	99	Aldrich

3. RESULTS

3.1. Influence of inert gases on the cloud point pressures

In this section the cloud-point pressures (de-mixing pressures) of the quasi-ternary systems copolymer/ethylene/inert gas [14, 15] are presented in dependence of mixture composition and temperature. The phase behaviour was investigated in the temperature range of 393 to 493 K. All solutions contained 15 wt% of the EH-copolymer or of the EVA-copolymer, respectively. Nitrogen, methane, carbon dioxide, helium and the alkanes ethane, propane, and n-butane were used as inert gases. The inert gas concentration w_{inert} was varied between 0 and 15 wt%. Due to the low molecular weight of helium, the upper limit of w_{helium} was 2 wt%.

3.1.1. Anti-solvent effects of nitrogen, methane, carbon dioxide and helium

The anti-solvent effects of several inert gases on solutions of the copolymers in supercritical ethylene are demonstrated in Fig. 3a/b to 6a/b. At constant temperature, the cloud point pressures of the systems copolymer/ethylene/inert gas increase when the concentration of nitrogen, methane, carbon dioxide or helium is raised. Due to their expanding impact on the two-phase region, these gases are anti-solvents.

Fig. 3a/b show the influence of nitrogen on solutions of the EH-copolymer (Fig. 3a) and of the EVA-copolymer (Fig. 3b) in supercritical ethylene. At constant temperature the cloud point pressures of both systems increase significantly with increasing nitrogen concentration.

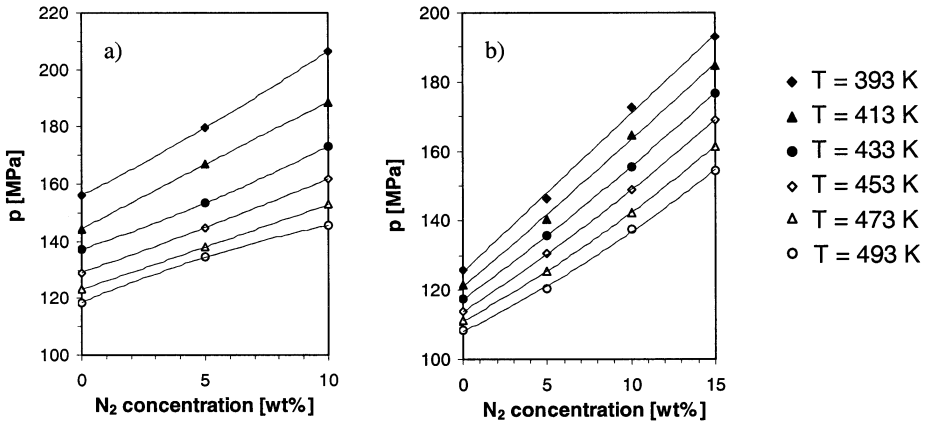

Fig. 3a/b. Cloud point pressures of the system EH-copolymer/ethylene/nitrogen (a) and EVA-copolymer/ethylene/nitrogen (b).

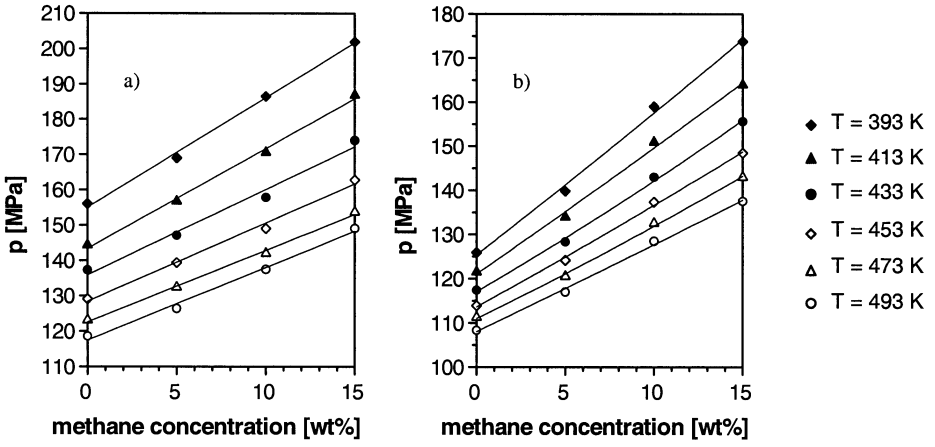

Fig. 4a/b. Cloud point pressures of the system EH-copolymer/ethylene/methane (a) and EVA-copolymer/ethylene/methane (b).

As can be seen from Fig. 4 a/b, methane is also acting as a strong anti-solvent on the copolymer solutions in supercritical ethylene. Whereas the addition of carbon dioxide (Fig. 5a/b) results only in a slight increase of the cloud point pressures, helium (Fig. 6a/b) is found to have the most significant anti-solvent effect. Compared to the helium-free mixtures the cloud point pressures of the solutions containing 2 wt% of the gas are higher by approximately 50 to 90 MPa (Fig. 6a/b).

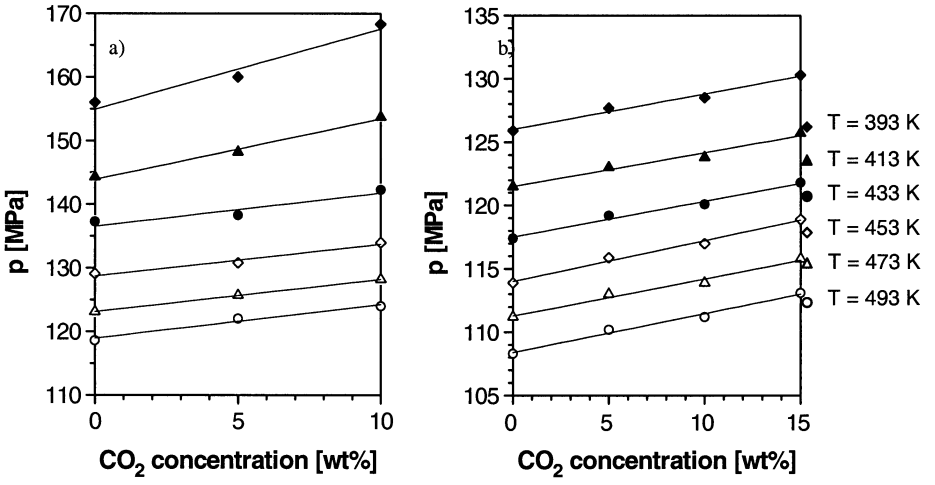

Fig. 5a/b. Cloud point pressures of the system EH-copolymer/ethylene/CO_2 (a) and EVA-copolymer/ethylene/CO_2 (b).

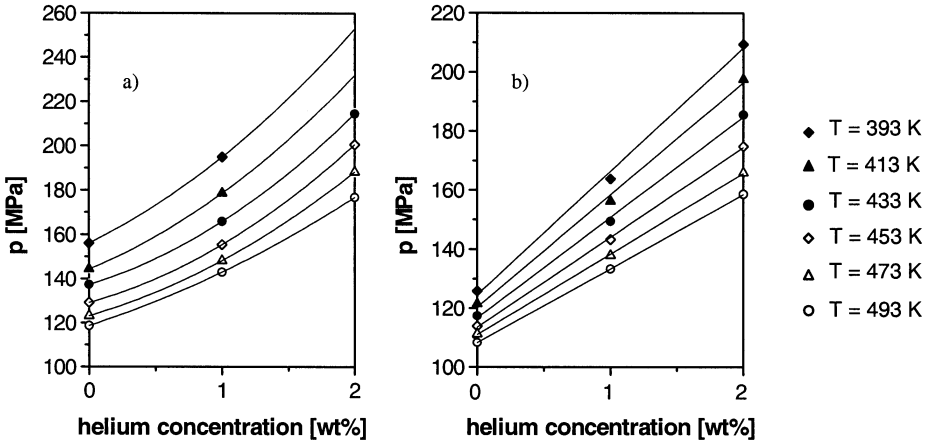

Fig. 6a/b. Cloud point pressures of the system EH-copolymer/ethylene/helium (a) and EVA-copolymer/ethylene/helium (b).

In order to explain the outstanding effect of helium, the low molar mass of the gas must be taken into consideration. In all cases, rising temperature is found to cause a decline of cloud point pressures and therefore to improve copolymer solubility, which is characteristic of the upper-critical-solution-temperature (UCST) behaviour.

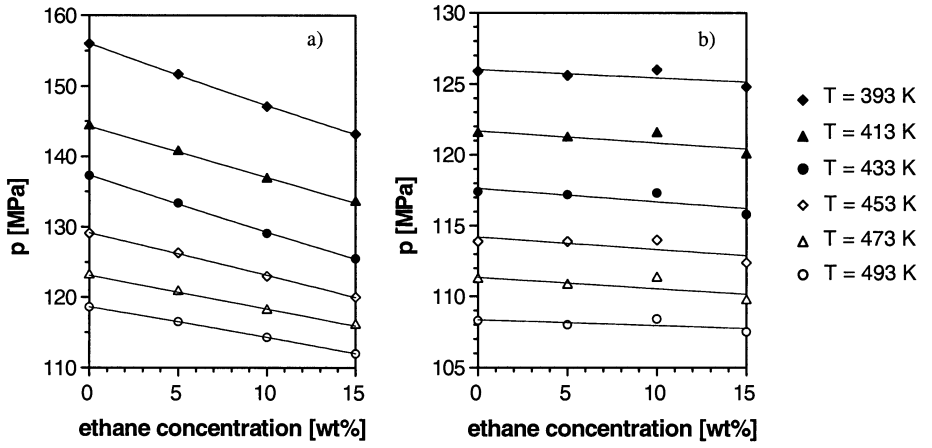

Fig. 7a/b. Cloud point pressures of the system EH-copolymer/ethylene/ethane (a) and EVA-copolymer/ethylene/ethane (b).

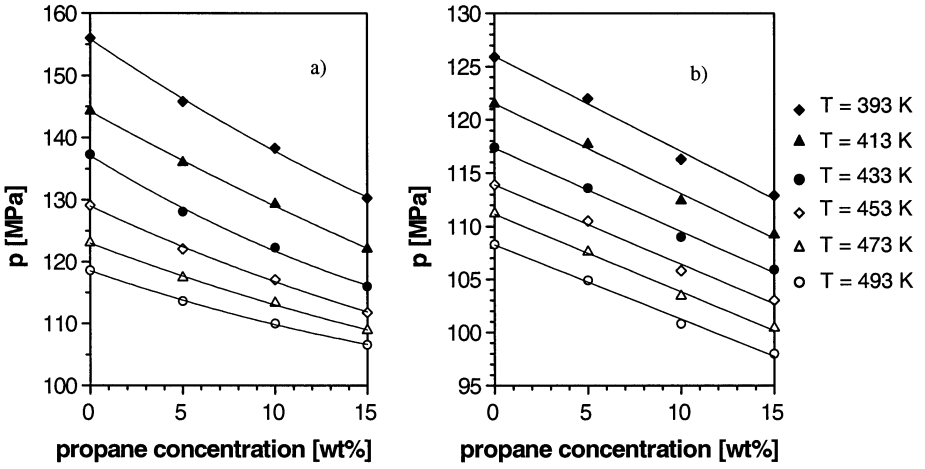

Fig. 8a/b. Cloud point pressures of the system EH-copolymer/ethylene/propane (a) and EVA-copolymer/ethylene/propane (b).

3.1.2. Co-solvent effects of ethane, propane, and n-butane

The alkanes ethane, propane, and n-butane act as co-solvents. At constant temperature, the addition of these inert compounds results in a de-mixing-pressure decrease, which is only slight for ethane (Fig. 7a/b), but more steep for propane (Fig. 8a/b) and especially for n-butane (Fig. 9a/b).

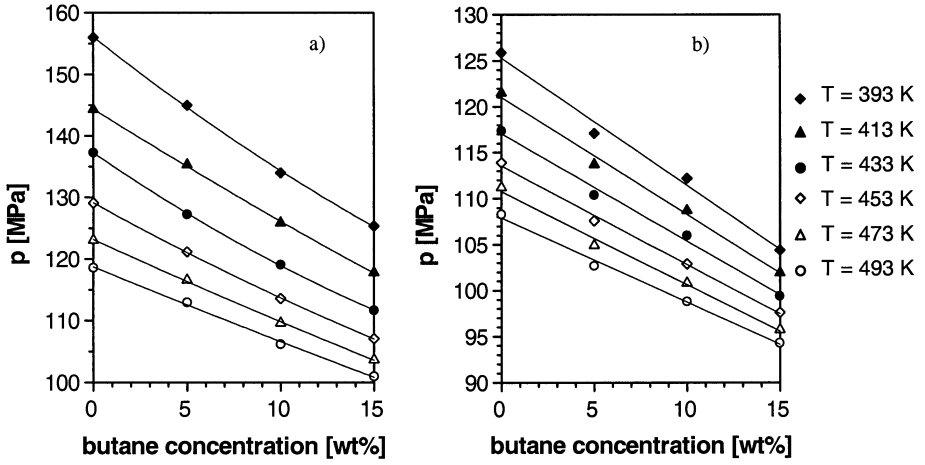

Fig. 9a/b. Cloud point pressures of the system EH-copolymer/ethylene/n-butane (a) and EVA-copolymer/ethylene/n-butane (b).

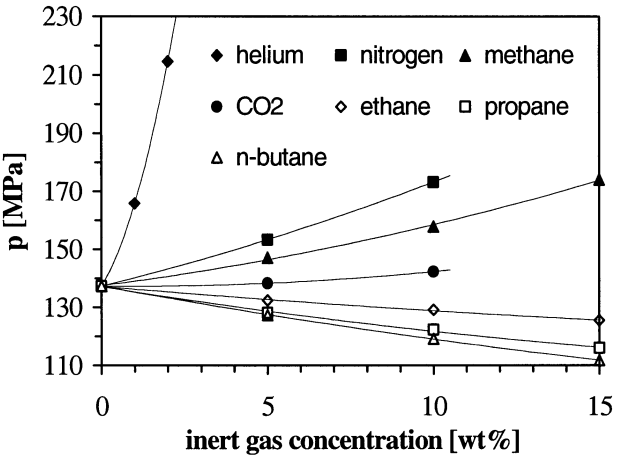

Fig. 10. Cloud points of the systems EH-copolymer/ethylene/inert gas; $T = 433$ K.

Fig. 10 and 11 give an overview of the effects of different inert compound on the phase boundaries of the systems EH-copolymer/ethylene/inert compound (Fig. 10) and EVA-copolymer/ethylene/inert compound (Fig. 11). The data are given for a temperature of 433 K. According to Prigogine's rules [16], the addition of gases which are soluble in the copolymer as well as in ethylene improves copolymer solubility. The alkanes ethane, propane and n-butane meet this rule, whereas the solubility of helium, nitrogen, methane and CO_2 in ethylene is much higher than in the copolymers. Therefore, these gases act as anti-solvents.

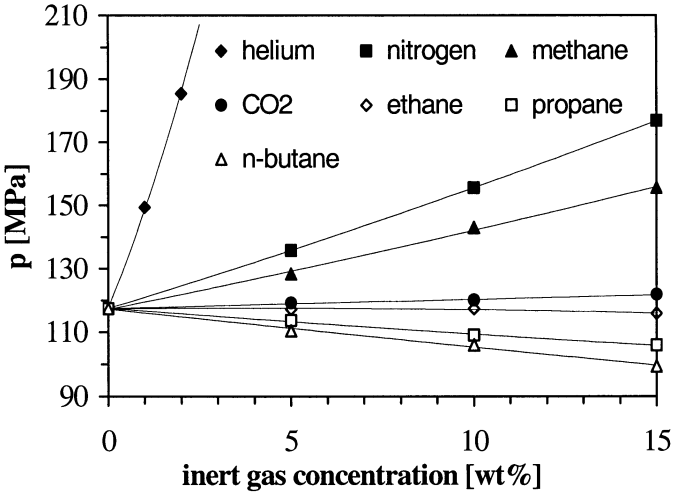

Fig. 11. Cloud points of the systems EVA-copolymer/ethylene/inert gas; $T = 433$ K.

3.2. Influence of co-monomers and inert compounds on the composition of phases

For determination of the composition of phases, coexistence curves were measured for solutions having an overall copolymer concentration of 15 wt% and a constant temperature of 433 K. The inert gas and co-monomer concentration was variable [15, 17, 18].

3.2.1. The phase behaviour of EVA solutions

In the following section the influence of the inert compounds on the phase behaviour of EVA solutions is discussed.

As reported before, different inert components have different effects on the cloud points of polymer solutions in supercritical ethylene. Some of them increase the cloud-point pressure and some of them decrease it. For example, the cloud-point pressures of the systems containing helium, nitrogen, methane, and carbon dioxide are higher than those of a reference system, which is free of these inert gases. The measurements of the coexistence curves confirm this finding as illustrated in Fig. 12. Generally the concentration of the polymer in the ethylene-rich phase (curves on the left hand side) decreases when the pressure is decreased and increases in the polymer-rich phase (curves on the right hand side).

Small spherical molecules, such as helium, nitrogen, methane, and carbon dioxide, act as anti-solvents. They reduce the mutual miscibility of EVA and ethylene. This means that the coexistence curves are shifted to higher pressures compared to the reference system without inert gas. We observed that helium and nitrogen have a relatively stronger anti-solvent effect than methane and carbon dioxide. For example, in the presence of helium or nitrogen a copolymer

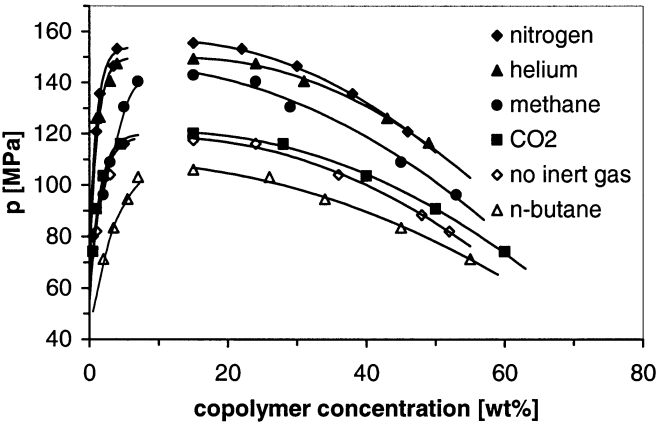

Fig. 12. Experimental coexistence curves for EVA/ethylene with and without inert gas; w(EVA) = 15 wt%; w(inert gas) = 10 wt%; w(helium) = 1 wt%; T = 433 K.

concentration of 40 wt% in the copolymer-rich phase is reached at pressures above 130 MPa, whereas in the absence of an inert gas, this copolymer concentration is reached at below 100 MPa. It is also observed that helium is the strongest anti-solvent among the inert gases studied in this work, about ten times stronger than nitrogen in terms of concentration. Therefore, the concentration of all inert gases was kept at about 10 wt%, whereas the concentration of helium was about 1 wt%.

The only co-solvent used in this work, n-butane, reduces the coexistence pressures by about 10 MPa relative to the reference system without inert gas.

In the quasi-quaternary system EVA/ethylene/VA/methane the methane concentration was kept constant at 10 wt%, whereas the mass ratio of VA/ethylene was varied, as shown in Fig. 13, which illustrates the influence of VA on the coexistence curves.

VA was found to act as a co-solvent in this quasi-quaternary system, increasing VA fraction substantially decreases the coexistence pressure. This means that, as the VA fraction increases, the EVA-rich phase becomes enriched with EVA and the ethylene-rich phase becomes enriched with ethylene. For example, to reach an EVA concentration of 40 wt% in the EVA-rich phase in the VA-free system, we need at least 120 MPa. By contrast, to reach such an EVA concentration in the EVA-rich phase in a system having a VA/ethylene ratio of 50/50 (shown with solid circles in Fig. 13), we need about 76 MPa. The corresponding pressure for the 75/25 ratio (solid squares) is below 43 MPa.

The coexistence curves of the EVA/ethylene/VA/inert gas system are presented in Fig. 14. The overall inert gas concentration is kept constant at 10 wt%, except for helium, which is 1 wt%. The mass VA/ethylene ratio is also kept constant, at about 50/50.

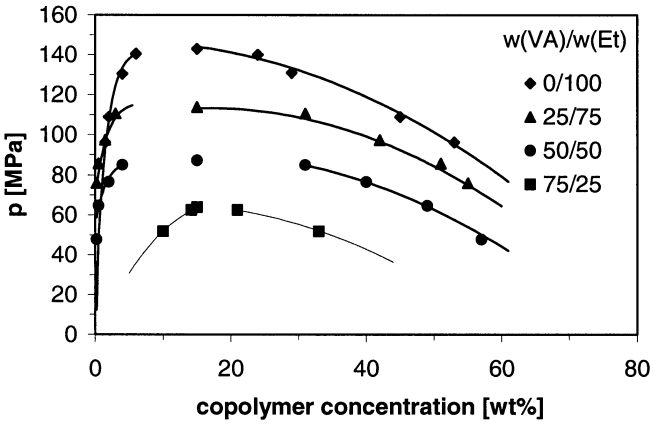

Fig. 13. Experimental coexistence curves for EVA/ethylene/VA/methane; w(EVA) = 15 wt%; w(methane) = 10 wt%; T = 433 K.

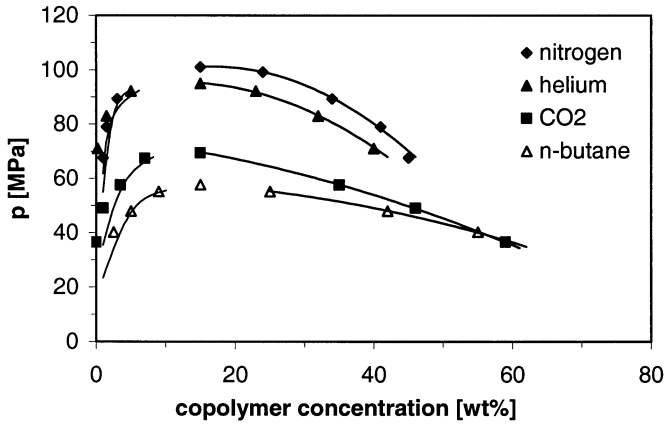

Fig. 14. Experimental coexistence curves for EVA/ethylene/VA/inert gas; w(EVA) = 15 wt%; w(inert gas) = 10 wt%; w(helium) = 1 wt%; w(VA)/w(ethylene) = 50/50; T = 433 K.

It is observed that the effect of the inert compounds on the phase behaviour of the quasi-quaternary systems is similar to that of the quasi-ternary systems; helium, nitrogen, methane, and carbon dioxide are found to reduce the miscibility while n-butane is found to increase it.

3.2.2. The phase behaviour of poly(ethylene-co-1-hexene) solutions

In the following section the influence of the comonomer and inert compounds on the composition of phases of poly(ethylene-co-1-hexene)-ethylene mixtures is discussed.

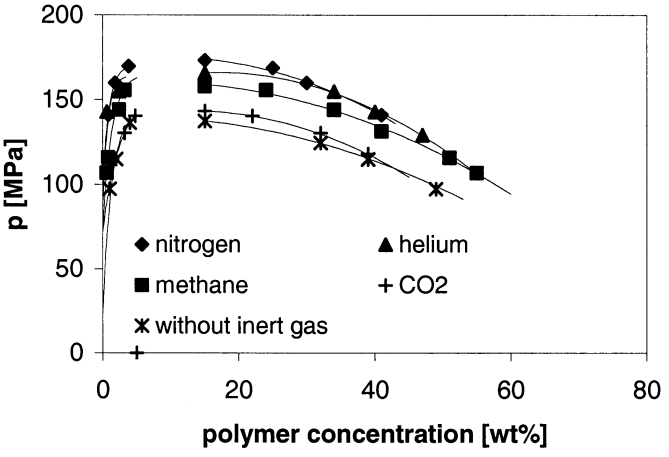

Fig. 15. Experimental coexistence curves for EH/ethylene/inert gas; w(EH) = 15 wt%; w(inert gas) = 10 wt%; w(helium) = 2 wt%; T = 433 K.

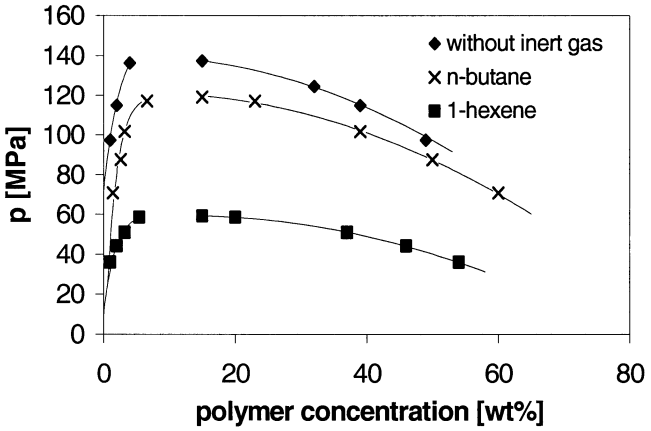

Fig. 16. Experimental coexistence curves for EH/ethylene/n-butane and EH/ethylene/1-hexene; w(EH) = 15 wt%; w(n-butane) = 10 wt%; ethylene/1-hexene ratio = 50/50; T = 433 K.

As described in Chapter 3.1 the inert compounds were found to behave in the same way as in the EVA-ethylene mixtures. Also the addition of the co-monomer 1-hexene has the same effect as in the case of EVA/ethylene mixtures.

The influence of nitrogen, helium, methane and carbon dioxide on the phase behaviour of an EH-ethylene mixture is presented in Fig. 15. It is obvious, that the small spherical molecules nitrogen and helium have the strongest anti-solvent effect, whereas methane and carbon dioxide do not act as such strong anti-solvents. The coexistence curves of the inert gas containing mixtures are shifted to higher pressure relative to the EH/ethylene mixtures.

Fig. 16 shows the coexistence curves of the EH/ethylene/n-butane and EH/ethylene/1-hexene mixtures. Both components lead to a better miscibility of the systems. The coexistence curves of both mixtures are shifted towards lower pressures relative to the binary system. The co-monomer 1-hexene exhibits the strongest effect.

3.3. Influence of the polymer molecular weight

As outlined in the last two sections, the cloud point pressures and the phase composition are steeply affected by the composition of the mixtures. Another point of interest is the influence of the molecular weights of the polymers on the cloud-point pressures.

Earlier investigations with n-alkanes and polyethylene waxes showed a linear dependence between molecular weight and increasing cloud-point pressure [19-21]. Experiments with LDPE (low density polyethylene) performed by Spahl [22] revealed a maximum of the cloud-point pressure at higher molecular weight.

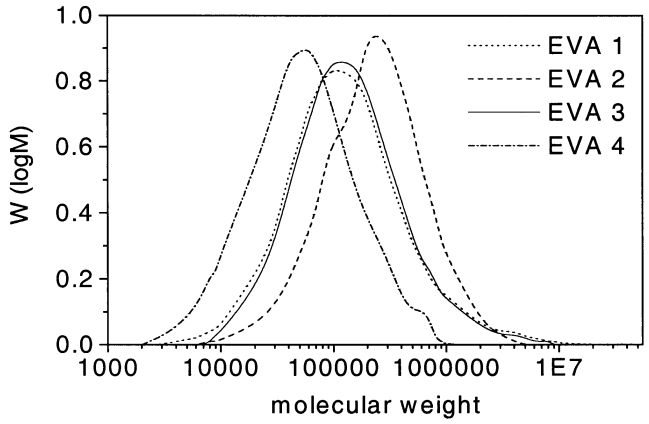

Fig. 17. Molecular weight distribution of the used copolymers EVA 1 – 4.

In order to analyse the influence of the molecular weight on the cloud point, four different copolymers with a vinyl acetate content of 27 wt% were used. The range of the number-average molecular weight was between 30,000 and 130,000, respectively between 91,000 and 379,000 for the weight-average molecular weight. The molecular weight distribution for the four copolymers is presented in Fig. 17.

All four copolymers show a symmetric and narrow molecular weight distribution. The copolymers have very similar polydispersities (M_W/M_N) between 2.9 (EVA 2) and 4.9 (EVA 1). This is of great importance for the cloud-point pressures because both polydispersity and symmetry influence the course of the cloud-point curves. By using copolymers from one production series the effect of molecular weight distribution could be eliminated [23].

Fig. 18 shows the cloud point pressures for the pseudo-binary system EVA-copolymer/ethylene. The mixtures contained 15 wt% copolymer and 85 wt% ethylene. The measurements were performed at temperatures between 413 K and 473 K. At low molecular weights the cloud-point pressure increases steeply. For high molecular weights the cloud-point pressures approach a maximum at about 120 MPa. A further interesting point is the influence of temperature. At high molecular weights the cloud-point pressure decreases with increasing temperature because of improved miscibility. At pressures below 70 MPa no temperature effect can be detected (LCST behaviour). As can be seen in Fig. 19, the temperature effect at lower pressures change its direction. At pressures below 65 MPa the cloud-point pressure increases with increasing temperature (UCST behaviour). This behaviour can be explained from explainable by looking on the density-pressure dependence of the solvent ethylene. Due to the high density

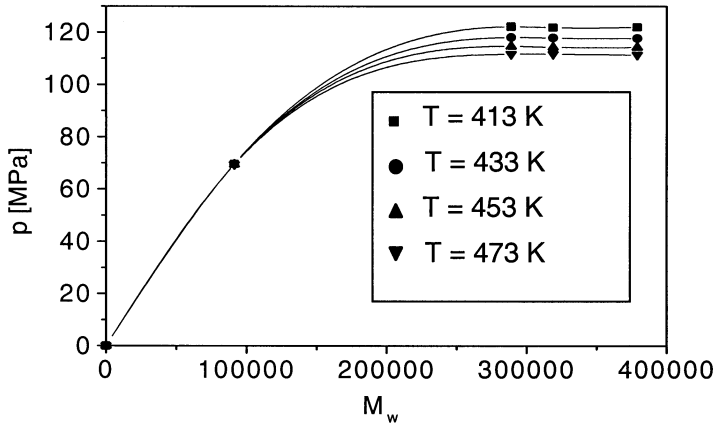

Fig. 18. Cloud-point pressures versus the weight-average molecular weight; w(polymer) = 15 wt%; w(ethylene) = 85 wt%.

of 0.5 to 0.6 g/ml at pressures above 70 MPa ethylene behaves like an organic solvent. At lower pressures ethylene behaves like a gas which has a decreasing capacity to solve high molecular materials.

Fig. 19 shows the cloud-point pressures of a pseudo-quaternary mixture composed of 15 wt% EVA-copolymer, 75 wt% solvent, consisting of ethylene and vinyl acetate and 10 wt% of the inert component carbon dioxide. In this case the cloud-point pressures increase up to an maximum of about 70 MPa. Due to

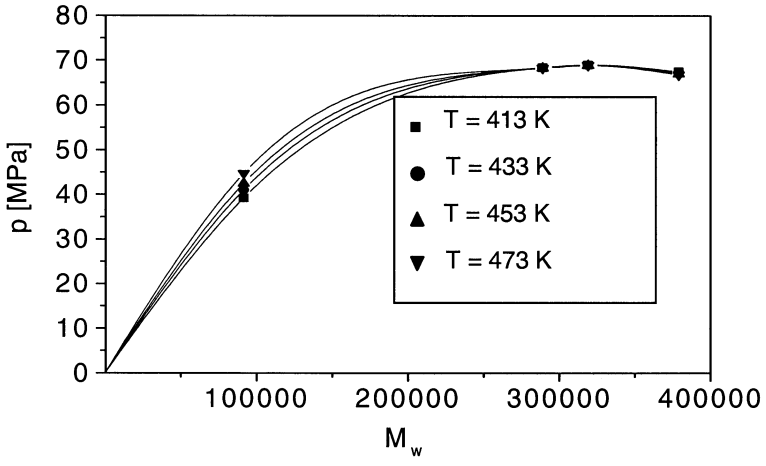

Fig. 19. Cloud-point pressures versus the weight-average molecular weight; w(EVA) = 15 wt%; w(ethylene) = 37.5 wt%; w(CO_2) = 10 wt%; w(vinyl acetate) = 37.5 wt%.

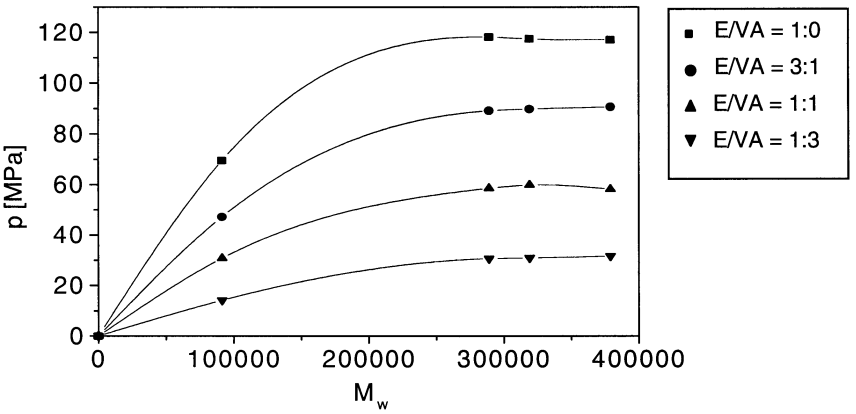

Fig. 20. Influence of the vinyl acetate fraction; w(polymer) = 15 wt%; T = 433 K.

the additional components the maximum pressure is significantly lower than in the example shown in Fig. 18. As mentioned before carbon dioxide acts as an anti-solvent but in this mixture the co-solvent effect of the co-monomer vinyl acetate overbalances the influence of carbon dioxide (Fig. 20 and 21).

In Fig. 20 the dependence of cloud-point pressures of the content of vinyl acetate for different molecular weights is shown. The uppermost curve represents a mixture without vinyl acetate. The parameters at the lower curves are 21.25, 42.5 and 63.75 wt% vinyl acetate. The content of copolymer is 15 wt% and the rest is ethylene. Only the data for 433 K are shown. The cloud-point pressures approach a maximum with increasing molecular weight. The dependence of the cloud point pressures on the vinyl acetate content appears to be linear for all molecular weights.

In Fig. 21 four different mixture compositions are shown to demonstrate the influence of the carbon dioxide. In this case, the copolymer fraction is again 15 wt% . The ethylene to vinyl acetate ratio is 1/1 and 3/1. For both experiments with 10 wt% and without carbon dioxide were performed. Two aspects are noticeable. First there is an anti-solvent effect by the carbon dioxide, the curves with carbon dioxide are slightly higher then those without. Furthermore we see the co-solvent effect of the vinyl acetate. The lower two curves are those with the higher vinyl acetate content.

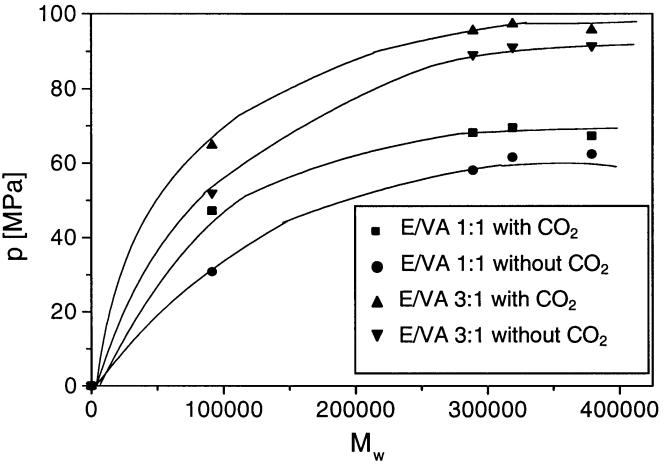

Fig. 21. Influence of additional components on cloud-point pressures; w(polymer) = 15 wt%; $T = 433$ K.

3.4. Modeling of inert gas effects on cloud-point pressures

This section gives an overview of the modeling of a subset of the cloud point data of Chapter 3.1 with a polymer equation of state. The experimental cloud point pressures of the EVA- and EH-copolymer solutions (polymer concentration = 15 wt%) in mixtures of ethylene and an inert gas (nitrogen, CO_2 or n-butane) were correlated using the Statistical Associating Fluid Theory (SAFT), described in [4, 24, 25]. The main goal was to capture the inert-component anti-solvent and co-solvent effects on the cloud-point pressures in the temperature range of 393 to 493 K at inert-component concentrations from zero to about 15 wt%.

According to Eq. (1), the SAFT compressibility factor consists of the hard-sphere, dispersion, chain, and association terms:

$$Z = \frac{pv}{RT} = 1 + Z^{hs} + Z^{disp} + Z^{chain} + Z^{assoc} \qquad (1)$$

Since this work deals with non-associating systems, the association term Z^{assoc} is set equal to zero. Following to Folie et al. [24], Z^{hs}, Z^{disp} and Z^{chain} can be calculated with three segment parameters for each polymeric and non-polymeric component: the temperature-independent segment volume v^{00}, the number of segments per molecule m, and the temperature-independent dispersion energy u^0/k. Their values are listed in Table 3.

Table 3
SAFT pure-component parameters

	MW [g/mol]	v^{00} [mL/mol]	m [-]	u^0/k [K]
EVA	61900	12.000	3154.600	210.00
EH	60000	12.000	3057.600	210.00
Ethylene	28.054	18.157	1.464	212.06
Nitrogen	28.013	19.457	1.000	123.53
Carbon dioxide	44.010	13.578	1.417	216.08
n-Butane	58.124	12.599	3.458	195.11

For ethylene and the inert components, these values are taken from literature [24]. As described in [4], we set v^{00} = 12 mL/mol and u^0/k = 210 K for the copolymers, and estimate the copolymer segment number parameter from the n-alkane corollary m = 0.05096 M_n, where M_n is the number-average molecular weight. Although the copolymers are polydisperse, they are treated as monodisperse components.

For mixtures, one binary parameter k_{ij} for each pair of components must be specified. In this work, these parameters are determined by fitting SAFT to the experimental cloud-point pressures, using the following objective function:

$$\mathrm{OF} = \sum_{i}^{N} \left| \frac{p_i^{exp} - p_i^{calc}}{p_i^{exp}} \right| \tag{2}$$

The k_{ij} parameters turn out to exhibit temperature dependence as follows:

$$k_{ij} = C_1 + C_2(T/\mathrm{K}) + C_2(T/\mathrm{K})^2 \tag{3}$$

The constants C_1, C_2 and C_3 are reported in Table 4. The impact of this temperature dependence of k_{ij} on the cross-segment energy u_{ij} is less than 5% within the temperature range of the experiment.

$k_{\text{copolymer-ethylene}}$ are fit to the experimental cloud-point pressures of the binaries copolymer/ethylene, $k_{\text{ethylene-inert}}$ to that of the binaries ethylene/inert gas, and $k_{\text{copolymer-inert}}$ to that of the ternaries copolymer/ethylene/inert gas. Since there are no experimental data available for the systems ethylene/N_2 and ethylene/CO_2, the corresponding k_{ij}'s are set zero.

Table 4
Binary parameters k_{ij} as function of temperature

	C_1	C_2	C_3
$k_{EVA\text{-}ethylene}$	0.0008	0.0002151	-0.00000019
$k_{EH\text{-}ethylene}$	-0.0209	0.0003340	-0.00000032
$k_{ethylene\text{-}N2}$	0	0	0
$k_{ethylene\text{-}CO2}$	0	0	0
$k_{ethylene\text{-}butane}$	0.1748	0	0
$k_{EVA\text{-}N2}$	-0.4582	0.0020308	-0.00000201
$k_{EVA\text{-}CO2}$	-0.0048	0.0001572	0
$k_{EVA\text{-}butane}$	0.2091	-0.0004248	0
$k_{EH\text{-}N2}$	0.3335	-0.0015481	0.000001963
$k_{EH\text{-}CO2}$	0.6887	-0.0030116	0.000003700
$k_{EH\text{-}butane}$	0.0142	-0.0000443	0

As suggested by Prigogine [16], the addition of an inert component to a copolymer solution in supercritical ethylene can result in an anti- or co-solvent effect. Fig. 22a/b illustrate the strong anti-solvent effect of N_2 on the solutions of the EVA-copolymer (Fig. 22a) and the EH-copolymer (Fig. 22b) in supercritical ethylene. For example, compared to the inert-free EVA-solution, the experimental cloud-point pressure of the mixture with an N_2 concentration of 15 wt% is shifted by about 60 MPa at 433 K (Fig. 22a).

Compared to nitrogen, the pressure shift for CO_2 is significantly lower, as can be seen from Figs. 23a/b. For the solution of the EVA-copolymer (Fig. 23a) the pressure increase is about 4 MPa at 433 K, when 15% of the inert gas are added. This anti-solvent-effect difference between nitrogen and CO_2 is well represented by SAFT.

Fig. 24a/b illustrate the co-solvent effect of n-butane on the solutions of the EVA-copolymer (Fig. 24a) and the EH-copolymer (Fig. 24b) in supercritical ethylene. The decreasing cloud-point pressures with increasing n-butane concentration and the UCST-like temperature behaviour are both well represented by SAFT. Compared to the n-butane co-solvent effect on the system

EVA/ethylene/n-butane (Fig. 24a), its co-solvent effect on the system EH/ethylene/n-butane (Fig. 24b) is stronger, because EH, in contrast to EVA, is non-polar.

Fig. 25a/b present a comparison of the three discussed copolymer/ ethylene/inert gas systems at 433 K. Fig. 25a shows the result for the system EVA/ethylene/inert gas, Fig. 25b for EH/ethylene/inert gas. n-Butane is found to be a strong co-solvent, CO_2 a weak anti-solvent, and N_2 a strong anti-solvent. All experimental co- and anti-solvent effects are in good agreement with the data obtained by SAFT.

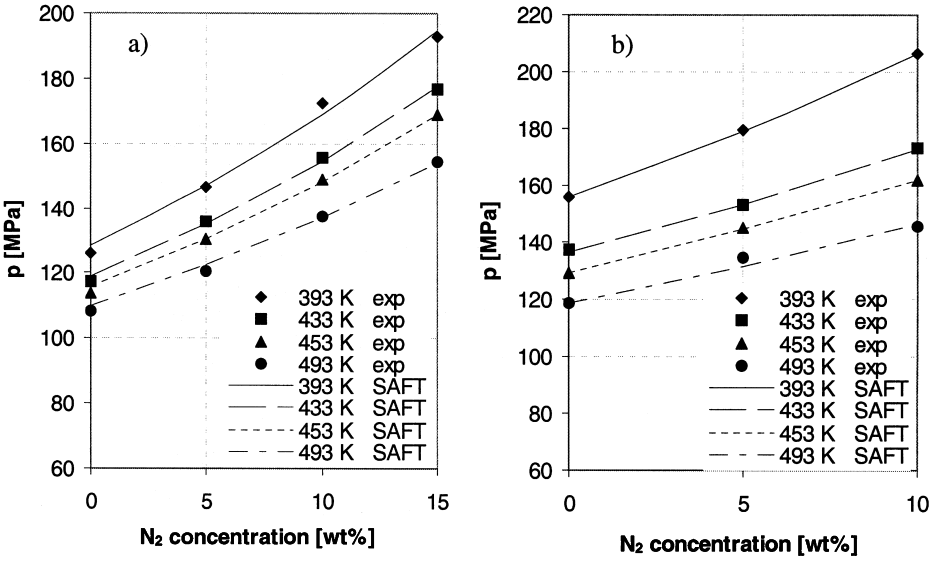

Fig. 22a/b. Experimental and calculated cloud-point pressures of the systems EVA/ethylene/ nitrogen (a) and EH/ethylene/nitrogen (b); w(copolymer) = 15 wt%.

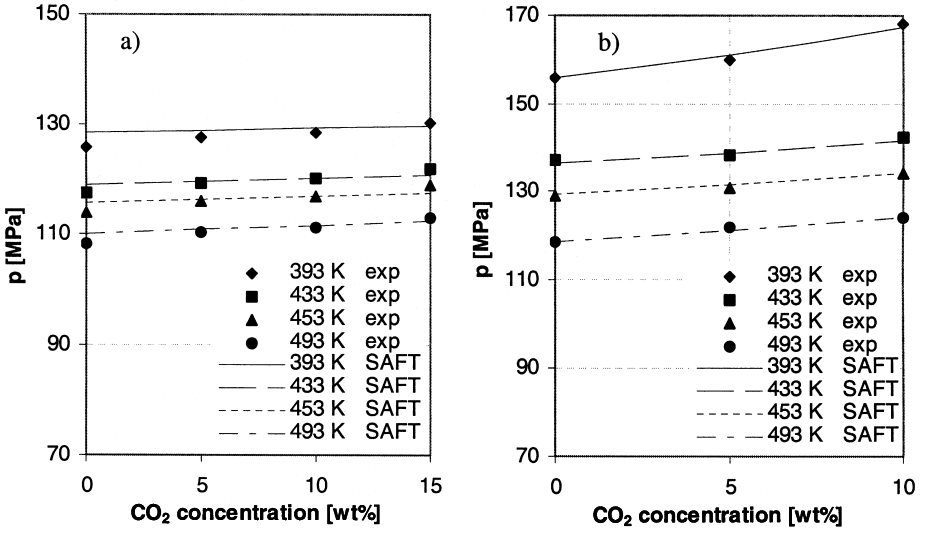

Fig. 23a/b. Experimental and calculated cloud-point pressures of the systems EVA/ethylene/ CO_2 (a) and EH/ethylene/ CO_2 (b); w(copolymer) = 15 wt%.

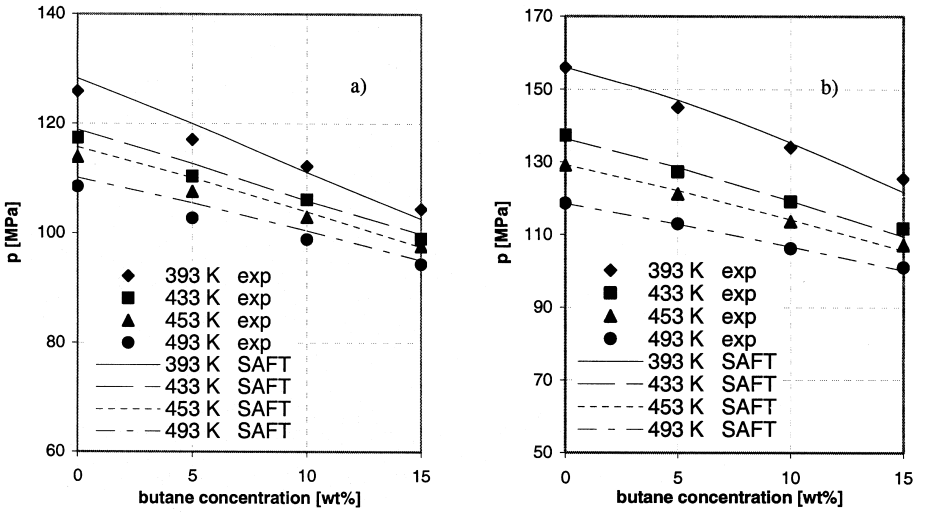

Fig. 24a/b. Experimental and calculated cloud-point pressures of the systems EVA/ethylene/ n-butane (a) and EH/ethylene/n-butane (b); w(copolymer) = 15 wt%.

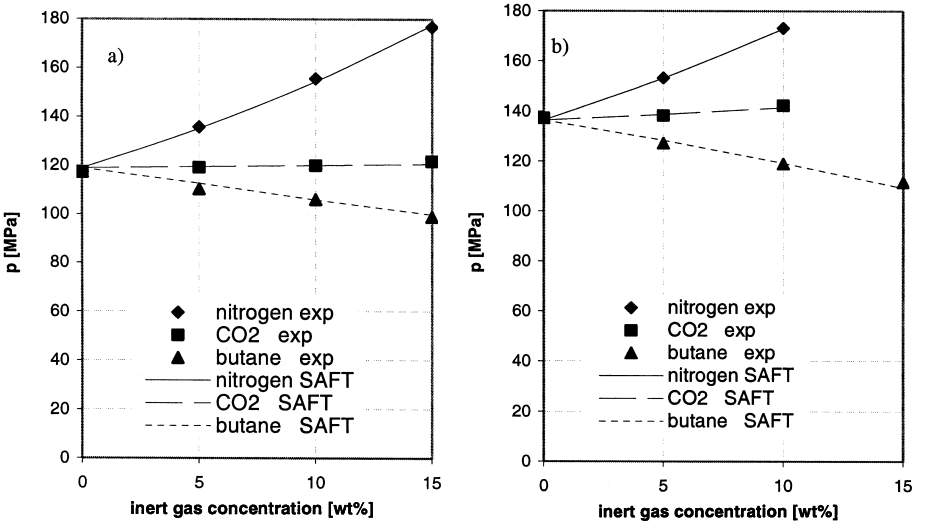

Fig. 25a/b. Experimental and calculated cloud-point pressures of the systems EVA/ethylene/ inert (a) and EH/ethylene/inert (b); w(copolymer) = 15 wt%; T = 433 K.

4. CONCLUSIONS

The solubility of EVA-copolymers in highly compressed ethylene is significantly improved by the addition of vinyl acetate and inert alkanes like propane, ethane and especially n-butane. These components are soluble in the copolymer

as well as in ethylene. In contrast, the solubility of small spherical molecules like helium, nitrogen, methane and carbon dioxide in the copolymer is much lower than in the solvent. Thus, in agreement with the rules of Prigogine, these inert gases act as anti-solvents. The anti-solvent effect decreases in the sequence helium > nitrogen > methane > carbon dioxide. The same tendencies were observed with the 1-hexene/ethylene-copolymer. Similarly to vinyl acetate also the co-monomer 1-hexene acts as a co-solvent.

It could be useful to add anti-solvents in the copolymerization of ethylene and high amounts of a co-monomer like vinyl acetate which increases steeply the solubility of the polymer. Otherwise the polymer separator must be operated at a low pressure to remove the polymer from the unreacted monomer which requires high energy to recompress the monomer and to feed it again into the polymerization reactor. Vice versa by the addition of solvents, polymerization processes in which the polymer, like an ethylene/acrylic acid copolymer, is less soluble could be run under single phase conditions to which preference is given.

REFERENCES

[1] G. Luft in A. Bertucco and G. Vetter (eds.), High Pressure Process Technology, Elsevier, Amsterdam, 2001.
[2] N. Koak, R.M. Visser, and Th.W. de Loos, Fluid Phase Eq. 158-160, 1999, 835-846.
[3] B. Folie and M. Radosz, Ind. Eng. Chem. Res., 34 (1995) 1501.
[4] B. Folie, C. Gregg, G. Luft and M. Radosz, Fluid Phase Eq., 120 (1996) 11.
[5] C. Wohlfahrt, Acta Polymerica, 35 (1984) 498.
[6] T. Heuer, G.P. Peuschel and M. Rätzsch, Acta Polymerica 40, (1989) 273.
[7] G. Luft and A. Lindner, Angew. Makromol. Chem., 56 (1976) 66.
[8] R. Spahl and G. Luft, Ber. Bunsenges. Phys. Chem., 87 (1983) 87, ibz. 86 (1982) 621, 85 (1981) 379.
[9] R. Wind and G. Luft, Chem.-Ing.-Tech., 64 (1992) 1114.
[10] G. Luft and M.S. Subramanian, Ind. Eng. Chem. Res., 26 No.4 (1987) 750.
[11] D. Constantin and J.P. Machon, Eur. Polym. J., 14 (1977) 703.
[12] H.A.J. Kennis, et al. Chem. Eng. Sci., 45 (1990) 1875.
[13] D. Heukelbach and G. Luft, Fluid Phase Eq., 146 (1998) 187.
[14] M. Kinzl, G. Luft, C. S. Ungar, Fluid Phase Equilib., 178 (2001), 179-189.
[15] M. Kinzl, G. Luft, H. Doerr, Fluid Phase Equilib., 178 (2001), 191-201.
[16] I. Prigogine, Chemical Thermodynamics (1954), VEB Leipzig.
[17] H. Dörr, Ph.D. Thesis, Darmstadt University of Technology, 2001.
[18] W. Kunz, Diploma Thesis, Darmstadt University of Technology, 1983.
[19] A. Fredenslund, J. Mollerup, K.R. Hall, J. Chem. Eng. Data., 21 (1976) 3, 301
[20] W.B. Kay, Ind. Eng. Chem. 40 (1948) 8, 1459
[21] H.H. Reamer, B.H. Sage, J. Chem. Eng. Data 7 (1962) 161.
[22] R. Spahl, Ph.D. Thesis, Darmstadt University of Technology, 1981
[23] D. Heukelbach, G. Luft, Fluid Phase Equilibria 146 (1998) 187-195.
[24] S. H. Huang, M. Radosz, Ind. Eng. Chem. Res., 29 (1990) 2284.
[25] S. H. Huang, M. Radosz, Ind. Eng. Chem. Res., 30 (1991) 1994.

Supercritical Fluids as Solvents and Reaction Media
G. Brunner (editor)

Chapter 1.3.

High pressure phase equilibria of copolymer solutions - Experiments and correlation

C. Beyer and L. R. Oellrich

Institut für Technische Thermodynamik und Kältetechnik,
Universität Karlsruhe (TH)
E-mail: oellrich@ttk.ciw.uni-karlsruhe.de

ABSTRACT

In the industrial high pressure polymerization process, manufacturing of ethylene-based copolymers like poly(ethylene-co-acrylic acid) has to be performed at very high pressures (up to 300 MPa) to avoid de-mixing due to unfavourable interactions between product (polymer) molecules and molecules of the educt mixture (ethylene and co-monomer). Suitable inert co-solvents may help to lower the operating pressure and yet still operate in a single phase region. In this project, phase equilibrium data have been accumulated for mixtures of ethylene and ethylene-co-acrylic acid copolymer with and without the application of various co-solvents in varying amounts. It was found that non-polar but dense co-solvents in varying amounts. It was found that nonpolar but dense co-solvents like n-heptane, iso-octane and n-decane are matching the co-solvent potential of a polar but non-associating substance like ethyl acetate, especially for the higher temperatures investigated. Strongly polar and associating fluids like ethanol and octanoic acid are superior co-solvents. However, for high concentrations of ethanol and lower temperatures, a shift in phase behaviour with rising de-mixing pressures (anti-solvent effect) has been observed which is attributed to self-association of excess ethanol molecules. This phenomenon can not be reported for ethyl acetate and octanoic acid.

In addition, cloud point data for mixtures of ethylene and poly(ethylene-co-ethyl acrylate) (EEA) and mixtures of ethylene and poly(ethylene-co-propyl acrylate) (EPA) are presented in the temperature range of 120 °C to 250 °C and for de-mixing pressures up to 2400 bar. The co-monomer content in the co-polymer varies between 0 and 100 mass-% for both copolymers examined. The polymer concentration was fixed at 5 mass-% in each experiment. Due to the unavailability of the copolymer under scrutiny, all polymer samples except for

the pure low-density polyethylene, poly(ethyl acrylate) (PEA) and poly(propyl acrylate) (PPA) had to be synthesized in a laboratory scale continuous high pressure polymerization setup in a joint effort with the Institute for Physical Chemistry at the University of Göttingen. With the present work, an important gap could be closed regarding the understanding of the phase behaviour of acrylate copolymers in low molecular weight hydrocarbons. Up to date, merely results for the de-mixing curves for ethylene/poly(ethylene-co-methyl acrylate) and ethylene/poly(ethylene-co-butyl acrylate) have been reported in the range of acrylates with short alkyl tails. These two systems exhibit strong differences in de-mixing behavior. Synthesis and phase behavior studies of an acrylate copolymer with an intermediate length alkyl tail provided further insight into the de-mixing pressure dependence on alkyl tail-length.

Like poly(ethylene-co-methyl acrylate), poly(ethylene-co-ethyl acrylate) exhibits a pronounced minimum in de-mixing pressure when the co-monomer concentration in the backbone of the polymer is increased. For poly(ethylene-co-propyl acrylate), no pronounced minimum but a light decrease in de-mixing pressure with rising co-monomer content was observed.

Experimental cloud point curves obtained were modeled using the Free-Volume- Theory, the SAFT- and PC-SAFT -Equation of State. The PC-SAFT - EOS was found to yield the most reliable representation of the experimental data with the lowest number of temperature-independent parameters to be fitted.

Being another important part of the project, selected results for the experimental determination of the composition of coexisting phases below the cloud point (coexistence curves) are shown. The experimental procedure to determine phase compositions via gravimetrical analysis was shown to work reliably. However, the size of the apparatus used limited the amount of obtained probes per experiment.

1. INTRODUCTION

In the industrial high pressure polymerization process, synthesis of polyethylene as well as ethylene-based copolymers has to be performed in a homogeneous phase to avoid a decrease in product quality due to overheating and possible fouling problems. On the other hand, a well-defined separation of the product from the educt mixture is aimed at in subsequent low pressure flash units. Hence, a need for reliable phase equilibrium data for mixtures of ethylene-based copolymers and low molecular weight hydrocarbons arises [1-3].

Numerous studies on high pressure polymeric phase behaviour have shown that the incorporation of a different co-monomer in the polyethylene chain can both increase or decrease the de-mixing pressure observed{or ethylene/-copolymer systems (Fig. 1).Changes in the phase behaviour may normally be

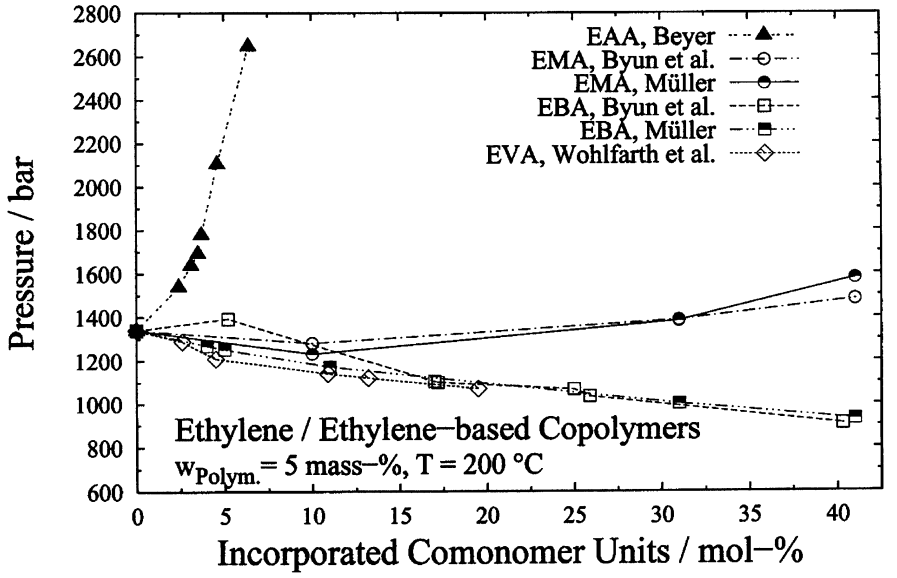

Fig. 1. Cloud point curves (isotherm/isopleth) for systems of ethylene/ethylene-based copolymers dependent on the co-monorner type and -content in the copolymer. Results for EAA obtained in this work are compared with results of Byun [6] and Müller [7] for EMA and EBA and Wohlfarth [8] for EVAc. The polymer concentration is fixed at 5 Ma.-%, the temperature at 200 °C.

attributed to either favourable or unfavourable intermolecular forces between mixing partners or changes in the free volume triggered by the incorporation of a co-monomer unit. The fundamentals of the phase behaviour of strongly asymmetric mixtures like the ones treated in this report are discussed elsewhere [4, 5].

A sharp increase in de-mixing pressure can be observed for systems of -ethylene/poly(ethylene-co-acrylic acid) (EAA) compared to the ethylene/-polyethylene system due to the acrylic acid unit's tendency to self-associate (dimerization) [9-13]. On the other hand, for systems of ethylene/-poly(ethylene-co-vinyl acetate) (EVA), a steady decrease of the cloud point curve has been reported by Wohlfarth et al. investigating EV A copolymers with VA contents from 7.5 mass-% up to 42.7 mass-% (or 2.6 mol-% up to 19.5 mol-%, respectively) [8], which can be attributed to favourable interactions between ethylene molecules and vinyl acetate repeat units as well as steric hindrance of the attachment of likewise polymer chains due to the existence of comparably large co-monomer units. However, Folie et al. also reporting decreasing de-mixing pressures while varying the co-monomer content in the polymer backbone from 0 to 27.5 mass-% VA, found a steep increase in cloud point pressure for the sys-

tem with EVA_{58} compared to the system with $EVA_{27.5}$ [14]. For the latter polymer with a polymer fraction of 15 mass-% and a temperature of 160 °C, the observed cloud point is located some 500 bar below the cloud point exhibited by the system with EVA_{58} (approx. 1250 bar and approx. 1750 bar, respectively). Folie et al. explain this behaviour with the occurrence of strong polar interactions between the polymer molecules which eventually override interactions between the highly quadrupolar ethylene molecules and the polar VA repeat units for high contents of incorporated VA. Folie's data could not be included in Fig. 1 as only data for a polymer mass fraction of 5% in the mixture have been considered for this plot.

Acrylic acid repeat units tend to establish intra-molecular and likewise inter-molecular hydrogen bonds (dimerization), thus shifting the de-mixing pressures required to higher values even if the acrylic acid content in the polymer backbone is relatively low (Fig. 1).

Owing to the high pressures needed to operate in a single phase region dealing with EAA-copolymers, it is economically and technically desirable to lower the pressures required by the addition of inert co-solvents capable of both establishing polar interactions with the co-monomer in the polymer chain and raising the density of the overall solvent mixture.

In this work, phase equilibrium data (cloud points) have been investigated for (quasi)binary and (quasi)ternary mixtures of ethylene/ethylene-co-acrylic acid copolymer (EAA) and ethylene/co-solvent/ethylene-co-acrylic acid copolymer, respectively.

As co-solvent model substances for lowering the de-mixing pressure, we have chosen ethyl acetate (EA) as a polar co-solvent and ethanol (EGH) and octanoic acid (GA) as both polar and associating co-solvents. In order to decouple co-solvency effects attributed merely to the increase in density triggered by the incorporation of a liquid co-solvent from those deriving from the co-solvent's ability to establish favourable interactions with the repeat units in the polymer chain, the following non-polar substances with comparable molecule size and *pvT* -behaviour have been employed as well: n- heptane, iso-octane and n-decane.

A number of studies dealing with the phase behaviour of ethylene/poly-(ethylene-co-(alkyl) acrylate) systems have been published showing that the incorporation of methyl acrylate in the polymer backbone (EMA) will decrease the de-mixing pressures observed until a co-monomer content of approx. 20 mol-% is reached [6, 7, 15, 16], Fig. 1. For higher contents of methyl acrylate, a rise of the experimental cloud point curve was observed, exceeding that observed for the ethylene/LDPE system. It was reported that pure poly(methyl acrylate) (PMA) could not be solved in ethylene up to 250 °C and 2500 bar [15]. Quite a different phase behaviour was observed for comparable mixtures with poly(ethylene-co-butyl acrylate) (EBA): adding butyl acrylate repeat units to the

backbone of the polymer continuously lowers the experimental cloud point curve. Pure poly(butyl acrylate) (PBA) readily dissolves in ethylene at pressures below 800 bar over a temperature range of 65 °C to 175 °C [6, 15]. A data point for pure PBA is not shown in Fig. 1 as no de-mixing pressure value is reported for 200 °C. However, due to the low temperature dependence of the ethylene/PBA cloud point curve reported by Byun et al., an estimated value of about 760 bar for 200 °C is expected.

In order to further understand and segregate the effect of alkyl acrylate tails of different length on the phase behaviour and close the gap of data published hitherto, the second aim of this study was to present cloud point data for systems of ethylene/poly(ethylene-co-ethyl acrylate) (EEA) and ethylene/poly(ethylene-co-propyl acrylate) (EPA), covering a broad range of copolymer composition. To the best of our knowledge, suitable EEA and EPA samples are not yet commercially available. Therefore, all EEA and EPA copolymers had to be synthesized in a laboratory scale continuous high pressure polymerization reactor in a joint effort with the Institute for Physical Chemistry at the University of Göttingen, Germany. Here, no attempt has been made to link de-mixing behaviour to different polymer molecular mass (all obtained mass average molecular mass numbers are found to be in a range from 72-258 kg/mol, s. Tables 1- 3) or different conditions of polymer synthesis but solely to different co-monomer concentration in the polymer backbone.

The knowledge of coexistence data, i.e. the exact composition of coexisting phases below the cloud point, is a fundamental prerequisite for designing phase equilibrium calculation models. After redesigning the apparatus used in this project in order to obtain more reliable coexistence data, several binary and quasi-binary analytical experiments have been conducted which will be presented shortly.

In addition, calculations have been performed within this project to model the experimental data obtained with up-to-date equations of state. The performance of earlier attempts to model the phase behaviour of highly asymmetric mixtures, like the Free-Volume-Theory, has been compared to the performance of lately developed Equations of State (EOS), like the Statistical Associating Fluid Theory (SAFT) and the Perturbed-Chain-SAFT-EOS. Representative results are displayed concluding this report.

Part of the work presented in this report has already been published in Helvetica Chimica Acta [13].

2. EXPERIMENTAL

2.1. Method

Cloud point data were collected using a high pressure variable volume cell made of an nonmagnetic nickel alloy (material code 2.4969). The cell has a length of 330 mm, an outer diameter of 85 mm and an inner diameter of 20 mm. Its working volume of -45 cm^3 is determined by calibration runs with CO_2. The cell is equipped with a steel bellows for volume (pressure) regulation, a sapphire window and an optical system for monitoring the phase behaviour. Pressure generation is accomplished by transferring water into the bellows with a syringe press. Cloud points were generally obtained starting with the highest temperature and lowering the temperature for the determination of the next cloud point. However, points were also taken while heating up the system to be able to rule out mutations due to thermal degradation or unintentional polymerization processes. For details of the procedure used to collect synthetic cloud point data, the reader is directed to [7]. For collecting samples from coexisting phases, the apparatus was redesigned with a longer window stamp. It can be pivoted from horizontal to vertical position. The pressure is lowered to the desired level at which sample taking will be commenced. The emerging light and heavy phases are allowed to de-mix completely within a time span of approx. 45 minutes. Samples are taken through two heated valves and heated tubing into thin-walled sample collecting vessels. The upper valve is designated to collect the light phase (Sol), the lower valve for collecting the heavy phase (Gel). The composition of the phases is determined by differential weighing, freezing the vessels in liquid nitrogen and removing the gaseous component under vacuum while defrosting.

2.2. Materials

The polymers examined in this study were pure low density polyethylene (LDPE) and ethylene-based random copolymers with 6, 7.5, 8, 9, 11 and 15 mass-% acrylic acid content (EAA_6, $EAA_{7.5}$, EAA_8, EAA_9, EAA_{11}, EAA_{15}) in the polymer backbone, respectively. All co-polymers are labeled according to the mass-% of co-monomer incorporated. Out of these, only the copolymers EAA_6, $EAA_{7.5}$ and EAA_9 were employed for the co-solvent studies. Data for LDPE (which also applies for the comparative experiments with EEA- and EPA-copolymers) and the AA-copolymers are listed in Table 1. The EAA-copolymers were kindly donated by EXXON Co., the LDPE was donated by BASF AG. On the EAA and LDPE polymer samples, Gel Permeation Chromatography was run against LDPE standards with kind support of BASF AG. Acrylic acid repeat units were turned into ester units first to avoid interaction with the GPC column. All co-solvents were purchased and used as received. Ethylene (purity 3.4) was donated by BASF AG and was used as received.

Table 1
Available data for the EAA-copolymers examined. The molecular mass data was collected by high temperature GPC against LDPE-standards, the composition data are according to manufacturer's specification.

Polymer	AA content [mass-%]	AA content [mol-%]	M_n [g/mol]	M_w [g/mol]	M_w/M_n [-]
LDPE	0	0	19235	164664	8.6
EAA_6	6.0	2.4	22713	258214	11.4
$EAA_{7.5}$	7.5	3.1	19932	235146	11.8
EAA_8	8.0	3.5	-	-	-
EAA_9	9.0	3.7	23443	227427	9.7
EAA_{11}	11.0	4.6	23730	205024	8.6
EAA_{15}	15.0	6.4	-	-	-

The other polymers examined in this study were ethylene-based random copolymers (EEA) with 4.4, 9.0, 13.3, 18.6, 28.9, 34.7 and 34.8 mol-% ethyl acrylate content in the polymer backbone, respectively, and pure poly(ethyl acrylate) (Table 2). The ethylene-co-propyl acrylate polymers examined contained 2.6, 4.3, 9.1, 14.3, 18.9, 24.2, 31.2 and 33.7 mol-% propyl acrylate in the polymer backbone, respectively, and pure poly(propyl acrylate). Data for these polymers are listed in Table 3. The LDPE was the same as above. PEA and PPA were purchased from SCIENTIFIC POLYMER PRODUCTS CO.. Since these two homo-polymers were supplied in a toluene solution, the sample was placed under vacuum for about 50 hours while slowly stirring with a magnetic stirrer and a stir bar placed inside the vial. The vacuum was kept until no more bubble formation could be observed.

All EEA and EPA copolymer samples were synthesized in the laboratories of the Institute for Physical Chemistry at the University of Göttingen using a laboratory scale continuous high pressure polymerization plant which is described in detail elsewhere [17, 18].

For determining the gel permeation chromatography results shown in Table 2 and 3, polymer samples were solved in tetra-hydrofurane at 30 °C. GPC was run against polystyrene standards in the laboratories of the Institute for Physical Chemistry, University of Göttingen.

To all systems with polymers containing acrylate monomer units, hydroquinone (RIEDEL-DE-HAËN CO., concentration 0.5% of the ethylene mass in the system [19]) was added as inhibitor. For the ethylene/LDPE and ethylene/EAA systems, 2,6-di-tert-butyl-p-cresol was used as inhibitor .

Table 2
Available data for the EEA-copolymers examined. The molecular mass data was collected by low temperature GPC against PS-standards, the composition data was collected using IR-spectroscopy. (For LDPE high temperature GPC against LDPE standards, for PEA (manufacturer's specification).

Polymer	EA content [mass-%]	EA content [mol-%]	M_n [g/mol]	M_w [g/mol]	M_w/M_n [-]
LDPE	0	0	19235	164664	8.6
$EEA_{14.1}$	14.1	4.4	-	-	-
$EEA_{26.1}$	26.1	9.0	-	-	-
$EEA_{35.4}$	35.4	13.3	36670	71950	2.0
$EEA_{44.9}$	44.9	18.6	44540	91410	2.1
$EEA_{59.2}$	59.2	28.9	-	-	-
$EEA_{65.5}$	65.5	34.7	64570	117900	1.8
$EEA_{65.6}$	65.6	34.8	46850	156460	3.3
PEA	100	100	29400	123000	4.2

Table 3
Available data for the EPA-copolymers examined. The molecular mass data was collected by low temperature GPC against PMMA-standards, the composition data was collected using IR-spectroscopy. (For LDPE high temperature GPC against LDPE standards, for PPA manufacturer's specification).

Polymer	PA content [mass-%]	PA content [mol-%]	M_n [g/mol]	M_w [g/mol]	M_w/M_n [-]
LDPE	0	0	19235	164664	8.6
$EPA_{9.8}$	9.8	2.6	-	-	-
$EPA_{15.5}$	15.5	4.3	-	-	-
EPA_{29}	29.0	9.1	-	-	-
$EPA_{40.4}$	40.4	14.3	46740	91714	2.0
$EPA_{48.7}$	48.7	18.9	54202	112170	2.1
$EPA_{56.5}$	56.5	24.2	50000	132800	2.7
$EPA_{64.9}$	64.9	31.3	78400	128600	1.6
$EPA_{67.4}$	67.4	33.7	64600	153800	2.4
PPA	100	100	-	≈140000	-

3. RESULTS

3.1. Synthetic Experiments

In Fig. 2, de-mixing (cloud point) curves for binary mixtures of 5 mass-% polymer in ethylene are presented. Compared to the results for pure polyethylene, the de mixing pressures are shifted to much higher values by acrylic acid repeat units in the backbone of the polymer .

For the polymer containing only 6 mass-% of acrylic acid at 150 °C, the cloud point is shifted up by approx. 600 bar. For EAA_{11}, a shift of this magnitude already takes place at 200 °C. The intermolecular forces accounting for this type of phase behaviour vary as a function of 1/T.This explains the high sensitivity of the de-mixing pressures in the lower temperature region [20] .

In Fig. 3, the impact of the addition of a small amount of co-solvent on the phase behaviour is shown. For these experiments, 5 mass- % of the co-solvents were added to the mixture of ethylene and EAA_6. It can be seen that similar results with only slight depression of the cloud point curve were obtained for the three nonpolar co-solvents and the polar substance ethyl acetate.

For the nonpolar co-solvents, the cloud point pressure could be depressed by about 45 to 150 bar over the whole temperature range. Compared to the other two substances, iso-octane at lower temperatures shows slightly better co-solvent behaviour at lower temperatures. While acting very similarly at higher temperatures, ethyl acetate (EA) can act as a better co-solvent at lower temperatures due to its polar nature.

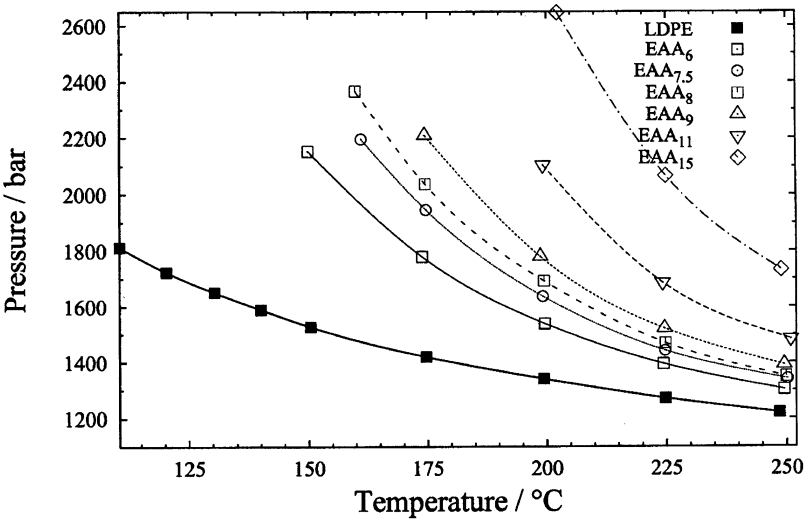

Fig. 2. Cloud point curves for quasi-binary systems of ethylene and EAA copolymers [13]. EAA mass fraction percentage of polymer mass is given as subscript. The polymer concentration is fixed at 5 mass-%.

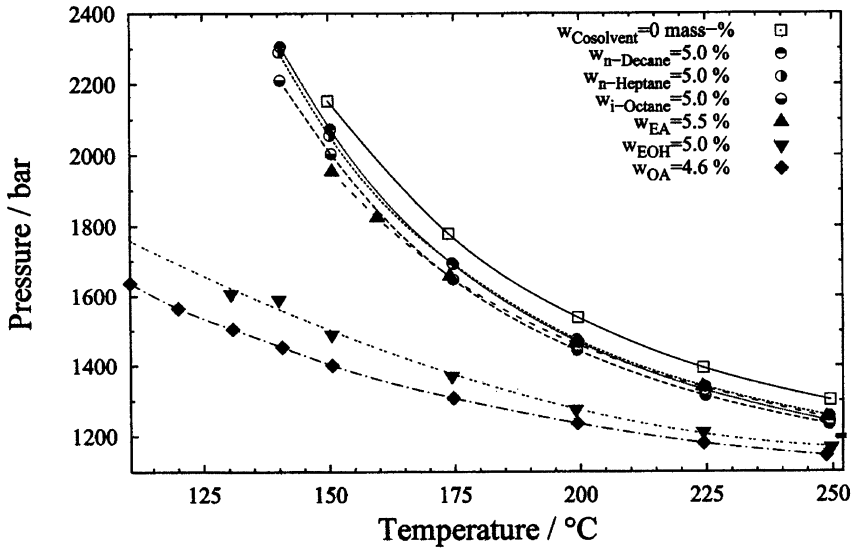

Fig. 3. Cloud point curves for quasi-ternary systems ofethylene/≈5% co-solvent/EAA_6 [13]. *w* is the co-solvent mass fraction in the system. The polymer concentration is fixed at 5 mass-%.

A significantly different performance could be observed for both, ethanol (EOH) and octanoic acid (OA). Especially at lower temperatures, both substances manage to lower the de-mixing pressure by several hundred bar, e.g. for 150 °C, the addition of 5 mass- % of octanoic acid to the system lowers the cloud point pressure by more than 700 bar. Compared to ethanol, octanoic acid acts as the better co-solvent here. This can be attributed to its carboxyl group and its higher molecular weight.

Fig. 4 shows the results obtained for the addition of 40 mass-% of co-solvent. For such a high mass fraction of dense (compared to ethylene) co-solvent, all systems shown exhibit cloud points lowered by at least 360 bar over the whole temperature range.

In these series, ethyl acetate even acts as a less efficient co-solvent than the nonpolar agents for higher temperatures. In the lower temperature region this effect is reversed showing ethyl acetate to be the superior co-solvent.

Octanoic acid once again shows a very powerful co-solvent behaviour over the entire temperature range. The cloud point curve is virtually independent of temperature, the cloud point pressure for 150 °C for instance is depressed by over 1400 bar .

However, quite a different phase behaviour was observed for ethanol. For higher values of temperature, the cloud points are located approx. 100 bar below the points observed for addition of n-heptane or ethyl acetate. For temperatures below 175 °C, though, the co-solvent power seems to decrease dramatically. For

140 °C, the de-mixing pressures for ethanol and n-heptane addition become nearly equal and are located approx. 750 bar above the corresponding value for octanoic acid. This phase behaviour can be attributed to strong self-association between ethanol molecules due to their excess concentration compared to the number of acrylic acid sites available in the polymer backbone.

Even though the occurrence of self-association for high concentrations of octanoic acid might be expected, too, we have not been able to observe this phenomenon for an octanoic acid mass fraction of up to 65 mass-%. Furthermore, as expected, no rising cloud point pressures could be observed for an addition of even 70 mass-% of ethyl acetate.

Our findings are consistent with the results published by McHugh and coworkers for the addition of ethanol to a system of butane and EAA-copolymer [21]. In that publication, a sharp rise in de-mixing pressure has been observed for adding 55.5 mass-% of ethanol to a mixture of butane and 5 mass-% of $EAA_{9.4}$ compared to adding 15.6 mass-% of ethanol. Wind reports continuously decreasing cloud points for adding acrylic acid as co-monomer to systems of ethylene and 13.5 mass-% of either EAA_3, EAA_6 or $EAA_{7.3}$ which is consistent with our results for adding octanoic acid to such systems. However, the highest acrylic acid content examined by Wind was 13.1 mass-%.

Fig. 5 and 6 show results obtained for quasi-binary systems of ethylene/EEA. All cloud point curves were taken with a polymer mass fraction of 5%.

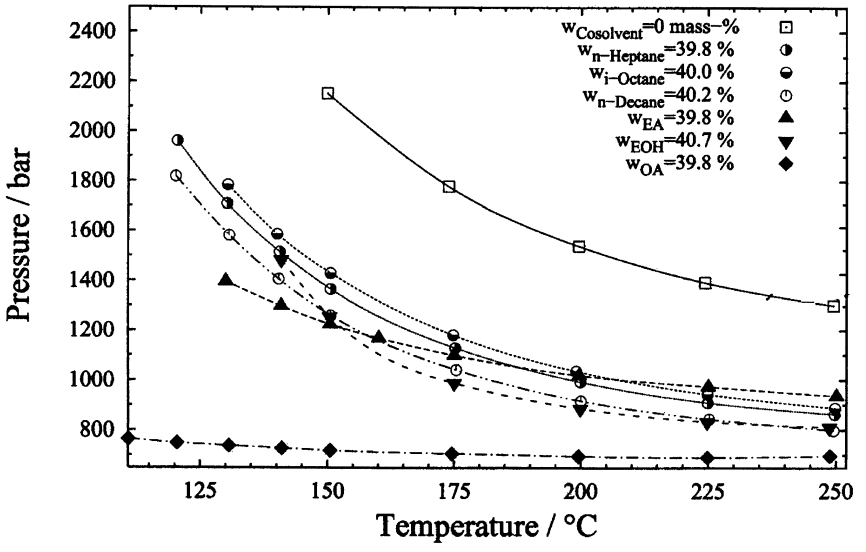

Fig. 4. Cloud point curves for quasi-ternary systems of ethylene/≈40% co-solvent/EAA_6 [13]. *W*: co-solvent mass fraction in the system. The polymer concentration is fixed at 5 mass-%.

For comparison, also the results for ethylene/LDPE and ethylene/PEA are included as the limiting ones. For better resolution, results for the systems with a co-monomer content up to 18.6 mol-% ($EEA_{44.9}$) in the polymer backbone are given in Fig. 5, results for higher co-monomer contents are given in Fig. 6.

In Fig. 5 it can be seen that the incorporation of small amounts of EA (4.4 mol-%/14.1 mass-%)) in the polymer backbone results in a decrease in de-mixing pressure of about 60 bar at 250 °C and about 250 bar at 120 °C compared to the experimental curve with LDPE. Increasing the co-monomer content to 9.0 mol-%/26.1 mass-% yields another pressure drop between about 150 bar and 250 bar, respectively. Comparable to methyl acrylate, butyl acrylate and vinyl acetate, the incorporation of small amounts of polar co-monomer units in the otherwise non-polar polyethylene chain seems to favour quadrupolar-polar ethylene-co-monomer interactions over likewise interactions between the polymer chains (intra- and/ or intermolecular) or the ethylene molecules (intermolecular) However, when increasing the EA content to values beyond about 26.1 mass-%, a rise of de-mixing pressures was observed. For both $EEA_{35.4}$ and $EEA_{44.9}$, similar values for the cloud point curve were determined. Both curves are located 40-60 bar above the one for $EEA_{26.1}$. This trend is amplified by further increasing the EA fraction in the polymer backbone (Fig. 6). Note that very similar de-mixing pressure values were found for 250 °C and varying the co-monomer content from 35.4 up to 65.6 mass-%. However, for $EEA_{65.6}$, the cloud point pressure determined for 120 °C is located about 220 bar above the corresponding value for $EEA_{35.4}$.

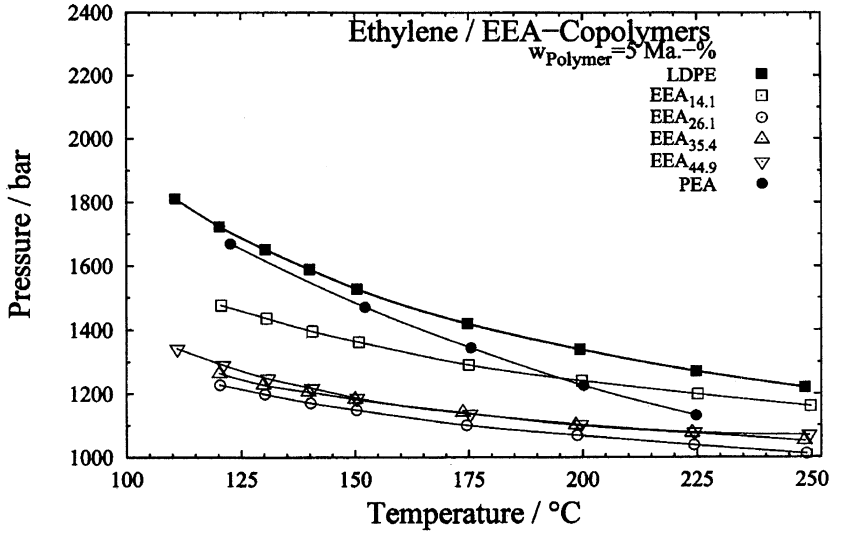

Fig. 5. Cloud point curves (isopleth) for systems of ethylene/EEA-copolymers for low co-monomer content in the polymer backbone. The polymer concentration is fixed at 5 mass-%.

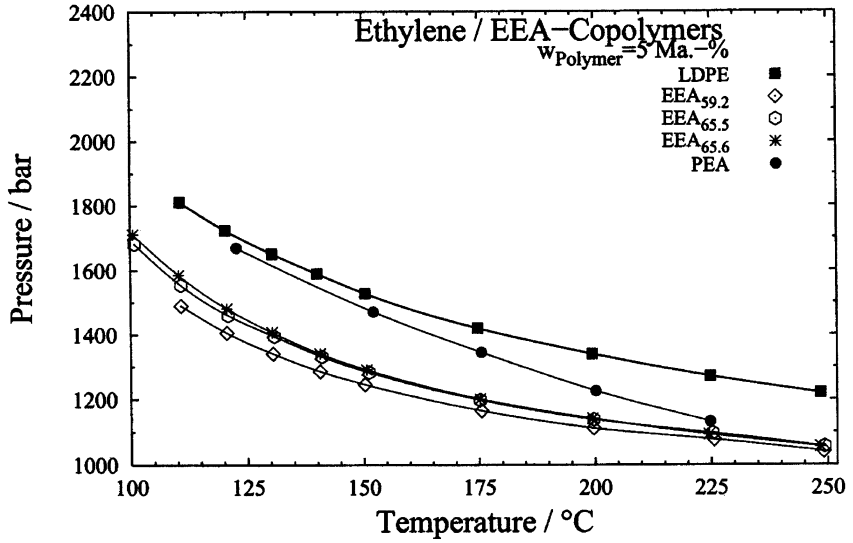

Fig. 6. Cloud point curves (isopleth) for systems of ethylene/EEA-copolymers for higher co-monomer content in the polymer backbone. The polymer concentration is fixed at 5 mass-%.

Taking into account that polar interactions vary as a function of $1/T$, it can be concluded that for higher EA contents the changes in the potential to establish polar interactions by incorporating polar ethyl acrylate in the polyethylene chain overrides the changes in the free volume which account for differences in phase behaviour in the high temperature region.

Being located between the curves for $EEA_{14.1}$ and $EEA_{35.4}$/$EEA_{44.9}$ for high temperatures, the obtained cloud point curve for the ethylene/PEA system intersects the $EEA_{14.1}$ curve at about 195 °C to assume values very similar to the LDPE system for low temperatures. Here, comparable to the homo-polymeric system with LDPE, the homogeneity of the polymer favours intermolecular attachment of polymer chains which hinders solvent molecules from enclosing the polymeric chains. The ethyl acrylate branch, although being strongly polar, seems to be too short to alter the mechanism of different polymer chains attaching.

Comparing the experimental data for $EEA_{65.5}$ and $EEA_{65.6}$, two co-polymers with only slightly differing EA content, two conclusions can be drawn: first, obtaining virtually identical cloud point curves for the two co-polymers confirms the reliability of the experimental procedure. Second, the impact of the co-monomer concentration in the polymer backbone on the phase behaviour clearly overrides that of different polymer molecular weight ($EEA_{65.5}$:

M_w=117900 g/mol, $EEA_{65.6}$: M_w=156460 g/mol, Table 2) for these systems which confirms results by de Loos for LDPE [22]. A cloud point curve for the ethylene/PEA (5 mass-%) system has been reported by Lora et al. [15] but could not be reproduced in this work without substantial deviations. For 225 °C, the de-mixing pressure observed in this work is about 125 bar above Lora 's data, for 120 °C, the difference is about 280 bar. Such large differences in experimental data can not be explained with different polymer properties, especially as the PEA sample Lora et al. used shows a very similar molecular weight (M_w=119300 g/mol (Lora), Mw=123000 g/mol (this work)) compared to the PEA sample used in this study. The reasons for the deviations observed could not be clarified conclusively up to date.

In Fig. 7 cloud point data for the poly(ethylene-co-propyl acrylate) co-polymers examined are presented. The plot includes the ethylene/LDPE system already displayed in previous figures as well as the homo-polymeric system ethylene/poly(propyl acrylate).

The de-mixing curve for $EPA_{9.8}$ is virtually identical with the LDPE curve in the higher temperature region. For lower temperatures, the curve for EP $A_{9.8}$ is located slightly below (the difference is 75 bar at 120 °C) , which may be attributed to augmented quadrupole-dipole interaction between the ethylene and the dipolar co-monomer .

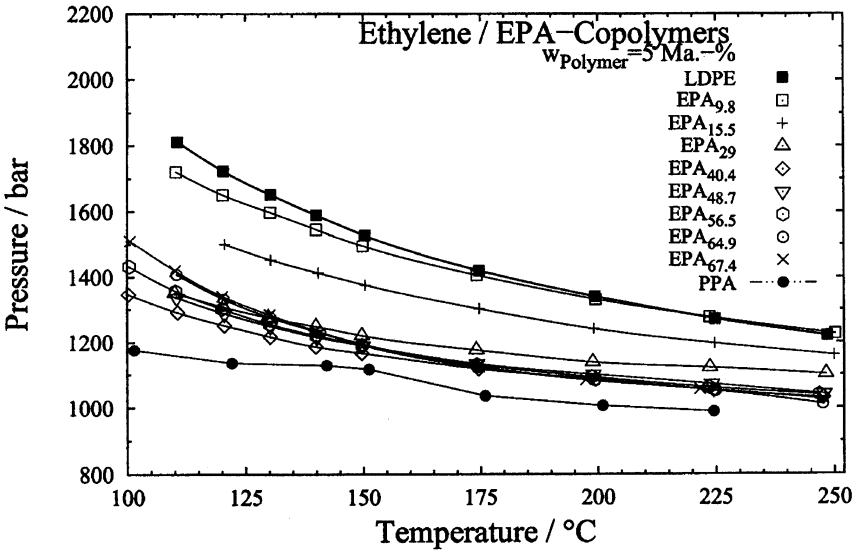

Fig. 7. Cloud point curves (isopleth) for systems of ethylene/EPA-copolymers. The polymer concentration is fixed at 5 mass-%.

When the PA-content is raised to 15.5 mass-% (4.3 mol-%), a further pressure drop is observed over the whole temperature range under investigation.

In the region of temperature above about 150 °C the cloud point curve for EPA_{29} is located above the very similar curves for $EPA_{40.4}$ to $EPA_{67.4}$. For lower temperature, though, this similarity is annulled; rising de-mixing pressures are observed for higher co-monomer content.

Unlike the de-mixing curve for PEA in Fig. 5 and 6, the curve for poly-(propyl acrylate) (PPA) is located well below those observed for both LDPE and all EPA co-polymers available. Here, compared to the other homo-polymer PEA, two factors apply: first, the impact of the polar acrylate group is weakened by the longer alkyl branch, second, this longer alkyl branch hinders attachment of likewise polymer chains thus favouring attachment of solvent molecules.

Hence, unlike the observations made with EEA-copolymers, no minimum in de-mixing pressure with rising co-monomer content has been observed at the higher temperatures (200 °C) here, but a steady decrease in cloud point pressure.

With the experimental results obtained in this study, Fig. 1 can be amended in order to further discuss the de-mixing behaviour of ethylene/poly(ethylene-co-(alkyl) acrylate) systems depending on the co-monomer alkyl tail length (Fig. 8).

Note that, unlike in Fig. 1, the axis of the abscissa comprises a co-monomer content range of 0 to 100 mol-%. Data for EEA and EPA collected in this

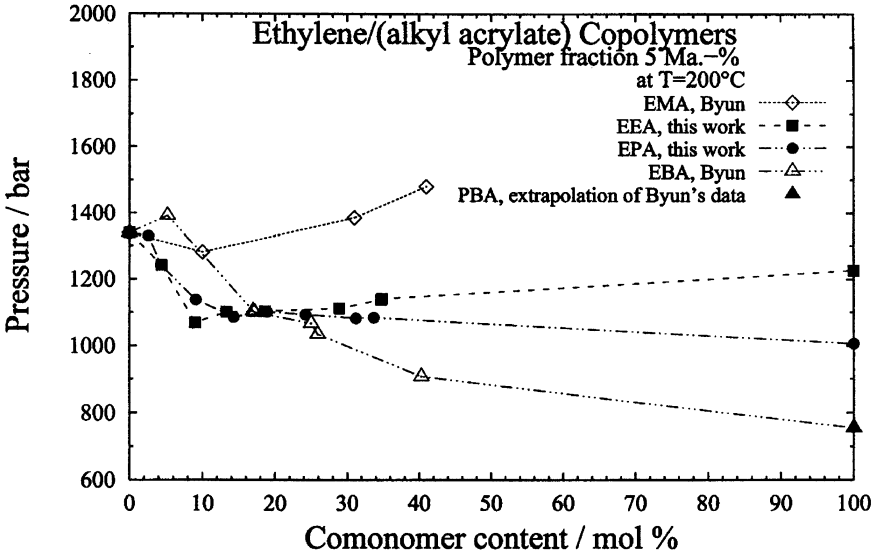

Fig. 8. Cloud point curves (isotherm/isopleth) for systems of ethylene/ethylene-based (alkyl acrylate) copolymers dependent on the co-monomer type and -content in the co-polymer. Own results for EEA and EPA are compared to results by Byun [6] for EMA and EBA. The polymer concentration is fixed at 5 mass-%, the temperature at 200 °C.

project is being compared to data by Byun [6] for both EMA and EBA. Here, the cloud point pressure for systems of ethylene and 5 mass-% of ethylene-based alkyl acrylate copolymers is displayed dependent on the co-monomer content in the polymer backbone for a temperature of 200 °C .

A de-mixing point for pure PMA in ethylene is not available in literature as no successful homogenization of this system could be accomplished up to 250 °C and 2500 bar [23]. Byun [6] communicates a de-mixing curve for ethylene/PBA in a temperature range of about 50 °C to 184 °C which was extrapolated to 200 °C for this plot which is felt to be tolerable due to the small temperature dependence of the de-mixing curve reported by Byun.

As indicated before, a pronounced minimum in pressure can be observed for EEA-copolymers at about 10 mol-% co-monomer content. Unlike this, no minimum but merely a flattening of the curve can be seen for EP A in the region of about 15 mol-% co-monomer content, with the curve steadily decreasing for higher co-monomer content.

3.2 Analytical Experiments

In this chapter, some of the analytical experiments undertaken in this study are presented. After redesigning the apparatus with a longer window stamp being designed to locate the phase boundary between two coexisting phases on a higher level between the two sample collection ports, the setup for collecting samples (heated tubing and valves, temperature control etc.) was taken into operation.

First coexistence data were collected using the binary system CO_2/squalane. For the first analytical experiment, a mixture of CO_2 and 30.3 mass-% of squalane was prepared in order to reproduce literature data by Liphard [24]. At 80 °C and pressures of 351 bar and 311 bar, respectively, samples were taken from coexisting phases and analyzed gravimetrically. For the higher pressure, the composition of the light phase could be reproduced with negligible deviations compared to Liphard, the concentration of the heavy 1 phase with a deviation of 6 mass-%. For the lower pressure, the composition of the heavy phase could be reproduced very exactly, the composition of the light phase with a deviation of about +5 mass- %.

In a second experiment with an initial concentration of 15.0 mass-% squalane and an experimental pressure of 301 bar (yet still at 80 °C) , the composition of the light phase could once again be reproduced exactly, while the composition of the heavy phase could be determined with larger differences of about 8 mass-%. With ethylene/LDPE, several experiments with different initial concentration of the mixture were undertaken. For an initial concentration of about 11.5 mass-% LDPE in ethylene and 200 °C, literature data by Spahl [25] were available for comparison. In his experiments, Spahl used an LDPE sample

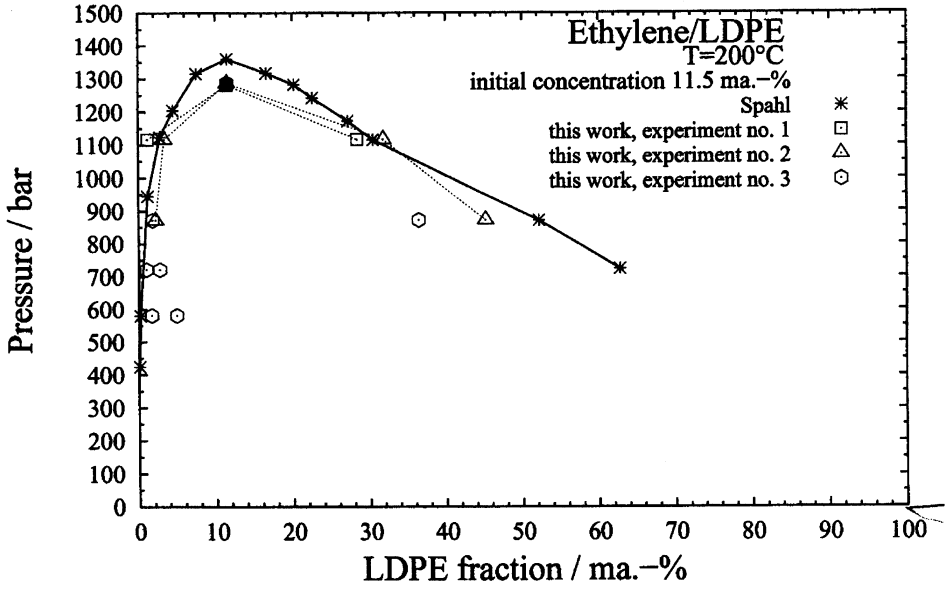

Fig. 9. Coexistence data for the quasi-binary system ethylene/LDPE at T=200 °C acquired with an initial concentration of 11.5 mass-% polymer in the system; own cloud point data plotted with full symbols; comparison to data by Spahl [25].

with M_w=192000g/mol, and M_n=19500 g/mol. The LDPE batch used in this work has an M_w=164700g/mol and M_n=19200g/mol (Table 1).

Three different experiments were run with different levels of pressure at which sample collecting was undertaken and with different number of samples taken (Fig. 9). Both sets of first samples taken at a pressure of about 1100 bar in experiment 1 and 2 showed very good reproduction of the literature data. In the second repetition of sample collecting in experiment 2, the LDPE content in the heavy phase was about 7 mass-% too low compared to Spahl's data. In the third experiment, sample collecting was not commenced until a pressure of about 900 bar was reached. Here, already the first sample of the heavy phase is faulty, for the second and third sample, practically pure light phase was collected also through the lower port which is dedicated to collect the heavy phase. Obviously, for low pressure or rising numbers of samples taken, the phase boundary is lowered below this port .

To avoid the dilution of the heavy phase by the lowering of the phase boundary, another experiment was run with an initial concentration of 30.0 mass-% of LDPE in ethylene (Fig. 10). The coexistence data obtained in this experiment could be compared to literature data by Spahl for an initial concen-

tration of 25.3 mass-% [25]. Here, quite the opposite effect could be observed: for the first run of sampling at a high pressure level (compared to the cloud point) and still a large quantity of LDPE in the system, the volume oft the heavy phase becomes so large that the phase boundary transcends the upper sampling port; the result for the light phase is obviously faulty. For the heavy phase in sampling 1 and both phases in sampling 2, good reproduction of the literature data was achieved. In the third and last sample drawing, again, the heavy phase was slightly diluted.

Concluding, it can be established that the reliability of the sample-drawing and analysis could be proved with the system CO2/squalane. For quasi-binary systems, reliable cloud point data also could be collected. Due to the limited size of the apparatus used and the small distance between the sample-drawing ports, the analytical procedure is limited in the size of the pressure range examined, the number of samples drawn and the initial concentration of the system investigated.

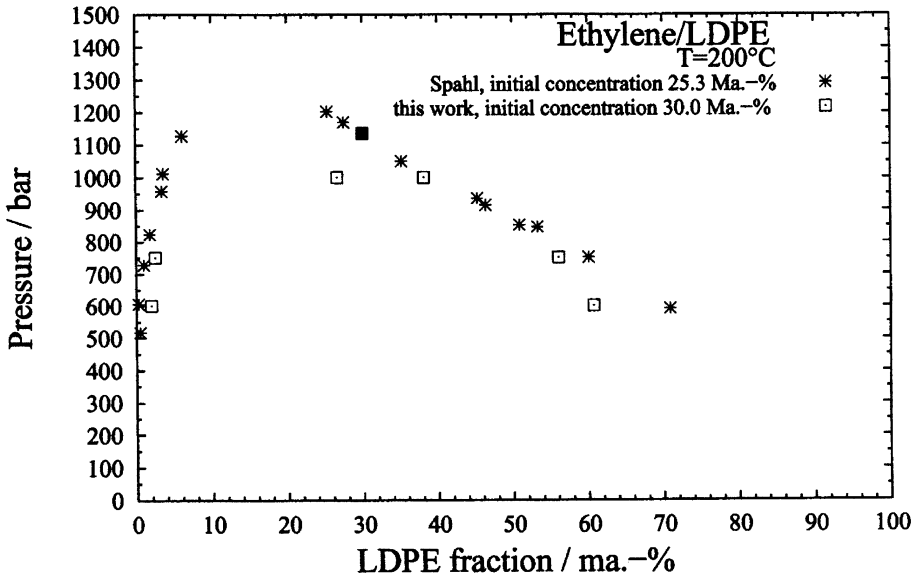

Fig. 10. Coexistence data for the quasi-binary system ethylene/LDPE at T=200 °C acquired with an initial concentration of 30.0 mass-% polymer in the system; own cloud point data plotted with full symbol; comparison to data by Spahl for an initial concentration of 25.3 mass-% [25].

4. MODELING

In this project, the experimental phase equilibrium data obtained was also modeled applying up-to-date equations of state. The performance of earlier attempts to model the phase behaviour of highly asymmetric mixtures, like the Free-Volume-Theory by Flory et al. [26, 27] is compared to the performance of lately developed EOS, like the Statistical Associating Fluid Theory [28-30] by Radosz et al.. The SAFT-EOS takes into account strong intermolecular forces like association, thus it should be applicable for the acrylic acid-copolymers and associating co-solvents used in this study. The Perturbed-Chain-SAFT is a further development of the SAFT -EOS by Sadowski and Gross [31, 32] taking into account that polymeric molecules are rather chains than spheres.

Due to restricted space, the reader is directed to the literature cited above for the theoretical background of the equations, mixing rules and parameters involved in the phase equilibrium models presented here. To exemplify, two systems modeled in this project will be shortly referred to in this report: ethylene/LDPE as a rather simple system and ethylene/EAA_6 (or ethylene/$EAA_{7.5}$, respectively) (Fig. 2) as a system for which association has to be considered to expect reasonable modeling of the experimental data.

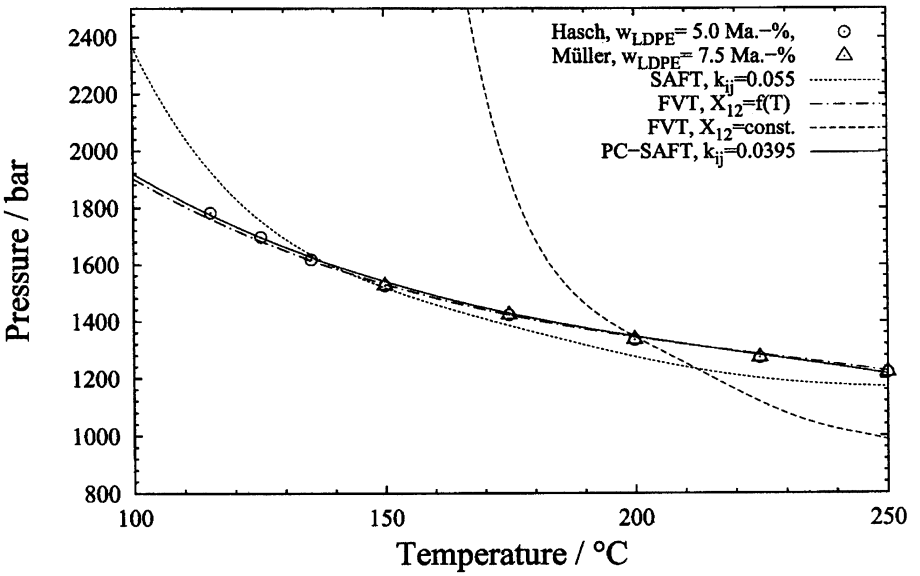

Fig. 11. Modeling results for cloud point data of the system ethylene/LDPE; comparison to experimental results by Müller and Hasch [7, 33].

For the system ethylene/LDPE, data available by Müller and Hasch [7, 33] have been modeled with the FVT, the SAFT- and PC-SAFT equations of state (Fig. 11). The FVT pure component parameters for LDPE were taken from Rodgers [34], temperature-dependent data for ethylene were found in [35] .

For both SAFT and PC-SAFT, the pure component parameters for ethylene were taken from literature [28, 31] .The pure component parameters for the polymer (i.e. m and v or σ, resp.) were attained by extrapolation of the homologous series of n-alkanes. The energy parameter u^0/k was fitted to experimental binary data. Then, the binary interaction parameter k_{ij} was fitted to the experimental data (SAFT and PC-SAFT); the FVT calculations were performed with both, a constant and temperature-dependent binary parameter X_{12}.

First, it can be seen in Fig. 11 that reasonable modeling of the system with FVT can only be achieved with a temperature-dependent interaction parameter X_{12}. The SAFT-EOS with a constant fitted binary interaction parameter k_{ij} reproduces the experimental data satisfactorily with larger deviations in the lower temperature region. The PC-SAFT -EOS, however, shows excellent results in mirroring the experimental data over the whole temperature range with one constant fitted k_{ij}. For the more complex systems examined in this project, modeling with the FVT was abandoned because of the necessity of a temperature-dependence of the binary interaction parameter (already for the simple systems) and because complex interaction like association is not accounted for in the underlying model.

Fig. 12 shows results for modeling the system ethylene/EAA_6 with both, the SAFT- and PC-SAFT-EOS. Due to acrylic acid being present in the polymer backbone, intermolecular association is accounted for by incorporating a respective term in the equation which is identical for both SAFT and PC-SAFT [36]. The number of associating sites (N_{sites}) per molecule can easily be computed knowing the average polymer molecular mass and the co-monomer content in the backbone.

The parameters ε_{AB}/k and v^{AB} describing the association energy for acrylic acid were proposed by McHugh and coworker for the SAFT-EOS [33, 37] and taken over for our calculations. For PC-SAFT, parameters were used which were fitted to pvT-data of pure acrylic acid. For the other pure component parameters the same values were used as for polyethylene

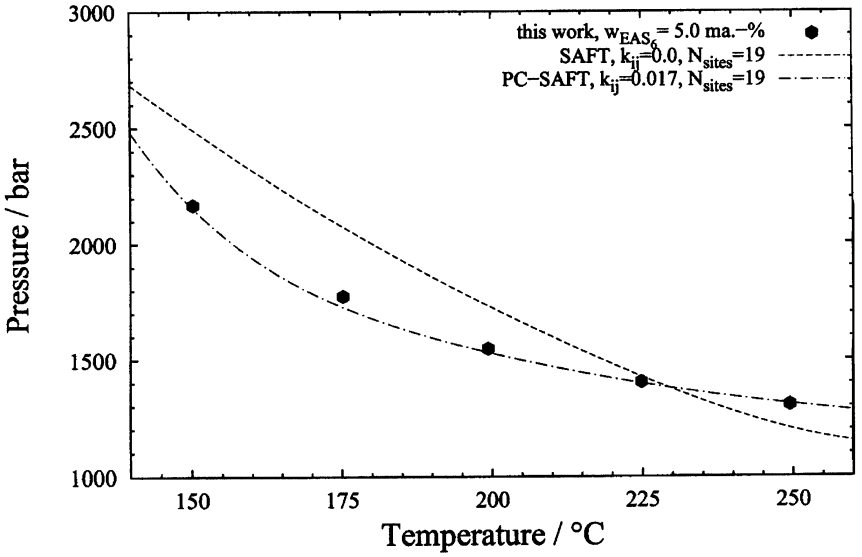

Fig. 12. Modeling results for cloud point data of the system ethylene/EAS_6; comparison to experimental results from this work (see Fig. 2).

because the acrylic acid content in the polymer backbone is very low (for PC-SAFT, the parameter u^0/k was fitted to binary data of the system ethylene/EAA_6).

Again, the reproduction of the experimental data is very good using the PC-SAFT-EOS with a constant, fitted binary interaction parameter (Fig. 12). The modeled curve for the SAFT -EOS with k_{ij}=0 cannot describe the data adequately. The result of tuning the number of associating sites and the value of the binary interaction parameter k_{ij} for the SAFT -EOS is displayed in Fig. 13. In order to improve the reproduction of the experimental data which was obtained for a fixed value of N_{sites} and k_{ij}=0 in Fig. 12 (for ethylene/EAS_6) , both values were varied slightly. That way, the position of the modeled curve could be enhanced significantly. However, opposed to the result obtained for PC-SAFT in Fig. 12, the modeled data show an inflection point.

Concluding the modeling part of the project, it can be stated that non-complex systems can only be modeled satisfactorily with the Free-Volume-Theory by adjusting a temperature-dependent binary interaction parameter. For modeling non-complex systems as well as mixtures with association, the advancement in the PC-SAFT-EOS provides clearly better reproduction of the experimental data.

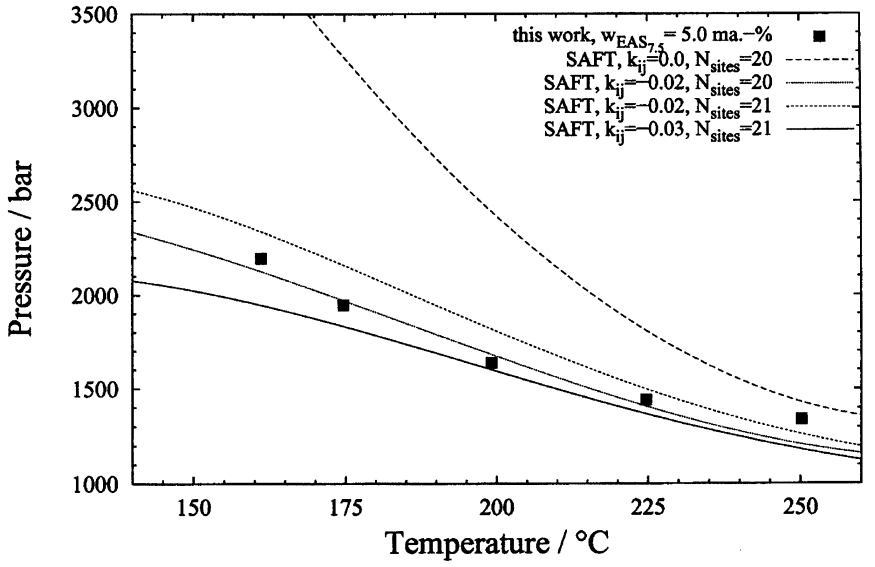

Fig. 13. Modeling results for cloud point data of the system ethylene/$EAS_{7.5}$ with SAFT; comparison to experimental results from this work (see Fig. 2).

5. CONCLUSIONS

In the present study, a high pressure phase equilibrium view cell suitable for both synthetic and analytical measurements was redesigned and taken into operation. A large number of experiments (both synthetic and analytical) on quasi-binary and quasi-ternary systems was conducted.

In mixtures of ethylene and poly(ethylene-co-acrylic) acid copolymers, non-polar but dense co-solvents can performed equally well compared to the polar but non-associating ethyl acetate.

For low temperatures with ethyl acetate or with associating co-solvents over the entire temperature range under investigation, though, the depression of the cloud points measured is remarkably higher. However, at high concentrations and low temperatures, ethanol loses its co-solvent strength due to the occurrence of self-association, even showing an anti-solvent-effect. Over the whole temperature range, octanoic acid acts as a very strong co-solvent in any concentration applied.

By examining the phase behaviour of both poly(ethylene-co-ethyl acrylate) and poly(ethylene-co-propyl acrylate) in ethylene, a major gap in experimental data published up to now for shorter acrylate chains could be closed.

In the analytical section of this work, coexistence data was acquired for both binary and quasi-binary asymmetric systems. The sample analysis proved to work reliably by good reproduction of available literature data, though the sample-drawing is affected by the size of the view cell, limiting the number of samples per run.

In the modeling section, it could be proved that the Perturbed-Chain--SAFT -equation of state showed superior results reproducing the experimental data for more simple systems like ethylene/polyethylene as well as for more complex systems like ethylene/poly(ethylene-co-acrylic acid) compared to the SAFT - equation of state.

ACKNOWLEDGEMENTS

The authors would like to thank Dipl. Chem. H. Latz and Prof. M. Buback, Institute of Physical Chemistry, University of Göttingen, Germany, for the fruitful cooperation synthesizing and examining the EEA- and EPA-copolymers; Dr. O. Müller and Dipl. Chem. H. Latz for preparing the EAA-copolymers for GPC analysis; Dr. D. Lilge, BASF AG, Ludwigshafen, Germany, for performing the GPC analysis for the EAA-copolymers, and Dr. J. Smits, EXXON Co., Machelen, Belgium, for providing the EAA-copolymer samples.

We would like to thank Dipl.-Ing. F. Tumakaka, Dr .-Ing. J. Gross, Prof. W. Arlt and Prof. G. Sadowski for valuable help for the modeling section of this work.

This work was supported by the Deutsche Forschungsgemeinschaft which is gratefully acknowledged.

REFERENCES

[1] G. Luft, Chem.-Ing.-Tech. 51 (1979) 960-969.
[2] A. Echte, Handbuch der Technischen Polymerchemie, VCH, Weinheim, 1993.
[3] Ullmann's encyclopedia of industrial chemistry, 5th Edition, VCH, Weinheim, 1992.
[4] R. Scott, Berichte der Bunsen-Gesellschaft 76 (1972) 296-308.
[5] M. McHugh, V. Krukonis, Supercritical Fluid Extraction, 2nd Edition, Butterworth-Heinemann, Boston, 1994.
[6] H. Byun, B. Hasch, M. Mc Hugh, F .-O. Mahling, M. Busch, M. Buback, Macromolecules 29 (1996) 1625-1632.
[7] C. Müller, Ph.D. thesis, Universitat Karlsruhe (TH) (1996).
[8] C. Wohlfarth, P. Wagner, M. Ratzsch, s. Westmeier, Acta Polymerica 33 (1982) 468-471.
[9] G. Luft, R. Wind, Chem.-Ing.-Tech 64 (1992) 1114-1117.
[10] R. Wind, Ph.D. thesis, TH Darmstadt (1992).
[11] B. Hasch, S.-H. Lee, M. McHugh, Fluid Phase Equilibria 83 (1993) 341-348.
[12] S.-H. Lee, M. McHugh, Polymer 38 (1997) 1317-1322.
[13] C. Beyer, L. Oellrich, Helvetica Chimica Acta 85 (2002) 659-670.
[14] B. Folie, C. Gregg, G. Luft, M. Radosz, Fluid PhaBe Equilibria 120 (1996) 11-37.

[15] M. Lora, F. Rindfleisch, M. McHugh, Journal of Applied Polymer Science 73 (1999) 1979-1991.
[16] B. Hasch, M. Meilchen, S.-H. Lee, M. McHugh, Journal of Polymer Science B 31 (1993) 429-439.
[17] M. Buback, M. Busch, K. Lovis, F .-O. Mahling, Chemie Ingenieur Technik 67 (1995) 1652-1655.
[18] M. Buback, M. Busch, K. Lovis, F. Mahling, Macromol. Chem. Phys. 197 (1996) 303-313.
[19] C. Müller, L. Oellrich, Acta Polymer. 47 (1996) 404-406.
[20] M. LoStracco, S.-H. Lee, M. McHugh, Polymer 35 (1994) 3272-3277.
[21] S.-H. Lee, M. LoStracco, M. McHugh, Macromolecules 29 (1996) 1349-1358.
[22] T. de Loos, Ph.D. thesis, Delft University Press (1981).
[23] B. HaBch, M. Meilchen, S.-H. Lee, M. McHugh, Journal of Polymer Science: Part B: Polymer Physics 30 (1992) 1365-1373.
[24] K. Liphard, G. Schneider, J. Chem. Thermodynamics 7 (1975) 805-814.
[25] R. Spahl, Ph.D. thesis, TH Darmstadt (1981).
[26] P. Flory, R. Orwoll, A. Vrij, Journal of the American Chemical Society 86 (1964) 3507-3514.
[27] P. Flory, R. Orwoll, A. Vrij, Journal American Chemical Society 86 (1964) 3515-3520.
[28] H. Huang, M. Radosz, Ind. Eng. Chem. Res. 29 (1990) 2284-2294.
[29] S. Huang, M. Radosz, Ind. Eng. Chem. Res. 30 (1991) 1994-2005.
[30] S. Huang, M. Radosz, Ind. Eng. Chem. Res. 32 (1993) 762.
[31] J. Gross, G. Sadowski, Ind. Eng. Chem. Res. 40 (2001) 1244-1260.
[32] J. Gross, G. Sadowski, Fluid Phase Equilibria 168 (2000) 183-199.
[33] B. Hasch, Ph.D. thesis, Johns Hopkins University, Baltimore (1994).
[34] P. Rodgers, Journal of Applied Polymer Science 48 (1993) 1061-1080.
[35] D. Bonner, D. Maloney, J. Prausnitz, Ind. Eng. Chem., Process Des. Develop. 13 (1974) 91-95.
[36] W. Chapman, K. Gubbins, G. Jackson, M. Radosz, Ind. Eng. Chem. Res. 29 (1990) 1709-1721.
[37] B. Hasch, M. McHugh, Journal of Polymer Science: Part B: Polymer Physics 33 (1995) 715-723.

Supercritical Fluids as Solvents and Reaction Media
G. Brunner (editor)

Chapter 1.4

Fluid Phase Equilibria of Binary Mixtures with Supercritical Solvents with *in-situ* Concentration Measurements by Raman Spectroscopy

A. Stratmann and G. Schweiger

Laseranwendungstechnik und Messsysteme, Maschinenbau, Ruhr-Universität Bochum, D-44780 Bochum, Germany

Phase equilibria data of the systems ethanol/carbon dioxide, 2-propanol/carbon dioxide and vinylacetic acid/ethylene at temperatures up to T=353 K and pressures up to p=9.6 MPa are presented. The measurements were made by Raman spectroscopy without the extraction of probes from the autoclave. To the authors knowledge it is the first use of Raman spectroscopy for phase equilibria investigations at high pressure with supercritical solvents. As far as available literature data show excellent agreement with our measurements.

1. INTRODUCTION

The knowledge of equilibrium states of binary or multicomponent mixtures is of high interest in chemical engineering, for example in separation processes. Generally, sampling techniques with, e.g., gas chromatographic analysis, are used for concentration measurements. The main limitations of these classical techniques are: possible disturbance of the equilibrium by the extraction of the probe, changes of the probe state between probe extraction and probe analysis, and the time delay between probe extraction and analysis.

Non-invasive spectroscopic methods, such as Raman [1–8] or NIR spectroscopy [9, 10], are free of these problems, but have other limitations. Spectroscopic techniques are difficult even impossible if the phases are not transparent. Effects on the spectra caused by temperature, pressure or molecular interaction can limit the quantitative evaluation of the spectra. Overlapping of the spectra of the individual components can make a quantitative interpretation of the spectra difficult even impossible. The experimental equipment is expansive especially for Raman spectroscopy. Progress in laser technique, light detection and spectroscopic equipment has caused a dramatic cost reduction in the last years. The easy access to powerful computing capacities has nearly eliminated

the problem of spectral overlapping. However, more work is needed for a better understanding and a broader database to quantify the effect of pressure, temperature, and intermolecular interactions on the spectra.

Raman spectroscopy is a well established method for concentration measurements in pure liquids and gases, mostly under ambient temperature and pressure. Raman investigations in mixtures can be found in [11–23], at higher pressure in [24–30], higher temperature in [31–34], higher pressure and temperature in [31], and in mixtures at higher pressure and/or temperature in [35–44]. Raman spectroscopy at very high pressure ($p \approx$ GPa) and covering a large pressure range, mostly treat the influence of the Raman line shape and position but no concentration measurement, are found in [45–62]. No phase equilibria studies of the vapor and liquid state in binary mixtures with supercritical solvents are known to the authors.

At high pressure or elevated temperatures interactions between molecules of the same kind as well as with that of the other component can affect the Raman spectra. Typically the intermolecular interactions cause line broadening and peak shifts in Raman bands. We will show that such effects are negligible for the investigated systems.

Our work is an extension of the phase equilibria investigations at moderate temperature [25] and pressure [32] to higher temperature and pressure with supercritical carbon dioxide and ethylene. First results have been published in [43, 44].

Supercritical carbon dioxide is an important solvent, as shown in e.g. [63–69, 69–85]. Further, it is non toxic, non explosive and inexpensive. These were the reasons to select carbon dioxide as the supercritical solvent. As second component we chose ethanol, a polar solvent, permitted in food industry. It is used as cosolvent together with supercritical carbon dioxide in extraction processes [77, 82]. This binary system was investigated by several authors [65, 66, 77, 86–91] allowing a comparison of our technique with the existing database. As second binary component we chose 2-propanol. 2-propanol is similar to ethanol, particulary the Raman spectra are similar. The limited existing database [75, 77, 88, 92] allowed a quantitative check of the Raman data and made an extension of the investigated equilibria by our technique promising. With supercritical ethylene and vinylacetic acid we investigate a binary system with complex molecules. Here we can show that intermolecular interactions have strong influences to the Raman spectra, but nevertheless quantitative analysis by Raman spectrocopy is possible. Vinylacetic acid and ethylene are used as comonomers in processes of polymerisation. The knowledge of the concentration ratio is necessary in the process reactions. In [93–95] some data for comparison exists.

2. RAMAN THEORY

2.1. Raman Radiant Flux

The radiant flux of the inelastic scattered light at the frequency ν_i can be expressed as

$$\Phi(\nu_i) = \int_V \int_\Omega c\, N_A \frac{\partial \sigma_{\nu_i}}{\partial \Omega}\, \phi_0\, d\Omega\, dV \tag{1}$$

where c denotes the density of the scattering molecules, N_A the Avogadro constant, $\partial\sigma_{\nu_i}/\partial\Omega$ the differential cross-section, and ϕ_0 the radiant flux density of the incident light.

The differential scattering cross-section for a vibrational transition of the frequency ν_i of a linear polarized Stokes Raman line, detected perpendicular to the laser beam, can be expressed as follows [96]

$$\frac{\partial \sigma_{\nu_i}}{\partial \Omega} = \left(\frac{\partial \sigma_i}{\partial \Omega}\right) \frac{2\rho_i + (1-\rho_i) sin^2\Theta}{1+\rho_i} \tag{2}$$

with the cross-section for $\Theta = 90°$

$$\left(\frac{\partial \sigma_i}{\partial \Omega}\right) = \frac{2^4\pi^4}{45}(\tilde{\nu}_0 - \tilde{\nu}_i)^4 b_i^2 g_i (45a_i^2 + 7\gamma_i^2) \left(1 - \exp\frac{hc\tilde{\nu}_i}{kT}\right)^{-1} \tag{3}$$

The depolarization ratio is given by

$$\rho_i = \frac{3\gamma_i^2}{45a_i^2 + 4\gamma_i^2} \tag{4}$$

with the wavenumber $\tilde{\nu}_0$ of the incident and $\tilde{\nu}_i$ of the scattered light, the zero point amplitude b_i, the degree of degeneracy g_i, and the specific molecular parameters a_i and γ_i; further, Planck's constant h, speed of light c, Boltzmann constant k and temperature T.

The influence of the refractive index on the incident light energy density is taken into account by the correction factor L. Eckhardt and Wagner [96] proposed

$$L = \frac{n_s}{n_0} \frac{(n_s^2+2)^2 (n_0^2+2)^2}{81} \approx \frac{(n^2+2)^4}{81} \tag{5}$$

The radiant flux density ϕ_0 of Eq. 1 has to be multiplied with this factor. Here n_s is the refractive index of the scattered light, n_0 of the incident light, and we assume that $n \approx n_0 \approx n_s$. Good agreement of measured and calculated correction factor L at different temperatures has been shown, e.g., in [31, 97, 98].

Neglecting interaction forces and the angular dependence of the differential scattering cross-section over the solid angle of observation Ω it follows

$$\Phi(\nu_i) \approx cLN_A \frac{\partial \sigma_{\nu_i}}{\partial \Omega} \int_V \int_\Omega \phi_0 \, d\Omega dV \tag{6}$$

where we have assumed that c is constant in the observated scattering volume. If we further assume the scattering volume as a point source emisson we can separate the integration of Ω from V, and if the scattered light of the laser beam is fully mapped on the entrance slit of the monochromator, we can replace the radiant flux density ϕ_0 by the laser power P_L

$$P_L := \int_{r=0}^{\infty} \int_{\varphi=0}^{2\pi} \phi r \, dr d\varphi = \frac{1}{2} \phi_0 \pi r_0^2 = \text{const.} \tag{7}$$

where $\phi(r_0) = \phi_0/\mathrm{e}^2$. This is no restriction of the following results because only relative measurements are evaluated.

Finally, it follows

$$\Phi(\nu_i) \approx cN_A L \frac{\partial \sigma_{\nu_i}}{\partial \Omega} \Omega P_L l \tag{8}$$

where the length of the scattering volume, defined by the magnification of the imaging optic and the monochromator entrance slit, is designated by l (systems with carbon dioxide: liquid phase $l \approx 10\,\text{mm}$, vapor phase $l \approx 5\,\text{mm}$; systems with ethylene $l \approx 3.3\,\text{mm}$).

The relative Raman intensity will be correlated with the density c by

$$\frac{\Phi_{1,x}}{\Phi_{1,0}} = \frac{c_{1,x}}{c_{1,0}} \frac{L_{1,x}}{L_{1,0}} \quad \text{and} \quad \frac{\Phi_{2,x}}{\Phi_{2,0}} = \frac{c_{2,x}}{c_{2,0}} \frac{L_{2,x}}{L_{2,0}} \tag{9}$$

where the subscript 1 and 2 denotes the components, 0 the pure components, and x the unknown mixture. In good approximation we assumed $L_{1,x}/L_{2,x} = 1$.

In the vapor phase $n_{1,0} \approx n_{2,0}$ and we can set $L_{1,0}/L_{2,0} = 1$.

2.2. Mole fraction

The relations between the mole fraction z and the density c is given by

$$z_1 = \frac{c_1}{c_1 + c_2} = \left(1 - \frac{c_2}{c_1}\right)^{-1} \quad \text{and} \quad z_2 = \frac{c_2}{c_1 + c_2} = 1 - z_1 \tag{10}$$

lead (by using Eq. 9) to

$$z_1 = \left(1 + \frac{\Phi_{2,x}}{\Phi_{1,x}} F\right)^{-1} \quad \text{and} \quad z_2 = 1 - z_1 \tag{11}$$

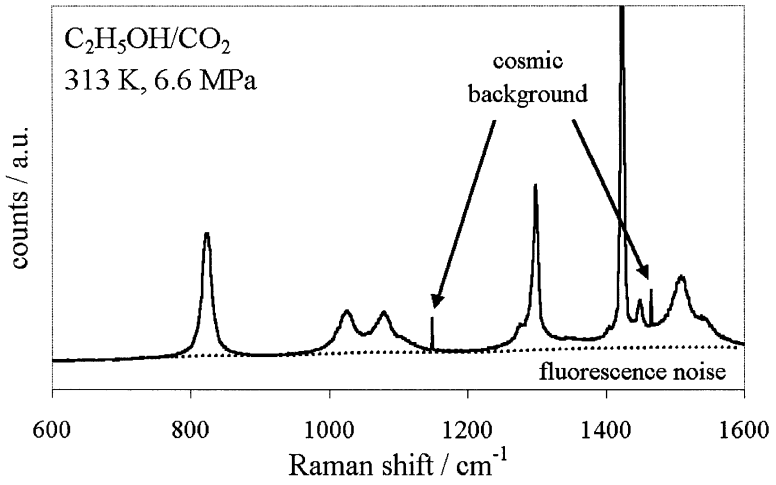

Fig. 1. Typical Raman spectra. Here the liquid phase of the mixture carbon dioxide/ethanol at $T = 313\,\mathrm{K}$ and $p = 6.6\,\mathrm{MPa}$ recorded within $t = 10\,\mathrm{s}$ and a laser power of $P_L = 0.4\,\mathrm{W}$.

with a form factor F

$$F = \frac{\Phi_{1,0}}{\Phi_{2,0}} \frac{L_{2,0}}{L_{1,0}} \frac{c_{2,0}}{c_{1,0}} \tag{12}$$

The determination of the mole fraction results from the determination of the Raman radiant flux ratio $\Phi_{1,x}/\Phi_{2,x}$ and the form factor F. This factor contains only physical values of the pure components and has to be determined once for the vapor F_V and once for the liquid phase F_L.

The flux ratio will determined from the Raman spectra. The form factor can be calculated or calibrated.

2.2.1. Raman Radiant Flux Ratio

The Raman flux ratio have to be determined from the Raman spectra. For evaluating Raman spectra various methods exist. The pros and cons are discussed in detail in, e.g., [6] and in particular for the presented data in [98].

A typical Raman spectrum is shown in Fig. 1. Region without overlapping can be seen ($\Delta\tilde{\nu} \approx 820\,\mathrm{cm}^{-1}$), as well as overlapping of the spectra of the pure components ($\Delta\tilde{\nu} \approx 1050\,\mathrm{cm}^{-1}$,$\approx 1250 - 1550\,\mathrm{cm}^{-1}$) and background noise caused by fluorescence and cosmic rays. The cosmic background are mathematically eliminated and the broadband fluorescence can easily separated from the Raman lines, because no temporal variations were observed. The fluorescence noise is caused by inpurities and has not effect on the Raman measurements, but we have no information whether the equilibria data are influenced.

For ethanol, 2-propanol and vinylacetic acid one can find Raman lines with no spectral overlapping as shown in the spectra below. Before evaluating the Raman band intensities a baseline is determined for each Raman band by connecting the minima on both side of the band. The peak intensity, that is, the vertical distance between the baseline and the maximum height, is assumed to be proportional to the radiant flux $\Phi_{1,x}$. We have compared this method with evaluating the area between the baseline and the Raman peak. Equivalent results in the mole fractions are achieved.

The carbon dioxide and ethylene peaks are partly overlapped by the Raman lines of the other component. The complicated structure of the (vibrational and rotational) carbon dioxide and ethylene spectrum makes it more difficult to separate it from the ethanol, 2-propanol or vinylacetic acid spectra. We use the following procedure to extract the carbon dioxide and ethylene spectrum from the Raman spectrum of the mixture: The amplitude of the Raman spectrum recorded from pure ethanol, 2-propanol or vinylacetic acid is numerically stretched or reduced so that the amplitude of the Raman peak free from overlapping (by carbon dioxide or ethylene) matches the corresponding peak in the spectrum of the mixture. Then this spectrum is subtracted from the spectrum of the mixture. The maximum height of the resulting carbon dioxide or ethylene signal is determined and assumed to be proportional to the radiant flux $\Phi_{2,x}$. Fig. 9 illustrates this procedure.

The Raman radiant flux ratio $\Phi_{1,x}/\Phi_{2,x}$ can then be calculated.

The determination of the radiant flux is principally not limitied to the existence of Raman lines free from spectral overlapping. This is discussed in the literature cited above.

Further, we have to keep in mind, that a pressure, temperature or/and composition induced shift or/and broadening of the Raman bands may need more sophisticated spectra analysis. We can show that our methods are sufficient for the investigated systems and with a special designed software the flux ratio is determined *in-situ*.

2.2.2. *Form Factor*

The form factor given by Eq. 12 can be calculated if the quantities L and c are available; Φ can be determined from the Raman spectra of the pure components. The result of this method is presented in [98] for the system toluene/cyclohexane ($p < 0.1\,\mathrm{MPa}$, $T = 323.15\,\mathrm{K}$). However, because the refractive indices under nonambient temperature are mostly unknown, the factor has to be determined by calibration.

If a mole fraction $z_{1,p}$ at temperature T_p and pressure p_p is given from a publication, the factor F can be calculated through measuring the Raman spectra of the mixture at that given T_p, p_p and determined radiant flux ratio $\Phi_{1,x}/\Phi_{2,x}$

to

$$F = \left(\frac{1}{z_{1,p}} - 1\right) \frac{\Phi_{2,x}}{\Phi_{1,x}} \tag{13}$$

This must be done once for the vapor phase ($z = y$) and once for the liquid phase ($z = x$). The calibration method is not self-consistent to Raman spectroscopy, but allows a fast survey about the accuracy of the Raman spectroscopic data if data from literature exists. This method is used for the investigated system vinylacetic acid/ethylene.

We also used a self-consistent method by filling the autoclave with a well-defined mixture. This mixture was generated by filling the autoclave with well-known masses of the different components ensuring that only one phase was existents in the autoclave. With the radiant flux ratio $\Phi_{1,x}/\Phi_{2,x}$ from the evaluated spectra of that mixture the factor F, respectively F_V and F_L, is then derived from a data point measurement at equilibrium

$$\left(1 + \frac{m_2}{m_1}\frac{M_1}{M_2}\right)^{-1} = z_1 = \left(1 + \frac{\Phi_{2,x}}{\Phi_{1,x}}F\right)^{-1} \tag{14}$$

to

$$F = \frac{m_2}{m_1}\frac{M_1}{M_2}\frac{\Phi_{1,x}}{\Phi_{2,x}} \tag{15}$$

This method is used for the investigated systems with carbon dioxide as supercritical solvent.

2.3. Equation of State

The Raman spectroscopic determined data of the systems ethanol/carbon dioxide and 2-propanol/carbon dioxide have been correlated by using the Peng-Robinson equation of state [99]

$$p = \frac{RT}{V^* - b} - \frac{a}{V^{*2} + 2bV^* - b^2} \tag{16}$$

In this equation, R is the the gas constant, T is the temperature, and V^* the molecular volume. The parameters a and b were calculated with the van der Waals one-fluid mixing rules

$$a = \sum_i \sum_j z_i z_j \sqrt{a_i a_j}\left(1 - \tilde{k}_{ij}\right) \qquad \text{and} \qquad b = \sum_i z_i b_i \tag{17}$$

with

Table 1
Parameters of the pure substances.
Chemicals (a), chemical formula (b,c), density / kg/m^3 at $T = 293.15$ K (d), molar mass / g/mol (e), melting point / K at $p = 1013$ hPa (f), boiling point / K at $p = 1013$ hPa (g), critical pressure / MPa (h), critical temperature / K (i), acentric factor (j), refractive index at $T = 293.15$ K, $\lambda = 589$ nm (k), supplier (l), purity / Vol.% (m). Data from supplier and [100–103].

(a)	2-propanol	ethanol	ethylene	carbon dioxide	vinylacetic acid
(b)	C_3H_8O	C_2H_6O	C_2H_4	CO_2	$C_4H_6O_2$
(c)	$CH_3CH(OH)CH_3$	C_2H_5OH			$CH_3COOCH=CH_2$
(d)	786	790			930
(e)	60.096	46.07	28.054	44.098	86.09
(f)	184.7	156.2	103.97	216.58	179.95
(g)	355.4	351.6	169.43	194.67	345.95
(h)	4.76	6.14	5.04	7.38	
(i)	508.3	513.92	282.35	304.13	
(j)	0.665	0.644		0.239	
(k)		1.3611			1.3954
(l)	Mallinckrodt-Baker Deventer (NL)	Merck Darmstadt (D)	Messer Griesheim Krefeld (D)	Messer Griesheim Krefeld (D)	Janssen Chimica Beerse (B)
(m)	99.5	99.8	> 99.7	99.0	99.0

$$a_i = 0.45724 \left(1 + f_i \left(1 - \sqrt{T_{c,i}/T}\right)\right)^2 \cdot R^2 T_{c,i}^2 / p_{c,i}$$
$$f_i = 1 + \left(0.37464 + 1.54226\omega_i - 0.26992\omega_i^2\right) \tag{18}$$

and

$$b_i = 0.0778\, RT_{c,i}/p_{c,i} \tag{19}$$

The binary interaction parameter has been modified to

$$\tilde{k}_{ij} = k_{12} - (k_{12} - k_{21})z_i \tag{20}$$

The indices i, j describe the components, c the critical parameters, and ω is the acentric factor as summerized in Table 1. This modification is used in [75] and so comparison is possible. Without the modification the calculated data will not fit to the measurement.

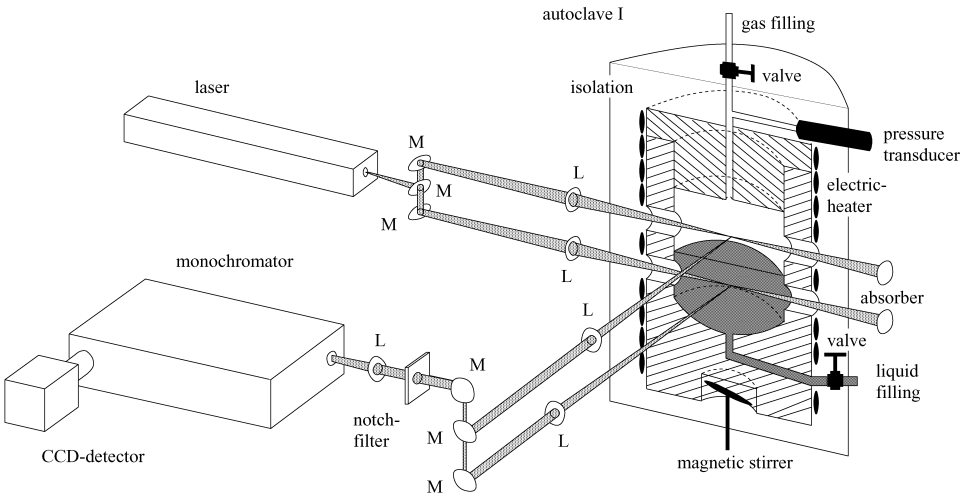

Fig. 2. Experimental setup with autoclave I (L≙lens, M≙mirror).

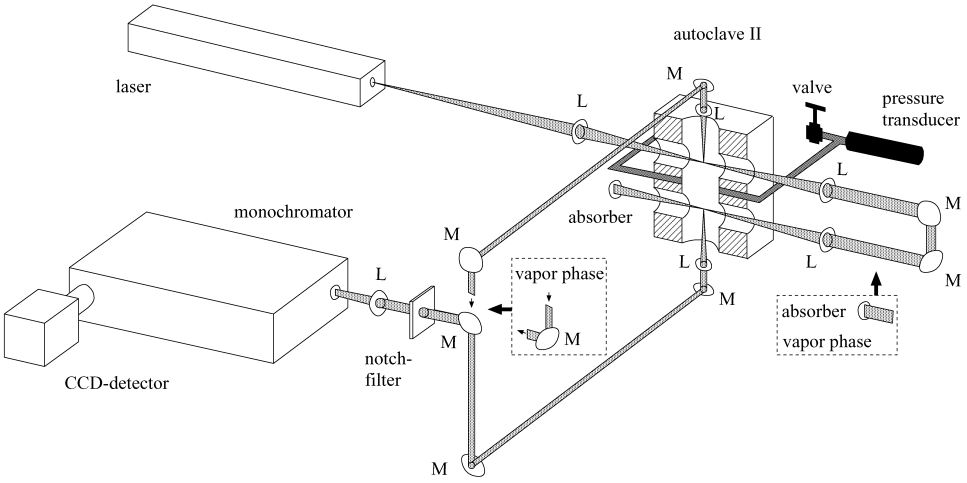

Fig. 3. Experimental setup with autoclave II (L≙lens, M≙mirror).

3. EXPERIMENTAL

The experimental setups are shown in Figs. 2 and 3. Main parts are the laser for the excitation of Raman scattering, the high pressure cell with temperature control, and the spectroscopic system. We have developed two high pressure cells. The main differences are the sample volume and the mixing technique.

3.1. Raman Excitation

Raman spectra are excited by a linear polarized Ar^+ laser (Innova 400, Coherent) at $\lambda = 514.5\,\text{nm}$ with $P_{L,max} = 10\,\text{W}$ or by a frequency doubled linear

polarized $Nd:YVO_4$ laser (Verdi V-5, Coherent) with $P_{L,max} = 5.5$ W at $\lambda = 532.0$ nm. For the systems ethanol/carbon dioxide and vinylacetic acid/ethylene at $T = 353$ K the Ar^+ laser was used. For the systems 2-propanol/carbon dioxide and vinylacetic acid/ethylene at $T = 323.15$ K the $Nd:YVO_4$ laser was used. The beam is focused into the temperature controlled high pressure autoclave I by a 150 mm biconvex lens and into autoclave II by a 80 mm biconvex lens. The long focal length reduces effects on the beam waist due to changes in the index of refraction caused by pressure and temperature changes and by variations of the mixing ratio. For Raman scattering with a typical detection time of about $t \leq 10$ s the laser output power is $P_L \approx 2.0$ W in the vapor phase and $P_L \approx 0.1$ W in the liquid phase. Only approximately half of the laser output power enters the scattering volume. The other half is lost by reflections on windows and mirrors.

3.2. High Pressure Cells

The autoclaves are made of stainless steel (material W 1.4571), designed for temperatures up to 473 K and pressures up to 25 MPa. They are described in detail in [98].

3.2.1. Autoclave I

This high pressure cell is an improvement of the autoclave described in [32] with a smaller sample volume and a electric heating system. It has a nominal filling volume of $\approx 280 \times 10^{-6}$ m^3 and has two pairs of windows mounted at different heights to pass the laser light. An additional pair of windows provides the optical access for the scattered light. The optical setup allows measurements in the vapor and in the liquid phase (cp. Fig. 2). The windows are specially hardened borosilicate glasses (Maxos, Schott Auer).

Liquids can be filled through the bottom by a high pressure membrane pump and gases can be filled through the top of the autoclave directly from a gas bottle. Further, we use a cell with two chambers divided by a movable piston. Using the pressure from a N_2 gas bottle ($p \approx 20$ MPa at room temperature) we can generate a desired gas pressure independent of the pressure of the carbon dioxide or ethylene gas bottle.

Temperature measurements are made by two Pt-100 sensors (ALMEMO-System, Ahlborn) with a system accuracy of $\Delta T = \pm 0.05$ K at 293 K and $\Delta T = \pm 0.1$ K at 373 K. The sensors are positioned near the two scattering volumes. The temperature stabilization is achieved by a computer controlled electric heater programmed with a special designed software. The whole autoclave is temperature isolated.

For the high pressure range up to 25 MPa a temperature calibrated (293 K-573 K) piezo resistive pressure transducer is used. This sensor (PAA-25HTC, Keller) has an absolute accuracy of $\Delta p = \pm 0.025$ MPa. For the low pressure

range from 10 kPa to 200 kPa, a second transducer (707.1.110, Leitenberger) is used with an absolute accuracy of $\Delta p = \pm 1.4$ kPa at 313.15 K.

To accelerate the mixing process, the sample is mixed by a "frit" inside the autoclave, which is driven by a magnetic rotator mounted outside of the autoclave. To avoid any contamination, all parts in contact with the fluid or the vapor are made of stainless steel, PTFE (pressure valves packing and seals), or glass.

3.2.2. Autoclave II

In this high pressure cell a new mixing technique is implemented (Fig. 3). Mixing is achieved by rotation of the whole autoclave. The autoclave has also a smaller sample volume ($\approx 40 \text{ x } 10^{-6}$ m^3) than autoclave II. So mixtures with higher viscosity can be investigated.

The same temperature controlling system is used as for autolcave I, but with only one Pt-100 sensor, positioned in the middle part of the cell. The pressure measurement at $T = 323.15$ K is done by the transducer (707.2.210, Leitenberger) with an absolute accuracy of $\Delta p \approx \pm 0.12$ MPa after calibration with the special sensor used at autoclave I. At $T = 353$ K the special sensor is used. Apart from that, the same techniques as for autoclave I are used.

3.3. Spectroscopic System

The scattered light is recorded perpendicular to the laser beam, collected through an $80/150$ mm (vapor/liquid) biconvex lens for autolcave I respectively 50 mm (vapor and liquid) for autoclave II. It is then passed parallel through a holographic notch filter (Kaiser Optical Systems) to suppress Rayleigh light and finally focused by a 100 mm achromatic lens on the entrance slit of the spectrometer. The image of the laser beam is orientated parallel to the height of the entrance slit. The spectroscopic system consist of a monochromator (HR 640, ISA, 1200 grooves/mm) and a liquid nitrogen cooled charged-coupled device (CCD) camera (Wright Instruments, 1152 x 300 pixels).

3.4. Principles of Operation

The autoclave is evacuated and heated to the desired temperature. Then the autoclave is filled with the gaseous component from the gas bottle or the piston cell and the liquid component is pumped into the vessel until the liquid level of the mixture is between the upper and lower window. After stable temperature and pressure are reached (mostly after less than one hour), Raman measurements (for that particular pressure and temperature) in the liquid and the vapor phase are made. By adding the liquid or the gaseous component, the next fluid-phase-equilibrium data point can be determined.

The Raman measurements are carried out at recording times of about $t \leq 10$ s and the detected spectra are then evaluated *in-situ* as described above to

determine the Raman radiant flux ratio and from that (with the form factor F) the mole fraction.

3.5. Form Factor Determination

3.5.1. Carbon Dioxide/Ethanol

The calibration factors F_V and F_L are determined by recording Raman spectra at two known single-phase states of the mixture. To calculate the calibration factor for the vapor state, the autoclave is filled with ethanol vapor. Keeping the pressure inside the autoclave lower than the vapor pressure of ethanol ($p_{C_2H_6O,V} = 17.92\,\text{kPa}$ at $313.15\,\text{K}$ [100]) guarantees that no liquid ethanol is inside the autoclave. The mass of ethanol is calculated by the ideal gas law

$$pV = \nu RT \qquad \text{and} \qquad m_{C_2H_6O} = \nu M_{C_2H_6O} \tag{21}$$

where pressure p and temperature T are known from measurements. Carbon dioxide is then added and with the known temperature and pressure, the density ρ_{CO_2} is calculated by the equation of Wagner and Span [101]. The possible presence of a small quantity of ethanol is neglected and it is assumed that only vapor of carbon dioxide is inside the autoclave. Finally, the mass of carbon dioxide is calculated with the density and the measured volume $V = (271.1 \pm 0.4)\,\text{x}\,10^{-6}\,\text{m}^3$ of the autoclave.

The determined masses

$$m_{C_2H_6O,V} = (0.057 \pm 0.006)\text{g} \qquad m_{CO_2,V} = (10.38 \pm 0.02)\text{g}$$

yield to the calibration factor for the vapor state, using Eq. 15:

$$F_V = 0.0966 \pm 0.0009 \tag{22}$$

To calculate the correction factor for the liquid state the autoclave is filled with a small quantity of carbon dioxide and the mass is calculated as mentioned before. A defined volume of ethanol is pumped into the autoclave until it is completely filled and therefore carbon dioxide is completely dissolved in ethanol. The mass of ethanol is now calculated using literature data for the density $\rho_{C_2H_6O}$ [104] and the measured volume and temperature of added ethanol. The calculated mass

$$m_{C_2H_6O,L} = (215.63 \pm 0.09)\text{g} \qquad m_{CO_2,L} = (6.98 \pm 0.01)\text{g}$$

introduced in Eq. 15 results in the calibration factor for the liquid state:

$$F_L = 3.90 \pm 0.02 \tag{23}$$

The indicated deviations in the correction factors were calculated using the Gaussian propagation law of errors, e.g. [105], and the deviations of the measured parameters (p, T, V), physical constants (R [106], $M_{C_2H_6O}$ [107], M_{CO_2} [108]) and the calculated values ($m_{C_2H_6O}$, m_{CO_2}, $\rho_{C_2H_6O}$, ρ_{CO_2}) from Eq. 15.

3.5.2. Carbon Dioxide/2-Propanol

The form factors of this system for the three investgated isothermal curves are calculated with nearly the same technique as described above for the system carbon dioxide/ethanol. To reduce a possible systematic error (the assumption of ideality, Eq. 21) the determination of the mass of 2-propanol of the vapor phase calibration is changed. Here we determined the 2-propanol volume by a measuring cup with a fine divided scale ($\Delta V = \pm 5 \text{ x } 10^{-9} \text{ m}^3$).

The following form factors were determined:

$F_V = 0.072 \pm 0.005$, $F_L = 1.745 \pm 0.002$ at $T = 313.15\,\text{K}$

$F_V = 0.066 \pm 0.004$, $F_L = 1.600 \pm 0.002$ at $T = 323.15\,\text{K}$

$F_V = 0.055 \pm 0.002$, $F_L = 1.464 \pm 0.002$ at $T = 333.15\,\text{K}$

3.5.3. Vinylacetic Acid/Ethylene

In this case, the form factors were determined by comparison with data from literature (cp. Eq. 13).

In [95] one can only find a calculated phase equlibria curve, unfortunately the measured data are not published. The form factors of our Raman results were determined by comparison with this calculated curve to:

$F_V = 5.500$, $F_L = 6.500$ at $T = 323.15\,\text{K}$

At $T = 353\,\text{K}$ the calibration is done in comparison with the data from [93–95] and yields to:

$F_V = 0.400$, $F_L = 0.005$ at $T = 353\,\text{K}$

4. DATA ANALYSIS

For quantitative spectroscopic analysis as described above, the amplitude or the integrated intensity of a particular Raman band of each component must be determined. Figs. 4-6 show the spectra of pure ethanol, 2-propanol and vinylacetic acid and Fig. 7 the spectra of carbon dioxide and ethylene.

The Raman bands used for the calculation of the Raman radiant flux ratio were measured simultaneously. Therefore, the aperture angle Ω, the laser power P_L, the size of the scattering volume l cancel. Transmission losses in the optical arrangement and the frequency dependence of the quantum efficiency of the CCD camera were also ignored.

The spectra are recorded within $t = 10\,\text{s}$, $t = 10\,\text{s}$, $t = 5\,\text{s}$, $t = 3\,\text{s}$ with a laser power of $P_L = 2.0\,\text{W}$, $P_L = 1.8 - 5.5\,\text{W}$, $P_L = 0.3 - 3.0\,\text{W}$, $P_L =$

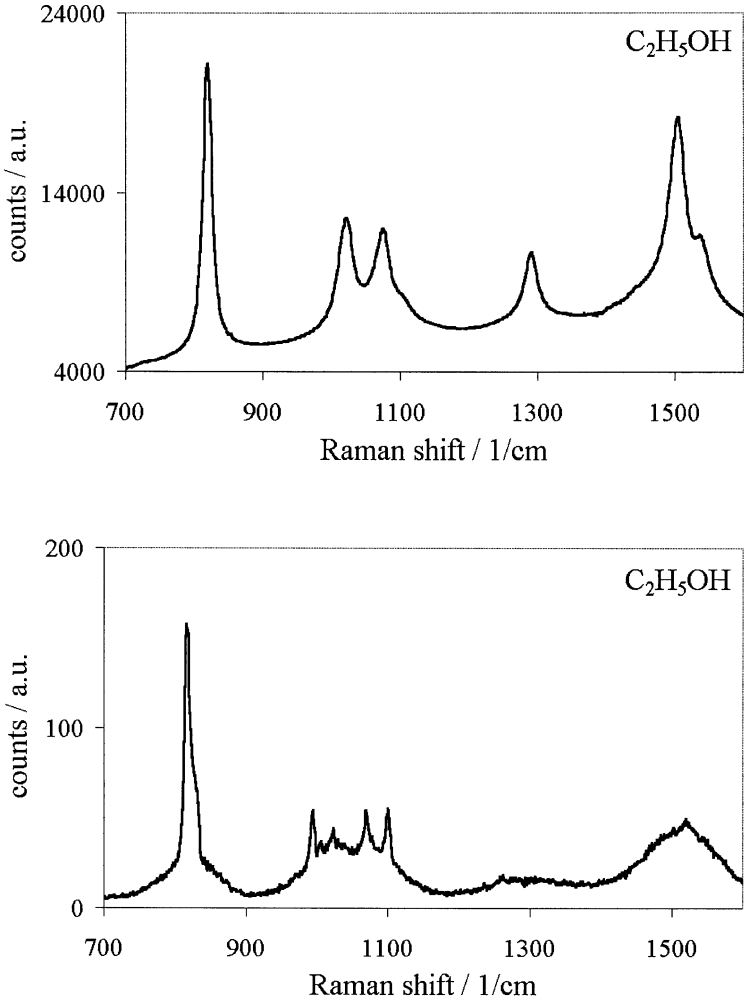

Fig. 4. Raman spectra of liquid (top) and gaseous (bottom) ethanol at $T = 313.06\,\mathrm{K}$ and $p = 17.4\,\mathrm{kPa}$.

$0.5 - 3.0\,\mathrm{W}$ for the vapor phase and $P_L = 0.2\,\mathrm{W}$, $P_L = 0.1 - 1.0\,\mathrm{W}$, $P_L = 0.1 - 0.3\,\mathrm{W}$, $P_L = 0.3 - 1.0\,\mathrm{W}$ for the liquid phase for the systems carbon dioxide/ethanol, carbon dioxide/2-propanol, vinylacetic acid/ethylene at $T = 323.15\,\mathrm{K}$, and $T = 353\,\mathrm{K}$. The temperature and pressure during recording of the spectra were measured and are shown in the data tables below.

The laser power is adjusted to achieve good Raman signals. A higher laser power for Raman scattering in the vapor phase will lead to a carbon dioxide and ethylene signal exceeding the maximum of the count rate of the camera (32 000 a.u.). The laser power has to be chosen appropriately to not exceed this

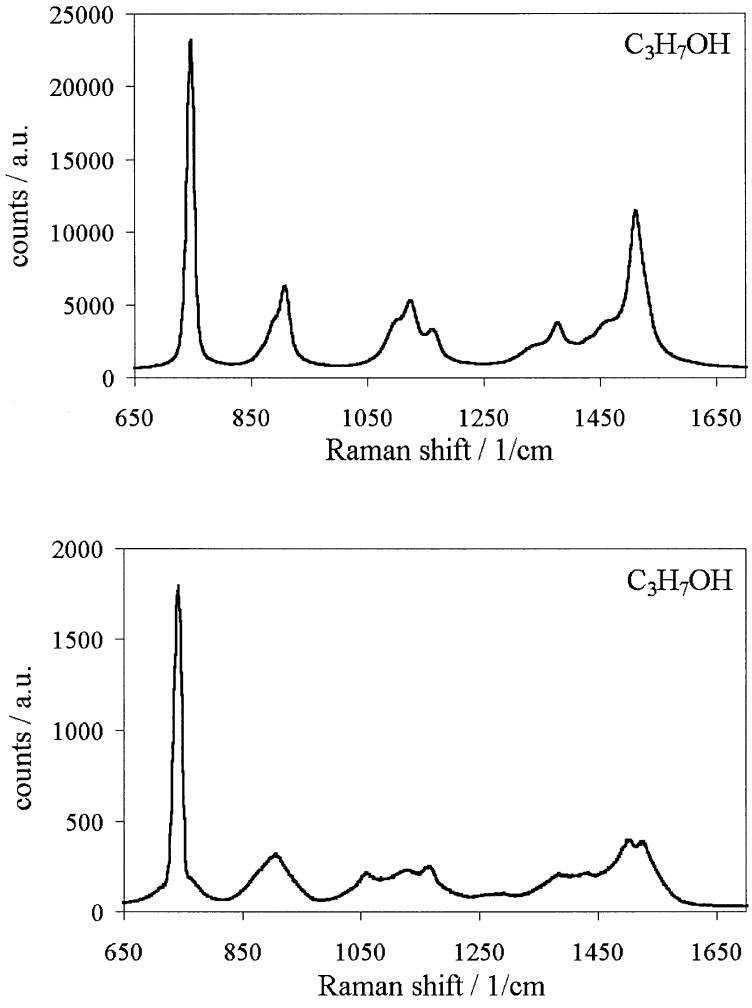

Fig. 5. Raman spectra of liquid (top) and gaseous (bottom) 2-propanol at $T = 323.11\,\mathrm{K}$ and $p = 23.6\,\mathrm{kPa}$.

dynamic range of the camera and to still get a sufficient signal-to-noise ratio for the ethanol, 2-propanol and vinylacetic acid signal.

In principle, small slit settings and high resolution would be desirable for the measurements to make discrimination of the various Raman bands easier. However, a narrow slit results in low intensity. In the present experiment the entrance slit width was chosen variable. The slit width was set between 140 μm and 300 μm.

To improve the data quality, ten spectra were recorded and averaged. All

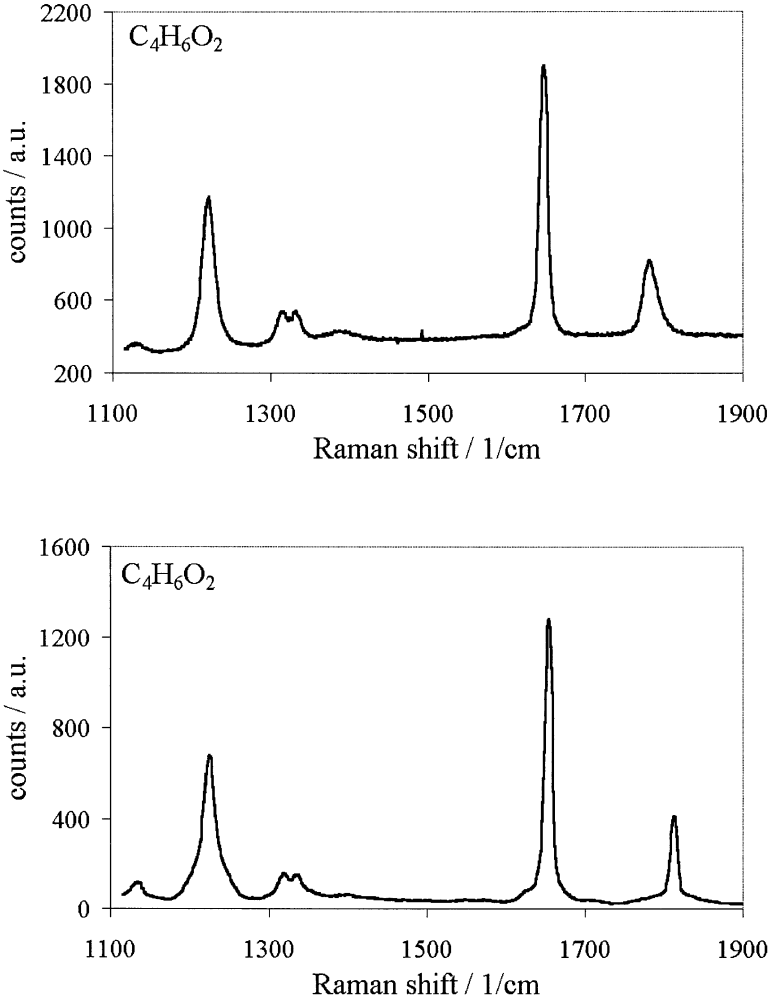

Fig. 6. Raman spectra of liquid (top) and gaseous (bottom) vinylacetic acid at $T = 323.15\,\mathrm{K}$ and $p < 0.1\,\mathrm{MPa}$.

disturbing cosmic background signals were mathematically eliminated. Possible local variations of the sensitivity of the CCD camera are not corrected. The evaluation procedure leads to a mean value of the Raman radiant flux ratio (cp. Eq. 11) for each data point

$$\frac{\Phi_{1,x}}{\Phi_{2,x}} := \overline{\Phi}_{1/2} = \frac{1}{10}\sum_{i=1}^{10}\frac{\Phi_{1,x,i}}{\Phi_{2,x,i}} \tag{24}$$

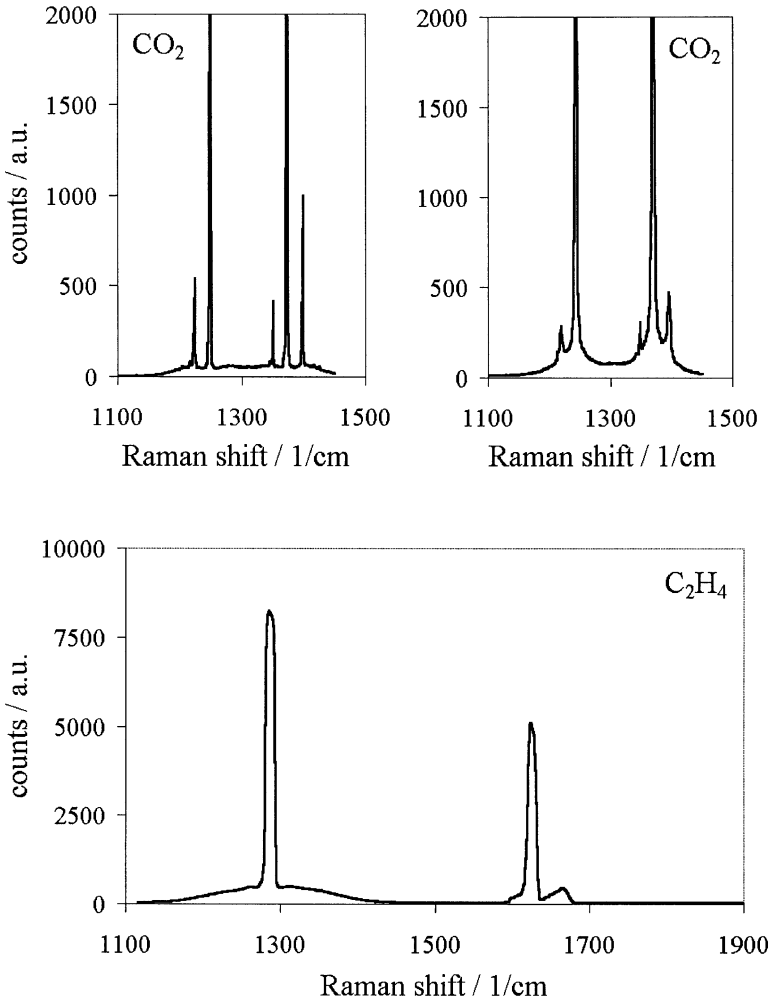

Fig. 7. Raman spectra of gaseous carbon dioxide (top, left; $T = 295,6\,\mathrm{K}$ and $p = 1.286\,\mathrm{Pa}$), liquid carbon dioxide (top, right; $T = 295,6\,\mathrm{K}$ and $p = 6.053\,\mathrm{Pa}$) and ethylene (bottom; $T = 295\,\mathrm{K}$ and $p = 2.0\,\mathrm{Pa}$).

and a deviation of this mean ratio, e.g. [105], of

$$\Delta\overline{\Phi}_{1/2} = \frac{s_{\overline{\Phi}_{1/2}}}{\sqrt{10}}\tau \tag{25}$$

with the standard error $s_{\overline{\Phi}_{1/2}}$ and the student factor $\tau = 1.06$ for ten data points within a confidence interval of $68.27\,\%$.

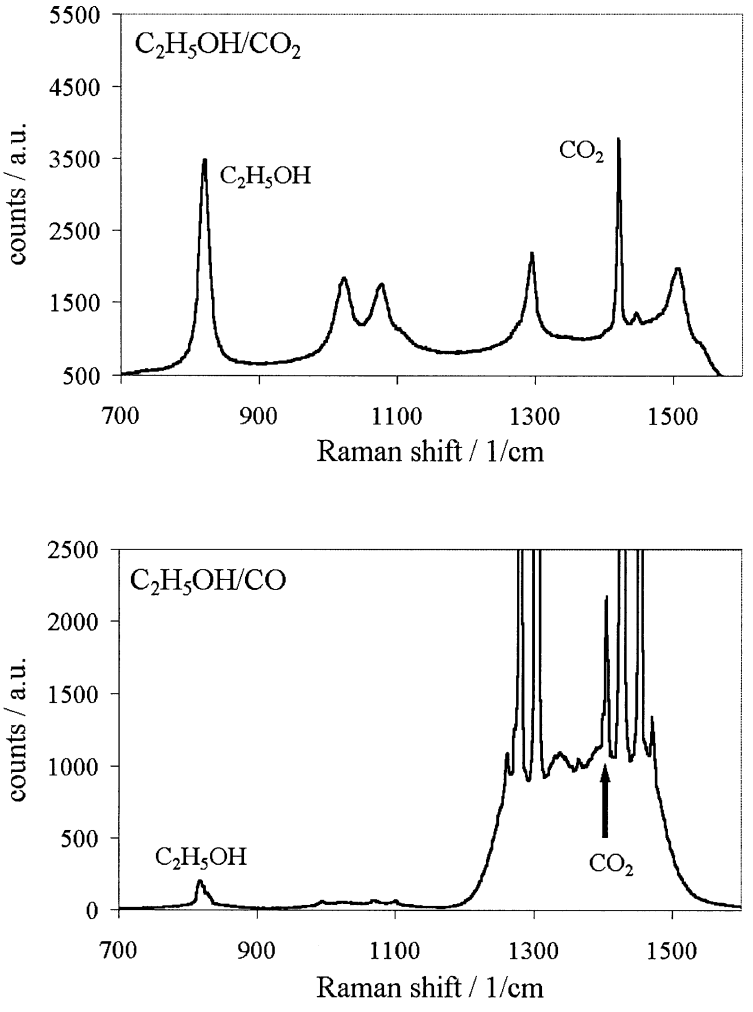

Fig. 8. Raman spectra of the liquid (top; $T = 312.95\,\mathrm{K}$, $p = 3.47\,\mathrm{MPa}$ and $x_{CO_2} = 0.1966$) and the vapor phase (bottom; $T = 313.20\,\mathrm{K}$, $p = 1.98\,\mathrm{MPa}$ and $y_{CO_2} = 0.9909$) of carbon dioxide/ethanol. The evaluated peaks are marked.

The deviations Δx and Δy in the calculation of the mole fraction of the liquid x and vapor state y (Eq. 11) depend on the deviation of the intensity ratio $\Delta(\overline{\Phi}_{1/2})$ and of the calibration factor ΔF_V resp. ΔF_L. They are calculated by Gaussian propagation law of errors.

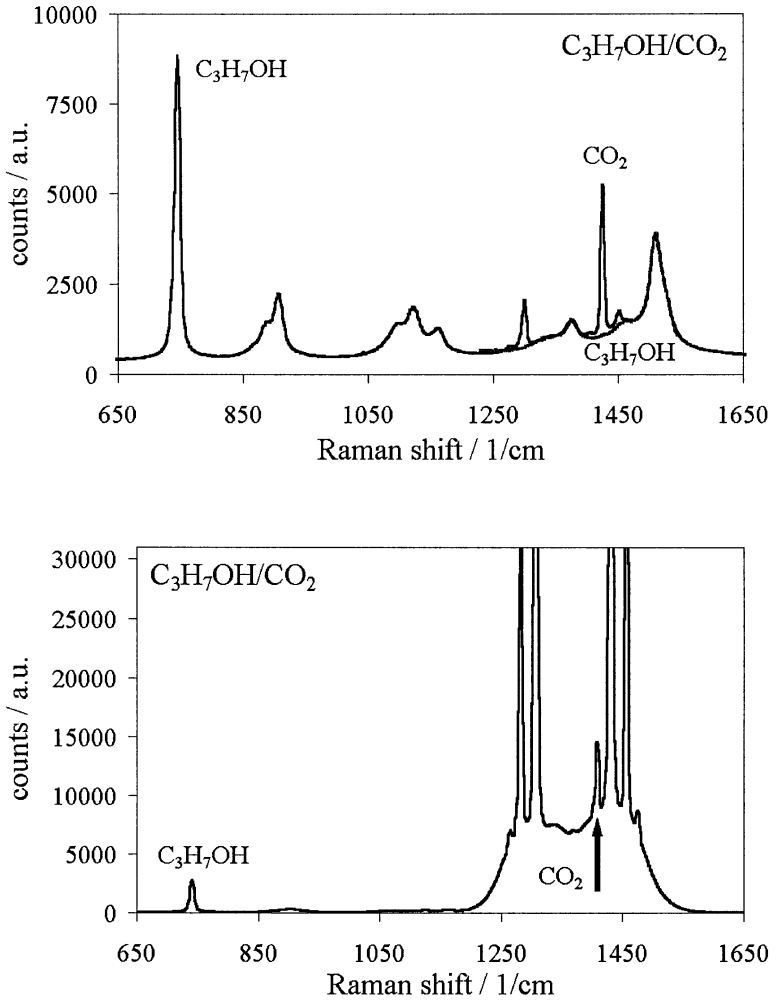

Fig. 9. Raman spectra of the liquid (top; $T = 323.22\,\mathrm{K}$, $p = 8.36\,\mathrm{MPa}$ and $x_{CO_2} = 0.6786$) and the vapor phase (bottom; $T = 323.24\,\mathrm{K}$, $p = 8.36\,\mathrm{MPa}$ and $y_{CO_2} = 0.964$) of carbon dioxide/2-propanol. The evaluated peaks are marked. In the spectra of the liquid phase the fittet spectra of pure 2-propanol is drawn as described above. It is the baseline for evaluating the carbon dioxide Raman peak.

5. RESULTS

The measurements were carried out and evaluated as described. The following diagrams show the vapor-liquid-equlibria of the investigated systems and the calculated Peng Robinson equation of state and, if exists, in comparision with data from literature. Our Raman data, including the calculated deviations, are summarized in the following tables. Because of some problems in the tem-

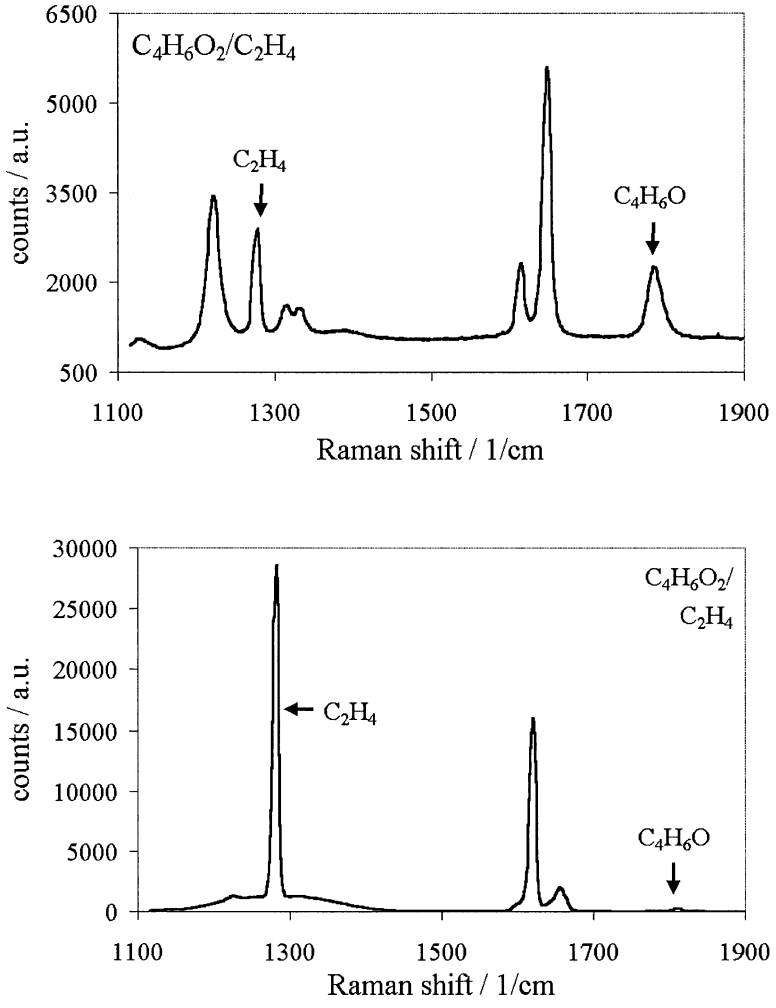

Fig. 10. Raman spectra of the liquid (top; $T = 323.11\,\mathrm{K}$, $p = 3.4\,\mathrm{MPa}$ and $x_{C_2H_4} = 0.20$) and the vapor phase (bottom; $T = 323.11\,\mathrm{K}$, $p = 3.4\,\mathrm{MPa}$ and $y_{C_2H_4} = 0.95$) of vinylacetic acid/ethylene. The evaluated peaks are marked.

perature regulation some measurements are at temperatures slightly different from the intended temperature. Nevertheless, these results are presented and the measured pressure and temperature during the data collection is indicated.

5.1. Raman Line Shift and Broadening

As described in the introduction, the Raman bands may be shifted and broadened due to the influence of pressure, temperature and concentration ratio

of the mixture. In Fig. 11 these influences on a pure carbon dioxide Raman band and on a vinylacetic acid band under pure and mixture conditions (vinylacetic acid/ethylene) are presented. The effect on carbon dixoide is very small and can be neglected. The band shift of the vinylacetic acid band at $\Delta\tilde{\nu} \approx 1810\,\mathrm{cm}^{-1}$ from gaseous to liquid state is about $\approx 30\,\mathrm{cm}^{-1}$. The other ethylene and vinylacetic acid bands in the investigated spectral range are not affected.

5.2. Carbon Dioxide/Ethanol

Fig. 12 shows our results and the data a summarized in Tab. 2. The precision of the mole fractions of the vapor phase are better the $\Delta y_{CO_2} = 10^{-3}$ as the diagram and the deviation calculation show.

The experimental results of this investigation are reproduced in the phase diagram shown in Fig. 13 together with data from the literature. The agreement of the liquid-phase line is excellent. In a (not shown) magnification the vapor-phase line has a systematic deviation less than $\Delta y_{CO_2} = 0.005$ in the mole fraction. Altering the form factor F_V numerically leads to good agreement between our data and those of the literature. The absolute position of the data depends mainly on the accuracy on the calibration factor and not of the Raman intensity measurement. For better results, the determination of the ethanol mass at the vapor state has to be improved (as is is done for the system carbon dioxide/2-propanol).

The results are published in [44].

In Fig. 12 our results are correlated with the Peng Robinson equation of state. At higher pressures, near the critical point, our computing method is unable to calculate mole fractions. This is a typical problem by using equation of states. Some effords to improve the routine may be done in future.

5.3. Carbon dioxide/2-Propanol

Fig. 14 shows our results and the data are summarized in Tab. 4, 5 and 6. The Raman spectroscopic determined equilibria data are consistent to one another. Strictly, only comparison with [75] at $T = 313.15\,\mathrm{K}$ is possible, at $T = 323.15\,\mathrm{K}$ and $T = 333.15\,\mathrm{K}$ the temperature data from literature is slighly different.

The comparison at $T = 313.15\,\mathrm{K}$ shows good comparison, as it is possible with one data-base from literature (cp. Fig. 15). At $T = 323.15\,\mathrm{K}$ and $T = 333.15\,\mathrm{K}$ our Raman data close a gap in equilibria data . If we leave the liquid phase data from [92] out of consideration the data around $T = 333\,\mathrm{K}$ are consistent to one another.

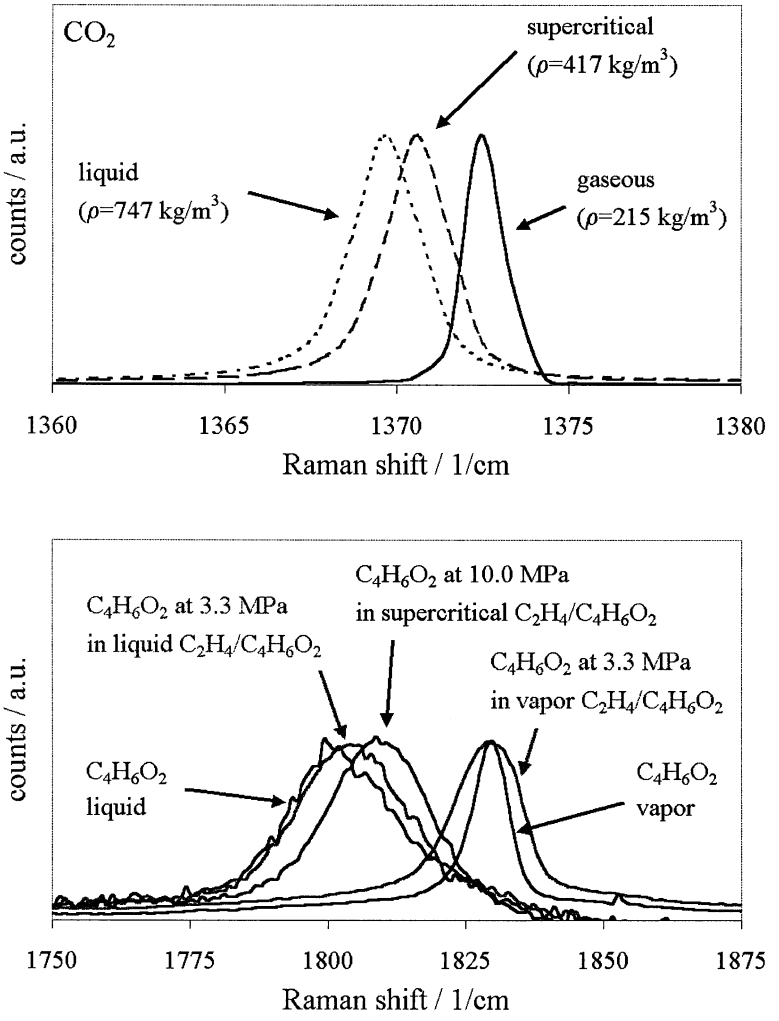

Fig. 11. Top: Influenceof the fluiddensity on a carbon dioxide Raman band. The line shifts and broadens from the gaseous (measurement conditions: $p = 1.3$ MPa, $T = 296$ K, $\Delta\tilde{\nu}_{max} = 1370.5\,\mathrm{cm}^{-1}$, FWHM $1.4\,\mathrm{cm}^{-1}$) via the supercritical (8.1 MPa, 309 K, $1372.4\,\mathrm{cm}^{-1}$, $2.2\,\mathrm{cm}^{-1}$) to the liquid state (6.5 MPa, 296 K, $1369.6\,\mathrm{cm}^{-1}$, $2.5\,\mathrm{cm}^{-1}$). The measurements are made with the experimental setup of autoclave I, the density is calculated from [101], and the lines are scaled to equivalent count rate.
Bottom: Influenceof pressure and mixing ratio on a vinylacetic acid Raman band at $T = 353$ K. The line shifts and broadens over a wide spectral range from the pure vapor via mixture of vinylacetic acid/ethylene and under supercritical conditions to pure liquid Raman line. The measurements are realized with the experimental setup of autoclave II and the lines are scaled to equivalent count rates.

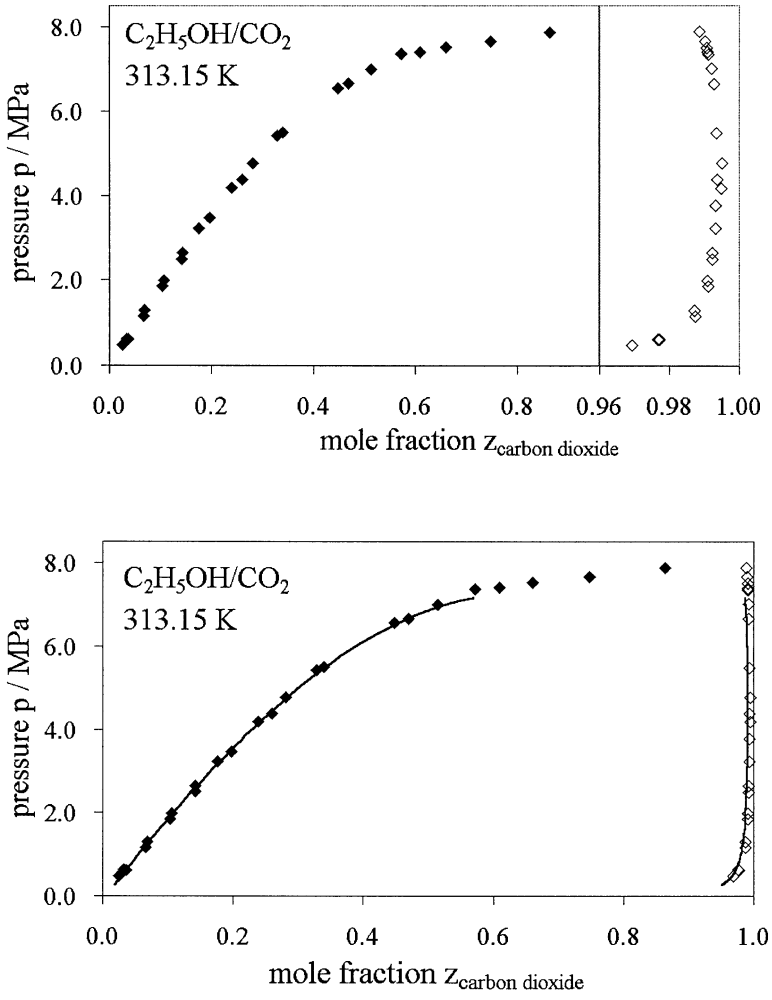

Fig. 12. Top: Vapor-liquid-equilibria of CO_2/C_2H_5OH measured by Raman spectroscopy. In the right part the mole fraction axis of the vapor phase (open diamonds) is enlarged.
Bottom: Comparison of our results with results calculated by the Peng-Robinsion equation of state and binary interaction parameters $k_{12} = 0.120$ and $k_{21} = 0.075$.

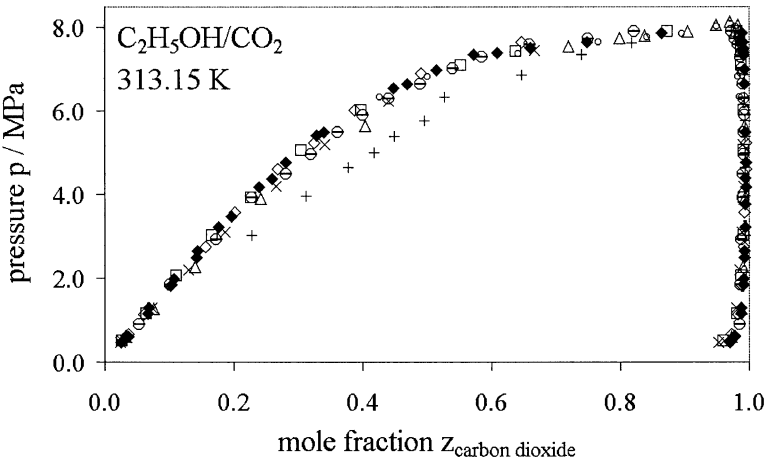

Fig. 13. Phase diagram of CO_2/C_2H_5OH. Our Raman spectroscopic results (filled ◇, [44]) in comparison with literature data from probe analysis (+ [86], □ [87], - [88], △ [89], ◇ [90], ○ [91], ○ [65], – [66], and × [77]).

Table 2
Liquid phase x_{CO2} and vapor phase y_{CO2} mole fractions of the system CO_2/C_2H_5OH with calculated standard errors Δx_{CO2} and Δy_{CO2} at meassured pressure p and temperature T.

x_{CO_2}	Δx_{CO_2}	p/MPa	T/K	y_{CO_2}	Δy_{CO_2}	p/MPa	T/K
0.0251	0.0003	0.48	313.29	0.9691	0.0005	0.48	313.28
0.0367	0.0005	0.61	313.32	0.9770	0.0005	0.61	313.50
0.0330	0.0003	0.62	313.15	0.9767	0.0003	0.62	313.20
0.0667	0.0006	1.16	313.24	0.9874	0.0002	1.16	313.07
0.0685	0.0006	1.29	313.00	0.9871	0.0003	1.29	313.01
0.1033	0.0009	1.85	312.88	0.9911	0.0002	1.85	313.01
0.1067	0.0007	1.98	313.18	0.9909	0.0002	1.98	313.20
0.1419	0.0011	2.50	312.79	0.9923	0.0001	2.50	312.78
0.1428	0.0007	2.65	313.18	0.9923	0.0001	2.65	313.16
0.1760	0.0009	3.22	313.04	0.9932	0.0001	3.23	313.08
0.1966	0.0010	3.47	312.95	0.9933	0.0001	3.77	312.89
0.2387	0.0010	4.18	313.13	0.9949	0.0002	4.18	313.12
0.2592	0.0014	4.38	313.15	0.9938	0.0002	4.39	313.19
0.2802	0.0012	4.78	313.15	0.9951	0.0001	4.78	313.16
0.3278	0.0059	5.42	313.15	0.9935	0.0001	5.49	313.28
0.3398	0.0012	5.50	313.22	0.9929	0.0002	6.66	312.53
0.4475	0.0014	6.56	313.21	0.9921	0.0002	7.01	313.33
0.4690	0.0014	6.66	312.58	0.9912	0.0002	7.35	313.80
0.5141	0.0014	6.70	313.18	0.9909	0.0002	7.39	313.25
0.5720	0.0016	7.37	314.03	0.9907	0.0002	7.50	313.00
0.6086	0.0016	7.40	313.30	0.9902	0.0002	7.65	312.81
0.6607	0.0015	7.52	313.06	0.9886	0.0001	7.87	313.02
0.7480	0.0011	7.66	312.81				
0.8644	0.0011	7.87	313.02				

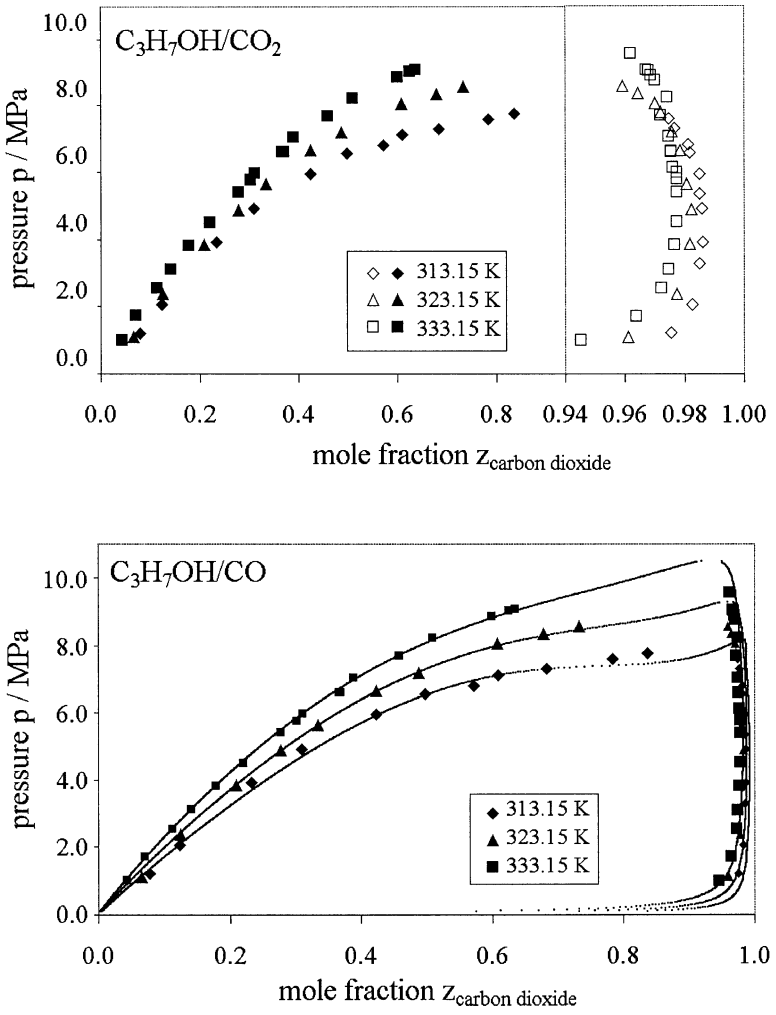

Fig. 14. Top: Vapor-liquid-equilibria of CO_2/C_3H_7OH measured by Raman spectroscopy. In the right part the mole fraction axis of the vapor phase (open tags) is enlarged.
Bottom: Comparison of our results with results calculated by the Peng Robinsion equation of state. The binary interaction parameters are summarized in Table 3.

Table 3
Binary interaction parameter for the system CO_2/C_3H_7OH

temperature / K	k_{12}	k_{21}
313.15	0.147	0.095
323.15	0.160	0.070
333.15	0.175	0.045

Table 4
Liquid phase x_{CO2} and vapor phase y_{CO2} mole fractions of the system CO_2/C_3H_7OH at $T = 313.15\,K$ with calculated standard errors Δx_{CO2} and Δy_{CO2} at meassured pressure p and temperature T.

x_{CO_2}	Δx_{CO_2}	p/MPa	T/K	y_{CO_2}	Δy_{CO_2}	p/MPa	T/K
0.0781	0.0001	1.21	313.02	0.976	0.002	1.21	313.06
0.1234	0.0002	2.06	313.19	0.983	0.002	2.06	313.17
0.1655	0.0001	3.28	313.41	0.985	0.001	3.29	313.02
0.2326	0.0003	3.92	313.14	0.986	0.001	3.92	313.11
0.3092	0.0006	4.91	313.14	0.986	0.001	4.91	313.14
0.3246	0.0002	5.36	313.12	0.985	0.002	5.36	313.12
0.4235	0.0004	5.95	313.16	0.985	0.001	5.95	313.14
0.5027	0.0003	6.56	313.23	0.982	0.002	6.57	313.30
0.5747	0.0004	6.81	313.05	0.981	0.002	6.81	313.04
0.6116	0.0003	7.12	313.15	0.977	0.002	7.31	313.39
0.6831	0.0003	7.31	313.39	0.974	0.002	7.60	313.17
0.7835	0.0002	7.60	313.15				
0.8371	0.0002	7.77	312.97				

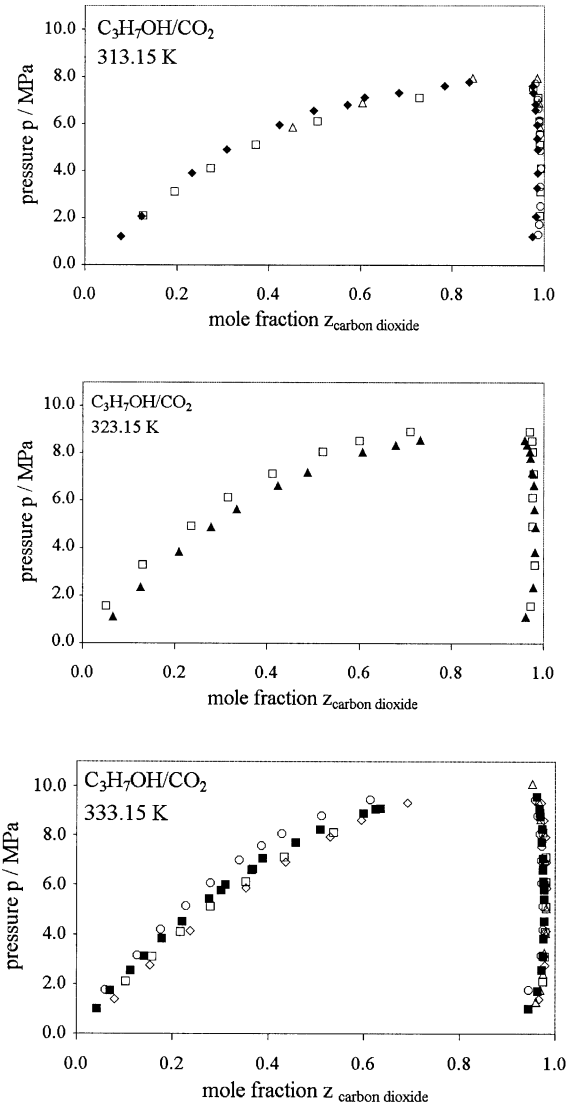

Fig. 15. Top: Phase diagram of CO_2/C_3H_7OH at 313.15 K. Our Raman spectroscopic results (filled ◇) at $T = 313.15$ K in comparison with literature data from probe analysis at $T = 313.15$ K (□ [75]), $T = 316.75$ K (△ [92]) and $T = 317.70$ K (○ [88]).
Middle: Phase diagram of CO_2/C_3H_7OH at 323.15 K. Our Raman spectroscopic results (filled △) at $T = 323.15$ K in comparison with literature data from probe analysis at $T = 324.70$ K (□ [77]).
Bottom: Phase diagram of CO_2/C_3H_7OH at 333.15 K. Our Raman spectroscopic results (filled □) at $T = 333.15$ K in comparison with literature data from probe analysis at $T = 333.10$ K (□ [75]), $T = 333.70$ K (△ [88]), $T = 333.70$ K (○ [77]) and $T = 334.85$ K (◇ [92]).

Table 5
Liquid phase x_{CO2} and vapor phase y_{CO2} mole fractions of the system CO_2/C_3H_7OH at $T = 323.15\,K$ with calculated standard errors Δx_{CO2} and Δy_{CO2} at meassured pressure p and temperature T.

x_{CO_2}	Δx_{CO_2}	p/MPa	T/K	y_{CO_2}	Δy_{CO_2}	p/MPa	T/K
0.0651	0.0002	1.11	323.15	0.961	0.002	1.11	323.18
0.1248	0.0003	2.37	323.16	0.978	0.002	2.37	323.19
0.1209	0.0003	2.99	323.08	0.977	0.002	2.99	323.11
0.2086	0.0003	3.85	323.15	0.9816	0.0009	3.85	323.20
0.2778	0.0004	4.88	323.16	0.9822	0.0008	4.88	323.12
0.3340	0.0005	5.65	323.20	0.9807	0.0009	5.65	323.17
0.3207	0.0003	5.92	323.17	0.978	0.001	5.92	323.19
0.424	0.002	6.66	323.20	0.979	0.001	6.66	323.23
0.4871	0.0004	7.20	323.18	0.976	0.002	7.20	323.16
0.6073	0.0003	8.07	323.14	0.972	0.002	7.80	322.96
0.6786	0.0003	8.36	323.22	0.970	0.002	8.07	323.20
0.7324	0.0003	8.57	323.16	0.964	0.002	8.36	323.24
				0.959	0.002	8.58	323.17

Table 6
Liquid phase x_{CO2} and vapor phase y_{CO2} mole fractions of the system CO_2/C_3H_7OH at $T = 333.15\,K$ with calculated standard errors Δx_{CO2} and Δy_{CO2} at meassured pressure p and temperature T.

x_{CO_2}	Δx_{CO_2}	p/MPa	T/K	y_{CO_2}	Δy_{CO_2}	p/MPa	T/K
0.0405	0.0001	1.01	333.10	0.945	0.002	1.01	332.98
0.0707	0.0001	1.73	333.40	0.964	0.001	1.71	333.39
0.1132	0.0001	2.54	332.92	0.9722	0.0008	2.55	332.92
0.1413	0.0002	3.12	333.35	0.9746	0.0007	3.11	333.30
0.1778	0.0002	3.83	333.25	0.9764	0.0007	3.83	333.00
0.2206	0.0002	4.51	333.06	0.9775	0.0006	4.53	332.96
0.2773	0.0002	5.42	333.20	0.9775	0.0006	5.40	333.09
0.3016	0.0003	5.78	332.86	0.9775	0.0006	5.80	332.86
0.3109	0.0002	5.99	332.97	0.9774	0.0006	5.99	332.89
0.3662	0.0006	6.61	333.27	0.9760	0.0007	6.14	333.38
0.3692	0.0003	6.61	333.20	0.9755	0.0007	6.59	333.42
0.3890	0.0003	7.06	333.22	0.9755	0.0007	6.62	333.10
0.4578	0.0003	7.70	333.52	0.9746	0.0007	7.06	333.26
0.5092	0.0003	8.23	333.00	0.9719	0.0008	7.71	333.61
0.5994	0.0003	8.88	333.20	0.9740	0.0007	8.24	333.00
0.6247	0.0003	9.05	333.20	0.9700	0.0008	8.76	333.60
0.6353	0.0003	9.08	333.92	0.9687	0.0009	8.90	333.50
				0.9678	0.0009	9.05	333.30
				0.9669	0.0009	9.07	332.87
				0.962	0.001	9.56	333.05

Table 7
Liquid phase x and vapor phase y mole fractions of the system $C_2H_4/C_4H_6O_2$ at $T = 323.15\,K$ at meassured pressure p and temperature T.

p/MPa	$y_{C_2H_4}$	T/K	$x_{C_2H_4}$	T/K
1.1	0.90	323.12	0.06	323.10
2.5	0.94	323.12	0.13	323.10
3.4	0.95	323.11	0.20	323.11
4.2	0.95	323.11	0.26	323.13
4.8	0.95	323.09	0.30	323.08
5.6	0.95	323.13	0.39	323.13
6.2	0.94	323.13	0.43	323.11
6.8	0.93	323.10	0.49	323.09

5.4. Vinylacetic Acid/Ethylene

First Raman results of the binary system vinylacetic acid/ethylene are presented in Fig. 16. The vapor-liquid-equilibria at $T = 323.15\,K$ and at $T = 353\,K$ are shown and the data are summarized in Tab. 7 and 8. The form factor is, as mentioned above, calibrated from literature data. In a next step we have to determine the form factors through mass-defined calibration (consistent in Raman spectroscopy).

Our aim is to show, that our Raman spectroscopic method can also be used for systems with molecules of complex structure and strong influences on the Raman bands, as shown in Fig. 11. Available literature data show relative large scattering. Our data fit well within this scattering range. To close the gap of the missing Raman phase equilibria data further measurements will be done in the future.

To check the influence of the Raman band shift and broadening we additionally evaluated different Raman bands (cp. Fig. 10) and different evaluating methods. The unshifted ethylene lines at $\Delta\tilde{\nu} \approx 1280\,cm^{-1}$ and $\Delta\tilde{\nu} \approx 1620\,cm^{-1}$ and the vinylacetic acid line at $\Delta\tilde{\nu} \approx 1210\,cm^{-1}$ were evaluated using the described spectra fitting method. The vinylacetic acid line at $\Delta\tilde{\nu} \approx 1800\,cm^{-1}$ were evaluated by peak height and band area. Same results in the mole fraction were achieved.

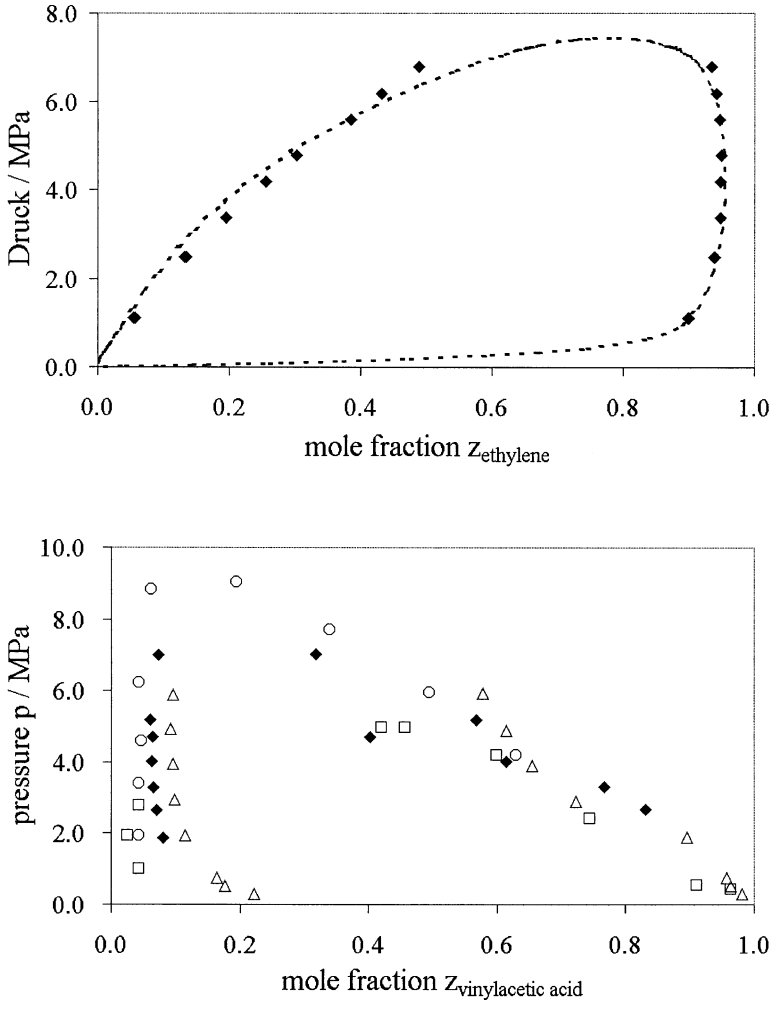

Fig. 16. Top: Phase diagram of vinylacetic acid at $T = 323.15$ K. Comparison of our results (filled ◇) with with the calculated phase curve from [95].
Bottom: Phase diagram of vinylacetic acid at $T = 353$ K. Comparison of our results (filled ◇) with results from literature data from probe analysis (△ [94], □ [93], ○ [95]).

Table 8
Liquid phase $x_{C_4H_6O_2}$ and vapor phase $y_{C_4H_6O_2}$ mole fractions of the system $C_2H_4/C_4H_6O_2$ at $T = 353\,K$ at meassured pressure p and temperature T.

$y_{C_4H_6O_2}$	p/MPa	T/K	$x_{C_4H_6O_2}$	p/MPa	T/K
0.080	1.88	353.17	0.832	2.67	352.78
0.070	2.66	352.4	0.766	3.30	352.91
0.066	3.30	352.86	0.614	4.01	353.09
0.063	4.01	353.06	0.403	4.70	352.90
0.064	4.71	352.86	0.318	7.34	352.98
0.061	5.19	353.02			
0.073	7.01	353.03			

6. CONCLUSION

We describe an experimental set-up for *in situ* measurements of fluid-phase equilibria at high pressure. Raman spectroscopy is used to determine the concentrations in the liquid phase as well as in the vapor phase of binary mixtures. Quantitative concentration analysis is presented. The results are in good agreement with data from the literature and some unpublished data are presented. The systems showed in the investigated pressure and temperature range ($p = 0.5 - 9.6\,MPa$, $T = 313.15\,K$, $323.15\,K$, $333.15\,K$ and $353\,K$) no effects of intermolecular forces on the Raman spectra or the effects can be neglected.

The Raman spectroscopic technique makes concentration measurements possible without the extraction of samples, as necessary by conventional techniques. Situations with a sensitive equilibrium (e.g., near the critical point), measurement at high pressure and temperature (where the extraction of samples may be difficult), or on-line control (of processes in chemical engineering) are the primary areas of applications of this technique.

The influence of intermolecular interactions to the evaluation of the Raman spectra at higher temperature, higher pressure and with complex molecules needs further investigations. The performance of this method at higher pressure and temperature should be tested. No principle limitations for an extension to multicomponent systems exist.

REFERENCE

[1] J. Brandmüller, H. Moser, Einführung in die Ramanspektroskopie, Steinkopff, Darmstadt, 1962.
[2] A. Anderson, The Raman Effect, Vol. 1, Dekker, New York, 1971, ISBN 0-8247-1014-2.
[3] A. Anderson, The Raman Effekt, Vol. 2, Dekker, New York, 1973, ISBN 0-8247-1015-0.

[4] D. Long, Raman Spectroscopy, McGraw-Hill, New York, 1977, ISBN 0-07-038675-7.
[5] A. Weber, Raman Spectroscopy of Gases and Liquids, Springer, Berlin, 1978, ISBN 3-540-09036-3.
[6] B. Schrader, Infrared and Raman Spectroscopy, VCH, New York, 1995, ISBN 3-527-26446-9.
[7] M. Pelletier, Analytical Applications of Raman Spectroscopy, Blackwell Science Ltd., Malden US, 1999, ISBN 0-632-05305-4.
[8] E. Davis, G. Schweiger, The Airborne Microparticle, Springer, Berlin, 2002, ISBN 3-540-43364-3.
[9] I. Swaid, D. Nickel, G. Schneider, Fluid Phase Equilibr. 21 (1985) 95–112.
[10] J. Friedrich, G. Schneider, J. Chem. Thermodyn. 21 (1989) 307–319.
[11] J. Evans, H. Bernstein, J. Chem. 34 (1956) 1127–1133.
[12] T. Wall, D. Hornig, J. of Chem. Phys. 45 (9) (1966) 3424–3430.
[13] H. Kroto, Y.-H. Pao, J. Opt. Soc. Am. 58 (4) (1968) 479–489.
[14] D. Bahnick, W. Person, J. Chem. Phys. 48 (3) (1968) 1251–1261.
[15] G. Fini, P. Mirone, P. Patella, J. Mol. Spectrosc. 28 (1968) 144–160.
[16] H. Clase, H. Kroto, Mol. Phys. 15 (2) (1968) 167–172.
[17] H. Kroto, J. Teixeira-Dias, Mol. Phys. 18 (6) (1970) 773–782.
[18] W. Hess, H. Hacker, H. Schrötter, J. Brandmüller, Z. f. angew. Physik 27 (1969) 233–238.
[19] J. Perchard, W. Murphy, H. Bernstein, Mol. Phys. 23 (3) (1972) 499–517.
[20] H. Kroto, J. Teixeira-Dias, Spectroch. Acta 28A (1972) 1497–1502.
[21] R. Ouillon, Y. Duff, Adv. Raman Spectrosc. 1 (1973) 428–435.
[22] W. Schindler, J. Jonas, J. Chem. Phys. 73 (8) (1980) 3547–3552.
[23] K. Tanabe, J. Hiraishi, Mol. Phys. 39 (6) (1980) 1507–1512.
[24] H. Welsh, P. Pashler, B. Stoicheff, J. Physics 30 (1952) 99–100.
[25] W. Reiff, Ph.D. thesis, Thermodynamik, Maschinenbau, Universität Duisburg (1985).
[26] S. Brunsgaard Hansen, Ph.D. thesis, Dep. Chem. and Dep. Chem. Eng., IVC-SEP, TU of Denmark, DK-2800 Lyngby, ISBN 87-986985-6-7 (2000).
[27] S. Brunsgaard Hansen, R. Berg, E. Stenby, Appl. Spectrosc. 55 (1) (2001) 55.
[28] S. Brunsgaard Hansen, R. Berg, E. Stenby, Appl. Spectrosc. 55 (6) (2001) 745.
[29] S. Brunsgaard Hansen, R. Berg, E. Stenby, J. Raman Spectrosc. 33 (2002) 160–164.
[30] M. Blatchford, S. Wallen, Anal. Chem. 74 (2002) 1922–1927.
[31] T. Fujiyama, B. Chem. Soc. Jap. 46 (1973) 87–89.
[32] T. Kaiser, C. Voßmerbäumer, G. Schweiger, Ber. Bunsenges. Phys. Chem. 8 (1992) 976–980.
[33] M. Pelletier, Appl. Spectrosc. 53 (1999) 1087.
[34] Y. Gu, Y. Zhou, E. Rothe, G. Reck, Appl. Phys. B 71 (2000) 865–871.
[35] D. Diller, R. Chang, Appl. Spectrosc. 34 (4) (1980) 411–414.
[36] D. Irish, T. Jarv, Appl. Spectrosc. 37 (1) (1983) 50–55.
[37] J. Thönnissen, Chem. Ing. Tech. 63 (12).
[38] S. Howdle, S. Best, J. Raman Spectrosc. 24 (7) (1993) 443–445.
[39] S. Howdle, V. Bagratashvili, Chem. Phys. Let. 214 (2) (1993) 215–219.
[40] S. Howdle, K. Stanley, V. Popov, V. Bagratashvili, Appl. Spectrosc. 48 (2) (1994) 214–218.
[41] P. Lalanne, S. Rey, F. Cansell, T. Tassing, M. Besnard, J. Supercrit. Fluids 19 (2) (2001) 199–207.
[42] P. Lalanne, T. Tassaing, Y. Danten, M. Besnard, J. Mol. Liq. 98-99 (2002) 201–212.
[43] A. Stratmann, G. Schweiger, Chem. Ing. Techn. 5 (2002) 649.
[44] A. Stratmann, G. Schweiger, Appl. Spectrosc. 56 (2002) 783–788.
[45] M. Buback, Ber. Bunsenges. Phys. Chem. 78 (1974) 1230–1235.

[46] M. Buback, K. Schulz, J. Phys. Chem. 80 (1976) 2478–2482.
[47] R. Eckel, M. Buback, G. Strobl, Colloid Polym. Sci. 259 (1981) 326–334.
[48] T. Zerda, J. Schroeder, J. Jonas, J. Chem. Phys. 75 (4) (1981) 1612–1622.
[49] R. Eckel, H. Schwickert, M. Buback, G. Strobl, Polym. Bull. 6 (1982) 559–564.
[50] W. Schindler, P. Sharko, J. Jonas, J. Chem. Phys. 76 (7) (1982) 3493–3496.
[51] R. Kruse, E. Franck, Ber. Bunsenges. Phys. Chem. 86 (1982) 1036–1038.
[52] W. Schindler, T. Zerda, J. Jonas, J. Chem. Phys. 81 (10) (1984) 4306–4313.
[53] F. Baglin, H. Versmold, U. Zimmermann, Mol. Phys. 53 (5) (1984) 1225–1238.
[54] T. Zerda, H. Thomas, M. Bradley, J. Jonas, J. Chem. Phys. 86 (6) (1986) 3219–3224.
[55] T. Zerda, X. Song, J. Jonas, Appl. Spectrosc. 40 (8) (1986) 1194–1199.
[56] V. Lemos, F. Camargo, J. Raman Spectrosc. 21 (1990) 123–126.
[57] X. Wang, Z. Shen, S. Tang, M. Kuok, J. Appl. Phys. 85 (1999) 8011–8017.
[58] M. Kooi, L. Ulivi, J. Schouten, Int. J. Thermophys. 20 (1999) 867–876.
[59] D. Freitag, C. Götz, G. Luft, A. van der Pol, K. Wierda, Appl. Spectrosc. 55 (2) (2001) 136–141.
[60] J. Michels, J. Schouten, J. Thermophys. (2001) 339–355.
[61] J. Schouten, J. Thermophys. 22 (1) (2001) 23–40.
[62] F. Perez Tejedor, O. Montoro, O. Rodriguez-Jimenez, V. Baonza, J. Nunez Delgado, Defect and Diffusion Forum 208-209 (2002) 121–124.
[63] M. Sato, M. Goto, T. Hirose, Ind. Eng. Chem. Res. 34 (1995) 3941.
[64] M. Sato, M. Goto, T. Hirose, Ind. Eng. Chem. Res. 35 (1996) 1906.
[65] C.-Y. Day, C. Chang, C.-Y. Chen, J. Chem. Eng. Data 41 (1996) 839.
[66] C. Chang, C.-Y. Day, C.-M. Ko, K.-L. Chiu, Fluid Phase Equilibr. 131 (1997) 243.
[67] J. Chiehming, C. Kou-Lung, D. Chang-Yih, J. Supercrit. Fluids 12 (1998) 223–237.
[68] H. Lee, H. Lee, Fluid Phase Equilibr. 150-151 (1998) 695–701.
[69] O. Pfohl, Ph.D. thesis, Verfahrenstechnik, TU Hamburg-Harburg, ISBN 3-18-357203-6 (1998).
[70] V. Riha, G. Brunner, J. Supercrit. Fluids 15 (1998) 33–50.
[71] K. Wagner, J. Zappe, A. Reeps, N. Dahmen, E. Dinjus, Fluid Phase Equilibr. 153 (1998) 135–142.
[72] M. Budich, G. Brunner, Fluid Phase Equilibr. 160 (1999) 759–773.
[73] C. Chang, C. Chen, Fluid Phase Equilibr. (163) (1999) 119–126.
[74] H. Lee, S. Mun, H. Lee, J. Chem. Eng. Data 44 (1999) 524–527.
[75] A. Bamberger, G. Maurer, J. Chem. Thermodyn. 32 (2000) 685–700.
[76] J. de la Fuente, S. Bottini, Fluid Phase Equilibr. 175 (2000) 45–52.
[77] L. Galicia-Luna, A. Ortega-Rodrigues, J. Chem. Eng. Data 24 (2) (2000) 265–271.
[78] T. Gamse, R. Marr, Fluid Phase Equilibr. 171 (2000) 165–174.
[79] M. da Silva, D. Barbosa, P. Ferreira, J. Mendonca, Fluid Phase Equilibr. 175 (2000) 19–33.
[80] M. da Silva, D. Barbosa, Ind. Eng. Chem. Res. 39 (2000) 4427–4430.
[81] G. Stuart, C. Dariva, J. Oliveira, Braz. J. Chem. Eng. 17 (2).
[82] A. Berna, A. Chafer, J. Monton, S. Subirats, J. Supercrit. Fluids 20 (2001) 157–162.
[83] A. Chafer, A. Berna, J. Monton, A. Mulet, J. Chem. Eng. Data 46 (2001) 1145–1148.
[84] S. Joung, C. Yoo, H. Shin, S. Kim, K.-P. Yoo, C. Lee, W. Huh, Fluid Phase Equilibr. 185 (2001) 219–230.
[85] H.-I. Chen, H.-Y. Chang, P.-H. Chen, J. Chem. Eng. Data 47 (2002) 776–780.
[86] S. Yoa, F. Liu, Z. Han, Z. Zhu, J. Chem. Eng. Chin. Univ. 3 (1989) 9.
[87] K. Suzuki, H. Sue, M. Itou, R. Smith, J. Chem. Eng. Data 35 (1990) 63.
[88] T. Suzuki, N. Tsuge, K. Nagahama, Fluid Phase Equilibr. 67 (1991) 213.
[89] J.-H. Yoon, H.-S. Lee, H. Lee, J. Chem. Eng. Data 38 (1993) 53.
[90] Y. Feng, Y. Hou, Petrochem. Technol. (China) 22 (1993) 803.

[91] J. Lim, Y. Lee, H. Chun, J. Supercrit. Fluids 7 (1994) 219.
[92] M. Radosz, J. Chem. Eng. Data 31 (1986) 43.
[93] M. Rätzsch, W. Schneider, D. Musche, J. Polymer Sci. Part A-1 9 (1971) 785.
[94] V. Zernov, V. Kogan, S. Ljubetskii, J. Appl. Chemistry (Moskow) 44 (8) (1971) 1837.
[95] A. Lindner, G. Luft, Ber. Bunsenges. 79 (5) (1975) 414–418.
[96] G. Eckhardt, W. Wagner, J. Mol. Spectrosc. 19 (1966) 407–411.
[97] H. Hatakeyama, T. Fujiyama, B. Chem. Soc. Jap. 51 (2) (1978) 431–433.
[98] A. Stratmann, Ph.D. thesis, submitted, Laseranwendungstechnik und Messsysteme, Maschinenbau, Ruhr-Universität Bochum (2003).
[99] D.-Y. Peng, D. Robinson, Ind. Eng. Chem. Fundam. I 15 (1976) 59.
[100] R. Reid, The Properties of gases and liquids, McGraw-Hill, New York, 1987, ISBN 0-07-051799-1.
[101] R. Span, W. Wagner, J. Phys. Chem. Ref. Data 25 (6) (1996) 1509–1596.
[102] J. Smukala, R. Span, W. Wagner, J. Phys. Chem. Ref. Data. 29 (5) (2000) 1053–1121.
[103] Merck, Chemie Datenbank: ChemDAT, http://www.merck.de (2002).
[104] H. Landolt, R. Börnstein, Numerical data and functional relationships in science and technology, Vol. IV/8G, Springer, Berlin, 2000, ISBN 3-540-66233-2.
[105] W. Walcher, Praktikum der Physik, 6th Edition, Teubner, Stuttgart, 1989, ISBN 3-519-03038-1.
[106] E. Cohen, B. Taylor, The 1986 Adjustment of the Fundamental Physical Constants, no. 63, Co Data Bull. Pergamon, Oxford, 1986.
[107] VDI, Wärmeatlas, 8th Edition, Springer, Berlin, 1997, ISBN 3-540-62900-9.
[108] IUPAC, J. Phys. Chem. Ref. Data 24 (1995) 1561.

Supercritical Fluids as Solvents and Reaction Media
G. Brunner (editor)

Chapter 1.5.

High-pressure solubility measurement of solids in near- and supercritical fluids

D. Tuma [a], B. Wagner [b] and G. M. Schneider [c]

[a] Universität Kaiserslautern, Fachbereich Maschinenbau und Verfahrenstechnik, Lehrstuhl für Technische Thermodynamik, 67663 Kaiserslautern

[b] Fachhochschule Aalen, Fachbereich Chemie, Beethovenstraße 1, 73430 Aalen

[c] Ruhr-Universität Bochum, Fakultät für Chemie, Physikalische Chemie, 44780 Bochum

1. INTRODUCTION

The development of supercritical fluid process design and technology up to now goes hand in hand with phase equilibrium thermodynamics from its (widely unnoticed) dawn in the late 1930s [1–3] over the 1960s, when chemical engineering has rediscovered the potential of the supercritical state [4], and has brought supercritical fluid extraction (SFE) to technical relevance. Collecting respective phase data remains a must in exploiting the solvent power of compressed gases both under near- and supercritical conditions. Brennecke and Eckert emphasize the importance of high-quality data acquisition in a journal review [5]. One key-statement of their treatise for a better fundamental understanding shall be repeated here in brief, because it characterizes the systems which will be discussed in this contribution in a lucid manner: Most binary systems (supercritical solvent + solute) fulfil what Brennecke and Eckert designate as "asymmetry", meaning the large differences in both size and intermolecular potential of the molecules involved. That is exactly true in view of the low-volatile, high-boiling organic substances and the particular solvent gases, from the non-dipolar but quadrupolar carbon dioxide to the polar chlorotrifluoromethane.

1.1. Objective and scope of our project

The objectives of our work as participants in the research program of the Deutsche Forschungsgemeinschaft (DFG) entitled "Supercritical Fluids as Solvents and Reaction Media" can be subsumed under the following statements. Our working intentions have been preceded by experiments on textile dyeing with dispersion dyestuffs dissolved in supercritical carbon dioxide in cooperation with the Deutsches Textilforschungszentrum Nord-West e. V. at Krefeld [6]. Already in those experiments, where dyeing has been performed under definite p,T-conditions, the necessity has arisen to investigate the solubility of those dispersion dyestuffs systematically. Pressure and temperature under which the colorant is dissolved strongly induce the coloration of the tissue, because these two parameters determine the dissolution, and the proper dyeing process with its peculiar thermodynamic and kinetic effects (such as dyestuff uptake, swelling of the tissue, etc.) is subordinate to the process of dissolution. The need for equilibrium data together with a rather well furnished equipment for high-pressure phase equilibria (e.g., sundry optical autoclaves applicable to maximum pressures of 100 and 200 MPa, respectively, spectrophotometers for UV-, VIS-, and NIR-investigation) as well first successful solubility investigations by means of NIR (cf. adamantane + CO_2 [7–9]) have motivated us to get a deeper insight to the solubility behaviour of dispersion dyestuffs in compressed gases. We have planned our experiments according to get highly precise equilibrium solubility data covering an extended p,ρ,T-range and also in other solvents than CO_2. Hereby, anthraquinone-based dispersion dyestuffs present themselves as model systems regarding the technique of measurement, because they are sufficiently stable during the experiment, and their spectral characteristics (i.e., their integrated molar absorption coefficient $B_{\tilde{\nu}}$) allow spectroscopic determination of even low concentrations ($\approx 10^{-5}$ mol dm^{-3}). All these facts help to ensure reproducibility of the experiments. Additionally, we have chosen β-carotene as a substance of preferential interest for supercritical extraction. In contrast to the anthraquinone derivatives, β-carotene, like many natural substances, is relatively unstable and well known to show stereomutation, but common to the anthraquinones is the suitability for spectroscopic investigations β-carotene has. Moreover, β-carotene is a substance where side effects, such as solvatochromism or isomerization (see chapter 4.1), can be studied.

As a second key-feature, we have collected data for modeling phase equilibria. It has been agreed that modeling should both correlate existing data and enable prediction in regions where experimental results are not available. Generally, thermodynamic models may help to reduce the number of data needed for a problem of process design. But at least as most models, corresponding mainly to equations of state and excluding any "closed form phenomenological models" like Chrastil's [10] work with adjustable parameters, a few experimental points

are needed for orientation. It is beneficial and reducing empirism to minimize the number of parameters and link those to real physical behaviour under maintenance of the theoretical framework of the equation. To have reliable and precise data over a large-scale p,T-area is a useful basis. Adjustable parameters are linked more closely to "thermophysical reality" and the applicability of the model may be extended to related systems. Selected data from experiments performed during this research program are subject to a new equation of state model by Kraska et al. and will be presented Chapter 1.10. of this book [11].

Our research has been experimental work, primarily high-pressure solubility experiments, with some auxiliary investigations concerning experimental handling and thermo-physical characteristics. Seven references can be designated as output directly related to this program [12–18], three additional papers deal with the aforementioned modeling [19–21]. Besides, the authors want to mention further five appertaining references which are anticipating [22–24] and immediately accompanying the duration of this research program [25,26]. Refs. 25 and 26 refer to a modified supercritical fluid chromatography technique, which has been adapted for solubility measurements, too, yet up to 20 MPa only. This equipment has served both for a purity check (cf. Ref. 15) of the substances and data production as well as reproduction. Results of our experiments have also been included in two review articles which outline the general activities in the field of supercritical fluids in our group at Bochum [27,28]. In short, our solubility investigations on the dispersion dyestuffs are subjects of the Refs. [12–14, 16, 18, 22–26], relevant for β-carotene are Refs. 13–15. The main characteristics for the understanding of the experiments will be presented in the corresponding sections of the present article, for further reading and detailed information the authors refer to the aforementioned references.

2. SOLUBILITY OF SOLIDS IN COMPRESSED GASES UNDER DISTINGUISHING HIGH PRESSURES

As already mentioned, we have performed our solubility experiments with particular attention to higher pressures than usually applied and reported in engineering and processing, especially in such techniques involving supercritical fluids. For example, at T = 313 K and p = 100 MPa CO_2 has a density ρ = 1102.5 kg m^{-3} [29], higher than water under normal conditions and far above the densities usually of a "SCF solvent" [5], which are approximately pending between 300 and 600 kg m^{-3}. The fact that very small pressure changes can give large density variations is one unique feature of the supercritical state, thus making it both interesting for, e.g., extractions and yet rather fastidious to handle.

That is a reason why solubility data for pressures of at least 100 MPa and more have been scarcely reported. The review of Bartle et al., which is related to the type substance of low volatility in CO_2 binary systems only, published in 1991 counts only 8 systems of totally 190 measured to pressures over 1000 atm [30]. A recently published review of Christov and Dohrn also covering solubility data published from 1994 to 1999 lists 824 binary systems, with 350 of the general sort carbon dioxide + X being the largest group [31]. From the altogether 13 systems of the latter which exceed the barrier of 100 MPa are not less than 10 originating from our group [22, 23, 32, 33]. If we classify all 824 tabulated binary systems by this criterion, a total of 56 references is found. We have been intensively engaged in the investigation at such high pressures, therefore a couple of characteristic features shall be delineated.

We measure the equilibrium solubility at T = const. ((low-volatile) solute = 2 and solvent = 1). The triple point of the solute is located at a significantly higher temperature than the critical point of the solvent 1. In this case, as pointed out by, e.g., van Konynenburg and Scott [34] and Schneider [35], the binary critical line (where l = g) in a $p(T)$-projection of a p,T,x-phase diagram is interrupted twice by the three phase line $s_2$lg. The two points of intersection represent the so-called lower and upper critical endpoint (LCEP and UCEP). Here, the two fluid phases, the gaseous and the liquid phase, become identical and the solid phase s_2 remains. Solubility measurements as well fluid extractions are performed in the temperature range between LCEP and UCEP.

From the total differentials of the chemical potential and from the material equilibrium condition combined with the Gibbs-Duhem-Margules relation we obtain for the pressure dependence of the mole fraction x_2'' of the solute in the fluid phase.

$$\frac{\mathrm{d}x_2''}{\mathrm{d}p} = -(V_2'' - V_{m,2}^{*\prime})\left(\frac{\partial x_2''}{\partial \mu_2''}\right)_{p,T} \qquad \text{at } T = \text{const.} \qquad (1)$$

In Eq. (1) $'$ stands for the pure solid phase (intrusion of solvent into the solid is neglected), $''$ for the fluid phase saturated with the solute 2. $V_{m,2}^{*\prime}$ is the molar volume of the pure solid, which we can take instead of the partial molar volume of solute V_2'. V_2'' is the corresponding partial molar volume of 2 in the fluid phase and μ_2'' its chemical potential. If $\left(\partial x_2''/\partial \mu_2''\right)_{p,T} > 0$, then the fluid phase is stable. For a qualitative description of the solubility behaviour it is recommended to eliminate its chemical potential. If we assume infinite dilution of 2

in the fluid phase, which is realistic due to the small concentrations, the Henry activity coefficient $f_2^{H//}$ can be set equal to unity.

$$\mu_2^{//} = \mu_2^{\infty//} + RT\ln\left(x_2^{//} f_2^{H//}\right) = \mu_2^{\infty//} + RT\ln x_2^{//} \tag{2}$$

$$\left(\frac{\partial\mu_2^{//}}{\partial x_2^{//}}\right)_{p,T} = \frac{RT}{x_2^{//}} \tag{3}$$

Eq. (3) describes the partial derivative of the chemical potential with respect to the mole fraction, and combination with Eq. (1) yields

$$\frac{\mathrm{d}\ln x_2^{//}}{\mathrm{d}p} = \frac{V_{m,2}^{*/} - V_2^{//}}{RT} \qquad \text{at } T = \text{const.} \tag{4}$$

Eq. (4) links the solubility $x_2^{//}$ with the pressure for a very small $x_2^{//}$. Fig. 1 illustrates a $p(x)$- (a) as well $p(c)$-isotherm (b) at T = const. Eq. (4) gives an extremum (e.g., a maximum of $x_2^{//}$) at $\mathrm{d}\ln x_2^{//}/\mathrm{d}p = 0$, i.e., at

$$V_{m,2}^{*/} - V_2^{//} = 0 \tag{5a}$$

$$\text{or } V_{m,2}^{*/} = V_2^{//} \tag{5b}.$$

More insight can be obtained, if the numerator on the right hand side of Eq. (4) is written as

$$V_{m,2}^{*/} - V_2^{//} = -(V_2^{//} - V_{m,2}^{*//}) - (V_{m,2}^{*//} - V_{m,2}^{*/}) \tag{6},$$

where $V_{m,2}^{*//}$ is the molar volume of the pure solute 2 in a (hypothetical) undercooled liquid state at the given values of pressure and temperature. The *second* term in brackets of Eq. (6) corresponds to the volume change of the (hypothetical) melting of pure solute 2; it is normally positive and small. The *first* term in brackets of Eq. (6), however, corresponds to the dissolution of the (hypothetical) pure liquid solute 2 in the fluid phase; since this term can be large and positive, negative or even zero, it determines the sign and the value of $\mathrm{d}x_2^{//}/\mathrm{d}p$. The change of sign of $\mathrm{d}x_2^{//}/\mathrm{d}p$ and the appearance of a maximum of $x_2^{//}$ with increas-

ing pressure (corresponding to $dx_2^{//}/dp = 0$) in Fig. 1a demonstrate the delicate balance between these two terms of Eq. (6).

Introduction of the solubility s_2 (in mol · volume^{-1} where – for very small solubilities as here – $s_2 = x_2^{//}/V_{m,1}^{*//}$) in Eq. (4) gives Eq. (7) where $\kappa_1^{*//}$ is the (isothermal) compressibility of the pure fluid solvent 1; here s^+ = unit solubility (see also Ref. 18):

$$\left(\frac{\partial \ln(s_2/s^+)}{\partial p}\right)_T = \frac{V_{m,2}^{*/} - V_2^{//}}{RT} + \kappa_1^{*//} \tag{7}$$

For the dependence of the solubility s_2 on density ρ, which is more frequently used than the dependence on pressure p, Eq. (8) holds (see again Ref. 18:

$$\left(\frac{\partial \ln(s_2/s^+)}{\partial \rho}\right)_T = \left(\frac{\partial \ln(s_2/s^+)}{\partial p}\right)_T \cdot \left(\frac{\partial p}{\partial \rho}\right)_T \tag{8}$$

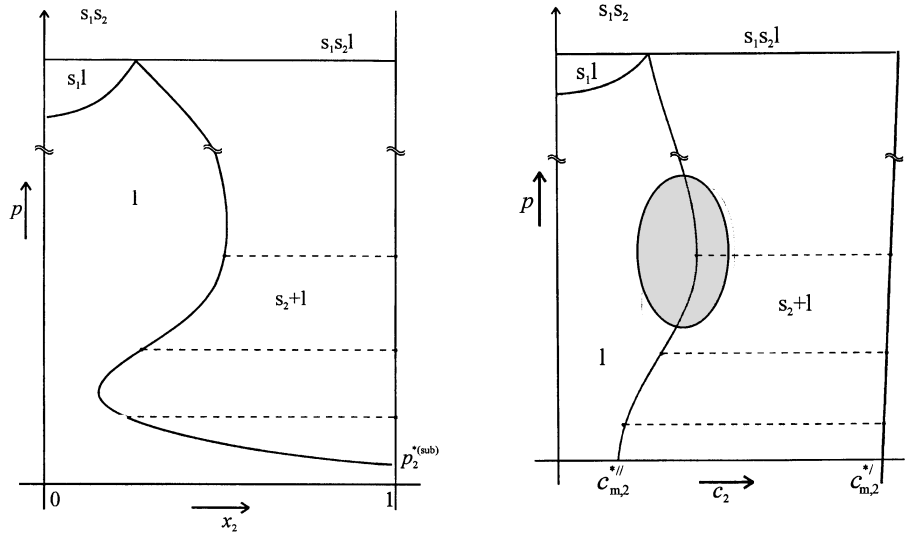

Fig. 1. Plot of a solubility isotherm as pressure vs. molar fraction (a) and pressure vs. concentration (b). The dashed curves represent lines of equal p and T. The inclination of the ordinate in (b) shall depict the compressibility of the solid. In reality, this effect is hardly observable and the ordinate practically perpendicular. The shaded area characterizes the pressures of our experiments.

The relevant criterion for the course of a solubility isotherm is the value of $(V_{m,2}^{*\prime} - V_2^{\prime\prime})$. At very low pressures (cf. Fig. 1a) the sublimation pressure $p_2^{*(sub)}$ determines the solubility practically alone giving $V_2^{\prime\prime} = RT/p_2^{*(sub)}$. With increasing solvent pressure the sublimation-originated contribution of the solute 2 in the gas phase decreases rapidly and passes a minimum. The "extraction effect" of the solvent remains at low pressures still low. This alters beyond the $p(x)$-minimum. In the $p(c)$-plot (Fig. 1b), however, there is no solubility minimum, since the number of solute molecules is related to the overall volume instead of the total amount of substance like in the $p(x)$-plot. At the bottom of the pressure axis in Fig. 1b the solute concentration is low and increases up to higher pressures.

Surprisingly, both solubility isotherms pass a solubility maximum, which means that a region of retrograde solubility despite further enhanced pressure is entered. After all, at ultrahigh pressures the solubility isotherms meet the s_1s_2l-phase border, both solvent and solute are in the solid state beyond this line. This at first sight odd behavior becomes more obvious, when we once again take a look at the value of $(V_{m,2}^{*\prime} - V_2^{\prime\prime})$. If $V_2^{\prime\prime} < V_{m,2}^{*\prime}$, then the right numerator in Eq. (4) becomes positive and the solute's molar fraction $x_2^{\prime\prime}$ increases with increasing pressures. At $V_2^{\prime\prime} = V_{m,2}^{*\prime}$ there is the extremum (either minimum or maximum), and when the relation changes into $V_2^{\prime\prime} > V_{m,2}^{*\prime}$, this numerator in Eq. (4) becomes negative, resulting in a retrograde course of $x_2^{\prime\prime}$ with increasing pressures. In the region of retrograde solubility behavior the solid state is thermodynamically favoured, since the highly compressed solvent hinders the further absorption of dissolved solute molecules. Prausnitz et al. have called this effect "squeezing out" [36]. The pressures where such a phenomenon can be observed for binary systems will strongly be different from each other, but predestined by thermodynamic rules as the ratio of $V_2^{\prime\prime}$ to $V_{m,2}^{*\prime}$ demonstrates. A high-pressure solubility maximum is neither an artifact nor a rare phenomenon [37]. Gitterman and Procaccia have derived a quantitative theory of supercritical solubility by a thermodynamic reflection of the slopes of the solubility curves [38]. Ultimately, this effect has been proven by the equation of state model developed by Kraska et al. [11, 19–21].

3. EXPERIMENTAL

3.1. Substances

The following substances have become involved into this project:
Carbon dioxide (CO_2), nitrous oxide (N_2O), fluoroform (CHF_3), chlorotrifluoromethane ($CClF_3$), and sulfur hexafluoride (SF_6) have been used as solvents.

The solutes chosen for high-pressure solubility measurements have been the anthraquinone derivatives, dispersion dyestuffs, and textile colorants 1,4-diamino-2-methoxyanthraquinone (Disperse Red 11, abbreviated DR11), 1-amino-4-methoxy-2-phenoxy-9,10-anthraquinone (Disperse Red 60, DR60) as well eight members of the 1,4-bis-(alkylamino)-9,10-anthraquinone series where "alkyl" is varying from methyl (Solvent Blue 78, AQ01) over ethyl (Solvent Blue 59, AQ02), propyl (AQ03), 1-methylethyl or isopropyl (Solvent Blue 36, AQiso03), butyl (Solvent Blue 35, AQ04), pentyl (Solvent Blue 14, AQ05), octyl (AQ08) to finally octadecyl (AQ18), as well β-carotene (β,β-carotene). The Refs. 13 and 16 provide further information, for example, on product specification and quality, of these chemicals.

3.2. Techniques of solubility measurements and systems investigated

Our high-boiling substances have to fulfil the qualification for UV/VIS-measurements. We demand from the dyestuff in interaction with the solvent that spectrophotometric analysis covering the *p*,*T*-capacities of our autoclaves can be performed. Because our cells have a fixed optical path length, the most important restriction which limits our experiment is a too high solubility manifesting in high values of absorbance.

Three different experimental devices have been used throughout this project. The first one is a SFC-apparatus modified in such a manner that dynamic solubility investigations to 20 MPa are feasible in addition to "normal chromatography". This specification has enabled us to analyze the purity of the raw material and, of greater importance for our experiments, to elute the troublesome by-products of better volatility in a continuous CO_2-flow. The analytical column is replaced by an extraction column without a customary stationary phase but filled with the dyestuff only. The carbon dioxide flowing through the column is charged with the dyestuff up to equilibrium solubility and is led through an optical cell which is connected to the detector by light guides. A diode array detector for ultraviolet and visible light serves to analyze the equilibrium absorbance (for solubility measurements) and the characteristic spectral pattern of the several components (in chromatographic analysis), respectively. As the diode array delivers a spectral profile over the wavelength range spectrum almost instantaneously, the dyestuff-filled column can be used in both experiments (solubility, purity control). A separation into components with individual retention times is not necessary, the components are determined by band analysis. Details of this

equipment are reported in Refs. 20 and 26, the second gives a schematic outline. The most profound description outside periodicals, however, is given by the doctoral theses of Kautz [39] and Wagner [40], respectively.

The other two installations are outlined by the static principle, which means the core piece is a high-pressure autoclave where a phase equilibrium is kept at constant p,T-conditions and observed by (the non-intrusive) UV/VIS-spectroscopy. The cell itself is made from a non-magnetic alloy, so that a magnetic stirrer within the sample space can be agitated from outside. The sample volume can easily be changed and measured by moving a piston of which the position can be determined inductively. A pressurizing fluid serves to induce the sample pressure. The first of the two autoclaves, equipped with two pairs of sapphire windows, is designed for a p_{max} of 100 MPa, the other with a single pair of windows for a p_{max} of 200 MPa, respectively. Fiber optics couple the sapphire windows to the spectrophotometer. For further reading of the static apparatuses, see the Refs. 13 and 28 for the 200-MPa device and the Refs. 15 and 41 for the other. Similar to the dynamic installation, a deeper insight into set-up as well operation is provided by the doctoral theses of Tuma [42] and Maiwald [43]. The proper solubility measurement is comparatively simple. After filling with the dyestuff ($\approx$ 0.01–0.02 g to ensure saturation at all p,T-conditions) and evacuating, the autoclave is adjusted to the particular temperature. Experience has shown that the best way is to record a solubility isotherm by a stepwise pressure increase to avoid any risk of supersaturation. Cross-check experiments have shown that more often than expected the investigated systems exhibit this effect, but without a regular trend. Equilibration time, however, depends largely on temperature conditions. Normally, at higher temperatures it becomes shorter. A time-drive tool in the spectrometer software allows to follow the course of equilibration.

The dynamic method has been applied to investigate AQ01, AQ02, AQ03, AQiso03, AQ04, AQ05, and AQ08 at pressures and temperatures between $299 \leq T/\mathrm{K} \leq 346$ and $7 \leq p/\mathrm{MPa} \leq 20$. All other substances have been investigated by the static method, with the p,T-ranges as follows: $330 \leq T/\mathrm{K} \leq 400$ and $17 \leq p/\mathrm{MPa} \leq 180$ for AQ18, $300 \leq T/\mathrm{K} \leq 340$ and $10 \leq p/\mathrm{MPa} \leq 140$ for DR11, $303.1 \leq T/\mathrm{K} \leq 332.7$ and $7.2 \leq p/\mathrm{MPa} \leq 97.6$ for DR60, and additionally AQ08 in the p,T-range $282.5 \leq T/\mathrm{K} \leq 341.5$ and $4.43 \leq p/\mathrm{MPa} \leq 107.5$, respectively. The p,T-frame has been $296.8 \leq T/\mathrm{K} \leq 326.0$ and $8 \leq p/\mathrm{MPa} \leq 180$ for β-carotene. The SFC-equipment has been exclusively operated with CO_2 as solvent, the other solvents have been applied in the static measurements in addition to CO_2, because the principle of an encapsulated sample of solvent + solute allows a rather easy exchange of the solvent. At best, one filling can be sufficient for the determination of more than one solubility isotherm (say three or four) covering the accessible pressure range. So, the solubility of AQ08 has as well

been investigated in N_2O, $CClF_3$, and SF_6, that of AQ18 in N_2O, of DR11 in N_2O and CHF_3, of DR60 in N_2O, $CClF_3$, and SF_6, and finally the solubility of β-carotene in N_2O and $CClF_3$. The corresponding references mentioned in Subsection 1.1 provide further details.

3.3. Experiments preparatory to solubility measurements and auxiliary investigations

3.3.1. Calibration in organic solvents and carbon dioxide

Prior to any solubility measurements in a compressed gas, a calibration function has to be determined. It is a common practice in spectroscopy to prepare stock solutions of the solute (i.e., the particular dyestuff) in an appropriate organic solvent (catchwords stability, sufficient solubility), commonly acetone, cyclohexane, ethanol, tetrahydrofuran, etc., and make a series of different concentrations by dilution.

Strictly speaking, both calibration and measurement should be done in the same solvent to get maximum spectral conformity. Practically, this means that for calibrations in organic solvents such solvents must be chosen where the molar absorption coefficient $B_{\tilde{\nu}}$ of the solute is most similar to that in, e.g., CO_2. We have been able to use the 100-MPa-autoclave for calibration in CO_2. It is realized as follows. An exactly defined amount of substance is introduced into the cell and dissolved by the CO_2. It is absolutely mandatory that this sample completely dissolves at any p,T-conditions. Different concentrations in the unit "moles per liter" are created by changing the cell volume (liter), thus opposite to the common dilution series where the amounts of substance (moles) are changed. By doing so, it can be proven whether an organic solvent is qualified for being used as calibration medium. We have verified this method exemplarily for the anthraquinone derivatives and discuss it in Ref. 15. We have also emphasized in this paper [15] in accordance with other authors that it is more advantageous to use integrated absorbances, meaning a full scan of the spectra instead of measuring at a fixed single wavelength and moreover with wavenumbers $\tilde{\nu}$ instead of wavelengths λ.

3.3.2. Calibration for β-carotene

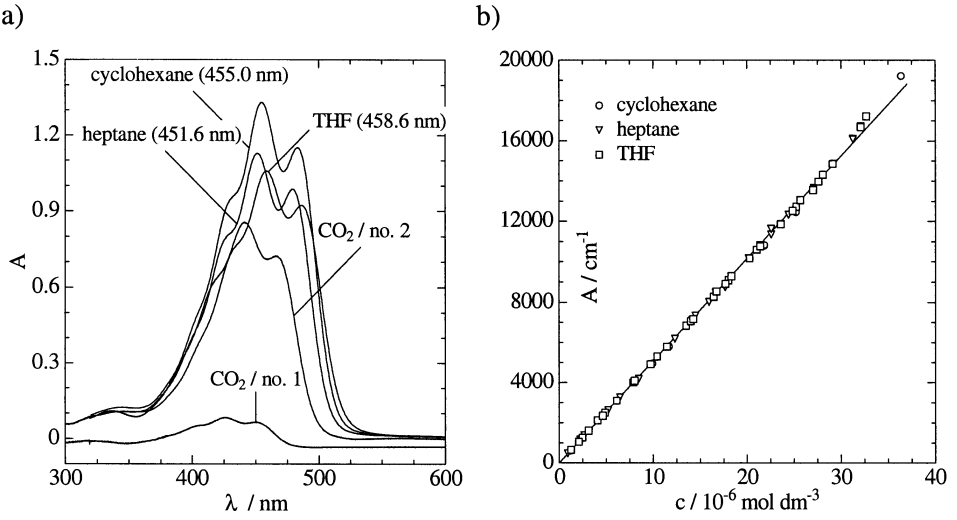

Fig. 2. a: Spectrum of β-carotene in different solvents and carbon dioxide (no. 1: T = 307.6 K, p = 8.5 MPa, λ_{max} = 425.9 nm; no. 2: T = 307.6 K, p = 180 MPa, λ_{max} = 441.4 nm). The wavelength indicates maximum absorbance. b: Calibration function of β-carotene in different solvents (reference optical path length d = 1 cm, quartz cuvettes). The $B_{\tilde{\nu}}$-values of β-carotene calculated from these lines are: $5.094 \cdot 10^9$ m mol^{-1} for cyclohexane, $5.074 \cdot 10^9$ m mol^{-1} for heptane, and $5.090 \cdot 10^9$ m mol^{-1} for THF.

These statements shall be pointed up guided by the calibration for β-carotene. Which solvents are to come into consideration? Solvatochromic studies applying the model developed by Kamlet, Abboud, and Taft performed by Maiwald show that carbon dioxide resembles cyclohexane [41]. Craft and Soares, jr. have investigated solubility, stability, and molar absorption coefficient of β-carotene in 18 different solvents [44]. They have found that the values for ε_{max} (i.e., at maximum absorbance of β-carotene) are located between the extrema 121300 l mol^{-1} cm^{-1} for DMSO and 142800 l mol^{-1} cm^{-1} for diethylether. Our sequence of $B_{\tilde{\nu}}$ (cf. Fig. 2b) fits in their ε_{max}-series. In the literature, ε_{max} for hexane (139200 l mol^{-1} cm^{-1} [45]) is often taken as so-called "reference absorptivity". In their experiments, Jay et al., for instance, have compared the molar absorption coefficient ($E_{1\%/1cm}$) of CO_2 at 50 MPa and 35 °C with that of hexane at normal conditions. Both values, 2624 ± 165 for CO_2 as well 2592 for hexane, are rather similar [46, 47]. Therefore, hexane or the less noxious cyclohexane can be used as calibration solvent for β-carotene [13]. Recently, $E_{1\%/1cm}$ = 2500 at maximum absorbance for β-carotene in cyclohexane

has been established as a standard [48, 49]. Notably, Jay et al. have recorded spectra of β-carotene both in various organic solvents and different near- and supercritical conditions for different gases [46, 47] and have seen a remarkable solvatochromism. As illustrated in Fig. 2a, we have observed the same. Thus, it is reasonable to work with the integrated absorbance, since supposing we would determine our β-carotene solubility by the absorbance of the central peak maximum (cf. Fig. 2a), maybe additionally set invariable throughout the experiment, we slip from the peak top onto the trailing edge, in other words, our results will be shifted to lower solubilities. If we record the complete spectrum, the solvatochromic shift can largely be compensated. What is now still remaining is the fact that the spectral pattern of β-carotene is also dependent on temperature and pressure. Reducing the temperature gives sharper peaks and shifts the spectrum to higher wavelengths [50–52], e.g., by 17.5 nm when going from room temperature to the temperature of liquid nitrogen (–185 °C). Throughout our experiments, however, the temperature range covered $\Delta T = 30$ °C only (instead of $\Delta T = 205$ °C in Loeb's experiment). Thus, this effect shall be negligible. A much more severe challenge for solubility experiments in general and in our opinion the main source of errors is the thermally induced isomerization and degradation. As closing statement, we would like to mention that Ngo et al. [53] refer to these particular points giving striking examples of how erroneous a spectral analysis can be when proceeding from false assumptions.

3.3.3. Auxiliary investigations

The auxiliary investigations primarily refer to crystal structure and polymorphism of the solid state for the different anthraquinone derivatives. The question has been whether and in which way they influence the solubility behavior in a series of similar solutes. Ref. 16 is dedicated to this matter, the major findings shall be discussed in Section 4.

4. RESULTS

The particular contribution of our group in technical terms and how we have pursued our objectives has been described so far. Leaving the technical part, we want to sketch the ideas behind our experiments, what has motivated us and, in particular, what we might consider as new scientific findings in the retrospect. Furthermore, this chapter shall provide a compilation of our findings and interpretations which otherwise have to be drawn from the various respective references.

4.1. Investigations on β-carotene

β-Carotene is one of the most important bio-molecules. Over decades, this substance has been subject to intensive studies on the application of multivariant extraction techniques. Since β-carotene is highly sensitive to stereomutation, the comparatively "mild" supercritical fluid extraction has established itself as a serious alternative. A recent database search giving 18 references only for β-carotene + CO_2 (we list 17 of them, this counting as well, in Ref. 19, in 2002 a paper by Gómez-Prieto et al. has been added [54]) expresses the outstanding importance of this system. We have considered β-carotene to be ideal for our measuring method and thus have taken up investigations. There are astonishing and evident discrepancies between published data, a problem many authors have figured out and sometimes comprehensively discussed in their contributions. Here, we would like to accentuate the two recently published papers by Sovová et al. [55] and Hansen et al. [56].

They compare their own results with the different existing data sets and point out possible reasons for the discrepancies among solubility results. Degradation and isomerization, solvatochromic shift, and different modifications are appointed as reasons for disagreeing results. In Fig. 3 our results for measurements in CO_2 and N_2O at $T = 322.9$ K are presented together with those results from literature which have been obtained at a similar temperature and give best agreement with ours. Fig. 3a shows that data agree remarkably well at lower densities (e.g., at $\rho = 700$ kg m^{-3} the most distant point is 43 % lower than our corresponding value), and the deviation increases when going to higher densities. Anyway, at $\rho = 850$ kg m^{-3} all data deviation still remains lower than a factor of 2. For N_2O, however, these deviations are more pronounced, at $\rho = 700$ kg m^{-3} (see Fig. 3b) the data of Subra et al. lie above our measurements by approximately a factor of 2.35 [57]. Hansen et al. give in their paper a statement that the solubility of β-carotene in CO_2 is not known to within better than a factor of 2 (at a temperature around 40 °C) [56].

Obviously, CO_2 is a very poor solvent compared to commonly used liquid organic extractants [44,47], therefore the question is how to get an improvement

which can make an economic extraction feasible. N_2O is physically similar to CO_2 and is a much better solvent for β-carotene at all p,T-conditions investigated. Thus, Subra et al. consider N_2O to be a serious alternative for the extraction of β-carotene [57] and other carotenoids. A restriction, however, is the risk of sudden decomposition of N_2O [60]. This explosion risk is certainly a reason why not only the research on carotenoid extraction but on extraction processing in general focuses on the addition of a co-solvent or entrainer (such as ethanol, methanol, or methylene chloride) to CO_2 as the mobile phase instead. For example, Jay et al. have found a tenfold enhancement in solubility at lower pressures up to 20 MPa by the presence of 6 % ethanol [46], Sovová et al. have found proportionality between the square root of ethanol concentration and the modified increase in β-carotene solubility [55].

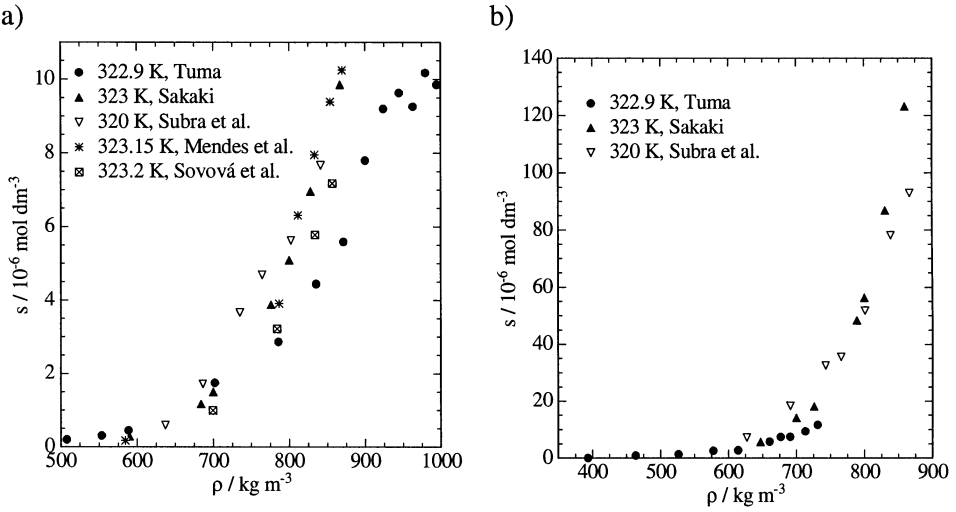

Fig. 3. Solubility of β-carotene in CO_2 (a) and N_2O (b). Comparison of our data with selected results from literature [55,57–59]. The entire data plotted of our solubility measurements for β-carotene can be found in Chapter 1.10. of this book [11].

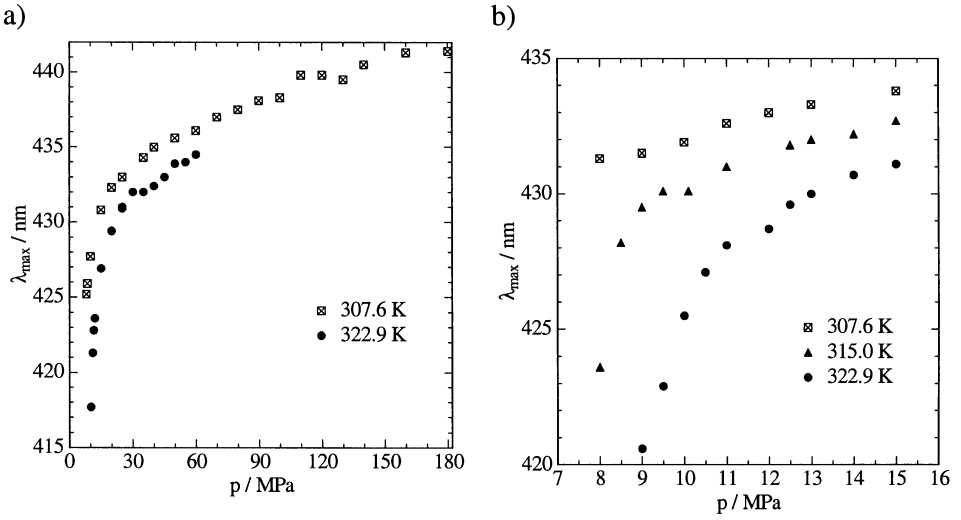

Fig. 4. Solvatochromism of β-carotene. Wavelength of maximum absorbance λ_{max} versus pressure p for CO_2 (a) and N_2O (b) at T = const.

The particular difficulties accompanying the investigation of β-carotene have already been mentioned. Our measuring technique gives us a full scan of the UV/VIS-spectrum for each datapoint which enables us to monitor solvatochromism simultaneously. Its influence must not be underestimated, as Fig. 4 illustrates.

The particular solvatochromism exhibited by β-carotene shows that higher pressures induce a bathochromic shift, whereas higher temperatures make a hypsochromic shift. The latter effect is distinctly smaller. It is striking to take a look at those pressures where extraction processes are normally operated. At T = 322.9 K λ_{max} is shifted by not less than 14.3 nm between 10.2 and 35 MPa.

Of greatest evidence, of course, is the inherent lability of β-carotene against thermally induced isomerization and decomposition [13]. Likewise, UV/VIS-spectroscopy gives the opportunity to observe any changes inside the solute. The distinctive mark is the so-called "cis-peak" in the UV-region, actually between 320 and 380 nm, which is contributed by the formation of (several) cis-isomers. The technique of static measurement confronts us with the following situation. Two kinetic processes, namely equilibrium solubility alignment is accompanied by an isomerization which is dependent on the particular p,T-conditions as well, and what we do is to record the total absorption spectrum in situ. The isomerization is known to be reversible and, of particular importance, the different cis-isomers of β-carotene are better soluble than the corresponding all-trans molecule [61]. We have no possibility to take a sample for analyzing its individual

composition, e.g., by means of HPLC. On the time-scale, we can see a continuous increase of the peak area during the experiment (cf. Fig. 6 in Ref. 13), except at higher temperatures when thermal decomposition becomes dominant [62,63]. As β-carotene is broken up into smaller fragments, the characteristic orange color diminishes rather quickly. An experiment at T = 349.9 K and p = 17.5 MPa showed an immediate decomposition reducing the total peak area within one hour by approximately 50 %. The molar absorption coefficient of these UV-active descendants is small. Therefore, it means, we have to find out two things only by looking at the structure of the recorded spectrum: When do we reach equilibrium solubility of the all-trans isomer? How do we quantify it by spectral analysis? For this purpose, we have applied a method proposed by Liaaen-Jensen [64] to estimate by analyzing the peak ratio of the λ_{max} absorption band and the longest wavelength absorption band and another absorption ratio between the λ_{max}-peak and the cis-peak. In Ref. 14 this model has been applied on our solubility measurements in CO_2 and N_2O. Saying that we "quantify" isomer content is somewhat exaggerated. We should not expect too much from an in-situ method here. Upon which these peak ratios, two dimensionless figures, give information is an alteration of the composition on a time scale [14]. Growing peak areas, for example, concurrent with these particular peak ratios remaining constant, indicate that no other than the dissolution process proceeds, meaning solubility equilibration. The results support our assumption to expect equilibrium solubility after one hour. Surprisingly, N_2O promotes isomerization less than CO_2 in addition to its enhanced solvent strength. Taking this into account, N_2O might be feasible for extraction, because compared to CO_2 lower pressures give higher yields with minor isomerization. Besides, Schierle et al. have developed a simple spectrophotometric method for fast routine measurements of total β-carotene in commercial products such as food additives that contain geometrical isomers in variable ratio [65].

Ultimately, a few statements should be given concerning modeling of these particular systems. Three of the four authors mentioned individually in Fig. 3 [57,59,60] have correlated their results using the density-based equation proposed by Chrastil [10]. The model gives a satisfactory correlation over the pressure (density) range which they have investigated, for all four authors not going further than 30 MPa as maximum pressure. Our own experiments, however, have included much higher pressures. At T = 307.6 K in CO_2, for example, we run through a solubility maximum at a pressure around 60 MPa. We defer further discussion until the next section. It shall be mentioned in advance that the validity of Chrastil's model fails at these high densities. Besides, Hansen et al. [56], who have tried to correlate our data with a similar model proposed by Méndez-Santiago and Teja [66], a modification of the Chrastil model, could not proceed with our data above 80 MPa. This correlation is also failing at high densities. We conclude that it is more reasonable to model the solubility, especially

when data over an extended p,T-range exist, by an equation of state. For more details we would once more like to refer to the contribution by Kraska et al. in this book, Chapter 1.10. [11].

4.2. Investigations on a series of anthraquinone derivatives, simultaneously used as dispersion dyestuffs

Since the possibility is discussed to replace conventional dyeing of polyester fabrics by a dyeing process in supercritical carbon dioxide, anthraquinone-type disperse dyestuffs have always been considered as preferential colorants. Contrary to β-carotene, which demands distinctive dedication by the operator on doing such high-pressure solubility experiments, this task is much easier with the anthraquinones. More, these kinds of substances are well-suited candidates for systematic investigations. Their solubilities in CO_2 and most other solvents used in supercritical fluid techniques are sufficiently low to exhaust our apparative possibilities, especially going up to pressures as high as 100 MPa or even more, they have proven to be stable under all measurement conditions, they show distinct and easy-to-analyze spectra in the visible region (blue and red colours), and, most important, the experiments can easily be reproduced. That has motivated us to establish a program for systematic measurements with the following leading ideas:

1) The application of two different methods (i.e., static and dynamic) provides high-quality data covering a larger p,T-region than usually reported in literature, meaning both liquid and supercritical state (temperature), and going from fluid-like to liquid-like densities (pressure / density).

2) Can we derive predictive rules for quantitative solubility from measuring homologous series, here, e.g., growing alkyl-substituents in a 1,4-bis-(alkylamino)-9,10-anthraquinone series?

3) What influences solubility most: Substituents, crystal structure as well polymorphism of the solid state, or yet primarily the solvent gas?

We have devoted much time and have taken painstaking efforts to bring some light into these complex and partly cryptic interrelations. We have employed further methods to achieve those ambitious goals, in particular for an additional investigation of the solid state, such as differential scanning calorimetry (DSC) to find phase transitions [67]. Besides, we have determined the molecular structure of one dyestuff, AQ02, by X-ray diffractometry [17]. Our results and argumentations relating thereto are tenor of a special paper [16]. In the following paragraph, we would like to sum up the main statements.

There is no monotonous function between increasing alkyl side-chains and solubility, although the melting temperature T_{fus} steadily decreases in the ascending sequence AQ01 to AQ08 (except AQiso03), reaches a minimum for AQ08, and again increases with further elongation of the alkyl chains [16]. The solubility is best not for AQ01, as might be assumed at first sight, but fluctuating

between AQ03 and AQ05. From a certain chain length on (AQ08 and higher) the solubility decreases. Which substance is best soluble in CO_2 depends also on the temperature, but the sequence is not really upset within the temperature interval investigated. AQiso03, however, remains in front throughout all *p,T*-conditions, its solubility being comparable to that of the unsubstituted 9,10-anthraquinone [68]. DR11 and DR60, both rather polar, belong to the poorly soluble dyestuffs, what is not really surprising. Anyway, quinizarin or 1,4-dihydroxy-9,10-anthraquinone is even better soluble than 9,10-anthraquinone [68]. There are chemists from the Islamic Republic of Iran (Shamsipur, Yamini, and co-workers) who perform similar comparative studies with different anthraquinone series in a dynamic apparatus up to (remarkably high) 40 MPa [69–71]. The results obtained from their studies cannot depict clear substituent-related trends, either. However, self-association and possible intra-molecular H-bonding in the solid state are considered to be relevant.

A further significant parameter determining solubility is the crystal structure and phase transitions in the solid state. As for β-carotene, it has been speculated that the structure of the solid might play a role. A crystalline solid will have a lower Gibbs energy and thus a lower solubility than the amorphous solid, and Sakaki (although no measurements with both modifications are reported from him) has picked up this idea to explain data discrepancies [58]. It seems obvious that a densely packed crystal does not favour dissolution, but on the other hand polymorphism and the weakening of the packing by temperature and solvent intrusion shall favour dissolution. Under the *p,T*-conditions of a supercritical fluid T_{fus} of the solid will drop significantly. Unfortunately, until now there is not enough information on the crystal structure of the 1,4-bis-(alkylamino)-9,10-anthraquinones available. From the solid densities published that of AQiso03 is the lowest, what is compatible with the high solubility. A remark by Bartle et al. [30], in their review paradoxically at a rather subordinate place, is noteworthy to be cited here. "When a solute or solute-rich phase undergoes a phase change, ... , there is no discontinuity in the solubility versus pressure curve, as can be supported by thermodynamic arguments." However, if the solute undergoes a first-order phase transition like melting, the transition enthalpy as well the transition volume have to be considered. When we look at our solubility isotherms, we cannot see any effect of a possible phase change, either. It is likely that the accuracy of our measuring technique is not sufficient.

If we vary the solvent instead of the solute, the outcome is drastically different. The effects discussed so far are downright eclipsed when we compare the solubility of our substances in different solvents. We have started varying the solvents in our investigations from the very beginning [22, 23]. For all our substances, the anthraquinone derivatives and β-carotene, N_2O has been found to be the best solvent, followed by CO_2, and after a big interval $CClF_3$ and SF_6. The unexpected high solubility of DR11 in CHF_3 may be associated with hydrogen

bonding between the acidic proton of fluoroform and the carbonyl groups on the anthraquinone ring [23]. Such comparisons, however, must be treated as conditional, since it is not really consistent to compare systematically the solubilities of a given solute in a rather unlikely series of chemically diverse gases. But the picture becomes much less confusing, as those solvents possess nearly equal critical temperatures.

Thus, we have tried to plot solubility versus the reduced density ρ/ρ_c for comparison, as shown in Figs. 5 and 6. There is no substantial difference between the two plots, even though DR60 is more polar than AQ08. Taking another example, it has been postulated that benzoic acid, due to its polarity, might be highly soluble in the likewise highly polar solvent CHF_3. The results, however, do not support this idea [72]. Measurements in $CClF_3$, which is also a polar solvent, have given similar results. Brunner and Peter have suggested, that polarity of the solvent does not appear to play a key-role in correlating the observed trends in supercritical fluid solubility [73]. Anyway, if we look at our β-carotene measurements and those in not less than 14 (near- and) supercritical solvents by Jay et al. [47], we see a similar picture as well. Like for the anthraquinone dyestuffs, N_2O appears to be the best, CO_2 a superior solvent, CHF_3 and $CClF_3$ follow in order of decreasing solubilizing power, SF_6 is the poorest solvent.

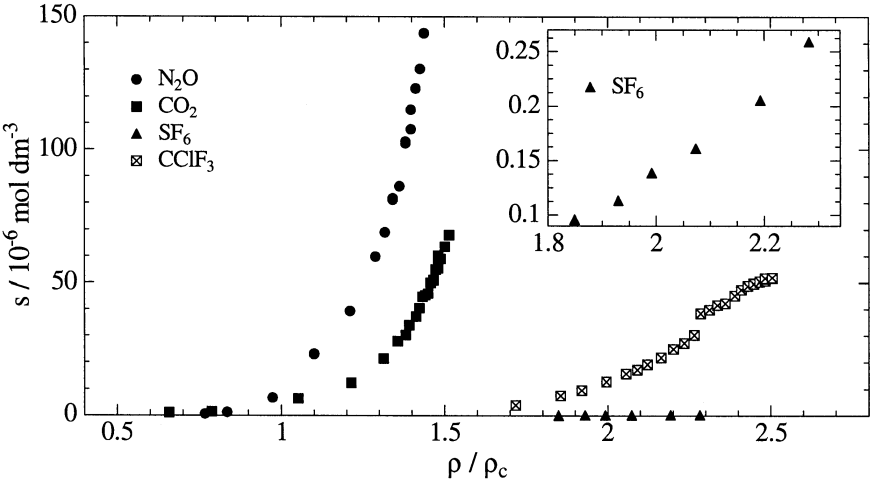

Fig. 5. Comparative solubility diagram of AQ08 in four solvents at $T = 315.7$ K (N_2O, CO_2, SF_6) and at $T = 314.6$ K ($CClF_3$). The density data source for the solvents here is given in Ref. 16. Solubility is plotted versus the reduced density, the inset showing the particular isotherm for AQ08 in SF_6 on a larger scale.

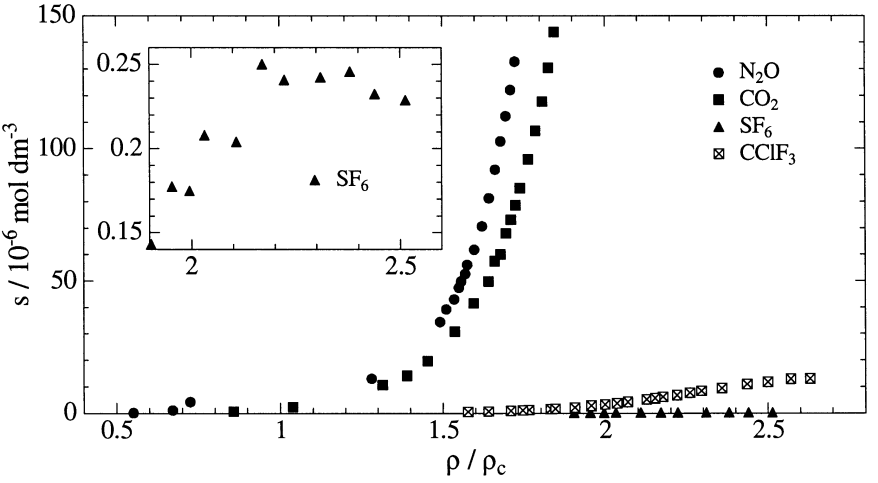

Fig. 6. Comparative solubility diagram of DR60 in four solvents at $T = 310.4$ K.

A phenomenon which we have kept track on from the beginning of our activities on high-pressure solubility measurements is the retrograde solubility at distinguishing high pressures, meaning when the isothermal plot solubility versus density or pressure goes through a maximum. In Chapter 2 we have pointed out that retrograde solubility is neither an artefact of data analysis nor an oddity. Sometimes, the existence of solubility maxima is still doubted, although it has been single subject of a paper by Kurnik and Reid published in 1981 [37]. We have spotted solubility maxima in dissimilar systems, in AQ18 + CO_2 and + N_2O [21,22], AQ16 + CO_2 [23], AQ08 + SF_6 [13], and β-carotene + CO_2 [19,24], but common to all the maximum has always occurred at liquid-like high solvent densities ($\rho \geq 1000$ kg m^{-3}). If such high densities (and corresponding pressures) can be achieved and analyzed – our static device is specially designed for this purpose – via such kind of solvent tuning, solubility maxima are likely to be found. The accomplishment of the criterion $V_2^{//} = V_{m,2}^{*/}$ is viable by tuning temperature and pressure (and thus density), the solvent itself (e.g., SF_6 has a critical density ρ_c of 736 kg m^{-3}), but also the solute (taking a substance of particularly low solubility). The quantitative solubility and if this value can be analyzed by the equipment or not is decisive. It is indicated by the characteristic curvature of the solubility isotherm at enhanced densities that the isotherm is approaching towards an extremum, as can be seen in Fig. 7 for the isotherms of the system AQ08 + CO_2 at 285.9 K, 291.0 K, and 303.2 K.

Many researchers, mostly chemical engineers, propagate Chrastil's model as an easy correlation tool which gives astonishing good results [10]. This model is based on the hypothesis that each solute molecule A associates with k (cf. Fig.

8) molecules of the solvent B to form a solvatocomplex AB_k which, in turn, is in equilibrium with the system. Chrastil's model is a simple three-parameter equation relating the solubility of the solute s to the solvent density ρ and the temperature T of the solvent. The plot of ln s (ln (s/s_0)) versus ln ρ (ln (ρ/ρ_0)) shall give a linear function over a wide range of solvent densities and temperatures. Strictly speaking, phenomenological models like Chrastil's are not capable of predicting unknown phase equilibria, although they serve a useful purpose in correlating existing data. For example, in all papers on anthraquinone solubilities of the aforementioned Iranian scientists density-based correlations analogous to Chrastil's equation [71] and the genuine model itself [69,70] show good agreement with the experimental data.

Its performance also to higher pressures than usually has attracted our interest. Fig. 8 distinctly shows that the linear function is kept within a restricted area only. If we look out for a distinctive feature in those double-logarithmic plots, there is rather often a deviation from linearity both at lowest and at the highest densities investigated. We have analyzed selected solubility data sets (AQ01 + CO_2 and AQiso03 + CO_2) in a way that two expressions for the molar solution energy, $\Delta_{sol}E_p$ and $\Delta_{sol}E_\rho$ have been derived from plots logarithm of the solubility versus the reciprocal temperature at constant pressure as well as constant density [18]. $\Delta_{sol}E_\rho$ obtained from isopycnic sections corresponds to the "total reaction heat" in Chrastil's model and is closely constant over a

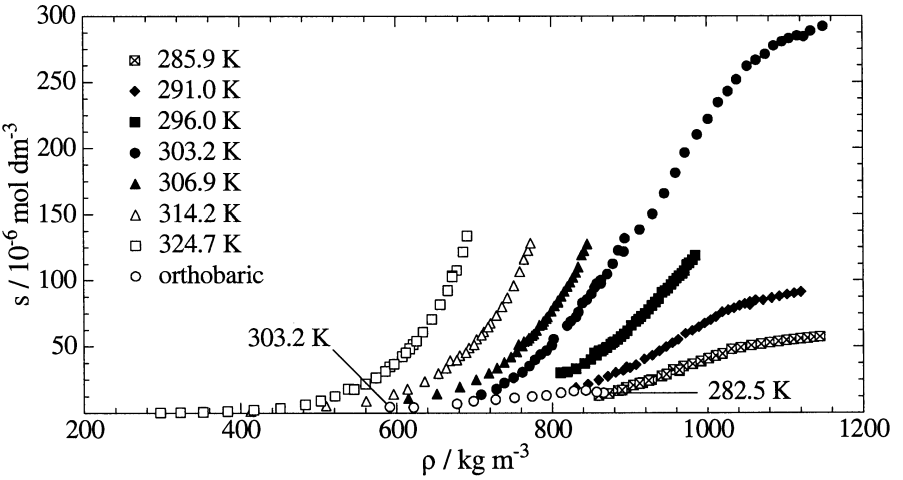

Fig. 7. Solubility of AQ08 in CO_2. The curvature of the isotherm alters at ρ = 956 kg m^{-3} for T = 291.0 K and ρ = 940 kg m^{-3} for T = 303.2 K, respectively. Supplementarily, solubility at orthobaric conditions (in the liquid phase along the vapor pressure curve) in a temperature range 282.5 ≤ T/K ≤ 303.2 are given.

considerable p,ρ,T-range and thus giving a linear function for ln s versus ln ρ. We maintain that Chrastil's model performs well approximately between 400 and 800 kg m^{-3} of solvent density. Furthermore, it seems reasonable that the proposed solvatocomplex shall be different at densities typical for the supercritical state, better for those density range exploited in supercritical fluid processing, and at liquid-like densities ($\rho \geq 800$ kg m^{-3}), since a supercritical fluid under these particular conditions has different thermo-physical properties than a liquid. Of course, this empirical correlation can be improved by making the k density-dependent and adding more parameters [74], but the model keeps being strictly adherent to the data and its quality. For those reasons, we favour the way via equations of state instead. With this key-word, the authors would like to lead over to the article of Kraska et al. in this book which goes more deeply into the field of equations of state [11].

5. CONCLUSIONS

Our specially designed high-pressure equipment, which enables us to surpass pressure regions usually inaccessible (or uninteresting) for most research groups, has motivated us to make a step towards the "terra incognita" of "supercritical fluids as solvents and reaction media" at densities even higher than water has at normal conditions. This is a region where rather unusual phenomena, such as retrograde solubility, can be observed. The primary stress of our contribution to

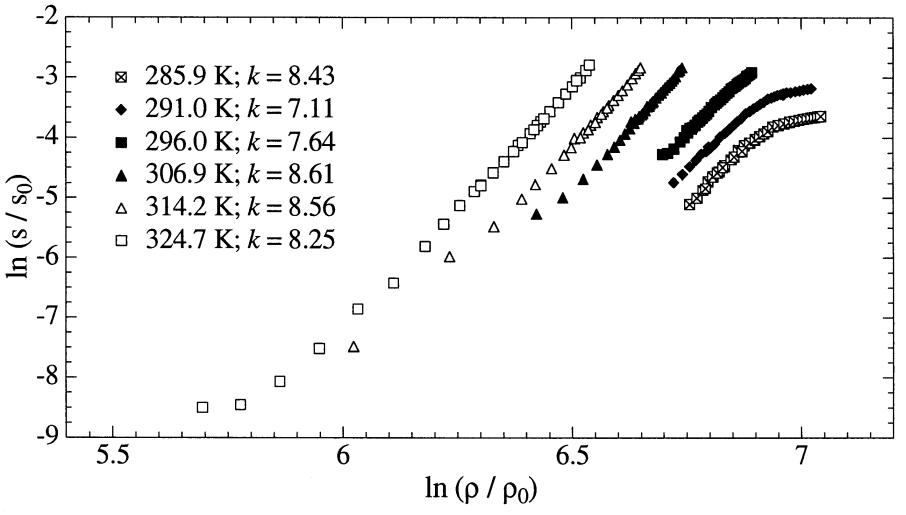

Fig. 8. Plot of the solubility isotherms of AQ08 in CO_2 according to Chrastil [10]. k exclusively refers to the linear region; $\rho_0 = 1$ kg m^{-3} and $s_0 = 1$ mol dm^{-3}.

this research program has been the experimental acquisition of high-precision solubility data which can later be evaluated from different points of view. Inspired by the literature we have chosen the technically challenging solubility behaviour of β-carotene in compressed gases with a view to supercritical fluid extraction. In the course of these investigations, we have been confronted with side effects, such as solvatochromism and isomerization, having a substantial impact on data quality. By adapting our procedure we have been able to prove solubility data from literature sources, to expand the investigated pressure range to almost 200 MPa, and eventually we could find a solubility maximum in the system β-carotene + CO_2. Another point of emphasis has been the systematic investigation of a substance class to study how a variation of structure and solvent characteristics influences the quantitative solubility behavior. We have decided on taking different anthraquinone derivatives for our investigations, because these substances have the attribute of a rather unproblematic handling in high-pressure solubility experiments. Research guided by this particular idea can frequently be found in the literature as well, and there have been many attempts to establish criteria which shall describe and predict the complex interactions between different substituents, their individual characteristics (e.g., hydrogen bonding), crystal structure and polymorphism in the solid state, and, of outstanding importance, the solvent gas. A notable result is that we have been able to find retrograde solubility for strongly dissimilar molecules just by "solvent tuning", meaning we have set the experimental conditions to liquid-like densities. The occurrence of this phenomenon is supported by thermodynamic considerations. Nevertheless, much speculation and many unresolved problems keep to remain in this field, as chemical interrelations have emerged to be ambiguous and much more complicated than the underlying thermodynamics.

ACKNOWLEDGEMENT

The authors thank the Deutsche Forschungsgemeinschaft (grant SCHN 98/22-1 to 22-4) and the Fonds der Chemischen Industrie e. V. for financial support. Additionally, we owe thanks to Professor Jae-Jin Shim, Yeungnam University, Korea, Professor Mamoru Nishioka, Anan College of Technology, Japan, and Professor William S. Sheldrick, University of Bochum, for their contributions to this project.

REFERENCES

[1] R. E. Wilson, P. C. Keith, R. E. Haylett, Ind. Eng. Chem., 28 (1936) 1065.
[2] I. R. Krichevskii, D. Yu. Gamburg, Zh. Fiz. Khim., 17 (1943) 215.
[3] D. Yu. Gamburg, Neft. Khoz., 25 (1947) 46.
[4] E. Klesper, A. H. Corwin, D. A. Turner, J. Org. Chem., 27 (1962) 700.
[5] J. F. Brennecke, C. A. Eckert, AIChE J., 35 (1989) 1409.
[6] K. Poulakis, M. Spee, G. M. Schneider, D. Knittel, H.-J. Buschmann, E. Schollmeyer, Chemiefasern / Textilindustrie, 41 / 93 (1991) 142.
[7] U. K. Deiters, I. Swaid, Ber. Bunsenges. Phys. Chem., 88 (1984) 791.
[8] U. K. Deiters, Fluid Phase Equilibria, 20 (1985) 275.
[9] I. Swaid, D. Nickel, G. M. Schneider, Fluid Phase Equilibria, 21 (1985) 95.
[10] J. Chrastil, J. Phys. Chem., 86 (1982) 3016.
[11] T. Kraska, K. O. Leonhard, J. Jurtzik, D. Tuma, G. M. Schneider, this book, Chapter 1.10..
[12] D. Tuma, G. M. Schneider, J. Supercrit. Fluids, 13 (1998) 37.
[13] D. Tuma, G. M. Schneider, Fluid Phase Equilibria, 158–160 (1999) 743.
[14] D. Tuma, G. M. Schneider, Wissenschaftliche Berichte FZKA, 6271 (1999) 155.
[15] B. Wagner, M. Nishioka, D. Tuma, M. Maiwald, G. M. Schneider, J. Supercrit. Fluids, 16 (1999) 157.
[16] D. Tuma, B. Wagner, G. M. Schneider, Fluid Phase Equilibria, 182 (2001) 133.
[17] G. M. Schneider, D. Tuma, M. Winter, B. Wagner, Z. Kristallogr. NCS, 216 (2001) 299.
[18] D. Tuma, B. Wagner, G. M. Schneider, Phys. Chem. Chem. Phys., 4 (2002) 968.
[19] T. Kraska, K. O. Leonhard, D. Tuma, G. M. Schneider, J. Supercrit. Fluids, 23 (2002) 209.
[20] T. Kraska, K. O. Leonhard, D. Tuma, G. M. Schneider, Fluid Phase Equilibria, 194–197 (2002) 469.
[21] T. Kraska, J. Jurtzik, D. Tuma, G. M. Schneider, Russ. J. Phys. Chem., in press.
[22] U. Haarhaus, P. Swidersky, G. M. Schneider, J. Supercrit. Fluids, 8 (1995) 100.
[23] P. Swidersky, D. Tuma, G. M. Schneider, J. Supercrit. Fluids, 9 (1996) 12.
[24] G. M. Schneider, C. B. Kautz, D. Tuma, in: Ph. Rudolf von Rohr, Ch. Trepp (eds.), Process Technology Proceedings 12, High Pressure Chemical Engineering, Elsevier, Amsterdam, 1996, pp. 259–264.
[25] C. B. Kautz, B. Wagner, G. M. Schneider, J. Supercrit. Fluids, 13 (1998) 43.
[26] B. Wagner, C. B. Kautz, G. M. Schneider, Fluid Phase Equilibria, 158–60 (1999) 707.
[27] G. M. Schneider, J. Supercrit. Fluids, 13 (1998) 5.
[28] G. M. Schneider, C. B. Kautz, D. Tuma, in: E. Kiran, P. G. Debenedetti, C. J. Peters (eds.), Supercritical Fluids – Fundamentals and Applications, NATO Science Series E: Applied Sciences – Vol. 366, Kluwer, Dordrecht, Boston, London, 2000, pp. 31–68.
[29] R. Span, W. Wagner, J. Phys. Chem. Ref. Data, 25 (1996) 1509.
[30] K. D. Bartle, A. A. Clifford, S. A. Jafar, G. F. Shilstone, J. Phys. Chem. Ref. Data, 20 (1991) 713.
[31] M. Christov, R. Dohrn, Fluid Phase Equilibria, 202 (2002) 153.
[32] T. P. DiNoia, M. A. McHugh, J. E. Cocchiaro, J. B. Morris, Waste Management, 17 (1997) 151.
[33] H. Pöhler, A. L. Scheidgen, G. M. Schneider, Fluid Phase Equilibria, 115 (1996) 165.
[34] P. H. van Konynenburg, R. L. Scott, Phil. Trans. Roy. Soc. (London) A, 298 (1980) 495.

[35] G. M. Schneider, in: E. Kiran, J. M. H. Levelt Sengers (eds.), Supercritical Fluids – Fundamentals for Application, NATO ASI Series E: Applied Sciences – Vol. 273, Kluwer, Dordrecht, Boston, London, 1994, pp. 91–115.
[36] J. M. Prausnitz, R. N. Lichtenthaler, E. G. de Azevedo, Molecular Thermodynamics of Fluid-Phase Equilibria, Second Edition, Prentice Hall, Englewood Cliffs, 1986.
[37] R. T. Kurnik, R. C. Reid, AIChE J., 27 (1981) 861.
[38] M. Gitterman, J. Procaccia, J. Chem. Phys., 78 (1983) 2648.
[39] C. B. Kautz, Fluidchromatographische Untersuchungen (SFC) an organischen Substanzen mit überkritischem Kohlendioxid: Bestimmung der Kapazitätsverhältnisse von Polyphenylen und substituierten Benzolderivaten sowie spektroskopische Löslichkeitsuntersuchungen an Anthrachinonfarbstoffen bis 20 MPa, Doctoral Thesis, Ruhr-Universität Bochum, Germany, 1996.
[40] B. Wagner, Untersuchungen zur Löslichkeit von Anthrachinonfarbstoffen in nah- und überkritischem Kohlendioxid mit einer Strömungsmethode bis 20 MPa, Doctoral Thesis, Ruhr-Universität Bochum, Germany, 1998.
[41] M. Maiwald, G. M. Schneider, Ber. Bunsenges. Phys. Chem., 102 (1998) 960.
[42] D. Tuma, UV/VIS-spektroskopische Hochdruckuntersuchungen in nah- und überkritischen Fluiden bis 180 MPa – Löslichkeit und Stabilität von Anthrachinonfarbstoffen und β-Carotin in CO_2, N_2O, $CClF_3$ und SF_6, Doctoral Thesis, Ruhr-Universität Bochum, Germany 1999.
[43] M. Maiwald, Solvatochromie in überkritischen Fluiden, Doctoral Thesis, Ruhr-Universität Bochum; Cuvillier, Göttingen, Germany, 1997.
[44] N. E. Craft, J. H. Soares, jr., J. Agric. Food Chem., 40 (1992) 431.
[45] B. H. Davies, in. T. H. Goodwin (ed.), Chemistry and Biochemistry of Plant Pigments, Second Edition, Vol. 2, Academic Press, London, New York, San Francisco, 1976, pp. 38–165.
[46] A. J. Jay, D. C. Steytler, M. Knights, J. Supercrit. Fluids, 4 (1991) 131; 199.
[47] A. J. Jay, D. C. Steytler, J. Supercrit. Fluids, 5 (1992) 274.
[48] US Pharmacopeia, 24-19 Edition, 2000, pp. 216–217.
[49] European Pharmacopeia, Third Edition, 1997, p. 465.
[50] J. N. Loeb, P. K. Brown, G. Wald, in: Staff of the Biological Laboratories of Harvard University, Cambridge, Mass., Photochemical and Stereochemical Properties of Carotenoids at Low Temperatures, Nature, 184 (1959) 614.
[51] L. Zechmeister, in: L. Zechmeister (ed.), Fortschritte der Chemie organischer Naturstoffe, Band 18, Springer, Wien, 1960, p. 223–349.
[52] H. Torii, M. Tasumi, J. Phys. Chem., 94 (1990) 227.
[53] T. T. Ngo, D. Bush, C. A. Eckert, C. L. Liotta, AIChE J., 47 (2001) 2566.
[54] M. S. Gómez-Prieto, M. M. Caja, G. Santa-María, J. Am. Oil Chem. Soc., 79 (2002) 897.
[55] H. Sovová, R. P. Stateva, A. A. Galushko, J. Supercrit. Fluids, 21 (2001) 195.
[56] B. N. Hansen, A. H. Harvey, J. A. P. Coelho, A. M. F. Palavra, T. J. Bruno, J. Chem. Eng. Data, 46 (2001) 1054.
[57] P. Subra, S. Castellani, H. Ksibi, Y. Garrabos, Fluid Phase Equilibria, 131 (1997) 269.
[58] K. Sakaki, Chem. Eng. Data, 37 (1992) 249.
[59] R. L. Mendes, B. P. Nobre, J. P. Coelho, A. F. Palavra, J. Supercrit. Fluids 16 (1999) 99.
[60] D. E. Raynie, Anal. Chem., 65 (1993) 3127.
[61] I. Gamlieli-Bonshtein, E. Korin, S. Cohen, Biotechnol. Bioeng., 80 (2002) 169.
[62] J. Byers, J. Org. Chem., 48 (1983) 1515.
[63] R. C. Mordi, J. C: Walton, G. W. Burton, L. Hughes, K. U. Ingold, D. A. Lindsay, D. J. Mofatt, Tetrahedron, 49 (1993) 911.

[64] G. Britton, in: G. Britton, S. Liaaen-Jensen, H. Pfander (eds.), Carotenoids: Spectroscopy, vol. 1B, Birkhäuser, Basel, Boston, Berlin, 1995, pp. 13–62.
[65] J. Schierle, T. Schellenberger, C. Fizet, R. Betz, Eur. Food Res. Technol., 215 (2002) 268.
[66] J. Méndez-Santiago, A. S. Teja, Fluid Phase Equilibria, 158–160 (1999) 501.
[67] S. Masberg, Differentialkalorimetrie (DSC) und Differentialthermoanalyse (DTA) bei hohen Drücken – Untersuchungen zum Phasenverhalten ausgewählter Triacylglycine, Flüssigkristalle und Anthrachinonfarbstoffe bis 200 MPa, Doctoral Dissertation, Ruhr-Universität Bochum, Germany, 1999.
[68] P. Coutsikos, K. Magoulas, D. Tassios, J. Chem. Eng. Data, 42 (1997) 463.
[69] M. R. Fat'hi, Y. Yamini, H. Sharghi, M. Shamsipur, J. Chem. Eng. Data, 43 (1998) 400.
[70] M. R. Fat'hi, Y. Yamini, H. Sharghi, M. Shamsipur, Talanta, 48 (1999) 951.
[71] M. Shamsipur, A. R. Karami, Y. Yamini, H. Sharghi, J. Chem. Eng. Data, 48 (2003) 71.
[72] W. J. Schmitt, R. C. Reid, J. Chem. Eng. Data, 31 (1986) 204.
[73] G. Brunner, S. Peter, Chem.-Ing. Tech., 53 (1981) 529.
[74] Y. Adachi, B. C.-Y. Lu, Fluid Phase Equilibria, 14 (1983) 147.

Supercritical Fluids as Solvents and Reaction Media
G. Brunner (editor)

Chapter 1.6.

Phase behaviour of organic solid solutes and supercritical fluids with respect to particle formation processes

M. Türk[a], A. Diefenbacher[b] and G. Upper[a]

[a]Institut für Technische Thermodynamik und Kältetechnik, Universität Karlsruhe (TH), Engler-Bunte-Ring 21, D-76128 Karlsruhe (mail: tuerk@ttk.uka.de)

[b]BASF-AG, GCT/C – L 540 D-67056 Ludwigshafen

1. INTRODUCTION

In recent years, there has been a growing interest in the formation of small particles of low volatile organic substances using supercritical fluids. Usually, in such processes mixtures composed of one solute (2) of low volatility differing appreciably from the supercritical solvent (1) in mass, size, interaction strength, polarity, and shape are involved. These "asymmetric mixtures" have interesting properties because of the different behaviours of the components. For example, since solubility increases exponentially on solvents density, loadings much greater than predicted by the vapour pressure of the solute can be attained.

Beside this, the phase behaviour of these mixtures shows some interesting particularities, which are depicted in Fig. 1. Usually, the triple point temperature of the organic solute is markedly higher than the critical temperature of the supercritical solvent. Beyond this, the solubility of the supercritical solvent in the liquid phase of the second component is limited. These facts lead to a melting point depression of the second component and in addition, the critical mixture curve (L=G) is interrupted at two distinguished points. Close to the critical temperature of the pure solvent, the lower branch of the critical locus ends at the lower critical endpoint (LCEP). At higher temperatures, the solid-liquid-gas three-phase-line (SLG-line) interrupts the critical mixture curve at the upper critical endpoint (UCEP). In general, two different kinds of SLG - behaviours may occur. If the melting temperature of the solute decreases continuously with increasing pressure, a Type I system behaviour (S_2LG I) is observed. A more complex behaviour shows the Type II system (S_2LG II); in these mixtures a temperature minimum in the p-T projection of the SLG-line is noticed. For a given binary mixture, there are two factors that influence the

temperature on the SLG-line. At low pressures, the increasing gas solubility in the liquid phase leads to a noticeable melting point depression. With increasing pressure, the influence of the hydrostatic effect of pressure, which increases the melting point of the pure solid (S_2=G_2), becomes predominantly. In the temperature range above the melting temperature of the second component, either a solid-fluid or a vapour-liquid equilibrium can be observed, depending on the global composition of the mixture. In the temperature range between the T_{LCEP} and T_{UCEP} (Typ I) or the minimum of the SLG-line (Typ II) only a solid-fluid two-phase equilibrium (S_2=G) exists for each pressure. In the region close to the two critical endpoints, small changes in pressure and temperature result in a considerable increase of the solubility of the organic solute in the supercritical solvent. Due to the higher solid solubility in the region around the UCEP in comparison to the LCEP, the former region is of major economic interest.

Until now, there are several methods for the formation of small low volatile organic substances. The primary techniques for particle formation involving supercritical fluids are: RESS (Rapid Expansion of Supercritical Solutions), PGSS (Particle Generation from Gas Saturated Solution), and GAS (Gas Anti-Solvent). Based on minor variations of the GAS-process, different techniques, including Aerosol Supercritical Extraction System (ASES), Precipitation with a Compressed Anti-solvent (PCA), Supercritical Anti-Solvent (SAS) and Solution Enhanced-Dispersion by Supercritical fluids (SEDS), are now in use.

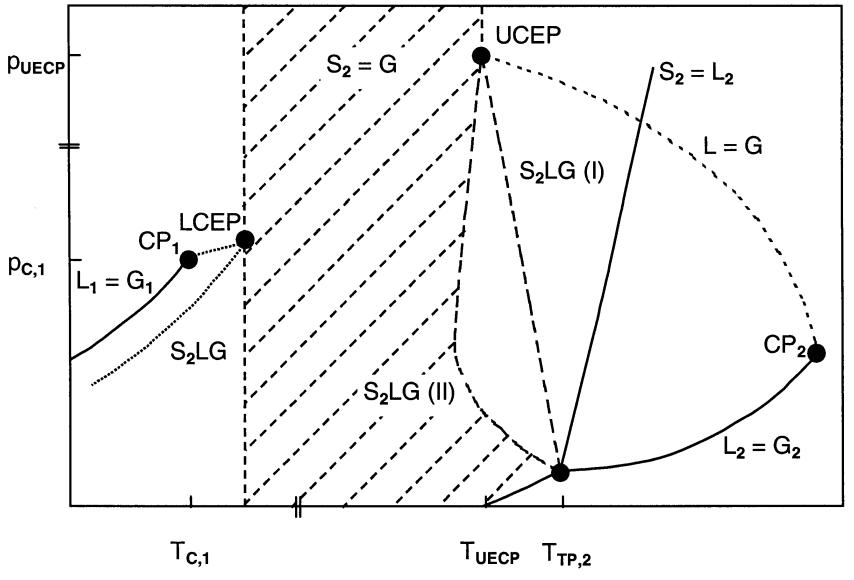

Fig. 1. Pressure versus temperature phase diagram for a typical asymmetric binary mixture [1].

To verify the feasibility of these processes, the knowledge of phase behaviour of the mixtures at the process conditions is essential. With regard to the PGSS-process, the ability of the supercritical solvent to melt the solid and to form saturated liquid phase is of major interest. In case of the RESS-process the solubility of the low volatile organic substance in the supercritical fluid is one of the key properties, since an insufficient solubility limits the practical application. Moreover, the solid-liquid-gas three-phase-line (SLG-line) of the systems involved has to be known, at least qualitatively. It was shown in literature, that the product properties (e.g. particle size and morphology) of the particles produced by RESS are often strongly influenced by the underlying phase behaviour [2, 3].

In order to overcome the lack of phase equilibrium data for the mixtures of interest, experiments were performed using two static equilibrium apparatuses. The first apparatus allows a visual determination of the SLG-line following the first melting point method and the second one enables solubility measurements [2, 3]. However, since reliable measurements of the phase behaviour of low volatile substances and supercritical fluids are time consuming and the cost of these measurements are quite high there is a need for reducing the experimental work by applying suitable equations of state (EoS). Thus, the primary object of our investigations is to evaluate and to compare different cubic equations of state for the correlation and reliable prediction of the solid-liquid-gas as well as the solid-gas equilibrium.

2. EXPERIMENTAL SETUP

For the measurements of the SLG - line, a static equilibrium apparatus (Fig. 2) was used. This apparatus is suitable in the temperature range from ambient temperature to 373 K at pressures up to 50 MPa. The equilibrium cell with an inner volume of 1.31 dm^3 is installed in a thermostated chamber. Due to controlled heating and cooling, it is possible to maintain a constant temperature within the limit of ±10 mK inside the chamber. During the measurements, the solute and the fluid investigated can be observed through two sapphire windows at both ends of the equilibrium cell. The temperature inside the equilibrium cell is measured with a calibrated Pt-100 thermometer within the total limit of ±30 mK. The reliability of the temperature measurement device was continuously proved by comparison with a Pt-25 thermometer (ITS-90). A high-precision standard dead weight gauge is used to measure the pressure. The dead weight gauge is separated from the test fluid inside the equilibrium cell by a thermostated pressure null indicator. By means of a very sensitive displacer, the pressure difference at the null indicator can be adjusted to less than ±0.1 kPa. The total uncertainty of the pressure measurement is within the limit of ±6 kPa.

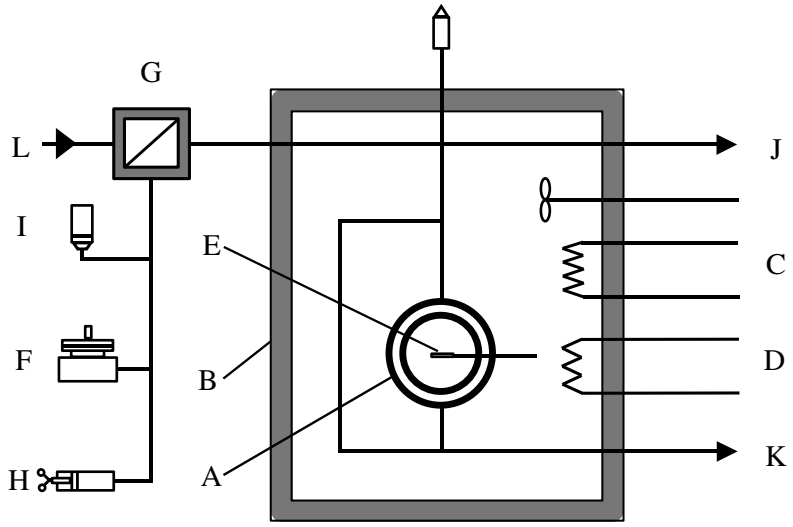

Fig. 2. Schematic diagram of the view-cell apparatus: **A** - equilibrium cell, **B** - thermostated chamber, **C** - heating, **D** - cooling, **E** - Pt-100 thermometer, **F** - standard dead weight gauge, **G** - pressure null indicator, **H** - displacer, **I** - pressure indicator, **J** – solvent, **K** – vacuum pump, **L** – nitrogen.

As proposed by Lemert and Johnston the first melting point method was used to determine the SLG-lines [1]. Thereby, the temperature was slowly increased until the onset of melting was observed. By the following temperature decrease by the same temperature span, a solidification of the solute was observed. This procedure was repeated several times in order to reduce the temperature span in which melting took place iteratively to less than 100 mK. For that reason, the first melting temperatures can be determined within an uncertainty of ±150 mK. A more detailed description of the apparatus and the experimental procedure is given in various publications [2, 3].

3. MODELING

For the description of the experimental results of the SLG-lines and the solubility of organic solid solutes in supercritical fluids various cubic equations of state where used. These equations can be written as follows:

$$p = \frac{R \times T}{(v-b)} - \frac{a(T)}{v^2 + v\times(b+c) - (b\times c + d^2)} \tag{1}$$

with $d = c = 0$ for the Redlich-Kwong-Soave-EoS and $c = b$ and $d = 0$ for the Peng-Robinson-EoS [4, 5]. Eq. (1) is also suitable to represent three parametric equations of state, such as the Trebble-Bishnoi-Salim-EoS ($d = v_C/3$) as well as the Patel-Teja-EoS ($d = 0$) [6, 7]. In Eq. (1), where p is the pressure, T the temperature, v the molar volume, $R = 8.31451$ J mol^{-1}K^{-1} the gas constant, only the parameter $a(T) = a_C \times \alpha(T)$ is treated as a function of temperature. The temperature dependence of the attraction parameter $\alpha(T)$ was represented using the equations proposed by the authors in the respective original publications. The cubic equations of state represented by Eq. (1) where applied to mixtures using the classical van der Waals mixing and combination rules:

$$a = \sum_{i=1}^{n}\sum_{j=1}^{n} x_i x_j \cdot a_{ij} \qquad \text{with} \quad a_{ij} = a_{ji} = \sqrt{a_i \cdot a_j} \cdot \left(1 - k_{ij}\right)$$

$$b = \sum_{i=1}^{n}\sum_{j=1}^{n} x_i x_j \cdot b_{ij} \qquad \text{with} \quad b_{ij} = b_{ji} = \frac{b_i + b_j}{2} \cdot \left(1 - l_{ij}\right) \tag{2}$$

$$c = \sum_{i=1}^{n}\sum_{j=1}^{n} x_i x_j \cdot c_{ij} \qquad \text{with} \quad c_{ij} = c_{ji} = \frac{c_i + c_j}{2} \cdot \left(1 - m_{ij}\right)$$

$$d = \sum_{i=1}^{n} x_i d_i$$

For comparison, the Redlich-Kwong-Soave-EoS and the Peng-Robinson-EoS were also used with the concentration-dependent combination rule of the cross-term a_{12} of the attraction parameter a proposed by Panagiotopoulos and Reid [8].

The SLG-line can be calculated by solving Eq. (3) - (5) simultaneously, where f is the fugacity calculated from the cubic equations of state.

$$f_k^G(T,p,y) = f_k^L(T,p,x) \tag{3}$$

$$f_i^G(T,p,y) = f_i^L(T,p,x) \tag{4}$$

$$f_{i,0}^S(T,p) = f_i^G(T,p,y) \tag{5}$$

In case that the solid-gas equilibrium (S_2=G) has to be calculated, Eq. (5) has to be solved only.

Due to the fact, that the solid state of a pure substance cannot be represented by an conventional equation of state, it is assumed that the fugacity of the pure solid can be related to that of a so-called sub-cooled liquid reference state at a given pressure and temperature [9, 10]. In Eq. (6), where Δh_i^{fus} is the enthalpy and T_i^{fus} the temperature of fusion at the triple point of the pure substance, the second term of the right hand side considers the pressure dependence. Of course, this expression neglects minor terms, which are a function of differences in heat capacities [1, 10].

$$ln\frac{f_{i,0}^{S}}{f_{i,0}^{L}} = \left[\frac{\Delta h_i^{fus}}{R \times T_i^{fus}}\left(1 - \frac{T_i^{fus}}{T}\right) + \int_{p^0}^{p} \frac{v_{i,0}^{S} - v_{i,0}^{L}}{R \times T} dp\right] \tag{6}$$

4. EXPERIMENTAL AND MODELING RESULTS

The p, T – projection of the p, T, x – diagram for the CO_2/naphthalene – mixture is shown in Fig. 3A. Beside the experimental data of our own measurements, literature data from various other authors are also shown for comparison. A good agreement with the experimental values published by Hong and Luks [11] and by Gmehling et al. [12] is observed. As described by Lemert and Johnston [1], the UCEP can be estimated by locating the intersection of the SLG-line with the apparent critical mixture curve. This procedure yields to a temperature of 333.45 ± 0.25 K and a pressure of 26.6 ± 0.2 MPa at the UCEP. A more detailed comparison of our experimental results with various data published in literature is given in literature [2, 3].

As the SLG-line depends strongly on the solubility of the supercritical solvent in the melt of the organic solute, both the melting point depressions and the location of the UCEP can be manipulated by changing the supercritical solvent or by using supercritical solvent mixtures. Fig. 3B shows experimental results for naphthalene melting points in the presence of CO_2, CO_2/CHF_3, and CHF_3 under high pressures [2]. For the mixtures investigated, the SLG-line was determined by observation of the first melting point. All SLG-lines of the mixtures investigated exhibit a slight temperature minimum, which is more distinct with increasing amount of CHF_3. Again, the value for the temperature and pressure at the UCEP of the mixture CO_2/CHF_3/naphthalene was determined by the intersection method. The UCEP of the mixture consisting of 70 mol-% CO_2 and 30 mol-% CHF_3 was determined at 337.2 K and 31.0 MPa. In the

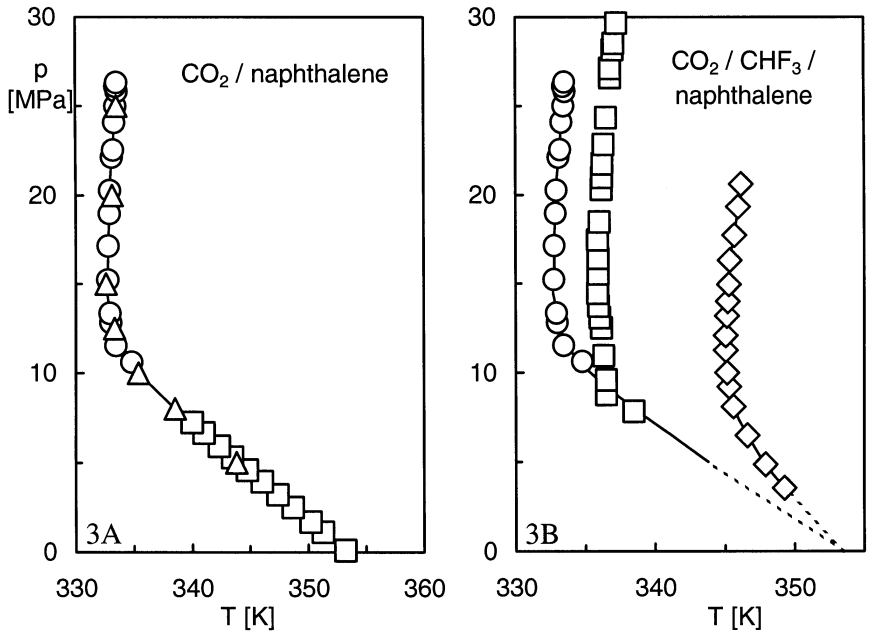

Fig. 3. Naphthalene melting points in the presence of CO_2, CHF_3 and a CO_2 / CHF_3 - mixture under high pressures, Fig. 3A, pure CO_2: ○ [2, 3], □ [11], △ [12], Fig. 3B: ○ pure CO_2, □ 70 mol-% CO_2, ◇ pure CHF_3 [2, 3].

CHF_3/naphthalene system, the pressure was to high to observe an UCEP because of experimental limitations.

The lines depicted in Fig. 4A have been calculated using the Redlich-Kwong-Soave-EoS and the Peng-Robinson-EoS. For comparison, both the classical van der Waals and the composition-dependent Panagiotopoulos - Reid mixing and combination rules were applied. As proposed by Kikic et al. [10], the binary interaction parameters k_{12} and l_{12} in case of the van der Waals mixing rules as well as n_{12} and n_{21} for the Panagiotopoulos - Reid mixing rule have been fitted to the location of the UCEP. Using these binary interaction parameters, the Redlich-Kwong-Soave-EoS yields to a somewhat better description of the SLG-line than the Peng-Robinson-EoS. It is shown elsewhere [2, 3], that no improvement of the calculated SLG-lines can be achieved by using the composition-dependent mixing rules. Since usually experimental data for the solid-gas equilibrium data are abundant, it is interesting to compare the results shown in Fig. 4A with those resulting from calculations using the binary interaction parameters regressed from solubility data. In Fig. 4B typical results for such SLG-line calculations are shown. Both the binary interaction parameter k_{12} and l_{12} regressed from solubility data at 308 K and 328 K describes the

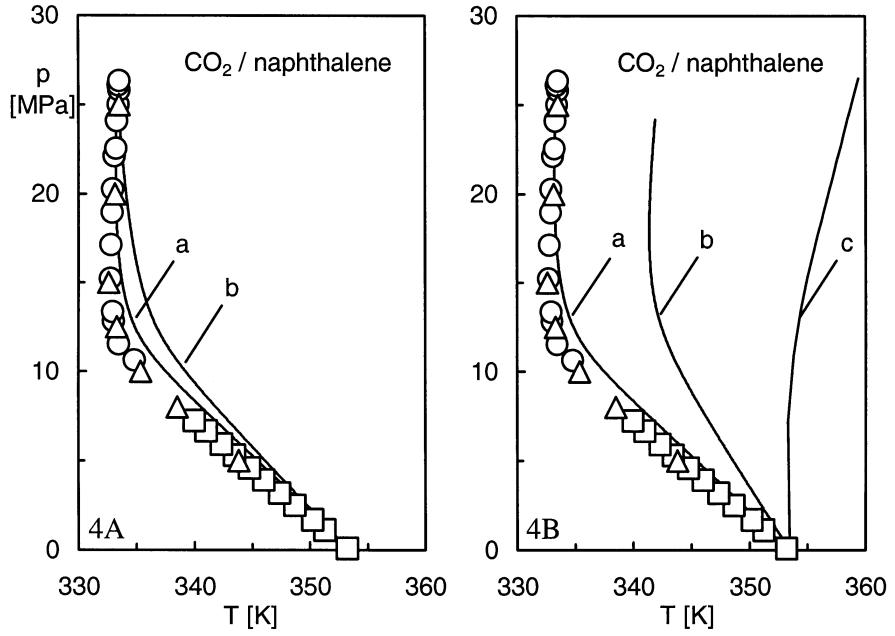

Fig. 4. Naphthalene melting points in the presence of CO_2 under high pressures, ○ [2,3], □ [11], △ [12], Fig. 4A: a) Redlich-Kwong-Soave-EoS, b) Peng-Robinson-EoS, Fig. 4B: Redlich-Kwong-Soave-EoS, a) k_{12} and l_{12} regressed from UCEP, b) k_{12} and l_{12} regressed from solubility data at 308 K, c) k_{12} and l_{12} regressed from solubility data at 328 K. The calculations using the binary interaction parameters regressed from the solubility data at 318 K were omitted because the results were close to those of 328 K.

experimental data insufficient. For the systems investigated, the values of the interaction parameters regressed from UCEP are listed in Table 1.

It is shown in Figure 4A, that both EoS are able to describe the naphthalene melting points in the presence of CO_2 acceptably well and that the position of the UCEP is accurately predicted. Similar results were obtained for the systems ethylene/naphthalene, and ethane/naphthalene [13].

Fig. 5 compares the prediction of the Redlich-Kwong-Soave- and the Peng-Robinson-EoS with experimental data for the systems CO_2/biphenyl and ethylene/biphenyl. For the later system and for both EoS an adequate agreement between experimental and calculated biphenyl melting points is noticed if the binary interaction parameters k_{12} and l_{12} were fitted to the location of the UCEP. In contrast to these results, markedly greater differences in the prediction of the SLG-line occur for the system CO_2/biphenyl. While the calculations performed with the Peng-Robinson-EoS lead to an insufficient description of the SLG-line, again a good agreement between experimental and calculated biphenyl melting points is noticed for the Redlich-Kwong-Soave-EoS.

Table 1
Mean absolute deviation between calculated and measured melting points and values of the binary interaction parameters regressed from UCEP.

System	EoS	$(\Delta T_M/T_M)$	k_{ij}	l_{ij}
CO_2 / naphthalene	RKS	0.31 %	0.080897	-0.036431
	PR	0.55 %	0.074388	-0.057526
CO_2 / biphenyl	RKS	0.29 %	0.081477	-0.010832
	PR	1.00 %	0.074021	-0.040882
ethylene / biphenyl	RKS	0.78 %	-0.012661	-0.015742
	PR	0.91 %	0.007078	-0.019500

In literature, several composition data are available along the SLG-line for the system CO_2/naphthalene and CO_2/biphenyl. Fig. 6 compares the prediction of the Redlich-Kwong-Soave- and the Peng-Robinson-EoS with these data using the binary interaction parameters that were obtained from the UCEP. Both EoS are able to predict the composition of liquid and vapour phases along the SLG-line qualitatively correct.

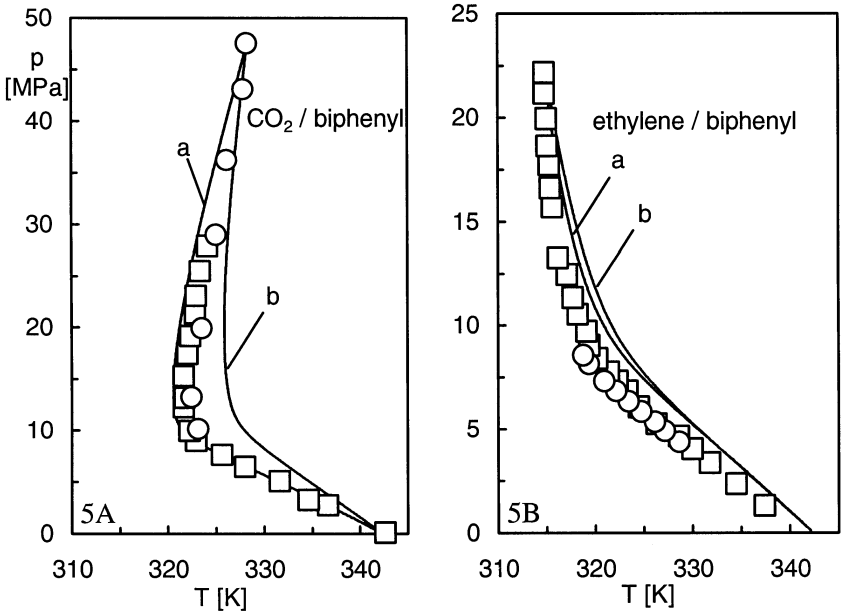

Fig. 5. Biphenyl melting points in the presence of CO_2 and of ethylene under high pressures, a) Redlich-Kwong-Soave-EoS, b) Peng-Robinson-EoS, Fig. 5A: ○ [14], □ [15], Fig. 5B: ○ [16], □ [17].

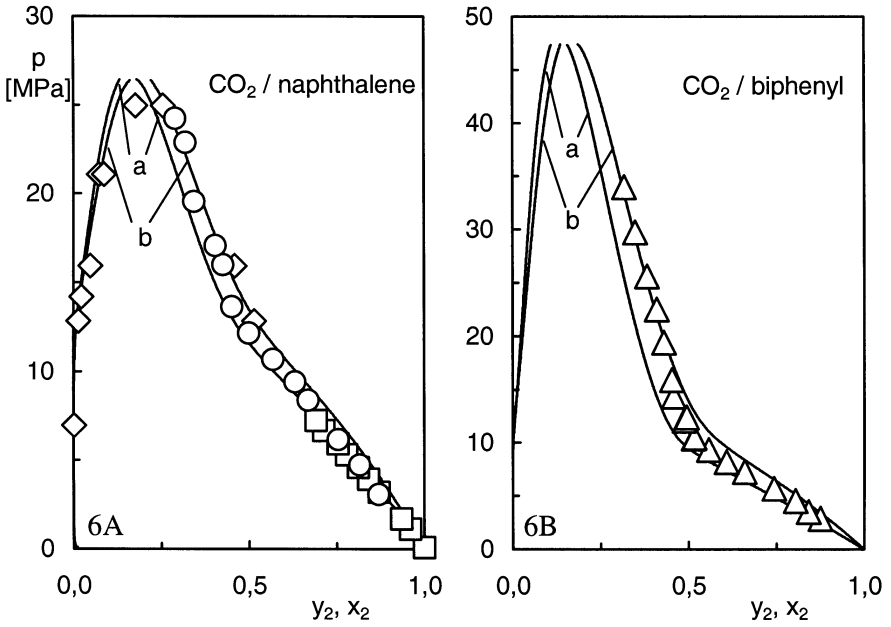

Fig. 6. Compositions along the SLG-line, Fig. 6A: CO_2 / naphthalene, Fig. 6B: CO_2 / biphenyl, a) Redlich-Kwong-Soave-EoS, b) Peng-Robinson-EoS, ◇ [11], ○, △ [18], □ [19].

As shown in Fig. 6, the calculated liquid and vapour compositions are in good agreement with various experimental data. However, both EoS are not able to predict the composition in the vicinity of the experimental UCEP accurately.

It was shown in Fig. 4, that for both EoS the use of the binary interaction parameters regressed from solubility data lead to an insufficient prediction of the experimental SLG-Line. Thus it is interesting to prove the ability to calculate the solute solubility in the supercritical solvent using those binary interaction parameters that are fitted exclusively to the UCEP. In Fig. 7, the solubility of naphthalene in pure CO_2 is plotted versus pressure at 308 K and at 328 K. These figures show a typical result for solubility calculations using the Redlich-Kwong-Soave-EoS and interaction parameters regressed from different data. Beside the calculated solubility data, own experimental data for the solubility of naphthalene in CO_2 [2, 3] are also shown. These data are in a good agreement with the data published by Tsekhanskaya et al. [20]. Both, the Redlich-Kwong-Soave prediction and the calculations using the binary interaction parameters obtained from solubility data at 308 K and 328 K were able to describe the experimental data qualitatively correct.

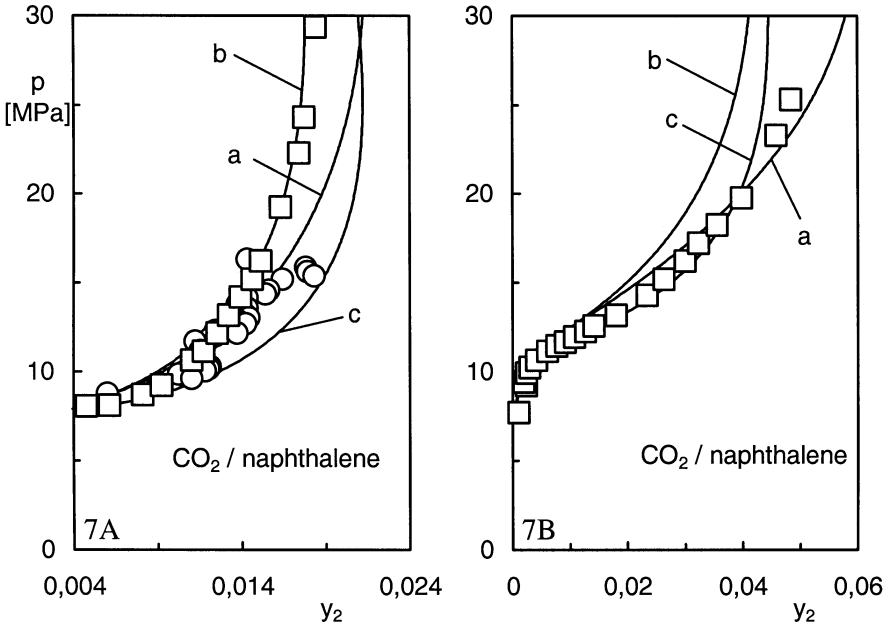

Fig. 7. Solubility of naphthalene in CO_2 at 308 K (7A) and 328 K (7B), O [2, 3], □ [20], solid lines Redlich-Kwong-Soave-EoS: a) k_{12} and l_{12} regressed from UCEP, b) k_{12} and l_{12} regressed from solubility data at 308 K, c) k_{12} and l_{12} regressed from solubility data at 328 K.

At both temperatures, the calculations using the binary interaction parameters regressed from solubility data at the respective temperature lead to the best description of the experimental data. On the other hand, the Redlich-Kwong-Soave prediction, using the binary interaction parameters obtained from the UCEP lead always to a slightly better result than those calculations using the binary interaction parameters regressed from solubility data at 328 K or 308 K respectively. A more detailed comparison between calculated and experimental solubility data shows, that the Redlich-Kwong-Soave-EoS leads to a slightly better description of the experimental data than the Peng-Robinson-EoS [3].

The behaviour of solute partial molar volumes in supercritical solvents displays some interesting features. Among others, unusually large negative values of the partial molar volume are reached in the vicinity of the solvents critical pressure where the pure solvent is most compressible. Eckert et al. [21] show that the ability to represent partial molar volume data correctly represents a very severe test for an EoS, since this procedure means that an EoS can be tested both in its first order form and in its differentiated form also (see Eq. (7) below).

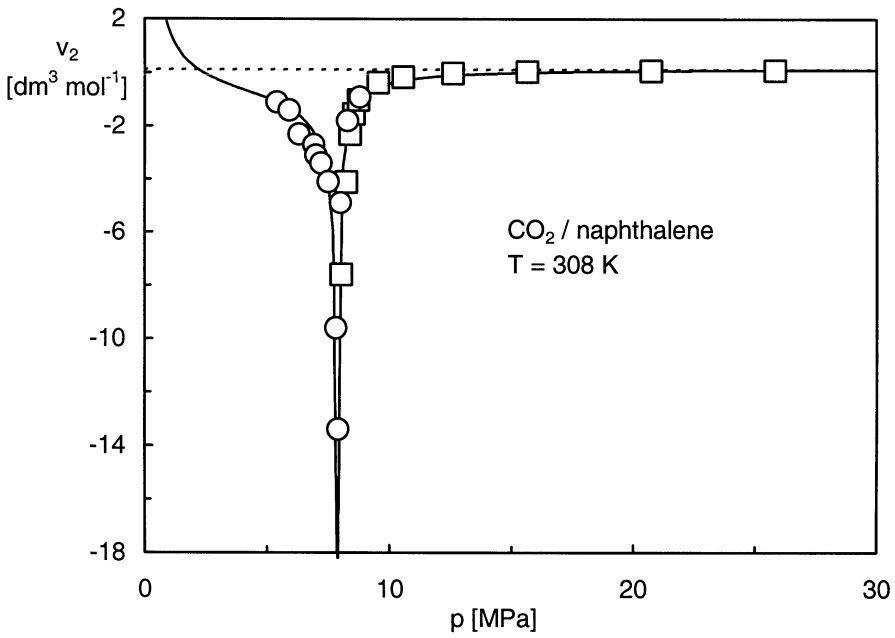

Fig. 8. Partial molar volume calculations for naphthalene dissolved in CO_2 at 308 K using the Redlich-Kwong-Soave-EoS and binary interaction parameters regressed from the UCEP, □ [21], ○ [23].

Fig. 8 shows a typical result for the partial molar volume calculations. The dashed line represents the molar volume of pure solid naphthalene (0.129 dm^3 mol^{-1}). The points of intersection between the solid molar volume and the partial molar volume can be attributed to the solubility minimum and maximum [22]. Both, the Peng-Robinson prediction and the calculations using the binary interaction parameters regressed from solubility data at 308 K were omitted for clarity because it was found to be very close to those of the Redlich-Kwong-Soave-EoS. In all cases, the description of the location of the minimum and the shape of the experimental data published by Eckert et al. [21] and van Wasen and Schneider [23] are qualitatively correct. However, the EoS investigated differs slightly in the absolute values of the calculated minimum.

$$v_2 = -n(\partial v/\partial p)_{T,n} \times (\partial p/\partial n_2)_{T,V,n_1} \tag{7}$$

In the CO_2/naphthalene system at 308 K, the minimum partial molar volume is approximately -18 dm^3 mol^{-1} at a fluid density of 7 mol dm^{-3}. These values indicate the existence of clusters of about 120 CO_2 molecules around a single naphthalene molecule. Certainly, this is mainly a consequence of the strength of

the solute - solvent interaction; also, the temperature range will be of influence. Additional calculations show, that the number of CO_2 molecules around a single naphthalene molecule decreases from 32 at 318 K to 17 at 328 K [3,24].

5. PHASE BEHAVIOUR AND PARTICLE SIZE

It has been already mentioned in the first section that the size of the particles produced by RESS is influenced by the underlying phase behaviour. It has been shown in an earlier investigation [25], that RESS experiments performed with naphthalene lead to particle sizes in the range of 1.5 - 2.5 μm (Fig. 9A). From Fig. 3 and Fig. 4 follows, that these pre-expansion temperatures are higher than the melting temperature of naphthalene and that a vapour-liquid equilibrium exists. By operating at these process conditions the formation of liquid droplets can already occur prior to expansion because the previously unsaturated mixture becomes supersaturated during heating up to the pre-expansion temperature. Thus large coalesced particles are formed which are principally formed from or via the liquid phase [26, 24, 2, 3].

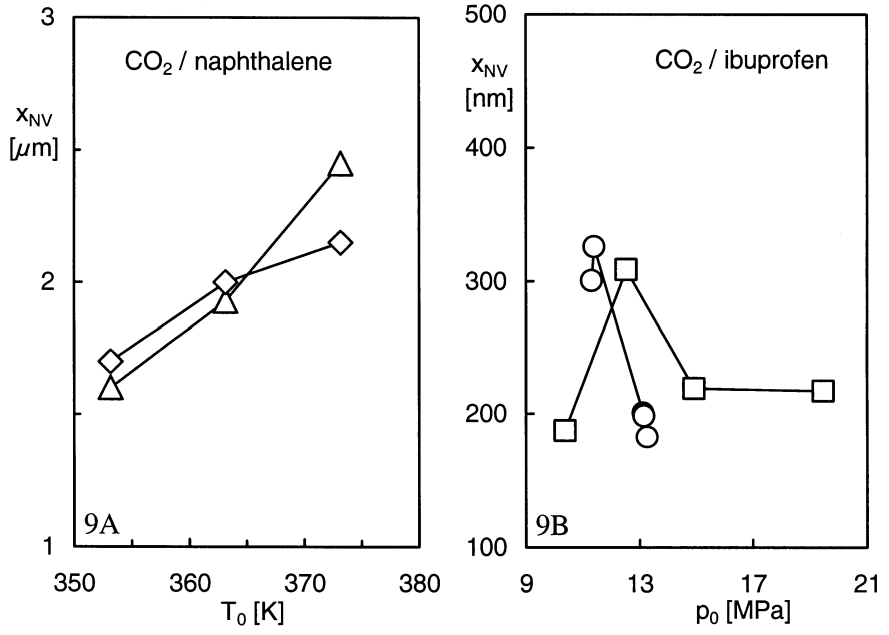

Fig. 9. Particle size of naphthalene (Fig. 9A: ◇ p_0 = 13 MPa, △ p_0 = 20 MPa) and of ibuprofen [27] (Fig. 9B: □ T_0 = 308 K, ○ T_0 = 318 K) obtained from different pre-expansion pressures, p_0, and temperatures, T_0).

This assumption is supported by the results obtained for ibuprofen. Fig. 9B shows that these experiments lead to particles in the range of 180 - 330 nm in diameter and no obvious dependence on the pre-expansion conditions on the particle size was observed. In opposite to naphthalene, these experiments were performed in the temperature range below the melting temperature of ibuprofen. Thus, in the pressure and temperature range considered, only a solid-fluid two-phase equilibrium exists and particle formation from or via a liquid phase can be excluded. These basic considerations given above clarify the importance of the knowledge of the SLG-line and of the phase behaviour of the systems involved for the production of nanoscale particles. In addition, these results were assisted by additional SEM-pictures of the precipitated particles. RESS-experiments performed in the region where a solid-fluid two-phase equilibrium exists lead always to small agglomerated particles consisting of primary particles with a particle size between 50 and 150 nm [24]. In contrast to these results, RESS-experiments performed at pre-expansion conditions higher than the melting temperature of the solute lead to large coalesced particles [26, 24].

6. CONCLUSIONS

Naphthalene melting points in the presence of pure CO_2, pure CHF_3, and a mixture composed of 70 mol-% CO_2 and 30 mol-% CHF_3 were determined visually. In case of the two former systems, the experimental UCEP was estimated by locating the intersection of the SLG-line with the apparent critical mixture curve. In the CHF_3/naphthalene system, the pressure was to high to observe an UCEP because of experimental limitations. All SLG-lines of the mixtures investigated exhibit a slight temperature minimum, which is more distinct with increasing amount of CHF_3. The experimental SLG-line is represented by the Redlich-Kwong-Soave- and the Peng-Robinson-EoS using two binary interaction parameters fitted exclusively to the UCEP. From an engineering point of view, these EoS are able to predict the solubility and the partial molar volume of a solute in a supercritical solvent as well as the liquid and vapour composition along the SLG-line reasonably well although neither solubility nor partial molar volume data were used to fit the binary interaction parameters. In addition, the importance of the knowledge of the SLG-line and of the phase behaviour of the systems involved for the production of nanoscale particles is clarified.

7. ACKNOWLEDGEMENTS

This work was supported by the grants Tu 93 / 2-1, -2, -3 and Tu 93 /4-1 of the Deutsche Forschungsgemeinschaft, (DFG), which is gratefully acknowledged. The authors are grateful to cand. chem. ing. M. Steurenthaler who performed parts of the calculations.

REFERENCES

[1] R.M. Lemert and K.P. Johnston, Fluid Phase Equilib., 45 (1989) 265.
[2] A. Diefenbacher and M. Türk, J. Supercrit. Fluids, 22 (2002) 175.
[3] A. Diefenbacher, doctoral thesis, Universität Karlsruhe (TH) (2001).
[4] D.Y. Peng and D.B. Robinson, Ind. Eng. Chem. Fundam., 15 (1976) 59.
[5] G. Soave, Chem. Eng. Sci., 27 (1972) 1197.
[6] M.A. Trebble and P.R. Bishnoi, Fluid Phase Equilib., 35 (1987) 1.
[7] N.C. Patel and A.S. Teja, Chem. Eng. Sci., 37 (1982) 463.
[8] A.Z. Panagiotopoulos and R.C. Reid, ACS Symposium, American Chemical Society, Washington DC, Series 300 (1986) 571.
[9] J.M. Prausnitz, R.N. Liechtenthaler, E. Gomez de Azevedo, Molecular Thermodynamics of Fluid Phase Equilibria, Prentice-Hall, Englewood Cliffs, (1999).
[10] I. Kikic, M. Lora, A. Bertucco, Ind. Eng. Chem. Res., 36 (1997) 5507.
[11] S.-P. Hong and K.D. Luks, Fluid Phase Equilib., 74 (1992) 133.
[12] M. Wilken, K. Fischer , J. Gmehling, Chemie Ingenieur Technik, 73 (2001) 1300
[13] M. Türk and G. Upper, unpublished results (2003).
[14] M.E. Paulaitis, M.A. McHugh, C.P. Chai, In Chemical Engineering at Supercritical Fluid Conditions, M.E. Paulaitis, J.M.L. Penninger, R.D. Grey, P. Davidson, Eds. Ann Arbor Science: Ann Arbor, MI, (1983).
[15] M.A. McHugh and T.J. Yogan, J. Chem. Eng. Data, 29 (1984) 112.
[16] G.A.M. Diepen and F.E.C. Scheffer, J. Phys. Chem., 57 (1953) 575.
[17] D. Zhang, A. Cheung, B.C.-Y. Lu, J. Supercritical Fluids, 5 (1992) 91.
[18] P.-L. Cheong, D. Zhang, K. Ohgaki, B.C.-Y. Lu, Fluid Phase Equilib., 29 (1986) 556.
[19] G.L. White and C.T. Lira, ACS Symposium, American Chemical Society, Washington DC, Series 406 (1989) Chapter 9.
[20] Y.V. Tsekhanskaya, M. Iomtev, E.V. Mushkina, Russ. J. Phys. Chem., 38 (1964) 1173.
[21] C.A. Eckert, D.H. Ziger, K.P. Johnston, T.K. Ellison, Fluid Phase Equilib., 14 (1983) 167.
[22] R.T. Kurnik and R.C. Reid, AIChE J., 27 (1981) 861.
[23] U. van Wasen and G.M. Schneider, J. Phys. Chem., 84 (1980) 229.
[24] M. Türk, professorial dissertation, Universität Karlsruhe (TH) (2001).
[25] S. Cihlar, M. Türk, K. Schaber, Proceedings of the World Congress on Particle Technology, Brighton, UK, 3 (1998) 380.
[26] S. Cihlar, doctoral thesis, Universität Karlsruhe (TH) (2000).
[27] M. Türk, P. Hils, B. Helfgen, R. Lietzow, K. Schaber, Part. Syst. Charact., 19 (2002) 327.

Supercritical Fluids as Solvents and Reaction Media
G. Brunner (editor)

Chapter 1.7.

Supercritical carbon dioxide as solvent for organic compounds present in aqueous salt solutions

G. Sieder and G. Maurer[a*]

[a]Lehrstuhl für Technische Thermodynamik, Universität Kaiserslautern, D-67653 Kaiserslautern, Germany,
[*] Corresponding author. Tel.: +49-631-2052410; fax: +49-631-2053835. Email address: gmaurer@rhrk.uni-kl.de (G. Maurer)

1. INTRODUCTION

The design of supercritical extraction processes requires a profound knowledge of the encountered phase equilibrium, for example, the high-pressure (vapor-liquid) equilibrium in multicomponent mixtures at temperatures above, but still close to, the critical point of the gas, and at pressures usually ranging from about 10 to 30 MPa. The open literature provides a lot of information on the phase equilibrium in binary systems supercritical gas + organic component (for a review see, for example, Dohrn and Brunner [1]). Adrian et al. [2] gave a review of the experimental available data for ternary systems supercritical gas + water + organic solvent. Little attention has been attributed to the influence of salts on such phase equilibria, although in industrial processes the aqueous phase often contains salts in rather large concentrations. From the liquid-liquid equilibrium as it turns up in standard extraction processes at ambient pressures it is known that salts can have an enormous influence on the composition of the coexisting phases.

In the present work the influence of the two salts (sodium chloride and sodium acetate) on the phase equilibrium of the system carbon dioxide + water + acetic acid is investigated experimentally and theoretically. Complementarily, the phase equilibrium of the ternary system carbon dioxide + water + acetic acid was also investigated. The experiments were performed with a continuous flow apparatus at temperatures from 313 K to 353 K at pressures up to 16 MPa.

The experimental results for the salt-free system are compared to predictions by the Peng-Robinson equation of state in the modification of Melhem et al. [3]. The interaction parameters were fitted to phase equilibrium

data of the binary subsystems. To improve the otherwise rather poor quality of the predictions the dimerization of acetic acid in both phases was taken into account by using a chemical theory. An extension of the Peng-Robinson equation of state is developed to allow for the presence of electrolytes. The extension consists of two additional terms which describe the long range interactions with ionic species.

2. EXPERIMENTAL

2.1. Apparatus

The experiments were performed with a flow technique apparatus. Only a short description of the experimental arrangement is given here, as more details are available elsewhere [4]. Fig. 1 shows a scheme of the experimental arrangement. Pure liquid carbon dioxide is taken from a gas cylinder, cooled down, and compressed by a diaphragm pump to a supercritical pressure. A second diaphragm pump delivers the liquid solvent. That solvent is a mixture of water, acetic acid, and the salt. The composition of the solvent is known from weighing the pure components before mixing. Both flows are mixed and throttled to the experimental pressure: The resulting two-phase flow is equilibrated in a preheater (stainless steel tube; outer and inner diameter: 8 and 7.7 mm; length: 7 m; filled with spheres of stainless steel, diameter: 3 mm). The equilibrated phases are separated gravimetrically in a high-pressure cell (volume: 38 cm^3). The phase boundary between the water-rich phase and the carbon dioxide-rich phase is observed visually through borosilicate windows. The phases are expanded separately by manually operated expansion valves to atmospheric pressure. The valves are handled so that the pressure is kept constant and the phase boundary in the view cell remains in a fixed position near the middle of the cell. The condensable components of each phase are separated from carbon dioxide by freezing out in cooled glass traps. Cooling is provided for the water-rich phase by an aqueous solution of an anti-freeze kept at 252 K and for the carbon dioxide-rich phase by ethanol at 200 K. Up to three traps are arranged in series to achieve complete separation. Suitable flow rates were determined in test runs. Lower flow rates are favorable for achieving the phase equilibrium, whereas larger flow rates are desired to reduce the period of time of an experiment. That time is mainly determined by the amount of condensate collected from the carbon dioxide-rich phase. A minimum of about 3 g is needed for a reliable analysis of that condensate. The collected amount of condensate from the carbon dioxide-rich phase was typically between 3 and 20 g. From the aqueous phase it was typically between 50 and 250 g. The condensates were analyzed for acetic acid by titration with sodium hydroxide. In some test runs the condensate from the carbon dioxide-rich phase was also analyzed (by ion chromatography) for the presence of salts. However, as no salt was detected in

these runs, most experiments were performed without such an analysis and the experimental results were evaluated assuming that the salts remain completely in the water-rich phase. The amount of carbon dioxide leaving the traps was determined volumetrically (after it was heated to ambient temperature) using wet-test meters.

Before each experiment the cooling traps are filled with carbon dioxide at ambient temperature and pressure. To determine the amount of separated solvents the traps are weighed before and after the experiment at room temperature. Special care was taken to avoid a loss of condensate when the valves were opened. More details of the analyzing procedure are available elsewhere [4].

2.2. Materials and uncertainties

Carbon dioxide (> 99.96 mass%) was provided by TV-Kohlensäure, Ludwigshafen a. Rh., Germany. Acetic acid (> 99,7 mass%) was from Carl Roth, Karlsruhe, Germany. Sodium acetate (> 99 mass%) and sodium chloride (> 99.5 mass%) were from Riedel de Haën, Germany. Those substances were used as supplied. Water was de-ionized.

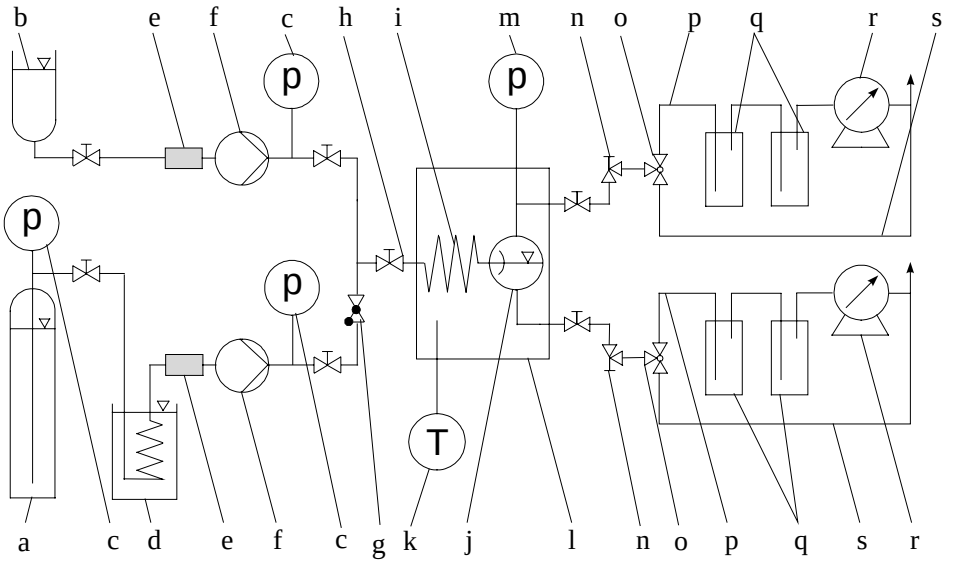

Fig. 1. Scheme of the experimental arrangement: (a) carbon dioxide, (b) mixture of solvents, (c) control pressure gauge, (d) cool bath, (e) filter, (f) diaphragm pump, (g) check valve, (h) throttle valve, (i) preheater, (j) equilibrium cell, (k) thermometer, (l) thermostat, (m) high precision gauge, (n) heated micrometer valve, (o) three-way valve, (p) head running, (q) cooling trap for freezing out, (r) wet-test meter, (s) first running.

The temperature in the thermostat (position k of Fig. 1) was measured by a calibrated platinum resistance thermometer with an estimated uncertainty of ± 0.1 K. The temperature in the wet-test meter was measured by liquid mercury thermometers with an uncertainty < ± 0.5 K. The pressure in the equilibrium cell was measured with an electronic pressure gauge (type 891.10.501, 0–40 MPa, Fa. WIKA, Klingenberg, Germany). The pressure gauge was calibrated with a precision pressure gauge (type 5200 S, Desgranges et Huot, Aubervilliers, France). The accuracy of the electronic pressure gauge is ± 15 kPa. However, oscillations in pressure caused by the diaphragm pumps as well as by the manual operation of the relief valves of the view cell, resulted in pressure fluctuations up to ± 25 kPa and up to ± 250 kPa at pressures below and above 8 MPa, respectively. The determination of the mass of carbon dioxide passing the wet-test meter requires the pressure of the gaseous effluent. That pressure was measured with a u-tube pressure gauge with an uncertainty of ± 60 Pa. The masses of the traps before and after the experiment were determined with a precision balance (type PM 1200, Mettler, Gießen, Germany) with an absolute uncertainty of ± 0.004 g. The acid concentration was analyzed by automatic titration (type DMS Titrino 716, Metrohm, Herisau, Switzerland). The relative uncertainty was better than 0.7 %. The experimental uncertainty of the gas volumes determined by the wet-test meter is < 0.5 % for the aqueous phase and < 1 % for the carbon dioxide-rich phase. The determined volumes of carbon dioxide were converted to the mass using the density of gaseous carbon dioxide calculated from the Bender equation of state [5]. The total relative uncertainty of the carbon dioxide mass is about 3 % for the aqueous phase and about 1 % for the carbon dioxide-rich phase.

The direct experimental results for the masses of all components were corrected for (a) the solubility of carbon dioxide in the frozen-out solvents, (b) the concentration of the solvents (water and acetic acid) in the vapor leaving the traps, and (c) the change of the gas phase volumes in the cooling traps. As shown in Table 1, these corrections are small (< 0.5 %). Table 1 also gives the average relative uncertainties of the mole fraction of carbon dioxide in the liquid phase and the mole fraction of water in the vapor phase. The maximum relative uncertainty of the mole fraction of carbon dioxide in the aqueous phase is about 4.5 %. As the water concentration in the vapor phase is rather small, its relative uncertainty may be as large as 25 %.

Table 1
Influence of the correction on the mass m_i of component i and the total experimental relative uncertainty of the mole fraction of carbon dioxide and water

	Corrections				uncertainties	
	aqueous phase		CO_2-rich phase		aqueous phase	CO_2-rich phase
	$\frac{\Delta m_{liq}}{m_{liq}}$ *	$\frac{\Delta m_{CO_2}}{m_{CO_2}}$	$\frac{\Delta m_{liq}}{m_{liq}}$ *	$\frac{\Delta m_{CO_2}}{m_{CO_2}}$	$\frac{\Delta x_{CO_2}}{x_{CO_2}}$	$\frac{\Delta y_{H_2O}}{y_{H_2O}}$
	%	%	%	%	%	%
CO_2 + water + acetic acid	0.09	0.40	0.22	0.02	2.1	6.4
CO_2 + water + acetic acid + sodium chloride	0.08	0.41	0.20	0.02	3.1	10.2
CO_2 + water + acetic acid + sodium acetate	0.07	0.33	0.20	0.02	2.9	11.1

* liq: water + acetic acid.

3. EXPERIMENTAL RESULTS

For the salt-free system carbon dioxide + water + acetic acid over 160 measurements were performed at 313, 333, and 353 K and pressures between 5 and 16 MPa. Generally, each combination of temperature and pressure was investigated with three different ratios of water to acetic acid in the carbon dioxide-free solution: $n_{water} : n_{acetic\ acid}$ = 2:1, 1:1, and 1:2, respectively. Some typical results for the phase equilibrium are shown in Fig. 2 to 4. For that salt-free system two types of phase behavior were observed. At "low" pressures (e.g., at 353 K and 10 MPa) the critical pressure of the binary system carbon dioxide + acetic acid is not exceeded and the two-phase region stretches between two binary systems: the carbon dioxide + acetic acid and the carbon dioxide + water systems (Fig. 2). As it was to be expected under those conditions, the solubility of acetic acid as well as of water in the vapor phase (which consists primarily of carbon dioxide) is small.

At "high" pressures (i.e., above the critical pressure of the binary system carbon dioxide + acetic acid) the miscibility gap starts only from the binary system carbon dioxide + water, but no longer extends to the binary system carbon dioxide + acetic acid (Fig. 3 and 4). The solubility of acetic acid in the carbon dioxide-rich phase is much higher, whereas the amount of water in that phase has not changed much. This effect results in a smaller slope of the tie-lines, as can be seen by comparing Fig. 2 with Fig. 3 and 4. The influence of pressure and temperature on the solubility of acetic acid in the carbon dioxide-rich phase can be summarized as following: Increasing the pressure results in

higher concentrations of acetic acid in the carbon dioxide-rich phase, whereas the opposite behavior is found when the temperature is lowered.

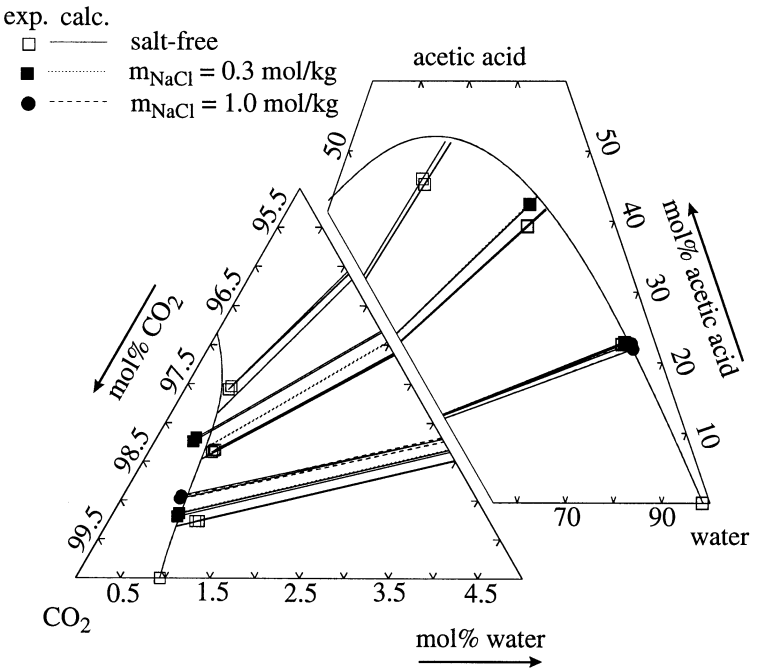

Fig. 2. Phase equilibrium of the system carbon dioxide + water + acetic acid (+ sodium chloride) at 353 K and 10 MPa.

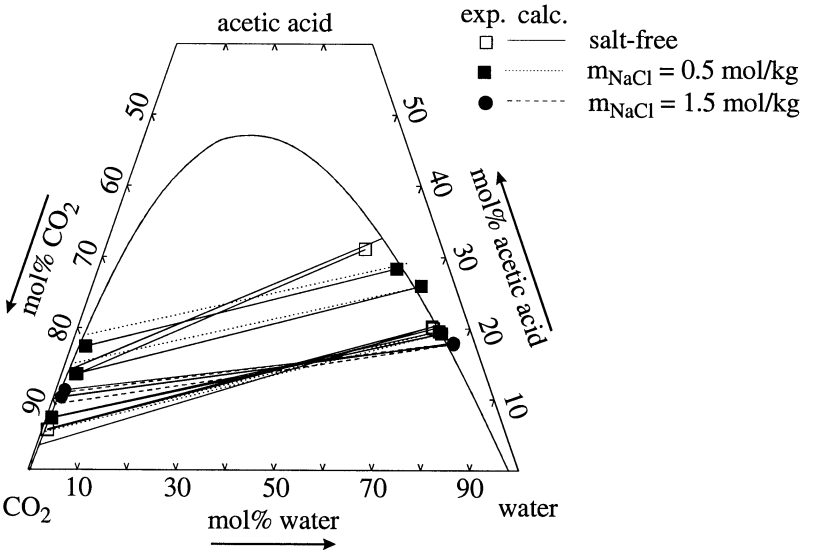

Fig. 3. Phase equilibrium of the system carbon dioxide + water + acetic acid (+ sodium chloride) at 313 K and 9 MPa.

The phase equilibrium of the quaternary system carbon dioxide + water + acetic acid + sodium chloride was investigated experimentally within the same pressure and temperature range as for the salt-free ternary system. The molality of sodium chloride in the carbon dioxide-free solvent mixture was varied between 0.3 and 1.5 molal. The molar ratio of water to acetic acid in the solvent was set either to 2:1 or to 1:1. Higher concentrations of acetic acid in the solvent mixture (e.g., 75 mol% acetic acid and 0.15 molal sodium chloride) were not realized, as sodium chloride precipitated when such solutions were pressurized by carbon dioxide. Fig. 2 and 3 demonstrate the influence of sodium chloride on the phase equilibrium. To present the experimental data in such triangular diagrams the concentrations of carbon dioxide, water, and acetic acid were calculated on a "salt-free" base. At constant temperature and pressure the presence of sodium chloride in the solvent mixture reduces the concentration of dissolved carbon dioxide. This effect (salting-out) is known from investigations of gas solubility in aqueous electrolyte solutions [6, 7]. The composition of the carbon dioxide-rich phase is also influenced by the presence of sodium chloride. At "low" pressures (Fig. 2) the influence is small. As sodium chloride reduces the activity of water in the aqueous phase, the amount of water in the vapor phase is lowered. Similarly, a small salting-out effect is also observed for acetic acid. At "high" pressures (Fig. 3) the salting-out effect on acetic acid is considerably increased. At high molalities of sodium chloride the concentration of acetic acid in the supercritical phase is almost twice that observed in the salt-free system at the same temperature and pressure.

Fig. 4 presents some typical results for the influence of a single sodium salt (either sodium chloride or sodium acetate) on the phase equilibrium of the quaternary system carbon dioxide + water + acetic acid. The molality of sodium acetate was varied between 0.5 and 3 mol kg^{-1}. Sodium acetate (as well as sodium chloride) results in a reduced solubility of carbon dioxide in the solvent mixture (i.e., salting-out is observed). However, sodium acetate in the liquid phase reduces the concentration of acetic acid in the carbon dioxide-rich phase, and increases the concentration of acetic acid in the liquid phase. Thus, a salting-in effect for acetic acid is observed. The opposite influences of the sodium chloride and sodium acetate on the partition of acetic acid are also shown in Fig. 5. The partition coefficient of acetic acid is defined as the quotient of the concentrations of acetic acid in the carbon dioxide-rich phase and in the aqueous phase. Fig. 5 shows this partition coefficient as a function of the density of the carbon dioxide-rich phase. That density has been approximated by the density of pure carbon dioxide which was calculated from the Bender equation of state [5].

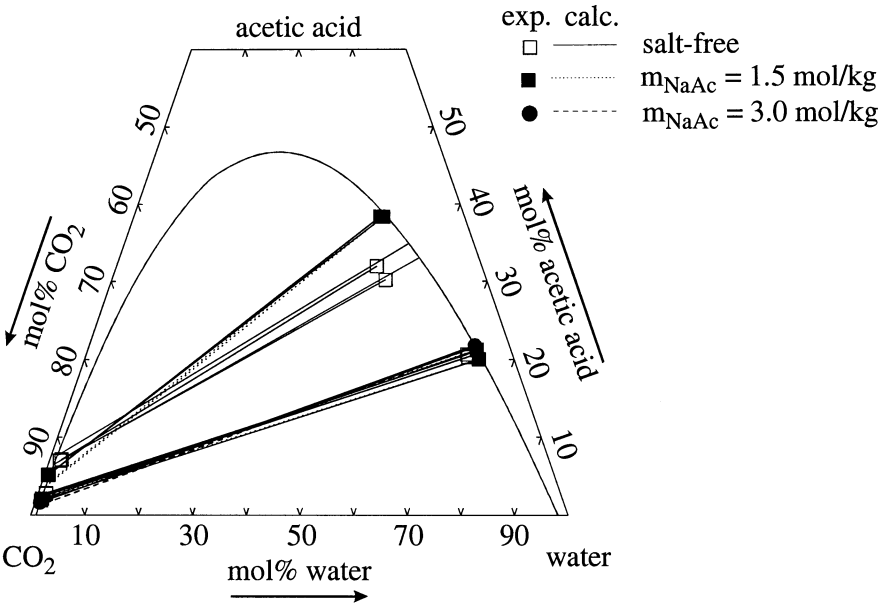

Fig. 4. Phase equilibrium of the system carbon dioxide + water + acetic acid (+ sodium acetate) at 353 K and 16 MPa.

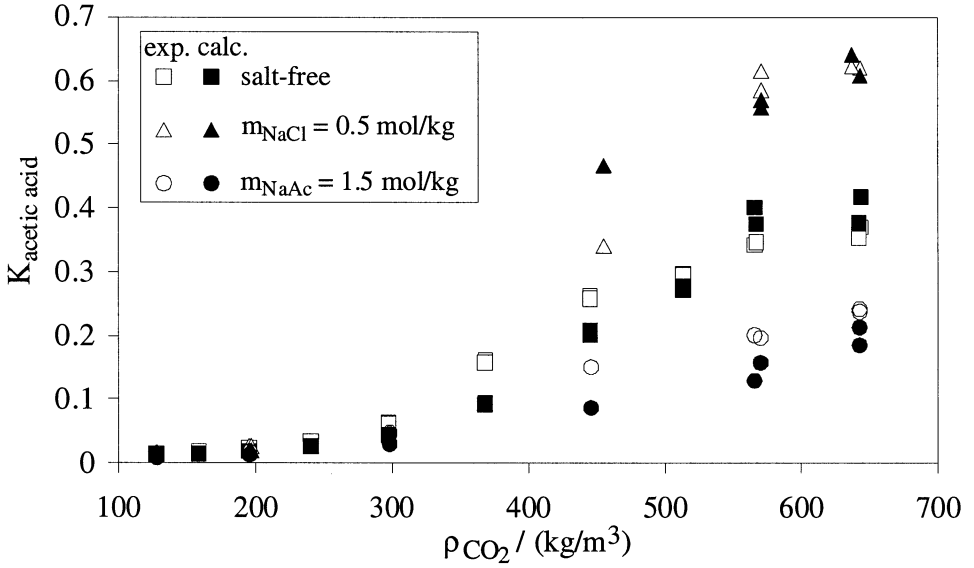

Fig. 5. Partition coefficient of acetic acid in the system carbon dioxide + water + acetic acid + salt at 333 K depending on the density of pure carbon dioxide for a CO_2-free solution with 50 mol% acetic acid.

The salting-out (salting-in) effect on acetic acid by sodium chloride (sodium acetate) is indicated by the increase (decrease) of the partition coefficient as compared to the salt-free systems.

4. MODELING

4.1. An extension of the Peng-Robinson equation of state to salt-containing systems

The equilibrium between fluid phases at high pressures is usually modeled with an equation of state, which commonly is derived from an expression for the free energy A as function of temperature T, volume V, and composition (e.g., mole numbers $\vec{n}$). It is common practice to split the free energy into two contributions:

$$A = A^{ideal} + \delta A^{real} \tag{1}$$

accounting for the properties in the ideal gas state (A^{ideal}) as well as for contributions caused by intermolecular forces (δA^{real}). General thermodynamics can be used to derive expressions for other state variables such as the pressure p

$$p(T,V,\vec{n}) = -\left(\frac{\partial A(T,V,\vec{n})}{\partial V}\right)_{T,\vec{n}}, \quad \wedge \tag{2}$$

the chemical potential μ_i of component I

$$\mu_i(T,p,\vec{x}) = \left(\frac{\partial A(T,V,\vec{n})}{\partial n_i}\right)_{T,V,n_j \neq n_i} \tag{3}$$

and the fugacity coefficient φ_i of component I

$$RT\ln\varphi_i = \left(\frac{\partial \delta A^{real}}{\partial n_i}\right)_{T,V,n_{j\neq i}} - RT\ln Z \tag{4}$$

It is common practice to split A^{ideal} into two contributions: A^0 is the free energy of the pure components in the ideal gas state at (T, p^0), and ΔA^{IG} accounts for the change of the free energy due to the mixing the ideal gases at (T, p^0) and changing the pressure to end up at volume V:

$$A^{ideal} = A^0 + \Delta A^{IG} \tag{5}$$

$$\Delta A^{IG}(T,V,\vec{n}) = RT\sum_{i=1}^{N_C} n_i \ln\frac{n_i RT}{Vp^0} \tag{6}$$

The contribution of the intermolecular forces to the free energy δA^{real} of a nonionic multicomponent mixture is separated into two terms resulting from repulsive and attractive forces, respectively.

$$\delta A^{real}_{nonionic} = \Delta A^{rep} + \Delta A^{att} \tag{7}$$

In the present work the Peng-Robinson equation of state [8] in the modification of Melhem et al. [3] is used to express those contributions:

$$\Delta A^{rep}(T,V,\vec{n}) = RT\sum_{i=1}^{N_C} n_i \ln\frac{V}{V - b\cdot n_T} \tag{8}$$

and

$$\Delta A^{att}(T,V,\vec{n}) = \frac{a(T)\cdot n_T}{2\sqrt{2}b}\ln\frac{V + b\cdot n_T\cdot(1-\sqrt{2})}{V + b\cdot n_T\cdot(1+\sqrt{2})} \tag{9}$$

where n_i and n_T are the mole number of component i and the total number of moles in the mixture, respectively. b is a covolume parameter

$$b = 0.07780\frac{RT_c}{p_c} \tag{10}$$

and a is an energy parameter (11)

$$a(T_c) = 0.45724\frac{RT_c^2}{p_c} \tag{12}$$

Subscript "c" denotes a property at the critical point.

As proposed by Melhem et al. [3], the influence of temperature on the attractive interaction parameter $\alpha(T)$ is approximated by:

$$\ln\alpha(T) = m(1 - T/T_c) + n\left(1 - \sqrt{T/T_c}\right)^2 \tag{13}$$

m and n are substance specific parameters.

Mixing rules have to be applied to describe the influence of the composition on a and b. A linear mixing rule without any adjustable parameter is used for the covolume parameter b:

$$b = \sum_{i=1}^{N_C} x_i \cdot b_i \tag{14}$$

where x_i and N_C are the mole fraction of component i and the number of components, respectively.

A quadratic mixing rule proposed by Panagiotopoulos and Reid [9] is used for energy parameter a:

$$a = \sum_{i=1}^{N_C} \sum_{j=1}^{N_C} (1 - K_{ij}) x_i x_j \sqrt{a_i a_j} \tag{15}$$

$$\text{with } K_{ii} = 0,\ K_{ij} = k_{ij} - (k_{ji} - k_{ij})\, x_i \text{ and } k_{ji} \neq k_{ij}\ . \tag{16}$$

Both binary interaction parameters (k_{ji} and k_{ij}) may depend on temperature (cf. Sect. 4.2).

An extension of that equation to mixtures with ionic species requires modifications for δA^{real}. Two assumptions are introduced. At first, it is assumed that both the covolume as well as the energy parameter of an ionic species are zero (i.e., ionic species do not have any vapor pressure). At second, two additional terms, ΔA^{DH} and ΔA^{iia}, are introduced to account for interactions with charged species.

$$A = A^0 + \Delta A^{IG} + \Delta A^{rep} + \Delta A^{att} + \Delta A^{DH} + \Delta A^{iia} \tag{17}$$

Table 2
Pure component parameters (cf. Ref. [4])

Component	T_c / K	p_c / MPa	m	n	References for experimental data
Carbon dioxide	304.2	7.38	0.6877	0.3813	[3]
Water	647.3	22.05	0.8795	0.0565	[3, 25–27]
Acetic acid (monomers)	416.3	5.11	0.3333	1.7215	[18–24]

Without ΔA^{DH} and ΔA^{iia} the presence of ionic species results only in a dilution of the mixture. ΔA^{DH} is a modified Debye-Hückel term. It considers long-range electrostatic interactions. The expression used here is based on the Debye-Hückel term in the G^E-model of Pitzer [10]. All nonionic components are considered to build up a nonionic solvent mixture with dissolved electrolytes (i.e., solutes).

$$\Delta A^{DH}(T,\vec{n}) = -n_{ges}RT\frac{4A_x I_x}{\chi}\ln(1+\chi\sqrt{I_x}) \tag{18}$$

I_x is the ionic strength based on mole fraction scale:

$$I_x = \frac{1}{2}\sum_{i=1}^{N_C} x_i z_i^2 \tag{19}$$

z_i is the charge number of solute i. χ is an empirical parameter

$$\chi = \frac{2}{\sqrt{M^*}} \tag{20}$$

adopted from Pitzer [10]. M^* is an average molecular mass:

$$M^* = \frac{1}{1000}\sum_{i=1}^{N_C} x_i^* M_i \tag{21}$$

and x_i^* is the mole fraction of solvent component i on a salt-free base.

The electrostatic properties of the solvent mixture are considered by a parameter A_x

$$A_x \frac{1}{3}\left(\frac{2\pi N_A}{v^*_{mix}}\right)^{1/2}\left(\frac{e^2}{4\pi\varepsilon_0\varepsilon_{mix}\cdot kT}\right)^{3/2} \tag{22}$$

N_A is Avogadro's number, v^*_{mix} is the molar volume of the solvent mixture, e is the charge of an electron, ε_0 is the permittivity of vacuum, ε_{mix} is the relative dielectric constant of the solvent mixture, and k is Boltzmann's constant. The molar volume v^*_{mix} is approximated by the covolume of the solvent mixture:

$$v^*_{mix} = \sum_{i=1}^{N_C} x^*_i b_i \tag{23}$$

The relative dielectric constant ε_{mix} is approximated by:

$$\varepsilon_{mix} = \frac{1}{v^*_{mix}} \sum_{i=1}^{N_C} x^*_i \cdot b_i \cdot \varepsilon_i \tag{24}$$

where ε_i is the relative dielectric constant of the pure solvent *i*. The influence of pressure on ε_i is neglected. The influence of temperature on ε_i is approximated by:

$$\varepsilon_i(T/K) = d_1 + \frac{d_2}{T/K} + d_3(T/K) + d_4(T/K)^2 + d_5(T/K)^3 \tag{25}$$

For the solvents of interest parameters d_i are given in Table 3.

Short range electrostatic interaction between ions and solvents are considered by a Margules term with binary and ternary interaction parameters:

$$\Delta A^{iia}(T,\vec{n}) = \frac{RT}{n_T} \sum_{i=1}^{N_C} \sum_{j=1}^{N_C} n_i n_j B_{ij} + \frac{RT}{n_T^2} \sum_{i=1}^{N_C} \sum_{j=1}^{N_C} \sum_{k=1}^{N_C} n_i n_j n_k C_{ijk} \tag{26}$$

At least one of the indices, (i or j) for B_{ij} (and i, j, or k) for C_{ijk}, stands for an ionic species. Introducing binary and ternary interaction parameters normally results in a large number of additional parameters. A few assumptions are introduced to reduce that number. At first, it is assumed that all binary (B_{ij}) and ternary (C_{ijk}) interaction parameters are symmetric. At second, all parameters for interactions between identical species are neglected ($B_{ii} = C_{iii} = 0$). At third, it was assumed that only parameters for interactions between ionic and neutral species are important, whereas parameters for interaction between ionic species are zero. When a single 1:1 salt (MX) is dissolved in a single solvent, there are

Table 3
Constants of Eq. (25) for the calculation of the relative dielectric constants

Component	d_1	d_2	d_3	d_4	d_5	Ref.
Carbon dioxide	1.6	-	-	-	-	[11]
Water	–19.2905	29814.5	–0.019678	$0.013189 \cdot 10^{-2}$	$-0.031144 \cdot 10^{-5}$	[12]
Acetic acid	3.33841	$0.953 \cdot 10^{-2}$	-	-	-	[13]

only one binary ($B_{S,MX}$) and two ternary ($C_{S,S,MX}$ and $C_{S,MX,MX}$) interaction parameters

$$B_{S,M^+} = B_{S,X^-} = B_{S,MX} \tag{27}$$

$$C_{S,S,M^+} = C_{S,S,X^-} = C_{S,S,MX} \tag{28}$$

$$C_{S,M^+,X^-} = C_{S,M^+,M^+} = C_{S,X^-,X^-} = C_{S,MX,MX} \tag{29}$$

As the experimental results did not give any hint for the presence of ionic species in the carbon dioxide-rich phase, it is worthwhile to mention that the extension to electrolyte solution (i.e., considering ΔA^{DH} and ΔA^{iia}) was only necessary for the water-rich phase, whereas the carbon dioxide-rich phase is treated as a nonionic mixture.

Additionally to the so called "physical" interactions, which have been described up to now, a "chemical" interaction leading to the dimerization of acetic acid was also taken into account (cf. Ref. [14]). The dimerization of acetic acid is taken into account in both phases. The procedure applied here is similar to the methods of Baumgärtner er al. [15] and of Grenzheuser and Gmehling [16]. Pure acetic acid is considered to be a mixture of monomers and dimers. The chemical equilibrium constant for the dimerization reaction

$$2\,CH_3COOH \leftrightarrow (CH_3COOH)_2 \tag{30}$$

$$\ln K(T) = \frac{2\mu_D(T,p^0) - \mu_M(T,p^0)}{RT} \tag{31}$$

was taken from Johnson and Nash [17]:

$$\ln K(T) = -16.641 + 6949.2/(T/K) \tag{32}$$

$\mu_D(T, p^0)$ and $\mu_M(T, p^0)$ are the chemical potentials of pure acetic acid dimers and monomers, respectively, at temperature T and standard pressure p^0 = 0.10325 MPa. The covolume b_D and the energy parameter a_D of acetic acid dimers are estimated from the parameters b_M and a_M of monomeric acetic acid:

$$b_D = 2 \cdot b_M \quad \text{and} \quad a_D(T) = 4a_M(T) \tag{33}$$

Furthermore, no binary parameter for interaction between acetic acid monomers and dimers is introduced (i.e., $K_{D,M} = 0$ for interactions between acetic acid monomers and dimers in Eq. (15)). Consequently, there is no difference between parameters for interactions between a component *i* on one side and either acetic acid monomers or acetic acid dimers on the other side: $k_{D,i} = k_{M,i}$ and $k_{i,D} = k_{i,M}$ (in Eq. (15)).

4.2. Interaction parameters

The method described above requires pure component and interaction parameters. The pure component parameters are given in Table 2. The parameters for "monomeric" acetic acid (critical temperature, critical pressure, as well as parameters m and n) were adjusted to give a good description of literature data for the vapor pressure [18-22] and the densities of coexisting liquid and vapor phase [23, 24] of pure acetic acid.

Tables 4 and 5 give the interaction parameters used for predicting the high pressure equilibria of the salt-free system carbon dioxide + water + acetic acid and the salt-containing systems carbon dioxide + water + acetic acid + (sodium chloride or sodium acetate). The binary interaction parameters of the mixing rule of Panagiotopoulos and Reid [9] were fitted to experimental results for the vapor-liquid equilibrium of the binary systems carbon dioxide + (water or acetic acid) and water + acetic acid. A linear influence of temperature on the interaction parameters had to be taken into account to achieve a good correlation of the experimental data. Parameter estimation was performed by minimizing the objective function SSQ:

$$SSQ = \sum_{i=1}^{N} \left[g_T \left(\frac{T^{\exp} - T^{cal}}{T^{\exp}} \right)^2 + g_P \left(\frac{p^{\exp} - p^{cal}}{p^{\exp}} \right)^2 + g_{x_1} \left(\frac{x_1^{\exp} - x_1^{cal}}{x_1^{\exp}} \right)^2 + g_{y_2} \left(\frac{y_2^{\exp} - y_2^{cal}}{y_2^{\exp}} \right)^2 \right]_i \tag{34}$$

For the determination of the interaction parameters between carbon dioxide + water, pressure, and temperature were preset (i.e., $g_T = g_P = 0$ and the relative deviations in the mole fraction of carbon dioxide in the liquid phase x_1 and of water in the vapor phase y_2 were minimized. No distinction was made between g_{x_1} and g_{y_2} ($g_{x_1} = g_{y_2} = 1$). In all other systems either the pressure or the temperature (for isobaric or isothermal experimental data, respectively) and the liquid phase composition were preset and the relative deviations in pressure (or temperature) and the vapor phase mole fraction of the solvent y_2 were minimized. Further details are available elsewhere (Sieder [4]). Predictions for

the phase equilibrium of the binary system carbon dioxide + acetic acid (without any binary parameter but considering the dimerization of acetic acid) agree with experimental data nearly as well as correlations which neglect the dimerization, but use an adjustable interaction parameter [14]. Thus, taking the dimerization of acetic acid into account results in an essential improvement in predictions for the phase behavior, as it allows to neglect any binary parameter. Therefore, in the work presented here, binary interaction parameters between carbon dioxide and acetic acid were neglected. All other binary interaction parameters (i.e., those for carbon dioxide + water and water + acetic acid) are given in Table 4. Table 5 gives a summarized comparison between correlated and experimentally determined vapor-liquid equilibrium data of the binary salt-free systems.

Table 4
Binary interaction parameter for the Peng-Robinson equation of state and the mixing rule of Panagiotopoulos and Reid [9] from the correlation of binary vapor-liquid equilibrium data

Component		T	p	$k_{12} = c_1^{(12)} + c_2^{(12)}\left(\frac{T/K}{1000}\right)$		$k_{21} = c_1^{(21)} + c_2^{(21)}\left(\frac{T/K}{1000}\right)$	
(1)	(2)	K	MPa	$c_1^{(12)}$	$c_2^{(12)}$	$c_1^{(21)}$	$c_2^{(21)}$
Carbon dioxide	Water	323–353	4–14	–0.4271	1.0337	–0.4516	1.9813
Carbon dioxide	Acetic acid	313–353	1–11	0.0	0.0	0.0	0.0
Water	Acetic acid	298–391	< 0.1	–0.5172	0.4286	–0.4286	0.1176

Table 5
Comparison between measured and calculated (Peng-Robinson equation of state and mixing rule of Pangiotopoulos and Reid [9]) results for the vapor-liquid equilibrium of the salt-free binary systems

Component		T	p	N_P	$\frac{\Delta x_1}{x_1^{exp}}$	$\frac{\Delta y_2}{y_2^{exp}}$	$\frac{\Delta p}{p}$	ΔT	References
(1)	(2)	K	MPa		%	%	%	K	
Carbon dioxide	Water	323–353	4–14	29	1.58	3.92	-	-	[14]
Carbon dioxide	Acetic acid	313–353	1–11	20	-	18.73	1.58	-	[14]
Water	Acetic acid	298–391	<0.1	169	-	4.87	0.91	0.42	[28–35]

Ionic interaction parameters ($B_{1,2}$, $C_{1,1,2}$, and $C_{1,2,2}$) were assumed to be independent of temperature. They were fitted to the osmotic coefficient of the binary systems water + sodium chloride and water + sodium acetate, to experimental data for the solubility of carbon dioxide in aqueous solutions of those single salts, and to experimental results for the influence of sodium chloride (and sodium acetate) on the vapor liquid equilibrium of the binary system water + acetic acid.

The data base for the osmotic coefficients of the binary systems water + sodium chloride and water + sodium acetate at temperatures from around 298 to 353 K was generated using Pitzer's model for the Gibbs excess energy of aqueous electrolyte solutions [10]. The resulting interaction parameters are given in Table 6. Using these parameters, the experimental results for the solubility of carbon dioxide in 4 to 6 molal aqueous electrolyte solutions by Rumpf et al. [6] and Xia et al. [7] were used to determine parameters for interaction between carbon dioxide on one side and sodium chloride or sodium acetate on the other side. Only a single binary parameter $B_{CO_2,NaCl}$ proved to be sufficient to reliably describe the solubility of carbon dioxide in aqueous solutions of sodium chloride. On the other side, all three parameters $B_{CO_2,NaAc}$, $C_{CO_2,CO_2,NaAc}$ and $C_{CO_2,NaAc,NaAc}$ had to be adjusted to give a good representation of the experimental data for the solubility of carbon dioxide in aqueous solutions of sodium acetate. Only scarce information is available on the influence of the single salts sodium chloride and sodium acetate on the vapor-liquid equilibrium of the binary system water + acetic acid (7 data points for the influence of sodium chloride and 9 data points for the influence of sodium acetate [37]).

Table 6
Ionic interaction parameter for the extended Peng-Robinson equation of state for salt containing systems (Sieder [4])

Component		T	p	m_{salt}	$B_{1,2}$	$C_{1,1,2}$	$C_{1,2,2}$
(1)	(2)	K	MPa	mol/kg			
Water	Sodium chloride	298–353	-	0–6	–2.7837	0.0	–1.0524
Water	Sodium acetate	298–333	-	0–6	–2.0085	0.0	0.0
Carbon dioxide	Sodium chloride	313–353	0–10	4–6	1.3631	0.0	0.0
Carbon dioxide	Sodium acetate	313–353	3–10	4–6	1.3370	4.7489	–6.6723
Acetic acid	Sodium chloride	379–390	1	0.1–6	6.7987	–5.2845	0.0
Acetic acid	Sodium acetate	-	1	2–3	2.3005	0.0	0.0

Using the parameters for the system water + salt and water + acetic acid, two binary parameters ($B_{CH_3COOH,NaCl}$ and $B_{CH_3COOH,NaAc}$) were adjusted to that data. The resulting interaction parameters are given in Table 6.

Table 7 presents a summarized comparison between the experimental data for the osmotic coefficient ϕ (for binary systems water + salt), the total pressure p (for the solubility of carbon dioxide in aqueous solutions of a single salt), and temperature and vapor phase composition in systems water + acetic acid + single salt (sodium chloride or sodium acetate). The average relative deviation is about 1 % for the osmotic coefficient, about 3 % for the solubility pressure, and about 5 % for the vapor-phase mole fraction of acetic acid, respectively.

Fig. 6 shows a comparison between the experimental data and the correlation for the vapor-liquid equilibrium of the system water + acetic acid + sodium chloride. Mole fractions of water and acetic acid are presented on a salt-free base. In the experiments the liquid phase was always saturated with sodium chloride – i.e., the results indeed represent a vapor + liquid + solid equilibrium. Therefore, the salt concentration in the liquid varies with varying water concentration. As the solubility of sodium chloride is small in acetic acid (below about 0.1 mol sodium chloride per kilogram of acetic acid) and large in water (about 6 mol per kilogram of water), the effect of the salt on the vapor liquid equilibrium is small at high acetic acid concentrations, whereas it is large at high water concentrations. For example, at 101 kPa the boiling temperature of an aqueous solution which is saturated by sodium chloride is nearly 10 K above that of pure water. Furthermore, the salt causes a shift in the volatility resulting in an azeotrope which is not observed in the salt-free system.

Table 7
Vapor-liquid equilibrium of salt containing systems: Comparison between experimental data and the correlation by the extended Peng-Robinson equation of state

Component			T	p	Salt molality	N_P	$\frac{\Delta\phi}{\phi_{exp}}$	$\frac{\Delta p}{p_{exp}}$	ΔT	$\frac{\Delta y_2}{y_2^{exp}}$	Ref
(1)	(2)	(3)	K	MPa	mol/kg		%	%	K	%	
H_2O	NaCl		298–353	-	0–6	84	0.7	-	-	-	[10]
H_2O	NaAc		298–333	-	0–6	39	1.3	-	-	-	[10, 36]
CO_2	H_2O	NaCl	313–353	0–10	4–6	38	-	2.7	-	-	[6]
CO_2	H_2O	NaAc	313–353	3–10	4–6	26	-	3.4	-	-	[7]
H_2O	CH_3COOH	NaCl	379–390	1	0.1–6	7	-	-	0.6	4.1	[37]
H_2O	CH_3COOH	NaAc	-	1	2–3	9	-	-	-	7.5	[37]

4.3. Prediction of high-pressure multicomponent phase equilibria

The methods (and parameters) describes above were applied to predict the high pressure phase equilibrium in systems of carbon dioxide + water + acetic acid without as well as with a single salt (sodium chloride or sodium acetate). As no parameter was adjusted to the new experimental results, the calculations are really predictions. In the calculation procedure the pressure, the temperature, and the molar ratio of acetic acid to water in the feed solution and – for the salt-containing systems – the salt concentration in the liquid feed were set and the compositions of the coexisting phases were calculated. Details of the calculation procedure are available elsewhere [4]. Fig. 2 to 5 show some typical comparisons between experimental phase equilibrium data and predictions.

For the ternary system carbon dioxide + water + acetic acid predictions for the tie-lines as well as for the binodal curve are shown. The agreement with the experimental data is good, although the miscibility gap is overestimated in particular at higher acetic acid concentrations. This overshooting is a well known phenomenon in particular for predictions of liquid-liquid phase equilibrium from parameters based on binary data alone. A good agreement is observed in particular at low pressures and low amounts of acetic acid (cf. Fig. 2). For higher amounts of acetic acid the solubility of carbon dioxide in the liquid phase is underestimated. But the predictions for the partitioning of acetic acid on the coexisting phases and the composition of the carbon dioxide-rich phase agree with the experimental results almost within experimental uncertainty. With increasing pressure the deviations increase (cf. Fig. 3 and 4), but the predictions for the slope of a tie-line nicely agree with the experimental results.

The influence of the salts on the phase equilibrium is also predicted with reasonable accuracy. The salting-out of both carbon dioxide and acetic acid by sodium chloride is predicted. The predictions for the partition coefficient of acetic acid agree with the experimental results nearly within experimental uncertainty (cf. Fig. 5 for a comparison for 333 K) for sodium chloride (where a salting-out effect is observed) as well as for sodium acetate (where salting-in occurs).

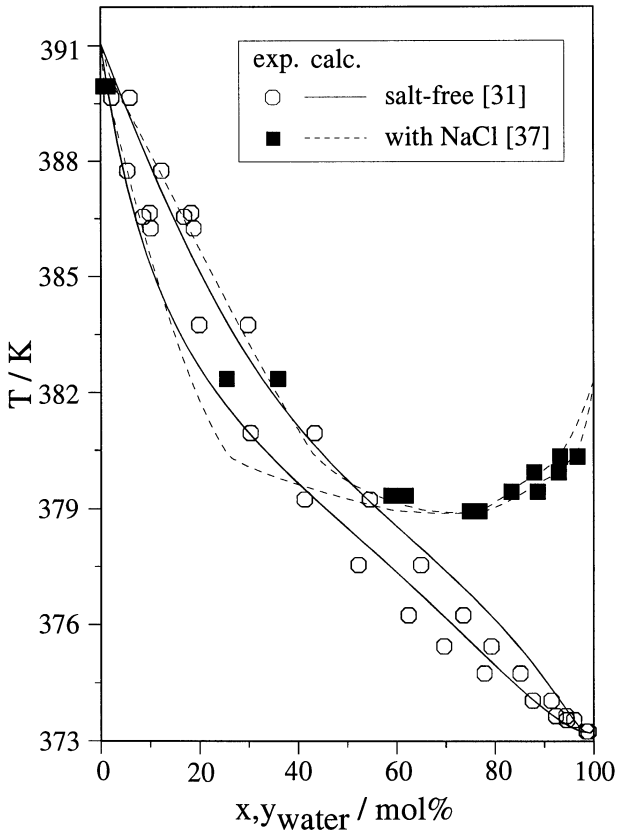

Fig. 6. Vapor-liquid equilibria in the system water + acetic acid + sodium chloride at 101 kPa: Experimental data and correlation.

5. CONCLUSION

The phase equilibrium of the ternary system carbon dioxide + water + acetic acid and the quaternary systems carbon dioxide + water + acetic acid + (sodium chloride or sodium acetate) was investigated experimentally for temperatures between 313 and 353 K at pressures up to 16 MPa. The measurements were performed with an apparatus realizing the continuous flow technique. The main focus of the experimental investigations was on the effects of the salts on the composition of the coexisting phases. The experimental result revealed that the concentration of carbon dioxide in the aqueous phase decreases in presence of both sodium chloride and sodium acetate, i.e., "salting-out" of carbon dioxide by these salts is observed. However, both salts reveal different effects on the concentration of acetic acid in the aqueous phase. The presence of sodium chloride reduces the concentration of acetic acid in the aqueous phase ("salting-

out"), whereas sodium acetate causes an increase in the concentration of acetic acid in the aqueous phase ("salting-in"). The experimental results are described by an extension of the Peng-Robinson equation of state. For salt-free mixtures the pure component parameters are determined using a proposal of Melhem et al. The properties of the salt-free mixtures are described using the mixing rules of Panagiotopoulos and Reid. In all cases it was important to consider the dimerization of acetic acid in both phases. With binary interaction parameters which were solely adjusted to binary data reliable predictions were possible for the high pressure phase equilibrium of the ternary salt-free system carbon dioxide + water + acetic acid. An extension of the Peng-Robinson equation of state is proposed to account for the presence of ionic species in the aqueous phase. The extension consists of two additional contributions to the free energy.

A term of Debye-Hückel type is introduced to account for unspecific long range electrostatic interactions. A contribution of Margules type with adjustable parameters is applied to account for specific short range interactions between ions on one side and ions and neutral species on the other side. The additional parameters were fitted to phase equilibrium data of binary and ternary salt containing systems. The so extended Peng-Robinson equation of state gives reasonable predictions for the influence of the single salts sodium chloride and sodium acetate on the compositions of the coexisting phases.

REFERENCES

[1] R. Dohrn, G. Brunner, Fluid Phase Equilibria, 106 (1995) 213.
[2] T. Adrian, M. Wendland, H. Hasse, G. Maurer, J. Supercrit. Fluids, 12 (1998) 185.
[3] G. A. Melhem, R. Saini, C. F. Leibovici, Fluid Phase Equilibria, 47 (1989) 189.
[4] G. Sieder, PhD Dissertation, Universität Kaiserslautern, Kaiserslautern, Germany, 2002.
[5] E. Bender, Proc. 5th Symp. Thermophys. Prop., (1970) 227.
[6] B. Rumpf, H. Nicolaisen, C. Öcal, G. Maurer, J. Sol. Chem., 23 (1994) 431.
[7] J. Xia, B. Rumpf, G. Maurer, Fluid Phase Equilibria, 155 (1999) 107.
[8] D.-Y. Peng, D. B. Robinson, Ind. Eng. Chem. Fundam., 15 (1976) 59.
[10] A. Z. Panagiotopoulos, R. C. Reid, Fluid Phase Equilibria, 29 (1986) 525.
[11] K. S. Pitzer, J. Phys. Chem., 77 (1073) 268.
[12] A. Michels, L. Kleerekoper, Physica, 6 (1939) 586.
[13] L. Chunxi, W. Fürst, Chem. Eng. Sci., 55 (2000) 2975.
[14] R. C. Weast, M. J. Astle, CRC Handbook of Chemistry and Physics, CRC Press Inc., West Palm Beach, 1978.
[15] A. Bamberger, G. Sieder, G. Maurer, J. Supercrit. Fluids, 17 (2000) 97.
[16] M. Baumgärtner, W. Rupp, H. Wenzel, Chem. Eng. Symp. Ser., 56 (1979) 31.
[17] P. Grenzheuser, J. Gmehling, Fluid Phase Equilibria, 25 (1986) 1.
[18] E. W. Johnson, L. K. Nash, J. Am. Chem. Soc., 72 (1950) 547.
[19] D. Ambrose, J. H. Ellender, C. H. S. Sprake, R. Townsend, J. Chem. Thermodyn., 9 (1977) 145.
[20] Engineering Sciences Data Unit International, No. 80029, London, 1980.
[21] F. H. MacDougall, J. Am. Chem. Soc., 58 (1936) 2585.

[22] R. A. McDonald, S. A. Shrader, D. R. Stull, J. Chem. Eng. Data, 4 (1959) 311.
[23] A. E. Potter, H. L. Ritter, J. Phys. Chem., 58 (1954) 1040.
[24] J. L. Hales, H. A. Gundry, J. H. Ellender, J. Chem. Thermodyn., 15 (1983) 211.
[25] S. Young, Sci. Proc. Roy. Dublin Soc., 12 (1909/10) 374.
[26] E. Schmidt, Properties of Water and Steam in SI-units, 2th ed., Springer, Berlin, 1981.
[27] K. Stephan, F. Mayinger, Thermodynamik, Band 1 Einstoffsysteme, 12. Auflage, Springer, Berlin, 1986.
[28] VDI-Wärmeatlas, 4. Auflage VDI-Verlag, Düsseldorf, 1984.
[29] I. Brown, A. H. Ewald, Austr. J. Sci. Reg. (1950) 306.
[30] A. N. Campbell, E. M. Kartzmark, J. M. Gieske, Can. J. Chem., 41 (1963) 407.
[31] R. Haase, M. H. Keller, K.-H. Dücker, Z. Naturf., A, 29 (1974) 1383.
[32] T. Ito, F. Yoshida, J. Chem. Eng. Data, 8 (1963) 315.
[33] T. M. Kushner, G. I. Tatsievskaya, V. A. Irzun, L. V. Volkava, L. A. Serafimov, Zh. Fiz. Khim., 40 (1966) 3010.
[34] M. S. Laazeva, N. P. Markuzin, Zh. Prikl. Khim., 46 (1973) 360.
[35] E. Sebastiani, L. Lacquaniti, Chem. Eng. Sci., 22 (1967) 1155.
[36] M. S. Vrevskii, K. P. Mishchenko, B. A. Muromtzev, J. Russ. Phys. Chem. Soc., 59 (1927) 598.
[37] J. Xia, Lehrstuhl für Technische Thermodynamik, Universität Kaiserslautern, Kaiserslautern, Germany; Unpublished data, 2001.
[38] S. Ohe, ACS Series No. 177: Advances in Chemistry, American Chemical Society, Washington, 1979.

Supercritical Fluids as Solvents and Reaction Media
G. Brunner (editor)

Chapter 1.8.

Correlation and prediction of high-pressure phase equilibria and related thermodynamic properties of simple fluid mixtures

U. K. Deiters*

Institute of Physical Chemistry, University of Cologne, Luxemburger Str. 116, D-50939 Köln, Germany
*deiters@xenon.pc.uni-koeln.de

ABSTRACT

The thermodynamic fundamentals of fluids and solids are shortly reviewed, and the criteria of phase equilibria discussed. The structure of the versatile *thermoC* program package is outlined, and its working demonstrated for several examples.

It is shown that complete phase diagrams involving solid–fluid and fluid–fluid phase equilibria can be predicted with a single parameter set, and that it is even possible to estimate pure-compound sublimation data from binary solid–fluid high-pressure phase equilibria.

Several mixing theories are applied to the correlation of the gas–gas equilibria of the (neon + krypton) system. It is shown that only mixing rules with density-dependent fractal exponents can achieve a quantitative agreement.

1. INTRODUCTION

At a first glance it might be astonishing that "simple fluid mixtures" can still be the topic of a publication after more than a century of research and development in thermodynamics. However, "simple" does not mean "easy": Especially the so-called simple mixtures show a surprising diversity of phase diagrams, when high pressures are taken into account.

The constituents of simple fluid mixtures are usually small molecules of fixed shape, interacting mostly by dispersion forces. Hydrogen bonds, polarity, internal rotations and vibrations do not occur or have no large influence on the thermodynamic properties. Molecules fulfilling these requirements are

- the noble gases,
- small alkanes (methane, ethane, ...),
- many refrigerants,

- carbon dioxide, nitrous oxide, sulphur hexafluoride,
- fluorine, chlorine, oxygen, nitrogen, and many other compounds.

Evidently, many of these substances and their mixtures play significant rôles in modern technology, e.g., mixtures of nitrogen, methane, or carbon dioxide with alkanes in the processing of natural gas, or carbon dioxide and nitrous oxide in supercritical fluid extraction technology. But also some chemically reactive mixtures must be mentioned in this context, e.g., (hydrogen + nitrogen) for the ammonia synthesis, and (hydrogen + oxygen) in rocket engines.

What makes these compounds and their mixtures so interesting and sometimes so hard to describe quantitatively is the extremely wide range of *reduced* properties spanned by many systems. For example, hydrogen at room temperature is at almost 10 times its critical temperature. Consequently, models and equations of state for hydrogen-containing mixtures have to cover a wide range of variables, and must be designed to be extrapolatable.

Another aspect of simple fluid mixtures is the asymmetry between the compounds, which is difficult to model and puts high demands on the mixing rule or equation of state. This asymmetry often leads to surprising phase separations.

Finally, simple molecules cannot be broken down into smaller groups, as the group contribution methods so efficiently do with larger molecules.

From the viewpoint of computational thermodynamics, simple fluid mixtures are benchmark systems for theories and models. For many of them not only experimental phase equilibrium data are available over wide ranges of temperatures and pressures, but also other properties like excess volumes, heats of mixing, or speed of sound. While it is always possible, by adjusting a few interaction parameters, to achieve of satisfying fit of a single VLE isotherm, the correlation of a set of isotherms is not always easy, and the simultaneous prediction of vapour–liquid, liquid–liquid, and solid–fluid equilibria as well as volumetric and caloric data is far from trivial.

Simple fluid mixtures are therefore worthwhile objects of study, after all. It is the goal of this work to outline the thermodynamic framework for calculations of their properties, to show some recent development in equations of state and mixing rules, and to discuss some aspects of computer programming.

2. THERMODYNAMIC FUNDAMENTALS

2.1. Thermodynamic properties of fluid phases

Thermal equations of state, $p(V_\mathrm{m}, T)$, connect three observable quantities, namely pressure, molar volume, and temperature, and are therefore valuable tools for the representation and correlation of volumetric data. For further calculations and predictions, however, it is advantageous to use one of the so-called fundamental equations, the Helmholtz energy equation $A_\mathrm{m}(V_\mathrm{m}, T)$ or the

Gibbs energy equation $G_{\mathrm{m}}(p,T)$. These two energies are usually not directly measurable, but since all other thermodynamic properties can be obtained from them by differentiation, these functions play a central rôle in all thermodynamic calculations. The fundamental equations of a fluid mixture of C components can be obtained from the thermal equation of state by

$$G_{\mathrm{m}}^{\mathrm{f}}(p,T,\vec{x}) = \sum_{i}^{C} x_i G_{\mathrm{m},i}^{\ominus}(p^{\ominus},T) + RT\sum_{i}^{C} x_i \ln x_i + \int_{p^{\ominus}}^{p} V_{\mathrm{m}}(p,T,\vec{x})\,\mathrm{d}p \quad , \quad (1)$$

where $\vec{x}$ denotes the vector of compositions (mole fractions).

The first term of this equation represents the intrinsic Gibbs energies of the mixture components in the perfect gas state. These intrinsic functions reflect, among other things, chemical energies and excitation of internal degrees of freedom; they usually cancel in calculations of isothermal processes in nonreacting mixtures. Because the molecules do not interact in the perfect gas state, their intrinsic functions are strictly additive.

The second term of Eq. (1) arises from the mixing of the components in the perfect gas state.

The third term represents the isothermal compression of the mixture from the perfect gas state to the final pressure p. Now there is the problem that $p(V_{\mathrm{m}},T,\vec{x})$ is always a single-valued function of its arguments, whereas $V_{\mathrm{m}}(p,T,\vec{x})$ is not. The mathematical difficulties inherent in this scheme can be circumvented by switching the variables (by means of partial integration):

$$\begin{aligned} G_{\mathrm{m}}^{\mathrm{f}}(p,T,\vec{x}) = {} & \sum_{i}^{C} x_i G_{\mathrm{m},i}^{\ominus}(p^{\ominus},T) + RT\sum_{i}^{C} x_i \ln x_i + pV_{\mathrm{m}}(p) \\ & - RT - \int_{V_{\mathrm{m}}^{\ominus}}^{V_{\mathrm{m}}} p(V_{\mathrm{m}},T,\vec{x})\,\mathrm{d}V_{\mathrm{m}} \quad , \end{aligned} \quad (2)$$

Because of $G_{\mathrm{m}} = A_{\mathrm{m}} + pV_{\mathrm{m}}$, this finally leads to

$$A_{\mathrm{m}}^{\mathrm{f}}(p,T,\vec{x}) = \sum_{i}^{C} x_i\big(A_{\mathrm{m},i}^{\ominus}(V_{\mathrm{m}}^{\ominus},T) + RT\ln x_i\big) - \int_{V_{\mathrm{m}}^{\ominus}}^{V_{\mathrm{m}}} p(V_{\mathrm{m}},T,\vec{x})\,\mathrm{d}V_{\mathrm{m}} \quad , \quad (3)$$

where $p(V_{\mathrm{m}},T,\vec{x})$ is the thermal equation of state for the mixture. Eq. (3) is the working equation for many older equations of state. Modern equations are usually based on a direct formulation of the residual Helmholtz energy,

$$A_{\mathrm{m}}^{\mathrm{f}}(p,T,\vec{x}) = \sum_{i}^{C} x_i\big(A_{\mathrm{m},i}^{\ominus}(V_{\mathrm{m}}^{\ominus},T) + RT\ln x_i\big) - RT\ln\frac{V_{\mathrm{m}}}{V_{\mathrm{m}}^{\ominus}} + A_{\mathrm{m}}^{\mathrm{r}}(V_{\mathrm{m}},T,\vec{x}) \quad , \quad (4)$$

and yield the thermal equation of state after differentiation,

$$p(V_\mathrm{m}, T, \vec{x}) = -\left(\frac{\partial A^\mathrm{f}_\mathrm{m}}{\partial V_\mathrm{m}}\right)_{T,x_i} \quad . \tag{5}$$

Upon this differentiation all intrinsic terms are lost. Conversely, the intrinsic terms cannot be obtained from the thermal equation of state by integration. Instead, one has to integrate experimental data for $C^{\ominus}_{p,\mathrm{m}}$, the isobaric molar heat capacity in the perfect gas state, to obtain these terms.

We finally note that the expression for the mixing entropy contains mole fractions, *not* volume fractions. The use of a Flory–Huggins type mixing entropy expression in an equation of state applicable to the perfect gas state, which previously had been proposed in literature, is not permissible.

2.2. Thermodynamic properties of solid phases

In contrast to vapor–liquid equilibria there is no path along which a continuous transformation of one phase into the other can be brought about. The consistent coupling of the thermodynamic functions of solid phases to those of fluid phases therefore requires some additional construction.

The customary approach to phase equilibria between a mixed fluid and a pure solid uses an extension of the "freezing point depression equation", in which the mole fraction of the solidifying compound is replaced by a fugacity ratio. This approach, however, ignores the effect of pressure on the solid phases. An alternative approach [1] starts from the observation that, at the sublimation pressure of a pure solid, p^sf, the relation

$$G^\mathrm{s}_\mathrm{m} = G^\mathrm{f}_\mathrm{m} \tag{6}$$

between the molar Gibbs energies of the solid and the fluid (vapour) phase holds. The Gibbs energy of the fluid phase can be obtained by means of the fluid equation of state, as shown above. The Gibbs energy of the solid at an *arbitrary* pressure p can then be expressed by

$$G^\mathrm{s}_\mathrm{m}(p,T) = G^\mathrm{f}_\mathrm{m} + \int_{p^\mathrm{sf}}^{p} V^\mathrm{s}_\mathrm{m}(p,T)\,\mathrm{d}p \quad . \tag{7}$$

Here $V^\mathrm{s}_\mathrm{m}(p,T)$ denotes the equation of state of the solid.

For small pressures it may be permissible to ignore the pressure dependence of the solid. But many organic compounds have very compressible, "soft" solid phases; examples are the rotator phases of the n-alkanes. In such cases the solid compressibility should be taken into account.

The simplest approach is to assume a constant solid compressibility,

$$\kappa_T^{\mathrm{s}} = -\frac{1}{V_{\mathrm{m}}^{\mathrm{s}}}\left(\frac{\partial V_{\mathrm{m}}^{\mathrm{s}}}{\partial p}\right)_T = \text{const} \quad . \tag{8}$$

The resulting solid equation of state is then

$$V_{\mathrm{m}}^{\mathrm{s}}(p,T) = V_{\mathrm{m}}^{\mathrm{s}}(p^{\mathrm{sf}},T)\exp\bigl(\kappa_T^{\mathrm{s}}(p-p^{\mathrm{sf}})\bigr) \quad . \tag{9}$$

A superior equation of state for solids is the Murnaghan equation [2], which makes use of the experimentally established relation

$$\frac{1}{\kappa_T^{\mathrm{s}}(p)} = \frac{1}{\kappa_T^{\mathrm{s}}(0)} + \lambda p \quad . \tag{10}$$

λ is an empirical constant, which turns out to be approximately the same for molecules of similar chemical constitution. The resulting expression for the volume is

$$V_{\mathrm{m}}^{\mathrm{s}}(p,T) = V_{\mathrm{m}}^{\mathrm{s}}(p^{\mathrm{sf}},T)\bigl(1+\lambda\kappa_T^{\mathrm{s}}(0)(p-p^{\mathrm{sf}})\bigr)^{-1/\lambda} \quad . \tag{11}$$

Eq. (7), in connection with one of the solid-state equations of state shown above, can then be used with the condition for phase equilibrium, $\mu_2^{\mathrm{s}} = \mu_2^{\mathrm{f}}$, to set up an equation for solid–fluid equilibria:

$$G_{\mathrm{m},2}^{\mathrm{f}}(p_2^{\mathrm{sf}},T) + \int_{p_2^{\mathrm{sf}}}^{p} V_{\mathrm{m},2}^{\mathrm{s}}(p,T)\,\mathrm{d}p = \mu_2^{\mathrm{f}}(p,T,x_2^{\mathrm{f}}) \tag{12}$$

It is assumed that component 2 is the one that solidifies. Eq. (12) is the working equation used here.

It is possible to replace the Gibbs energies or chemical potentials by fugacities,

$$\mu_2^{\mathrm{f}} = \mu_2^{\ominus} + RT\ln\frac{x_2^{\mathrm{f}} f_2}{p^{\ominus}} \quad . \tag{13}$$

As sublimation pressures are usually very low, it is a common simplification to replace the integral by $V_{\mathrm{m},2}^{\mathrm{s}}(p-p_2^{\mathrm{sf}}) \approx pV_{\mathrm{m},2}^{\mathrm{s}}$ and the Gibbs energy on the l.h. side by $\mu_2^{\ominus} + RT\ln(p_2^{\mathrm{sf}}/p^{\ominus})$. Then the equilibrium condition can be rearranged into

$$\ln x_2^{\mathrm{s}} = \ln\frac{p_2^{\mathrm{sf}}}{f_2} + \frac{pV_{\mathrm{m}}^{\mathrm{s}}}{RT} \quad . \tag{14}$$

This equation, which contains several simplifications, is found in many textbooks [3].

For the evaluation of the Gibbs energy of a solid it is therefore necessary to know the sublimation pressure (which can be obtained from the triple point pressure and the sublimation enthalpy by means of the Clausius–Clapeyron equation), the solid molar volume, and preferably some solid compressibility data. It should be noted that the solid equation of state contributes approximately $V_{\mathrm{m}}^{\mathrm{s}}(p - p^{\mathrm{sf}})$ to the Gibbs energy Eq. (7), even in the case of an incompressible solid. This contribution is sometimes overlooked [4].

2.3. Stability and equilibrium

It is common textbook knowledge that the necessary condition for two-phase equilibrium in a mixture is

$$\mu_i' = \mu_i'' \,, \quad i = 1, \ldots, C \quad , \tag{15}$$

where the μ_i are the chemical potentials of component i as defined by

$$\mu_i(V_{\mathrm{m}}, T, \vec{x}) = \left(\frac{\partial A_{\mathrm{m}}}{\partial n_i}\right)_{V_{\mathrm{m}},T,n_k\neq i} \quad . \tag{16}$$

Together with the conditions of mechanical equilibrium,

$$p = p(V_{\mathrm{m}}', T, \vec{x}') = p(V_{\mathrm{m}}'', T, \vec{x}'') \quad , \tag{17}$$

the phase equilibrium condition yields a system of algebraic equations, which can then be solved for the equilibrium compositions.

An acceptable solution must furthermore fulfill the criterium of diffusional stability (local convexity of the Gibbs energy function); for a binary mixture this so-called spinodal criterium is

$$\left(\frac{\partial^2 G_{\mathrm{m}}}{\partial x_1^2}\right)_{p,T} > 0 \quad . \tag{18}$$

It can be shown that a phase fulfilling this criterium also does not fail the mechanical stability test, $\kappa_T > 0$.

However, the above conditions do not guarantee that the calculated phase equilibrium is a stable one. This can only be verified by a global search for the minimum of the Gibbs energy.

A little known stability criterium is offered by the Third Law: It turns out that some fluid equations of state predict negative total entropies at high densities. The density at which this happens must be regarded as an upper boundary to the solidification density [5].

3. THE *thermoC* PROGRAM

3.1. Concept

The amount of computer program code required for the determination of parameters of equations of state, for their storage and retrieval, and for the calculation of several kinds of phase equilibria, critical states, and volumetric and caloric data, is rather large, even for a single equation of state.

When it comes to comparisons between many equations of state or between different mixing theories, the programming effort can become prohibitive.

The logical answer to this problem is a structured program package with clearly distributed scopes of its components. The *thermoC* program package, which had been developed by us over the previous years, uses the following program code classes:

1. *general mathematical subroutines:*
   These are, for example, root finders, minimizers, differentiation algorithms, linear algebra subroutines.
2. *basic thermodynamic subroutines:*
   These subroutines represent general thermodynamic relations, e.g., the relation between the equation of state and the critical properties, the Gibbs energy, or caloric data. Subroutines in this class are independent of the thermodynamic model (equation of state) or of the main program within which they are used.
3. *model-specific thermodynamic subroutines:*
   These rather small sets of subroutines contain each the characteristics of an equation of state or a mixing rule. Subroutines in this class are independent of the context in which they are used.
4. *main programs:*
   These calculate the thermodynamic properties and thus define the program context, e.g., calculation of a vapour pressure curve or a critical curve. They are independent of the equation of state or mixing rule used.

The propagation of informations like EOS parameters from the main programs to the subroutines is not achieved by global variables (in Fortran77: common blocks), but by "structures", a special feature of the programming language C. The difference between the C and the Fortran programming style can be demonstrated with the following example:

Declaration of the structure holding parameters for a pure compound:

C:

```
typedef struct {
char name[20], comment[40];
int id;
double pcr, Tcr, vcr;
double par[20];
struct ideal1 ideal;
} species;
```

Fortran77:

no equivalent

The informations stored are the name of the compound, a comment line indicated the source of the parameters, an identity number (there may be more than one parameter set for a single compound), the critical data, and the parameter vector. Furthermore, there is a reference to another structure storing caloric data of the perfect gas state.

Reserving memory for the parameters (pure fluid program):

C:

```
species s;
```

Fortran77:

```
COMMON /PARS/CHARACTER NAME(20),
+COMMENT(40), INTEGER ID,
+REAL*8 PCR, TCR,VCR, PAR(20)
COMMON /IDEAL1/ ...
```

Invocation of a subroutine (e.g., pure fluid pressure):

C:

```
p = press1(&s, v, T);
```

Fortran77:

```
P = PRESS1(V, T)
```

So far the programming languages seem to be approximately equivalent. But what happens, if we want to deal with more than one compound?

Reserving memory for the parameters (binary mixture program):

C:

```
species s[2];
```

Fortran77:

```
COMMON /PARS/CHARACTER NAME(20),
+COMMENT(40),INTEGER IDENTNO,
+REAL*8 PCR, TCR, VCR, PAR(20)
COMMON /PARS2/CHARACTER
+NAME2(20,2),COMMENT2(40,2),
+INTEGER IDENTNO2(2),
+REAL*8 PCR2(2), TCR2(2),
+VCR2(2),PAR2(20,2)
COMMON /IDEAL1/ ...
```

Invocation of the pure fluid pressure subroutine within the mixure main program:

C:

```
p[i] = press1(&s[i], v, T);
```

Fortran77:

```
PCR = PCR2(K)
TCR = TCR2(K)
VCR = VCR2(K)
DO K=1,NPARAMS
PAR(K) = PAR2(K,I)
END DO
P(I) = PRESS1(V, T);
```

Even this little example shows how difficult extensions of code can be with Fortran, and that it is necessary to maintain huge common blocks — with the risk of name clashes increasing with the size of the program.

3.2. Model-specific subroutines

The number of model-specific subroutines should be as small as possible, in order to facilitate the implementation of new models. On the other hand there is a minimum of subroutines required for a smooth and efficient computation of thermodynamic properties. Our choices for minimal sets of subroutines are listed in Table 1 for pure compounds and in Table 2 for binary mixtures.

It should be noted that the volume finder subroutine is a model-specific, not a globally defined subroutine. For cubic equations of state the volume finder subroutine can invoke a special cubic root finder, e.g., Cardano's method (which is neither safe nor optimal [6]!), or more complicated iterative algorithms in other cases. There is no principal limitation: The *thermoC* program can accommodate equations of state of arbitrary complexity.

That no explicit pressure subroutine appears in the list of mixture subroutines is intended: There are complicated mixing theories with density-dependent parameters, for which the analytical differentiation of the Helmholtz energy

Table 1
Model-specific subroutines required for pure-fluid equations of state.

subroutine	purpose
ident1()	declaration of the EOS name and number of parameters, eventually loading tables of universal constants
limits()	declaration of the physically meaningful range of EOS parameters
ares1()	residual Helmholtz energy
press1()	pressure (the EOS itself)
vcalc1()	calculation of molar volumes for given pressure and temperature
xinit()	estimated (not necessarily exact) values of reduced critical properties

Table 2
Model-specific subroutines required for equations of state of mixtures.

subroutine	purpose
ident2()	declare mixing rule name and number of parameters
ares2()	residual Helmholtz energy
vcalc2()	calculation of molar volumes for given pressure, temperature, and composition

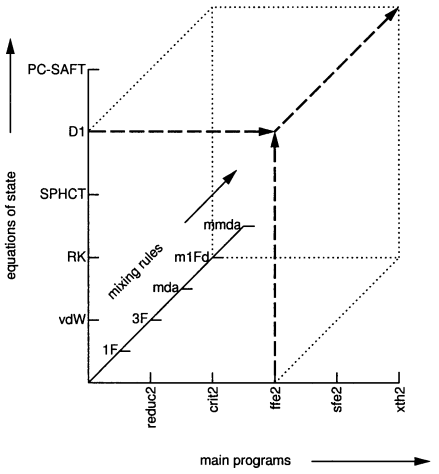

Fig. 1. Illustration of the creation of executable programs by dynamic loading. For explanations of the abbreviations see Tables 4 (main programs) and 5 (equations of state).

equation is highly impractical. As *thermoC* offers a volume finder subroutine which relies on numerical differentiation of the Helmholtz energy, a binary pressure equation is not necessary (although it can be specified if the user desires).

3.3. Main programs

The main programs have been formulated in such a way that they are completely independent of the equation of state or mixing theory used. In *thermoC* the model-specific subroutines are compiled as dynamically loadable libraries, which are invoked by the main programs at run time. This way any thermodynamic property (represented by the appropriate program) can be calculated with any equation of state (represented by its model-specific subroutine set).

For mixtures it is furthermore possible to combine a pure-fluid equation of state with different mixing rules (1-fluid theory, 3-fluid theory, mean density approximation, ...). The resulting three-dimensional linking scheme is illustrated by Fig. 1.

Table 3
Main programs for the calculation of pure-fluid properties.

main program	purpose
ffe1()	vapour pressure curve
reduc1()	parameter fitting
sfe1()	sublimation pressure curve
sle1()	melting pressure curve
spinodal1()	spinodal curve
vir1()	virial coefficients
xth1()	thermodynamic data of fluids (single phase state)
xth1s()	thermodynamic data of solids

Table 4
Main programs for the calculation of mixture properties.

main program	purpose
crit2()	critical curves
ffe2()	vapour–liquid and liquid–liquid equilibria
mix2_Hp()	isenthalpic-isobaric mixing
mix2_HS()	isenthalpic-isentropic mixing
reduc2()	binary parameter fitting
sfe2()	solid–fluid equilibria
spinodal2()	spinodal curves of mixtures
transit2()	transitiometer† simulation
xth2()	thermodynamic data of fluid mixtures (single phase)

† a very versatile high-pressure apparatus which can record — among other thermodynamic properties — the heat flow caused by a pressure or temperature scan [7]

It should be noted that the dynamic loading of model libraries makes use of special features of the programming language C: pointer arithmetics and the possibility to "overload" function pointers with new values at run time.

A list of the main programs recently contained in *thermoC* is given in Tables 3–4. Furthermore, Table 5 lists the equations of state which are available at present; for many of them the application to mixtures is possible, too.

3.4. Mathematical and general thermodynamics subroutines

thermoC makes heavy use of numerical differentiation. For long, complicated equations of state, this may even be more accurate than analytical differentiation. Nevertheless, the loss of numerical precision by differentiation is a problem that needs to be addressed.

Table 5
Equations of state recently implemented in *thermoC*.

cubic	semiempirical noncubic	empirical noncubic
PR: Peng–Robinson [8]	CSRK: Carnahan–Starling + Redlich–Kwong [9]	IUPAC_C6H6: benzene [10]
RK: Redlich–Kwong [11]	CSvdW: Carnahan–Starling + van der Waals [9]	IUPAC_CO2: carbon dioxide [12]
RKS: Redlich–Kwong–Soave [13]	D1: Deiters [14,15]	IUPAC_CH4: methane [16,17]
TBS: Trebble–Bishnoi–Salim [18]	Mxw2RK: soft sphere + Redlich–Kwong [19,20]	IUPAC_N2: nitrogen [21]
vdW: van der Waals [22]	Mxw2vdW: soft sphere + van der Waals [19,20]	IUPAC_O2: oxygen [23]
	PC-SAFT: perturbed chain stat. associated fluid [24]	IAPWS_H2O: water [25,26]
	SL: Sanchez–Lacombe [27]	Nicolas: Lennard-Jones fluid [28]
	SPHCT : simplified perturbed hard chain theory [29]	
	YKchvdW: Yelash–Kraska + van der Waals [30,31]	

For some equations of state variants are available with correction terms for association or quantum effects.

Within *thermoC* only differentiation formulas are used which eliminate at least errors of the order $O(\delta x)$, where δx is the numerical differentiation increment of the mole fraction. Sometimes even higher orders are eliminated by Romberg's method (also known as Ridder's method [32]).

A special problem, which is rarely addressed in mathematical text books, is the finite domain size of some variables; e.g., mole fractions should always remain within [0;1]. This sometimes requires asymmetric differentiation formulas, which consequently have been implemented in *thermoC* .

4. PREDICTION OF THERMODYNAMIC PROPERTIES

4.1. Phase diagrams of pure compounds

With most 3-parameter equations of state it is not difficult to reproduce the vapour pressure curve over an appreciable temperature interval. It is not always easy, however, to obtain good predictions of the liquid densities and the vaporization enthalpies at the same time.

Fig. 2 represents a severe test of an equation of state as well as the computational software: Tetracosane is known two have two solid phases, a rotator

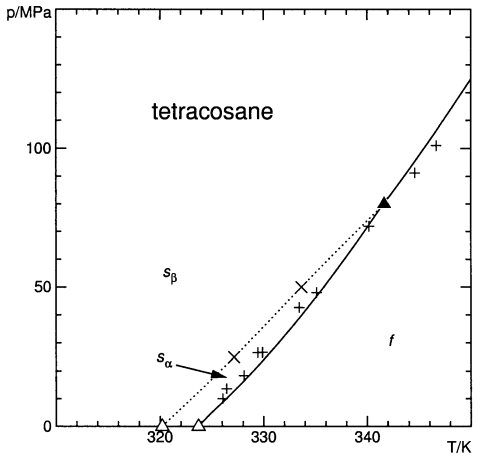

Fig. 2. Phase diagram of tetracosane. —: predicted melting pressure curves using the Deiters equation of state, · · ··: estimated solid–solid transition line, △;: experimental triple points, ▲, predicted triple point, +, ×: experimental phase transition points [34,35].

phase s_α and a normal crystalline phase s_β. An equation of state [14,15] was fitted to the liquid density and the pressure at the $s_\alpha lg$ triple point. Furthermore, the pressure of the $s_\alpha s_\beta g$ triple point was estimated from the experimentally known phase transition enthalpies and volumes [33]. From these data the melting pressure curve was predicted. It can be seen from Fig. 2 that even the upper triple point, $s_\alpha s_\beta l$ could be predicted almost within the experimental uncertainty.

4.2. Phase diagrams of mixtures involving solidification

In typical correlations of fluid–fluid phase equilibria, shortcomings of the equation of state or the mixing rules can be compensated to some degree by the use of adjustable binary parameters. However, this path is no longer available if phase diagrams are to be calculated which contain both fluid–fluid and solid–fluid equilibria: If the binary parameters are fitted, e.g., to the critical curve, no leeway for adjustment is left for the solid–fluid equilibria, and vice versa. Therefore such calculations offer a particularly stringent test of thermodynamic models.

An example, the phase diagram of the binary mixture (ethene + naphthalene) is shown in Fig. 3: An *slg* three-phase line issues from the triple point of naphthalene, runs first towards lower temperatures with increasing pressure (the usual melting point depression effect in mixtures), but then turn to higher temperatures (a pressure effect). It ends in a critical endpoint, *sl=g*, where it meets the critical curve originating from the critical point of naphthalene. This

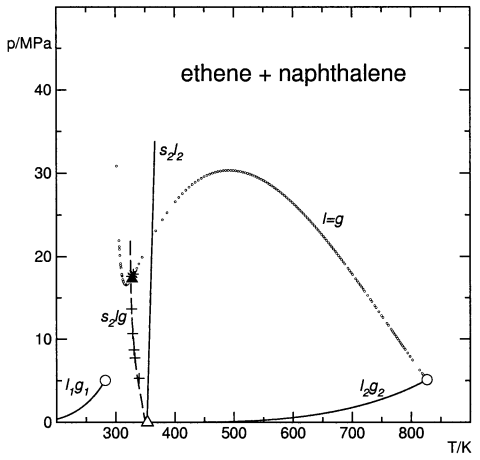

Fig. 3. Phase diagram of the system (ethene + naphthalene). Calculations were made with the Deiters equation of state and density-dependent mixing rules [36], experimental data are from Diepen and Scheffers [38,39]. —: pure component vapor pressure and melting pressure curves, – – –: *slg* 3-phase curve (predicted), ○: binary critical state (predicted), ◯: pure component critical point, +: *slg* 3-phase state (experimental), △: triple point, ▲: critical endpoint, ×: binary critical state (experimental).

critical curve is also terminated and can no longer continue towards high pressures.

The modelling of such asymmetric mixtures requires equations of state and mixing rules which take into account packing effects in the compressed liquid or gas state very accurately. Fig. 3 was obtained with the Deiters equation and a modified, density-dependent 1-fluid mixing theory [36], which is described below (Eq. (29). This mixing rule has been found to be superior to the van der Waals 1-fluid mixing rule if the mixture components are of approximately spherical shape and rigid.

The (ethene + naphthalene) system is sometimes quoted as an example of a simple binary mixture with an (in principle) continuous critical curve connecting the pure-fluid critical points, which is only interrupted by the crystallization phase equilibria. But the computations shown here cast some doubt upon this view: Fig. (3) also shows the metastable part of the critical curve, which is not accessible to experiments, but easy to obtain from the calculations. The shape of this metastable part shows that (ethene + naphthalene) should be regarded as a class III system in the nomenclature of Scott and van Konynenburg [37].

It should be noted that this phase diagram was obtained with a single, temperature-independent set of parameters, which was used for all curves of the phase diagram.

4.3. Estimation of sublimation pressures

One of the most frustrating aspects of calculations of solid–supercritical fluid phase equilibria is generally the lack of reliable sublimation data: The experimental determination of sublimation or vapour pressure data at pressures below 100 Pa is extremely difficult and costly.

A feasible alternative to a direct ultra-low pressure experiment might be a special evaluation of a high-pressure solid–fluid equilibrium curve.

In a typical solid–fluid equilibrium the concentration of the crystallizing compound in the fluid phase is very low. Consequently, mixing rule terms characterizing the interactions between solute molecules play a minor rôle only, and can be estimated sufficiently well even by crude methods. In a 1-fluid set of mixing rules like Eq. (29) one can therefore fit ϵ_{12} and σ_{12}, and then estimate ϵ_{22} and σ_{22} by means of the Berthelot–Lorentz combining rules. Furthermore, because of the low solute concentrations the exact shape of the mixing rules also becomes insignificant — as long as the interaction parameters are fitted, there is no significant difference between a simple 1-fluid theory and a complicated scheme like Eq. (29). In the end, only 4 indispensable parameters of the solute remain to be determined: ϵ_{12}, σ_{12}, p^{sf}, and $V_{\mathrm{m}}^{\mathrm{s}}$; and of course the molar volume of the solid and the collision diameter can be expected to be correlated.

We have tested this approach for the (carbon dioxide + adamantane) system. The latter is a roughly spherical compound (tricyclodecane, $C_{10}H_{16}$) with a rather high triple point temperature, and thermodynamic data of the solid phase are available in the literature.

Fig. 4 shows a typical solid–fluid phase diagram of this system, with the typical dramatic increase of the adamantane concentration in the fluid phase above the critical pressure of carbon dioxide. At still higher pressures the adamantane concentrations begin to decline [1].

The Deiters equation of state, here in conjunction with 1-fluid mixing rules, was then fitted to the experimental data. Table 6 compares the sublimation pressures obtained by this fit with experimental values for the sublimation pressures of adamantane [41]. The agreement is reasonably good, and even the sublimation enthalpy of adamantane is obtained. One has to realize, however, that the sublimation pressure is very sensitive to small deviations of the experimental data: The determination of sublimation pressures from high-pressure binary phase equilibria amounts to an extrapolation of an isotherm (Fig. 4) to zero pressure — a difficult task, but not an impossible one.

For the extrapolation to succeed it would be helpful to have binary solid–fluid equilibrium data down to lower pressures, at least to the critical pressure of the solvent fluid.

The molar volume and the compressibility of the solid required for these calculations were taken from literature [42,43]. In principle the molar volume

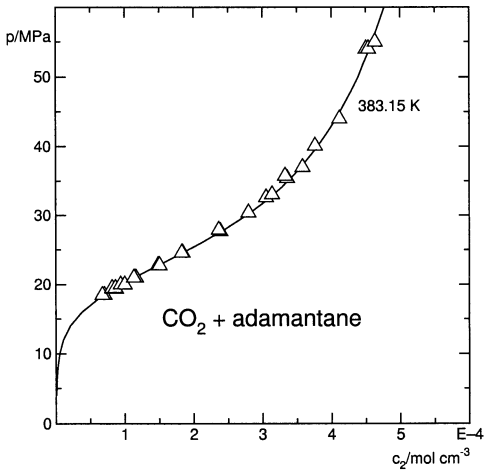

Fig. 4. Solid–fluid phase diagram of the system (carbon dioxide + adamantane). —: calculated with Deiters equation of state (interaction parameters of adamantane and sublimation pressure fitted to exp. data), △: experimental data [1,40].

Table 6
Sublimation pressures of adamantane. Results from fitting an equation of state to high-pressure phase equilibrium data of (carbon dioxide + adamantane) and from direct experimental determination at very low pressures [41].

T/K	p^{sg}/kPa	
	fitted	experimental
343.15	0.65	0.44
363.15	1.74	1.25
383.15	4.22	3.19
403.15	9.36	7.45
	$\Delta_{sub l}H_m$/kJ mol^{-1}	
	51.2	54.3

can also be obtained from the fitting procedure, but for an accurate prediction the input data have to cover an extremely wide pressure range. If only the calculation of solid–fluid equilibria at high pressures is intended, it is usually sufficient to estimate the solid molar volume from the covolume parameter of the equation of state.

4.4. Mixing theories

The calculation of fluid phase equilibria at high pressures depends mainly on two elements — equations of state and mixing theories. However, it is not

the goal of this paper to discuss equations of state. A short summary of the requirements to be fulfilled by equations of state has already been published elsewhere [44]. For discussions of specific programming problems and pitfalls related to cubic equations of state the reader is referred to recent literature [45,6].

Equations of state are usually formulated for pure compounds only. For use with mixtures they have to be generalized, and this is accomplished by means of mixing rules or, more generally, by mixing theories.

From the viewpoint of statistical thermodynamics it is often advantageous to describe the local structure of a fluid by means of the radial distribution function $g(r)$. This function represents the local particle density — or, more accurately, the deviation of the local particle density from the bulk density — in the vicinity of a given particle:

$$\mathrm{d}N = 4\pi r^2 \rho g(r)\,\mathrm{d}r \tag{19}$$

Here $\rho = N/V$ is the number density; the given particle is assumed to be at $r = 0$. Then the contribution of the intermolecular forces to a thermodynamic property, e.g., the residual internal energy, can be written as

$$U^{\mathrm{r}} = \frac{1}{2}\sum_{i}^{N}\sum_{k}^{N} u_i k = \frac{2\pi N^2}{V}\int_0^\infty u(r)g(r)r^2\,\mathrm{d}r \quad . \tag{20}$$

Introducing reduced variables,

$$\begin{aligned} u(r) &= \epsilon_0 \tilde{u}(\tilde{r}) \\ r &= \sigma_0 \tilde{r} \\ g(r) &= \tilde{g}(\tilde{r}) \quad , \end{aligned} \tag{21}$$

then leads to

$$U^{\mathrm{r}} = \frac{2\pi N^2}{V}\epsilon_0\sigma_0^3\int_0^\infty \tilde{u}(\tilde{r})\tilde{g}(\tilde{r})\tilde{r}^2\,\mathrm{d}\tilde{r} \tag{22}$$

This equation implies that the molecules interact by pair potentials only, and that these pair potentials depend on distance only, not on orientation. The equation can easily be adapted to other thermodynamic properties like the pressure or the compression factor.

For mixtures Eq. (22) becomes

$$U^{\mathrm{r}} = \frac{2\pi N^2}{V}\sum_{i}^{C}\sum_{k}^{C} x_i x_k \int_0^\infty \tilde{u}_{ik}(\tilde{r})\tilde{g}_{ik}(\tilde{r})\tilde{r}^2\,\mathrm{d}\tilde{r} \quad . \tag{23}$$

The problem, of course, is to find plausible approximations for the radial distribution functions $g_{ik}(r)$.

In order to present a stringent comparison of several such approximations, we present calculations for a single high-pressure system only, namely (neon + krypton). This systems exhibits a gas–gas immiscibility of the second kind and represents a challenge to the computational models. For the following calculations always the same equation of state [14,15] is used, which is known to be reasonably good for small molecules and noble gases. Therefore deviations from or agreement with the experimental data can be attributed to the quality of the mixing rules.

The mixing theories outlined in the following sections are applied to the attractive part of the equation of state only; for the repulsive part the mixing functions are provided by theory of hard sphere mixtures.

4.4.1. 1-fluid theories

The most widely used mixing theory is probably the van der Waals 1-fluid theory (*1F*). Here it is assumed that the pair potentials are conformal, i.e., they are the same for all pair interactions in the mixture when expressed with reduced properties:

$$u_{ik}(r) = \epsilon_{ik}\tilde{u}(\tilde{r}) \quad \text{with} \quad \tilde{r} = \frac{r}{\sigma_{ik}} \tag{24}$$

Furthermore it is assumed that the radial distribution functions can be made to coincide when expressed with reduced distances:

$$g_{ik}(r) = \tilde{g}(\tilde{r}) \tag{25}$$

With these simplifications, Eq. (23) can be transformed into

$$U^{\mathrm{r}} = \frac{2\pi N^2}{V} \sum_i^C \sum_k^C x_i x_k \epsilon_{ik} \sigma_{ik}^3 \int_0^\infty \tilde{u}(\tilde{r}) \tilde{g}(\tilde{r}) \tilde{r}^2 \, \mathrm{d}\tilde{r} \quad . \tag{26}$$

Now the integral does no longer depend on the species. Comparison with Eq. (22) finally leads to

$$\begin{aligned} U^{\mathrm{r}} = U_0^{\mathrm{r}} \quad \text{with} \quad \epsilon_0 \sigma_0^3 &= \sum_i^C \sum_k^C x_i x_k \epsilon_{ik} \sigma_{ik}^3 \\ \sigma_0^3 &= \sum_i^C \sum_k^C x_i x_k \sigma_{ik}^3 \quad , \end{aligned} \tag{27}$$

i.e., the mixture can be represented by a hypothetical pure fluid with parameters (ϵ_0, σ_0). As any residual molar property can be written as a function of reduced properties only, we finally obtain the working equation

$$U_{\mathrm{m}}^{\mathrm{r}} = U_{\mathrm{m},0}^{\mathrm{r}} \left(\frac{k_{\mathrm{B}} T}{\epsilon_0}, \frac{V}{N \sigma_0^3} \right) \quad . \tag{28}$$

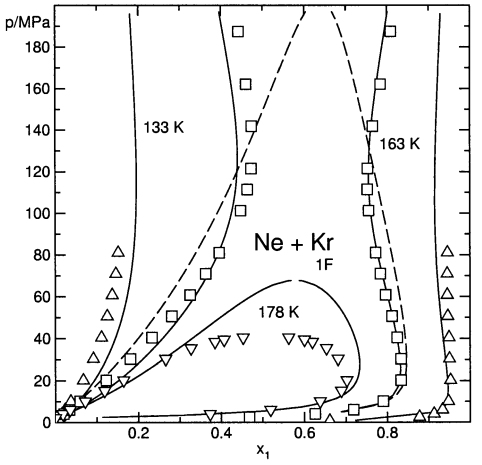

Fig. 5. Phase diagram of the (neon + krypton) system. —: Deiters EOS, 1-fluid theory, – – –: Redlich–Kwong EOS, symbols: exp. data [46].

Expressed with words: The *parameters* of the equation of state are averaged over the species, and the resulting values are used with the pure-fluid equation of state.

It should be noted that not every mixing rule containing double sums similar to Eq. (27) is a true van der Waals 1–fluid mixing theory: Some equations have rather peculiar definitions of their parameters, e.g., for the Redlich–Kwong equation $a_{\mathrm{RK}} \sim \epsilon^{3/2}\sigma^3$ [11]. A double sum over such parameters is not compatible with Eq. (27).

Fig. 5 shows the phase diagram of the (neon + krypton) system, correlated with the 1-fluid theory. It should be noted that all isotherms were calculated with the same parameter set.

It is possible to relax the restriction Eq. (25) somewhat by introducing the concept of fractal dimensions. The resulting mixing theory, the *modified density-dependent 1-fluid theory (m1Fd)*, accounts very accurately for size differences of the mixture components [36]:

$$
\begin{aligned}
U_{\mathrm{m}}^{\mathrm{r}} = U_{\mathrm{m},}^{\mathrm{r}}0 \quad \text{with} \quad \epsilon_0\sigma_0^{\gamma} &= \sum_i^C \sum_k^C x_i x_k \epsilon_{ik} \sigma_{ik}^{\gamma} \\
\gamma &= 3(1-\xi^2) \\
\sigma_0^3 &= \sum_i^C \sum_k^C x_i x_k \sigma_{ik}^3
\end{aligned}
\tag{29}
$$

Here γ is a fractal exponent accounting for packing efficiency. The density dependence given here is for a square-well potential wit h a range of 1.5σ,

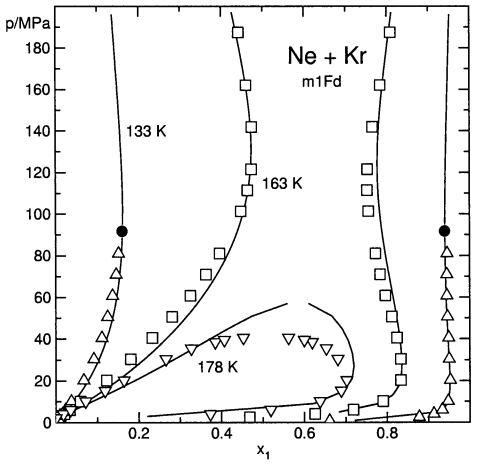

Fig. 6. Phase diagram of the (neon + krypton) system. —: modified 1-fluid theory (*m1Fd*), •: calculated endpoint $s_{\mathrm{Kr}}lg$, open symbols: exp. data [46].

which is the pair potential underlying the equation of state used in this work. ξ is the reduced density with respect to the occupied volume, $\xi = \frac{\pi}{6}\frac{N}{V}\sigma^3$.

Application of the *m1Fd* mixing theory leads to a significant improvement of the representation of the phase equilibria in the neon–krypton system (Fig. 6).

4.4.2. 3-fluid theories

In very asymmetric mixtures the radial distribution functions of the various species differ not only in the location of their peaks (which can be accounted for by 1-fluid theories), but also in their general shapes: E.g., in a mixture of neon and krypton at 150 K the neon is supercritical and consequently should have a rather featureless radial distribution function, whereas the krypton is subcritical, and its radial distribution function should have a high peak at the distance of the first solvation shell.

To overcome this problem the so-called *3-fluid theory* has been proposed. Its equations can be derived from Eq. (23) by assuming that each $g_{ik}(r)$ is the same as that of a pure fluid with the parameters $(\epsilon_{ik}, \sigma_{ik})$ at the same volume and temperature as the mixture:

$$U_{\mathrm{m}}^{\mathrm{r}} = \sum_i^C \sum_k^C x_i x_k U_{\mathrm{m},0}^{\mathrm{r}}\left(\frac{k_{\mathrm{B}}T}{\epsilon_{ik}}, \frac{V}{N\sigma_{ik}^3}\right) \tag{30}$$

It can be shown that this mixing theory is exact in the limit of low densities; it gives correct second virial coefficients. However, it fails catastrophically for

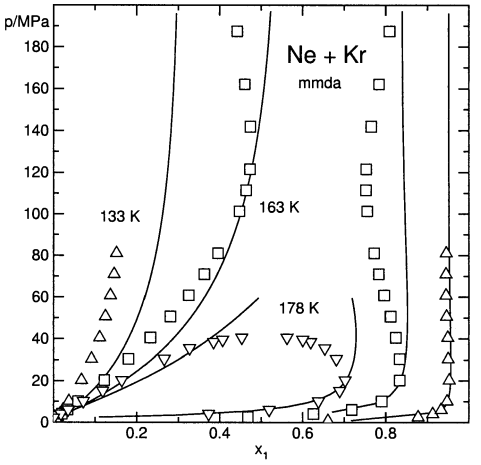

Fig. 7. Phase diagram of the (neon + krypton) system. —: modified mean density approximation (*mmda*), symbols: exp. data [46].

asymmetric mixtures at high densities, because the reduced density of the larger component, $N\sigma_{22}^3/V$, can easily exceed the physically possible range.

4.4.3. Mean density approximations

To overcome this weakness, and as a compromise between the 1-fluid and 3-fluid theories, the *mean density approximation (mda)* averages over the size parameters, but not over the energy parameters of an equation of state:

$$U_{\mathrm{m}}^{\mathrm{r}} = \sum_i^C \sum_k^C x_i x_k \frac{\sigma_{ik}^3}{\sigma_0^3} U_{\mathrm{m},0}^{\mathrm{r}}\left(\frac{k_{\mathrm{B}}T}{\epsilon_{ik}}, \frac{V}{N\sigma_0^3}\right) \quad \text{with} \quad \sigma_0^3 = \sum_i^C \sum_k^C x_i x_k \sigma_{ik}^3 \tag{31}$$

In analogy to the 1-fluid theory, a more detailed modelling of the fluid structures at high densities leads to a *modified mean density approximation (mmda)*, in which the weight factor σ_{ik}^3/σ_0^3 is replaced by $\sigma_{ik}^\gamma/\sigma_0^\gamma$; γ is a density-dependent fractal dimension, which has already been explained above.

The phase diagram of the test system neon–krypton for this mixing theory is shown in Fig. 7. It is clearly not an improvement over the previous mixing theories.

4.4.4. Combination theory

In spite of the good theoretical foundations of the *mmda* theory, the representation of high-pressure phase equilibria leaves to be desired. The reason for this is the interaction with (unlike) neighbour molecules, which prevents each mixture component to assume its own, undisturbed radial distribution function.

Consequently, the *mmda* turns out to inferior to the *m1Fd* theory at high densities.

On the other hand, the *mmda* converges against the theoretical low-density limits, which is not always guaranteed for 1-fluid theories.

It is therefore appealing to combine both theories. The logical measure of the translational "freedom" of molecules is the free volume, which for hard spheres is given by

$$V_{\mathrm{m}}^{\mathrm{free}} = fV_{\mathrm{m}} \quad \text{with} \quad f = \exp\left(-\frac{4\xi - 3\xi^2}{(1-\xi)^2}\right) \quad . \tag{32}$$

The resulting mixing theory, *mmda1F*, can then be summarized as

$$U_{\mathrm{m}}^{\mathrm{r}} = \sum_i^C \sum_k^C x_i x_k \frac{\sigma_{ik}^\gamma}{\sigma_0^\gamma} U_{\mathrm{m},0}^{\mathrm{r}}\left(\frac{k_{\mathrm{B}}T}{e_{ik}}, \frac{V}{N\sigma_0^3}\right)$$

$$\text{with} \quad \sigma_0^3 = \sum_i^C \sum_k^C x_i x_k \sigma_{ik}^3 \tag{33}$$

$$\epsilon_0 \sigma_0^\gamma = \sum_i^C \sum_k^C x_i x_k \epsilon_{ik} \sigma_{ik}^\gamma$$

$$e_{ik} = f\epsilon_{ik} + (1 - f\epsilon_0)$$

The resulting phase diagram for (neon + krypton) is shown in Fig. 8. Except for slight deviations at extreme pressures (which may be attributed to quantum effects), the new theory is even better than the *m1Fd* theory. Especially the "hourglass" contour of the middle isotherm, which is very difficult to calculate, is rendered quite well.

5. CONCLUSION

The adequate correlation and prediction of high-pressure phase equilibria requires a rather accurate modelling of the local structure of the fluid phases involved. Simple 1-fluid mixing theories turn out to be not sufficient, even for noble gas mixtures.

On the other hand, improved mixing theories are available which permit a quantitative representation of the phase equilibria over wide ranges of pressures and temperatures. These theories, *m1Fd* and *mmda1F*, contain density-dependent fractal exponents which are derived from computer simulations.

The use of these mixing theories within equations of state to generate phase envelopes is not easy; the density dependence of the effective dimensionality of space leads to extremely complicated expressions for the pressure, the chemical potentials, and other derivatives. However, it is possible to circumvent this

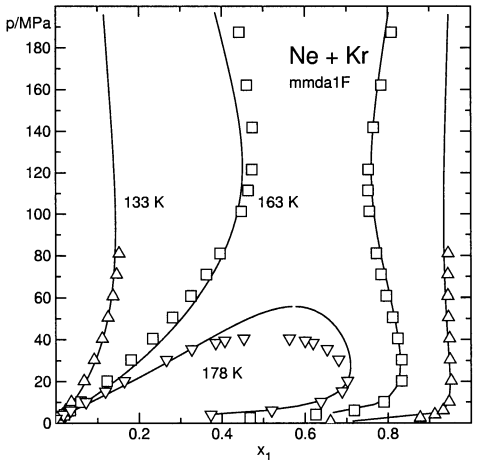

Fig. 8. Phase diagram of the (neon + krypton) system. —: combination theory (*mmda1F*); symbols: exp. data [46].

problem by numerical differentiation. The *thermoC* program package uses this technique to implement these and other complex mixing theories and equations of state.

With equations of state of sufficient quality it is possible to predict fluid–fluid and solid–fluid phase equilibria from the same parameter set. The internal consistency of the thermodynamic model can even be utilized to estimate sublimation pressures of pure solid compounds from high-pressure binary solid–fluid equilibrium data.

6. ACKNOWLEDGMENTS

We wish to thank Prof. Gabriele Sadowski (University of Dortmund, Germany) and Dr. Abdel Fenghour (Imperial College, U. K.) for supplying parameter sets and test data for their equations of state, as well as Dr. Thomas Kraska and Dr. Leonid V. Yelash for their work on the correlation of solid–fluid equilibria.

Financial support by the Deutsche Forschungsgemeinschaft (project De 391/13) is gratefully acknowledged.

Symbols

A Helmholtz energy
C number of components
f free volume factor
$g(r)$ radial distribution function
G Gibbs energy
H enthalpy
k_B Boltzmann's constant
n amount of substance
N number of molecules
p pressure
R universal gas constant
T temperature
$u(r)$ pair potential
U internal energy
V volume
x mole fraction
γ density-dependent fractal dimension
κ_T isothermal compressibility
λ Murnaghan parameter
μ chemical potential
ρ number density

Superscripts

f fluid (liquid, gas, supercritical) phase
r residual property
s solid phase
$\ominus$ reference state (perfect gas)

Subscripts

i component i
m molar property

REFERENCES

[1] U. K. Deiters, I. Swaid, Ber. Bunsenges. Phys. Chem. 88 (1984) 791–796.
[2] D. C. Wallace, Thermodynamics of Crystals, John Wiley & Sons, New York, 1972.
[3] G. T. Preston, J. M. Prausnitz, Ind. Eng. Chem. Process Design Develop. 9 (1970) 264.
[4] M. Teller, H. Knapp, Ber. Bunsenges. Phys. Chem. 87 (1983) 532.
[5] J. F. Kenney, Phys. Chem. Chem. Phys. 1 (1999) 3277–3285.
[6] U. K. Deiters, AIChE J. 48 (2002) 882–886.
[7] S. L. Randzio, D. J. Eatough, E. A. Lewis, L. E. Hansen, J. Chem. Thermodynamics 20 (1988) 937–948.
[8] D. Y. Peng, D. B. Robinson, Ind. Eng. Chem. Fundam. 15 (1976) 59–64.
[9] N. F. Carnahan, K. E. Starling, J. Chem. Phys. 51 (1969) 635–636.
[10] A. Fenghour, K. M. de Reuck, A. Elhassan, J. Kilner, An analytic equation of state for benzene from the triple point to 725 K and 400 MPa, in: Proceedings of the ICCT-2002 (IUPAC International Conference on Chemical Thermodynamics), University of Rostock (Germany), 2002, p. 47.
[11] O. Redlich, J. N. S. Kwong, Chem. Reviews 44 (1949) 233–244.
[12] R. Span, W. Wagner, J. Phys. Chem. Ref. Data 25 (1996) 1509–1596.
[13] G. Soave, Chem. Eng. Sci. 27 (1972) 1197–1203.
[14] U. K. Deiters, Chem. Eng. Sci. 36 (1981) 1139–1146.
[15] U. K. Deiters, Chem. Eng. Sci. 36 (1981) 1146–1151.
[16] U. Setzmann, W. Wagner, J. Phys. Chem. Ref. Data 20 (1991) 1061–1155.
[17] W. Wagner, K. M. de Reuck, Methane, Vol. 13 of IUPAC International Tables of the Fluid State, Blackwell Science, London, 1996.
[18] P. H. Salim, M. A. Trebble, Fluid Phase Equil. 65 (1991) 59–71.
[19] U. K. Deiters, Mol. Phys. 74 (1991) 153–160.
[20] U. K. Deiters, S. L. Randzio, Fluid Phase Equil. 103 (1995) 199–212.
[21] S. Angus, K. M. de Reuck, B. Armstrong, Nitrogen, Vol. 6 of IUPAC International Tables of the Fluid State, Pergamon, Oxford, 1979.

[22] J. D. van der Waals, On the Continuity of the Gaseous and Liquid States, Vol. XIV of Studies in Statistical Mechanics, North-Holland, Amsterdam, 1988.
[23] W. Wagner, K. M. de Reuck, Oxygen, Vol. 9 of IUPAC International Thermodynamic Tables of the Fluid State, Blackwell Science, London, 1987.
[24] J. Gross, G. Sadowski, Fluid Phase Equil. 168 (2000) 183–199.
[25] A. Saul, W. Wagner, J. Phys. Chem. Ref. Data 18 (1989) 1537–1564.
[26] W. Wagner, A. Pruß, J. Phys. Chem. Ref. Data 31 (2002) 383–355.
[27] I. C. Sanchez, R. H. Lacombe, J. Phys. Chem. 80 (1976) 2352–2362.
[28] J. K. Johnson, J. A. Zollweg, K. E. Gubbins, Mol. Phys. 78 (1993) 591–618.
[29] C.-H. Kim, P. Vimalchand, M. D. Donohue, S. I. Sandler, AIChE J. 32 (1986) 1726–1734.
[30] L. V. Yelash, T. Kraska, U. K. Deiters, J. Chem. Phys. 110 (1999) 3079–3084.
[31] L. V. Yelash, Development of equations of state for complex fluids (Ph. D. thesis), Vol. 745 of Fortschritts-Berichte VDI Reihe 3, VDI Verlag, Düsseldorf, 2000.
[32] W. H. Press, S. A. Teukolsky, W. T. Vetterling, B. P. Flannery, Numerical Recipes (in Fortran), 2nd Edition, Cambridge University Press, 1992.
[33] U. Domanska, D. Wyrzykowska-Stankiewicz, Thermochim. Acta 179 (1991) 265–271.
[34] E. Flöter, T. W. de Loos, J. de Swaan Arons, Fluid Phase Equil. 127 (1997) 129–146.
[35] A. Würflinger, G. M. Schneider, Ber. Bunsenges. Phys. Chem. 7 (1973) 121–128.
[36] U. K. Deiters, Fluid Phase Equil. 33 (1987) 267–293.
[37] P. H. van Konynenburg, R. L. Scott, Philos. Trans. Royal Chem. Soc. London Ser. A 298 (1980) 495–540.
[38] G. A. M. Diepen, F. E. C. Scheffer, J. Amer. Chem. Soc. 70 (1948) 4085.
[39] G. A. M. Diepen, F. E. C. Scheffer, J. Phys. Chem. 57 (1953) 575.
[40] I. Swaid, D. Nickel, G. M. Schneider, Fluid Phase Equil. 21 (1985) 95–112.
[41] L. Malaspina, R. Gigli, G. Bardi, J. Chem. Phys. 59 (1973) 387.
[42] W. Florian, Z. Phys. Chem. 61 (1968) 319.
[43] S. N. Vajdya, G. C. Kennedy, J. Chem. Phys. 55 (1971) 987–992.
[44] U. K. Deiters, K. M. de Reuck, Pure & Appl. Chem. 69 (1997) 1237–1249.
[45] I. Polishuk, J. Wisniak, H. Segura, Phys. Chem. Chem. Phys. 4 (2002) 879–883.
[46] N. J. Trappeniers, J. A. Schouten, Physica 73 (1974) 546–555.

Supercritical Fluids as Solvents and Reaction Media
G. Brunner (editor)

Chapter 1.9.

Development of simplified equation of states for molecular fluids and their applications for the investigation of supercritical chain molecule solutions and mixtures.

L. V. Yelash and Th. Kraska

Universität zu Köln, Institut für Physikalische Chemie, Luxemburger Str. 116, 50939 Köln

1. INTRODUCTION

For modeling and simulation of processes based on supercritical fluids the thermophysical properties of the supercritical solvent and its mixtures are required. A commonly used approach for modeling these data is to use equations of state which relate the parameters of state such as the pressure of a system to the density, temperature and composition. Historically the first equation of state which is able to describe the gas phase, the liquid phase, vapour-liquid equilibria and the critical point is the van der Waals equation of state [1]. It has been derived by considering the attraction between molecules and their volume. These two molecular properties are not accounted for in the ideal gas law which is only valid at low density. The resulting equation consists of two additive terms: a repulsion term containing the volume parameter of the molecules, and an attraction term containing the attraction parameter. It has been shown by van Laar [2] and later more detailed and accurate by van Konynenburg and Scott [3,4] that the van der Waals equation of state is able to generate several different main types of binary phase diagrams with many subtypes such as azeotropic phase diagrams. However, although the van der Waals equation of state can be used for qualitative modeling of the phase behaviour of pure fluids and their mixtures, it is not able to give satisfactory quantitative description of fluid phase equilibria. Therefore, empirical modifications of the van der Waals equation of state have been developed. These modified van der Waals equations, of which here the well known Redlich-Kwong [5], Soave [6] and Peng-Robinson [7] equations can be mentioned, are known as cubic equations of state. The modifications usually affect the attraction term while the van der Waals repulsion term remains unchanged.

Empirical modifications of the van der Waals equation improve the quantitative description in the state region in which they were introduced. However, they can also lead to unphysical behaviour outside this region of state. Furthermore, there is not necessarily a direct relation between the parameters of empirical equations of state and the molecular properties of the substances.

In order to address these problems, molecular based equations of state have been developed in recent decades. The background for these equations of state is statistical thermodynamics which gives the relation between the properties of single molecules and the macroscopic properties of an ensemble of molecules. While this approach is formally exact, it cannot be applied rigorously because of its mathematical complexity. For this reason several approximations have to be made in course of the derivation of a molecular based equations of state. A common approximation is, for example, to describe the macroscopic properties based on pair interactions while neglecting three-body potentials. Another common approach is the so-called virial series which is a Taylor expansion in the density. The coefficients of this series are called virial coefficients and represent the n-body interaction [8]. Often they can be calculated numerically only based on two-body potentials within the superposition approximation. Other numerical approaches are the integral equations which give, based on a pair potential, the pair correlation function describing the probability to find one molecule at a certain distance to another molecule [8,9]. This pair correlation function represents the microscopic structure in a fluid and can also be used for calculating macroscopic properties. Furthermore, the molecular perturbation theory is based on the separation of a pair interaction into different additive contributions. One of these contributions is the molecular interaction of a reference system which has to satisfy some requirements. The microscopic and macroscopic properties for such reference system should be know very well. Furthermore, the mathematical model of a reference system should be simple enough for applying it within the perturbation theory. Finally, the pair potential reference system should be as close as possible to the total pair potential. A commonly employed reference system is the hard-sphere fluid which consists of non-penetrating spheres without attraction. A perturbation of this reference system can be attractive or soft repulsive interactions between the molecules [10,11] or dipolar interactions [12]. Often only the second and third terms of the perturbation expansion can be calculated with reasonable effort, which restricts the applicability of such models to small perturbations such as small dipole moments, for example. In some cases extrapolation equations accounting for higher terms have been proposed successfully [12].

A general problem of molecular based equations of state is their mathematical complexity. They are usually non-cubic in the molar volume. This practically means that the numerical solver to calculate the molar volume for given pressure and temperature implemented for cubic equations of state in some

commercial packages, cannot be applied. Furthermore, the molecular equations of state are not optimised with experimental data; they rather describe a model fluid with a model pair interaction. Since a potential model is never identical with the real molecular interactions, there are always differences between the calculations and the experimental data. A general problem of cubic equations of state as well as molecular equations of state is the description of the near critical region. This problem is addressed in detail in another chapter in this book [13] and therefore will not be discussed here.

In technical applications it is sometimes necessary to have very accurate data of working fluids. This is, for example, the case for the calculation of the mass of liquefied gas going through a pipeline for given temperature, pressure and volume flow rate. Such modeling is required for the calculation of the cost of a gas. For these cases neither the cubic equations of state nor the molecular based equations of state give accurate enough values. In recent decades so called reference equations of state have been developed which are able to describe the properties of some technically important fluids very accurately by using a large number of adjustable parameters. The number of parameters can vary from 40 to 60 depending on the desired accuracy of the generated data [14,15]. The equations are empirically optimized and no relation to molecular properties is claimed. The extension of these equations into meta-stable regions or to mixtures, however, is difficult because of the numerous terms and parameters, which are not related to physical properties.

Considering the above mentioned advantages and shortcomings of the different approaches for the development of equations of state it becomes obvious that there is no unique way which can be applied to several different problems. A promising way to obtain an optimised equation of state is to combine the advantages while avoiding the shortcomings. This requires the combination of the molecular and the empirical approaches, for example, by designing an empirical function taking into account the physical constraints such as the limiting behaviour of functions or the curvature related to a certain thermodynamic property. Another way is to force the results obtained from a molecular theory into a simplified equation of state structure. There are several different mathematical procedures possible to accomplish this approach. The method to combine molecular based models and a simple mathematical structure we here call mapping approach. In course of this procedure we include the constraints given by the molecular models, thermodynamic properties, and molecular simulation data.

The rest of the chapter is organized as follows: first we report about our investigation of certain important equation of state properties; secondly, we describe the development of simplified molecular equation of state models based on prior investigations including the global phase diagram method; finally, we present investigations of critical phenomena in polymer systems based on a newly developed equations of state.

2. INVESTIGATION OF EQUATION OF STATE PROPERTIES

2.1. The repulsion term

Equations of state are usually build up by additive terms representing different molecular contributions. Cubic equations of state consist of two terms: the repulsion term and the attraction term. Most cubic equations of state are based on the original van der Waals repulsion term while the modifications are accomplished with the attraction term. It is known from experience that the cubic equations of state are not accurate for saturated liquid densities. A simple analysis shows that the reason for this shortcoming is the incorrect high density limit of the van der Waals repulsion term.

$$p_{\mathrm{rep}} = \frac{RT}{V-b} \tag{1}$$

One can rewrite this equation in terms of the compressibility factor:

$$Z_{\mathrm{rep}} = \frac{p_{\mathrm{rep}} V_{\mathrm{m}}}{RT} = \frac{1}{1-4y} \tag{2}$$

Here the packing fraction $y = b/4V_{\mathrm{m}}$ is introduced. The packing fraction is the fraction of space filled with the molecules. For spherical molecules the highest possible packing fraction is about 0.7405 which corresponds to the face centred cubic or the hexagonal close packing. A cubic primitive packing gives a packing fraction of 0.52. Random close packing is at about 0.64 [16]. Taking a look at Eq. (2) one finds that the compressibility factor and also the pressure diverges to infinity at y=0.25. This so called pole packing fraction is the largest possible packing fraction of the van der Waals repulsion term. The value 0.25 is far below the largest values for spherical molecules and also far below the typical packing fractions in liquid phases of around 0.5. This explains why equations including the van der Waals repulsion term are not accurate in the liquid region.

An alternative hard-sphere repulsion term has been proposed by Carnahan and Starling (CS) in 1969 [17] based on the virial equation. The values of the virial coefficients for the hard-sphere fluid have been calculated by Ree and Hoover [18,19]. The CS repulsion term accurately describes the properties of hard sphere molecules including liquid densities. It is the most used reference and repulsion term in molecular based equations of state. Its derivation is based on the virial equation for the compressibility factor:

$$Z = 1 + B_2 y + B_3 y + B_4 y + B_5 y + \ldots \tag{3}$$

Here the B_i are the virial coefficients representing the i-particle interactions. The relation between the virial coefficients and the i-particle interactions have been derived in the framework of statistical mechanics in the 1950s [8] by combining a virial series of the pressure and a virial expansion of the density. For the hard-sphere fluid the virial coefficients have been calculated up to B_4 analytically and the higher virial coefficients up to B_8 have been calculated by means of numerical Monte-Carlo integration [18,19]. With rounded values of these virial coefficients one can obtain a closed form for the series:

$$Z = 1 + 4y + 10y + 18y + 28y + \ldots = 1 + \sum_{i=1}^{\infty} (3i + i^2) y^i = \frac{1 + y + y^2 - y^3}{(1-y)^3} \tag{4}$$

This equation is the Carnahan-Starling equation. The pole packing fraction y=1 of this equation is too high compared to the largest packing fraction of hard spheres. However, in the range up to liquid state and the random close packing the Carnahan-Starling equation is very accurate.

In order to investigate the differences between the van der Waals repulsion and the Carnahan-Starling repulsion one can calculate the virial coefficients given by Eq. (5):

$$Z = \frac{1}{1-4y} = 1 + 4y + 16y^2 + 64y^3 + 256y^4 + \ldots \tag{5}$$

The second virial coefficient of the van der Waals repulsion is correct but all other virial coefficients are significantly overestimated. We have worked out the relation between the virial coefficient and the pole packing fraction recently [20,21,22]. It turns out that the pole packing fraction is related to the limiting slope of the function $\ln(B_i)$ of i for infinite i.

$$\lim_{i \to \infty} \frac{\Delta \ln B_i}{\Delta i} = \ln\left(\frac{1}{y_{\text{pole}}}\right) \tag{6}$$

or

$$\lim_{i \to \infty} \frac{B_i}{B_{i+1}} = y_{\text{pole}} \tag{7}$$

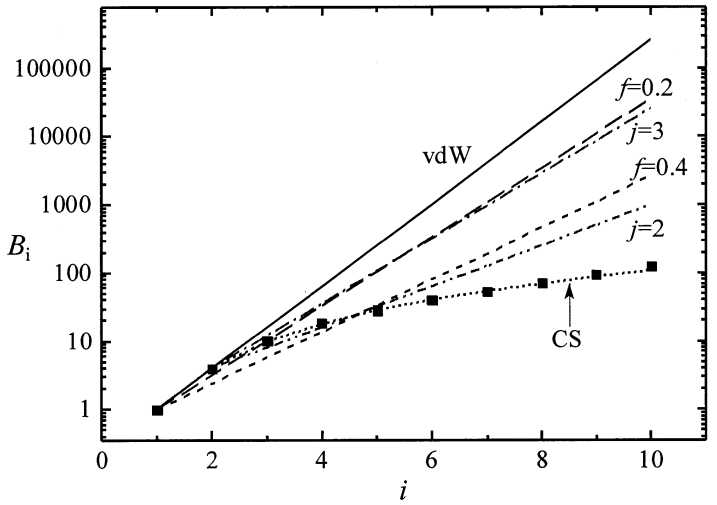

Fig. 1. Logarithm of the virial coefficient B_i as function of its index i. Comparison of the theoretical values with the CS equation, the vdW equation, the coefficients obtained from Eq. (8) for different values of j, and the coefficients obtained from the volume translation approach (Eq. (10)) for different values of the translation parameter f.

Fig. 1 shows the plot of $\log(B_i)$ against i. One can see that the van der Waals repulsion is given by a linear function in this plot. It is a linear extrapolation from the ideal gas limit over the second virial coefficient towards high densities. The mathematically more complicated Carnahan-Starling equation is given as a curved function in Fig. 1 due to the corrections of the virial coefficients at higher densities. The limiting slope is zero which corresponds to a pole packing fraction of unity.

A general approach to derive the equation of state of hard-spheres is based on a detailed analysis of the structure of the virial series resulting in a generic equation for repulsion terms [20,21]. This generic equation reproduces several repulsion terms which are known from the literature and originally have been developed by several different methods.

Knowing the results of this investigation one can systematically improve the repulsion terms. A simple repulsion term such as the van der Waals repulsion (Eq. (2)) gives a linear function in the plot $\log(B_i)$ of i. The slope in this plot is related to the high density limit of the equation according to Eq. (6). One can now derive another simple repulsion term with improved ability to describe the liquid phase by moving the linear function of the van der Waals equation to lower $\log(B_i)$ values, i.e. by decreasing the slope and hence increasing the pole packing fraction. Other equations of state have a different pole packing fraction such as the Scott equation with the value 0.5 [23]. In course of an investigation of the balance between repulsion and attraction terms [24] an empirical interpo-

lation between the van der Waals and the Scott equations has been obtained by introducing a parameter j in the repulsion term:

$$Z_{\text{rep}} = \frac{p_{\text{rep}} V_{\text{m}}}{RT} = \left(\frac{1 + y(4 - j)}{1 - y\, j} \right) \tag{8}$$

This equation can be represented as zeroth order approximation within the generic hard sphere equation mentioned above by relating the parameter j to the pole packing fraction y_∞ by $j = 1/y_\infty$ [21]. The virial coefficients obtained from this equations are also plotted in Fig. 1 for different j values. One can see that decreasing j values move the virial coefficients towards the theoretical values, however, on cost of the accuracy of some intermediate virial coefficients. It also increases the pole packing fraction towards realistic values for liquid phases. This can be easily seen from the decreasing slope in Fig. 1 keeping in mind Eq. (6).

Another approach to improve the liquid density is the volume translation technique [25-28]. The volume translation can be introduced by replacing the volume V_{m} by $V_{\text{m}}+c$ as for example in the van der Waals equation of state:

$$p = \frac{RT}{V_{\text{m}} + c - b} - \frac{a}{(V_{\text{m}} + c)^2} \tag{9}$$

Here we discuss the effect of a temperature-independent volume translation parameter only. While the volume translation affects the repulsion and the attraction terms, we are here interested only in the repulsion term. It can be rearranged by introducing the packing fraction y and a dimensionless volume translation parameter $f = c/b$ [29]. The resulting compressibility factor is then given by:

$$Z = \frac{pV}{RT} = \left(\frac{1}{1 - (4 - 4f)y} \right) \tag{10}$$

The Taylor expansion of this term

$$Z_{\text{rep}} = 1 + \sum_{i=1}^{\infty} B_{i+1,rep}\, y^i \tag{11}$$

gives the expressions of the repulsive virial coefficients:

$$B_{i+1,\mathrm{rep}} = (4-4f)^i \tag{12}$$

The repulsive virial coefficients can again be analysed in a recently proposed way in a $\log(B_{i,\mathrm{rep}}(i))$ diagram [20,21] shown in Fig. 1 as discussed above. This figure shows the virial coefficients of the vdW equation of state with different volume translation parameter up to f=0.4. One can see that all virial coefficients are represented by straight lines with different slopes. The fix point for all lines is the ideal gas limit at i=1. Increasing the volume-translation parameter shifts the virial coefficients towards the theoretical values. The curvature of $\log(B_{i,\mathrm{rep}})$ as function of i, however, cannot be represented by a linear function. The slope of these lines is related to the pole packing fraction y_{pole} given for this type of volume translation by:

$$y_{\mathrm{pole}} = \frac{1}{4-4f} \tag{13}$$

Based on this analysis of the pole one can also show that a temperature-dependent volume-translation parameter can lead to an isotherm crossing at high pressure [28, 30, 31]. Similar crossing has also been found for a temperature-dependent co-volume as obtained from perturbation theory for the soft-sphere fluid. However, this discussion is beyond the scope of this chapter and the reader is referred to the literature for further reading [28].

One can conclude that the accuracy of a repulsion term for describing the hard-sphere reference fluid in general depends on the complexity of its mathematical form. However, there are possibilities to develop an optimized mathematical structure which is simple and reasonably represents the properties of the hard-sphere fluid. Furthermore, it turns out that empirical approaches are not necessarily unphysical. A detailed investigation can exhibit the physical relevance of an empirical approach. It can then be employed for the simplification of the mathematical structure of molecular based equations of state.

2.2. The attraction term.

As mentioned earlier, most changes of empiric cubic equations of state deal with the attraction term. A generalized Peng-Robinson-attraction term consists of a temperature dependent function and a function depending on the molar volume. It can be written in the following way [32]:

$$p_{\mathrm{att}} = -\frac{a(T)}{(V_{\mathrm{m}}+mb)(V_{\mathrm{m}}+kb)} \tag{14}$$

First, we here focus on the molar volume dependence of the attraction term. With certain values of the parameters m and k one can recover known attraction terms. For example, for k=0 and m=0 one obtains the van der Waals attraction term, for k=1 and m=0 the Redlich-Kwong term and for $k = 1-\sqrt{2}$ and $m = 1+\sqrt{2}$ one obtains the Peng-Robinson term. With the generalized term given by Eq. (14) one can systematically investigate different attraction terms and develop an improved term. Similar as for the repulsion term a Taylor expansion in the packing fraction is helpful for this analysis:

$$Z_{\text{att}} = -\frac{4a}{RTb}\frac{y}{(1+4my)(1+4kb)} = -\frac{4a}{RTb}\sum_{i=2}^{\infty}(-4)^{i-2}\left(\frac{m^{i-1}-k^{i-1}}{m-k}\right)y^{i-1} \qquad (15)$$

Depending on the values of the parameter set (k,m), the attraction term can exhibit negative virial coefficients, as it should be expected from the physical point of view. However, it is also possible that the virial coefficients can have alternating signs as function of their index. An exception is the van der Waals-attraction term, for which the second virial coefficient has a positive value while all higher virial coefficients are zero. One can show that the van der Waals equation is at the boundary $k = -m$ between parameter sets (k,m) which generate attractive virial coefficients with alternating signs and parameter sets which generate negative values for all attractive virial coefficients [32]. Empirical cubic equations of state such as the Redlich-Kwong or the Peng-Robinson equation give attractive virial coefficients with alternating signs. The reason for this unphysical behaviour is that the critical compressibility factor calculated with cubic equations of state can only be lowered towards the experimental values below $Z_c = 0.3$ if the attractive virial coefficients have alternating signs [32].

In Fig. 2 the general attraction term combined with the van der Waals repulsion term is analysed in a plot of the parameter sets (k,m). At the dashed curves in this diagram the critical compressibility factor Z_c is a constant value given in the boxes at the curves. One can see that these iso-Z_c contour curves have low values of Z_c on the right hand side of the boundary line $k = -m$, i.e. for attractive virial coefficients with alternating signs. One can furthermore see that the Redlich-Kwong and the Peng-Robinson equations are located in this region as well as parameter sets for many real substances represented by the dark shaded area.

The discussion of the density dependence of the attraction term up to here is based on a general attraction term related empirical extensions of the van der Waals attraction. So far not much is said about a density dependence which can

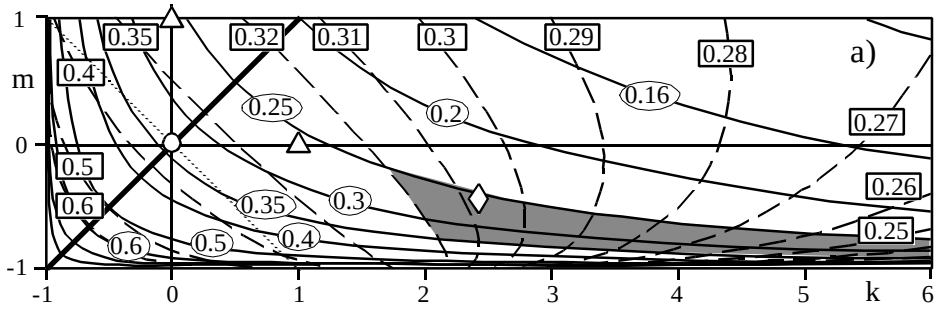

Fig. 2. Curves with constant critical compressibility factor (dashed curves, numbers in boxes) in a section of the (k,m) plane. These curves are calculated with Eq. (14) and Eq. (2). In addition, curves for a constant values of close-packing density divided by the critical density are shown (solid curves, numbers in ovals). This ratio characterises the ability of an equation of state to describe the saturated liquid densities. The dark shaded region represents sets of parameters which are usually obtained from experimental data. (○) Van der Waals equation; (Δ) Redlich-Kwong equation; (◊) Peng-Robinson equation. The dotted line is the boundary at $k=-m$.

be derived from theoretical considerations. This can, for example, be obtained from molecular thermodynamics. There are several different attraction terms developed in recent years based on thermodynamic perturbation theory such as the SAFT-VR attraction term [33]. It consists of two contributions which have been derived by perturbation theory. Using a recently developed method we have shown that it is possible to map the resulting rather complicated SAFT-VR attraction term by a generalized Peng-Robinson attraction [34]:

$$Z_{\text{att}} = -\left(\frac{4a}{bRT}\right)\left(q\frac{4y^2}{b} + \frac{14/3\ y}{(1+4my)(1+4ky)}\right) \tag{16}$$

For SAFT-VR one obtains two solutions for the parameter sets (q,m,k) having the values (6.89977, 0.405274, -0.162346) or (8.55684, 0.371495, -0.0397963). These parameter sets ensure a monotonically decreasing attraction term for increasing density as is should be and which is not the case for some perturbation approaches.

The empirical models have been optimised by comparison to experimental data. For example, the $1/\sqrt{T}$ function of the Redlich-Kwong attraction term is the result of the observation that the correlation of the attraction term to experimental systems gives an averaged temperature dependence of $T^{-0.48}$ which was then rounded to $T^{-0.5}$. Later by Soave [6] this temperature dependence has been further developed. The result for the attraction parameter a is a quadratic

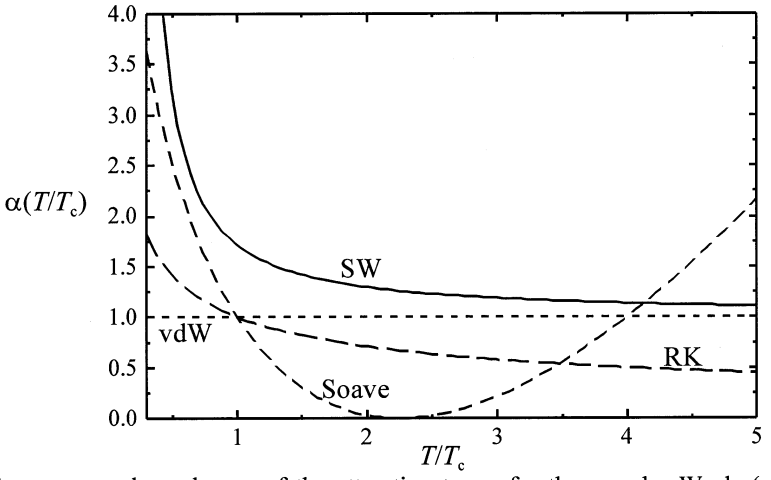

Fig. 3. Temperature dependences of the attraction terms for the van der Waals (vdW), the Redlich-Kwong (RK), the Soave and the theoretically based dependence for the square well fluid (SW).

function in $\sqrt{T}$ with a new parameter $k(\omega)$ which has been related to the acentric factor ω proposed by Pitzer within the extended corresponding states principle [35].

$$\alpha(T) = \left(1 + k(\omega)\left(1 - \sqrt{T_r}\right)\right)^2 \tag{17}$$

Fig. 3 shows the temperature dependence of the van der Waals, the Redlich-Kwong, and the Soave equations of state. In addition a temperature dependence of the square well potential is plotted in this diagram. The Redlich-Kwong temperature dependence and that of the square-well potential behave similarly. A difference is the high temperature limit which is zero for the Redlich-Kwong function while the square-well function converges to the vdW limit. The Soave temperature dependence has a minimum above the critical temperature and hence beyond that minimum they increase with temperature. This is not consistent with molecular theory, however, in several cases which only consider the phase equilibria below this minimum no unphysical behaviour can be expected. On the other hand, extrapolating the region of interest for supercritical fluid processes one should be aware of artificial behaviour [24,36].

As is has been shown not only empirical approaches can lead to artificial behaviour. Similar to a temperature dependent volume translation [31], a temperature dependent co-volume can lead to a crossing of the isotherms [28,30,31]. The temperature dependence of the co-volume can be derived, for example, from the Barker-Henderson perturbation theory [10]. The Barker-Henderson

theory yields a model for soft-sphere repulsion based on a hard-sphere reference system. In general, perturbation theories work well for small perturbations, for example, at low densities. However, at high densities, at which the repulsion becomes dominant, such theories can fail. This is a similar failure as for a temperature dependent co-volume for the SAFT-VR attraction term at high densities as discussed above.

One can conclude that empiric as well as molecular-based equations of state have advantages as well as shortcomings. Both approaches can lead to artificial behaviour under certain conditions. For empiric equations this can appear if it used outside the range of state in which they have been correlated. In case of molecular models, one always has to keep in mind the approximations made in course of their development. These approximations can lead to limited range of applicability. The mathematical complexity of molecular based equations can furthermore lead to artificial behaviour. In the next section we describe a new approach for the development of equations of state in which we combine advantages of both methods for developing equations of state.

3. DEVELOPMENT OF NEW SIMPLIFIED EQUATIONS OF STATE

In course of the investigation of different equations of state with respect to their advantages and shortcomings, it turns out that empirical and theoretical approaches have several features in common. It is our aim to work out these features since they are of special interest for the development of equations of state. Within our approach we choose a simple appropriate mathematical structure for the equation of state onto which we map the molecular models.

This mapping approach can be accomplished mathematically in different ways. One possibility is to relate the virial coefficients of the simple frame equation to the virial coefficients of a molecular based equation of state. This method works rigorously for simple models describing non-spherical shapes [37] but also for anisotropic attractive forces such as dipolar interactions [34, 38].

As a simple example we here introduce the mapping approach in terms of the virial expansion which we have accomplished in a series of papers on different molecular properties [20, 37, 39]. As a molecular based reference equation we employ the Carnahan-Starling (CS) equation for the hard-sphere fluid [17]. The virial expansion is given by Eq. (4). As simplified equation for mapping of the CS equation we employ our BQ75 term [20-22, 37].

$$Z = \frac{pV_m}{RT} = \left(\frac{3 + Ay + By^2}{(1-y)(3-4y)} \right) \tag{18}$$

From the virial series of the BQ75 equation

$$Z = 1 + B_2 y + B_3 y^2 + \cdots = 1 + \frac{A+7}{3} y + \frac{3B + 7A + 37}{9} y^2 + \cdots \tag{19}$$

one can obtain the values of A and B by comparing the virial coefficients to the hard-sphere values B_2=4, B_3=10:

$$A = 5 \qquad B = 6 \tag{20}$$

Similarly we obtained for the regular TPT1 approach the following values for the coefficients A and B as function of the chain length parameter m [39].

$$A = 5 + \frac{9}{2}(m-1) \tag{21}$$

$$B = 6 + \frac{45}{4}(m-1) \tag{22}$$

One can easily recognize that these coefficients consist of the constant contribution of the hard-sphere term and a contribution of the chain term which vanishes for m=1. In order to include the flexibility of the chain molecule we have in addition introduced the Prigogine c-factor in the repulsive residual term [40]:

$$Z = 1 + cm\left(\frac{2y(6+y)}{(1-y)(3-4y)}\right) + (m-1)\left(\frac{37y^2 - 30y}{4(1-y)(3-4y)}\right) \tag{23}$$

As a result for an equation of state for chain molecules of certain flexibility within the TPT1 approach we obtain the following expressions for A and B [40]:

$$A = \frac{2 - 30m + 48cm}{4} \tag{24}$$

$$B = \frac{-21 + 37m + 8cm}{4} \tag{25}$$

The complete equation of state developed in this way consists of the combined repulsion and chain term and the van der Waals attraction term modified for chain molecules. This attraction term has been chosen because of its mathematical simplicity and because it is able to capture the main features of the real dispersive attraction.

$$p = \frac{RT}{V_m}\left(\frac{3 + Ay + By^2}{(1-y)(3-4y)}\right) - \frac{16a_{seg}}{b^2}y^2 \tag{26}$$

Here a_{seg} is the van der Waals attraction parameter for one segment and y the packing fraction including the chain length parameter $y = mb/4V_m$.

In order to investigate the phase behaviour of chain molecules and their mixtures systematically, the dependence of the equation of state parameters is required. There are different ways of fitting the dependence of the parameters m and cm on the number of molecular repeating units n, which is the number of the carbon atoms in case of the n-alkanes. For practical reasons, the parameters a and b have been calculated for m=1 and c=1 for methane in this model. Then the dependence of the parameters on the number of molecular repeating units n is correlated with the model chain length parameter m and the entropic factor cm.

$$m = 1 + 0.3770(n-1) + 0.2660\frac{n-1}{n} \tag{27}$$

$$cm = 1 + 0.3426(n-1) - 0.4212\frac{n-1}{n} \tag{28}$$

One can expect different dependencies of the parameters $m(n)$ and $cm(n)$ on the number of real segments n for different chain flexibility. In a simple approach one can use the n-alkane series as reference series and account for different flexibility by a factor of c such as:

$$c = c_{n-alkanes} \cdot c_i \tag{29}$$

Since our investigations presented here are of qualitative or semi-quantitative nature we have set c_i =1 for all calculations.

4. APPLICATIONS OF THE EQUATION OF STATE MODEL FOR THE INVESTIGATION OF CRITICAL PHENOMENA

Based on the above developed simplified equation of state we have investigated several critical phenomena in binary mixtures of low molecular weight substances, oligomer and polymer solutions and polymer blends. The equation of state used here is simple enough to perform an analysis of critical behaviour in complex systems; on the other hand the equation is based on a molecular model which makes it possible to discuss phase phenomena in terms of molecular in-

teractions. Besides the calculation of the binary phase diagrams we employ the method of global phase diagram for a general understanding of the relation between molecular properties and phase behaviour in supercritical systems.

4.1. Co- and Anti-solvent effects in polymer solutions

There are few investigations of anti-solvent effects based on correlations of experimental data for specific experimental systems [41,42,43]. We here follow the topological change of the phase diagrams which is a less quantitative but more general approach to investigate such effects. In specific we are interested in the relation between the molecular properties of a certain additive for a desired effect on the phase behaviour in supercritical solutions. Once this relation is established one has the possibility for an appropriate choice of an additive. The calculations are based on a quasi-binary approximation and neglect polydispersity in order to reduce the number of parameters.

The effect of an additive on the solubility of a substance in a supercritical solvent can be twofold, it can increase the solubility (co-solvent) or can decrease the solubility (anti-solvent). An application for an anti-solvent effect in supercritical fluid processes is discussed in another chapter in this book [44]. The overall effect of an additive can be represented in a pressure-temperature projection of the phase diagram. Although the mole fraction is not shown in such diagrams they give sufficient information concerning the discussion of the solubility. While an additive can affect the phase behaviour quantitatively by a shift of the characteristic curves in a p,T diagram, it can also change the phase behaviour qualitatively.

There are several topologically different phase diagram types which are usually classified by six main types according to the nomenclature by van Konynenburg and Scott [3, 4] who found the first five of these types (Fig. 4) in calculations with the van der Waals equation of state. Also an alternative, more systematic nomenclature has been proposed [45]. In the context of this work, only four binary phase diagram types are of interest which are the types III, III_m, IV, and V.

For mixtures of low molecular weight substances the vapour pressure curve of the less volatile substance is usually chemically stable above its critical temperature. In this case the phase diagram is complete. Low volatile organic substances including polymers often degenerate before reaching the critical temperature. In such cases the critical point of the less volatile compound does not exist and the phase diagram is incomplete. With increasing chain length of the less volatile compound the solubility decreases continuously. In Fig. 5 this effect is shown for calculations with Eq. (26). One can see that while the

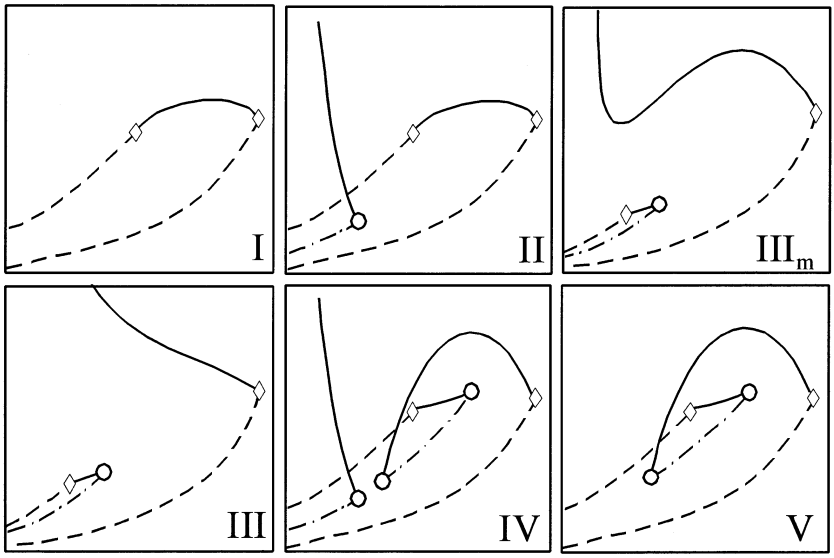

Fig. 4. Phase diagram types of interest in the context of this work. (III, III$_m$, IV, V). Dashed curves: vapour pressure curves of the pure substances; solid curves: binary critical curves; dot-dashed curves: three-phase curves; (◊): critical points of pure substances; (○) critical end points.

solubility over a wide temperature and pressure range decreases the phase diagram undergoes different topological changes from type I for a monomer/solvent system towards type III for a *n*-mer/solvent system. For further investigations of the solvent effects we have employed the 1000-mer/solvent system with the same co-volume for the chain segments and the solvent molecules. Once the co-volumes and the chain length are fixed there are three variable parameters left in the model. These are the van der Waals attraction parameters of the solvent molecules a_{11}, of the segments of the chain molecules a_{22} and the cross attraction parameter a_{12} for the interaction of the solvent molecules and the chain segments. Since we here are interested in a qualitative investigation and not a quantitative correlation of experimental data we can reduce the number of variable parameters from three to two by using dimensionless differences of the three van der Waals attraction parameters. Such dimensionless attraction parameters have been introduced by van Konynenburg and Scott [3,4]:

$$\varsigma = \frac{d_{22} - d_{11}}{d_{22} + d_{11}} \tag{30}$$

$$\lambda = \frac{d_{22} - d_{12} + d_{11}}{d_{22} + d_{11}} \tag{31}$$

with

$$d_{ij} = \frac{a_{ij} b_{ij}}{b_{ii} b_{jj}} \tag{32}$$

Since here the co-volumes are all the same $b_{11}=b_{22}=b_{12}$, one can replace the d_{ij} by a_{ij} in Eq (30) and (31). The two dimensionless attraction parameters λ and ζ are the axis of a so-called global phase diagram. Each binary system is represented by one point in the global phase diagram. Depending on the values of the global attraction parameters the phase diagram type can be different. In the global phase diagram one can locate regions in which a certain phase diagram type is present. These regions are separated by boundary curves. A direct way to locate these regions is to calculate these boundary curves between these regions. In the context of this work, three boundary curves are of interest. These are the double critical end point (DCEP), the critical pressure step point (CPSP) and the zero-Kelvin boundary (ZKP). At the ZKP a liquid-liquid critical curve vanishes at zero Kelvin which is a boundary between type II and type I phase behaviour. Some of the important boundary states are sketched in Fig. 6 as *p,T* diagrams.

The thermodynamic conditions of these boundary states are well known [3, 4, 46-50] and can be calculated with an equation of state model. The basis function is the Helmholtz energy which can be calculated by an integration of equation of state (Eq. (26)) over the volume.

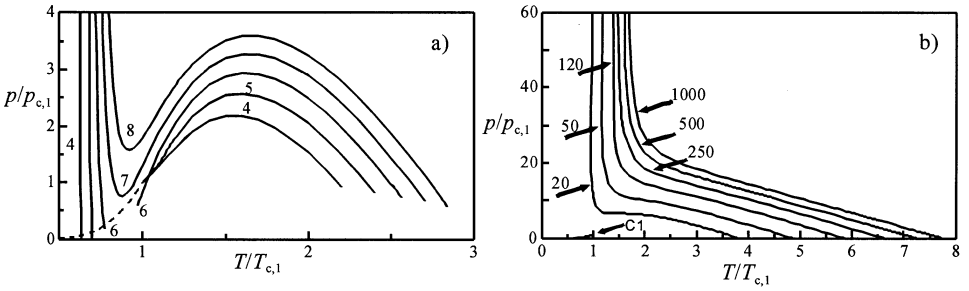

Fig. 5. Development of the critical curve as function of the chain length (numbers at curves). a) Topological transitions for short chain length molecules. b) Decreasing miscibility over a wide range of pressure and temperature with increasing chain length.

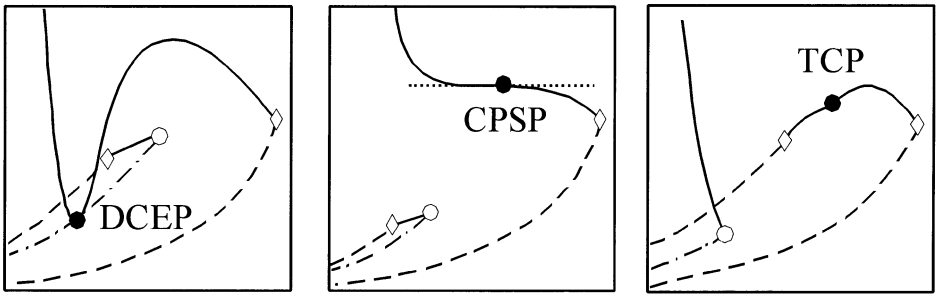

Fig. 6. Boundary states of interest in the context of this work: the double critical end point (DCEP) is a boundary between types III and IV; the critical pressure step point (CPSP) is a boundary between types III and III_m; the tricritical point (TCP) is a boundary, for example, between type II and IV.

$$A = -\int p(V,T,x)\ dV \tag{33}$$

The derivatives of the Gibbs energy, which are necessary for the evaluation of the thermodynamic conditions for the boundary states, can be obtained by regular Jacobi transformation from the derivatives of the Helmholtz energy. Below the Jacobi transformations for the second and third derivative of the Gibbs energy with respect to the mole fraction, being zero for a binary critical state, are given.

$$G_{2x} = A_{2x}^2 - \frac{A_{Vx}^2}{A_{2V}} \tag{34}$$

$$G_{3x} = A_{3x}^2 - 3A_{2xV}\left(\frac{A_{Vx}}{A_{2V}}\right) + 3A_{x2V}\left(\frac{A_{Vx}}{A_{2V}}\right)^2 - A_{3V}\left(\frac{A_{Vx}}{A_{2V}}\right)^3 \tag{35}$$

with

$$A_{ixjV} = \left(\frac{\partial^{i+j} A(V,T,x)}{\partial x^i \partial V^j}\right)_T \tag{36}$$

The abbreviations of the Gibbs energy derivatives are defined accordingly. The higher derivatives can be obtained similarly by Jacobi transformation. They can be used to calculate boundary states, for example, the tri-critical point with the conditions:

$$G_{2x} = G_{3x} = G_{4x} = G_{5x} = 0 \tag{37}$$

At a double critical endpoint a critical phase (Eq. (38)) is in equilibrium with a non-critical phase (Eq. (39)). At this point in addition the slope of the critical curve (left side of Eq. (40)) and the slope of the three-phase curve (right side of Eq. (40)) are identical. The thermodynamic conditions for the double critical end point are hence given by the following set of equations:

$$G_{2x} = G_{3x} = 0 \tag{38}$$

$$\mu_i^c = \mu_i^n \tag{39}$$

$$\frac{S_{2x}^c}{V_{2x}^c} = \frac{S_m^c - S_m^n - (x_1^c - x_1^n)S_x^c}{V_m^c - V_m^n - (x_1^c - x_1^n)V_x^c} \tag{40}$$

The critical pressure step point is a binary critical state at which the slope and the curvature of the binary critical curve are zero in the pT diagram. The corresponding conditions are [47]:

$$G_{2x} = G_{3x} = 0 \tag{41}$$

$$G_{2xT} = 0 \tag{42}$$

$$G_{4x}G_{2x2T} - G_{3xT}^2 = 0 \tag{43}$$

The boundary states can be calculated by solving the thermodynamic conditions numerically. As a result one obtains the critical properties and one global coordinate, e.g. λ for a given other global parameter, e.g. ζ. The resulting boundary curves are shown in Fig. 7 for the 1000-mer/solvent system investigated here. The regions of the different phase diagram types are labelled in the figure. Based on the global phase diagram of the 1000-mer/solvent system one can rather easily analyse the co- and anti-solvent effects. This can be accomplished by relating the effect of an additive to a path in the global phase diagram. It is, for example, known that the addition of carbon dioxide to polysterene/cyclohexane solution [41,43] decreases the solubility. It is discussed that the reason for the anti-solvent effect is that the CO_2 molecules screen the attraction between the solvent and the solute. In terms of the global parameters this corresponds to an increasing λ-value (decreasing a_{12}). This path is shown in Fig. 7 by an arrow marked with an "A" for anti-solvent. The corresponding pT diagrams along this path are shown in Fig. 8a.

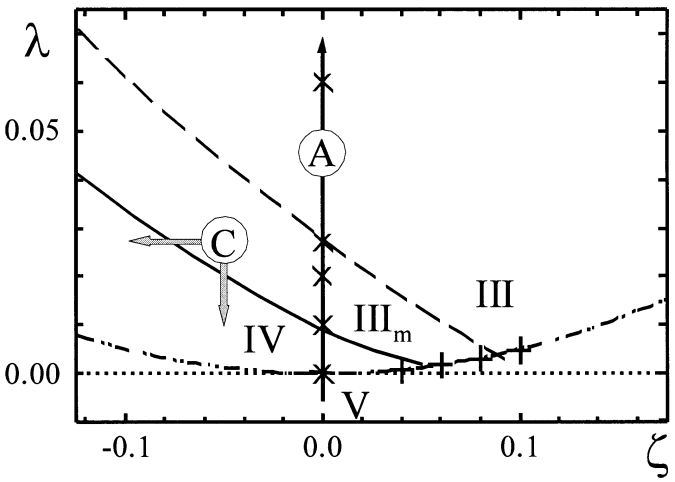

Fig. 7. Global Phase diagram for a 1000-mer/solvent system. The solvent has the same co-volume as a chain segment (b_{11}=b_{22}). Dashed curve: critical pressure step point boundary; solid curve: double critical end point boundary; dotted curve: zero Kelvin boundary; dot-dashed curve: geometric mean curve ($a_{12} = \sqrt{a_{11}a_{22}}$). The crosses and pluses mark the anti-solvent paths (A). The cosolvent paths (C) are marked by grey arrows.

Another possibility is to decrease a_{12} while keeping the geometric mean $a_{12} = \sqrt{a_{11}a_{22}}$. This is possible by choosing an anti-solvent path along the geometric mean curve which is also plotted in Fig. 7. The corresponding p,T diagrams along the geometric mean curve are also shown in Fig. 8b. One can recognize significant differences in the change of the phase behaviour for the two different paths. While the direct anti-solvent path (Fig. 8a) leads to simultaneous

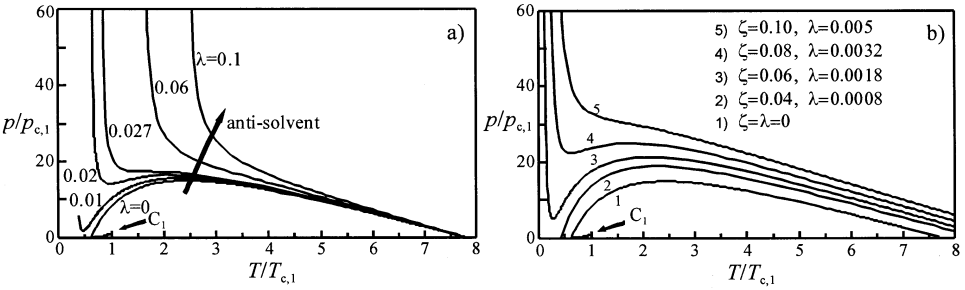

Fig. 8. Binary systems corresponding to the antisolvent paths shown in Fig. 7: a) Antisolvent paths at constant ζ value (only the cross attraction is decreased, (x) in Fig. 7). b) Antisolvent paths along the geometric mean curve (the ratio between the pure attraction parameters is varied, (+) in Fig. 7).

decrease of the solubility in temperature and pressure directions, the anti-solvent path along the geometric mean (Fig. 8b) mostly affects the solubility in the pressure direction.

Similarly we have investigated the effect of different types of a co-solvents on the binary phase behaviour. We have chosen two different paths, one affecting a_{12} or λ only, the other one affecting ζ only and λ not at all. Both paths are marked by "C" in Fig. 7. In Fig. 9 the p,T diagrams corresponding to these paths are shown. Here one can again find differences in the different ways the attraction of solvent and polymer is affected by the co-solvent. A co-solvent which mainly affects the self-attraction of the compounds has strong effect on both the temperature and the pressure-shift of the immiscibility curves. If a co-solvent mainly affects the cross attraction, the temperature shift of the critical curve is weak.

We can conclude that the effect of an additive on the phase behaviour of a binary mixtures, such as a monodispers polymer solution, strongly depends on the way the additive molecules affect the interactions of the components of the mixture. We have shown how a systematic investigation by the method of global phase diagrams can be employed for the relation of the molecular properties of the substances and the phase behaviour. The different effects of the additives can be characterized by paths in the global phase diagram. We here have investigated idealised additive paths. A more quantitative representation of additive effects by a path in the global phase diagram requires the correlation of experimental data of polymer solutions with different additives followed by the representation in a global phase diagram.

4.2. Miscibility windows in two polydispers blends.

In a recent paper is it reported about miscibility windows in polymer blends [51]. Miscibility windows are not new phenomena. They have for example been found in ternary systems related to supercritical fluid extraction [52-54]. Such

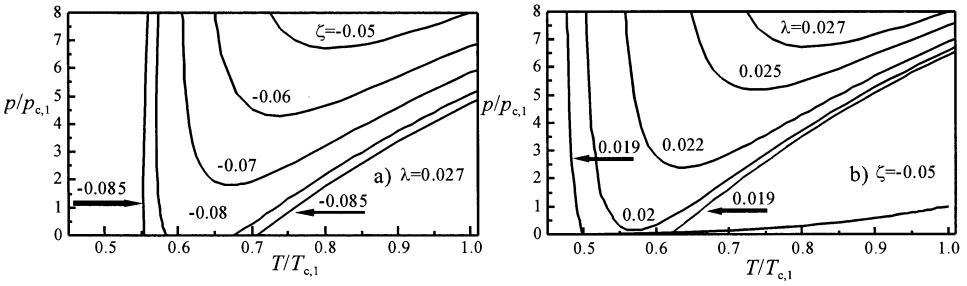

Fig. 9. Binary systems corresponding to the cosolvent paths shown in Fig. 7. a) Cosolvent path at constant λ value. Along this path only the cross attraction is increased. b) Cosolvent path at constant ζ value. Along this path the ratio between the pure attraction parameters is changed.

miscibility windows are of interest since they are small regions of miscibility in systems which are usually immiscible. For processing of polymer blends one has to find a miscible region which is often at very high pressure for polymer blends. A possibility to decrease the processing pressure can be important for the realisation of a process. In addition, such special phase phenomenon are of interest for a fundamental investigation of molecular interactions and phase phenomena. For choosing polymer systems which exhibit such miscibility windows one has to know the corresponding molecular parameters. The method of global phase diagram is the method of choice here since it relates molecular interaction parameters to phase behaviour.

For the investigation we employ the same equation of state (Eq. 26-28) as in section 4.1 for the investigation of the co- and antisolvent paths. However, since here both substances are oligomers or polymers, the mixing rules have to be used in a general form with chain length parameters m_i for both substances:

$$m = x_1 m_1 + x_2 m_2 \tag{44}$$

$$b = \frac{x_1 m_1 b_1 + x_2 m_2 b_2}{x_1 m_1 + x_2 m_2} \tag{45}$$

$$c = \frac{x_1 m_1 c_1 + x_2 m_2 c_2}{x_1 m_1 + x_2 m_2} \tag{46}$$

$$a_{\text{seg}} = \frac{x_1^2 m_1^2 a_{11} + 2 x_1 m_1 x_2 m_2 a_{12} + x_2^2 m_2^2 a_{22}}{\left(x_1 m_1 + x_2 m_2\right)^2} \tag{47}$$

There are two requirements for obtaining a miscibility window in polymer blends: first, the cloud point curve of the blend must be bimodal (Fig. 10b), and secondly, the UCST curve has to exhibit a temperature minimum (Fig. 10a) [55]. In Fig. 10 the appearance of such miscibility windows is sketched. With decreasing temperature from T_1 to T_2 the extremes of the bimodal cloud point curve merge. As a results the homogeneous region between the extremes form a miscibility window at T_2 (Fig. 10c). In this work we focus on the investigation of the appearance of a critical temperature minimum (CTM). In order to locate the parameter sets which generate a critical temperature minimum we have calculated curves at which a CTM exists at a certain given pressure in the global phase diagram.

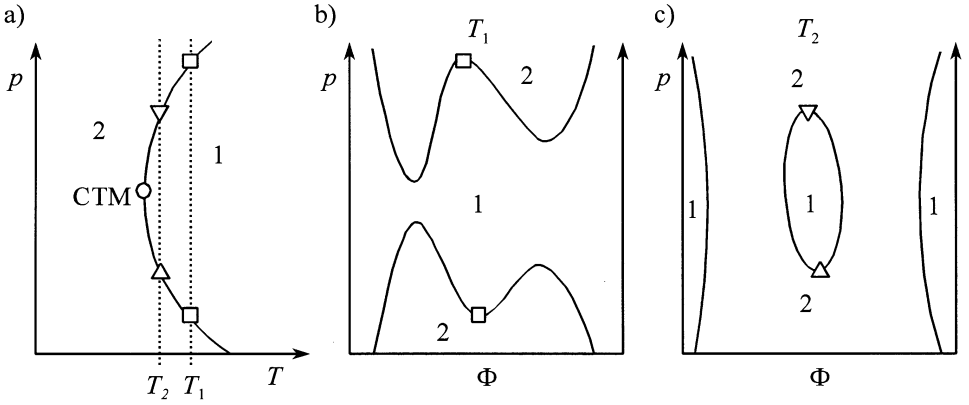

Fig. 10. Sketch of the appearance of a miscibility window in polymer blends. The symbols are critical points. Here Φ is the volume fraction of one of the polymers. a) The UCST curve has a critical temperature minimum (CTM). b) Intersection in diagram 10a at T_1: The cloud point curve has to be bimodal with two precipitation thresholds (extremes) which can be caused by the polydispersity of both polymers. c) Intersection in diagram 10a at T_2: Close to the CTM the precipitation thresholds at high and low pressure can join and form a miscibility window.

For the direct calculation of such curves the thermodynamic conditions of the CTM have to be known. The thermodynamic conditions of extremes in binary critical curves can be found in the literature [47,56]. The slope of the binary critical curve in the pressure-temperature diagram is related to the second derivatives of the volume and the entropy with respect to the mole fraction.

$$\left(\frac{\partial p}{\partial T}\right)_c = \frac{S_{2x}}{V_{2x}} \tag{48}$$

A critical temperature extreme ($dp/dT = \pm\infty$) exists for V_{2x}=0. With $V = (\partial G/\partial p)_T$ the resulting conditions for critical temperature minimum are

$$G_{2x} = G_{3x} = G_{2xp} = 0 \tag{49}$$

with the following abbreviation for the derivatives:

$$G_{nxkp} = \left(\frac{\partial G^{n+k}}{\partial x^n \partial p^k}\right)_T \tag{50}$$

In a recent paper we have discussed the semi-quantitative appearance of a miscibility window in the system polydimethylsiloxane/polyhexylmethyl-

siloxane (PDMS/PHMS) [55]. It is the objective to find interaction parameter sets which generate a critical temperature minimum for given chain length of the two oligomers or polymers. Therefore, we have calculated CTM curves in a global phase diagram for different systems, represented by the number of segments, at different constant pressure. At the crossing of such isobaric CTM curves one obtains attraction parameter sets for systems with a CTM which varies with pressure depending on the chain length of one component.

The results of this investigation show that it is possible to obtain a critical temperature minimum (CTM) in the critical curve of polymer blends [55]. With the global phase diagram method one can locate the interaction parameters which generates such behaviour. Since the interaction parameters represent specific substances, one can locate possible blend systems which exhibit a miscibility window. This investigation also shows that a CTM can shift below zero pressure. It follows that there are possibly blends which have a CTM at negative pressure which is likely to be overseen in typical experiments at positive pressure.

4.3. Chain length dependence of the critical volume fraction

It has been shown in the previous sections that the knowledge of the chain length dependence of the critical properties is crucial for locating specific phase phenomena such as miscibility windows. Especially the chain length dependence of the critical polymer concentration has been subject of controversial discussion in recent years. A very common approach to describe the chain length dependence of the critical volume fraction is a power law:

$$\phi_c = AN^r \tag{51}$$

Here A is a substance-dependent parameter and r is an exponent which is believed to have an universal value. From Flory-Huggins theory one can calculate the value of this exponent in the infinite chain length limit $r = -0.5$. The same value has been obtained by de Gennes based on a renormalisation group analysis [57] and also by Duplantier [58]. In another approach which includes three-body interactions, Muthamkar [59] has obtained the value $r = -1/3$. In several molecular simulation studies a variety of values in the range from 0.36 to 0.38 have been reported [60-63]. Yan and de Pablo [64] have extrapolated their simulation data with a generalized Flory expression and obtained a value close to –0.5. From experimental investigations, values ranging from –0.16 to –0.4 for oligomer and polymer solutions have been estimated.

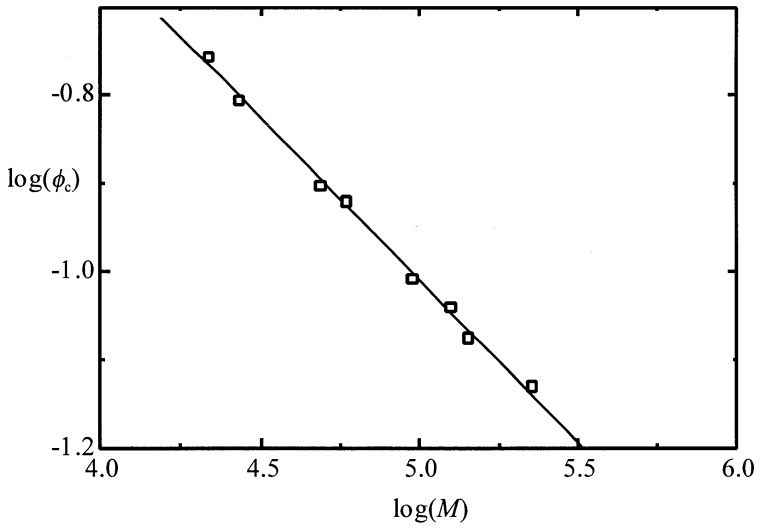

Fig. 11. Double logarithmic plot of the critical volume fraction against the molar mass of the systems PMMA in 3-octanone. The experimental data are taken from reference [65]. The exponent r of Eq. (51) is the slope in this plot. The resulting value here is $r = -0.367$.

For the analysis of experimental data the measured volume fractions ϕ_c are plotted in a $\log(\phi_c)$-$\log(N)$ diagram. In such diagram the data can often be regressed by a linear function. The slope of this function is the exponent r. This procedure is shown in Fig. 11 for the system PMMA in 3-octanone with data taken from the literature [65]. One can see that although there is some scattering, the data seem to be represented by a linear function fairly well. In order to investigate the chain length dependence of the critical volume fraction systematically and to understand the values of the exponent r we employ our equation of state model presented in section 3. With this equation we calculate critical points at a given constant pressure for chain molecules dissolved in a solvent with the same co-volume as the segments of the chains. From the investigation in section 4.1 we know that with increasing chain length the oligomer or polymer solutions can pass through different phase diagram types. These transitions can affect the values of the exponent r. Therefore, we have to locate certain sets of attraction parameters which are free of such transitions while varying the chain length. Here the global phase diagram can be a useful tool. As mentioned earlier the boundaries in the global phase diagram move with increasing chain length. This movement becomes slower with increasing chain length and the diagram of the 1000-mer/solvent system shown in Fig. 7 can be regarded as good approximation for the long chain length limit.

Being on the left side of the boundary curve means that the phase diagram type does not change with increasing chain length and possible artefacts due to a

topological change can be excluded. Hence, we have chosen three sets of attraction parameters (C1: ζ=0.0, λ=0.0; C2: ζ=-0.1, λ=0.03; C3: ζ=-0.2, λ=0.03). Two of these systems C2 and C3 are type IV with an UCST and a LCST while the third C1 is type V without UCST curve. For these three systems we have calculated the critical points at constant pressure and increasing N. As value for the pressure we chose somewhat arbitrary the critical pressure of the solvent (p_r=1). In experimental investigations usually atmospheric pressure is employed. In Fig. 12 the results of the calculations are shown for all three systems. One can see that the equation of state calculations follow the same trend as the molecular simulation data added in this diagram. The offsets are due to the differences in the models and in the attraction parameters as one can recognize from the differences of the results for the three systems C1, C2 and C3. More interesting is the slope not being constant, which means that the exponent r is also not constant. Fig. 13 shows the exponent r calculated from Fig. 12 as function of log(N). It appears that the value of the exponent decreases with increasing chain length. The limiting value for all data and models shown in this diagram seems to converge to –0.5 which is the Flory value.

As a main conclusion of this investigation which is in detail accomplished in recent papers [66,67] it follows that the power law (Eq. (51)) with a constant exponent is not suitable for analysing experimental data of the critical volume fraction over a wide range of chain length. It can rather be applied locally only, while the Flory value is valid in the infinite chain length limit only. Based on the

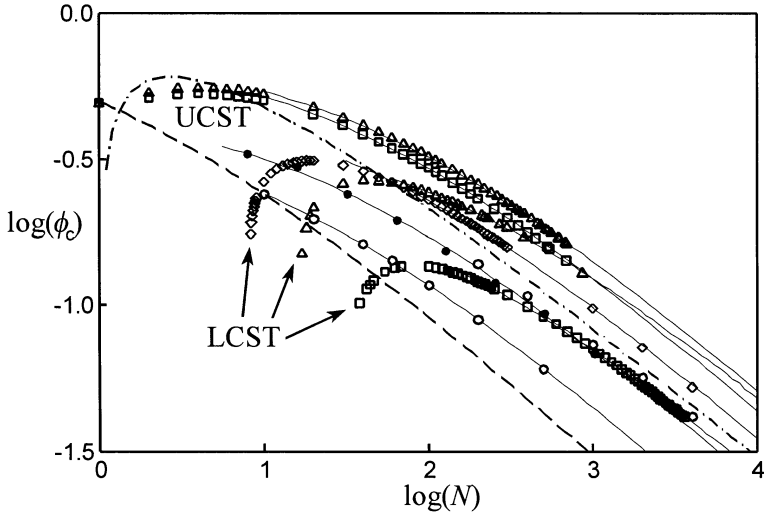

Fig. 12. Double logarithmic plot of the critical volume fraction against the chain length calculated with Eq. (26) (C1 (rhombi), C2 (triangles), C3 (squares)). In addition molecular simulation data [60-64] are added (circles). The Flory theory is plotted as dashed curve, and the renormalization group model is added as dot-dashed curve. All other curves are to guide the eye.

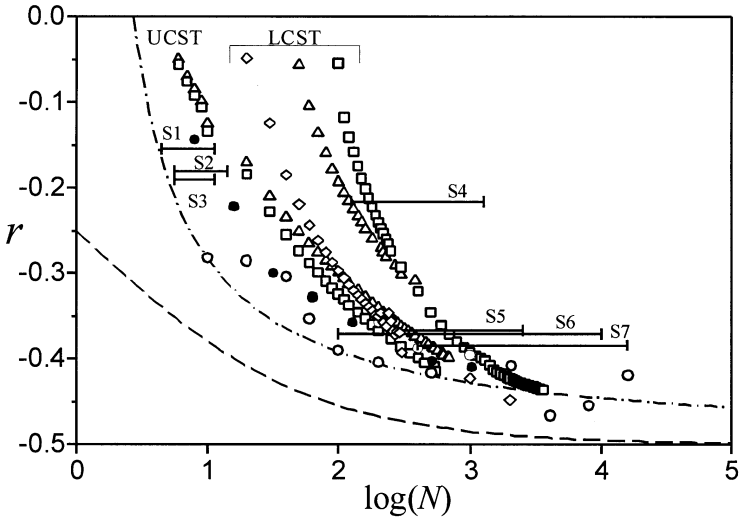

Fig. 13. Plot of the exponent r against the logarithm of the chain length. For legend see Fig. 12. In addition experimental data for the UCST are added. Exponents for experimental systems as calculated in Ref. [55] from data taken from the literature: S1: n-alkanes/N,N-dimethylacetamide; S2: n-alkanes/nitrobenzene S3: n-alkanes/dimethyl maleate; S4: polystyrene/nitroethane; S5: PMMA/3-octanone S6: polystyrene/methylcyclohexan; S7: polystyrene/cyclohexane. C1 (rhombi), C2 (triangles); C3 (squares).

analysis given above we have developed a simple correlation equation which can be used for the correlation of oligomer solution data including the monomer limit and the infinite chain length limit:

$$\phi_c = \frac{\sqrt{P_2 + P_3 \ln(N)}}{P_1 + \sqrt{N}} \tag{52}$$

This equation is also able to represent a maximum of the exponent r in the oligomer range and it can be used for extrapolations of the critical volume fraction to very long chain molecules. In Fig. 14 correlations with Eq. (52) are shown for some systems for which data are available up to chain length of 10^5. One can see that Eq. (52) gives a good correlation and especially that it is more suitable for extrapolation to long chain length than a power law. The parameters of Eq. (52) have no physical meaning, however, since they are related to the topology of the log(ϕ)-log(N) diagram they cannot be varied freely. In case of the UCST, for example, all parameters P_i should be positive.

We can conclude that the extrapolation of the critical volume fraction to long chain polymer solutions can be inaccurate with the usually employed

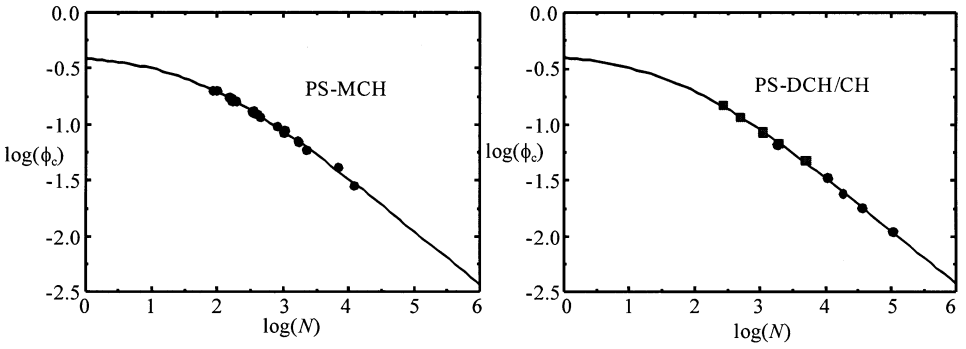

Fig. 14. a) Correlation of experimental data for the systems polystyrene/methylcyclohexane [68-70] with Eq. (52). b) Correlation of experimental data for the systems polystyrene/deuterated cyclohexane (squares) [71] and polystyrene/ cyclohexane (circles) [72] with Eq. (52).

power law. A non-linear function based on the Flory and a renormalisation model such as Eq. (52) can be useful for a more accurate extrapolation.

5. CONCLUSIONS

In course of the investigations summarized here we have treated several phenomena in critical and supercritical solutions. These investigation have been accomplished with a relatively simple equation of state model. This model has been developed based on the TPT1 approach by mapping on a mathematical simplified equation of state. This equation is one result of our investigation of empirical cubic and molecular based equations of state. Simple and molecular based equations are important in order to avoid artificial behaviour which can appear with mathematically complicated equations, especially in the context of complex phase behaviour as investigated here. With this equation we have qualitatively and semi-quantitatively investigated co- and antisolvent effects in supercritical oligomer and polymer solutions. Based on the systematic investigation in a global phase diagram we established different paths which represent different effects of an additive on the phase behaviour. Each of such paths corresponds to different kind of molecular interactions of an additive with the solvent and solute. Such approach can be useful for choosing a specific additive.

Furthermore, we have applied this equation of state to the investigation of miscibility windows in critical polymer blends. With the global phase diagram method, attraction parameter sets have been located which can exhibit such miscibility windows.

Finally, we have investigated the chain length dependence of the critical volume fraction with our equation of state model. As a result we reported that

the usual power law approach has a local character and can hardly be applied for extrapolations over a wide range of chain length in critical polymer solutions. We therefore propose an alternative correlation equation which can be used for extrapolation to very long chain molecules.

6. ACKNOWLEDGEMENT

This work has been supported by the Deutsche Forschungsgemeinschaft (DFG grants KR 1598/3-1/3-2).

REFERENCES

[1] J. D. van der Waals, "On the Continuity of the Gaseous and Liquid States" PhD thesis 1873, in Studies in Statistical Thermodynamics, Vol. XIV, ed. By J. S. Rowlinson, North-Holland, Amsterdam (1988).
[2] J. J. van Laar, Proc. Royal Acad. Amsterdam, Vol. VIII, 646 (1905).
[3] R. L. Scott, P. H. van Konynenburg, Discuss. Faraday Soc. 49 (1970) 87.
[4] P. H. van Konynenburg, R. L. Scott, Philos. Trans. 298A (1980) 495.
[5] O. Redlich, J. N. S. Kwong, Chem. Rev. 44 (1949) 233.
[6] G. Soave, Chem. Eng. Sci., 27 (1972) 1197.
[7] D. Y. Peng, D. B. Robinson, Ind. Eng. Chem. Fundam. 15 (1976) 59.
[8] D. A. McQuarrie, Statistical Mechanics, Harper Collins Publishers, New York (1976).
[9] L. L. Lee, Molecular Thermodynamics of Nonideal Fluids. Butterworth, Boston, (1988).
[10] J. A. Barker, D. Henderson, J. Chem. Phys. 56 (1972) 3013.
[11] J. D. Weeks, D. Chandler, H. C. Anderson, J. Chem. Phys. 54 (1971) 5237.
[12] G. Stell, J. C. Rasaiah, H. Narang, Mol. Phys., 27 (1974) 1393.
[13] T. Kraska, K.O. Leonhard, J. Jurtzik, D. Tuma, G. M. Schneider, this book.
[14] R. Span, W. Wagner, J. Phys. Chem. Ref. Data, 25 (1996) 1509.
[15] R. Span, W. Wagner, J. Phys. Chem. Ref. Data, 27 (1974) 1393.
[16] J. D. Bernal, S. V. King, in Physics of simple liquids, North-Holland Publ. Co., Amsterdam (1968).
[17] N. F. Carnahan, K. E. Starling, J. Chem. Phys. 51 (1969) 635.
[18] F. H. Ree, W. G. Hoover, J. Chem. Phys. 40 (1964) 939.
[19] F. H. Ree, W. G. Hoover, J. Chem. Phys. 46 (1967) 4181.
[20] L. V. Yelash, T. Kraska, Phys. Chem. Chem. Phys., 3 (2001) 3114.
[21] L. V. Yelash, Dissertation, University Cologne, Nov. 2000, VDI-Verlag (2002).
[22] L. V. Yelash, T. Kraska, U. K. Deiters, J. Chem. Phys. 110, (1999) 3079.
[23] R. L. Scott, in Physical Chemistry, An Advanced Treatise, ed. D. Henderson, Academic Press, New York, Vol. 8A, ch. 1, p. 1 (1971).
[24] I. Polishuk, J. Wisniak, H. Segura, T. Kraska, Ind. Chem. Eng. Res. 41 (2002) 4414.
[25] A.Peneloux, E. Rauzy, R. Fréze, Fluid Phase Equilibria 8 (1982) 7.
[26] P. Ungerer, C. Batut , Revue de l'Institut Francais di Pétrol 52 (1997) 609.
[27] J. Ahlers, J. Gmehling, Fluid Phase Equilibria 191 (2001) 177.
[28] L. V. Yelash, T. Kraska, AIChE J., 49 (2003) 1569.
[29] B. S. Jhaveri, G. K. Youngren, SPE Reservoir Engineering, 8 (1988) 1033.
[30] P. H. Salim, M. A. Trebble, Fluid Phase Equilibria 65 (1991) 59.
[31] O. Pfohl, Fluid Phase Equilibria 163 (1999) 157.

[32] L. V. Yelash, T. Kraska, Fluid Phase Equilibria, 162 (1999) 115.
[33] A. Gil-Villegas, A. Galindo, P. J. Whitehead, S. J. Mills, G. Jackson, J. Chem. Phys., 106 (1997) 4168.
[34] L. V. Yelash, T. Kraska, Phys. Chem. Chem. Phys. 2 (2000) 4734.
[35] K. S. Pitzer, J. Am. Chem. Soc. 77 (1955) 3427.
[36] I. Polishuk, J. Wisniak, H. Segura, Chem. Eng. Sci., 55 (2000) 5705.
[37] L.V. Yelash, T. Kraska, E. A. Müller, N. F. Carnahan, Phys. Chem. Chem. Phys., 1 (1999) 4919.
[38] L. V. Yelash, T. Kraska, Fluid Phase Equilibria, 182 (2001) 27.
[39] L. V. Yelash, T. Kraska, Phys. Chem. Chem. Phys., 1, (1999) 2449.
[40] L. V. Yelash, T. Kraska, Phys. Chem. Chem. Phys., 1, (1999) 4315.
[41] B. Bungert, G. Sadowski, W. Arlt, Proceedings of the GVC-Fachausschuß "High Pressure Chemical Engineering, March 3-5, Karlsruhe, Germany (1999).
[42] C. F. Kirby, M. A. Mc Hugh, Chem. Rev. 99 (1999) 565.
[43] J. Groß, G. Sadowski, this book.
[44] A. Weber, T. Kraska, R. Kümmel, this book.
[45] U. K. Deiters, K. M. DeReuck, Fluid Phase Equilibria 161 (1999) 206.
[46] U. K. Deiters, I. L. Pegg J. Chem. Phys., 90 (1989) 6632.
[47] L. Z. Boshkov, Ber. Bunsen-Ges. Phys. Chem. 96 (1992) 940.
[48] T. Kraska und U. K. Deiters, J. Chem. Phys., 96 (1992) 539.
[49] T. Kraska, Ber. Bunsenges. Phys. Chem., 100 (1996) 1318.
[50] L. V. Yelash and T. Kraska, Ber. Bunsenes. Phys. Chem., 102 (1998) 213.
[51] A. R. Imre, Macromolecular Symposia, 198 (2003) 11.
[52] A. Kordikowski, G. M. Schneider, Fluid Phase Equilibria 90 (1993) 149.
[53] H. Pöhler, G. M. Schneider, Fluid Phase Equilibria 110 (1995) 151.
[54] K. Gauter, C. J. Peters, A. L. Scheidgen, G. M. Schneider, Fluid Phase Equilibria 171, 127 (2000).
[55] A. Imre, T. Kraska, L. V. Yelash, Phys. Chem. Chem. Phys. 4 (2002) 992.
[56] G. M. Schneider, Ber. Bunsenges. Phys. Chem. 70 (1966) 497.
[57] P. G. de Gennes, Scaling Concepts in Polymer Physics, Cornell University Press, Ithaca, Chap.4, Sec.3 (1979).
[58] B. Duplantier, J. Phys. (France) 43 (1982) 991.
[59] M. Muthukumar, J. Chem. Phys. 85 (1986) 4722.
[60] N. Wilding, M. Müller, K. J. Binder, Chem. Phys. 105 (1996) 802.
[61] A. Z. Panagiotopoulos, V. Wong, M. A. Floriano, Macromolecules 31 (1998) 912.
[62] A. D. Mackie, A. Z. Panagiotopoulos, S. K. Kumar, J. Chem. Phys. 102 (1995) 1014.
[63] H. Frauenkron, P. Grassberger, J. Chem. Phys. 107 (1997) 9599.
[64]Q. Yan, J. J. de Pablo, J. Chem. Phys. 113 (2000) 5954.
[65] K. Q. Xia, X. Q. An, W. G. Shen, J. Chem. Phys. 105 (1996) 6018.
[66] L. V. Yelash, T. Kraska, A. R. Imre, S. J. Rzoska, J. Chem, Phys. 118 (2003) 6110.
[67] L. V. Yelash, T. Kraska, Fluid Phase Equilibria, in press (2004).
[68] T. Nose, T. van Tan, J. Polym. Sci., Polym. Lett. Ed. 14 (1976) 705.
[69] M. Heinrich, B. A. Wolf, Polymer 33 (1992) 1926.
[70] T. Dobashi, M. Nakata, M. Kaneko, J. Chem. Phys. 72 (1980) 6685.
[71] Y. B. Melnichenko, M. A. Anisimov, A. A. Povodyrev, G. D. Wignall, J. V. Sengers, W. A. Van Hook, Phys. Rev. Let. 79 (1997) 5266.
[72] M. A. Anisimov, A. F. Kostko, J. V. Sengers, Phys. Rev. E 65 (2002) 051805.

Supercritical Fluids as Solvents and Reaction Media
G. Brunner (editor)

Chapter 1.10.

Correlation of the solubility of low-volatile organic compounds in near- and supercritical fluids based on an accurate equation of state

Th. Kraska [a], K. O. Leonhard [a], J. Jurtzik [a], D. Tuma [b] and G. M. Schneider [c]

[a] Universität zu Köln, Institut für Physikalische Chemie, Luxemburger Str. 116, 50939 Köln

[b] Universität Kaiserslautern, Fachbereich Maschinenbau und Verfahrenstechnik, Lehrstuhl für Technische Thermodynamik, 67663 Kaiserslautern

[c] Ruhr-Universität Bochum, Fakultät für Chemie, Physikalische Chemie, 44780 Bochum

1. INTRODUCTION

A key challenge in pursuing supercritical fluid processes is how to model and predict phase equilibria in the systems represented, because this matter strongly determines the economic feasibility of such kind of process. Recently, an article entitled "Solubility prediction in supercritical CO_2 using minimum number of experiments" has been published [1]. In that article different solubility models have been investigated with a minimum amount of experimental data. Any solubility modeling basically ranges between two extremes, on the one hand fully ab initio methods, meaning no information from experiment is required, and on the other hand a phenomenological methodology strictly based on experimental information.

The complexity of supercritical fluid systems keeps the first method very much in the background. To the best knowledge of the authors no articles on solubility modeling in a system low-volatile solute + supercritical solvent using ab initio calculations are known. In contrast to this, there exists a vast variety of phenomenological models which serve well in correlating existing solubility data, but they are at least limitedly if at all applicable for predictions. The optimum, however, shall be a compromise somewhere in between. For example,

when equations of state are used to correlate solubility data, the solid-fluid interaction parameter k_{ij} must be correlated from existing data.

Therefore, our suggestion for this compromise, which is presented in this chapter, is an equation of state model which can accurately model the *pVT*-behaviour of the (supercritical) solvent over a wide range of state combined with a fugacity approach for the implementation of the low-volatile solute. The latter has the intention to reduce the number of tunable mixing rules and substitute them by thermophysical solute-related parameters instead. Coming back to Ref. [1], the authors take the view that it is best, of course, to rely on precise experimental data. It is not so much a matter of the number of data points, rather a matter what state region is covered by those data.

This chapter is a synopsis of three feature articles [2–4] on high-pressure solubility correlation. These papers result from a cooperation between two groups of physical chemists in Bochum and Cologne. The experimental work is the result of frontier research on high-pressure phase equilibria, with dominant participation of supercritical fluids, over more than one decade in Bochum. Methods and several experimental highlights, which have been achieved in the period of this research program, will be presented in another chapter of this book [5]. Based on these data we have evaluated an innovative correlation model which we developed and programmed for describing the solubility in supercritical fluids. In this work we delineate the model and emphasize its capabilities towards more severe conditions, meaning extraordinarily high pressures up to approximately 200 MPa, and its particular preference to physically realistic parameters.

1.1. Equation of state for the critical region

The modeling of the thermophysical properties in the critical region of a supercritical solvent is a challenging problem, since all analytical equations of state exhibit a limiting behaviour near the critical point, which is different to that of the experimental data. This asymptotic behaviour affects the thermophysical properties in the region around the critical point. One can describe the behaviour of a fluid in the critical region by power laws which are exactly valid in the limit of the critical point. Exemplarily, we here consider the power law describing the critical isotherm near the critical point.

$$\Delta p = A\,\Delta\rho^{\delta} \tag{1}$$

Here ΔX is $(X - X_c)/X_c$, p is the pressure, ρ the density, A the critical amplitude, being a substance dependent parameter, and δ the critical exponent. For analytical behaviour one can calculate the exponent δ from a Taylor expansion of the pressure:

$$p = p_c + \left(\frac{\partial p}{\partial \rho}\right)(\rho - \rho_c) + \frac{1}{2}\left(\frac{\partial^2 p}{\partial \rho^2}\right)(\rho - \rho_c)^2 + \frac{1}{6}\left(\frac{\partial^3 p}{\partial \rho^3}\right)(\rho - \rho_c)^3 + \ldots \quad (2)$$

At critical conditions the second and third term vanish. Close to the critical point terms of higher order become negligible and hence the leading term is the fourth term of Eq. (2):

$$p = p_c + \frac{1}{6}\left(\frac{\partial^3 p}{\partial \rho^3}\right)(\rho - \rho_c)^3 \quad (3)$$

After rearranging this equation

$$p - p_c = A(\rho - \rho_c)^3 \quad (4)$$

one finds that the exponent of the power law (Eq. (1)) takes the value $\delta = 3$ for any analytical equation of state, which can be expanded in a Taylor series. However, experiments yield the value $\delta = 4.76$. Such difference can be found also for other critical exponents and is related to the diverging fluctuations in a fluid at the critical point. All equations of state based on the mean field approach are not able to describe these diverging fluctuations and hence give the so called classical exponents rather than the non-analytical or non-classical exponents. More detailed investigations and analysis of the near-critical behaviour are given in review papers [6–8].

In recent decades, much effort has been undertaken in order to develop equations of state which are accurate in the critical region. Early approaches using a power law [9,10] were limited to the region very close to the critical point. To extend the range of the power laws, so called corrections to scaling have been introduced [11]. A few years later, the combination of the power law for the critical region and a classical equation of state, such as a van der Waals-like equation, have been combined empirically, for example, by a switch function [12–14]. While such an approach gives good representation of the *pVT*-data both in the critical region and in the vapour-liquid region, it can lead to artificial behaviour in the derivatives [14]. This artificial behaviour is related to an inflection point in the switch function.

More recently, physically based approaches for the crossover from classical to non-classical behaviour have been proposed [15]. These methods have been elaborated and applied to several different classical equations of state models, such as the Landau expansion [15], cubic equations of state [16], or the statistical associating fluid theory [17]. With such approaches the thermophysical properties can be modeled properly. On the other hand, due to the fact the resulting equation of state is a non-analytical equation of state, a

numerical evaluation is necessary. Furthermore, the extension of this particular approach to binary mixtures is difficult and has been accomplished so far only for few rather simple types of binary systems [18].

Another possibility to describe the critical behaviour as well as the vapour-liquid region properly are multi-parameter reference equations of state [19]. However, they have been developed for a handful important pure fluids (e.g., CO_2, H_2O, CH_4, N_2) only and require a lot of adjustable parameters, especially when the critical region should be modeled accurately.

In this work we have developed an equation of state which is based on a semi-empirical approach. The aim of this approach is to obtain an equation giving accurate results in the critical region, in the low-pressure vapour-liquid region, and in the high-pressure region at least up to several hundred MPa. Further requirements are that the number of parameters should be much lower than for the multi-parameter reference equations of state. Furthermore, the parameters should also be related to physical properties. In engineering applications and also in investigations of the solubility in supercritical solvents it is not necessary that the model exhibits the non-classical exponents at the critical point, in other words, the equation of state can be analytical at the critical point. Hence, the resulting equation of state proposed here is an analytic equation with an exponent δ, which increases towards the critical point, and only very close to the critical point it is fixed at the classical value $\delta = 3$.

1.2. Solubility of low-volatile substances in supercritical fluids

Since the 1960s, when supercritical fluids have become apparent as solvents [20], actually for the extraction of caffeine from coffee beans, a huge manifold of processes with supercritical fluids have been developed. Many of these processes have in common that a low-volatile substance, which can be a liquid or a solid, has to be dissolved in the supercritical solvent. In a considerable number of applications we are confronted with the situation that the solute (i.e., the substance subject to treatment) is polar and the solvent, like CO_2, unpolar. Hence, the understanding of the solubility behaviour and its modeling for such systems is important for the design of processes with supercritical fluids. There are two challenges for such a task: first, the solubility is often very low in the order of 10 or 100 micromole per litre, secondly, as described in the first section of the introduction, it is difficult to model the pVT-behaviour in the critical and supercritical region with equations of state accurately.

There are different approaches for the solubility modeling which are mainly keyed to specified applications. For solubility data up to medium pressures of 20 MPa one can apply the Chrastil method, a purely phenomenological model, which is based on some rather simple physical arguments and gives a linear relation between the logarithm of the solvent density and the solubility [21]. A significant drawback of Chrastil's method is that the model is solely founded on

experimental solubility data at low and medium pressure. For higher pressures this linear relation is not valid any more and other, more sophisticated approaches have to be used. A common correlation method is based on the cubic equations of state which are empirical descendants evaluated on basis of the van der Waals equation. In order to model the solubility in supercritical fluids a fugacity approach is employed. The delicate problem here is that the cubic equations of state are not accurate in the critical region, and hence the accuracy of the solubility data is only ensured up to a certain pressure. Furthermore, there are difficulties to describe a solubility maximum appearing at higher pressure with this approach.

In our project, we combine the semi-empirical equation of state describing the solvent with a fugacity approach for the extension to a solute. Since the equation of state accurately models the solvent's *pVT*-behaviour, one can expect physically relevant parameters and solute properties from the correlation of the solubility data. In several examples presented, particularly for adamantane + CO_2 (cf. 5.1), our method gives satisfying results as surrogate for saturation pressure experiments.

2. EQUATION OF STATE MODEL

The background of the differences between the classical behaviour, as obtained from mean field equations of state, and the experimentally observed non-classical behaviour in the critical region are large density fluctuations. These fluctuations become very large close to the critical point, and diverge at the critical point. Models which assume a uniform density throughout the fluid cannot capture such fluctuations and hence must fail in the critical region. An effective way of accounting for non-uniform density distributions in fluids has been proposed ten years ago [22]. This method treats the density fluctuation as perturbation to the average density of the fluid $\bar{\rho} = N/V$. The deviation of the local density from the average density is described by a density distribution function for which the Gauss distribution is used. The mathematical formalism for the development of the perturbation term is a convolution of a mean field equation of state with the density distribution. For performing this convolution it is necessary to use a density expansion of the mean field equation of state rather than the closed form which is usually given. As reference equation we use a Carnahan-Starling-van der Waals kind of equation of state given by:

$$p_{\mathrm{ref}} = \frac{RT}{V_{\mathrm{m}}}\left(1 + \frac{4\xi - 2\xi^2}{(1-\xi)^3}\right) - \frac{8RbT^*}{V_{\mathrm{m}}^2}\Psi(T) \tag{5}$$

Here, $\xi / b/V_m = b\rho$, $\Psi(T) = 1 + f_T^*(T_c - T)/T_c$ with $f_T^* = f_T$ for $T \leq T_c$, and $f_T^* = 0.25 f_T$ for $T > T_c$. If we now perform the convolution of the Taylor expansion of Eq. (5)

$$p_{ref} = RT\rho + \sum_{i=2} f_i(T)\ \rho^i \tag{6}$$

with a density distribution, we obtain for the residual part (second term in Eq. (6)):

$$\left\langle p_{ref,res} \right\rangle_\rho = \sum_{i=2} f_i(T)\ I_i \tag{7}$$

Due to the convolution, the density powers are replaced by integrals over ρ^i multiplied by the density distribution:

$$I_i = \int_{-\infty}^{\infty} \rho^i \cdot P_{gauss}(\rho, \mu, \sigma)\ \mathrm{d}\rho \tag{8}$$

Here, σ is the width of the density distribution, and $\mu = \bar{\rho}$ the average value of the Gauss distribution which we set equal to the average density. In order to extract the perturbation term from Eq. (7), we have to separate the terms including the width-parameter σ from the terms without this particular parameter. The terms without the σ-parameter represent the reference equation and can be written in a closed form after separation. For the perturbation term, however, it is not possible to obtain a closed form.

$$\left\langle p_{ref,res} \right\rangle_\rho = \sum_{i=2} \left[f_i(T) + g_i(\sigma, T) \right]\ \rho^i = \sum_{i=2} f_i(T)\ \rho^i + \sum_{i=2} g_i(\sigma, T)\ \rho^i$$
$$= p_{ref,res} + p_{pert,res}(\sigma) \tag{9}$$

This equation of state is able to account for density fluctuations effectively. It is, however, still a classical equation of state in the context of the divergences at the critical point. A thorough analysis has shown that the effective critical exponent δ increases towards the non-classical behaviour on the way to the critical point and takes the classical value only very close to the critical point [22]. Since this is the case for approaching the critical phase from the liquid as well the gas phase, there remains only a narrow gap in which the critical exponents have the explicitly classical value. Generally, this narrow gap is not of importance for practical applications of supercritical fluids, because processes with supercritical fluids are often operated significantly above the critical point

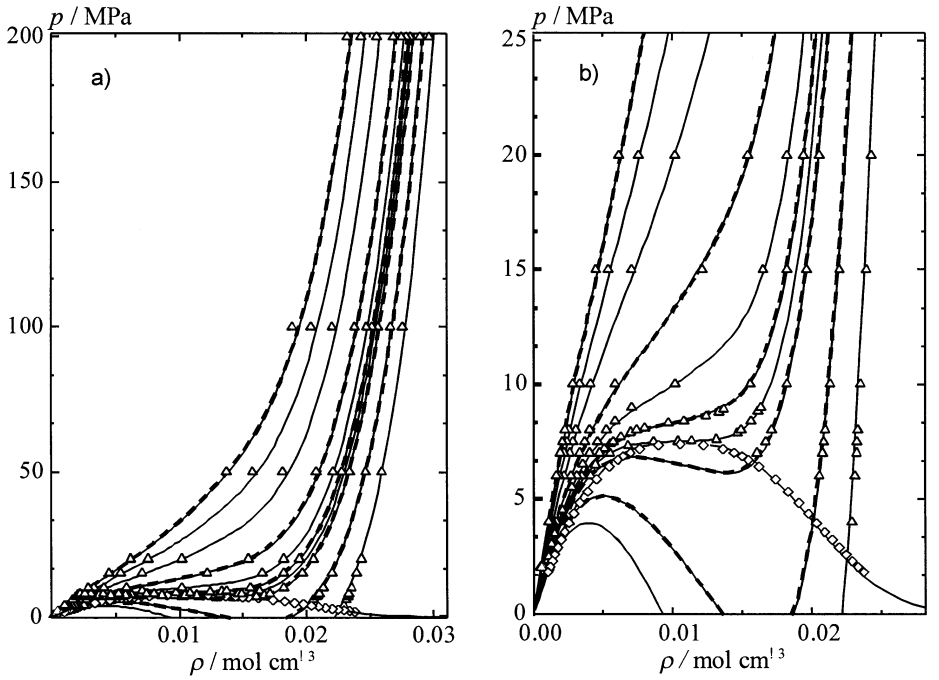

Fig. 1. Isotherms and coexistence curve for carbon dioxide up to high pressures (a) and in the critical region (b) calculated with the original equation [24] and the simplified form (solid dashed curves) compared to experimental data (symbols) taken from the tables of Span and Wagner [25]. The simplified equation is almost indistinguishable from the original equation of state. Ten isotherms are plotted in the range from T = 260 to 460 K (beginning from the right T = 260 K, 280 K, 300 K, 304.21 K, 310 K, 320 K, 340 K, 380 K, 420 K, 460 K).

in order to avoid the negative influence of the critical slowing down of the diffusion coefficient [23].

In Eq. (9) there remains one unknown variable, namely the parameter σ. This parameter is treated as semi-empirical parameter and adjusted to data of the critical isotherm of argon [24]. Argon has been chosen as reference fluid, because it is a simple substance with isotropic van der Waals interactions. The correlation function for the density and the temperature dependence of σ is designed in order to be able to transfer it to other substances:

$$\sigma = \sigma_{\mathrm{c}} \cdot \xi \left(\frac{1}{\xi_{\mathrm{c}}} - \frac{B_\xi}{\xi_{\mathrm{c}}^2} y + \sum_{i=2}^{n} C_{\mathrm{i}} y^{\mathrm{i}} \right) \cdot \exp\left(- \left(\frac{\Delta T}{B_{\mathrm{T}}} \right)^2 \right) \tag{10}$$

with $y = (\xi - \xi_{\mathrm{c}}) / B_\xi$ and $\Delta T = (T - T_{\mathrm{c}}) / T_{\mathrm{c}}$. Here, the substance-dependent parameters B_ξ and B_{T} are used for transferring Eq. (10) to other substances which do not differ too much in the molecular interactions from argon. Since

most supercritical solvents are small non-polar molecules, Eq. (10) can be applied to several supercritical fluids. The parameter σ_c is the value of σ at the critical point. The coefficients C_i are substance-independent and listed in an earlier paper together with further details on the equation of state [24].

The correlation of these equation of state parameters requires two steps: first, the parameters a, b, and σ_c are calculated from the critical conditions, secondly, B_ξ can be calculated from data of the critical isotherm of the substance, and finally B_T and f_T from data of the coexistence curve. The parameters and figures showing the agreement between the equation of state calculations and the experimental data are given in Ref. [24].

The evaluation of the double sum in the perturbation requires some computer time, since for convergence at high density up to 40 terms are required. This can limit the application of Eq. (9) in cases which require numerous evaluation of the equation of state. Since, as mentioned earlier, it is not possible to transform the perturbation term into a closed form, we have correlated the repulsive part of the perturbation term with a comparatively simple equation given as [2]:

$$p_{\text{pert,res,repulsion}} = \frac{RT}{V_m}\left(\frac{A\xi + B\xi^2 + C\xi^3}{(3-4\xi)(1-c_1\xi)}\right) \tag{11}$$

$$A = 4.757\cdot 10^{-5}\,\sigma_n + 12.22\,\sigma_n^2 - 0.5568\,\sigma_n^3 \tag{12}$$

$$B = -0.001692\,\sigma_n + 47.57\,\sigma_n^2 - 1.886\,\sigma_n^3 \tag{13}$$

$$C = \frac{-0.0204\,\sigma_n + 189.3\,\sigma_n^2 + 434.2\,\sigma_n^3 - 1711\,\sigma_n^4}{1 + 2.35\,\sigma_n} \tag{14}$$

$$c_1 = 1.424 - 0.1\,\sigma_n + 8.114\,\sigma_n^2 - 4.916\,\sigma_n^3 \tag{15}$$

$$\sigma_n \equiv \frac{\sigma V_m}{b_0} \tag{16}$$

Here, $b_0 = 1$ dm^3 mol^{-1} is the volume unit. Eq. (11) can be used as replacement for the double sum in Eq. (9). In Fig. 1 the pVT-data of carbon dioxide are compared to the calculation with the original perturbation term (Eq. (9)) and calculations with the simplified term (Eq. (11)). One can see that both equations give almost identical results and agree well with the experimental data of the vapour-liquid equilibrium, the critical region, and the high-pressure data.

A complete list with the meaning of all symbols which appear in our model, as far as not explained in the text, is given in Ref. [2].

3. SOLUBILITY CORRELATIONS

Since for many of the low-volatile substances investigated here only few thermophysical properties are available in the literature, we have chosen to employ a simple model for the solutes instead of a full equation of state model. Based on the assumption that the solute in equilibrium with the solution is a pure substance, mixing rules for the pure solute phase can be skipped. The solute is described within a fugacity approach [26] by its saturation pressure, molar volume, and by its compressibility where available.

$$x_2 = \frac{p_2^{\text{sat}}}{p\ \varphi_2(x_2)} \exp\left(\frac{V_{\text{m},2}(p - p_2^{\text{sat}})}{\text{RT}}\right) \tag{17}$$

Here, x_2 is the mole fraction of the solute in solution, $V_{\text{m},2}$ is the molar volume of the pure solute, p_2^{sat} the saturation pressure of the pure solute, and φ_2 the fugacity coefficient of the solute in solution. The parameters of the solute have been obtained from the correlation to the solubility data. These are the attraction parameter of the pure solute T^*_{22}, the volume parameter b_{22}, and the corresponding cross parameters k_{12} and l_{12} (cf. Eqs. (20) and (21)). Simple quadratic one-fluid mixing rules are used for the mixture parameters T^* and b.

$$b = x_1^2 b_{11} + 2x_1 x_2 b_{12} + x_2^2 b_{22} \tag{18}$$

$$T^* = \frac{x_1^2 b_{11} T_{11}^* + 2x_1 x_2 b_{12} T_{12}^* + x_2^2 b_{22} T_{22}^*}{b} \tag{19}$$

$$b_{12} = l_{12} \frac{b_{11} + b_{22}}{2} \tag{20}$$

$$T_{12}^* = k_{12} \sqrt{T_{11}^* T_{22}^*} \tag{21}$$

All other equation of state parameters are treated as composition independent, meaning that the solute generates only a small perturbation of these solvent parameters.

Since saturation pressure data for many solutes are not available in the literature, we have to chose an indirect way of estimating the saturation pressures. Based on the solubility isotherms for different temperatures, we have obtained the saturation pressure of the low-volatile solute and described its temperature dependence with the following two-parameter equation:

$$p_{\mathrm{sat}} = p_0 \exp\left(-\frac{A_{\mathrm{sat}}}{T} + B_{\mathrm{sat}}\right) \tag{22}$$

Here, $p_0 = 1$ MPa is the unit pressure. This equation resembles the structure of the Clausius-Clapeyron equation. The parameters A_{sat} and B_{sat} have been treated as adjustable parameters similar to the equation of state parameters. These parameters as well as the equation of state parameters have been optimised by least-square minimization to experimental data of solubility isotherms. In order to obtain A_{sat} and B_{sat}, it is necessary to use several solubility isotherms simultaneously for fitting. Another possibility is to obtain p_{sat} for each solubility isotherm separately and correlate the data points (T, p_{sat}) with Eq. (22) afterwards. For the rare cases for which the vapour pressure of the solute is known from experiments, its separate calculation is a good test for the internal consistency of the model.

The isothermal compressibility κ_{T} of the solute has been taken from the literature where available. It affects the molar volume of the pure solute according to Eq. (23):

$$V_{\mathrm{m},2} = \left(1 - \kappa_{\mathrm{T}}(p - p_2^{\mathrm{sat}})\right) V_{\mathrm{m},2}^{p=p_2^{\mathrm{sat}}} \tag{23}$$

In those cases, when no experimental compressibility data are available, it was possible to improve the results by using the compressibility as adjustable parameter. Ultimately, the molar volume of the solute $V_{\mathrm{m},2}$ has been taken from the literature where available or likewise treated as adjustable parameter.

4. EXPERIMENTAL

We have measured the high-pressure saturation equilibrium of a low-volatile high-molecular organic substance in a compressed gas under conditions from the liquid to the supercritical state for the following systems: adamantane in CO_2 [2], β-carotene (more precisely β,β-carotene [27]) in CO_2, N_2O, and $CClF_3$ [2], and finally the anthraquinone derivatives and dispersion dyes 1-amino-4-hydroxy-2-phenoxy-9,10-anthraquinone (Disperse Red 60, abbreviated DR60) [3] in CO_2 and three 1,4-bis-(alkylamino)-9,10-anthraquinones (with "alkyl" starting from the short "propyl" (AQ03) over "octyl" (AQ08) to finally "octadecyl" (AQ18)) in CO_2 and also N_2O for the last dye mentioned. The structures of the mentioned organic substances are given in Fig. 2.

In situ analysis by spectroscopy is common to all experimental investigations. The entire experimental procedure is briefly sketched in the corresponding experimental chapter in this book [5], the p,T-conditions of the experiments will be quoted in the subsections of paragraph 5. For further

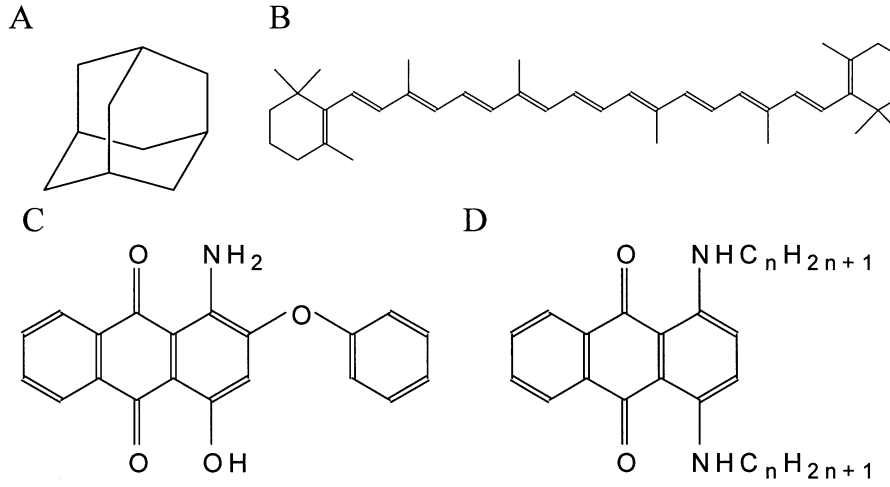

Fig. 2. Structures of: adamantane (A), β-carotene (B), 1-amino-4-hydroxy-2-phenoxy-9,10-anthraquinone (Disperse Red 60) (C), and 1,4-bis-(alkylamino)-9,10-anthraquinone (D), where alkyl = propyl (n = 3), octyl (n = 8), and octadecyl (n = 18).

reading see the references cited therein and above all the respective parts of the three feature articles [2–4].

5. RESULTS

Our correlation model has been applied to the solubility of several different low-volatile organic compounds in different supercritical fluids. We have chosen adamantane as a test substance with a simple molecular structure and relatively high solubility in supercritical carbon dioxide. Several thermophysical properties of adamantane are available in the literature, which is another reason for testing our model with this particular substance. The other substances investigated belong to the class of organic dyes. β-Carotene is a common natural dye of outstanding technical importance [28]. It is employed as a reference substance for biomolecules [29] and, for example, used as food additive and for food dyeing [30]. Besides, it is important for technical applications to know how a possible change in the molecular structure due to the application of pressure affects the solubility behaviour of a biomolecule. Since the functionality of biomolecules is related to its structure, this knowledge can be important for a specific process.

Apart from this natural dye, we have investigated a series of synthetic dispersion dyes, namely anthraquinone derivatives. This series includes AQ03, AQ08, and AQ18 as an example for molecules with two growing side chains. Another anthraquinone dye investigated here is Disperse Red 60 (DR60) with polar groups. These specific substances have been chosen for several reasons:

they are stable under the experimental conditions, as members of a homologous series they are suitable for a systematic investigation, they are commonly used in conventional dyeing processes [31,32] and potential candidates for supercritical dyeing [33], and for some of the pure anthraquinone dyes thermodynamic data are available in the literature which is especially important here.

5.1. Adamantane

Adamantane is a simple globular molecule interacting by van der Waals forces only. Its saturation pressure is therefore relatively high compared to those dyes investigated later in this work. Thus, the solubility in supercritical solvents is relatively high. Swaid [34] has measured four solubility isotherms of adamantane dissolved in supercritical carbon dioxide at 343 K, 362.5 K, 382 K, and 402 K in a pressure range from 10 MPa to 85 MPa. In Fig. 3 two correlations of the solubility data with slightly different parameters are shown. For the calculations, the compressibility of adamantane ($\kappa_T = 2.27 \cdot 10^{-4}$ MPa^{-1} [35]) has been taken from the literature as well as its molar volume ($V_{m,s} = 125.9$ cm^3 mol^{-1}, calculated from X-ray data given by Hara et al. [35]). One can see that our model is able to describe the solubility over a wide range from 0.01 to 0.8 mol dm^{-3}. The solubility values reach a maximum which is shifted to higher pressures with increasing temperatures. Our equation of state is able to give a good correlation in the overall pressure range, whereas the

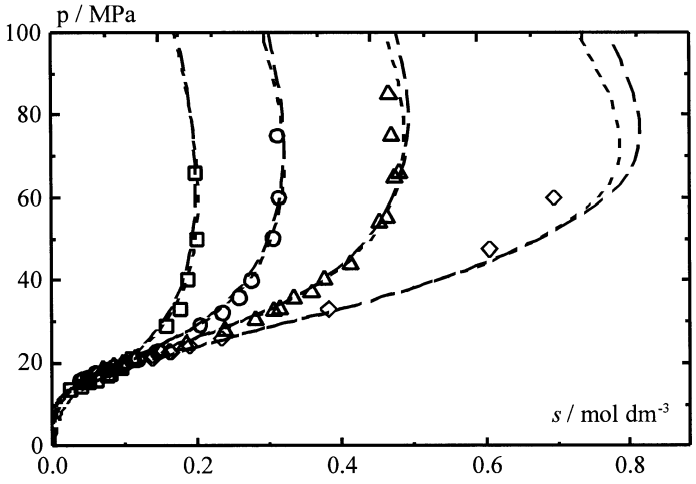

Fig. 3. Correlation of the solubility of adamantane in CO_2. The symbols are the experimental data at 343 K (□), 362.5 K (○), 382 K (Δ), and 402 K (◊). The long dashed curves correspond to the parameter set no. 2 in Table 1, whereas the short dashed curves correspond to the parameter set no. 3 in Table 1. In the latter correlation the average compressibility of the solid is used rather than the compressibility in the low pressure limit.

Redlich-Kwong equation of state, as reported earlier [36, 37], cannot represent solubility maxima. The deviation between experimental data and correlation increases slightly with increasing temperature. This may be caused by Eq. (22) which restricts the temperature dependence of the saturation pressure to a linear function of $\ln p$ as function of $1/T$. Another possible reason is the high value of the solubility at 402 K. At this temperature it can happen for certain parameter sets that the model does not find a solution in course of the solubility calculation, which indicates complete miscibility. In such a case the parameters overestimate the solubility, but it does not happen for the isotherms with lower solubility. For these correlations we used the molar volume $V_{m,s} = 125.9\ cm^3\ mol^{-1}$ [35]. On the other hand, for the saturation pressure we did not take experimental data, we used the saturation pressure as adjustable parameter instead. Since we correlated four isotherms at the same time, we could directly obtain the parameters A_{sat} and B_{sat} of Eq. (22). With these parameters it is possible to estimate the saturation pressure of pure adamantane. In Fig. 4 the saturation pressure is plotted against the temperature for three different parameter sets and compared to experimental data. One can see that all three parameter sets predict the experimental data fairly well. The two estimations corresponding to the two solubility correlations shown in Fig. 3 are almost identical. The solid curve in Fig. 4 corresponds to that correlation which suggest complete miscibility at 402 K in a certain pressure range. If we include two more values with high solubility above 0.07 g cm^{-3} at $T = 402.0$ K in the correlation, a solubility maximum is found. It appears that small variations of the solute parameters can change the topology of the solubility behaviour at high temperature for this system, while it leaves the correlations at lower temperatures almost unchanged. Reiser et al. have also calculated saturation pressures on CO_2-solubility basis [39]. Mokbel et al. have stated that sublimation takes place in their experiments up to the maximum temperature at 462.0 K [38]. It is important to consider that each phase transition in the analysed temperature range requires a separate Eq. (20). For globular molecules such as adamantane, solid-solid phase transitions are reported in the literature [40–42], However, these transitions do not affect the pT-range of the solubilities in CO_2 discussed here.

Table 1
Parameters of the solute and the binary interaction as obtained by the correlation of the solubility. The corresponding correlations are shown in the figures indicated in the first column.

System	T^*_{22} / K	b_{22} / $cm^3\ mol^{-1}$	k_{12}	l_{12}	A_{sat} / K	B_{sat}	κ_T / MPa^{-1}	$V_{m,s}$ / $cm^3\ mol^{-1}$
Adamantane + CO_2; no. 1 (Figs. 3, 4)	744.71	45.48	1.0	1.0	7466	13.58	0.000227	125.9
Adamantane + CO_2; no. 2 (Figs. 3, 4)	735.246	42.8871	1.0	1.0	7424.82	13.69	0.000227	125.9
Adamantane + CO_2; no. 3 (Figs. 3, 4)	742.628	42.6433	1.0	1.0	7410.43	13.63	0.000450	125.9
β-Carotene + CO_2 (Fig. 5b)	594.8	124.5	0.9483	1.0689	8285.0	0.0	0.0	536.8
β-Carotene + $CClF_3$ (Fig. 5a)	594.8	124.5	1.1028	1.0136	8285.0	0.0	0.0	536.8
β-Carotene + N_2O (Fig. 5c)	594.8	124.5	1.0109	0.9321	8285.0	0.0	0.0	536.8
DR60 + CO_2; T = 303.1 K (Fig. 6)	799.872	81.7009	1.0	1.0	9200.0	5.80788	0.0	312.0
DR60 + CO_2; T = 314.8 K (Fig. 6)	790.23	84.7281	1.0	1.0	9200.0	5.58534	0.0	312.0
DR60 + CO_2; T = 322.5 K (Fig. 6)	784.632	85.3309	1.0	1.0	9200.0	5.83209	0.0	312.0
DR60 + CO_2; T = 393.15 K (Fig. 6)	749.937	80.5537	1.0	1.0	9200.0	5.37428	0.0	312.0
DR60 + CO_2; T = 423.15 K (Fig. 6)	794.369	80.3058	1.0	1.0	9200.0	5.70381	0.0	312.0
DR60 + CO_2; 303.1 ≤ T / K ≤ 322.5, (Fig. 6)	705.714	94.1156			7709.73	1.25074		364.37
AQ03 + CO_2; 305 ≤ T / K ≤ 340, (Fig. 8)	754.423	80.5019			10423.5	11.8918		322.4
AQ08 + CO_2; 310.1 ≤ T / K ≤ 340.1, (Fig. 9)	758.937	127.691			15730.4	21.4659		462.7
AQ18 + CO_2 (Fig. 10a)	651.773	162.879	1.0	1.0	19910.2	28.129	0.0000182	562.449
AQ18 + N_2O, no. 1 (Figs. 10b, c)	651.773	162.879	1.05299	0.907738	19910.2	28.129	0.0000182	562.449
AQ18 + N_2O, no. 2 (Figs. 10b, c)	651.773	162.879	1.05299	0.907738	p_{sat} / 10^{-14} MPa 1036.1		0.0000182	562.449

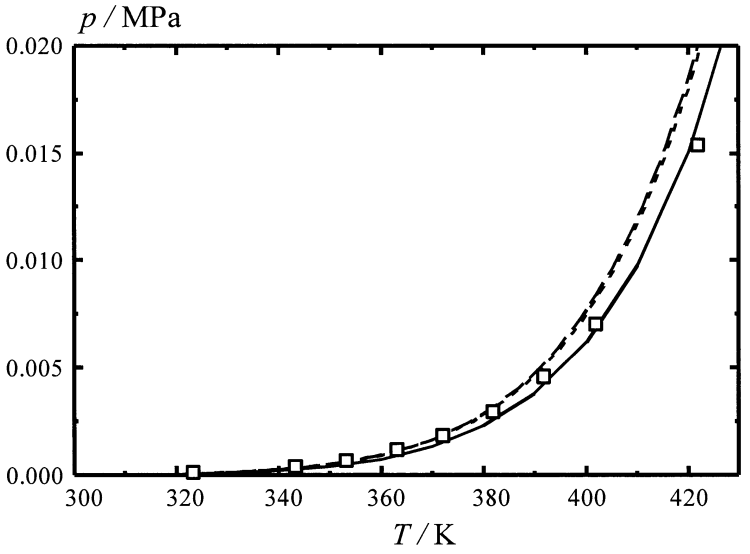

Fig. 4. Plot for saturation pressures p_{sat} of adamantane as obtained from the solubility data. The squares are experimental data taken from Mokbel et al. [38], the lines show the fit from solubility isotherms. The three curves represent those three parameter sets listed in Table 1. Solid curve: set 1; long dashed curve: set 2; short-dashed curve: set 3. Apparently, the value of the compressibility of the solute has minor influence on the prediction of the saturation pressures (compare long- and short-dashed curves).

5.2. β-Carotene

β-Carotene is a substance which is of interest from several different point of views. It is a widely used natural dye, for example, for food and pharmaceuticals. It is also used as a representative for biological molecules. In this particular context not only the solubility but also the effect of changes in the molecular structure such as isomerization and its influence on the solubility is of interest. For this investigation we employed solubility data of β-carotene in three different solvents: carbon dioxide, chlorotrifluoromethane and nitrous oxide. Experimental data up to 200 MPa are used in the correlation. For the solubility of β-carotene in nitrous oxide only data at low pressure up to 15 MPa are available [43, 44]. Due to the good solubility of β-carotene in nitrous oxide at this pressure, the limit of the experimental setup for the concentration measurement is reached. Since the solubility of β-carotene in carbon dioxide is drastically lower, the solubility maximum could be reached and detected with the same experimental setup [43, 44] at 307.6 K. The solubility of β-carotene in chlorotrifluoromethane is even lower than in carbon dioxide and data up to 200 MPa are available for the temperature range from 296 K to 326 K [43, 2]. All these solubility data have been correlated by using the same parameters for the

pure β-carotene. For the molar volume we used $V_{m,s} = 536.8\ cm^3\ mol^{-1}$ which has been obtained from X-ray data [45]. Since the parameters for the pure solvent are also fixed, only the deviations from the Lorentz-Berthelot combining rules have been treated as adjustable parameters. In Fig. 5 the results for the correlations are shown.

The importance of this binary system is illustrated by the plenty of papers which have been reported on the system β-carotene + CO_2 (see Ref. [2] and further references cited therein). In several of these publications data are correlated with density-based empirical models such as the Chrastil model [21] or with cubic equations such as the Peng-Robinson and the Redlich-Kwong equations and their modifications. To summarize these results so far, the density-based model gives satisfactory results only up to pressures of approximately 30 MPa. At pressures where the solubility deviates from monotonous dependence of solvent density, e.g., when a solubility maximum occurs, that model fails. With an equation of state better agreement between experimental data and correlations have been found. Cygnarowicz et al. [46], who have measured three isotherms of β-carotene in CO_2 (at 40, 60, and 70 °C and up to 44 MPa), present an extrapolation up to even 100 MPa, where the solubility continuously grows. Our own experimental results, however, disagree with that prediction [2].

The solubility maxima found for the isotherm at $T = 307.6$ K in Fig. 5b coincides well with the calculated values from our equation of state. The deviation of the experimental data at pressures above 125 MPa is supposed to be an outcome of isomerization caused by an enrichment of cis-isomers in the solution, while the all-trans β-carotene is squeezed out of the solution and crystallizes. A more detailed depiction of these effects, especially observation of isomerization kinetics by spectral analysis, is given in a dissertation [43]. Due to their technical relevance, they shall be subject to further investigation.

In Fig. 5a the correlation of the solubility of β-carotene in $CClF_3$ is shown. Apparently, the correlation is less accurate as for β-carotene in CO_2. The solubility maximum is predicted at lower pressure and lower solubility than the experimental data suggest. In order to move the solubility maxima to higher pressure and higher solubility one has to increase the saturation pressure of the pure β-carotene. Then, it can happen that the saturation pressure becomes too high compared to the total pressure of the system and can lead to the appearance of an artificial solubility maximum at low system pressure, which has not been found experimentally yet to the knowledge of the authors. So, it is rather an indication that the saturation pressure of the pure solute is too high in the model.

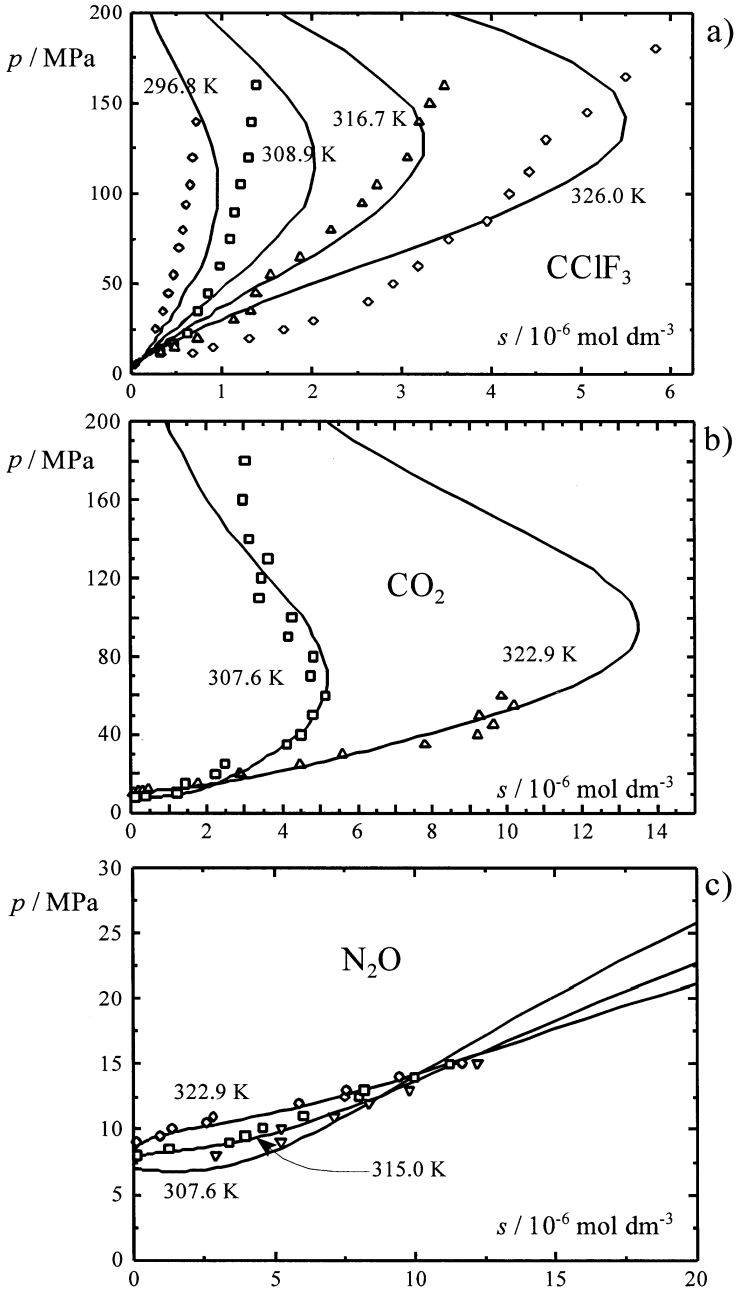

Fig. 5. Experimental (symbols) and calculated solubility of β-carotene in $CClF_3$ (a), CO_2 (b), and N_2O (c) for a common saturation pressure and common van der Waals parameters of β-carotene. The corresponding parameters are listed in Table 1. The solubility of β-carotene in the three solvents increases from $CClF_3$ over CO_2 to N_2O.

Another possible reason for the difference between model and experiment for $CClF_3$ is the use of amorphous instead of crystalline β-carotene as taken for the solubility measurements in CO_2 and N_2O [44]. Sakaki has reported a slightly higher solubility of amorphous β-carotene compared to the crystalline species [47]. The comparison of our present data in CO_2 with earlier results published in 1996 [48], where amorphous β-carotene has been applied as well, gives a similar finding. The reason is that the Gibbs energy of the crystalline modification is lower than of the amorphous one. One can use this observation systematically as sign for the upper limit of the solute saturation pressure.

The largest deviations between experiment and correlation can be observed for $CClF_3$, which is the poorest solvent for β-carotene. The solubility in N_2O (Fig. 5c) is comparatively high, and with the experimental method employed, data in the region of the crossing of the solubility isotherms are available. It should be noted that our model predicts a solubility maximum also for N_2O at high solubility at $s = 180 \cdot 10^{-6}$ mol dm^{-3} and $p = 190$ MPa for $T = 307.6$ K. The solubility in CO_2 (Fig. 5b) takes the intermediate place amongst the systems investigated here.

5.3. 1-Amino-4-hydroxy-2-phenoxy-9,10-anthraquinone (DR60) + CO_2

The dye Disperse Red 60 (DR60) is one of four anthraquinone dyes subject to correlation in this work. In Fig. 6 solubility data obtained experimentally and two correlations are plotted for the system DR60 + CO_2 [3]. With increasing temperatures the isotherms at $T = 303.1$ K, 314.8 K, and 322.5 K become less steep, meaning a stronger solubility increase within a given pressure interval. Beyond approximately 40 MPa the increase of solubility diminishes as characterized by the distinct curvature. The mutual intersection of the isotherms at $p \approx 20$ MPa does not appear when the isotherms are plotted against density instead. The correlations reproduce the complete course of the measured data satisfactorily. One can improve the correlation by making the characteristic temperature and van der Waals parameter T^* and the covolume parameter b temperature dependent. This modification is very useful for the estimation of the solute saturation pressure. However, such empirical extensions should be carried out carefully, especially with a view to extrapolations. All equation of state parameters are listed in Table 1.

Several investigations on this particular system have been published, and the relating references can be drawn from Ref. [3]. If we compare these data sets both mutually and to our own results, large discrepancies are noticed. Our data coincide best with those of Sung and Shim [49], their data being approximately 25 % higher than ours as, for example, for our value taken for comparison at $p = 32.83$ MPa and $T = 314.8$ K.

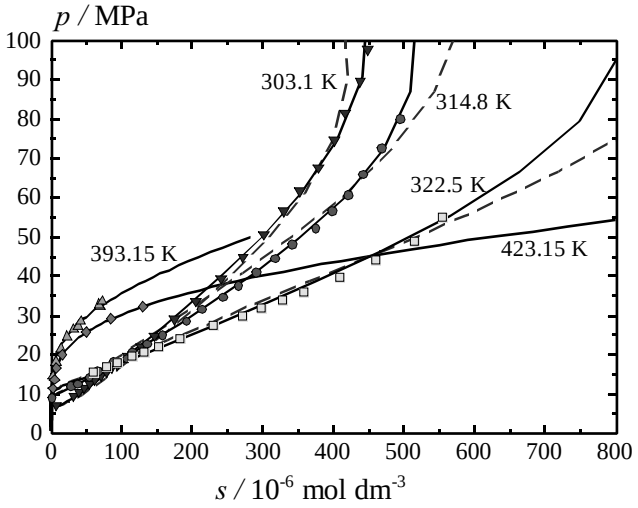

Fig. 6. Experimental (symbols) and calculated solubilities of Disperse Red 60 in CO_2. The solid curves correspond to a temperature-dependent parameter set (T^*, b), whereas the dashed curves result from temperature-independent parameters. The parameters are listed in Table 1. The data at T = 393.14 K and at 423.15 K are taken from the literature [49].

Sung and Shim have applied two solubility-density relations originating from Chrastil's model [21] to correlate their results, the $s(\rho)$-plot in semilog and log-log presentation. Additionally, they have optimised their correlation by the introduction of a temperature-dependent parameter [49]. However, correlations of this type prove to be inapplicable for an extended density range, as we have investigated for this system. Due to the significant curvature of the isotherms shown in Fig. 6, both the semi-log and the log-log relation between solubility and density do not give straight parallel lines for the solubility isotherms any more [55]. The same will, of course, be the case when we do such a data analysis for the systems β-carotene + CO_2 and + $CClF_3$. Our equation of state overcomes this shortcoming. It is generally applicable and not restricted to a limited density region, where Chrastil's conceptions are applicable.

As already pointed out, the saturation pressure of the solute required for the correlation has to be estimated indirectly from the solubility isotherms. As shown in Fig. 7, there are several data on saturation pressures for sublimation and vaporization of DR60 available, because of its particular use in, e.g., thermal sublimation printing or textile dyeing [56–59]. The saturation pressures we obtain from the solubility data of Sung and Shim [49] coincide well with the correlation given by Nishida et al. [50]. The saturation pressures obtained from our own measurements at lower temperatures is a little bit above the extrapolation of Nishida's function [50]. Nevertheless, one can conclude that the estimated saturation pressure is in the correct order of magnitude.

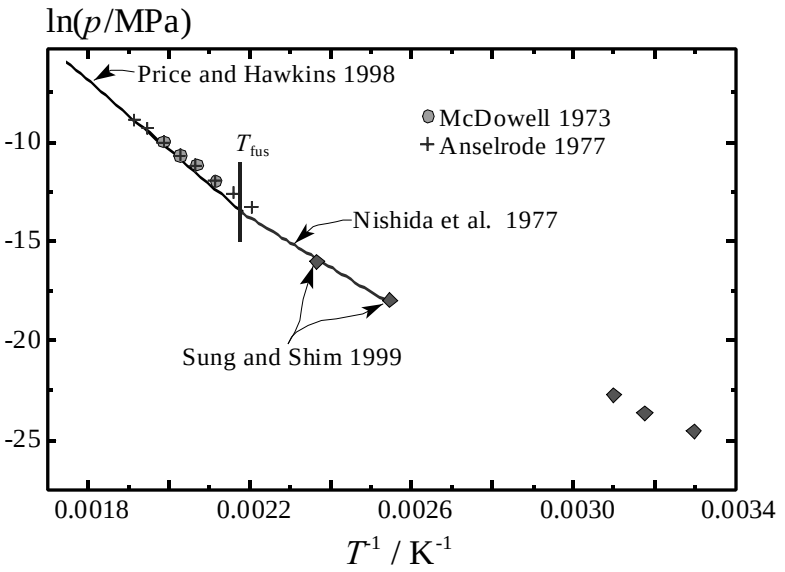

Fig. 7. Comparison of the sublimation and vapour pressure of Disperse Red 60 obtained from solubility correlations (diamonds, derived from the three isotherms shown in Fig. 6) and from direct measurements. In order to fill the gap between our data at low temperature and the directly measured vapour pressures at high temperature [50–53], we have also calculated the vapour pressure from the solubility data of Sung and Shim [49]. The temperature of fusion T_{fus} = 459 K has been taken from Ref. [54].

5.4. 1,4-Bis-(alkylamino)-9,10-anthraquinone (AQ*n*) + CO_2 and + N_2O

Fig. 8 shows the experimental data [60] as well as the calculated curves for the system 1,4-bis-(propylamino)-9,10-anthraquinone (AQ03) + CO_2 [3]. We find a good agreement within the investigated *p*,*T*-range. In contrast to DR60, also Chrastil's equation gives remarkably good results [60], mainly since the particular *p*,*T*-range (pressure region not exceeding 20 MPa) for this system can comply with the specific requirements concerning validity and applicability.

The results of the correlation of the system 1,4-bis-(octylamino)-9,10-anthraquinone (AQ08) + CO_2 is shown in Fig. 9. The agreement is similar to that of AQ03 + CO_2, with the correlations even better [3]. In contrast to AQ03, no vapour pressure data have been published so far for AQ08. That is the reason why we used the saturation pressure as adjustable parameter.

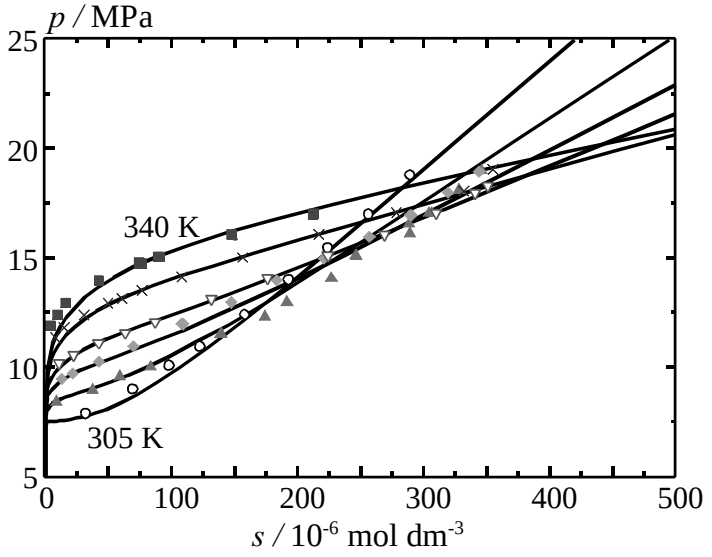

Fig. 8. Experimental (symbols) [60] and calculated solubility isotherms for AQ03 in CO_2 for the temperatures 305 K, 310 K, 315 K, 320 K, 330 K, and 340 K. The corresponding parameters are listed in Table 1, being temperature-independent.

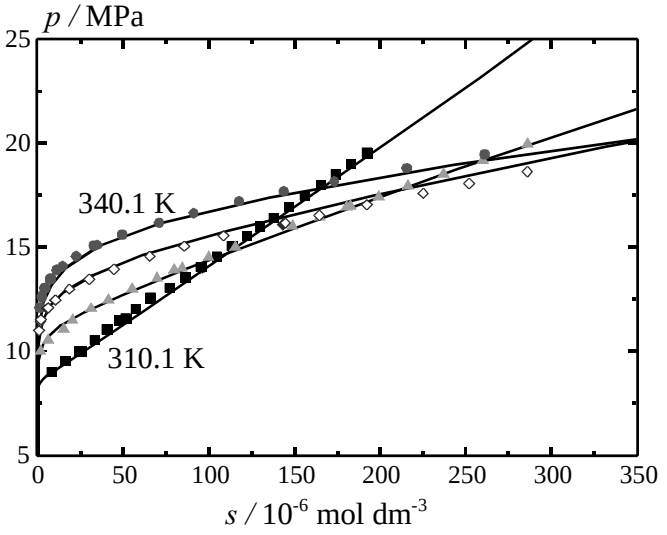

Fig. 9. Correlation of solubility isotherms for AQ08 in CO_2 for the temperatures 310.1 K, 320 K, 330 K, and 340.1 K [61]. The corresponding parameters are listed in Table 1, likewise temperature-independent.

Fig. 10a shows both experimental data [62,63] and calculated solubility isotherms [4] for the system 1,4-bis-(octadecylamino)-9,10-anthraquinone (AQ18) + CO_2. The parameter set of the model is given in Table 1. The model is able to describe the solubility data once again well considering the low solubility. The solubility maximum which has been found experimentally for 330 K, 340 K, and 345 K and which is also indicated by the experimental data at 350 K can be described by the model well, too. At the temperatures 380 K, 400 K, and perhaps also 360 K, due to the melting point drop under CO_2-pressure, AQ18 is most probably molten. However, the $p(s)$-curves in Fig. 10a show no peculiar features indicating this phase change.

Finally, we correlated the solubility of AQ18 in N_2O. For this correlation we used the AQ18 parameters obtained from the correlation of the AQ18 + CO_2 system and took only the cross-interaction parameters k_{12} and l_{12} as adjustable parameters. The obtained values are listed in Table 1. The correlation itself is shown in Fig. 10b. Again, the model is able to correlate the solubility maxima, for which we have data at 310 K, 320 K, and 360 K. This statement is true for the pressure at the maxima. But, the extrapolation of the correlation linked to data up to $s = 60 \cdot 10^{-6}$ mol dm^{-3} towards the high solubility data at 360 K shows deviations in the value of the solubility at the maximum (Fig. 10c). We have then correlated the isotherm at 360 K by adjusting the saturation pressure only. The result is shown as dotted curve in Fig. 10c. The parameters for the latter correlation is listed in Table 1 as parameter set no. 2, whereas the correlation up to $s = 60 \cdot 10^{-6}$ mol dm^{-3} is related to parameter set no. 1 in Table 1. Besides, one can also see well that the isotherm crossing at low pressure is represented by the model.

In Fig. 11 the saturation pressures estimated from the solubility isotherms of the AQ03 + CO_2, AQ08 + CO_2, and AQ18 + CO_2 system are shown in comparison. The saturation pressure obtained in this way appears to show a systematic trend. There is a phase change (melting) in the temperature range for AQ18 and hence the saturation pressure cannot be described by one single function. Since we do not have sufficient data for the supposed phase change, we chose here only one function for the estimation of the saturation pressure.

In Fig. 12 the parameters obtained from the correlation of the solubility data are plotted against the length of the side chains (number of C-atoms) of the AQn series. Fig. 12a shows the chain length dependence of the two volume parameters required in this model. These are the molar volume of the pure solute $V_{m,s}$ and the equation of state volume parameter of the solute b_{22}. One can see that both parameters increase with increasing chain length as expected.

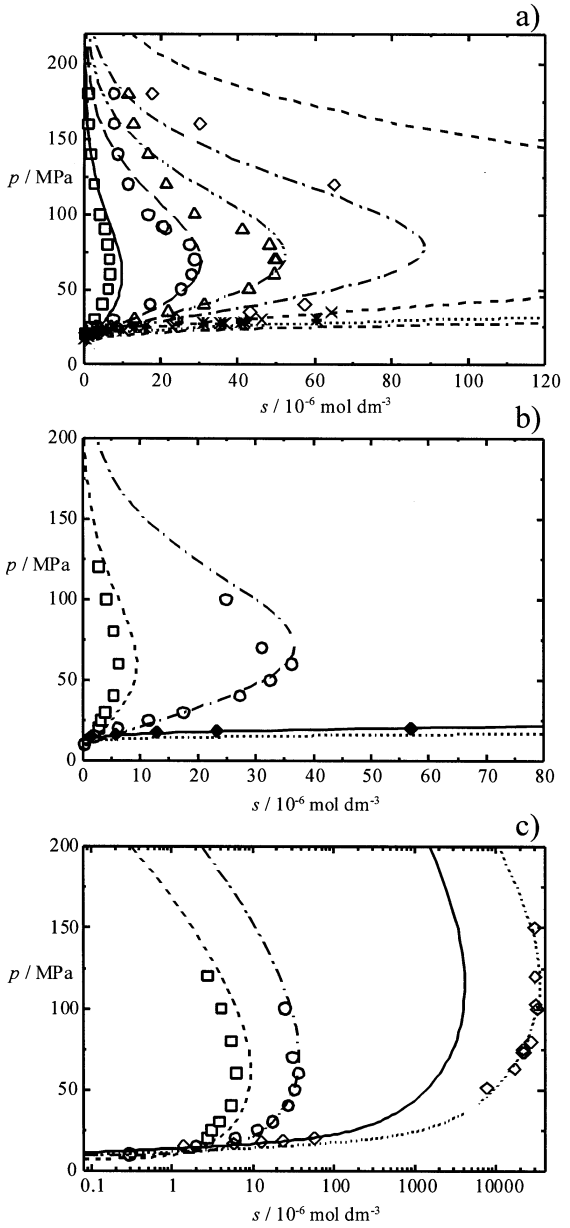

Fig. 10. a) Correlation of the solubility of AQ18 in CO_2. The symbols are the experimental data at the following temperatures: $T = 330$ K (□), $T = 340$ K (○), $T = 345$ K (Δ), $T = 350$ K (◊), $T = 360$ K (+), $T = 380$ K (*), $T = 400$ K (x). b) Correlation of the solubility of AQ18 in N_2O (parameter set 1 in Table 1). The symbols are the experimental data at the following temperatures: $T = 310$ K (□), $T = 320$ K (○), $T = 360$ K (◊), dotted curve: correlations with separate saturation pressure(parameter set 2 in Table 1). c) As b), but in logarithmic scale due to high solubility.

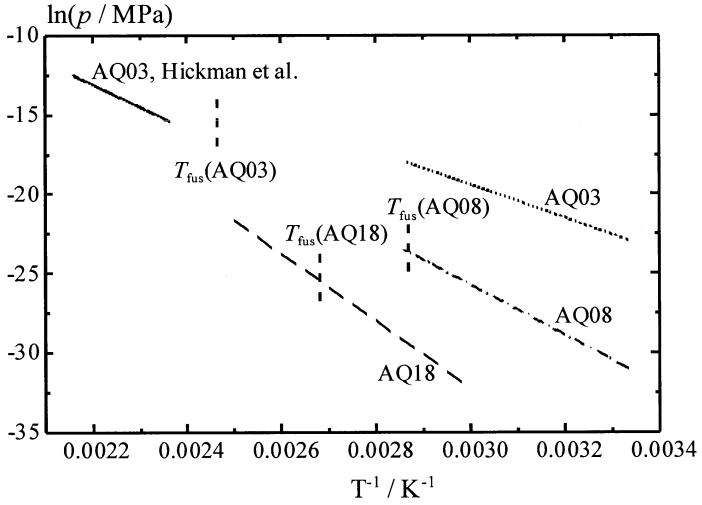

Fig. 11. Comparison of the saturation pressure of AQ18 obtained from the solubility correlations (dashed line). Also shown for comparison are the sublimation pressures of AQ03 and AQ08 as obtained from the solubility correlation (dot-dashed line). The solid line represents direct determination of Hickman et al. [64]. The melting temperatures T_{fus} of AQ03, AQ08, and AQ18 are 406 K, 349 K, and 373 K, respectively [54].

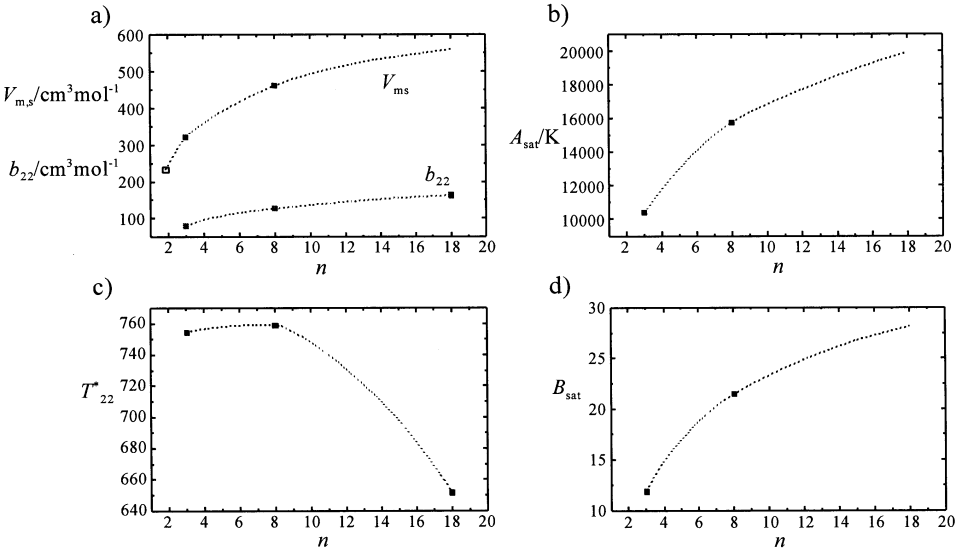

Fig. 12. Correlated equation of state parameters and properties of the pure solid as function of the chain length n of the anthraquinone dyes AQn. a) molar volume of the pure solute $V_{m,s}$ and the equation of state parameter b_{22}; b) parameter A_{sat} of the temperature dependence of the saturation pressure; c) equation of state parameter T^*_{22}; d) parameter B_{sat} of the temperature dependence of the saturation pressure.

The value of the molar volume of AQ02, which has been obtained from X-ray measurements [65], is added in this diagram for comparison. It appears that this value fits into the trend obtained from the analysis of the solubility data done here. The ratio of these two volume parameters is for all systems close to the value four, which is expected from the definition of the *b*-parameter used here. It should be mentioned that these two volume parameters have been correlated independently. As far as one can draw conclusions from these three data sets, it seems that the chain length dependence of the volume parameters decreases with increasing chain length. The two parameters of the saturation pressure equations behave similar, as shown in Fig. 12b and 12d. The only exception is the attraction parameter of the solute T^*_{22}, which increases when going from AQ03 to AQ08 and then decreases towards AQ18, as shown in Fig. 12c. The inverted trend towards lower values with increasing chain length might be explained by the fact that the weakly interacting side chains become larger and the more strongly dipolar interaction by the oxygen atoms (cf. Fig. 2) becomes less dominant or even shielded by the flexible side chains. A similar effect can be observed in the chain length dependence of the melting temperature [54]. In Fig. 11 one can see that the dependence of the melting temperature on the length of the side chain is also not monotonous. Usually, with increasing molecular weight or chain length the triple point temperature and the critical temperature of a substance increase. Hence, one would expect an increasing melting temperature and attraction parameter T^*_{22} for the solute also in the AQ*n* series with increasing *n*. As mentioned above, strong dipolar interaction of the oxygen atoms can be screened by the alkyl-nature side chains. This effect rather leads to a decreasing melting temperature as well attraction parameter with increasing chain length. However, while the attraction parameter T^*_{22} decreases from AQ08 to AQ18, the melting temperature decreases from AQ03 to AQ08. This shift might be explained by packing effects which become important at the melting transition.

6. CONCLUSIONS

A new non-cubic equation of state has been presented and, first of all, successfully applied to correlate the *pVT*-behaviour of several supercritical solvents, such as the customary CO_2 as well as $CClF_3$ or N_2O. In the next step, this equation of state has been successfully applied on the modeling of solubility behaviour of low-volatile organic compounds in these solvents. These are four anthraquinone derivatives, β-carotene, and adamantane. Solubilities in a remarkably broad density range of the solvent have been modeled showing congruity between our theory and the experiments. It is moreover noteworthy to mention that our model predicts the occurrence of solubility maxima regardless whether independently determined or along solubility isotherms fitted saturation pressures are considered. As an additional result, the saturation pressure of the

particular solute, that is the low-volatile substance, can be deduced from the solubility isotherms. The obtained values are in good agreement with literature data if available.

The correlation of the solubility of the anthraquinone dyes shows that the model reliably describes the properties in a homologous series of bis-alkylamino-anthraquinones and that special effects in the molecular interactions can be captured. Above all, the parameters obtained from these correlations have a consistent physical meaning and can thus be employed for the correlation of the low-volatile organic compound in other solvents.

7. ACKNOWLEDGEMENT

The authors thank the Deutsche Forschungsgemeinschaft (DFG; grants KR 1598/3-1, 3-2, as well SCHN 98/22-1 to 22-4) and the Fonds der Chemischen Industrie e. V. for financial support. One of us (K.O.L.) wishes to thank the Käthe-Hack-Stiftung for support. T.K. also acknowledges the support by the Arbeitsgemeinschaft industrieller Forschungseinrichtungen (AiF) and the Bundesministerium für Wirtschaft und Technologie.

REFERENCES

[1] A. Jouyban, M. Rehman, B. Y. Shekunov, H.-K. Chan, B. J. Clark, P. York, J. Pharm. Sci., 91 (2002) 1287.
[2] T. Kraska, K. O. Leonhard, D. Tuma, G. M. Schneider, J. Supercrit. Fluids, 23 (2002) 209.
[3] T. Kraska, K. O. Leonhard, D. Tuma, G. M. Schneider, Fluid Phase Equilibria, 194–197 (2002) 469.
[4] T. Kraska, J. Jurtzik, D. Tuma, G. M. Schneider, Russ. J. Phys. Chem., 77, Suppl. 1 (2003) 51.
[5] D. Tuma, B. Wagner, G. M. Schneider, High-pressure solubility measurement of solids in near- and supercritical fluids, Chapter 1.5., this book.
[6] J. M. H. Levelt-Sengers, Pure & Appl. Chem., 55 (1983) 437.
[7] A. Aharony, M. E. Fisher, Phys. Rev. B, 27 (1983) 4394.
[8] A. M. H. Levelt-Sengers, J. V. Sengers, Phys. Rev. A, 12 (1975) 2622.
[9] B. Widom, J. Chem. Phys., 43 (1965) 3898.
[10] P. Schofield, Phys. Rev. Lett., 22 (1969) 606.
[11] F. J. Wegner, Phys. Rev. B, 5 (1972) 4529.
[12] G. A. Chapela, J. S. Rowlinson, J. Chem. Soc. Faraday Trans. I, 70 (1974) 584.
[13] J. R. Fox, Fluid Phase Equilibria, 14 (1983) 45.
[14] H. W. Wooley, Int. J. Thermophys., 4 (1983) 51.
[15] Z. Y. Chen, P. C. Albright, J. V. Sengers, Phys. Rev. A, 41 (1990) 3161.
[16] A. Krostowicka Wyczalkowska, M. A. Anisimov, J. V. Sengers, Fluid Phase Equilibria, 158–160 (1999) 523.
[17] S. B. Kiselev, J. F. Ely, I. M. Abdulagatov, J. W. Magee, Int. J. Thermophys., 21 (2000) 1373.
[18] S. B. Kiselev, Fluid Phase Equilibria, 128 (1997) 1.
[19] R. Span, Multiparameter Equations of State, An Accurate Source of Thermodynamic Property Data, Springer, Berlin, Heidelberg, New York, 2000.

[20] E. Stahl, K.-W. Quirin, D. Gerard, Verdichtete Gase zur Extraktion und Raffination, Springer, Berlin, Heidelberg, New York, 1987.
[21] J. Chrastil, J. Phys. Chem., 86 (1982) 3016.
[22] T. Kraska, Entwicklung einer Zustandsgleichung für fluide Reinstoffe unter Berücksichtigung des nahkritischen Gebietes, Doctoral Thesis, Ruhr-Universität Bochum, Germany, 1992.
[23] P. C. Hohenberg, B. I. Halperin, Rev. Mod. Phys., 49 (1977) 435.
[24] K. Leonhard, T. Kraska, J. Supercrit. Fluids, 16 (1999) 1.
[25] R. Span, W. Wagner, J. Phys. Chem. Ref. Data, 25 (1996) 1509.
[26] S. Garnier, E. Neau, P. Alessi, A. Cortesi, I. Kikic, Fluid Phase Equilibria, 158–160 (1999) 491.
[27] B. C. L. Weedon, G. P. Moss, in: G. Britton, S. Liaaen-Jensen, H. Pfander (eds.), Carotenoids: Isolation and Analysis, vol. 1A, Birkhäuser, Basel, Boston, Berlin, 1995, pp. 27–70.
[28] G. Britton, S. Liaaen-Jensen, H. Pfander (eds.), Carotenoids, vols. 1–3, Birkhäuser, Basel, Boston, Berlin, 1995–1998.
[29] R. Hartono, G. A. Mansoori, A. Suwono, Chem. Eng. Sci., 56 (2001) 6949.
[30] J. Bauernfeind (ed.), Carotenoids as Colorants and Vitamin A Precursors – Technological and Nutritional Applications, Academic Press, New York, 1981.
[31] Y.-C. Chao, N.-T. Wang, Jiemian Kexue Huizhi (J. Chin. Colloid Interface Soc.), 13 (1990) 27.
[32] Y. C. Chao, Y. L. Chung, C. C. Lai, S. K. Liao, J. C. Chin, Dyes and Pigments, 40 (1998) 59.
[33] M.-W. Park, H.-K. Bae, J. Supercrit. Fluids 22 (2002) 65.
[34] I. Swaid, NIR-spektroskopische Untersuchung zum Phasenverhalten von Decan + CO_2, Adamantan + CO_2 sowie Octacosan + CO_2 im Temperaturbereich 300 bis 450 K und bei Drücken bis 1 kbar, Doctoral Thesis, Ruhr-Universität Bochum, Germany, 1984.
[35] K. Hara, Y. Katou, J. Osugi, Bull. Chem. Soc. Jpn., 54 (1981) 687.
[36] U. K. Deiters, I. Swaid, Ber. Bunsenges. Phys. Chem., 88 (1984) 791.
[37] U. K. Deiters, Fluid Phase Equilibria, 20 (1985) 275.
[38] I. Mokbel, K. Růžička, V. Majer, V. Růžička, M. Ribeiro, J. Jose, M. Zábranský, Fluid Phase Equilibria, 169 (2000) 191.
[39] J. Reiser, E. McGregor, J. Jones, R. Enick, G. Holder, Fluid Phase Equilibria, 117 (1996) 160.
[40] T. E. Jenkins, J. Lewis, Spectrochim. Acta, 36A (1980) 259.
[41] K. Rapcewicz, J. Przystawa, Physica B, 205 (1995) 115.
[42] V. Vijayakumar, A. B. Garg, B. K. Godwal, S. K. Sikka, Chem. Phys. Lett. 330 (2000) 275.
[43] D. Tuma, UV/VIS-spektroskopische Hochdruckuntersuchungen in nah- und überkritischen Fluiden bis 180 MPa – Löslichkeit und Stabilität von Anthrachinonfarbstoffen und β-Carotin in CO_2, N_2O, $CClF_3$ und SF_6, Doctoral Thesis, Ruhr-Universität Bochum, Germany 1999.
[44] D. Tuma, G. M. Schneider, Fluid Phase Equilibria, 158–160 (1999) 743.
[45] D. R. Lide (ed.), CRC Handbook of Chemistry and Physics, 74th ed., CRC Press, Boca Raton, Ann Arbor, London, Tokyo, 1993–1994.
[46] M. L. Cygnarowicz, R. J. Maxwell, W. D. Seider, Fluid Phase Equilibria, 59 (1990) 57.
[47] K. Sakaki, Chem. Eng. Data, 37 (1992) 249.
[48] G. M. Schneider, C. B. Kautz, D. Tuma, in: Ph. Rudolf von Rohr, Ch. Trepp (eds.), Process Technology Proceedings 12, High Pressure Chemical Engineering, Elsevier, Amsterdam, 1996, p. 259.

[49] H.-D. Sung, J.-J. Shim, J. Chem. Eng. Data, 44 (1999) 985.
[50] K. Nishida, E. Ishihara, T. Osaka, M. Koukitu, J. Soc. Dyers Colour., 93 (1977) 52.
[51] L. Anselrode, J. Soc. Dyers Colour., 93 (1977) 201.
[52] D. M. Price, M. Hawkins, Thermochim. Acta 315 (1998) 19.
[53] W. McDowell, J. Soc. Dyers Colour., 89 (1973) 177.
[54] D. Tuma, B. Wagner, G. M. Schneider, Fluid Phase Equilibria, 182 (2001) 133.
[55] D. Tuma, G. M. Schneider, Wissenschaftliche Berichte FZKA 6271 (1999) 155.
[56] J. Eibl, W. Tröger, K.-H. Sender, Melliand Textilber., 58 (1977) 844.
[57] F. Somm, F. Palacin, Melliand Textilber., 64 (1983) 834.
[58] N. Harada, T. Suzuki, Jpn. Kokai Tokkyo Koho JP 2000272251 A2, 2000.
[59] R.-M. Zhou, Y.-Y. Hu, L. Sun, H.-B. Li, Y.-J. Shen, Huadong Ligong Daxue Xuebao (J. East China Univ. Sci. Tech.), 26 (2000) 438.
[60] B. Wagner, Untersuchungen zur Löslichkeit von Anthrachinonfarbstoffen in nah- und überkritischem Kohlendioxid mit einer Strömungsmethode bis 20 MPa, Doctoral Thesis, Ruhr-Universität Bochum, Germany, 1998.
[61] C. B. Kautz, Fluidchromatographische Untersuchungen (SFC) an organischen Substanzen mit überkritischem Kohlendioxid: Bestimmung der Kapazitätsverhältnisse von Polyphenylen und substituierten Benzolderivaten sowie spektroskopische Löslichkeitsuntersuchungen an Anthrachinonfarbstoffen bis 20 MPa, Doctoral Thesis, Ruhr-Universität Bochum, Germany, 1996.
[62] U. Haarhaus, Spektroskopische Hochdruckuntersuchungen zur Löslichkeitsbestimmung von Dispersionsfarbstoffen in überkritischen Gasen bei Drücken bis zu 2 kbar und Temperaturen zwischen 300 und 410 K, Doctoral Thesis, Ruhr-Universität Bochum, Germany, 1992.
[63] U. Haarhaus, P. Swidersky, G. M. Schneider, J. Supercrit. Fluids 8 (1995) 100.
[64] K. C. D. Hickman, J. C. Hecker, N. D. Embree, Ind. Eng. Chem. Anal. Ed. 9 (1937) 264.
[65] G. M. Schneider, D. Tuma, M. Winter, B. Wagner, Z. Kristallogr. NCS, 216 (2001) 299.

Supercritical Fluids as Solvents and Reaction Media
G. Brunner (editor)

Chapter 1.11.

Thermo- and fluiddynamic aspects of the hydrogenation of triglycerides and esters in presence of supercritical fluids

E. Weidner, C. Brake and D. Richter

Process Technology, Ruhr-University of Bochum, Universitätsstraße 150, 44780 Bochum, Germany

1. INTRODUCTION

Since about 100 years hydrogenation of fats and fat derivatives is a widely applied high pressure reaction. Several ten millions of tons of liquid oils of biological origin are hydrogenated annually in order to increase the melting point by reducing the number of (C=C)-double bonds in the fatty acid side chains of the unsaturated triglycerides. The so-called hardened fats are e.g. used for the production of margarine or serve a basis for further chemical transitions [1, 2].

The production of fatty alcohols from fatty acid methyl esters is an example where hydrogenation is applied to fat derivatives. Fatty alcohols are an essential raw material for the production of emulsifiers or detergents. In 1985 about 750000 tons long-chained alcohols (fatty alcohols) were produced by hydrogenation of an ester group at temperatures between 473 and 573 K and pressures between 20 and 30 MPa [3].

Typically the conversion rates for the hydrogenation of liquid compounds as triglycerides or long-chained esters are slow [4]. One reason for that slow conversion is the limited solubility of hydrogen in liquid oils. In order to increase the solubility of hydrogen and thus the reaction rates, hydrogenations are typically carried out at elevated temperature (the solubility of hydrogen in oil increases with rising temperature [2] and pressure in presence of a catalyst. But even then, rather long residence times (minutes to hours) are required to achieve the desired yield. Therefore the typical hydrogenation reactor is either a stirred vessel or a loop reactor, which both allow to establish sufficient contact times and to remove the heat of reaction from the system. The use of large reactor volumes or high circulation rates (in case of a loop reactor) requires sophisticated safety concepts. Additionally the high temperatures and long residence times may result in unwanted byproducts. In case of triglycerides such byproducts are e.g. trans fatty acids, which are considered to be physiologically unfavorable [5].

The hydrogenation of esters to fatty alcohols might lead to alkanes, which requires an additional (and expensive) purification step.

These and other limitations of the classical technologies gave reason to search for alternatives. In the 90´s several proposals on hydrogenation of fats in presence of a supercritical fluid (SCF) were published [6-10]. All authors report on a considerable increase of space velocities compared to conventional techniques. In lab-scaled reactors the reaction rates were several hundred times faster then those of hydrogenations in absence of supercritical fluids.

Comparison of reactions in presence of different supercritical solvents indicate that the kind of supercritical fluid plays an important role on the overall conversion. Härröd e.g. found that the space velocity for the hydrogenation of triglycerides is increased by a factor of 60 in presence of carbon dioxide and by a factor of 700 in presence of propane [8].

It is of high interest to understand why a solvent, which does not take part in the chemical reaction itself, has such a pronounced effect on the overall conversion rate and why different SCF have such different effects.

The thermo- and fluiddynamic behavior under reaction conditions is considered as key for the understanding of the role of the SCF during hydrogenation. In Fig. 1 the phases in the classical reactions are shown qualitatively [11]. The substrate to be hydrogenated is liquid, whereas the hydrogen forms a separate gas phase. The two compounds react with each other on the surface of a solid catalyst. To reach the catalyst, the hydrogen has to be dissolved in the liquid phase. The maximum solubility is defined by the thermodynamic equilibrium, which depends on pressure and temperature. Due to the consumption of hydrogen by the reaction, the equilibrium is disturbed. A concentration gradient is established in the liquid phase and subsequently also at the gas-liquid interface and in the gas phase (see Fig. 1). As the solubility of hydrogen in the liquid is low, the concentration of hydrogen at the surface of the catalyst is also low and thus might limit the rate of reaction.

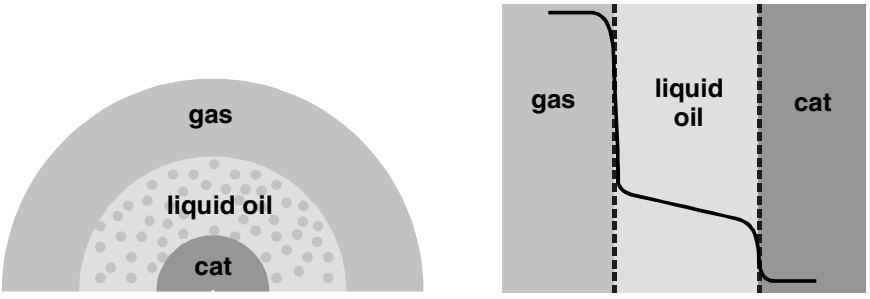

Fig. 1. Hydrogenation of triglycerides by heterogeneous catalysis -number of phases and concentration profile of hydrogen (qualitatively).

The role of the SCF in that system is studied for two different reactions:

- the hydrogenation of triglycerides in presence of carbon dioxide, propane and dimethyl ether at pressures up to 18 MPa and temperatures up to 403 K and
- the hydrogenation of fatty acid esters to fatty alcohols in presence of propane and dimethyl ether at pressures up to about 20 MPa and temperatures up to 573 K at the
  - ♦ reactor inlet for mixtures of methyl esters or ethyl esters with SCF and hydrogen and at the
  - ♦ reactor outlet for mixtures of fatty alcohols, SCF, hydrogen and methanol or ethanol.

Additionally viscosities and densities of selected mixtures were measured.

2. HYDROGENATION OF TRIGLYCERIDES

During hydrogenation of triglycerides double bonds in the fatty acid side chains of the triglyceride molecule are saturated. This reaction results in a considerable increase of the melting point of the hydrogenated product. The type of reaction can be described by the following principle equation:

If the triglycerides are considered as a pure substance or as a pseudo component the reaction system comprises four compounds. It is known that the miscibility of the oils/fats with supercritical fluids at temperatures far above the melting temperature (as they are typical for the reaction) does not depend very strongly on the degree of saturation [12]. So compound A and C possess a similar miscibility with SCF, which allows to reduce the quaternary system to a pseudo ternary system containing triglycerides (A and C), hydrogen (B) and SCF.

The phase behavior of (pseudo-)binary and pseudo ternary mixtures of soybean oil, hydrogen and the supercritical fluids carbon dioxide or propane or dimethyl ether were measured. In addition densities, dynamic viscosities and flow behavior of selected coexisting liquid phases were analysed. For that purpose an integrated plant was used. The principle flow scheme is presented in Fig. 2. For details please see Ref. 11 and 13. The experiments were performed at temperatures of 373 and 403 K in a pressure range between 0,1 and 18 MPa.

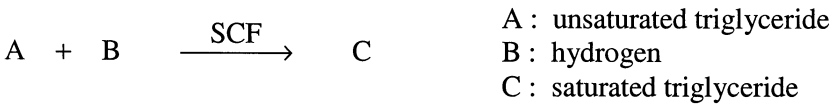

Fig. 2. Reaction scheme of the hydrogenation of triglycerides.

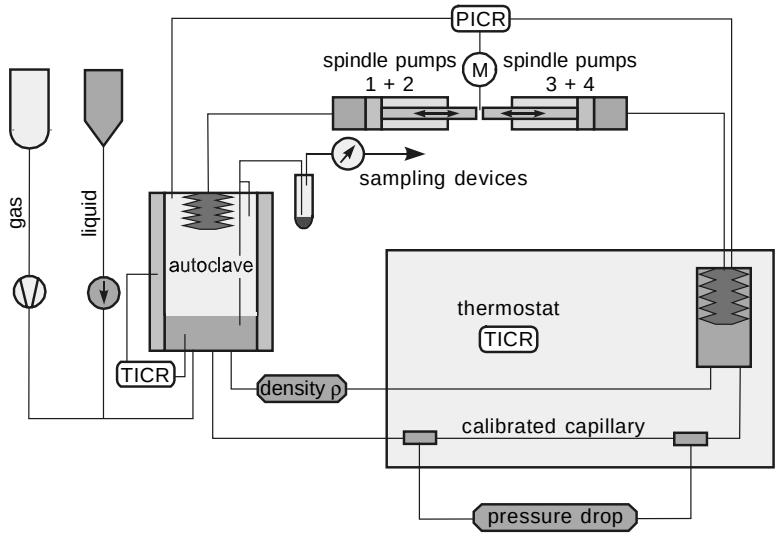

Fig. 3. Simplified flow sheet of the integrated apparatus for measuring phase equilibria, densities, viscosities and flow behavior [13].

The soybean oil is equilibrated in the autoclave in presence of a known amount of SCF and hydrogen. Samples of the upper and the lower phase in the autoclave were taken and analyzed with respect to the mass of triglycerides and the composition of the gases by gas chromatography. Densities were determined by a Paar densitometer. Viscosities were measured by means of a capillary viscosimeter. A sample of the lower phase in the autoclave is conveyed through a calibrated capillary at different volume flows by means of a spindle press system. The pressure drop over the capillary is measured and from flow, density and geometric dimensions of the capillary the viscosity is derived. Performing experiments at different flows allows to investigate the flow behavior of the gas saturated liquids. The flow behavior of the pure oil is newtonian. Also the gas saturated oils flow mostly newtonian.

2.1. Phase behavior of triglycerides and hydrogen with CO_2

A typical ternary diagram of soybean oil, hydrogen and carbon dioxide at pressures and temperature above the critical conditions of carbon dioxide is shown in the center of Fig. 4.

The rectangles on the sides of the triangle represent the phase equilibria of the binary mixtures in pressure-composition plots at two different temperatures. From the rectangle on the right side it can be taken, that carbon dioxide and hydrogen are completely miscible at the investigated conditions, which are supercritical with respect to the critical data of carbon dioxide (7.383 MPa and 304.19 K). The lower rectangle displays the phase behavior between soybean oil and

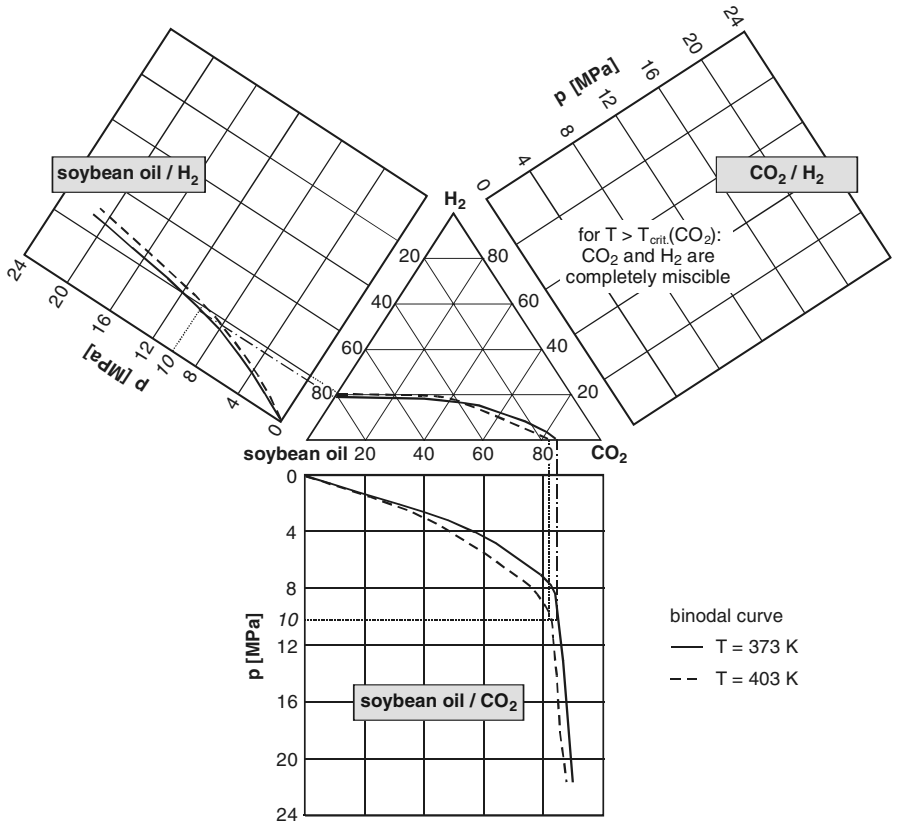

Fig. 4. Phase behavior of soybean oil, hydrogen and carbon dioxide (qualitative).

carbon dioxide. The solubility of oil in the carbon dioxide is very low. Therefore the isotherm is almost identical with the ordinate on the right side.

Whereas carbon dioxide does practically not dissolve the oil, it has a rather good solubility in the oil phase. The solubility of the gas in the oil increases with increasing pressure and/or decreasing temperature.

The binary system hydrogen and soybean oil (left rectangle) shows a different temperature dependency: with increasing temperature, the solubility of hydrogen in oil increases. Additionally the solubility of hydrogen in oil is much lower than that of carbon dioxide.

The dash and dot lines in the binary diagrams illustrate how the binary solubility data are to be transferred into the ternary diagram for a given temperature and pressure. The binary mixing gaps on the lower and left side of the triangle are connected with the binodal curve, which was determined experimentally (for quantitative diagrams see Ref. 11 and 13 and chapter 2.5).

The dotted lines show the transfer of the binary data into the ternary data for a higher temperature at the same pressure. Due to the different temperature dependency of the gas solubilities (carbon dioxide resp. hydrogen) in soybean oil, the binodal isotherms of the ternary system must have an intersection, what was also verified experimentally.

The shaded area in Fig. 4 represents the region where a gas saturated liquid phase coexists with a gas phase, containing mainly hydrogen and carbon dioxide. Due to the very low solubility of soybean oil in the gases the composition of the gas phase is almost identical with the right side of the triangle. The area below the binodal curve corresponds to a one phase region, where the gas mixture is homogeneously miscible with soybean oil.

2.2. Phase behavior of triglycerides and hydrogen with propane

The phase behavior of soybean oil, hydrogen and propane at different pressures and temperatures is shown in Fig. 5.

The hydrogenation reaction in the presence of SCF is typically performed at temperatures around 373K, which is near the critical temperature of propane (369,85 K). Depending on the applied pressure, the binary system propane - hydrogen may either be completely miscible if the temperature is higher than the critical temperature, or show a mixing gap between liquid propane and gaseous hydrogen for subcritical temperatures. In Fig. 5 phase behavior with complete

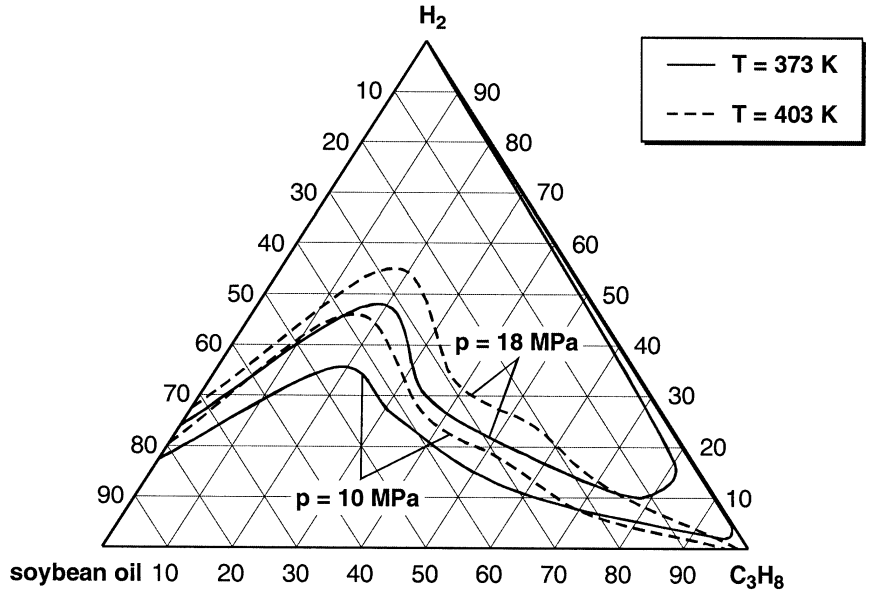

Fig. 5. Phase behavior of soybean oil, hydrogen and propane at different pressures and temperatures [13].

miscibility of the gas and SCF (right side of the triangle) is shown. The lower side of the triangle depicts the solubility between soybean oil and propane. Depending on the pressure also complete miscibility between triglycerides and propane may occur [12]. For a principle study on the different types of ternary phase diagrams to be derived from the binary boundaries see Ref. [13].

As it is shown in Fig. 5 the solubility of hydrogen in soybean oil increases in the presence of small amounts of propane (vicinity of the left side of the triangle). The same behavior was found in the system sunflower oil, hydrogen and propane [14]. The bimodal curves are shown for pressures of 10 and 18 MPa. The solid lines represent the binodal curves at a temperature of 373 K, while the dashed lines are valid for 403 K. The increase in hydrogen solubility in the liquid phase is more distinct at 18 MPa than at 10 MPa. Propane seems to act as a co-solvent. Measurements of the phase behavior at lower pressures (e.g. 2 MPa and 4 MPa) show that the co-solvency disappears. It should be mentioned that the shape of the binodal curve could indicate the presence of a third phase (liquid-liquid de-mixing), but experiments in optical cells did not verify that assumption. On the other hand it is known that such three-phase areas might exist in a very narrow concentration range, which is difficult to reach experimentally.

At higher propane concentration the hydrogen solubility in the liquid oil phase passes a maximum, followed by a minimum. This behavior differs from that of the carbon dioxide systems and can be understood from the different solubilities in the binary systems (see above). The region of complete miscibility between hydrogen, propane and soybean oil is much larger, than that in the carbon dioxide system.

2.3. Phase behavior of triglycerides and hydrogen with dimethyl ether

The ternary diagram of soybean oil, hydrogen and dimethyl ether (DME) at different temperatures and pressures is shown in Fig. 6.

The principle behavior is similar to that in the propane system. At a temperature of 403 K also a maximum-minimum shape of the binodal curve is found. At a temperature of 373 K dimethyl ether is subcritical (T_{crit}= 400,29 K) and thus a mixing gap between liquid DME and gaseous hydrogen occurs.

The region of complete miscibility between soybean oil, dimethyl ether and hydrogen is larger than that in the propane system, which indicates that dimethyl ether is a slightly better solvent than propane.

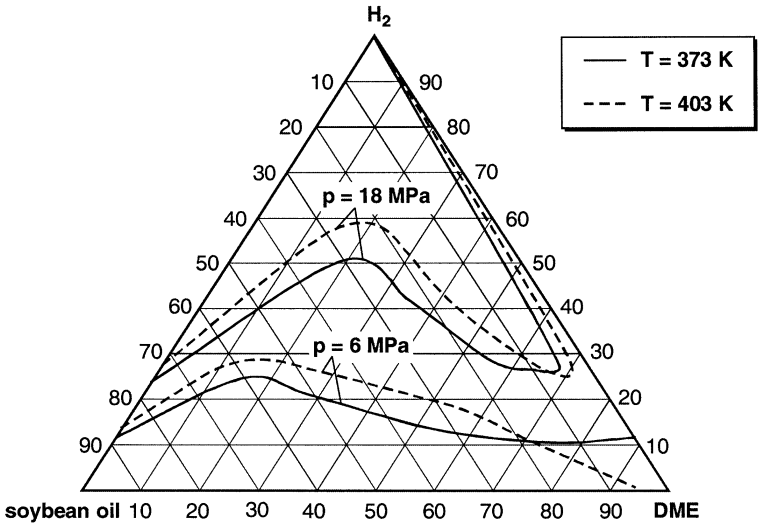

Fig. 6. Phase behavior of soybean oil, hydrogen and dimethyl ether at different temperatures and pressures [13].

2.4. Density and dynamic viscosity

Adding SCF to a mixture of soybean oil and hydrogen changes the phase behavior considerably. Additionally, the properties of the gas saturated liquids are to be taken into account in order to analyze the differences in space velocities of the hydrogenation reaction (see above).

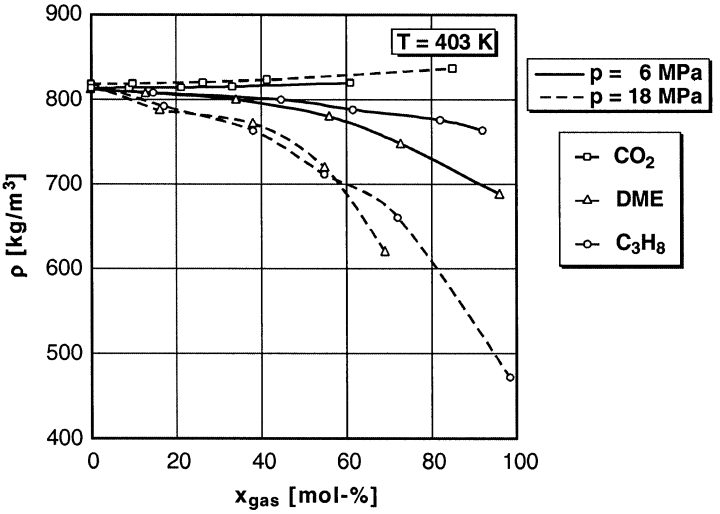

Fig. 7. Influence of supercritical fluids on the density of the gas saturated liquid phase [13].

Adding a supercritical fluid to a mixture of soybean oil and hydrogen influences the density of the gas saturated liquid considerably (Fig. 7). In ternary systems the density of the liquid phase slightly rises with increasing concentration of carbon dioxide. This behavior was found for both investigated temperatures (T = 373 K not shown in Fig. 7). It is quite similar to known density dependencies in binary systems with carbon dioxide (see e. g. Ref. 14-16).

Contrary to the systems with carbon dioxide, adding increasing amounts of propane or dimethyl ether to soybean oil that is saturated with hydrogen leads to a reduction of the density. The effect of dimethyl ether is slightly larger than that of propane.

The influence of the supercritical fluids on the dynamic viscosity of the gas-saturated oil rich liquid phase is shown in Fig. 8.

At low concentrations of SCF all three investigated SCFs act as a diluent, which means that the viscosity of the oil rich phase is reduced. At higher concentrations propane and dimethyl ether further reduce the viscosity, while adding more carbon dioxide results in a viscosity increase.

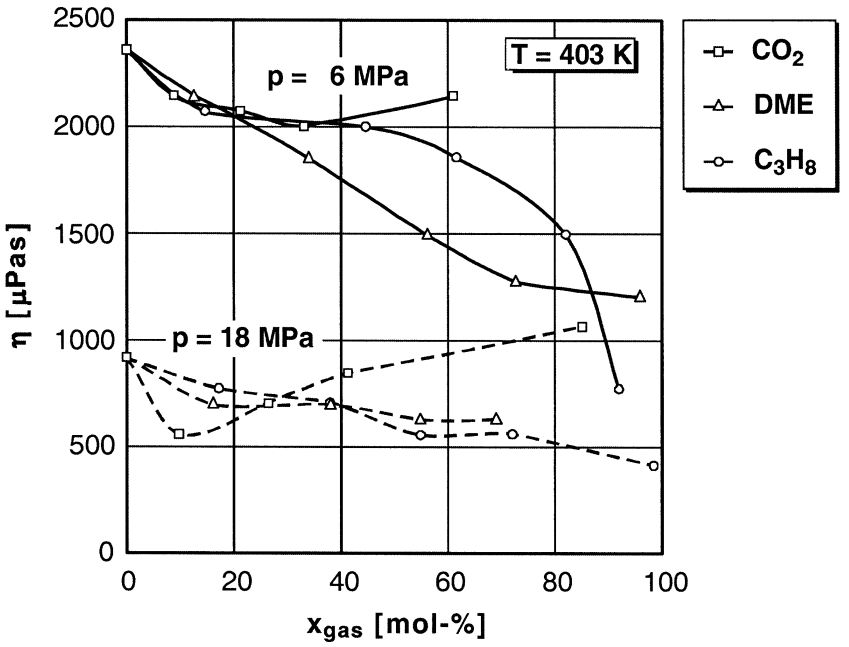

Fig. 8. Influence of supercritical fluids on the dynamic viscosity of the gas saturated liquid phase [13].

2.5. Discussion

Phase behavior and viscosity help to understand the differences in space velocities of the hydrogenation of double bonds in triglycerides in the presence of different supercritical fluids.

In Fig. 9 the phase behavior in the system soybean oil, hydrogen and carbon dioxide is shown quantitatively in molar concentrations. To hydrogenate one double bond per molecule of triglyceride the stoichiometric demand is one mol of hydrogen per mol triglyceride, which corresponds to a concentration of 50 mol% in the binary mixture (left side of the triangle). The solubility of hydrogen in pure oil is far below that value (10 to 28 mol-%, depending on the applied pressure). Thus the required hydrogen has to be delivered from a gas phase, which leads to a reaction system with a gas-liquid interface (see Fig. 1).

Adding carbon dioxide to a 50/50 mixture of soybean oil and hydrogen is represented by the straight mixing line in Fig.. The mixing line lies in the two-phase area over the whole concentration range. The observed increase in space velocity in presence of carbon dioxide might be attributed to a change in the ratio between hydrogen and oil in the liquid phase. This is illustrated for the tangential point between the binodal curve and the mixing line at 18 MPa. At this point (approx. 55 mol-% carbon dioxide) the molar ratio between hydrogen and oil reaches 1 : 1. On the one hand carbon dioxide reduces the overall concentration of triglycerides and hydrogen, but on the other hand the ratio between the two compounds is shifted towards the minimum required stoichiometry. As the viscosity of the oil rich phase increases with the addition of larger amounts of

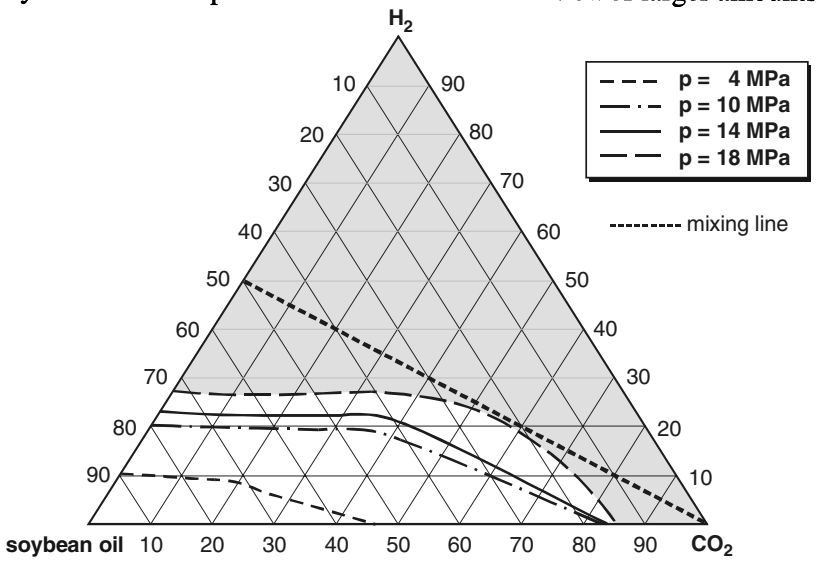

Fig. 9. Hydrogenation of triglycerides in presence of supercritical carbon dioxide - phase behavior and mixing line.

carbon dioxide (see Fig. 8) it is concluded that the viscosity is of less relevance for the increase in space velocity than the stoichiometric ratio.

The diagram shown in Fig. 10 illustrates phase conditions during hydrogenation in presence of supercritical dimethyl ether both at low pressure and high pressure. The mixing line once again starts at 50 mol-% of hydrogen in oil. At low pressure (6 MPa) it can be seen that a gas phase and a liquid oil rich phase are present up to a concentration of approx. 80 mol-% of dimethyl ether (T = 373K). Above that concentration the mixture is present in one homogeneous phase. The number of interfaces in the reactor is reduced and the stoichiometric ratio between hydrogen and soybean oil can be chosen in a wide range of composition, independent from phase equilibrium restrictions.

As it is shown in Fig. 10 the homogeneous region is reached at much lower dimethyl ether concentrations at a pressure of 18 MPa, which allows even higher ratios between hydrogen and oil than at 6 MPa. The same observations are made for propane, but with propane slightly higher concentrations of SCF are required to achieve complete miscibility.

The increase of reaction rates in presence of SCFs as solvents for hydrogenation of triglycerides is to be understood via

- a shift of the stoichiometric ratio between hydrogen and oil in the liquid, oil-rich phase to higher values if carbon dioxide is applied and
- the formation of a homogeneous reaction mixture at moderate pressures if propane or dimethyl ether are used. Mass transfer resistances of the transport of hydrogen prevailing in the traditional heterogeneous system are overcome.

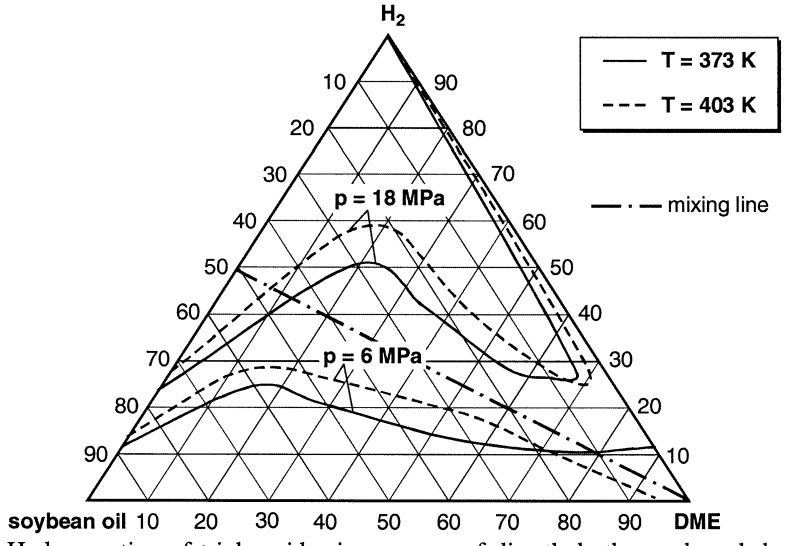

Fig. 10. Hydrogenation of triglycerides in presence of dimethyl ether - phase behavior and mixing lines.

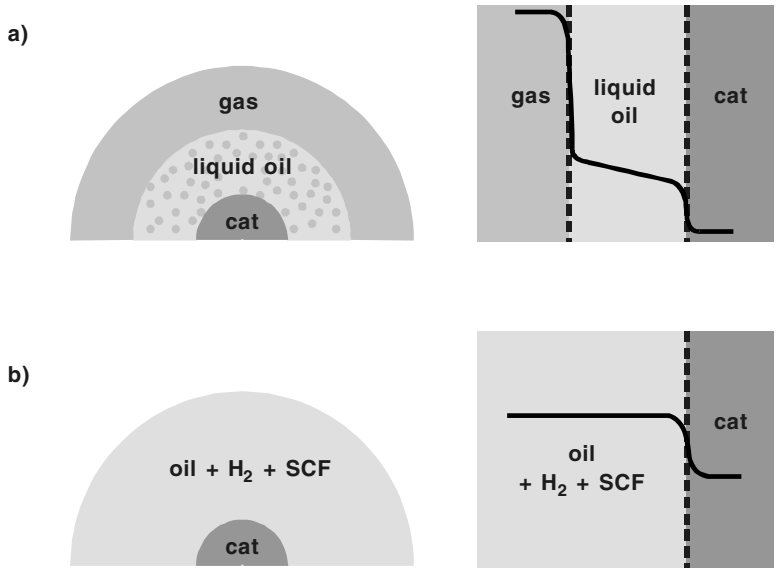

Fig. 11. Hydrogenation of triglycerides by heterogeneous catalysis - number of phases and concentration profile (qualitatively) at a) classical hydrogenation and at b) hydrogenation in presence of suitable SCF.

This is further illustrated in Fig. 11, where the number of phases during the classical hydrogenation and the hydrogenation in presence of dimethyl ether or propane are compared with each other.

The ratio between hydrogen and oil can almost freely be chosen if a suitable SCF and conditions (p, T) are applied. From the reduction of the number of interfaces the considerable differences between the effect of different SCF on the hydrogenation of triglycerides can be understood.

3. HYDROGENATION OF FATTY ACID ESTERS

The principle reaction scheme of the hydrogenation of fatty acid esters is more complex than that of the hydrogenation of triglycerides (compare Fig. 2 and Fig. 12).

$$D + E \xrightarrow{SCF} F + G$$

D : fatty acid ester
E : hydrogen
F : fatty alcohol
G : short-chain alcohol

Fig. 12. Reaction scheme of the hydrogenation of fatty acid esters.

Starting material for the generation of fatty acid esters can be triglycerides. By a homogeneous catalyzed reaction between triglycerides and a short-chained alcohol (mostly methanol, seldom ethanol) fatty acid esters (D) are formed. The ester group reacts with hydrogen (E) to form the fatty alcohol (F) and a short-chained alcohol (G, which is either methanol or ethanol).

If unsaturated triglycerides are used, the fatty acid esters (D) contain double-bonds. Depending on the catalyst, these double-bonds may hydrogenate in a second reaction (not shown in Fig. 12). As the thermo- and fluiddynamic boundary conditions of the hydrogenation of double-bonds is described above, the second part of the paper is focused only on the hydrogenation of the ester group.

As the esters does not as readily react with hydrogen as the double bond, higher pressures and temperature (20 - 30 MPa, 473 - 573 K) have to be applied [3, 17]. Also for the hydrogenation of the ester group a considerable increase in space velocities and reaction rates are reported [18, 19]. As can be seen from Fig. 12, at least five components are present in the reaction mixture. In contrast to the reaction product of the hydrogenation of triglycerides (saturated triglycerides), which possess a similar solubility in SCF like the unsaturated compounds, the reaction products of the hydrogenation of fatty esters (fatty alcohols and short-chained alcohols) are known to have a different phase behavior with SCFs than the fatty acid esters [20-24]. Additionally the short-chained alcohol formed during the reaction has to be removed before the hydrogen and the SCF are recycled.

This requires a closer look not only on the reaction, but also on the removal of the fatty alcohol, the separation of the short-chained alcohol and the recycling of hydrogen and SCF. A detailed experimental thermodynamic study of such a complex system would be very time consuming and expensive. Therefore an approach is demonstrated, where a combination of process analysis, predictive modelling and experimental verification allows to study the influence of the SCF on the overall hydrogenation process.

Based on the reaction a simplified block diagram for the process was developed (Fig. 13). The shaded process steps are considered to be most relevant for the process analysis.

Reactor: Similar to the hydrogenation of (C=C)-double bonds, high reaction rates of the hydrogenation of fatty acid esters are reached, if the reaction proceeds in homogenous phase [18, 19]. So it is necessary to determine the one phase region, depending on the composition of the reaction mixture (three compounds: fatty acid ester, hydrogen, SCF), pressure and temperature at the reactor inlet. Assuming complete conversion (without byproducts like e. g. alkanes), the mixture leaving the reactor contains four compounds (fatty alcohol, short-chained alcohol, hydrogen (surplus) and SCF). Because the one phase region should prevail during the whole reaction, also the phase behavior at the reactor outlet has to be studied.

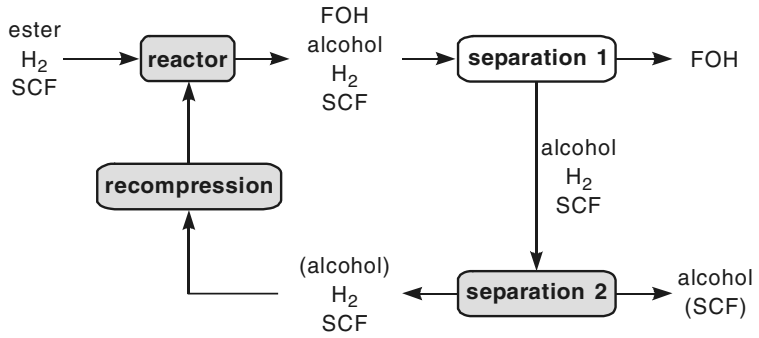

Fig. 13.Block diagram for the hydrogenation of fatty acid esters to fatty alcohols.

Separation 1: Fatty alcohols have a boiling point which is distinctly higher than that of all other compounds leaving the reactor. Therefore the separation of the fatty alcohol ("separation 1", see Fig. 13) can be achieved quite easily by reducing pressure and temperature in a first flash expansion stage. The fatty alcohol precipitates from the homogeneous reaction mixture and is withdrawn as a liquid from the bottom of separator 1. It has to be further purified by removing traces of short-chained alcohols, SCF and hydrogen (not shown in Fig. 13). Separation 1 and the purification of the fatty alcohol is not described in this paper.

Separation 2: The removal of the short-chained alcohol from the mixture leaving separation 1 is a crucial step of the whole process, because the hydrogen and SCF has to be recycled preferably without any residual reaction product. The phase behavior of the mixtures of this second separation step was analyzed in order to determine what qualities of bottom and top product can be obtained (bottom product = short-chained alcohol, top product = hydrogen and SCF).

Recompression: Temperature, pressure and the dimensions of the columns/apparatuses used in separation 2 are derived from the maximum allowable content of short-chained alcohol to be recycled into the reactor. The underlying phase behavior depends on the kind of supercritical fluid used. So the SCF does not only influence the reaction, but is also of significant influence on product recovery and gas recompression. Therefore the effect of two different supercritical fluids (propane and dimethyl ether) was studied.

Methods [24, 25]: The phase behavior was measured as well as calculated with several equations of states (EoS). The measurements were performed in a high-pressure view cell with a variable volume between 24 to 57 cm^3 and a maximum measuring temperature of 473 K. Methyl and ethyl oleate were used as model substances for fatty acid esters and propane and dimethyl ether were used as supercritical fluids. Pure 1-octadecanol was taken as product of the hydrogenation. The compositions of the mixtures for the thermodynamic study

were chosen according to those that are published to give highest reaction rates [18].

The calculations were performed with Aspen Plus®, version 11.1. The following equations-of state were used:

- Standard Peng-Robinson (PENG-ROB),
- Standard Redlich-Kwong-Soave (RK-SOAVE),
- Soave-Redlich-Kwong (SRK),
- Predictive Soave-Redlich Kwong (PSRK),
- Schwarzentruber-Renon for polar compounds (SR-POLAR),
- Redlich-Kwong-Aspen (RK-Aspen).

The binary interaction parameters, except those for the fatty components, were taken from the data base of the simulation program or calculated by regression of vapor-liquid-equilibria [26-38]. The results of calculations were compared with the experimental data in all cases. The best fitting equations were determined and applied for further modelling of the process steps.

3.1. Phase behavior in the reactor for systems containing propane

The EoS by Schwarzentruber and Renon gave the best description for mixtures containing propane. As an example, the measured pT-envelope of a mixture of ethyl oleate, hydrogen and propane is compared to the calculated data in Fig. 14 (for further information see Ref. 25).

The region above the *p,T*-envelope indicates pressures and temperatures, where the mixture of that specific composition is present in one homogeneous phase. Below the *p,T*-envelope two or more phases are present.

In general the SR-POLAR EoS calculates slightly higher pressures (0,5 to 1,5 MPa) for the phase envelope as actually measured.

The calculated *p,T*-envelopes of mixtures containing methyl oleate respectively ethyl oleate are compared in Fig. 15. In the lower temperature range, there are only small differences in the mixtures vapor pressure. Here the solubility of the supercritical fluid is dominating the phase behavior. At higher temperatures systems with methyl oleate require lower pressures to reach the one phase area, which is probably due to the lower boiling temperature compared to ethyl oleate.

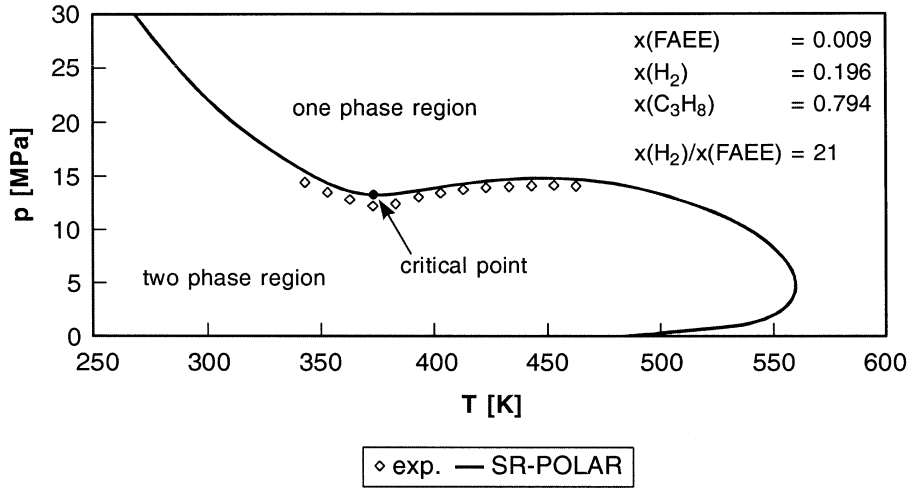

Fig. 14. Measured and calculated pT-envelope of a mixture of ethyl oleate (FAEE), hydrogen and propane (C_3H_8).

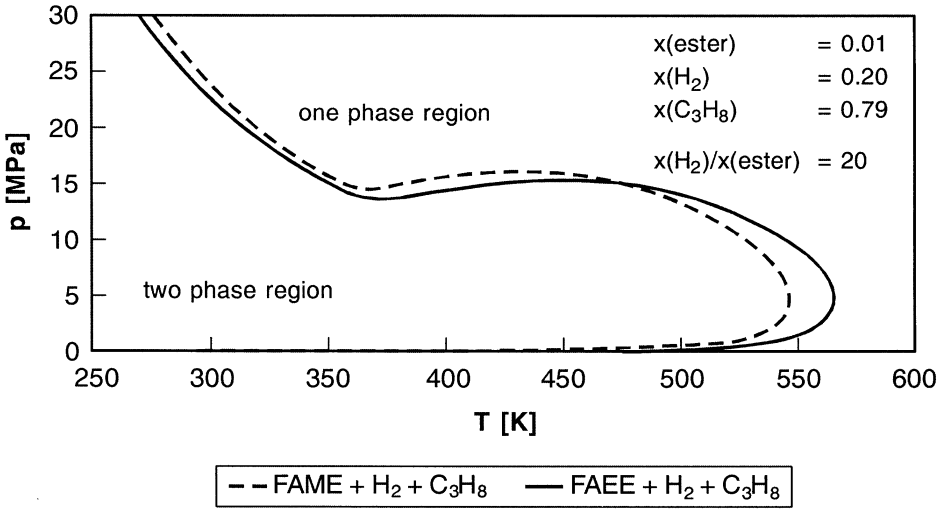

Fig. 15. Calculated pT-envelope of mixtures containing of methyl oleate (FAME) respectively ethyl oleate (FAEE), hydrogen and propane (C_3H_8).

3.2. Phase behavior in the reactor for systems containing dimethyl ether

Like for propane systems, all equations predict higher vapor pressures. Again the SR-POLAR EoS turned out to give the best fit (see Fig. 16) also for mixtures containing dimethyl ether.

The p,T-envelopes of mixtures containing methyl oleate respectively ethyl oleate are compared in Fig. 17. A similar behavior like in the systems with propane was found.

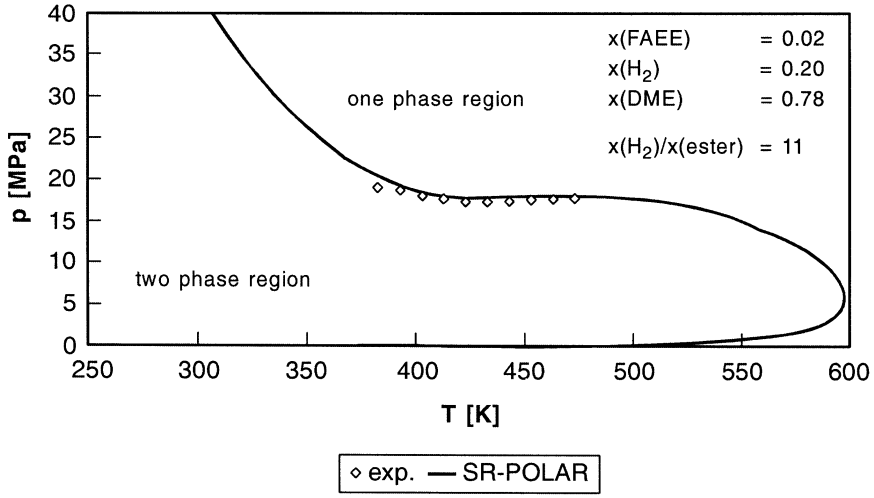

Fig. 16. Measured and calculated pT-envelope of a mixture of ethyl oleate (FAEE), hydrogen and dimethyl ether (DME).

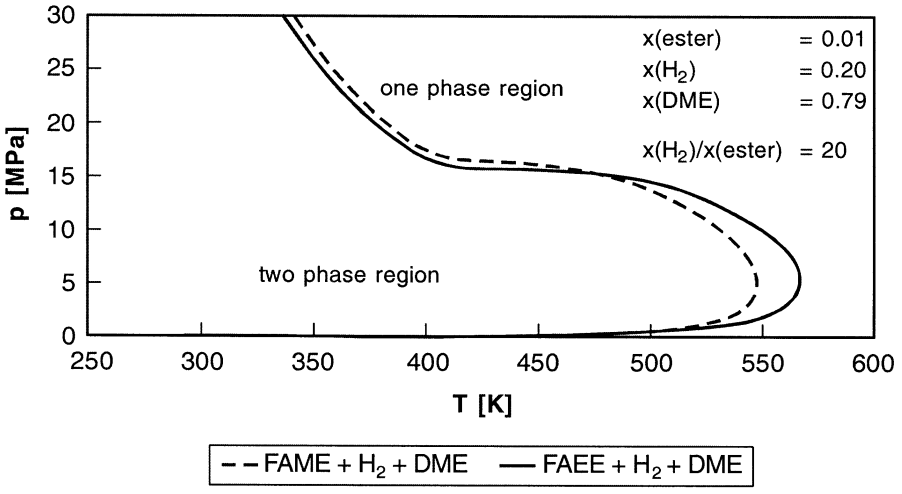

Fig.17. Calculated pT-envelopes of mixtures containing of methyl oleate (FAME) respectively ethyl oleate (FAEE), hydrogen and dimethyl ether (DME)

At low temperatures, the vapor pressures in the systems with propane and dimethyl ether are in the same range. With DME, the two-phase area is extended to slightly higher temperatures than with propane. The phase envelopes depend very strongly on the composition. At higher concentrations esters and/or higher hydrogen surplus, considerably higher pressures are required to reach the one phase region. For further information see Ref. 25.

As mentioned above, additionally the phase behavior at the reactor outlet was investigated. It was found that the deviations in the phase envelopes between inlet and outlet are in the same range as between ethyl esters and methyl esters [25]. Having in mind that a certain distance to the vapor pressure has to be kept in a "real reactor" to take care of pressure losses and uncertainties of the phase behavior of intermediate products and byproducts, it can be concluded that a first approach to one phase conditions can be derived from the ternary phase behavior in the system fatty acid ester, hydrogen and propane or dimethyl ether.

3.3. Phase behavior in separation

While methanol is formed when methyl oleate is used as educt, ethanol is generated in case of ethyl oleate as educt for the production of 1-octadecanol. So the phase behavior in the separation step has to be investigated regarding not only the supercritical fluid but also the short-chained alcohol.

The phase envelope of ternary mixtures containing propane, hydrogen and either methanol or ethanol can be described best by the PSRK EoS (Fig. 18). For systems containing dimethyl ether, a better fit with experimental data was achieved by the PENG-ROB EoS (Fig. 19).

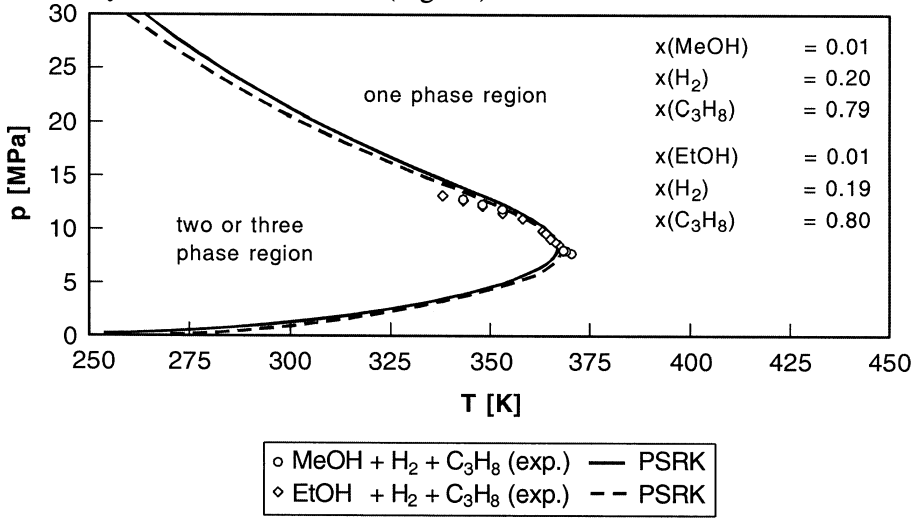

Fig. 18. Measured and calculated pT-envelopes of mixtures containing methanol (MeOH) respectively ethanol (EtOH), hydrogen and propane (C_3H_8).

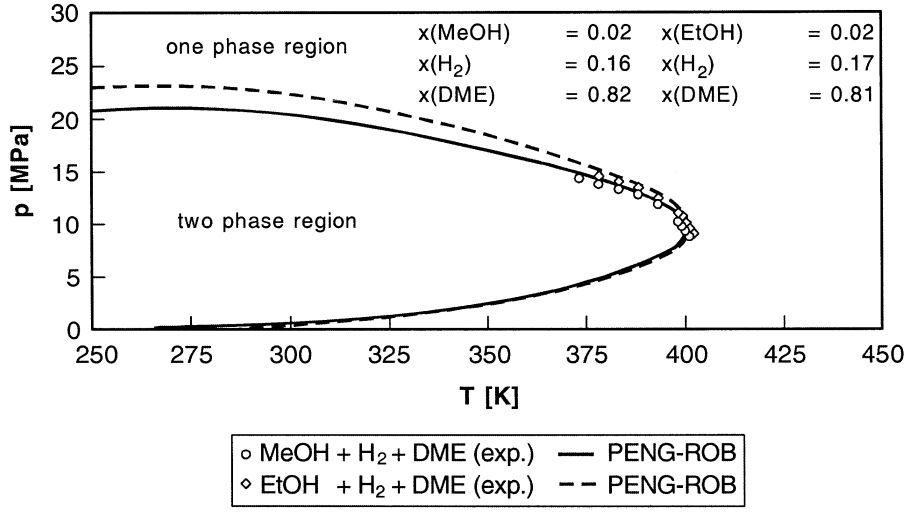

Fig. 19. Measured and calculated pT-envelopes of mixtures containing methanol (MeOH) respectively ethanol (EtOH), hydrogen and dimethyl ether (DME).

The *p,T*-envelopes for both short-chained alcohols differ only slightly. A comparison of the *p,T*-envelopes at identical molar compositions (Fig. 20) shows that the two phase area in DME-systems extends to considerably higher pressures than in systems containing propane.

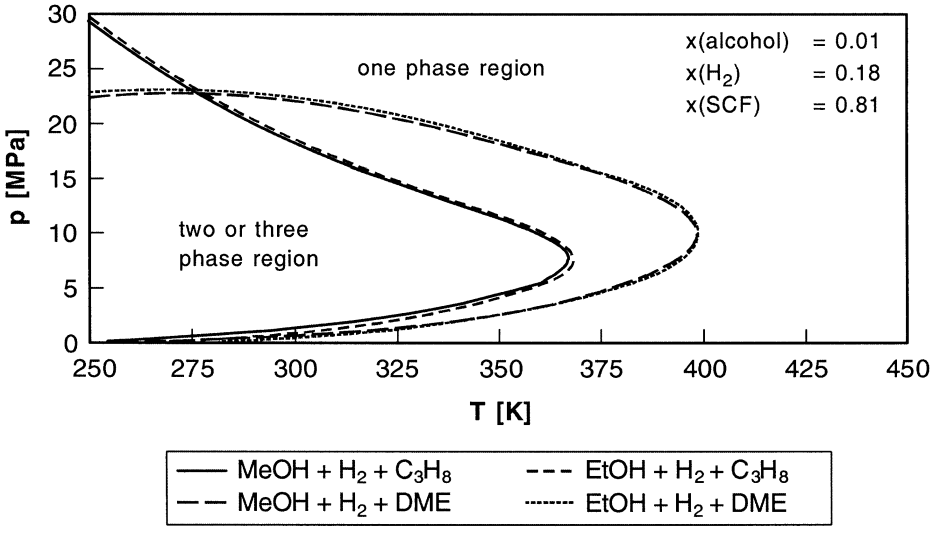

Fig. 20. Calculated pT-envelopes of mixtures containing methanol (MeOH) respectively ethanol (EtOH), hydrogen and propane (C_3H_8) respectively dimethyl ether (DME).

The removal of the alcohols from hydrogen and SCF in separation 2 can be achieved by distillation. In case of dimethyl ether, the pressure and temperatures at which the distillation is carried out are considerably higher than for the propane systems. Concerning the costs for recompression of hydrogen and SCF, which are a dominating part of the operation costs, higher pressures in separation 2 are to be preferred. Concerning product quality and especially the residual alcohol content in the gases removed as top product of separation 2, it is not sufficient to consider only phase envelopes. Additionally separation factors must be taken into account.

Binary systems of propane and methanol form an azeotrope at elevated pressure [36], which, as indicated by equilibrium calculations, probably exists also in the presence of hydrogen. Thus the concentration of methanol in the recycling gas is given by the azeotropic composition. If that concentration is unacceptable for the reaction an additional purification step for breaking the azeotrope is required. This could be achieved either by

- a second distillation, operated at a different pressure or by
- operating separation 2 at very low pressures where the azeotrope disappears or by
- absorption/extraction of methanol, e.g. with ethylene glycol [39].

All these methods are connected with increased technical complexity of the plant and/or increased costs. Alternatively it can be considered to avoid systems where azeotropes are formed by choosing an appropriate SCF or short-chained alcohol.

Propane and ethanol for example do not form an azeotrope; so if ethyl esters are hydrogenated in presence of propane, in principle pure mixtures of hydrogen and SCF can be recycled into the reactor. Similar behavior was found for combinations of DME with methyl esters or ethyl esters.

4. 3. Recompression

The phase envelopes for mixtures of alcohols, hydrogen and SCF indicate that pressures between 0,5 and 4 MPa have to be established in separation 2. To reach homogeneous conditions in the reactor, pressures of about 15 - 30 MPa are required.

The binary phase diagram (T,x,y) between propane and hydrogen serves to illustrate several possibilities for recompressing hydrogen and SCF.

The gaseous mixture of hydrogen and SCF leaving separation 2, which is represented by V1 in the vicinity of the dew line in Fig. 21, can be recompressed by means of a gas compressor (Version 1). Depending on the compressibility, several stages can be required. The size of the compressor heads can be derived from the density ratio between suction and discharge pressure. The calculated densities ratios are shown in Fig. 22.

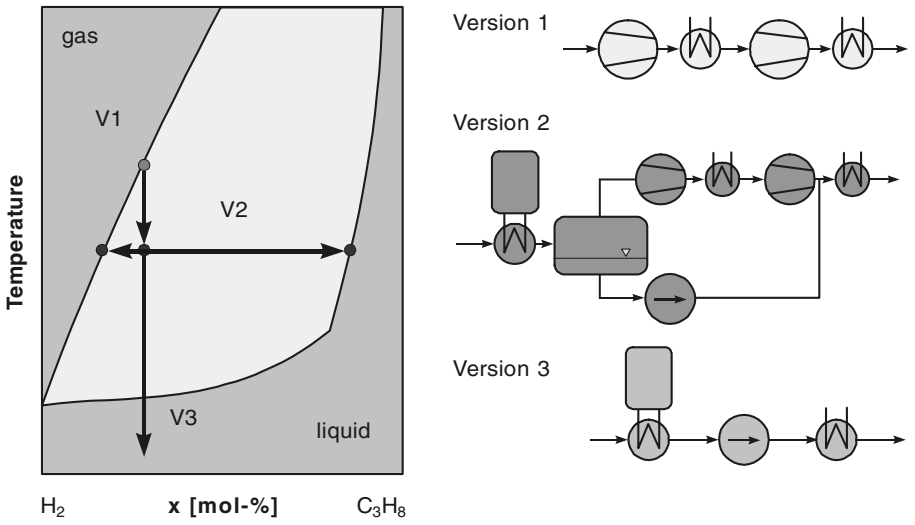

Fig. 21. Recompression of hydrogen and SCF.

To generate this diagram, densities of various mixtures of hydrogen and propane were measured by a magnetic suspension balance. The PSRK EoS, which was also suitable for the vapor-liquid phase equilibria of the binary mixture, fits the experimental data very good. The densities on the suction side of the compressor are calculated for a pressure in separation 2 of 0,5 MPa for using pro-

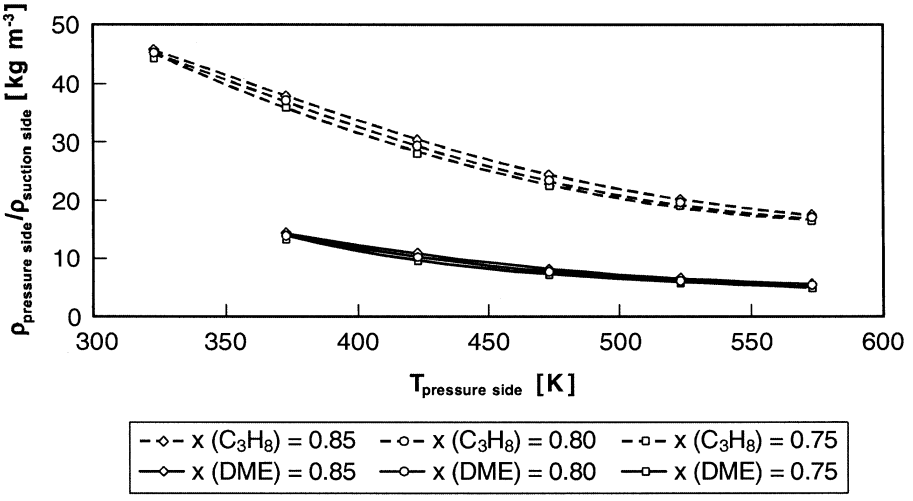

Fig. 22. Calculated density ratios for the recompression of hydrogen and propane (C_3H_8) respectively dimethyl ether (DME) [PSRK EoS].

pane and 2 MPa for using dimethyl ether as SCF. The densities on the pressure side were calculated at different end temperatures and at a pressure of 20 MPa.

The density ratios of mixtures containing dimethyl ether are lower than those of mixtures containing propane, which means that in case of recompressing gaseous mixtures by a multistage compressor smaller pump heads and less energy are required.

Nevertheless for the final concept alternative technical solutions should be considered. To reduce the volume to be recompressed, the gaseous mixture of hydrogen and propane can be cooled. If the temperature lies in the two phase area, a condensed liquid propane phase that contains less hydrogen than the initial mixture (see Fig. 21 , V2), can be compressed by means of a pump, while the hydrogen rich coexisting gas phase can either be vented or recompressed by a gas compressor (Version 2). Considering that hydrogen is rather expensive, it is probably recommendable to recycle it.

A third alternative, illustrated by V3 in Fig. 21, allows to recompress the whole mixture by a single liquid pump (Version 3). The gaseous mixture is completely liquified and subcooled. Due to the low boiling temperature of hydrogen complete condensation requires rather low temperature (typically lower then 200 K, depending on the pressure in separation 2). In that case the advantage of using a single liquid pump is at least partly reduced by the costly equipment for generating the low temperatures.

3.5. Discussion

Similar to the rate of hydrogenation of double bonds in triglycerides, the rate of hydrogenation of the ester group in fatty acid esters can be increased considerably in presence of supercritical fluids. By a combination of selected experiments and calculation of phase behavior it was shown, that in a reactor both for methyl esters and ethyl esters homogeneous mixtures with hydrogen can be established either in presence of propane or dimethyl ether. At comparable compositions, dimethyl ether requires slightly lower pressures than propane. The pressure increases considerably with rising concentration of esters, which is favorable with respect to the throughput through a given reactor volume. The pressure also rises with increasing hydrogen surplus, which would increase the reaction rate.

By combination of experiment and modeling, suitable EoS for describing the phase behavior were identified. Integrating the EoS in a simulation program like Aspen Plus® allows to calculate the phase behavior in a rather short time for a wide range of composition, temperature and pressure. Suitable thermodynamic conditions for carrying out the reaction can be derived both for the reactor inlet and outlet. It is recommendable to verify experimentally the calculated values, e. g. by measuring the phase envelope at a given composition in an optical cell.

To answer the question which SCF is to be preferred, it is required not only to consider the reaction, but the overall process. For this purpose a simplified flow scheme was proposed and the key steps were identified. Again the combination of experiments, literature data (in case of binary equilibria) and calculations helped to analyze the process and to define thermodynamic boundary conditions for product recovery and the recycling of hydrogen and SCF. The removal of the reaction product with intermediate volatility (short-chained alcohol) requires a separate separation step. In the performance of that specific stage, large differences occur when either propane or dimethyl ether are used. The differences in product recovery (e.g. the avoidance of azeotropes) are probably of higher relevance for the overall performance of the process than those in the reactor.

4. SUMMARY

Hydrogenation of liquids in presence of supercritical solvents can be much faster than at conventional conditions. SCF may increase the ratio between "available" (= liquid-dissolved) hydrogen. If SCF with better solvent properties are applied, even homogeneous conditions can be established, which result in higher rates than just adding a supercritical solvent to a two phase system. If the rate is to be maximised, the SCF with the best solubility for the substance to be hydrogenated allows to run the reaction at the highest concentration and/or lower pressures or temperatures.

For the hydrogenation of (C=C)-double bonds in triglycerides it was found, that the solvent power of the SCFs increases from carbon dioxide over propane to dimethyl ether. For carbon dioxide it was not possible to reach a homogeneous mixture, which corresponds to the finding that the rates in the presence of carbon dioxide are lower than in the presence of propane, which is a solvent, that allows to reach homogeneous conditions at rather moderate pressures.

The knowledge of the typically complex phase behavior in near- or supercritical systems is essential for planning hydrogenations and for interpretation of the results. For binary or ternary systems, experimental studies on thermo- and fluiddynamics are feasible. For systems with a larger number of compounds, a combination of predictive modeling, experimental verification and optimization of the models is a suitable method for choosing and comparing SCFs, identifying boundary conditions of the reactions and for designing processes.

On the example of hydrogenation of fatty acid esters to fatty alcohols, it was demonstrated that a suitable SCF should not only be identified considering the reaction. Comparing dimethyl ether with propane showed that the recovery strategies for the reaction mixtures depend strongly on the phase behavior. Azeotropes which require additional purification steps are avoidable via choosing the right solvent. Additionally suitable and effective strategies for recom-

pression of SCF and hydrogen depend strongly on the phase behavior of the near-critical mixtures.

If hydrogenations in presence of supercritical fluids are planned, it is highly recommendable to consider the thermo- and fluiddynamics already at the earliest stage of research and development. Only the combination of kinetic and thermodynamic information allow to make use of the fascinating and promising capabilities of SCF. The actual development shows that hydrogenation with SCF is at the edge of technical application. Two industrial plants for R&D have been taken into operation in 2002 [40-43]. These plants demonstrate the suitability of hydrogenations in presence of supercritical fluids in larger scale.

ACKNOWLEDGEMENT

The authors wish to thank Magnus Härröd and Sander van den Hark for many useful hints and discussions and the Deutsche Forschungsgemeinschaft for the financial support of the project.

REFERENCES

[1] M. Bockisch, Fats and oils handbook, AOCS Press, 1998.
[2] Die Hydrierung von Fetten, Gemeinschaftsarbeit der Deutschen Gesellschaft für Fettwissenschaft e.V., Sonderdruck aus Fette - Seifen - Anstrichmittel 78 (1976) 385, 79 (1977) 181 und 465, 80 (1978) 1, Industrieverlag von Hernhaussen KG, Hamburg.
[3] Ullmann's Encyclopedia of Industrial Chemistry, 6th Edition, 2001.
[4] M. Baerns, H. Hofmann and A. Renken, Chemische Reaktionstechnik, Lehrbuch der Technischen Chemie. Band 1, 3., checked Edition, Wiley-VCH, Weinheim, 1999.
[5] M.-B. Macher, Supercritical Hydrogenation of vegetable Oils, Ph. D. Thesis, Chalmers University of Technology, Göteborg, Sweden, 2001.
[6] K.H. Pickel, R. Steiner, Supercritical Fluid Solvents for Reactions, Proc. Of the 3rd Int. Symp. on Supercritical Fluids, Strasbourg, 1994.
[7] T. Tacke, S. Wieland, P. Panster, Hardening of Fats and Oils in Supercritical CO_2, Proceedings of the 3rd Int. Symp. on High Pressure Chem. Eng., Zürich, 1996.
[8] M. Härröd and P. Møller, Hydrogenation of Fats and Oils at Supercritical Conditions in P. Rudolf von Rohr and C. Trepp (eds.), High Pressure Chemical Engineering, Elsevier Sciene, Amsterdam, 1996.
[9] Degussa AG, WO 95/22591, Hydrogenation of Unsaturated Fats, Fatty Acids or Fatty Acid Esters, 1995.
[10] Poul Möller Ledelses- og Ingeniörrådgivning APS, WO 96/01304, Hydrogenation of Substrate and Products Manufactured According to the Process, 1996
[11] D. Richter and E. Weidner, Influence of Supercritical Carbon Dioxide and Propane on the Solubility and Viscosity of systems containing Hydrogen and triglycerides (Soybean Oil), 6th Meeting on Supercritical Fluids – Chemistry and Materials, Nottingham, 1999.
[12] H. G. A. Coorens, C. J. Peters, J. De Swan Arons, Phase Equilibria in Binary Mixtures of Propane and Tripalmitin, Fluid Phase Equilibria, 40 (1988), 135.

[13] D. Richter, Phasenverhalten und Viskosität in Systemen aus Triglyceriden, Wasserstoff, Kohlendioxid, Propan und Dimethylether, Ph. D. Thesis, Universität Erlangen, Germany, 2000.
[14] H. Schiemann, Die Grenzflächenspannung von Lipiden in Gegenwart verdichteter Gase, Ph. D. Thesis, Universität Erlangen, 1993.
[15] S. Peter, A. Blaha-Schnabel, H. Schiemann, E. Weidner, Interfacial Tension in Binary Systems Containing a Dense Gas, H.Kiran, J.M.H.Levelt-Sengers (eds.), Supercritical Fluids, 731 - 738, Kluwer Academic Publishers, 1994.
[16] H. Schiemann, E. Weidner, S. Peter, Interfacial Tension in Binary Systems containing a Dense Gas, J. of Supercrit. Fluids, 6 (1993) 181.
[17] mg engineering Lurgi Life Science, Fatty Alcohol Technology, company brochure, 1999.
[18] S. van den Hark, The Use of Supercritical Fluids to Reduce the Number of Phases in Catalytic Hydrogenation: The Reaction of Fatty Acid Methyl Esters to Fatty Alcohols, Ph. D. Thesis, Chalmers University of Technology, Göteborg, Sweden, 2000.
[19] S. van den Hark, M. Härröd and p. Møller, Hydrogenation of fatty Acid Methyl Esters to Fatty Alcohols at Supercritical Conditions, JAOCS, 76 (1999), No. 11.
[20] H. Inomata, et al. Vapour Liquid Equilibria for Binary Mixtures of Carbon Dioxide and Fatty Acid Methyl Esters, Fluid Phase Equilibria, 46 (1989), 41.
[21] C. Crampon, G. Charbit, E. Neau, High-Pressure Apparatus for Phase Equilibria Studies: Solubility of Fatty Acid Esters in Supercritical CO2, J. of Supercrit. Fluids, 16 (1999) 11.
[22] J.-S. Yau and F.-N. Tsal, Solubilities of 1-Hexadecanol and 1-Octadecanol in Subcritical and Supercritical Carbon Dioxide, J. Chem. Eng. Data, 37 (1992), 285.
[23] D.-S. Jan, C.-H. Mai, and F.-N. Tsai, Solubility of carbon Dioxide in 1-Tetradecanol, 1-Hexadecanol, and 1-Octadecanol, J. Chem. Eng. Data, 39 (1994) 384.
[24] C. Brake, D. Richter, E. Weidner, Thermodynamic Study on the Hydrogenation of Fatty Acid Esters in the Presence of Supercritical Fluids, Proc. Of the 4th Intern. Symp. On High Pressure Process Technology and Chemical Engineering, Venice, 2002.
[25] C. Brake, Ph. D. Thesis, Ruhr-Universität Bochum 2003, in preparation.
[26] W. L. Burriss, N. T. Hsu, H. H. Reamer, and B. H. Sage, Ind. Eng. Chem., 45 (1953) 210.
[27] R. B. Williams and D. L. Katz, Ind. Eng. Chem., 46 (1954) 2512.
[28] D. B. Trust and F. Kurata, AIChe J., 17 (1971) 86.
[29] A. Jónasson, O. Persson, and P. Rasmussen, J. Chem. Eng. Data, 40 (1995) 1209.
[30] E. Brunner and W. Hültenschmidt, J. Chem. Thermodyn., 22 (1990) 73.
[31] E. Brunner, W. Hültenschmidt, and G. Schlichthärle, J. Chem. Themodyn., 19 (1987) 273.
[32] K. Bezanehtak, G. B. Combes, F. Dehghani, and N. R. Foster, J. Chem. Eng. Data, 47 (2002) 161.
[33] M. Gómez-Nieto and G. Thodos, AIChE J., 24 (1978) 672.
[34] M. S. Zabaloy, H. P. Gros, S. B. Bottini, and E. A. Brignole, J. Chem. Eng. Data, 39 (1994) 214.
[35] E. Brunner, J. Chem. Thermodyn., 17 (1985) 871.
[36] A.-D. Leu, D. B. Robinson, S. Y.-K. Chung and C.-J. Chen, Can. J. Chem. Eng., 70 (1992) 330.
[37] M. M. Elbaccouch and J. R. Elliott, J. Chem. Eng. Data, 45 (2000) 1080.
[38] M. Teodorescu and P. Rasmussen, J. Chem. Eng. Data, 46 (2001) 640.

[39] D. S. Brands, The Hydrogenolysis of Esters to Alcohols over Copper Containing Catalysts, Ph. D. Thesis, University of Amsterdam, Netherlands, 1998.
[40] S. K. Ross, F. R. Smail, M. Sellin, R. Amandi, P. Licence and M. Poliakoff, Chemical Reactions in Supercritical Carbon Dioxide: From Laboratory to Commercial Plant, Proc. Of the 4th Intern. Symp. On High Pressure Process Technology and Chemical Engineering, Venice, 2002
[41] http://www.thomas-swan.co.uk/
[42] M. Härröd, S. van den Hark, A. Holmquist, P. Møller, Hydrogenation at Supercritical Single-Phase Conditions, Proc. Of the 4th Intern. Symp. On High Pressure Process Technology and Chemical Engineering, Venice, 2002
[43] http://www.harrod-research.se/

Supercritical Fluids as Solvents and Reaction Media
G. Brunner (editor)

Chapter 1.12.

Perturbed-Chain-SAFT: development of a new equation of state for simple, associating, multipolar and polymeric compounds

J. Gross [a] and G. Sadowski [b]

[a] Technische Universität Berlin, Fachgebiet Thermodynamik und Thermische Verfahrenstechnik, Straße des 17. Juni 135, 10623 Berlin, Germany, Present address: BASF AG, Conceptual Process Engineering GIC/P - Q 920, 67056 Ludwigshafen, Joachim.Gross@alumni.tu-berlin.de

[b] Technische Universität Berlin, Fachgebiet Thermodynamik und Thermische Verfahrenstechnik, Straße des 17. Juni 135, 10623 Berlin, Present address: Universität Dortmund, Lehrstuhl für Thermodynamik, Emil-Figge-Strasse 70, 44227 Dortmund, G.Sadowski@ct.uni-dortmund.de.

ABSTRACT

A new physically based equation of state is proposed which is suitable for molecules of any molecular mass (from gases to polymers) as well as for associating and polar substances and their mixtures. The model is termed Perturbed-Chain SAFT (PC-SAFT) and is derived by extending the perturbation theory of Barker and Henderson to chain molecules. Whereas earlier versions of the SAFT equation of state assume the hard-sphere fluid as a reference system for the attractive (dispersive) interactions, the hard-chain fluid is here consistently considered for the dispersion term. The molecular model is refined by individually accounting for molecular association (hydrogen-bonding) and polar interactions (dipolar and quadrupolar). Three pure-component parameters are required for non-polar and non-associating substances, two further parameters characterise association and one additional parameter is needed for polar interactions. Copolymers can conveniently be modelled using the pure-component parameters of the appropriate homopolymers and one additional interaction parameter, only. Using one constant k_{ij} parameter, convincing results are obtained for systems containing non-polar as well as associating and polar substances, gases, solvent molecules, homopolymers or copolymers.

1. INTRODUCTION

The prediction or correlation of thermodynamic properties and phase equilibria with equations of state remains an important goal in chemical and related industries. While the use of equations of state was for a long time restricted to systems of simple fluids, there is an increasing demand for models suitable also for complex compounds. They include polymers as well as compound with specific interactions like association and dipolar interactions. Along with an increasing complexity of thermodynamic systems on the molecular level, often times the experimental data also gets scarce. This is the case e.g. for many biochemical problems.

Significant progress towards equations of state suitable for such complex systems is being made by applying theories from statistical thermodynamics. Many recent studies account for non-spherical molecular shape by assuming molecules to be chains of freely jointed spherical segments. Despite its simplicity, this molecular model accounts for size and shape effects and has successfully been applied to simple as well as large polymeric fluids and their mixtures. The molecular model can further be refined by assuming the segment to have association sites or partial charges (e.g. dipoles). Detailed reviews are available in the literature [1-3].

The first widely applied equation of state based on this molecular view was the Perturbed Hard-Chain Theory (PHCT) equation of state developed by Beret and Prausnitz [4] and by Donohue and Prausnitz [5]. Multipolar interactions were considered by Vimalchand and Donohue [6]. The success of their work has been the inspiration for further developments. A more recent equation of state concept for chain molecules is based on Wertheim's Thermodynamic Perturbation Theory [7-10]. By applying Wertheim's theory and extending it to mixtures Chapman et al.[11-12] derived the Statistical Associating Fluid Theory (SAFT) equation of state for chain mixtures. Although many modifications of the SAFT model were suggested, one of the most successful modification remains the SAFT model suggested by Huang and Radosz [13-14]. The non-spherical shape of molecules, however, is not accounted for in their dispersion term.

In earlier studies [15-16] the authors have developed a theory for chain molecules, where the chain structure of the molecules is consistently considered also in the dispersion term. The theory is based on a perturbation theory of Barker and Henderson [20-21] by extending it to chain molecules and is referred to as the Perturbed-Chain SAFT (PC-SAFT). This theory was compared to simulation data of square-well chains and was found to give good results [15]. It was subsequently modified to describe real fluids by adjusting model constants to pure-component properties of n-alkanes [16] and was applied to associating [17] and polymeric systems [18-19].

In this study we summarize the basic ideas behind the PC-SAFT equation of state and seek to present a brought overview of calculation results obtained with this model. In order to evaluate the PC-SAFT model, comparisons are made to the SAFT version of Huang and Radosz (subsequently referred to as SAFT).

2. DEVELOPMENT OF A NEW EQUATION OF STATE

Even for simple model fluids, like the Lennard-Jones fluid, it is not possible to derive exact and engineering-like (analytic) equations of state. Perturbation theories are often used to deliver simple approximate solutions for a given molecular model. The underlying idea is to divide the total intermolecular forces into repulsive and attractive contributions. The repulsive interactions are approximated through a 'reference-fluid', for which a reliable description has to be available. Within this work, the reference fluid is the hard-chain fluid (section 2.2.1).

The attractive intermolecular forces are in the Perturbed-Chain SAFT equation of state further divided into different contributions, so that the reduced residual Helmholtz energy is written as

$$\frac{a^{res}}{kT} = \frac{a^{hc}}{kT} + \frac{a^{disp,chain}}{kT} + \frac{a^{assoc}}{kT} + \frac{a^{DD}}{kT} + \frac{a^{QQ}}{kT} \tag{1}$$

where the right hand side of Eq. 1 are the expression for the hard-chain fluid as well as contributions due to dispersion, association, dipolar and quadrupolar interactions. For a defined molecular model, theories from statistical thermodynamics can be applied for the different contributions.

2.1. Molecular model

An equation of state derived from statistical thermodynamics requires the definition of a molecular model. The molecular model underlying the Perturbed-Chain SAFT equation of state is depicted in Fig. 1. Molecules are assumed to be chains of freely jointed spherical segments. The segments may possess association sites, exhibiting specific (often strong) short-range interactions, thus mimicking hydrogen-bonding. Moreover, they may carry partial charges. Dipolar segments have two partial charges (positive and negative), whereas quadrupolar segments carry three charges, i.e. poitive-2×negative-positive (e.g. nitrogen or acetylene) or negative-2×positive-negative (e.g. carbon dioxide).

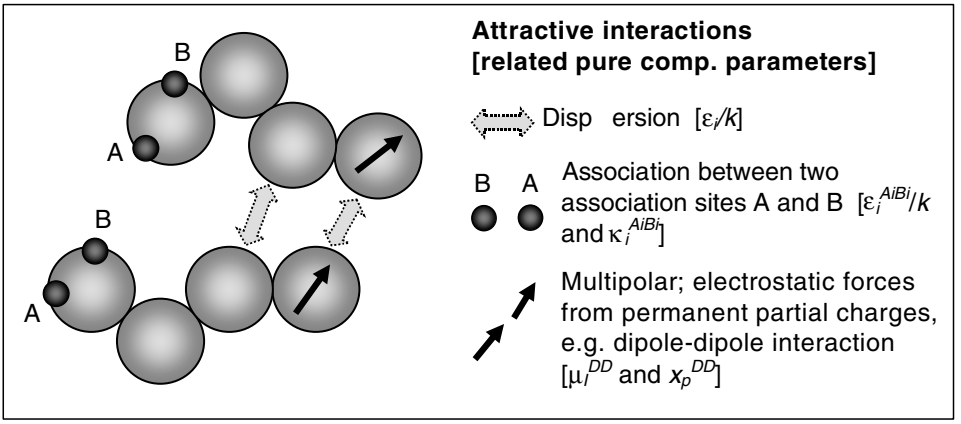

Fig. 1. Molecular model underlying the Perturbed-Chain SAFT equation of state. Schematic illustration of dispersive attractions, association and multipolar interactions.

2.2. A new dispersion term for chain molecules

A new dispersion expression for chain molecules was developed by extending a perturbation theory to chain molecules. First the hard-chain reference equation of state is introduced (section 2.2.1), then the extension of the perturbation theory is discussed (section 2.2.2), the treatment of mixtures is described (section 2.2.3), a comparison of the theory to molecular simulations is given (section 2.2.4), and the modification of the model for representation of real fluids is presented (section 2.2.5).

2.2.1. Reference equation of state

The hard-chain reference fluid consists of chain-molecules as depicted in Fig. 1 with no attractive interactions. Chapman et al. [11] have developed an equation of state for the hard-chain fluid based on Wertheim's first order thermodynamic perturbation theory [7-10]. For chains comprising m segments, the reduced Helmholtz energy is

$$\frac{a^{hc}}{kT} = \overline{m} \cdot \frac{a^{hs}}{kT} - \sum_i x_i (m_i - 1) \cdot \ln g_{ii}^{hs}(\sigma_{ii}) \tag{2}$$

where x_i is the mole fraction of chains of component i, m_i is the number of segments in a chain, g_{ii}^{hs} is the radial pair distribution function for segments at collision-distance in the hard sphere system, and $\overline{m}$ is the mean segment number in the mixture, with

$$\overline{m} = \sum_i x_i m_i \tag{3}$$

The Helmholtz energy of the hard-sphere fluid required in Eq. (2) is given on a per-segment basis [22-23]:

$$\frac{a^{hs}}{kT} = \frac{1}{\zeta_0}\left[\frac{3\zeta_1\zeta_2}{(1-\zeta_3)} + \frac{\zeta_2{}^3}{\zeta_3(1-\zeta_3)^2} + \left(\frac{\zeta_2{}^3}{\zeta_3{}^2} - \zeta_0\right)\cdot \ln(1-\zeta_3)\right] \tag{4}$$

and the radial distribution function of the hard-sphere fluid is:

$$g_{ij}^{hs} = \frac{1}{(1-\zeta_3)} + \left(\frac{d_i d_j}{d_i + d_j}\right)\frac{3\zeta_2}{(1-\zeta_3)^2} + \left(\frac{d_i d_j}{d_i + d_j}\right)^2 \frac{2\zeta_2{}^2}{(1-\zeta_3)^3} \tag{5}$$

with ζ_n defined as:

$$\zeta_n = \frac{\pi}{6}\rho\sum_i x_i m_i d_i{}^n \qquad n \in \{0,1,2,3\} \tag{6}$$

According to the perturbation theory applied in section 2.2.2 the segment diameter d_i is a function of temperature. A correlation suggested by Chen and Kreglewski [24] is applied, where

$$d_i = \sigma_i \cdot \left(1 - 0.12 \cdot \exp\left(-3 \cdot \frac{\varepsilon_i}{kT}\right)\right) \tag{7}$$

and σ_i is the segment diameter (temperature independent) of component *i*.

2.2.2 Extension of a perturbation theory to chain molecules

The perturbation theory of Barker and Henderson [20-21] is used for dispersive interactions within this work. It was originally derived for spherical molecules using the hard-sphere fluid as a reference fluid. Since chain molecules are of interest here, an extension of the Barker-Henderson theory to chain molecules is required. The basic idea of the perturbation approach is that the Helmholtz energy of a system can be expressed as an expansion in inverse temperature around the Helmholtz energy of a reference system. The perturbation expansion is fast convergent for dispersive interactions and can be truncated after the second term [25]. For chain molecules the residual part of the Helmholtz energy is given by

$$\frac{a^{disp,chain}}{kT} = -2\pi\rho\cdot\left(\frac{\varepsilon}{kT}\right)\sigma^3\sum_{\alpha}^{m}\sum_{\beta}^{m}\int_1^{\lambda} g_{\alpha\beta}^{hc}(m,w,\rho)w^2dw$$
$$-\pi\rho\, m\, kT\left(\frac{\partial\rho}{\partial P}\right)^{hc}\left(\frac{\varepsilon}{kT}\right)^2\sigma^3\frac{\partial}{\partial\rho}\left[\rho\sum_{\alpha}^{m}\sum_{\beta}^{m}\int_1^{\lambda} g_{\alpha\beta}^{hc}(m,w,\rho)w^2dw\right] \tag{8}$$

with

$$kT\left(\frac{\partial\rho}{\partial P}\right)^{hc} = \left(1+m\frac{8\eta-2\eta^2}{(1-\eta)^4}+(1-m)\frac{20\eta-27\eta^2+12\eta^3-2\eta^4}{[(1-\eta)(2-\eta)]^2}\right)^{-1} \tag{9}$$

where w is the reduced radial distance around the segments ($w=r/\sigma$), η denotes the packing fraction (a dimensionless density, $\eta=\zeta_3$), and $g_{\alpha\beta}{}^{hc}(m,w,\rho)$ is the radial distribution function of the hard-chain reference fluid. For chain molecules the overall intermolecular interaction is calculated as the sum of all individual segment-segment interactions in Eq. (8). Only pair-wise interactions of segments α and β located on different chains are considered within the summation, because the intermolecular radial distribution function $g_{\alpha\beta}{}^{hc}$ is considered.

Chiew [26] has proposed expressions for $g_{\alpha\beta}{}^{hc}(m,w,\rho)$ based on the integral equations applying the closure of Percus und Yevick [27] and further obtained an approximation for the average intermolecular radial distribution function $g^{hc}(m;w,\rho)$, given as

$$g^{hc}(m;w,\rho) = \frac{1}{m^2}\sum_{\alpha}^{m}\sum_{\beta}^{m} g_{\alpha\beta}^{hc}(m;w,\rho) \tag{10}$$

In the formulation of the perturbation theory given above (Eq. (8)), all segment-segment interactions have to be considered individually. However, we can introduce an averaging into the perturbation theory analogous to that proposed by Chiew, i.e. Eq. (10). For a pure chain-fluid the perturbation theory is rewritten as

$$\frac{a^{disp,chain}}{kT} = -2\pi\rho\cdot m^2\left(\frac{\varepsilon}{kT}\right)\sigma^3\underbrace{\int_1^{\lambda} g^{hc}(m,w,\rho)w^2dw}_{I_1(m,\eta)}$$
$$-\pi\rho\, m\, kT\left(\frac{\partial\rho}{\partial P}\right)^{hc} m^2\left(\frac{\varepsilon}{kT}\right)^2\sigma^3\underbrace{\frac{\partial}{\partial\rho}\left[\rho\int_1^{\lambda} g^{hc}(m,w,\rho)w^2dw\right]}_{I_2(m,\eta)} \tag{11}$$

Eq. (11) represents a perturbation theory for chain molecules, with the hard-chain fluid consistently used as a reference fluid. The radial distribution

function delivers information about chain length and structure into the dispersion term.

Solving Eq. (11) is numerically tedious and we aim at a simpler representation of the integrals I_1 and I_2 in Eq. (11). The integrals I_1 and I_2 depend only on density and the segment number and it was found possible to substitute I_1 and I_2 with simpler expressions without a recognizable loss of information. First of all, as in previous investigations [28-29] a power series in density is assumed for I_1 and I_2, according to

$$I_1(\eta, m) = \sum_{i=0}^{6} a_i(m) \cdot \eta^i \qquad \text{and} \qquad I_2(\eta, m) = \sum_{i=0}^{6} b_i(m) \cdot \eta^i \tag{12}$$

where the coefficients $a_i(m)$ and $b_i(m)$ are functions of the segment number. Liu and Hu [30-31] have derived expressions covering the chain-length dependence of a chain fluid, as

$$a_i(m) = a_{0i} + \frac{m-1}{m} a_{1i} + \frac{m-1}{m}\frac{m-2}{m} a_{2i} \tag{13}$$

$$b_i(m) = b_{0i} + \frac{m-1}{m} b_{1i} + \frac{m-1}{m}\frac{m-2}{m} b_{2i} \tag{14}$$

The second terms on the right-hand side of Eq. (13) and (14) account for the fact, that a segment is bond to a nearest-neighbour segment and the last terms account for the effect of next-to-nearest neighbour segments. It was possible to show, that model constants a_{0i}, a_{1i}, and a_{2i} as well as b_{0i}, b_{1i}, and b_{2i} can be fitted so that the integrals I_1 and I_2 in Eq. (11) can be substituted with Eq. (12)-(14) for the complete relevant parameter range ($1 \le m \to \infty$ and $0 \le \eta \le 0.74$, where $\eta = 0.74$ is the closest packing of segments) [15]. The equation of state requires three pure-component parameters (for non-associating and nonpolar components): the segment number m, the segment diameter σ, and the depth of the pair potential ε/k.

2.2.3. Extension to mixtures

The equation of state can be extended to mixtures by applying one-fluid mixing rules. The chain structure does not introduce complications, because the theory is segment-based. Applying the van der Waals one-fluid mixing rules to the perturbation theory leads to

$$\frac{a^{disp,chain}}{kT} = -\ 2\pi\rho \cdot I_1(\eta,\overline{m}) \cdot \sum_i \sum_j x_i x_j m_i m_j \left(\frac{\varepsilon_{ij}}{kT}\right) \sigma_{ij}^{\ 3}$$
$$-\ \pi\rho\,\overline{m}\,kT \left(\frac{\partial\rho}{\partial P}\right)^{hc} \cdot I_2(\eta,\overline{m}) \cdot \sum_i \sum_j x_i x_j m_i m_j \left(\frac{\varepsilon_{ij}}{kT}\right)^2 \sigma_{ij}^{\ 3} \tag{15}$$

where the power series I_1 and I_2 (Eqs. (12)-(14)) as well as Eq. (9) can now be evaluated for the mean segment number $\overline{m}$ of the mixture, i.e. Eq. (3).

The parameters for mixtures are obtained by conventional Berthelot-Lorentz combining rules introducing one adjustable binary interaction parameter k_{ij}

$$\sigma_{ij} = \frac{1}{2}\left(\sigma_i + \sigma_j\right) \tag{16}$$

$$\varepsilon_{ij} = \sqrt{\varepsilon_i \varepsilon_j} \cdot \left(1 - k_{ij}\right) \tag{17}$$

The equation of state as given in Eq. (15) in combination with Eq. (12)-(14) can conveniently be solved analytically. Equations for pressure, fugacity coefficients and the caloric properties are given elsewhere [16].

2.2.4. Evaluation of the perturbation theory through comparison with simulation results

Molecular simulations can be used to rigorously test molecular theories when an identical molecular model is considered. The square-well chain fluid was extensively investigated in the literature. In order to evaluate the above described perturbation theory, the square-well chain fluid was considered in Eq. (11) as an intermediate step towards the Perturbed-Chain SAFT equation of state. An analytic expression for $g^{hc}(m;w,\rho)$ according to Chiew's so-called PY2-approximation given by Tang and Lu [32] was used. The integration in

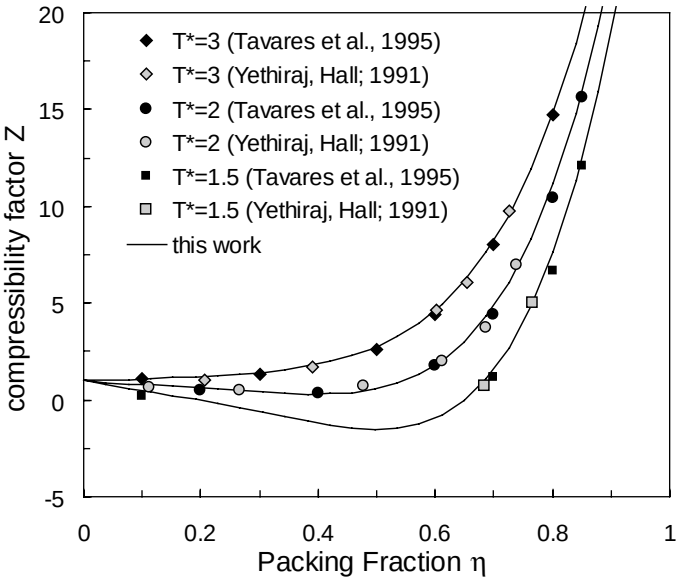

Fig. 2. Compressibility factor of pure 4-mer square-well chains at three reduced temperatures ($T^*=T/(\varepsilon/k)$). The solid lines are model calculations. Symbols are Monte Carlo simulation from the literature.

Eq. (11) was calculated numerically. Thus, the calculation results presented in Fig. 2 were obtained with no adjustable parameter - neither in the theory given in Eq. (11), nor through molecular parameters. Fig. 2 compares molecular simulations (from the literature) for a fluid with 4 segment (m=4) with predictions of theory. The theory is in good agreement with the simulated values.

2.2.5. Modification for real components

To date, the most successful equations of state for chain molecules were developed by applying statistical thermodynamic theories and readjusting model constants to better represent pure-component behavior of real substances [5, 24, 33]. Introducing information of real substances into the equation of state compensates weaknesses in the molecular model and in the applied theory.

In order to incorporate information about the chain-length dependence of real molecules, parameters of Eq. (13) and (14) were fitted to pure-component data of n-alkanes, leading to the PC-SAFT equation of state. The homologous series of n-alkanes is suited for this step, since molecular interactions apart from repulsion and dispersion can be neglected (ethane was excluded due to its small quadrupolar moment) [16].

The pure-component parameters for the n-alkane components, however have to be available in advance in order to fit the power-series coefficients of the first order term a_{0i}, a_{1i} and a_{2i} as well as those of the second order term b_{0i}, b_{1i} and b_{2i} in Eq. (13) and (14). As a first step, these pure-component parameters were determined assuming a Lennard-Jones potential in Eq. (11), applying the average radial distribution function $g^{hc}(m,w,\rho)$ for hard-chains proposed by Chiew [26]. In a subsequent step, the coefficients a_{0i}, a_{1i}, a_{2i}, b_{0i}, b_{1i}, and b_{2i} were regressed using the pure-component parameters determined before. Vapor pressures and liquid, vapor, and supercritical densities were considered in the regression, applying a Levenberg-Marquardt algorithm. The appropriate values are treated as universal model constants of the Perturbed-Chain SAFT equation of state.

2.3. Further contributions to the PC-SAFT equation of state

2.3.1. Association contribution

Based on Wertheim's work [7-10] Chapman et al. [11-12] have derived an association term which is suited for specific, short-range interactions. Wertheim's theory represents a powerful framework, because the considered fluid (associating fluid) is allowed to have a different molecular structure than the reference fluid (i.e. a different radial distribution function). The theory is applicable for such cases because temporary dimers resulting from the specific interactions are conceived to be a different molecular species.

In addition to the three pure-component parameters for simple fluids there are two pure-component parameters determining the associating interactions between the association site A_i and B_i of a pure-component i: the association energy ε^{AiBi}/k and the effective association volume κ^{AiBi}. All associating components are here assigned two association sites (often referred to as the 2B model [13]). Although the majority of associating compounds show significant multi-polar moments, the multi-polar interactions are at this point neglected.

It is generally non-trivial to define the strength of cross-associating interactions between two associating substances. Within the scope of this study, however, those interactions are determined by applying simple mixing and combining rules. The combining rules were suggested by Wolbach and Sandler [34] from considering gas phase association at the low pressure limit, as

$$\varepsilon^{A_iB_j} = \frac{1}{2}\left(\varepsilon^{A_iB_i} + \varepsilon^{A_jB_j}\right) \tag{18}$$

$$\kappa^{A_i B_j} = \sqrt{\kappa^{A_i B_i} \cdot \kappa^{A_j B_j}} \left(\frac{\sqrt{\sigma_{ii} \cdot \sigma_{jj}}}{\frac{1}{2}\left(\sigma_{ii} + \sigma_{jj}\right)} \right)^3 \tag{19}$$

where, within this work, no binary correction parameter is introduced.

The combining rules Eq. (18) and (19) are different to the ones most commonly encountered for SAFT models. The remainder of the association term is unchanged compared with several other SAFT versions (including the one by Huang and Radosz) and the equations are not presented here.

2.3.2. Multipolar contribution

Scientists are long aware of the important role multipolar interactions (like dipole-dipole or quadrupole-quadrupole) play [6, 35, 36]. The challenge with all interactions resulting from permanent charges is due to the fact that perturbation theories are difficult to apply to long-range forces. Those perturbation theories suggested for multipolar contributions are usually of 3rd order and are written in the Padé approximation.

An alternative route was taken by Saager and Fischer [37] and Saager et el. [38] who extensively performed molecular simulations and obtained a dipole-dipole term and a quadrupole-quadrupole term by fitting empirical expressions to the simulation data. A two-center Lennard-Jones molecule was considered in their simulations. Since the development of the PC-SAFT equation of state (as described in section 2.2.5) is based on the Lennard-Jones potential, it is possible to adopt the multipolar contributions derived by Saager and Fischer. In order to extend the expressions to chain molecules, we apply a theory proposed by Jog and Chapman [39] where dipolar segments are allowed within chain-molecules.

Two additional parameters are introduced when dipolar interactions are accounted for: the fraction of segments x_p^{DD} in the chain containing a dipole, and the dipolar moment μ_i. Analogously, x_p^{QQ} and the quadrupolar moment Q_i* are the parameters for quadrupolar molecules. However, it is here suggested to reduce the number of parameters to one for each multipolar interaction.

A significant induction effect is observed for strong dipolar fluids in dense (liquid) state. Hence, the effective dipolar moment is higher than the value determined for vacuum. It is therefore suggested to use the dipolar moment μ_i^{DD} as an adjustable parameter and set the parameter x_p^{DD} to $x_p^{DD}=1/m_i$. This defines the dipolar moment to be located on one segment only. For molecules with multiple functional groups however, both of the dipolar parameters should be fitted or thoroughly be defined.

The induction effect of quadrupolar moments is usually weaker than the one from dipolar moments. It is suggested to apply quadrupolar moments as

tabulated in the literature for molecules in vacuum. The remaining pure-component parameter, the segment-fraction x_p^{QQ} containing the quadrupolar moment, is adjusted to pure-component data.

2.4. Copolymers

Many technical polymers are composed of different types of repeat units and thus have to be declared as copolymers. The molecular model depicted in Fig. 1 can be refined by allowing segments to have different diameters and different dispersive interactions. The treatment of copolymers is particularly appealing with this molecular model, because the properties of a copolymer can be calculated from knowledge of the homopolymers (and optionally a correction parameter) and it is thus possible to account for different repeat-unit "compositions" without having to adjust pure-component parameters. The theoretical framework for extending the PC-SAFT equation of state was developed by Shukla and Chapman [40] and Banaszak et al. [41]. One fluid mixing rules are applied in the dispersion term for different segment-types in the chain.

In order to apply the copolymer-concept, a sequence in which the different segments are arranged in the chain needs to be defined. Copolymers with a statistical distribution of the repeat-units in the chain require an assumption on the sequence of neighboring repeat units. A simple approach for defining a sequence was suggested by the authors [19].

3. RESULTS

3.1. Pure components

All pure-component parameters were regressed by simultaneously fitting pure-component vapor pressure data and liquid density data [16].

3.1.1. Non-associating weakly polar components

The PC-SAFT model requires three pure-component parameters for simple fluids, namely the segment number m, the segment diameter σ, and the segment energy parameter ε/k. The ability to accurately correlate vapor-liquid equilibria of pure substances is important, because systematic errors observed in such calculations will usually propagate into mixture

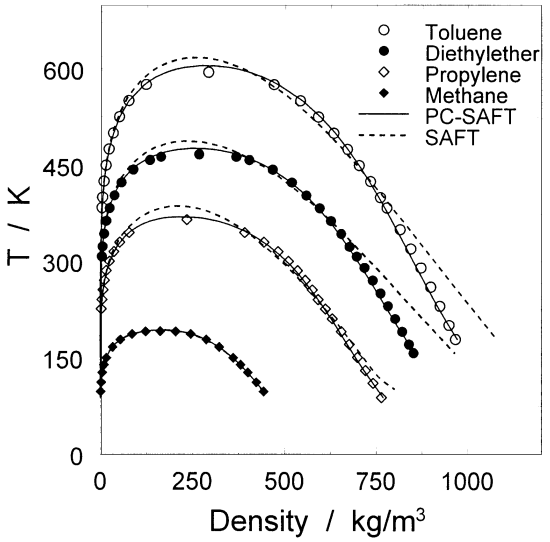

Fig. 3. Saturated liquid and vapor densities for methane, propylene, diethylether, and toluene. Comparison of PC-SAFT and SAFT to experimental data [42]. Reprinted with permission from IEC Res. 40(2001)1244-1260. Copyright 2003 American Chemical Society.

calculations. Fig. 3 shows the vapor-liquid equilibrium of methane, propylene, diethylether and toluene in a T-ρ-diagram. The densities of the coexisting phases are well described by the PC-SAFT equation of state. Even for moderately non-spherical molecules, the PC-SAFT equation of state gives considerably improved results compared with SAFT for the liquid phase at low temperature and in the vicinity of the critical point.

Fig. 4A shows the deviations between PC-SAFT vapor pressure results and experimental data for some arbitrarily chosen representatives of different homologous series. For comparison, results of SAFT are presented in Fig. 4B using the same scale of the diagram axis. Fig. 4B reveals systematic errors of the SAFT model in representing pure-component vapor pressures, whereas no obvious systematic deviation is observed for the PC-SAFT equation of state. It should be noted, that the pure-component parameters of the SAFT equation of state were for this comparison refitted to the same pure-component data as for the PC-SAFT model. Due to the wide temperature range considered, the errors observed for the SAFT model were more pronounced, when the original pure-component parameters derived by Huang and Radosz [13] were used.

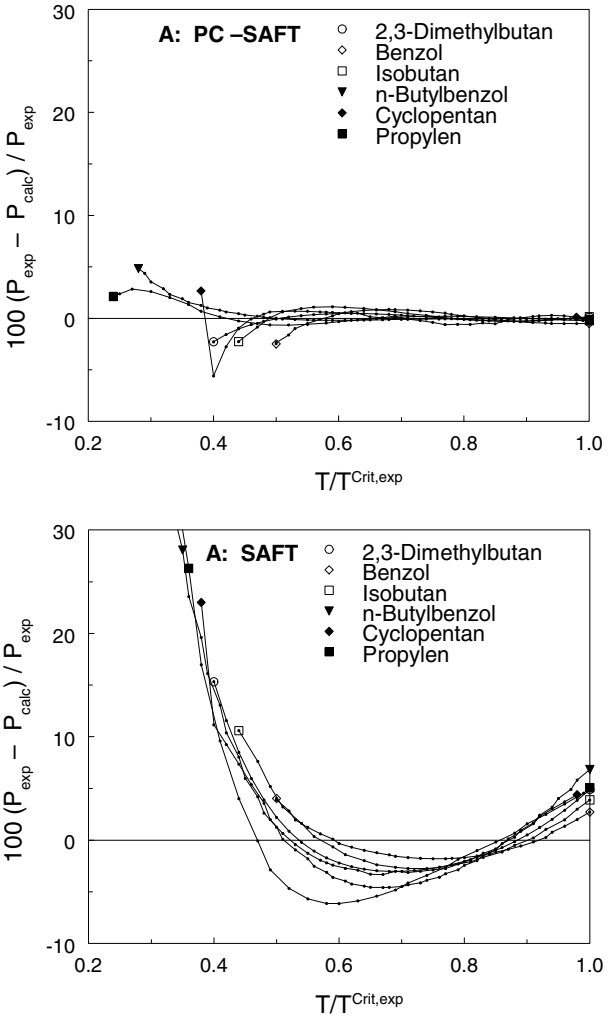

Fig. 4. Relative deviation of theory to experiment in vapor pressure. The deviation to each experimental point is displayed with a small point; lines are for optical guidance. A: PC-SAFT, B: SAFT (given in same scale). Reprinted with permission from IEC Res. 40(2001)1244-1260. Copyright 2003 American Chemical Society.

The calculation of caloric properties requires temperature derivatives of the Helmholtz energy. Here, the dispersion term plays a dominant role and the application of an equation of state to caloric data is a meaningful test for the dispersion term. Caloric data was not included in the regression of pure-component parameters. Fig. 5 and 6 compare experimental heats of vapori-

zation and experimental liquid heat capacities to results from the PC-SAFT model and the SAFT equation of state. The PC-SAFT equation of state is capable of predicting these caloric properties confirming a proper temperature behavior of the model.

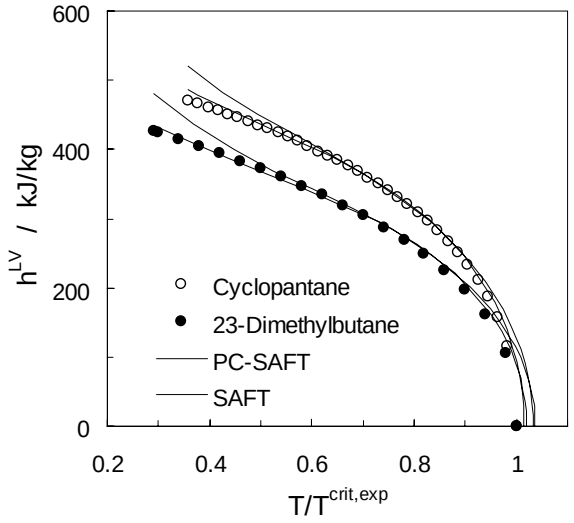

Fig. 5. Heat of vaporization for Cyclopentane and 23-Dimethylbutane. Comparison of PC-SAFT (solid lines) and SAFT (dashed lines) to experimental data [42].

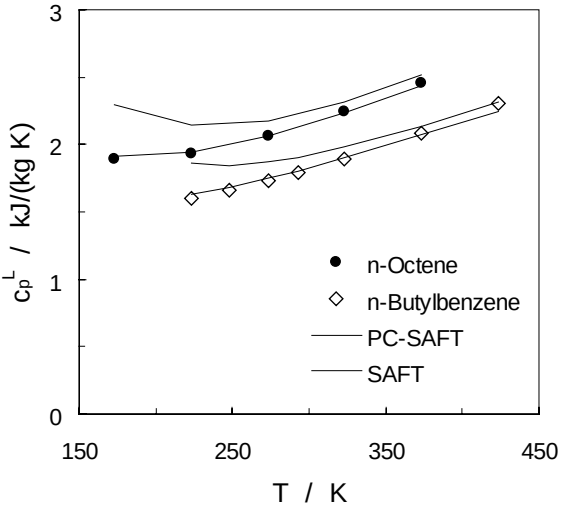

Fig. 6. Liquid heat capacities for n-Octene and n-Butylbenzene. Comparison of PC-SAFT (solid lines) and SAFT (dashed lines) to experimental data [42].

3.1.2. Associating components

Fig. 7 displays the vapor-liquid equilibrium of three alkanols in a T-ρ-diagram. The densities of the coexisting phases are well described by the PC-SAFT model. Results of the SAFT model obtained with pure-component parameters determined by Huang and Radosz [13] are given for comparison. It is seen from Fig. 7, that an improved description of dispersive interactions also leads to advanced result for associating compounds.

3.1.3. Multipolar components

Fig. 8 shows the vapor-liquid region of carbon dioxide, from triple point to critical point as well as sub- and supercritical isotherms up to pressures of 10^3 bar and temperatures up to 450 K. The PC-SAFT equation of state describes the densities of the fluid region of carbon dioxide with good precision up to elevated pressures. A quadrupolar moment independently determined for carbon dioxide in vacuum (Q^*=4.18D, ref. [47]) was considered. The only remaining pure-component parameter related to the quadrupole term (x_p^{QQ}, the fraction of segments carrying the polar moment) along with the three regular pure-component parameters were fitted to pure-component data of carbon dioxide. The absolute average deviation in vapor pressure is only 0.12% for the complete vapor pressure curve from triple point to critical point. When the quadrupolar interactions are neglected, the error in vapor pressure is 2.78%.

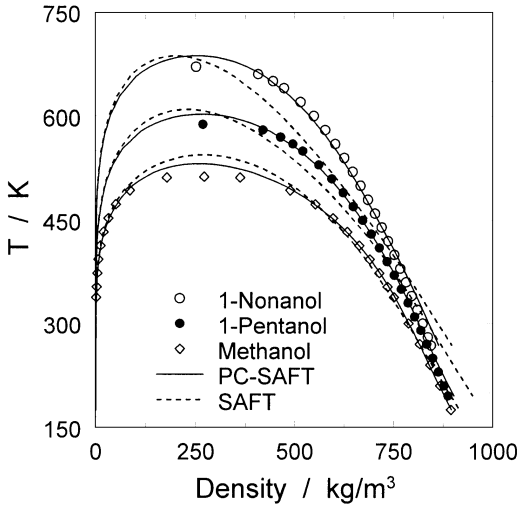

Fig. 7. Saturated liquid and vapor densities for methanol, 1-pentanol, and 1-nonanol. Comparison of PC-SAFT & SAFT to experimental data [42,43]. Reprinted with permission from IEC Res. 41(2002)5510-5515. Copyright 2003 American Chemical Society.

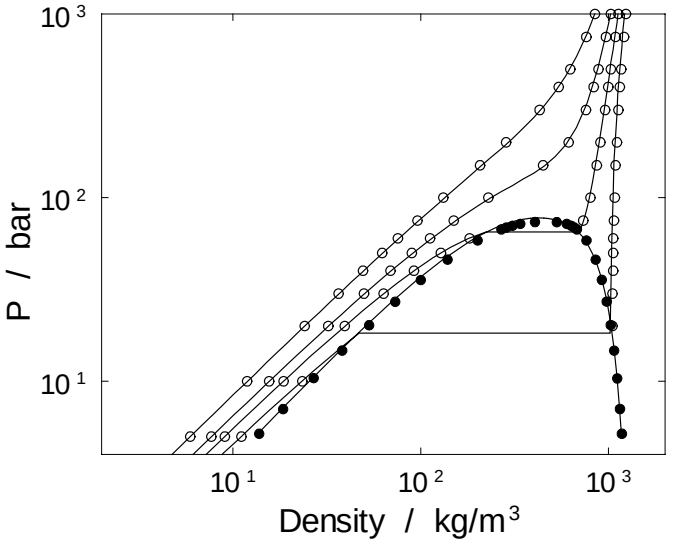

Fig. 8. *PρT* behavior of carbon dioxide. Subcritical and supercritical isotherms and coexisting densities from triple point to critical point from experiment (symbols, [44]) and PC-SAFT equation of state (solid lines). Reprinted with permission from IEC Res. 40(2001)1244-1260. Copyright 2003 American Chemical Society.

3.2. Mixtures

3.2.1. Mixtures of non-associating components

Engineers in chemical and petroleum industries often depend upon predictive capabilities of an equation of state. In this section, the PC-SAFT model will be applied to binary mixtures with k_{ij} set to zero in order to explore its ability to predict the phase behavior of asymmetric mixtures of non-polar components. Fig. 9-10 show *P-x*-diagrams of methane–butane mixtures and ethane–n-decane mixtures at various temperatures. The PC-SAFT equation of state is in good agreement with the experimental data in all cases. When compared to SAFT, the PC-SAFT equation of state seems to be more predictive for liquid and vapor phase compositions and in particular in the vicinity of the critical point. It is a general trend, that the SAFT model predicts mixture critical points at too high concentrations of the light (supercritical) components, whereas the PC-SAFT equation of state is seen to be more reliable here.

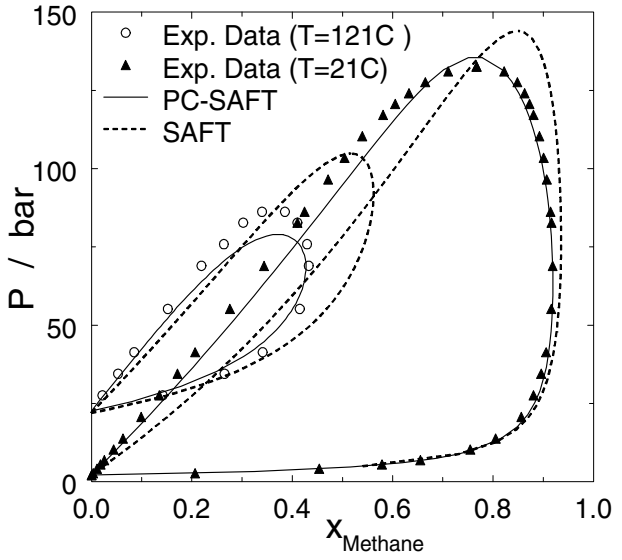

Fig. 9. Vapour-liquid equilibrium of n-butane-methane mixtures at two temperatures. Comparison of PC-SAFT and SAFT predictions (k_{ij}=0 in both cases) to experimental data [45]. Reprinted with permission from IEC Res. 40(2001)1244-1260. Copyright 2003 American Chemical Society.

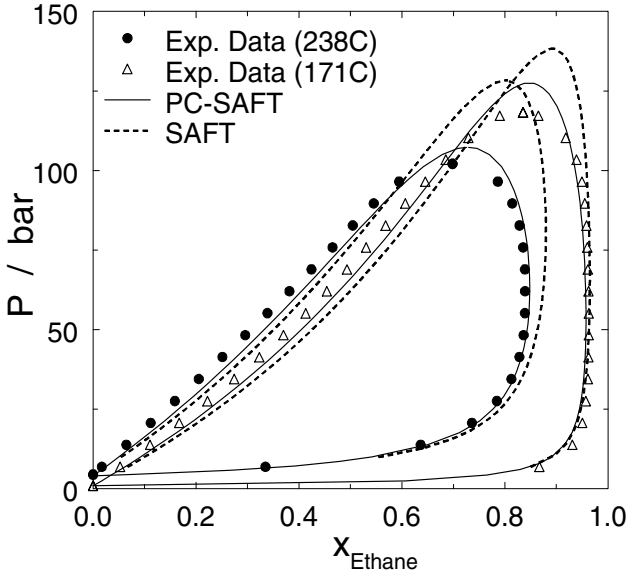

Fig. 10. Vapour-liquid equilibrium of n-decane-ethane mixtures at two temperatures. Comparison of PC-SAFT and SAFT predictions (k_{ij}=0 in both cases) to experimental data [46]. Reprinted with permission from IEC Res. 40(2001)1244-1260. Copyright 2003 American Chemical Society.

3.2.2. Mixtures with associating components

Mixtures with only one associating substance (self-association) do not require mixing rules for the association term. The phase behavior of methanol and cyclohexane at normal pressure is displayed in Fig. 11. This system exhibits an azeotropic vapor-liquid equilibrium at higher temperatures and a liquid-liquid equilibrium at lower temperatures. Fig. 11 demonstrates, that the association term enables the PC-SAFT model to simultaneously correlate VLE and LLE of self-associating mixtures with only one constant binary interaction parameter over wide ranges of temperature.

Modeling mixtures where associating interactions occur between different substances is particularly demanding for molecular theories. The phase behavior of water and 1-pentanol at P = 1.013 bar is depicted in Fig. 12 in a T-x-diagram. The system shows a liquid-liquid equilibrium at lower temperatures and a hetero-azeotropic vapor-liquid equilibrium. The k_{ij} parameter of both models were fitted to the 1-pentanol-rich liquid concentration of the vapor-liquid-liquid equilibrium. Both models deviate somewhat from the vapor-liquid data. The PC-SAFT equation of state is found to better agree with the liquid-liquid data.

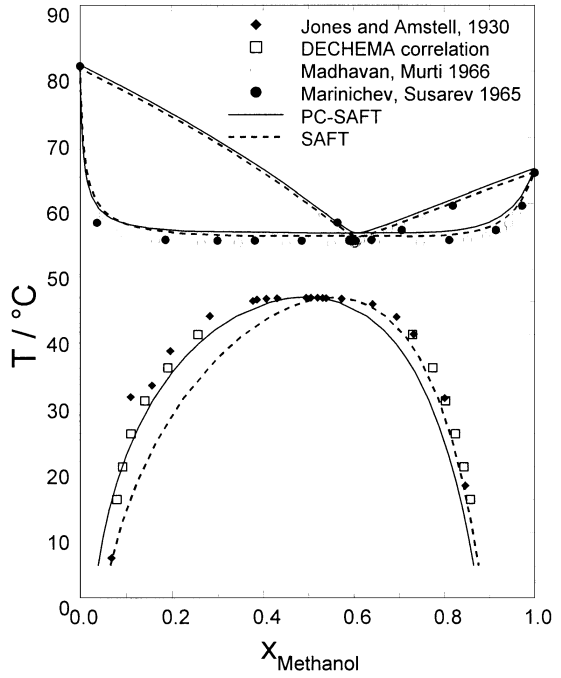

Fig. 11. Isobaric vapour-liquid and liquid-liquid equilibrium of methanol-cyclo-hexane at P=1.013bar. Experimental data and calculation results of PC SAFT (k_{ij}=0.051) and SAFT (k_{ij}=0.044). Reprinted with permission from IEC Res. 41(2002)5510-5515. Copyright 2003 American Chemical Society.

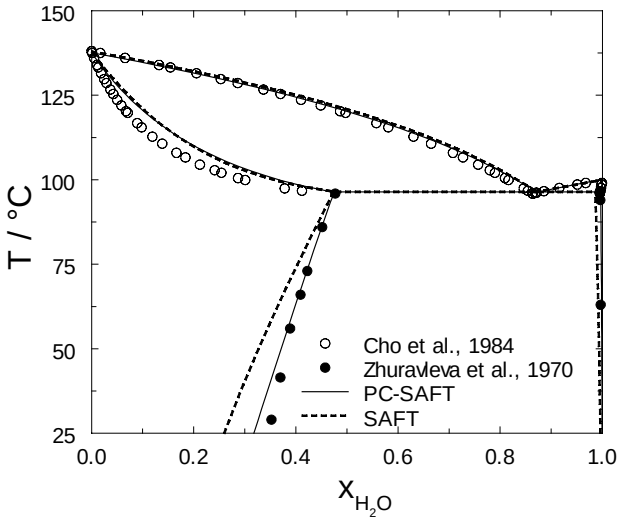

Fig. 12. Isobaric vapour-liquid and liquid-liquid equilibrium of water–1-pentanol at P=1.013bar. Comparison of experimental data to calculation results of PC SAFT (k_{ij}=0.016) and SAFT (k_{ij}= - 0.069). Reprinted with permission from IEC Res. 41(2002)5510-5515. Copyright 2003 American Chemical Society.

3.2.3. Mixtures with multipolar components

It was shown earlier [16-17], that mixtures with carbon dioxide (one of the strongest quadrupolar compounds) can be well described with the PC-SAFT equation of state, when the specific quadrupolar interactions are ignored. However, very large binary interaction parameters k_{ij} are required. Table 1 gives a comparison of k_{ij} parameters for various carbon dioxide mixtures, when the quadrupolar interactions are separately accounted for and when they are ignored. It becomes apparent, that the k_{ij} parameters are considerably smaller when the multipolar interactions are properly considered. The k_{ij} parameters then deviate only little from zero suggesting that a value of zero may also give good results. Fig. 13 and 14 confirm, that mixtures of carbon dioxide with non-polar (and non-polymer) components can be reliably predicted using k_{ij}=0. It should be noted, that results of the SAFT equation of state (without quadrupole-term) represent a best-fit, where again large values for the k_{ij} parameter are required.

Table 1

Comparison of regressed binary interaction parameter for PC-SAFT with and without quadrupole term.

	PC-SAFT	
	with quadrupole term	**without** quadrupole term
	k_{ij}	k_{ij}
CO_2 - Propane	-0.003	0.105
CO_2 - Butane	0.006	0.114
CO_2 - Pentane	0.017	0.120
CO_2 - Heptane	0.013	0.117
CO_2 - Cyclohexane	0.008	0.123
CO_2 - Methylcyclohexane	0.007	0.116
Absolute Average	**0.009**	**0.116**

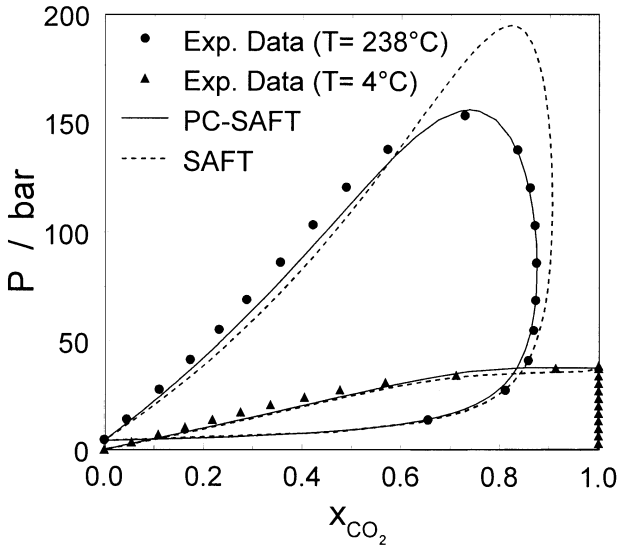

Fig. 13. Vapor-liquid equilibrium of n-decane-CO2 mixtures at two temperatures. Comparison of PC-SAFT predictions (k_{ij}=0) and SAFT correlation results (k_{ij}=0.115) to experimental data [48].

3.2.4. Polymer systems

Martin et al. have published experimental cloud points for polypropylene – n-pentane mixtures [51]. Fig. 15 compares results obtained from the PC-SAFT equation of state with experimental liquid-liquid data at three temperatures. In consideration of a relatively narrow molecular mass distribution, a monodisperse polymer of molecular mass M=M_w=50.4kg/mol was assumed. The correlation results are in good agreement with the experimental phase behavior. The SAFT model does not properly correlate liquid-

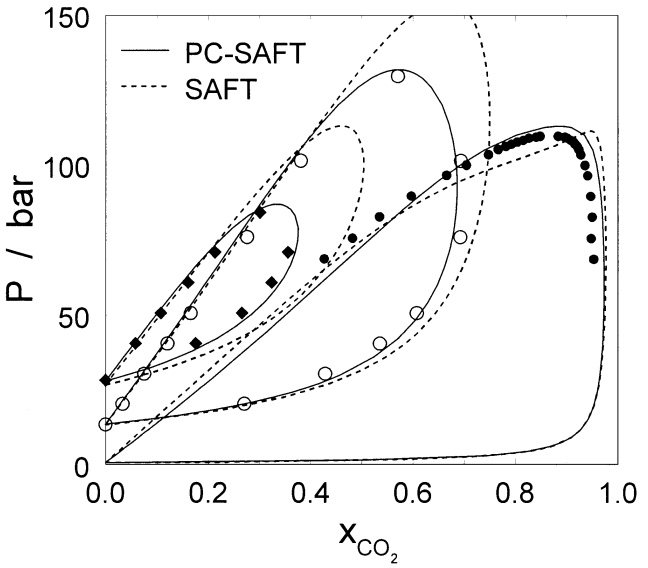

Fig. 14. Vapour-liquid equilibrium of cyclo-hexane-CO_2 mixtures at three temperatures (full spheres: T=71°C, open spheres: T=200°C, diamonds: T=250°C). Comparison of PC-SAFT predictions (k_{ij}=0) and SAFT correlations (k_{ij}=0.135) to experimental data [49, 50].

liquid equilibria of polypropylene systems using pure-component parameters of ref. [13] so that a comparison to the SAFT model is not given.

The use of compressed gases for separating polymers from solvents and for fractioning polymers, as well as the use of supercritical gases as a continuous phase in polymer reactions has given rise for some novel perspectives in process engineering [52]. Martin et al. [51] have presented cloud point measurements for ternary mixtures of polypropylene – n-pentane – CO_2 for various CO_2 contents (Fig. 16). The binary k_{ij} parameter for polypropylene – n-pentane is given above (k_{ij} = 0.0137, Fig. 15) and the binary parameter for n-pentane – CO_2 is set to zero. The k_{ij} parameter between polypropylene and CO_2 was obtained from the ternary mixture, adjusted to the highest point of pressure (at 42-wt% CO_2, Fig. 16). This pragmatic approach seems to give improved results, when the CO_2 content is significantly higher in the ternary system (42-wt% CO_2) than in available binary mixtures of polymer and gas (here: 12-wt% CO_2 [53]).

Applying this approach, the PC-SAFT equation of state describes the shift of the LCST-demixing (lower critical solution temperature) with varying CO_2 concentrations correctly in Fig. 16 using k_{ij}=0 for the pentane-CO_2 binary and two constant k_{ij} (temperature-independent) parameters.

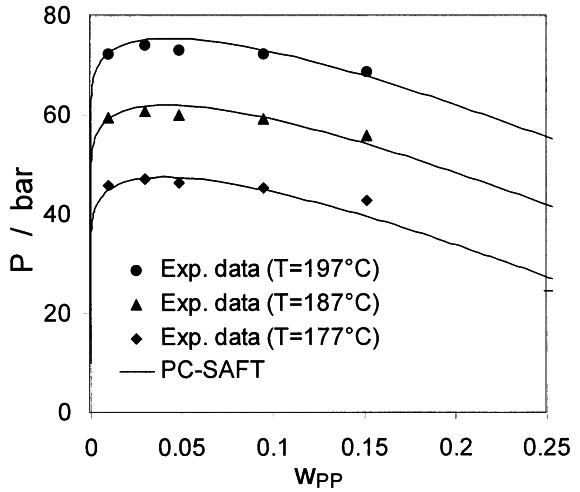

Fig.15. Liquid-liquid equilibria of polypropylene (PP) – n-pentane at three temperatures. (PP: M_w=50.4kg/mol, M_w/M_n=2.2). Comparison of experimental cloud points [51] to PC SAFT calculations (k_{ij}=0.0137). The polymer is assumed monodisperse. Reprinted with permission from IEC Res. 41(2002)1084-1093. Copyright 2003 American Chemical Society.

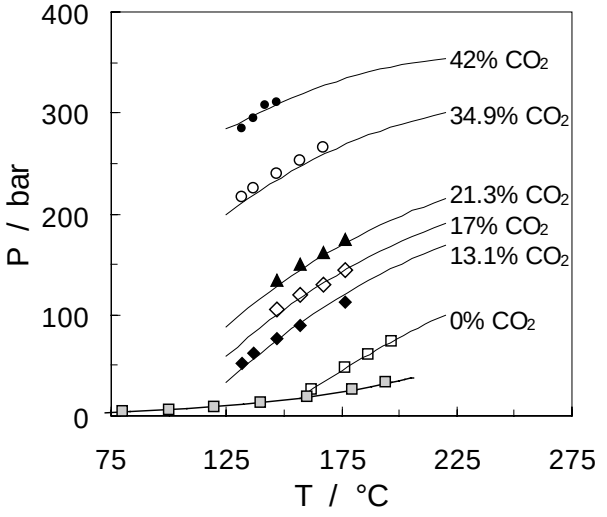

Fig.16. Cloud point curves polypropylene (PP) – n-pentane – CO_2 for various CO_2 contents. Initial PP mass fraction w_{PP}=0.03 (before the addition of CO_2). Comparison of experimental cloud points [51] to PC SAFT calculations (PP–n-pentane: k_{ij}=0.0137, PP–CO_2: k_{ij}=0.06, n-pentane–CO_2: k_{ij}=0). Reprinted with permission from IEC Res. 41(2002)1084-1093. Copyright 2003 American Chemical Society.

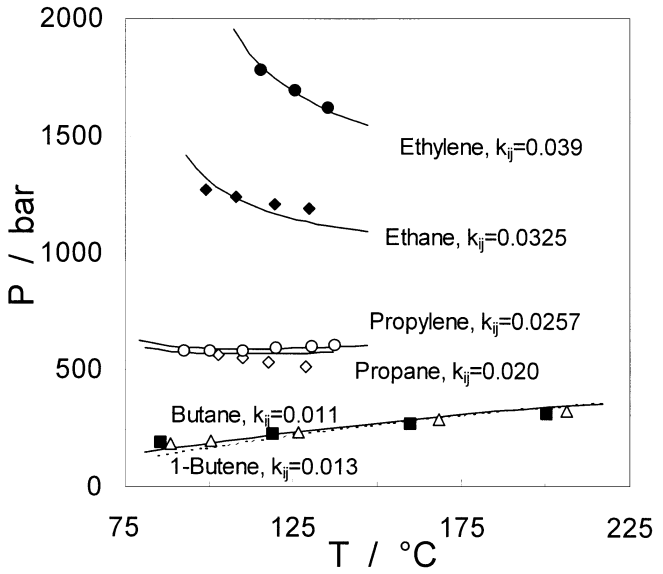

Fig. 17. High pressure equilibrium for polyethylene (LDPE) with varying solvents: ethylene, ethane, propylene, propane, butane, and 1-butene. (w_{LDPE}=0.05; M_w=106 kg/mol, M_n=20.1 kg/mol). Comparison of experimental data [55] to the PC-SAFT model. (LDPE- 1-butene: open triangles and dashed line). Reprinted with permission from IEC Res. 42(2003)1266-1274. Copyright 2003 American Chemical Society.

Cloud point measurements for LDPE in mixture with several solvents are displayed in Fig. 17. The PC-SAFT equation of state was applied to all of the appropriate mixtures with constant k_{ij} parameters resulting in good agreement to the experimental data for the given temperature range.

Fig. 18 presents measurements of Wohlfarth [54] for vapor-liquid mixtures of polyethylene and toluene at T = 120 °C. The two polyethylene systems are well described by the PC-SAFT equation of state with k_{ij} = 0 including a correct representation of the molecular mass.

3.2.5. Copolymer systems

The phase behavior of mixtures of random poly(ethylene-co-1-butene) (PEB) and propane was investigated by Chen et al. [56] by measuring cloud points of the liquid-liquid equilibrium at high pressures as depicted in Fig. 19. The repeat-unit composition of the PEB copolymer ranges from polyethylene to almost pure polybutene (PEB with 97 mass-% 1-butene). Fig.19 gives a comparison between experimental data and calculation results of the PC-SAFT equation of state. The k_{ij} parameters of polyethylene-propane and polybutene-propane were determined from the experimental data of PEB

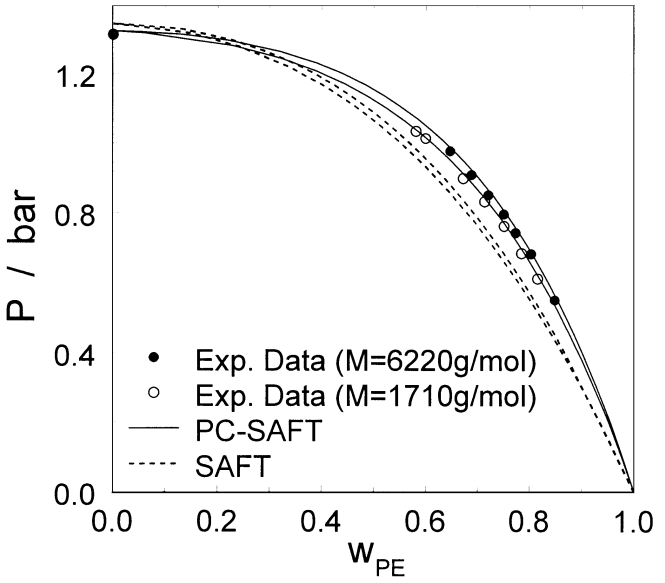

Fig. 18. Vapor-liquid phase equilibrium of polyethylene – toluene at T=120°C in a pressure - mass fraction plot. Comparison of experimental data [54] to correlation results of PC-SAFT ($k_{ij}=0$) and SAFT ($k_{ij}=0$).

with 0 mass-% 1-butene in backbone and PEP with 97 mass-% 1-butene in the backbone, respectively. The remaining internal $k_{i\alpha i\beta}$ parameter correcting the interactions between polyethylene-segments and polybutene-segments of PEB was fitted to be k_{ij}=0.008. The solubility of PEB in propane improves considerably with increasing amounts of 1-butene repeat units in the PEB. Over the temperature range of about 200 K and over the entire range of repeat-unit composition the PC-SAFT equation of state is in good agreement to the experimental data using constant k_{ij} parameters.

4. CONCLUSION

This work summarizes the basic ideas that have led to the development of the Perturbed-Chain SAFT (PC-SAFT) equation of state.
As opposed to many of the earlier models, where the non-spherical shape of molecules are only considered in the repulsive molecular interactions, PC-SAFT accounts for the non-spherical molecular shape also in the dispersive interactions. A new dispersion expression for chain molecules was developed by extending the perturbation theory of Barker and Henderson to chain molecules.

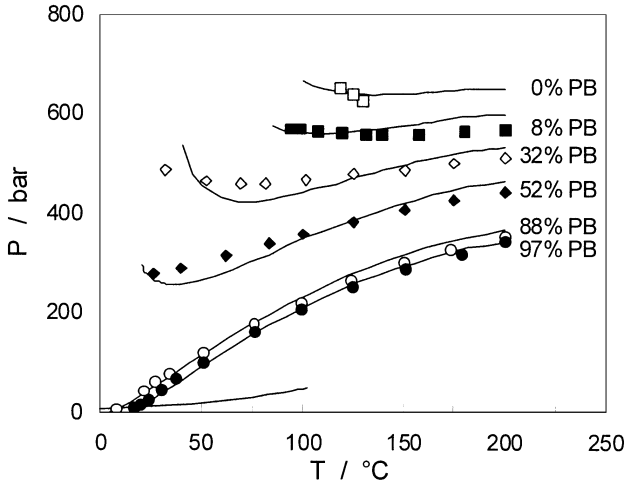

Fig. 19 Cloud-point curves for mixtures of poly(ethylene-co-1-butene) (PEB) and propane with varying repeat-unit composition (from 0 mass-% to 97 mass-%) of 1-butene (w_{PEB}=0.053, M=62 kg/mol to 120 kg/mol). Experimental cloud points [56] and calculation results of the PC-SAFT equation of state (PE and PB segments: $k_{i\alpha i\beta}$=0.008, PE– propane: k_{ij}=0.0206, PB– propane: k_{ij}=0.025).

The PC-SAFT equation of state is based on a well defined molecular model with various contributions of molecular interactions individually accounted for. Besides repulsion and dispersion, those include molecular association (e.g. contribution due to hydrogen-bonding), dipole-dipole and quadrupole-quadrupole interactions. Considering the different contributions to the overall intermolecular interactions separately increases the predictive capabilities of this model. The proposed equation of state is suitable for compounds of any molar mass, from gases to polymers as well as for polar and associating substances and their mixtures.

Non-polar, non-associating compounds are characterized by three pure-component parameters, associating substances require two further parameters. Dipolar and quadrupolar components are each defined with two additional pure-component parameters, however one of these can often be determined independently. Pure-component parameters are adjusted by fitting vapor pressure and liquid density data. The equation of state gives good fit to these properties and agrees well with caloric properties, like enthalpy of vaporization or heat capacities. The comparison to the SAFT version of Huang and Radosz reveals systematic improvements.

When applied to vapor-liquid equilibria of mixtures the PC-SAFT equation of state shows substantial predictive capabilities and good correla-

tion results. Comparisons to the SAFT model again show clear advantages of the proposed model.

Both, vapor-liquid and liquid-liquid equilibria of self-associating as well as cross-associating mixtures were correlated using one constant binary interaction parameter (k_{ij}), correcting the dispersive interactions. Simple combination rules were used for the cross-associating interactions.

Considering the quadrupolar interactions of carbon dioxide individually allows to predict mixtures with non-associating and non-polymer systems very satisfyingly.

The phase equilibria of polymer systems, which often involve high-pressure liquid-liquid mixtures as well as vapor-liquid equilibria at lower pressures were investigated. The PC-SAFT equation of state was found to give good correlation results of the appropriate phase behavior over wide ranges of conditions. The addition of a supercritical compound, like carbon dioxide to a polymer-solvent mixture shifts the liquid-liquid equilibrium (LCST) towards higher pressures and lower temperatures. This behavior is effortless modeled with the proposed model using constant k_{ij} parameters.

The PC-SAFT equation of state can conveniently be applied to copolymer systems. The copolymer is conceived to be composed of segments of the constituting homopolymers. Poly(ethylene-co-butene) with varying composition of butene repeat-units in the backbone can for example be modeled based solely on the pure-component parameters of polyethylene and polybutene and one additional parameter which corrects the interactions between the unlike copolymer segments. As before, the PC-SAFT equation of state revealed to be suitable to model the phase equilibrium over wide ranges of temperature with constant k_{ij} parameters.

REFERENCES

[1] Y.S. Wei and R.J. Sadus, AIChE J. 46 (2000) 169.
[2] E.A. Müller and K.E. Gubbins, Ind. Eng. Chem. Res. 40 (2001) 2193.
[3] I.G. Economou and M.D. Donohue, Fluid Phase Equilib. 116 (1996) 518.
[4] S. Beret and J.M. Prausnitz, AIChE J. 21 (1975) 1123.
[5] M.D. Donohue and J.M. Prausnitz, AIChE J. 24 (1978) 849.
[6] P. Vimalchand and M.D. Donohue, Ind. Eng. Chem. Fundam. 24 (1985) 246.
[7] M.S. Wertheim, J. Stat. Phys. 35 (1984) 19.
[8] M.S. Wertheim, J. Stat. Phys. 35 (1984) 35.
[9] M.S. Wertheim, J. Stat. Phys. 42 (1986) 459.
[10] M.S. Wertheim, J. Stat. Phys. 42 (1986) 477.
[11] W.G. Chapman, G. Jackson, K.E. Gubbins, Mol. Phys. 65 (1988) 1057.
[12] W.G. Chapman, K.E. Gubbins, G. Jackson, M. Radosz, Ind. Eng. Chem. Res. 29 (1990) 1709.
[13] S.H. Huang and M. Radosz, Ind. Eng. Chem. Res. 29 (1990) 2284.
[14] S.H. Huang and M. Radosz, Ind. Eng. Chem. Res. 30 (1991) 1994.
[15] J. Gross and G. Sadowski, Fluid Phase Equilib. 168 (2000) 183.

[16] J. Gross and G. Sadowski, Ind. Eng. Chem. Res. 40 (2001) 1244.
[17] J. Gross and G. Sadowski, Ind. Eng. Chem. Res. 41 (2002) 1084.
[18] J. Gross and G. Sadowski, Ind. Eng. Chem. Res. 41 (2002) 5510.
[19] J. Gross, O. Spuhl, F. Tumakaka, G. Sadowski, Ind. Eng. Chem. Res. 42 (2003) (accepted).
[20] J.A. Barker and D. Henderson, J. Chem. Phys. 47 (1967) 2856.
[21] J.A. Barker and D. Henderson, J. Chem. Phys. 47 (1967) 4714.
[22] T. Boublik, J. Chem. Phys. 53 (1970) 471.
[23] G.A. Mansoori, N.F. Carnahan, K.E. Starling, T.W. Leland, J. Chem. Phys. 54 (1971) 1523.
[24] S.S. Chen and A. Kreglewski, Ber. Bunsen-Ges. 81 (1977) 1048.
[25] D. Henderson, J. Chem. Phys. 61 (1974) 926.
[26] Y.C. Chiew, Mol. Phys. 73 (1991) 359.
[27] R.L. Rowley, Statistical Mechanics for Thermophysical Property Calculations, Prentice-Hall, Englewood Cliffs, New Jersey, 1994.
[28] H.S. Gulati and C.K. Hall, J. Chem. Phys. 107 (1997) 3930.
[29] T. Hino and J.M. Prausnitz, Fluid Phase Equilib. 138 (1997) 105.
[30] H. Liu and Y. Hu, Fluid Phase Equilib. 122 (1996) 75.
[31] Y. Hu and H. Liu, J. Chem. Phys. 104 (1996) 396.
[32] Y. Tang and B.C.-Y. Lu, J. Chem. Phys. 105 (1996) 8262.
[33] Y. Song, S.M. Lambert, J.M. Prausnitz, Ind. Eng. Chem. Res. 33 (1994) 1047.
[34] J.P. Wolbach and S.I. Sandler, Ind. Eng. Chem. Res. 37 (1998) 2917.
[35] K.E. Gubbins, C.H. Twu, Chem. Eng. Sci. 33 (1978) 863.
[36] R.L. Cottermann, B.J. Schwarz, J.M. Prausnitz, AIChE J. 32 (1986) 1787.
[37] B. Saager and J. Fischer, Fluid Phase Equilib. 72 (1992) 67.
[38] B. Saager, J. Fischer, M. Neumann, Molec. Simul. 6 (1991) 27.
[39] P.K. Jog and W.G. Chapman, Mol. Phys. 97 (1999) 307.
[40] K.P. Shukla and W.G. Chapman, Mol. Phys. 91 (1997) 1075.
[41] M. Banaszak, C.K. Chen, M. Radosz, Macromolecules 29 (1996) 6481.
[42] VDI-Wärmeatlas, VDI-Gesellschaft Verfahrenstechnik und Chemieingenieurwesen (GVC), Düsseldorf, 1994.
[43] American Petroleum Institute Research Project 44: Selected Values of Properties of Hydrocarbons and Related Compounds, Table 23-2-(1.101)-kb, 1974.
[44] S. Angus, B. Armstrong, K.M. de Reuck, International Union of Pure and Applied Chemistry - Carbon Dioxide, Pergamon Press, London, 1973.
[45] B.H. Sage, B.L. Hicks, W.N. Lacey, Ind. Eng. Chem. 32 (1940) 1085.
[46] H.H. Reamer and B.H. Sage, J. Chem. Eng. Data 7 (1962) 161.
[47] D.E. Stogryn and A.P. Stogryn, Molec. Phys. 11 (1966) 371.
[48] H.H. Reamer and B.H. Sage, J. Chem. Eng. Data 8 (1963) 508.
[49] N. Nagarajan and R.L.Jr. Robinson, J. Chem. Eng. Data 32 (1987) 369.
[50] I.R. Krichevskii and G.A. Sorina, Russ. J. Phys. Chem. 34 (1960) 679.
[51] T.M. Martin, A.A. Lateef, C.B. Roberts, Fluid Phase Equilib. 154 (1999) 241.
[52] B. Bungert, G. Sadowski, W. Arlt, Ind. Eng. Chem. Res. 37 (1998) 3208.
[53] Y. Sato, K. Fujiwara, T. Takikawa, Sumarno; S. Takishima, H. Masuoka, Fluid Phase Equilib. 162 (1999) 261.
[54] C. Wohlfarth, Vapour-Liquid Equilibrium Data of Binary Polymer Solutions, Physical Sciences Data 44, Elsevier, Amsterdam, 1994
[55] B.M. Hasch, S.-H. Lee, M. A. McHugh, J. Appl. Polym. Sci. 59 (1996) 1107.
[56] S.-J. Chen, M. Banaszak, M. Radosz, Macromolecules 28 (1995) 1812.

Supercritical Fluids as Solvents and Reaction Media
G. Brunner (editor)

Chapter 1.13.

Extractability of As-Chelates and Solubility of different Rh, Pd-Chelates in Supercritical Fluid CO_2

B. W. Wenclawiak, A. Wolf and S. Wilnewski

Analytical Chemistry, Department of Chemistry, University of Siegen,
Adolf Reichwein Str. 9, D-57078, Siegen, Germany

1. INTRODUCTION

In analytical chemistry supercritical fluids are mainly applied for selective extraction of analytes from solid and liquid matrices (supercritical fluid extraction, SFE) or as mobile phases in chromatographic separations (supercritical fluid chromatography, SFC) [1]. The combined characteristic of gaseous transport of substances and liquid-like dissolving power gives the supercritical carbon dioxide properties, which are already used in different fields of chemistry. In reviews the scope of application of the supercritical fluid technology is described in detail [2].

Apart from analytical scale or technical scale supercritical fluid extraction (SFE) supercritical fluids are also used for the following purposes [3, 4]:

- Supercritical Fluid Reaction (SFR)
  Organic synthesis in supercritical fluids is of growing interest [3]. Synthesis with homogeneous or heterogeneous catalysts, most often precious metal compounds are predominant in sc CO_2. The yields of reaction products are controlled by the solubility of the catalysts [5]. The kinetic rate constants are larger for reactions in sc CO_2 as compared to those in solvents.

- Crystallization from Supercritical Solution, CSS
  The generation of nano particles with the supercritical fluid technology is described in detail by Jung and Perrut [6].

- Rapid Expansion of Supercritical Solvents, RESS
  Nanostructured chelate crystals can be generated by rapid expansion of Supercritical chelate solutions which in turn can be further processed to super conductors of the $YBa_2Cu_3O_7$ – type [7].

- Gas Anti-Solvent Precipitation, GASP
  The Gas Anti-Solvent (GAS) process can be used for crystallization of substances, which are only slightly soluble or not soluble in supercritical fluid. Briefly, the process is performed by first dissolving the substance of interest in the organic solvent. When the supercritical fluid is added to the solution the substance precipitates [8,9].

Metal ions are insoluble in sc CO_2 and thus must be converted into soluble compounds. This can easily be achieved by adding chelators to the metal ion solution. The chelator has to compensate the charge of the metal ion and -very simplified- coat the metal ion with an organic lipophilic layer, which makes the whole chelate soluble in sc CO_2. The metal ion or better the centre ion is usually coordinated via two or more heteroatoms such as sulphur, oxygen, nitrogen, or phosphorus. The heteroatoms are part of a carbon backbone. The residual or carbon side chains/groups influence the solubility of the whole chelate [10, 11]. We have studied the solubility in supercritical carbon dioxide of Palladium, Rhodium and Arsenic - chelates with different systematically modified ligands of the dialkyldithiocarbamate type and ß-diketonate type.

Metal chelates can be catalysts, precursors for catalysts, can be suitable as model compounds, or can be used in many other applications. Some dithiocarbamates are used as fungicide (Ziram®, Maneb®, Zineb® etc.) or in the mineral industry [12]. Recent research shows that Palladium-dialkyldithiocarbamates can be used for the production of Pd-nano particles [H. Beer, unpublished results]. They can also function in medicine as antagonists of the anti-tumor agent cis-platinum [13-15]. Platinum (II) and Palladium (II)-compounds with dithiocarbamates and amines show cytostatic activity [16].

1.1. Dialkyldithiocarbamate (DTC)

Carbamates are salts of the disubstituted carbamine acid, which is unknown as free acid. Dialkyldithiocarbamine ligands (DTC's) are synthesized from carbon disulfide and aliphatic or aromatic amines in an alkaline solution {1} [17, 18]:

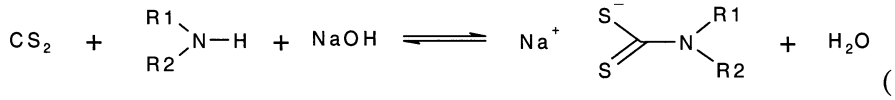

(1)

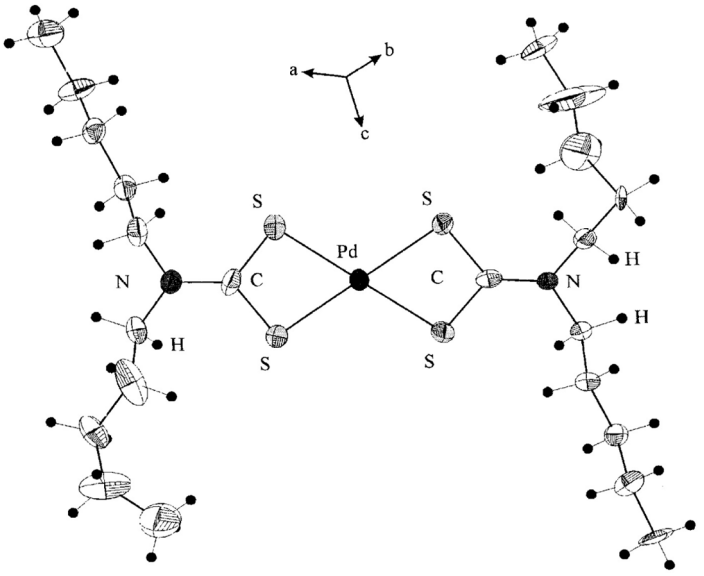

Fig. 1. X-ray structure of Pd $(DPeDTC)_2$ with ellipsometric vibration.

Further reaction of the sodium salt with metal ions yields the respective metal dithio dialkyl carbamate or simply the Me-DTC chelate. The ease of handling made the DTC chelates a preferred way of quantitative determinations for metal ions in liquids by photometric measurements in the past [19]. The detection limits for metals are at the ultra trace level (some $pg \cdot L^{-1}$). A detailed description of the absorption bands of the Palladium- and Rhodium-dialkyldithiocarbamates in different solvents can be found in [20].

Some DTC chelates are sufficiently stable to be analyzed via high-pressure liquid chromatography (HPLC) [21-23] or gas chromatography [24-27].

1.2. β-Diketonates

Pentane-2, 4-dione (acetylacetone or acac) is a liquid at ambient conditions and the simplest representative of the β-diketone-ligands. Replacing the residual methyl groups in pentane-2, 4-dione (R_1 and R_2 in figure 2) by alkyl or aryl groups yields a wide variety of different ß-diketone-ligands. Metal ions react with the β-diketone to yield the corresponding β-diketonate, which is soluble in organic solvents or sc CO_2.

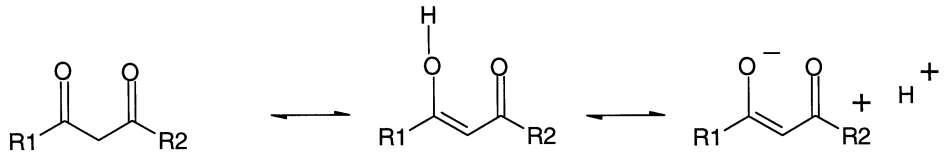

Fig. 2. ß-diketonate.

Adduct formations of β-diketonates and organo phosphorous compounds are reported [28]. It is for instance possible to separate adducts of ß-diketonates and tributylphosphate by SFC [29].

1.3. The relevant central ions of this study

Rhodium and Palladium and their alloys are used in dentistry, in industry, for jewellery, and electrical engineering. In medicine Platinum and Palladium are used in cancer therapy [16].

The greatest demand for precious metals is their use in modern catalytic exhaust converters. The recovery of the precious metals Palladium and Rhodium applies mainly liquid-liquid extraction [30, 31].

In order to reduce the consumption of the organic solvents sc CO_2 might be one alternative.

Arsenic is an element of particular interest because of its high toxicity. Still it is found in a variety of minerals in the environment (*arsenic pyrite* ("$FeAs_2$ * FeS_2"), as *realgar* (As_4S_4) and as *auripigment* (As_2S_3)). Arsenic is used for alloys (lead alloys for gun pellets, copper-tin alloys for mirrors) and for the production of semiconductors (GaAs, InAs). It is no longer used in medicine and in pesticides. It can form very toxic (arsenite, arsenate) or moderately toxic compounds (DMA = Dimethylarsinic acid (V), MMA = Monomethylarsonic acid (III)). Sodiummonomethylarsonate was used in the past as herbicide (3.3 Mio. pounds in the USA 1977). Photo reduction metabolizes sodium mono methyl arsonate into (herbicide active) arsenite which affects the enzyme NADP+ which then reacts to malic acid), and apparently non-toxic (arsenobetaine, "arseno-sugars") compounds.

In ecology the potential hazard of a compound depends decisively on the nature of the compound or the so-called species. Different species of the same element can exhibit a very different behavior with respect to reactivity, toxicity, bio-disposability, solubility and bioaccumulation.

One of the most widely used techniques for pre concentration and separation of arsenic compounds from solid and liquid samples is chelation combined with solvent extraction. These procedures are usually time - and labor - intensive, especially for solids where leaching procedures are required to

release the arsenic ions before complexation and solvent extraction. Furthermore solvent extraction requires the use of toxic organic liquids in some cases.

In recent years supercritical fluid extraction of arsenic compounds has gained acceptance as an alternative sample preparation technique because it is relatively fast and its selectivity can be controlled [32, 33].

There are two ways of modifying the solubility of metal chelates in sc CO_2 reported in literature [34].

a) Change of the residual group – e.g. replacement of hydrogen by fluorine or increase the carbon chain length.
b) Adding an additional modifier e.g. TBP (Tributylphosphate).

Our study focuses mainly on the solubility of different palladium, rhodium, and arsenic chelates. Some others are added for better comparison. The main goal is to find the optimum ligand, that is one, which provides maximum solubility without a fluorine attached.

2. CLASSIFICATION OF LIGANDS

All ligands and chelates were prepared according to methods described in the literature [35, 36]. In Table I the ligands selected for our study are given.

The chelates have been determined by means of elementary analysis and melting points (Table 2). The DTC chelates have also been characterized by FAB-mass spectrometry and ^{1}H-NMR.

Table 1
Dialkyldithiocarbamine and ß-Diketone ligands used in this study.

Formula	*Chemical name*	*Abbreviation*
$[S_2CN(C_2H_5)_2]^-$	Diethyldithiocarbamate	DDTC
$[S_2CN(C_3H_7)_2]^-$	Diisopropyldithiocarbamate	DiPDTC
$[S_2CN(C_4H_9)_2]^-$	Dibutyldithiocarbamate	DBDTC
$[S_2CN(C_4H_9)_2]^-$	Diisobutyldithiocarbamate	DiBDTC
$[S_2CN(C_5H_{11})_2]^-$	Dipentyldithiocarbamate	DPDTC
$[S_2CN(C_6H_{13})_2]^-$	Dihexyldithiocarbamate	DHDTC
$[S_2CN(C_8H_{17})_2]^-$	Dioctyldithiocarbamate	DODTC
$[S_2CN(C_2H_2F_3)_2]^-$	Trifluoroethyldithiocarbamate	FDDTC
	(Phenyldithiocarbamate)	PhenDTC
	(Diphenyldithiocarbamate)	DPhenDTC
$CH_3COCH_2COCH_3$	Acetylaceton	acac
$C_2H_5COCH_2COC_2H_5$	3,5-Heptandion	hd
$C_4H_9COCH_2COC_4H_9$	2,2,6,6-Tetramethyl-3,5-heptandion	thd

Table 2
Melting points of some Pd and Rh dialkyldithiocarbamates

Ligand	Pd	Rh
DDTC	225-226	>235
DPTC	>300	>235
DBTC	105-106	nd
DHDTC	65-66	176-177

3. EXPERIMENTAL SETUP AND PROCEDURE

A 250mL high-pressure syringe pump was used to pressurize and to deliver carbon dioxide to the system. A schematic of the apparatus is shown in Fig. 3.

The CO_2 is compressed to the necessary pressure and flows through a heat exchanger (1.5 m coiled capillary tubing) into the extraction cell. Heat exchanger and extraction cell are kept at the desired temperature usually above the critical temperature of sc CO_2 The extraction cell is made from of high-quality stainless steel and has metal frits at its outlets, to hinder particles of the sample from leaving the cell.

A heated variable restrictor maintains pressure in the system. Beside the variable restrictor sometimes fixed types – fused silica or stainless steel capillaries, with a small internal diameter from 10 to 40 μm – were applied. However the variable restrictor was more comfortable to use.

Extracts were collected in a solvent. When a defined/measured volume of CO_2 had passed the cell, the flow was stopped and the quantity of the extract was determined either photo metrically or by spectroscopy.
Usually the procedure was as follows:

- Fill the extraction cell with the chelate.
- Pressurize to the desired pressure.
- Heat the system to the desired temperature with the restrictor closed until the equilibrium is reached. After 30 minutes open the restrictor and collect the extracted chelate in a suitable solvent (dynamic extraction).
- Determine metal content in the solvent (off line determination).

For some experiments we used an apparatus that has been described elsewhere [15]. A schematic of the apparatus for these experiments is shown in Fig. 4. It consists of a modified Suprex MPS 225 (Suprex Corp. Pittsburgh, PA). A 250 mL syringe pump is used to pressurize CO_2. All heated components, except the pneumatic driven valve and the capillary connected to the detector are placed in an oven. The pressure of the sc CO_2 and the temperature of the

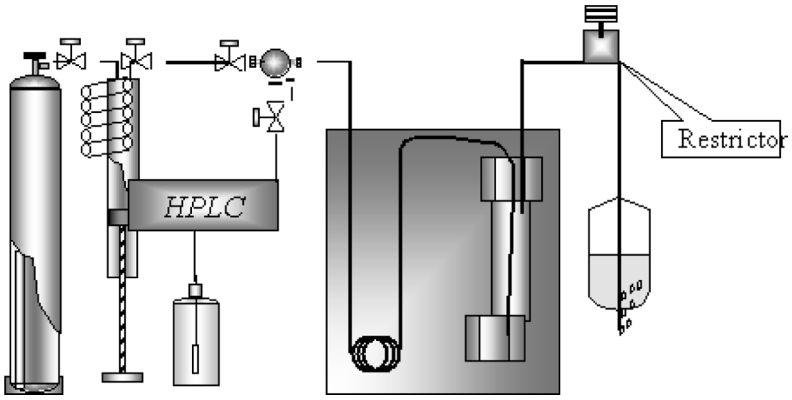

Fig. 3. Schematic of apparatus for dynamic measurement.

oven, detection cell and of the restriction system can be programmed via a control panel. The CO_2 was heated in a 1.0 m preheating coil of 1.6 mm x 762 μm i.d. (1/16 in. x 0,03 in.) stainless steel tubing and then passes through the saturation cell (V=1,027 mL, 14,5 mm x 9,5 mm i.d. SFE cell, Keystone Scientific, Bellfonte, PA) containing approx. 100 mg of the chelate. The saturation cell with the chelate was equilibrated to the desired temperature before CO_2 was filled in. The preheating coil was necessary to ensure that the

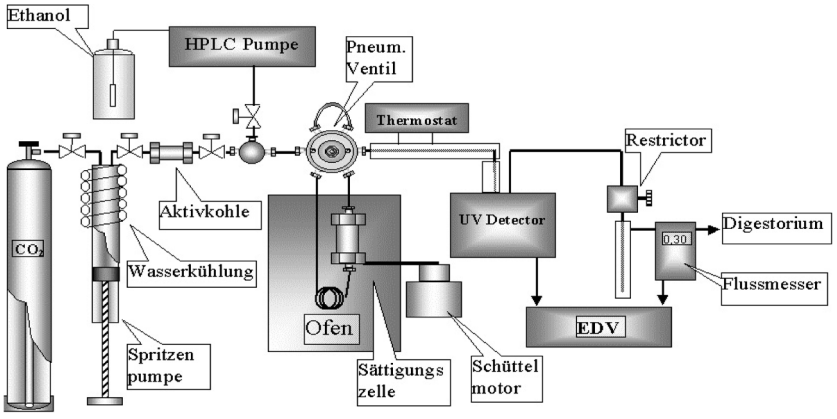

Fig. 4. Apparatus for online dynamic-spectroscopic measurement of chelate solubility.

CO_2 is at operating temperature prior to entering the saturation cell. After pressurizing the cell the pneumatic valve is switched to the "load" position where the sc CO_2 flows directly from the pump to the detector. In this position, the flow rate is adjusted to a value of 0.3 mL/min while the chelate dissolves in the fluid.

The dissolution of the chelates is accelerated by shaking the cell with a mixer motor (Cenco Instrumenten, Netherlands). After equilibration the valve is switched for 500 ms to a position where the saturation cell is flooded and an aliquot of the saturated solution is transferred to a "Spectra Focus" (Spectra Physics) forward scanning absorbance detector where the absorbance of the chelate aliquot is measured time-resolved. The flow rate, measured by an Aalborg mass flow meter is recorded in parallel with the signal of the UV detector. The spectra of five extractions were recorded and afterwards the chelate is eluted from the steel capillary and restrictor by pumping ethanol through it. The ethanol of the extract is removed and the chelate is treated with hydrochloric acid (1:5 v:v). This solution is analyzed with an ICP-OES (Leeman Labs, Inc.). To calibrate the system a correlation between known amounts of dissolved chelates and the area of the time resolved chelate absorption was derived. With the analyzed quantity of five extractions, the known switching time of valve and the measured flow rate, the concentration of the extracted solution can be calculated. This calculated concentration is set in relationship to the area under the spectra measured. Therefore a correlation between the area of the on line absorption area of the chelate aliquots and the solubility was found.

The system was calibrated by determination of the solubility of $Cu(thd)_2$ figure 5 [37] and comparison with the literature values. The triangles are values from Lagalante et al. The rhombs are values from our experiments.

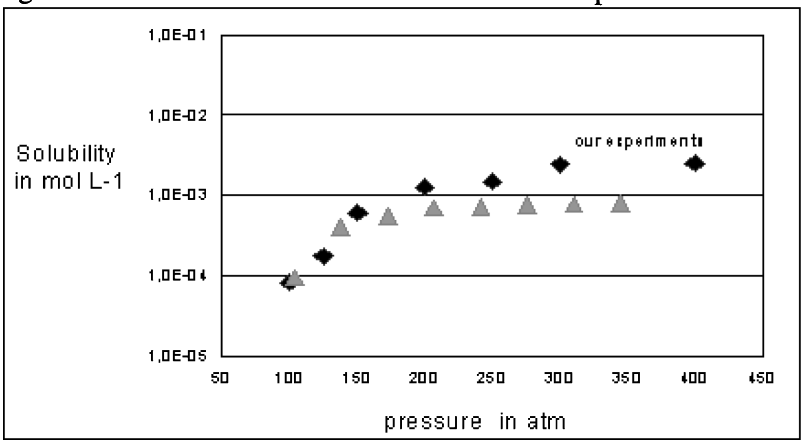

Fig. 5. Solubility of $Cu(thd)_2$ at 40°C and different pressures [37].

Solubility was determined by a UV-VIS-spectroscopic measurement of $Cu(thd)_2$ directly in the supercritical fluid cell [37]. Our solubility data for $Cu(thd)_2$ were gravimetrically determined, after collection in a solvent and drying. Our solubility corresponds well up to a pressure of 150 bar with the literature values. Above 150 atm the gravimetrically determined solubility are slightly higher.

A conversion of the solubility from mol/L^{-1} to mg/L^{-1} shows that the solubility difference are in the range of 50 mg $Cu(thd)_2$ per liter sc CO_2. Our slightly higher solubility might be due to additionally attached solvent (from the collection step), which could not be removed during drying before gravimetric determination of crystallized $Cu(thd)_2$.

4. RESULTS

4.1. Determination of the extraction yields of different arsenic chelates

Extractabilities for a series of different arsenic disubstituted dithio carbamine chelates (DDTC, DiPDTC, DBDTC, DiBDTC, DPDTC, DHDTC, DODTC, FDDTC, PhenDTC, DPhenDTC) were determined in the pressure range from 200 to 400 atm and the temperature range from 50 to 150 °C. The procedure here is different than our common procedure as described above. It is extractability, which is measured here, and not solubility. Still it delivers valuable data, which can be compared with solubility data.

A certain quantity of arsenic (200μg) and DTC ligand (10mg) was added to the extraction cell. A certain defined volume of CO_2 was flushed through the cell and then the extracted quantity of arsenic chelate was determined. This extraction procedure was selected, because it resembles more the non-continuous one vessel strategy as very common in industrial processes. Arsenic was determined in the extracts by inductively coupled plasma atomic emission spectrometry (ICP-AES). Conditions for ICP standard mode are given in Table 3, those for hydride mode are given in Table 4. The results are thus described as recoveries.

Table 3
ICP parameters for Arsenic standard determination

Auxiliary flow	0,0 l/min
Coolant flow	10 l/min
Nebulizer pressure	45 psi
Pump rate	1,0 ml/min

Table 4
ICP parameters for the hydride operation modus

Auxiliary flow	1,2 l/min
Coolant flow	15 l/min
Nebulizer pressure	35 psi
Pump rate	1,3 ml/min

Table 5
Limit of detection (LOD) and limit of determinations (LODet) of arsenic (standard and hydride mode)

Limit		Standard operation Arsen (III)	Hydride operation Arsen (III)
LOD	DFG	1,00 ppm	0,93 ppb
	DIN	0,28 ppm*	0,29 ppb
LODet	DFG	1,50 ppm	1,40 ppb
	DIN	1,80 ppm	1,51 ppb**

*0,1ppm[38]
**0,001ppm[39]

Each extraction was performed three times for statistical reasons. Each extract was measured three times. LOD`s for standard mode and hydride mode are given in Table 5.

Results for extractability of arsenic are plotted in 3D for better comparability (Fig. 6).

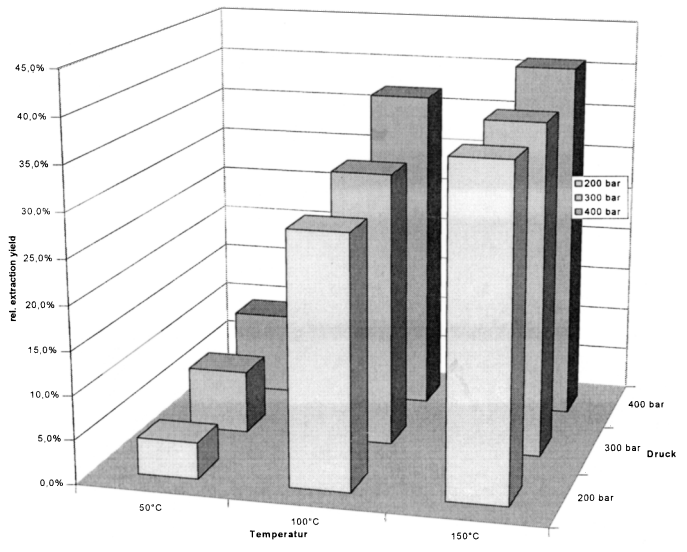

Fig. 6. Relative extraction yields of As (III) with iBDTC.

The results depicted in Fig. 6 are similar for all As-DTC's with respect to the conditions selected: With increasing pressure and with increasing temperature the solubility increases (Fig. 7).

Comparing the solubility of all studied arsenic chelates under the same extraction conditions an unexpected trend was observed: From DDTC to DBDTC solubility increases and then decreases again (Fig. 7).

Wai et al. reported that the solubility of chelates under supercritical conditions follows a trend: Longer residual alkyl chains increase the solubility [40]. It is obvious that the properties of the chelates change with a change of the residual substituent, e.g. melting point [table II] or diffusion coefficient.
However the syntheses of the long-chain chelates is often very difficult, because they do not crystallize and are thus difficult to purify.

Fluorinated dithiocarbamates exhibit a much higher solubility for many metal ions [40,41]. Fluorination of the alkyl chain in dithiocarbabamates as for example in the case of Bis(trifluoroethyl)dithiocarbamate, will increase the solubility of the metal chelates significantly [40].

Yet due to environmental concern for technical applications fluorinated ligands are not desired. Still we have determined extraction yields of As (III) with Na-FDDC at pressures from 200 to 400 bar and temperatures from 50 to 150°C is very similar. There is no significant difference in extractability for any condition studied. Even at 50°C the extraction yield is almost 100 %. Which is in agreement with the reported superb solubility of fluorinated chelates.

The solubility of arsenic diphenyldithiocarbamate is significantly lower than those of alkyl dithiocarbamates [42].

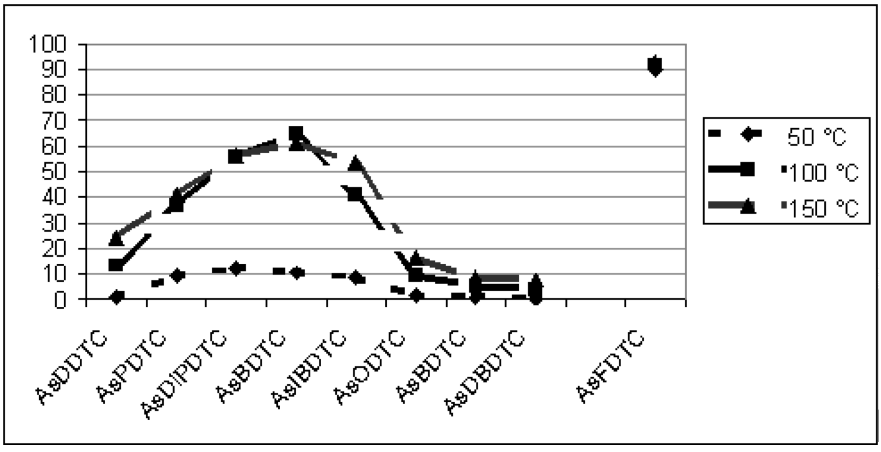

Fig. 7. Dependence of the extraction yields on the length of the chain of the chelates.

It is reported in the literature that the solubility of Cu, Zn, and Hg dithiocarbamates follows the order[43, 44]:

$M(FDDTC)_2 > M(DHDTC)_2 > M(DBDTC)_2 > M(DPDTC)_2 > M(DDTC)_2 > M(DPhenDTC)_2$

(DPhenDTC = Diphenyldithiocarbamate). It is also reported that increasing pressure and temperature will increase the solubility of dialkyldithiocarbamates in the pressure range 100 to 400 and temperature range 50 to 150 °C [43].

Ligands substituted by phenyl show a considerably lower solubility in supercritical CO_2 than the aliphatic substituted ligands and are therefore very seldom used. Our results of the change of the arsenic extraction yields with respect to increasing side chain length are in general in agreement with previous reports. However we do observe a decreasing extractability when the alkyl side chain is bigger than butyl. Comparing the extraction yields of our experiments for As(III)DDTC and As(III)FDDTC shows, that the extraction of As(III)FDDTC is quantitative, while that of e.g. As(III)DDTC is only at about 25% at 150°C and only 1% at 50°C.

4.2. Solubility of different metal chelates

In a comparative study the solubility of three different representative ligands (DIPDTC; THD, MTG) and of three different metal ions (Pd, Rh, Pb) in sc CO2 was studied Table VI.

The conditions of solubility determination were: Pressure between 15 and 40 MPa and temperatures of 50, 60 and 70°C respectively. They are compiled in Table VI. It is apparent that the solubility differences of Pd/Rh DTC and ß-diketone are sufficiently large that selective extraction becomes possible.

Table 6
Solubility [mol L^{-1}] of different metal chelates in sc CO_2

50 °C			
Ligand	Pd	Rh	Pb
DiDTC	10^{-5}	2.4 10^{-4}	6.7 10^{-4}
THD	1.7 10^{-2}	2.2 10^{-4}	-
MTG	9.3 10^{-5}	1.5 10^{-4}	-
60 °C			
DiDTC	1.65 10^{-5}	3.4 10^{-4}	7.5 10^{-4}
THD	1.8 10^{-2}	3.0 10^{-4}	-
MTG	1.1 10^{-4}	2.1 10^{-4}	-
70 °C			
DiDTC	2.2 10^{-5}	3.8 10^{-4}	1.39 10^{-3}
THD	1.9 10^{-2}	3.8 10^{-4}	-
MTG	4.9 10^{-5}	3.6 10^{-5}	-

A series of four 3D plots illustrates the dependences of T and p on solubility (Fig. 8-11).

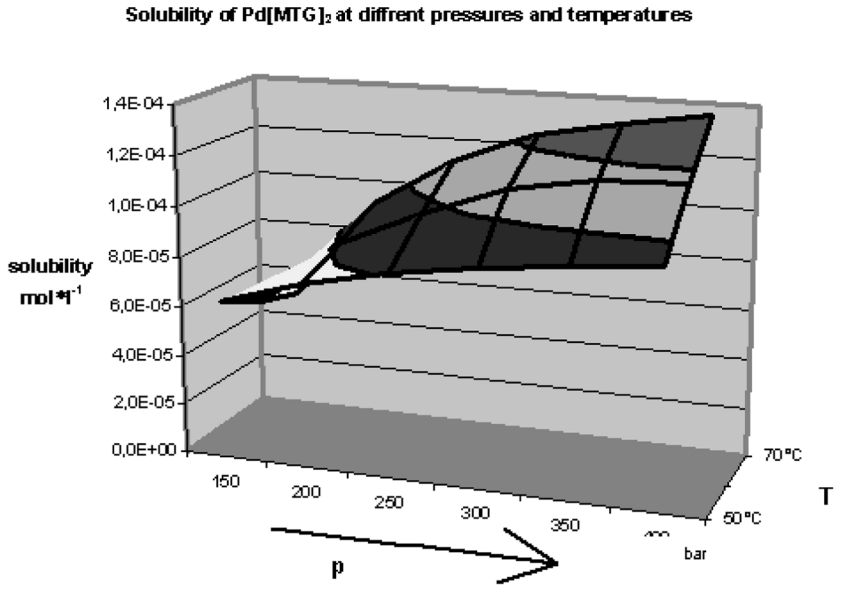

Fig. 8. Solubility of $Pd(MTG)_2$.

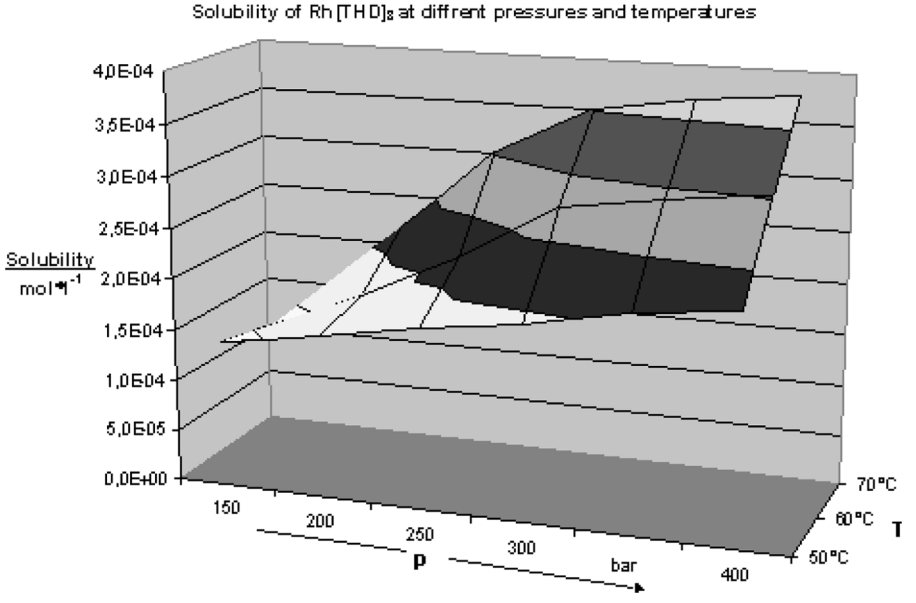

Fig. 9. Solubility of Rh(III) THD_3 .

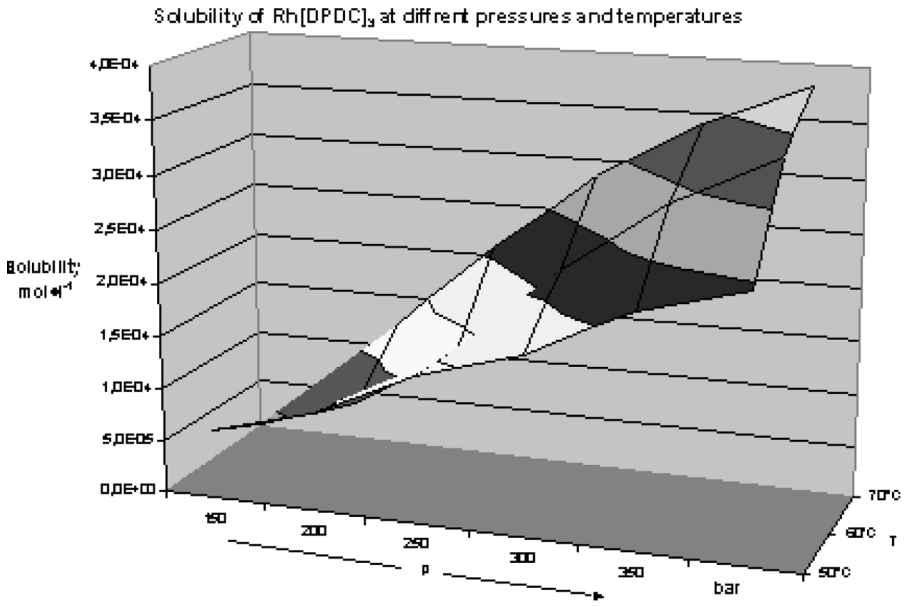

Fig. 10. Solubility of Rh(III)DPDTC$_3$.

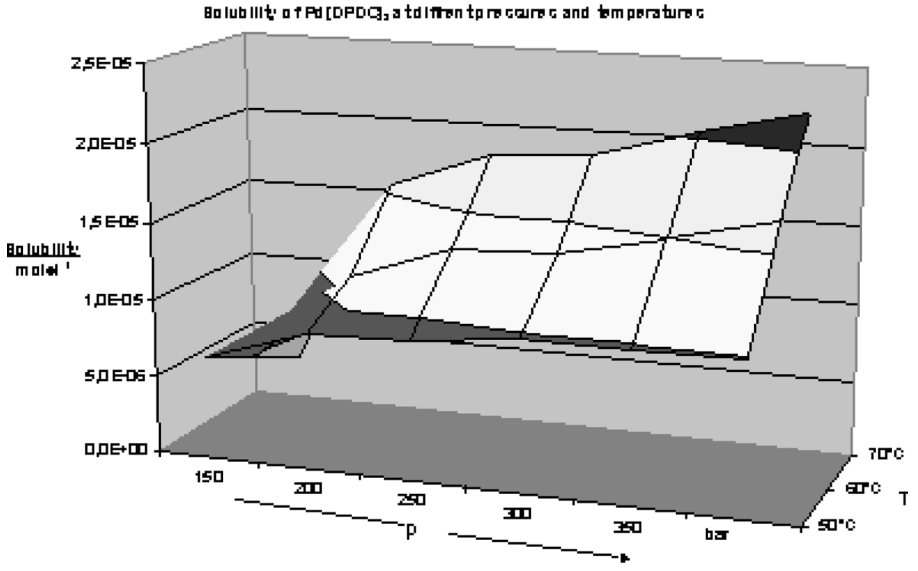

Fig. 11. Solubility of Pd (II)-DPDTC.

In general the solubility increases with increasing pressure and above 200 bar also with increasing temperature.

As a general rule it can be concluded, that the solubility for DiPDTC chelates increases from Pd via Rh to Pb and the solubility for MTG chelates follows the same trend (Pb does not form a MTG chelate). For the β-diketones this is not the case. The solubility of Pd $(thd)_2$ is two orders of magnitude bigger than the corresponding Rh $(thd)_3$. We do not know if this is due to a modifier or solvent present.

Recently we have focused on solubility of dialkyl dithio carbamates of Pd and Rh. Again the influence of the dtc alkyl chain length on the Pd/Rh chelate solubility in sc CO_2.is studied. Pressure was 300 bar and the temperature varied only between 50°C for Palladium and 60 °C for Rhodium. In Figure 12 comparison of the solubility is presented.

Once more the largest solubility were measured for a butyl di thio carbamate. The influences of the geometry, size and molecular mass of the chelates on the solubility have to be studied in more detail.

The differences in solubility for Pd and Rh cannot be attributed to the slightly different temperatures. We assume that the octahedral coordination of rhodium with three ligands results in a higher solubility than the corresponding two ligand coordination of palladium. It is (well) known that chelates with the coordination number Z = 3 always have a larger solubility than the analogous compounds with the coordination number Z = 2. For Z=2 a square (quadrate) plane or tetrahedral structure is possible. The spatially (sterically) stronger protection of the central atom at the octahedral coordination with nonpolar alkyl

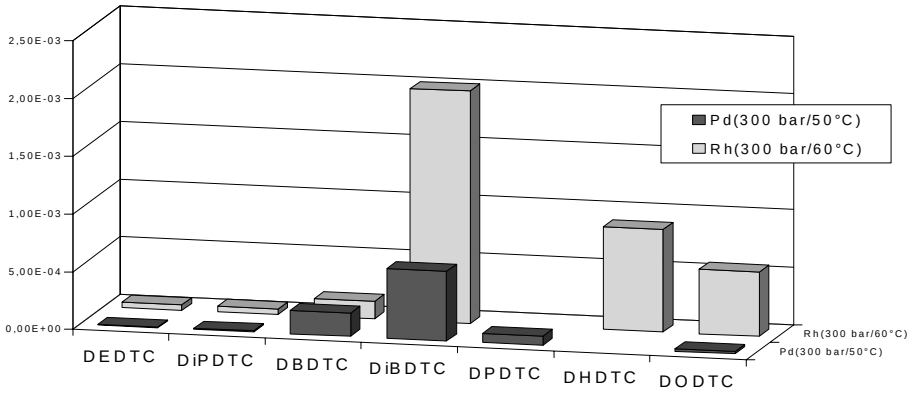

Fig. 12. Solubility of different PdDDTC at 300bar/50°C and RhDDTC at 300bar/60°C.

substituents results in a decrease of the chelate polarity and respectively in an increase of the sublimation pressure of the chelate, which is directly connected with the solubility. Consequently the solubility of the dialkyldithiocarbamates in sc CO_2 strongly depends on the structure of the alkyl side chains.

5. CONCLUSIONS

The solubility in sc CO_2 of different metal chelates with systematically modified ligands was studied. For dialkyl dithiocarbamates the maximum solubility for all studied conditions was observed when a butyl substituent was attached to the chelate ligand. Fluorination will further increase the solubility however fluorinated ligands are of major environmental concern and thus not derived in technical processes.

Attaching of aryl instead of alkyl does not increase the solubility. This is in accordance of literature data [2].

The dialkyldithiocarbamate ligands are suitable for an efficient extraction of the precious metals; this holds also true because this ligand can be synthesized without great expense and because the basic chemicals are relatively moderate in price (ca. 2 €/L^{-1}).

To improve the understanding of the relation structure and solubility in sc CO_2 further studies are necessary.

Solubility of metal chelates in sc CO_2 are relatively low and thus currently not suitable for technical applications. Modifier in CO_2 or additional complexing agents might improve the solubility and should be studied.

ACKNOWLEDGEMENT

We wish to thank the German science foundation (DFG) for the support through grants We 1073/9-1+2 and 13-1+2+3. We thank Dr. R. Nagel for the x-ray structure of Pd(DPeDTC)2.

REFERENCES

[1] T. L. Chester, J.D. Pinkston, D. E. Raynie: Supercritical Fluid Chromatography and Extraction. Anal. Chem. 70, 1998, 301R-319R.

[2] A. Baiker: Supercritical Fluids in Heterogeneous Catalysis, Chem.Rev., 99, 1999, 453-473.

[3] A. V. Yazid, E. J. Beckmann: Design, Synthesis and Evaluation of Novel, Highly CO2-Soluble Chelating Agents for Removal of Metals:Ind. Enrg. Chem. Res., 35, 1996, 3644-3652.

[4] H. O. Ohde, F. Hunt, C. M. Wai: Synthesis of Silver and Copper Nanoparticles in a Water-in-Supercritical-Carbon Dioxide Microemulsion, Chem. Mater.,13, 2001, 4130-4135.
[5] P. G. Jessop, W. Leaner: Chemical Reactions using Supercritical Fluids, VCH, 2000.
[6] J. Jung, M. Parrot: Particle design using supercritical fluids; Literature and patent survey. J. Supercritical Fluids, 20, 2001, 179-219.
[7] R. Maharani, J. F. Bouquet, K. Chhor, C. Pommier: Solubility and Decomposition Studies on Metal Chelates in Supercritical Fluids for Ceramic Precursor Powder Synthesis. J. Supercritical Fluids, 4, 1991, 55-59.
[8] F. E. Wubbolts, R.E. A. Buijse, O. S. I. Bruinsma: Semi-batch gas anti-solvent precipitation of poly (2,6 dimethyl-1,4-phenyl-ether). Delft University of Technology, Laboratory for Process Equipment. Sept., 1996, 13th Symposium, Toulouse, France.
[9] U. Förter-Barth, U. Teipel, H. Krause: Formation of Particles by Applying the GAS-Process. Frauenhoffer Institut für Technologie, Pfinztal, I.S.A.S.F., April 1999, Nottingham.
[10] B. W. Wenclawiak, H. Beer, A. Ammann, A. Wolf: Solubility and modifications of metal chelates in supercritical carbon dioxide. ACS, 2003, in print.
[11] Y. Lin, R. Brauer, K. E. Laintz, C. M. Wai: Supercritical Fluid Extraction of Lanthanides and Actinides from Solid Materials with Fluorinated ß-Diketones. Anal. Chem., 65, 1993, 2549-2551.
[12] K. W. Weissmahr, C. L. Houghton, D. L. Sedlak: Analysis of the Dithiocarbamate Fungicides Zriam, Menab, and Zineb and the Flotation Agent Ethylxanthogenate by Ion-Pair Reversed-Phase HPLC. Anal.Chem.,70, 1998, 4800-4804.
[13] M. A. Malik, P. O'Brien, N. Revaprasadu: Synthesis of TOPO-capped PtS and PdS nanoparticles from $[Pt(S_2CNMe(Hex))_2]$ and $[Pd(S_2CNMe(Hex))_2]$. J. Mat. Chem.,12(1), 2002, 92-97.
[14] L., Sindellari, L. Trincia, M. Nicolini, M. Carrara, L. Cima, S. Zampiron: Dithiocarbamates as antagonists of cisplatin toxicity. Inorg. Chim. Acta, 137(1-2), 1987, 109-113.
[15] H. Ohde,C. M. Wai, H. Kim, J. Kim, M. Ohde,: Hydrogenation of Olefins in Supercritical CO_2 catalyzed by Palladium Nanoparticles in a Water-in-CO_2 Microemulsion. J. Am. Chem. Soc.,124, 2002, 4540-4541.
[16] G. Faraglia, D. Fregona, S. Sitran, L. Giovagnini, C. Marzano, F. Baccichetti, U. Casellato, R. Graziani: Platinum(II) and palladium(II) complexes with dithiocarbamates and amines; synthesis, characterization and cell assay. J. Inorg. Biochem. 83(1), 2001, 31-40.
[17] A. Uhlin, S. Åkerström: The Association of Alkali Metal N,N-Dialkyldithiocarbamates in Solution. Acta Chemica Scandinavica. 25, 1971, 393-410.
[18] A. Hulanicki: Complex Reactions of Dithiocarbamates. Talanta, 14, 1967, 1371-1392.
[19] H. Bode: Systematische Untersuchungen über die Anwendbarkeit der Diäthyldithiocarbamate in der Analyse. Fres. Z. Anal. Chem., 144, 1995, 165-186.
[20] Beer, H.: Synthese und Charakterisierung von Diisopropyldithiocarbamaten des Bleis, Rhodiums und Palladiums, Studienarbeit, Universität Siegen, 1994.
[21] B. W. Wenclawiak, P. Schulze, V. Uebis: Micro Reversed Phase Liquid Chromatography of Cd, Ni, Zn, Cu, Co, Hg-Diethyldithiocarbamates at Pictogram Level. Microchimica Acta, II, 1984, 251-262.
[22] B. W. Wenclawiak, F. Bickmann: Liquid Chromatographic Separation of some Platinoid Metal 8-Hydroxychinolates. Bunseki Kagaku, 33, 1984, E67-E72.

[23] S. Dilli, P. Tong: Liquid chromatography of metal chelates. Chromatographic studies of homologous dialkyldithiocarbamates. Analytica Chemica, 395, 1999, 101-112.
[24] M. A. Arain, M. Y. Khuhawar, M. I. Bhanger: Capillary Gas Chromatography of Metal Chelates of Diethyl Dithiocarbamates. Chromatographia, 55, 2002, 349-352.
[25] K. Kristsotakis, H. J. Tobschall: Gas-chromatographic separation of the noble metals gold, platinum, palladium, rhodium, and iridium as bis(trifluoroethyl)dithiocarbamate chelates. Fres. Z. Anal. Chem., 320(2), 1985, 152-155.
[26] M. L. Riekkola: Capillary Gas Chromatography of Some Metal Chelates of Dipropyl- and Dibutyldithiocarbamic Acids. Microchimica Acta, I, 1982, 327-334.
[27] Y. Lin, H. Wu, C. M. Wai, N. G. Smart: Separation of divalent transition metal ß-diketonates and their adducts by supercritical fluid chromatography. Talanta, 52, 2000, 695-701.
[28] E. B. Sandell, H. Onishi: Photometric Determination of Traces of Metals, John Wiley & Sons, New York, 1978.
[29] Y. Lin, H. Wu, C. M. Wai, N. G. Smart: Separation of divalent transition metal β-diketonates and their adducts by supercritical fluid chromatography. Talanta, 52, 2000, 695-701.
[30] K. E. Jarvis, S. J. Parry, J. M. Piper: Temporal and Spatial Studies of Autocatalyst-Derived Platinum, Rhodium, and Palladium and Selected Vehicle-Derived Trace Elements in the Environment, Environ. Sci. Technol., 35, 2001, 1031-1036.
[31] F. Zereini, F. Alt, B. Skerstupp, J. Messerschmidt, J. Müller, Tagungsband Edelmetall-Forum, Frankfurt am Main, 1999.
[32] P. L. Buldin, S. Cavalli, A. Trifido: State-of-the-art ion chromatographic determination of inorganic ions in food. J. of chromatog. A: 789, 1997, 529-548.
[33] B. W. Wenclawiak, M. Krah: Reactive supercritical fluid extraction and chromatography of arsenic species, Fresenius J Anal Chem., 351, (1995), 134-137.
[34] Knothe, M.: Untersuchungen zur Extraktion der Pt-Metalle mit Tributylphosphat aus salzsauren Lösungen. Z. anorg. Allg. Chem., 1980, 470, 216-226.
[35] W. Cross, A. Akgerman: Determination of Metal-Chelate Complex Solubilities in Supercritical Carbon Dioxide. Ind. Eng. Chem. Res., 35(5), 1996, 1765-1770.
[36] C. M. Wai, S. Wang, Y. Liu, V. Lopez-Avila, W. F. Beckert: Evaluation of dithiocarbamates and ß-diketones as chelating agents in supercritical fluid extraction of Cd, Pb and Hg from solid samples. Talanta, 43, 1996, 2083-2091.
[37] A. F. Lagalant, B. N. Hansen, T. J. Bruno, R. E. Sievers: Solubilities of Copper (II) and Chromium (III) ß-Diketonates in Supercritical Carbon Dioxide. Inorg. Chem., 34, 1995, 5781-5785.
[38] DIN EN ISO 11885, LAWA, Merkblatt P3/1.
[39] DIN EN ISO 11969 (D18).
[40] C. M. Wai, S. Wang: Solubility Parameters of Metal Dithiocarbamates in Supercritical Carbondioxide. Anal. Chem., 68, 1996, 3516-3519.
[41] J. Wang, W. D.Marshall: Anal. Chem., 66, 1994, 1658.
[42] B.W. Wenclawiak, S. Uttich, H. J. Deiseroth, D.Schmitz: Studies on bulky residual group substituted arsenic(III) dithiocarbamate structures, Inorg. Chim. Acta, 348, 2003, 1-7.
[43] C. M. Wai, S. Wang: Supercritical Fluid Extraction: metals as complexes, J. of chromat. A, 785, 1997, 369-383.
[44] M. Ashraf-Khorassani, L. Taylor: Supercritical Fluid Extraction of mercury (II) ion in situ chelation and pre-formed mercury complexes from different matrices. Anal. Chem. Acta, 379, 1999, 1-9.

Supercritical Fluids as Solvents and Reaction Media
G. Brunner (editor)

Chapter 2.1.

p,T- dependence of molecular mobility in supercritical fluids studied by high pressure NMR

T. Groß[a], Liuping Chen[b], and H.-D. Lüdemann[a]

[a]Institut für Biophysik, Universität Regensburg, D-93040 Regensburg, Germany
[b]Institute of Physical Chemistry, School of Chemistry and Chemical Engineering, Zhongshan (Sun Yat-Sen) University, Guangzhou 510275, People's Republic of China

1. INTRODUCTION

The studies described in this chapter were undertaken with the aim to learn more about the dynamic behaviour of compressed supercritical neat fluids and their binary mixtures. The knowledge of the kinetic properties of these fluids is important for the optimisation of technological processes that make use of the unique properties of the supercritical state [1]. Another reason for the investigation of the systems studied below being that a quantitative analytical theory of molecular dynamics is still lacking. Experimental data of fairly simple fluid systems can provide a data basis against which the validity of newer approaches for the solution of this classical problem can be checked [2,3]. In the following, the self diffusion coefficients D_i for some simple fluids (hydrogen, deuterium, carbon dioxide, and ammonia) measured over a wide p,T -range will be discussed. Also the intradiffusion coefficients D_{ii} for some binary fluids with ammonia resp. carbon dioxide as one component will be presented.

For the most basic model of the neat fluid state, the hard sphere (HS) model, extensive and critically evaluated computer simulations as function of the density exist. The density and temperature dependences of the dynamic properties of this HS model system are commonly described as functions of the packing fraction by empirical polynomia. The comparison of experimental D_i for simple fluids is possible only, if p,V,T-data are known for the system to be studied. For the four compounds given above these data are also available. Attempts to describe the D_{ii} in binary mixtures by HS-models would demand a large set of MD-simulations in which the composition, the density, the mass- and the diameter- ratios would have to be varied. Simulations of that kind are

only partially available[4,5]. Furthermore no experimental densities exist for the binary fluids studied in this investigation.

2. EXPERIMENTAL

The self diffusion coefficients were measured in a strengthened glass cell proposed by Yamada [6]. Modifications introduced by our group to this design as well as the filling procedures have been published [7,8]. The high pressure apparatus was assembled from commercial parts. For the work given below, it proved essential to have a reliable separation system to prevent the pressurising liquid from contaminating the sample. A home made sliding piston design was used. It is customary to use O-rings for sealing the sliding piston. However, ammonia as well as carbon dioxide are absorbed in the O-ring at elevated pressures thus swelling the ring. A piston sealed in this way becomes leak after a rather short period. The attempt to use any other O-ring material available to us resulted in little improvement. After several futile attempts to design a more reliable seal, the use of an indium ring in the sliding piston described in detail in Fig. 1 proved to be the best solution. The separation of pressurizing liquid and fluid sample was reliable for periods of up to a week and the isotopically enriched compounds could be recovered without impurities and reused. The disadvantage of this setup is that after prolonged use a fraction of the indium is squeezed into the annular space between piston and cylinder and thus the friction in the seal increases with time. In order to determine the sample pressure precisely it is necessary to mount a strain gauge at the sample filled side of the separation volume. This strain gauge and a double stem three way valve were mounted at the right side of the separation volume. These details are not shown in Fig.1.

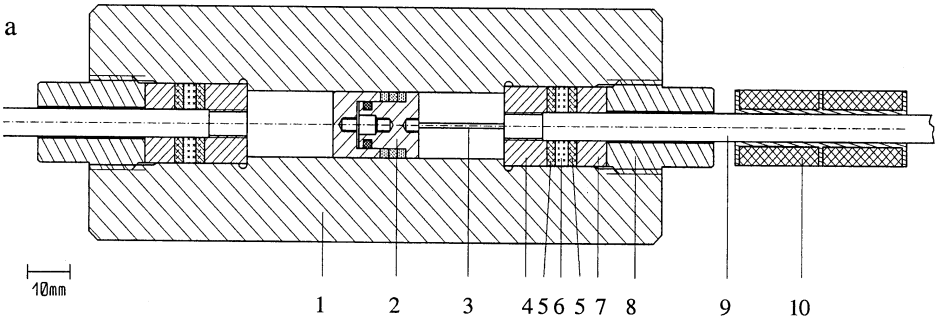

Fig. 1 a) Separation volume: 1: Cylinder (Material; nonmagnetic TiAl6V4), 2: self sealing gliding piston (Material, TiAl6V4), 3: rod with ferromagnetic tip, 4: Bridgman seal, 5: POM rings, 6: Indium seal ring, 7: Support ring (TiAl6V4), 8: Retaining screw (TiAl6V4), 9: Commercial 6mm high pressure tube, 10: linear position transducer.

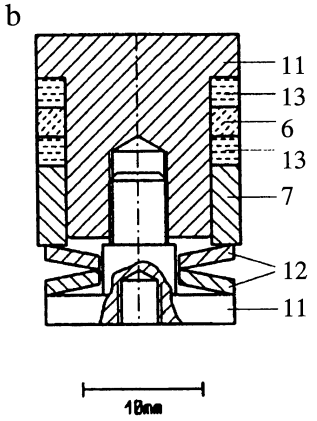

Fig. 1b. Details of self sealing piston: 6: Indium seal ring ,7: Support ring (TiAl6V4), 11: Body of gliding piston (TiAl6V4), 12: CuBe Belleville springs, 13: Copper support rings.

3. THEORY

The self diffusion data for the neat substances are analysed with the rough hard sphere (RHS) model proposed by Chandler [10,11]. This model combines results from the gas kinetic theory by Chapman and Enskog [2,12] with molecular dynamics simulation for the smooth hard sphere (HS) model system[13,14]. The diffusion coefficient D_{0HS} for a dilute gas composed of hard spheres is given by [1]

$$D_{0HS} = \frac{3}{8\rho\sigma^2}\left(\frac{k_B T}{m\pi}\right)^{1/2} \tag{1}$$

with ρ the number density, σ the hard sphere diameter, k_B Boltzmann's constant, T the absolute temperature and m the mass of the spherical particle. For denser gases Enskog scaled this expression with the value of the radial distribution function $g(\sigma)$ at contact distance σ.

$$D_{EHS} = D_{0HS} / g(\sigma) \tag{2}$$

MD-simulations by Alder and his group [13] on the HS model system revealed the existence of correlations between the molecular velocities of nearest neighbour molecules. As a consequence the self diffusion coefficient

D_{HS} of the HS liquid has to be expressed by an empirical polynomial P(n) of the packing density n, with $n = \rho \cdot \sigma^3$ leading to the expression:

$$D_{HS} = D_{0HS} \cdot P(n) \tag{3}$$

Speedy [15] critically reassessed the existing HS-MD simulations and derived for $P(n)$:

$$P(n) = \left(1 - n/1.09\right) \cdot \left[1 + n^2\left(0.4 - 0.83n^2\right)\right] \tag{4}$$

Chandler's [9,10] comparisons of the early experimental high pressure D_i with the HS MD-simulations led to the observation that in real fluids at equal values of T and ρ D_i is always lower than D_{HS}. He ascribed this to the fact that real molecules deviate from spherical symmetry and thus rotation-translation coupling must occur, leading to a reduction of D_i . The observed reduction is described by an empirical parameter A named rotation translation coupling parameter. By definition follows $A \leq 1$.

$$D_i \approx D_{RHS} = AD_{HS} \tag{5}$$

This treatment needs 2 free fit parameters for the description of D_i, the A parameter and the HS-diameter σ. It is generally agreed upon that for real molecules σ should decrease slightly with increasing temperature, since the repulsive part of the interaction of real hard spherical molecules cannot be infinitely steep. Experimentally it was found [14] that in most fluid systems the A parameter is decreasing with falling temperature. Speedy [15] concluded from this observation that for most real liquids attractive interactions contribute to the reduction of D_i .

4 RESULTS NEAT FLUIDS

The analysis of the four neat systems studied here by application of the RHS-model yielded some remarkable surprises that will be discussed next.

The D_i data for NH_3 [16] are given in Table 1. The rotation-translation coupling parameter A and the RHS diameter σ derived from the data are given in Table 2.

The results of Table 2 are typical for substances like CH_4 [17] and CF_4 [18], which are non-polar and in good approximation spherical. Among the compounds studied hitherto these two would be expected to behave most similar to the HS-model system. In these fluids $A \approx 1$ in the whole range studied and

Table 1
D_i (m^2s^{-1}) of fluid NH_3

T(K)	10MPA	50MPa	100MPa	150MPa	200MPa
203	2.61E-9	2.37E-9	1.90E-9	1.67E-9	
213	3.40E-9	2.93E-9	2.54E-9	2.23E-9	1.88E-9
223	4.13E-9	3.69E-9	3.03E-9	2.77E-9	2.39E-9
243	6.02E-9	5.29E-9	4.61E-9	4.10E-9	3.56E-9
273	9.30E-9	8.10E-9	7.01E-9	6.20E-9	5.57E-9
299	1.28E-8	1.11E-8	9.50E-9	8.31E-9	7.65E-9
332	1.98E-8	1.67E-8	1.42E-8	1.23E-8	1.09E-9
373	4.92E-8	2.56E-8	2.01E-8	1.72E-8	1.52E-8
423		3.95E-8	2.89E-8	2.45E-8	2.18E-8
473		5.30E-8	3.85E-8	3.21E-8	3.01E-8

Table 2
A-parameter and RHS diameter σ for NH_3 (Mean standard deviation ±1.5%)

T(K)	213	223	243	273	299	332	373	423	473
A	1.00	1.00	0.91	0.87	0.90	1.00	1.00	1.00	1.00
σ(nm)	0.33	0.33	0.32	0.32	0.32	0.31	0.31	0.30	0.30

thus independent of temperature, σ is reduced by ~5% with increasing temperatures (between 160K and 450K).

In chemistry textbooks NH_3 is introduced as one of the fluids similar in hydrogen bonding to hydrogen fluoride and the alcohols. In these liquids *A* decreases dramatically with falling temperature at the lowest temperatures to $A \approx 0.01$ [8,19]. While the RHS-diameters σ show a much lower *T*-dependence (a decrease of ~5% in the T-range investigated) and are very close to the mean diameter taken from molecular models. Also the diameter of NH_3 derived from the RHS-analysis are close to the results obtained from crystal data and mechanical models. The *A*-parameter shows no significant change with temperature.

These data give no indication of any influence of hydrogen bonding upon the molecular dynamics. Other spectroscopic evidence for hydrogen bonding [20-22] is controversial. Recently a model was derived from MD-computer simulations [23,24] that explained the high molecular mobility in fluid NH_3 by the transient formation of ammonia dimers with two cyclic hydrogen bonds between two molecules. These bonds should provide a low energy pathway for the molecular reorientation and facilitate diffusion. Studies on the three methyl amines [25] and some of their mixtures with NH_3 [26] make a significant contribution of these cyclic intermediates to the molecular dynamics in ammonia very unlikely.

Also the analysis of D_i for carbon dioxide [27] showed some unexpected features. In Fig. 2 isotherms of D_i (CO_2) are presented. These results were taken with carbon-13 enriched carbon dioxide (99% C-13). NMR experiments with the C-13 nucleus have because of its low gyromagnetic ratio a sensitivity that is about two orders of magnitude ($1.59 \cdot 10^{-2}$) lower than for hydrogen. Thus these experiments consumed plenty of instrument time and could at the higher temperatures not be extended to the lower pressures. Etesse at al. [28] working with a more voluminous NMR probe that confined their work to $p < 50$MPa could cover some of the low pressure region.

To our surprise it proved very simple to undercool CO_2 deeply. We could without extreme efforts extend our high pressure data 70K below the melting pressure curve. The solid line drawn through the data in Fig. 2 gives the approximate position of the melting pressure curve.

These data could be well within the limits of the precision of the data fitted by the RHS model. However the results derived showed for most of the isotherms an A-parameter $A \geq 1$ which is physically without meaning. Also the RHS-diameter σ reveals a very unsystematic T-dependence. The most probable explanation for these findings is that the good fit is fortuitous and that fluid CO_2 should rather be described by a hard dumbbell. Unfortunately systematic MD-simulations of the hard dumbbell system are lacking.

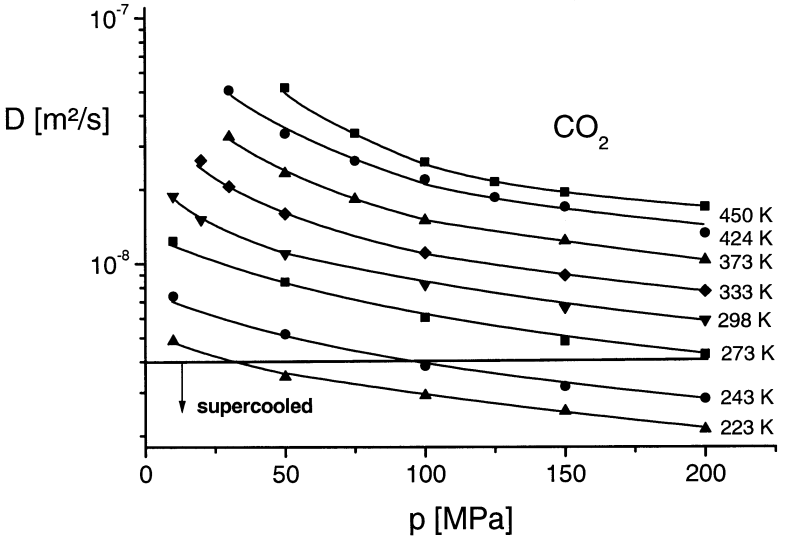

Fig. 2. Isotherms of D_i of neat CO_2. The full approximately horizontal line gives the position of the melting pressure curve. All data below this line belong to the metastable undercooled state.

The data obtained for the CO_2 and for the fluids discussed next, H_2 and D_2 , [29] could only be obtained with the newly developed gliding piston separator with indium seal described above. Fig. 3 shows the isotherms for D_i (D_2). Although the data extend to a maximum pressure of 200 MPa, they are confined to rather low packing densities, and thus the fit of the data to the RHS model is not very sensitive. Also the available published p,V,T-data cover only part of the pressure and temperature range of our experiments and had to be extrapolated.

Thus the most simple RHS fit with setting the rotation translation coupling parameter A to A = 1 was done. This yielded reasonable values for σ ($\sigma(H_2$, 274K) = 0.264nm, $\sigma(H_2$, 373K) = 0.2249nm, $\sigma(D_2$, 274K) = 0.243nm, $\sigma(D_2$, 373K) = 0.238nm). However the attempts to fit the experimental D_i with A as a free parameter yielded inconsistent parameters and lead to the suspicion that the hydrogen isotopes should rather be compared to a hard dumbbell fluid.

From the analysis of these four simple neat fluids it becomes apparent that the attempts to characterise real fluids by the RHS model yields interesting but semi-quantitative information. Previous work on a wide variety of fluids like alkanes and halo-methanes but also the lower alcohols [30, 31] showed that the parameter A for most fluids decreases strongly with decreasing temperature. Its interpretation as a sterical factor, measuring the deviation from spherical symmetry of the particles in a fluid cannot explain this finding. Rather A should be taken as an empirical parameter that monitors the contributions from attractive interactions and the deviations from spherical shape to the molecular dynamics.

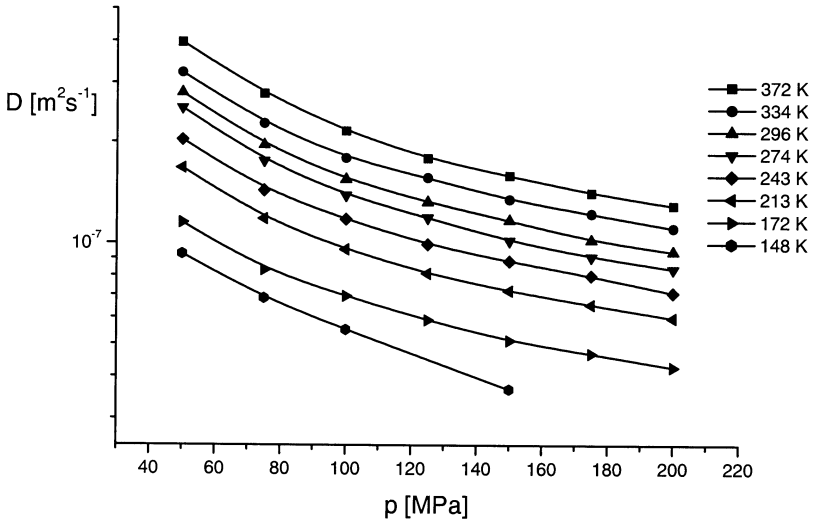

Fig.3. Isotherms of the self diffusion coefficient D_i for neat deuterium.

However our knowledge of the condensed fluid dynamics is even more incomplete. From Eq. (1) it follows, that the dynamics for a pair of molecules of identical shape and chemical composition (the typical examples being isotopomers, M and N), should scale with the square root of the mass ratio. The reduced diffusion coefficient $D_{r,\,p,T}$ is defined by:

$$D_{r,p,T} \equiv \frac{D_M}{D_N} = \sqrt{\frac{m_M}{m_N}} = m_r \tag{6}$$

It should be independent of T and p. In Fig. 4, 100MPa isobars of $D_{r,\,p,T}$ for several pairs of isotopomers are given. They all show a pronounced temperature dependence. $D_{r,\,p,T}$ in all cases decreasing with increasing temperature. For most compounds $D_{r,p,T}$(exp) is found significantly larger then the value derived from Eq. (6). The pair H_2/D_2 being until now the only example where the experimental result is lower than the value calculated from Eq. (6) ($m_r = 2^{1/2} = 1.41$).

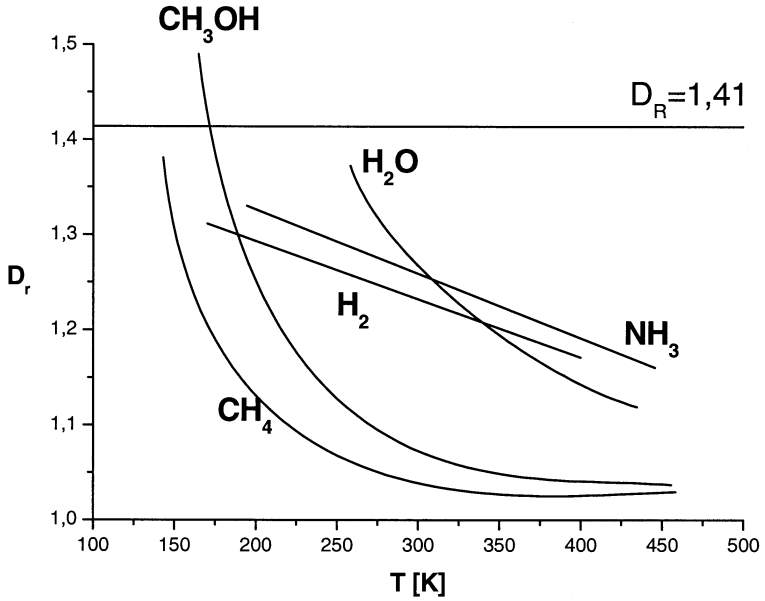

Fig.4. 100MPa isobars of $D_{r,p,T}$(exp) defining the dynamic isotope effect defined by Eq.(6).

5. RESULTS BINARY MIXTURES

For the description of the translational molecular mobility in a homogeneous binary mixture the term intradiffusion coefficient D_{ii} has been introduced [31]. It is defined by:

$$\frac{\partial c_1}{\partial t} = D_{ii} \frac{\partial^2 c_1}{\partial x^2} \quad (c\text{-gradient}_{t=0} = 0) \tag{7}$$

Only a few high pressure intra-diffusion studies exist that extend over a wide c,T -range. Older work has been reviewed [8]. Recent experiments deal with simple hydrocarbon mixtures [5, 33] and with the influence of dipole moments and hydrogen bonds upon the molecular dynamics in mixtures consisting of approximately spherical molecules [34].

The analysis of these data is hampered by the lack of reliable density data. Also comprehensive hard sphere MD-simulations for binary mixtures are still wanted.

In the following the temperature and pressure dependence of the D_{ii} is described by the activation energy $\Delta E^{\neq}_p$ at constant pressure and the activation volume $\Delta V^{\neq}$ given by:

$$\Delta E_p^{\neq} = -R\left(\frac{\partial \ln D_{ii}}{\partial 1/T}\right)_p \quad \text{and} \quad \Delta V^{\neq} = -RT\left(\frac{\partial \ln D_{ii}}{\partial p}\right)_T \tag{8}$$

It is generally agreed upon that the concept of a defined activated transition state is not applicable to transport processes in fluids. The data that will be presented below should only be taken as a convenient concept for the brief description and comparison of the T,p dependence of D_{ii} in different fluids.

5.1. Binary mixtures with carbon dioxide

Three binary mixtures of CO_2 with nonpolar molecules have been studied. The full data are compiled in [35, 36]. The mixtures with benzene as the second component show the typical behaviour for this group of compounds that is also observed in the ammonia mixtures studied below. In Fig. 5 the D_{ii} at 298K for both compounds are given as functions of the mole fraction $x(C_6H_6)$ for three pressures. In the log D_{ii} versus x plots the isobars are almost linear, thus it is possible to interpolate reliably the D_{ii} for the whole concentration range from experimental data obtained from two to three strategically chosen mixtures. Also it becomes obvious from the inspection of the full data [35, 36] that the pressure and temperature dependence are changing smoothly with pressure and it is thus

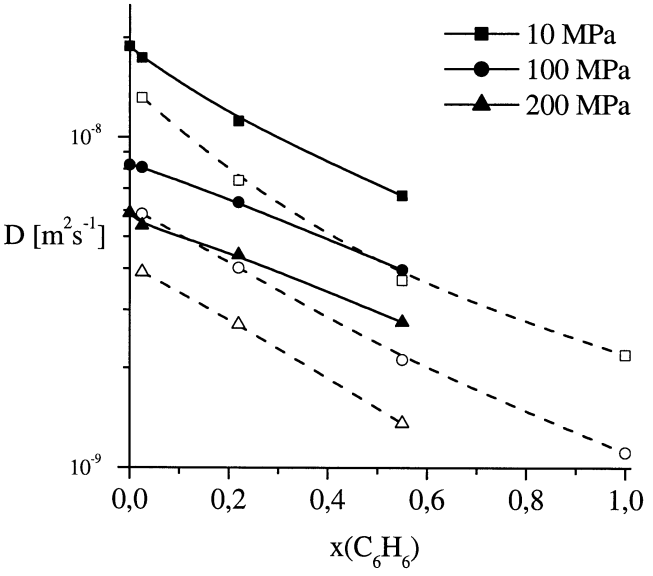

Fig. 5. Isobars of D_{ii} for both components in the system CO_2/C_6H_6 at 298K as function of the mole fraction $x(C_6H_6)$ (open symbols: C_6H_6, closed symbols: CO_2).

reliable to extrapolate the data presented considerably to pressures and temperature not covered by experiment.

In Fig. 6 the 100MPa isobars of D_{ii} as function of $x(H_2)$ in the mixtures of CO_2 and H_2 are given for three temperatures. These show contrary to the system C_6H_6/CO_2 a pronounced curvature, small additions of H_2 to CO_2 lead to a strong increase of D_{ii}. Most probably this results from the large reduction of the particle number density caused by the addition of H_2. Inspection of Fig. 5 and 6 reveals that the pressure and temperature dependences of the D_{ii} for the two components are almost identical. It becomes even more obvious from the activation parameters given in Table 3. This in our opinion indicates that the temperature and pressure dependences of the molecular dynamics of a liquid mixture are a collective property of the fluid.

In Fig. 7 some isotherms of D_{ii} for a dilute solution of palmitic acid methyl ester (PME) in CO_2 are given. This mixture was studied as an example for the typical solutes encountered in technical supercritical extraction. Although the size, shape and mass of the two components are very different, the temperature and pressure dependences of the D_{ii} are very similar, the activation energies for PME being only slightly larger than $\Delta E^{\neq}_{p}$ (CO_2) (see Table 3).

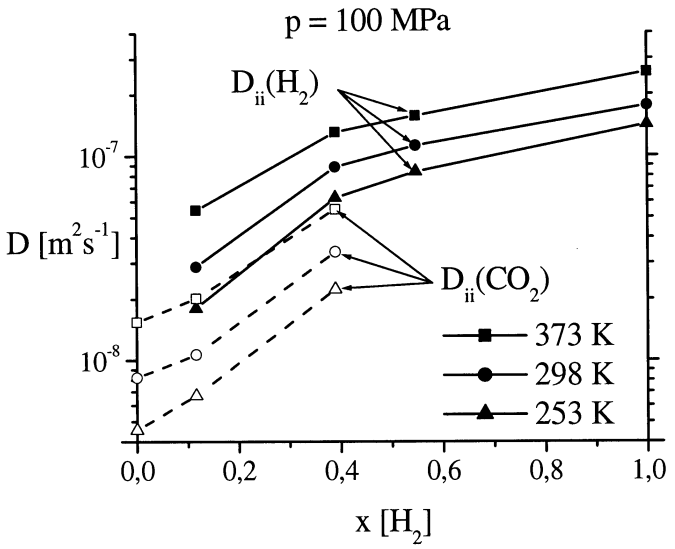

Fig.6. 100 MPa isobars of D_{ii} in mixtures of CO_2/H_2 as function of the mole fraction $x(H_2)$ (open symbols: CO_2, full symbols: H_2).

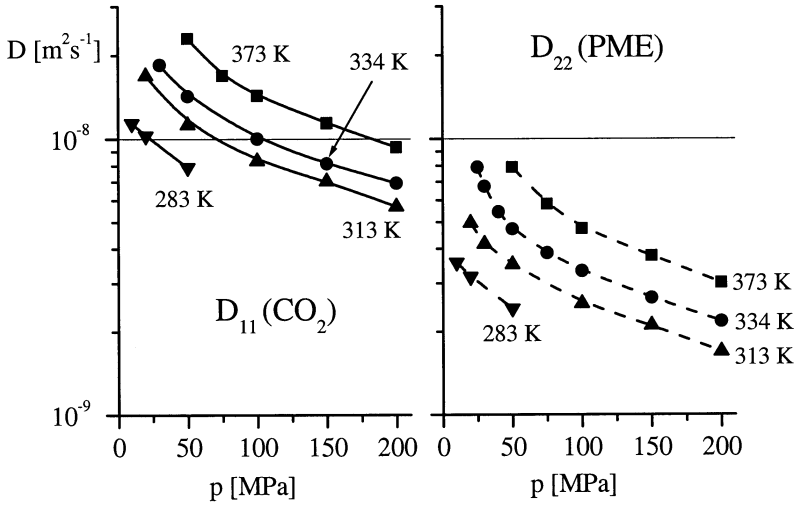

Fig. 7. Isothermal pressure dependence of the D_{ii} in a dilute solution of palmitic acid methyl ester (PME) in CO_2. x(PME)= 0.022.

In the next two binary fluids presented, molecules that may form hydrogen bonds (acetic acid and methanol) were added to carbon dioxide. The study of these systems should reveal the influence of hydrogen bonding upon the molecular dynamics and should prove, whether the carbonyl groups of the CO_2 molecules can participate in the hydrogen bonding via their lone electron pairs as acceptors.

Solutions of the mono carboxylic acids in non-polar solvents are known to form with their carboxyl groups cyclic hydrogen bonded dimers [37]. The formation of these dimers can be most sensitively followed by studying the proton chemical shift of the hydroxyl proton. Increasing temperature must lead to an increase in dissociation of these dimers. Inspection of the D_{ii} for both compounds [35, 36] indicates that the CO_2 does not participate in the H-bonding and also shows that even at the highest temperature reached by our experiments (425K) a significant fraction of the acid molecules is in dimeric form.

Pure fluid mono alcohols form via their hydroxyl group hydrogen bonded transient associates that because of the 1:2 donor/acceptor stoichiometry of the hydroxyl group can only consist of chains, branched chains and rings.

The extent of hydrogen bond formation can also be monitored by the hydroxyl proton chemical shift δ(OH). In Fig.8 $\Delta = \delta(OH) - \delta CH_3$) at constant

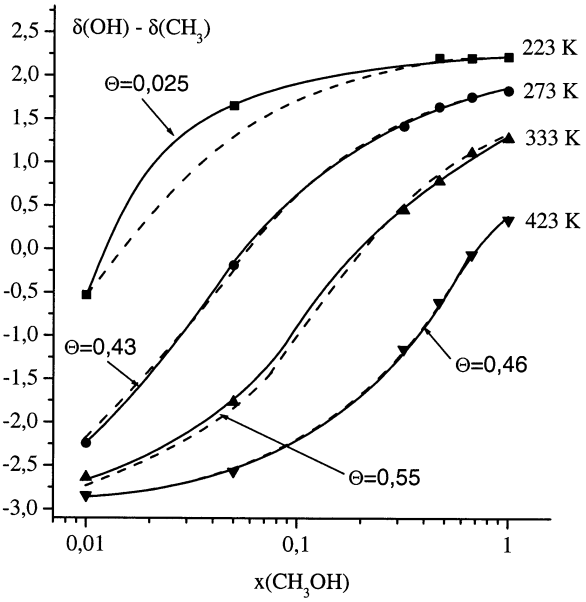

Fig.8. 100 MPa isotherms of the hydroxyl proton chemical shift δ, referenced to the methyl group of methanol, as function of x(CH_3OH). The lines through the experimental points result from fitting δ to a linear association model with Θ the free nucleation parameter The broken lines were obtained with a Θ fixed to 0.5. For details see [35].

pressure (100 MPa) is plotted as function of $x(CH_3OH)$. The data are fitted to a cooperative linear association model with a nucleation parameter Θ for the description of the dimer formation. The enthalpy for hydrogen bond formation ΔH= 16±1 kJ/mol is derived. The mathematical details for this analysis are given in [35]. This analysis proves that also in the CO_2/CH_3OH mixture the CO_2 does not participate in the hydrogen bonding.

Also the D_{ii} of the CO_2/CH_3OH system show clearly, that the CO_2 is not involved in the hydrogen bond formation. In Fig. 9 isotherms of the D_{ii} at 100MPa as function of $x(CH_3OH)$ are given for some temperatures. The concentration dependence of the $D_{ii}(CO_2)$ show in this presentation the normal nearly linear concentration dependence, as it is found in the system C_6H_6/CO_2 (Fig. 6), while the $D_{ii}(CH_3OH)$ show very pronounced deviation from this behaviour, the deviation from the normal x-dependence becoming larger with decreasing temperature. For $x(CH_3OH) \rightarrow 0$ both compounds have almost the same D_{ii}, with increasing concentration the translational mobility of the alcohol decreases much faster than the $D_{ii}(CO_2)$. This is a clear indication that transient hydrogen bonded associates are formed by the alcohol molecules. In view of the discussion given above about the incomplete understanding of the general size and mass dependence of the D_{ii} it becomes obvious that any attempt to describe the x-dependences of $D_{ii}(CH_3OH)$ by the quantitative association models presented for the chemical shift measurements is futile.

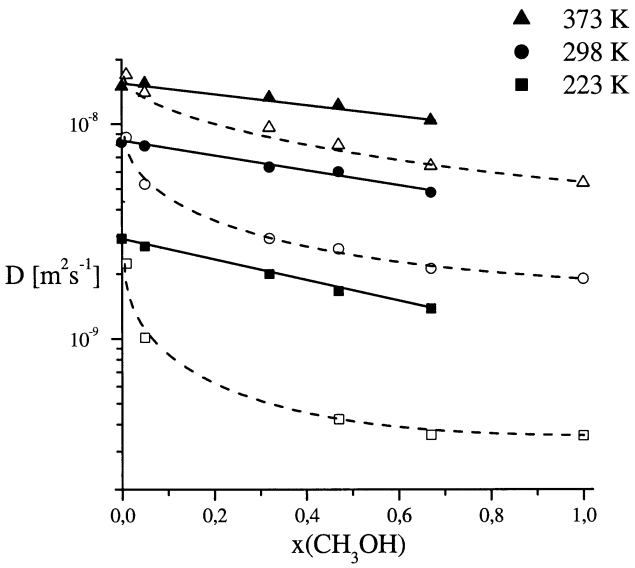

Fig.9. Concentration dependence of the D_{ii} in CO_2/CH_3OH mixtures (full symbols: CO_2, open symbols: CH_3OH).

5.1. Binary mixtures with ammonia

In the literature fluid ammonia is often described as a "waterlike" solvent. The analysis of the data for neat NH_3 given above did not show any of the unusual properties typical for liquid water [35, 38].

The D_{ii} for the binary mixture C_6H_6/NH_3 were studied as model system for a non-polar compound dissolved in ammonia [35, 39]. These mixtures show the typical behaviour that was observed also for C_6H_6/CO_2 given above (Fig. 5). The isotherms of the log D_{ii} versus x diagrams are nearly linear.

In order to learn more about the influence of large dipole moments upon the x,p,T-dependences of the D_{ii} the system acetonitrile/NH_3 was studied. Some data collected are given in Fig. 10 together with the benzene/NH_3 results.
Comparison of the two diagrams shows that the large dipole moment of CH_3CN of 3.92 Debye does not lead to a significant reduction of mobility. Another rather unexpected result of these studies is that either of these systems shows regular solution behaviour. None of the peculiarities in the concentration dependence observed in aqueous solutions of hydrophobic solutes [40] are found in these ammonia systems. The comparison of the absolute values of the D_{ii} in the C_6H_6 systems of NH_3 and CO_2 also does not show large differences that could be interpreted as the formation of hydrogen bonded associates in ammonia.

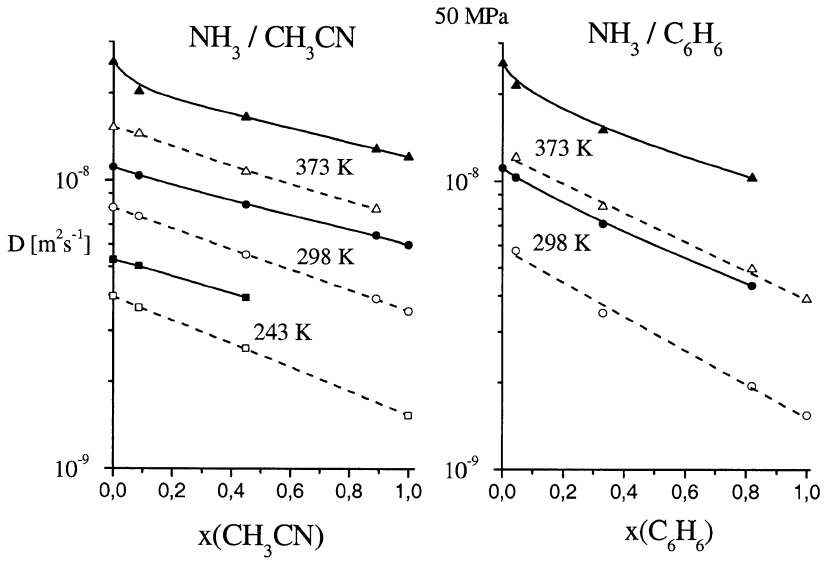

Fig. 10. Comparison of the concentration dependence of the D_{ii} in binary mixtures of benzene and acetonitrile (at 50MPa) in NH_3, (open symbols: C_6H_6 or CH_3CN, full symbols: NH_3).

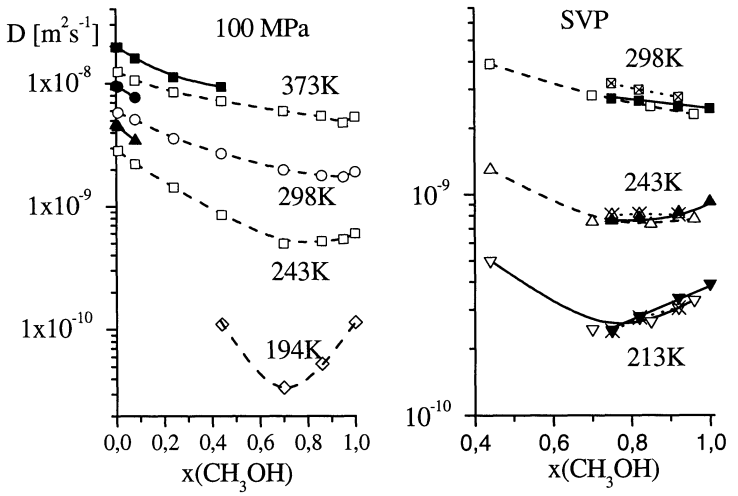

Fig.11. left. Concentration dependence of the D_{ii} in NH_3/CH_3OH mixtures at 100 MPa (full symbols: NH_3 ,open symbols: CH_3OH).
Fig.11. right. Concentration dependence of the D_{ii} at saturation vapour pressure (SVP) in the system $^{15}NH_3/CH_3OH$. (full symbols: $^{15}NH_3$, open symbols CH_3OH, open crossed symbols: D_{ii} (methanol) obtained from a slight extrapolation of the high pressure data that end at a minimum pressure of 10MPa.

In Fig. 11 the D_{ii} for the binary system CH_3OH/NH_3 are given. The ammonia protons and the hydroxyl proton do exchange chemically. Thus for most of the x,p,T range the two proton signals for these atoms coalesce into one signal and the $D_{ii}(NH_3)$ cannot be determined by Proton NMR. For technical reasons the rare ^{15}N isotope has to be used for the D_{ii} (NH_3) measurements. Even for a 100% ^{15}N enriched sample of ammonia the sensitivity of the NMR experiment is compared to the proton reduced by a factor of $1.04 \cdot 10^{-3}$. With the low filling factor of our high pressure cells ^{15}N diffusion measurements are not feasible. Only saturation vapour pressure data could be obtained in sealed thick walled commercial 10mm NMR glass tubes.

For this mixture the isotherms of D_{ii} (CH_3OH) as function of the mole fraction x run at lower temperature through minima. The minima become more pronounced with decreasing temperature and increasing pressure. This enforces the rather puzzling conclusion that the ammonia molecules must form hydrogen bonds with the hydroxyl group of the alcohol. Mass spectrometric studies of alcohol/amine mixtures show clearly that in the gas phase mixed hydrogen bonded dimers are formed in which the amines act via their lone electron pair as acceptors [41]. However if the ammonia would participate only in mixed

hydrogen bonds with methanol by acting as an acceptor, the experimental facts shown in Fig. 11 could not be explained. As stated above in the discussion of the CH_3OH/CO_2 system the hydroxyl group can contribute to the formation of the hydrogen bonded associates 2 acceptor sites and 1 donor site, adding to this liquid another molecule with one more acceptor site must result in a reduction of the mean size of the associates. This should lead to an increase in mobility, which is opposite to our observation. The pronounced minima observed in the low temperature isotherms demand that the ammonia must participate also with its three hydrogen atoms as donors.

An average stoichiometry of 4 donors and 3 acceptors per pair of NH_3 and CH_3OH allows the formation of three dimensional networks and must thus lead to the effects observed. Obviously this is a qualitative statement only and it does not claim that all mixed hydrogen bonds possible between the two molecules have the same bond energy. However the conclusion that all types of the hydrogen bond interaction between the two constituents of this mixture must exist in the fluid rests on safe experimental evidence. This conclusion is further corroborated by a comparison of the D_{ii} found in CH_3OH/CO_2 (Fig. 9) with the data presented in the left diagram of Fig. 11. Here the $D_{ii}(NH_3)$ obtained by ^{15}N NMR are compared to $D_{ii}(CH_3OH)$. Contrary to the observations in the CH_3OH/CO_2 mixtures, where the differences between the diffusivities become larger with falling temperature, both compounds show for $T \leq$ 298K within experimental error identical D_{ii}.

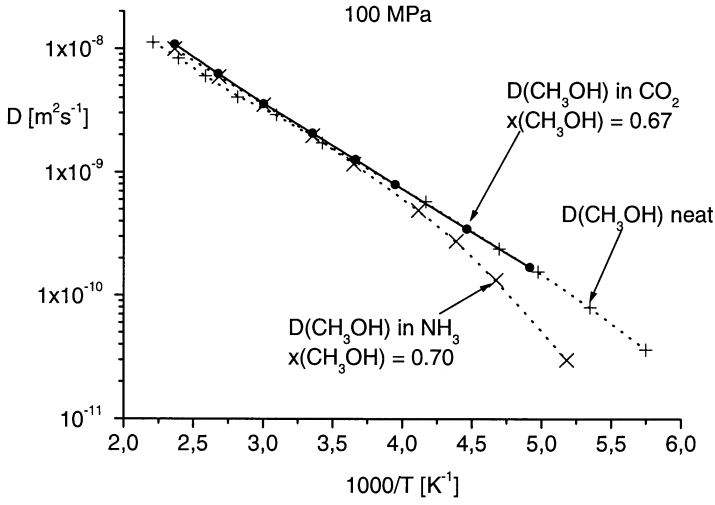

Fig. 12. Comparison of the 100MPa isobars for the diffusion of methanol in the neat CH_3OH [43] and in the binary systems with CO_2 resp. NH_3.

Supplementary experimental evidence for this conclusion is presented in Fig. 12. Here the 100MPa isobar of D_i for neat methanol [43] is compared to of $D_{ii}(CH_3OH)$ for the two binary systems with NH_3 and CO_2 with $x(CH_3OH) \approx 0.7$. For all three isotherms the slope increases with decreasing temperature which is typical for all glass forming liquids. While the isobars for neat CH_3OH and for the mixture with CO_2 show an identical T-dependence, the $D_{ii}(CH_3OH)$ for the CH_3OH/NH_3 system decreases at the lower temperatures much steeper than the other two isobars. This very steep decrease of molecular mobility is typical for liquids that can form transient three dimensional hydrogen bonded networks. The most striking example for this statement is supercooled water [8] which also shows this very strong reduction of D_i with falling temperature.

6. CONCLUSIONS

The self diffusion studies on neat fluids have come to a stage where it is quite clear, that our present understanding of the molecular dynamics of the condensed fluid state is rather limited. However by now sufficient experimental data have been collected that could form a solid basis for the test of future theoretical developments. Although even for the neat systems surprisingly few sufficiently precise density data that cover a large range of the p,T-space do exist. Through the experimental data it also has become clear, where the quantitative shortcomings of the established models are to be found.

Compared to these neat systems the theoretical concepts for the description of diffusion in fluid mixtures are even more rudimentary. A quantitative analytical "ab initio"-description of the dynamic properties is not in sight. In order to outline some general properties of the binary systems described above, the activation energies and the activation volumes, as defined by Eq. (7) and (8), were derived from the data. They are collected in Table 3. The general conclusion from the inspection of these results is that these activation parameters, i.e. the temperature and pressure coefficients of the translational molecular mobility in the binary systems that are made up of non-polar as well as highly polar substances are a collective property of the fluid. Within the limits of the precision of the values derived they are identical for the two components and do not reflect the individual properties of the individual compounds like mass, shape, and dipole moment. The system CO_2/CH_3OH in which hydrogen bonded associates can be formed is an exception to this observation. Here the diffusional mobility of the alcohol molecules decreases much faster with decreasing temperature than the $D_{ii}(CO_2)$, reflecting the formation of hydrogen bonded associates between the alcohol molecules only.

The mixture NH_3/CH_3OH shows some unexpected chemical properties, the experimental data can be explained only with the existence of hydrogen bonded

Table 3
Activation energies at constant pressure $\Delta E^{\neq}_p$(kj mol^{-1})and activation volumes $\Delta V^{\neq}$(cm^{3}mol^{-1}) at 300K and 100MPa for intra diffusion in some binary mixtures and their neat constituents.

.	Fluids	with	CO_2			Fluids	with	NH_3	
Subst.	x^a	$\Delta E^{\neq}_p{}^b$	$\Delta V^{\neq c}$	Ref.	Subst.	x^a	$\Delta E^{\neq}_p{}^b$	$\Delta V^{\neq c}$	Ref.
CO_2	1	7.5	12.0	27	NH_3	1	8.5	7.0	16
CO_2	0.975	7.5	13.0	36	NH_3	0.956	8.5	7.0	39
C_6H_6	0.025	8.0	13.0	36	C_6H_6	0.044	9.1	8.0	39
CO_2	0.78	8.1	11.0	36	NH_3	0.67	8.7	9.0	39
C_6H_6	0.22	8.9	12.0	36	C_6H_6	0.33	9.8	10.0	39
CO_2	0.45	9.3	12.0	36	NH_3	0.18	11.0	15.0	39
C_6H_6	0.55	10.6	13.0	36	C_6H_6	0.82	11.9	16.0	39
C_6H_6	1	12.7	16.0	42	C_6H_6	1	12.7	16.0	42
CO_2	0.88	7.0	13.0	36	NH_3	.0912	8.2	7.0	39
H_2	0.12	7.2	17.0	36	CH_3CN	0.088	8.1	8.0	39
CO_2	0.61	5.8	17.0	36	NH_3	0.55	8.4	7.0	39
H_2	0.39	4.8	24.0	36	CH_3CN	0.45	8.4	7.0	39
H_2	0.55	4.0	18.0	36	NH_3	0.11	8.4	7.0	39
H_2	1	2.7	11.0	29	CH_3CN	0.89	8.7	8.0	39
CO_2	0.978	8.2	12.0	36	CH_3CN	1	9.1	8.0	44
PME	0.022	9.6	12.0	36	[d]) The	System	NH_3 +	CH_3OH	
CO_2	0.93	9.9	17.0	36	CH_3OH	1	12.0	7.0	43
PME	0.07	11.1	18.0	36	CH_3OH	0.96	12.5	7.0	39
AcA [e])	0.015	8.1	12.0	36	CH_3OH	0.85	13.3	7.0	39
CO_2	0.86	8.8	12.0	36	CH_3OH	0.70	13.2	8.0	39
AcA [e])	0.14	8.9	12.0	36	CH_3OH	0.44	12.4	7.0	39
CH_3OH	001	9.2	12.0	36	CH_3OH	0.24	10.2	6.0	39
CO_2	0.95	8.3	13.0	36	CH_3OH	0.08	8.9	8.0	39
CH_3OH	0.05	12.8	12.0	36					
CO_2	0.68	9.1	12.0	36					
CH_3OH	0.32	13.8	10.0	36					
CO_2	0.53	9.2	11.0	36					
CH_3OH	0.47	13.8	9.0	36					
CO_2	0.33	8.8	9.0	36					
CH_3OH	0.67	12.9	9.0	36					
CH_3OH	1	12.0	7.0	43					

[a]) mole fraction x of compound in column 1 resp 6 [b]) Activation energy at constant pressure $\Delta E^{\neq}_p$(100MPa) since some of the isobars show a slight curvature $\Delta E^{\neq}_p$ was derived from the slope at 300K [c]) activation volume determined from the 300K isotherm at a pressure of 100MPa [d]) as explained in the text only the D_{ii} (CH_3OH) could be obtained in this mixture [e]) ACA= acetic acid.

associates in which both compounds must participate as acceptors and donors. The isobaric temperature dependence of the D_{ii}(CH_3OH) in this system can be described by the Adam-Gibbs theory with the VTF-equation as well as by the mode coupling (MCT) theory (for details see [39]).

The next steps in the evaluation of the diffusion data presented here would be the determination of the p,V,T-data for some strategically chosen mixtures. Also it seems timely to start a comprehensive set of Hard Sphere MD-simulations for the binary mixture under systematic variation of the packing fraction, and the diameter- and mass ratios.

ACKNOWLEDGEMENTS

The DFG supported T. Groß and provided generous material support for the experiments. Prof. Liuping Chen was recipient of a grant from the China Scholarship Council. The reliable and continuing support by the Fonds der Chemischen Industrie is acknowledged. Only the excellent technical support by the workshops of our faculty made these experiments feasible. Especially Mr. J. Gamez-Weingärtner , S. Heym , G. Niesner, and G. Wührl helped beyond the call of duty.

REFERENCES

[1] G. Brunner, Gas Extraction, Steinkopf Darmstadt, Springer New York 1994.
[2] S. Chapman and T. G. Cowling, The Mathematical Theory of Non-Uniform Gases, Cambridge University Press, Cambridge, 1952.
[3] C. G: Gray and K. E. Gubbins, Theory of Molecular Fluids, Vol. 1: Fundamentals, North Holland Publishing Company, Amsterdam, 1984.
[4] A. J. Easteal and L. A. Woolf, Chem. Phys., 88 (1984) 101.
[5] I. Tarassov, S. Wappmann and H.-D. Lüdemann, Z. Phys. Chem., 193 (1996) 1.
[6] H. Yamada, Rev. Sci. Instrum., 45 (1974) 640.
[7] E. O. Stejskal and J. E. Tanner, J. Chem. Phys., 42 (1965) 288.
[8] E. W. Lang and H.-D. Lüdemann, Prog. Nucl. Magn. Reson. Spectrosc., 25 (1993) 507.
[9] W. E. Price and H.-D. Lüdemann, in High Pressure Techniques in Chemistry and Physics: A Practical Approach, W. B. Holzapfel and N. S. Isaacs (eds) Oxford University Press, ch.5, 225 (1997).
[10] D. Chandler, J. Chem. Phys., 60 (1974) 3596.
[11] D. Chandler, J. Chem. Phys., 62 (1075) 1358.
[12] D. Enskog, Kungl. Svenska Vet. Ak. Handl., 63 (1922) 4.
[13] B. Alder, D. M. Gass and T. E. Wainwright, J. Chem. Phys., 53 (1970) 3813.
[14] J. Jonas (ed.) NMR Basic Principle and Progress, High Pressure NMR, Springer Verlag Berlin, 24 (1991).
[15] R. J. Speedy, F. X. Prielmeier, T. Vardag, E. W. Lang and H.-D. Lüdemann, Mol. Phys., 66 (1989) 577.
[16] T. Groß, J. Buchhauser, W. E. Price, I. N. Tarassov and H.-D. Lüdemann, J. Mol. Liquids, 73,74 (1997) 433.
[17] A. Greiner Schmid, S. Wappmann, M. Has and H.-D. Lüdemann, J. Chem. Phys., 94 (1991) 5643.
[18] M. Has and H.-D. Lüdemann, J. Mol. Liquids, 46 (1990) 7.
[19] N. Karger and H.-D. Lüdemann, J. Chem. Phys., 109 (1998) 3301.

[20] J. J. Carolan and T. A. Scott, J. Magn. Reson., 2 (1970) 243.
[21] W. M. Litchman and M. Alei jr., J. Chem. Phys., 56 (1972) 5818.
[22] J. G. Powles and M. Rhodes, Mol. Phys., 12 (1967) 399.
[23] F. M. Tao and W. Klemperer, J. Chem. Phys., 99 (1993) 5976.
[24] S. M. Cybulski, Chem. Phys. Lett., 228 (1994) 451.
[25] Liuping. Chen, T. Groß and H.-D. Lüdemann, Phys. Chem. Chem. Phys., 1 (1999) 3503.
[26] T. Groß, Liuping Chen, J. Buchhauser and H.-D. Lüdemann, Phys. Chem. Chem. Phys., 3 (2001) 3701.
[27] T. Groß, J. Buchhauser and H.-D. Lüdemann, J. Chem. Phys., 109 (1998) 4518.
[28] P. Etesse, J. A. Zega and Kobayashi, J. Chem Phys., 97(1992) 2022.
[29] Liuping Chen, T. Groß, H. Krienke and H.-D. Lüdemann, Phys. Chem. Chem. Phys., 3 (2001) 2025.
[30] H.-D. Lüdemann, Rev. High Presure Science and Technol., 11 (2001) 315.
[31] H.-D. Lüdemann and Liuping Chen, J. Phys.: Condens. Matter, 14 (2002) in print.
[32] H. J. V. Tyrrell and K. R. Harris, Diffusion in Liquids, Butterworth London, (1984).
[33] I. N. Tarassov, S. Wappmann and H.-D. Lüdemann, Polish J. Chem., 71 (1997) 1763.
[34] Liuping Chen, T. Groß and H.-D. Lüdemann, J. Mol. Liquids, 98-99 (2002) 27.
[35] T. Groß, Thesis Universität Regensburg, (2000).
[36] T. Groß, Liuping Chen, J. Buchhauser and H.-D. Lüdemann, Phys.Chem.Chem.Phys., 3 (2001) 2845.
[37] A. Streitwieser, C. H. Heathcock and E. M. Kosower, Organische Chemie ,VCH Verlag, Weinheim, 2nd edition (1994) 489.
[38] F. Franks ed., Water a comprehensive treatise, Plenum Press New York, vol.1 (1972).
[39] T. Groß, Liuping Chen, J. Buchhauser and H.-D. Lüdemann, Phys.Chem. Chem. Phys.,3 (2001) 3701.
[40] F. Franks ed., Water a comprehensive treatise, Plenum Press New York, vol.2 (1973).
[41] L. A. Curtis and M. Blander, Chem. Rev., 88 (1988) 827.
[42] H. J. Parkhurst and J. Jonas, J. Chem. Phys., 63 (1975) 2698.
[43] N. Karger, T. Vardag and H.-D. Lüdemann, J. Chem. Phys., 93 (1990) 3437.
[44] R. L. Hurle and L. A. Woolf, J. Chem. Soc. Faraday Trans., 78 (1982) 2233.

Supercritical Fluids as Solvents and Reaction Media
G. Brunner (editor)

Chapter 2.2.

Interfacial Phenomena in Countercurrent and Spray Processing Using Supercritical Fluids

R. Eggers, P. Jaeger [a]

[a] Process Engineering II, Heat- and Mass Transfer, Technical University Hamburg-Harburg, D-21071 Hamburg

1. INTRODUCTION

Performance and efficiency of industrial processes are generally influenced by interfacial effects. In any process involving more than one homogeneous phase, interfaces appear that either determine the procedure itself like in liquid - liquid extraction or the final product like magarines or coatings. High pressure processes are affected in the same way, only that interfacial phenomena are not so easily accessible to observation. Often, certain effects are assumed to occur just by deduction from the final result. Recently, methods have been developed in order to quantify dominating interfacial properties at high pressures. Among these, the interfacial tension plays an important role since this measure resembles the energy for creating new interface. While the interfacial tension is used to describe fluid interfaces, the analogous measure for solid - fluid interfaces is directly named interfacial energy. The interfacial energy on its turn is related to the wetting behavior of liquids on solid surfaces. Hence, it becomes quite clear that any liquid - fluid mass transfer operation is strongly influenced by the interfaces being present within the process. Since the rate of transferred moles is directly related to the extension of the interface by

$$\dot{M} = k\, A\, \Delta c \tag{1}$$

and k as the mass transfer coefficient is influenced among others by interfacial convection the variety and complexity of the associated interfacial phenomena becomes apparent.

Table 1 gives an overview on different types of interfacial phenomena as they affect high pressure processes that involve supercritical fluids.

Table 1
Interfacial phenomena in supercritical fluid processing

Phenomena	Process	Physical Property
Drop formation	Spraying (RESS, GAS, etc.)	IFT, drop size, drop velocity
Bubbles	Bubble column	IFT, bubble size/shape
Wetting	Packed column	Contact angle, wetting
Foam	Bubble column	Foam stability, IFT
Nucleation	Polymer processing	Crit. Pressure difference, IFT
Emulsion	Reverse micelles	Phase behavior
Interfacial convection	Mass transfer operations	Refraction
Coalescence	Mixer-Settler	Coalescence rate

2. MATERIALS AND METHODS

Since the thirties of the past century the pendant drop method is known for determining interfacial tension from drop shapes that are generated inside a view chamber at elevated pressure. During decades experimental values were subject to fairly high errors due to analogous photographing images and an empirical evaluation method [1]. Later, electronic data processing allowed to digitalize drop images and solve the theoretical equation of a drop profile exactly meeting physical laws [2]. The measuring principle is based on the pressure difference resulting from curvature of fluid interfaces which is described by Laplace' law:

$$\Delta P = \sigma\left(\frac{1}{R_1}+\frac{1}{R_2}\right) \tag{2}$$

As a consequence of this relation a liquid flows spontaneously into a capillary in case of wetting of the inner surface which is also called capillary action. Applied to a pendant drop the hydrostatic pressure needs to be accounted for in order to obtain an equation that describes the Laplace pressure at any height of the drop:

$$\Delta P = \sigma\left(\frac{1}{R_1}+\frac{1}{R_2}\right)=\frac{2\sigma}{R_0}-\Delta\rho g z \tag{3}$$

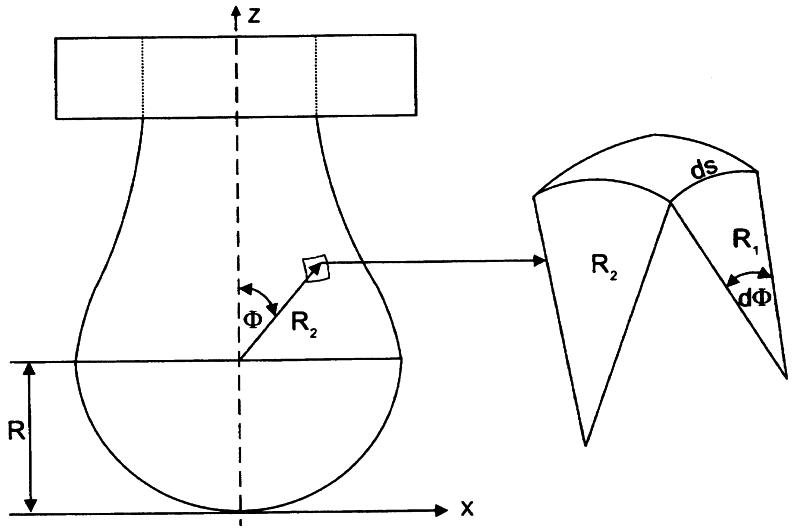

Fig. 1. Coordinates of a pendant drop.

For adaptation of the pendant drop measuring principle to high pressure, drops are generated within a high pressure view chamber like shown in Fig. 2.

After recording by means of a CCD – camera connected to a personnel computer, drop shapes are evaluated for determination of the interfacial tension with help of the DSA (drop shape analysis) programme from KRÜSS, Hamburg.

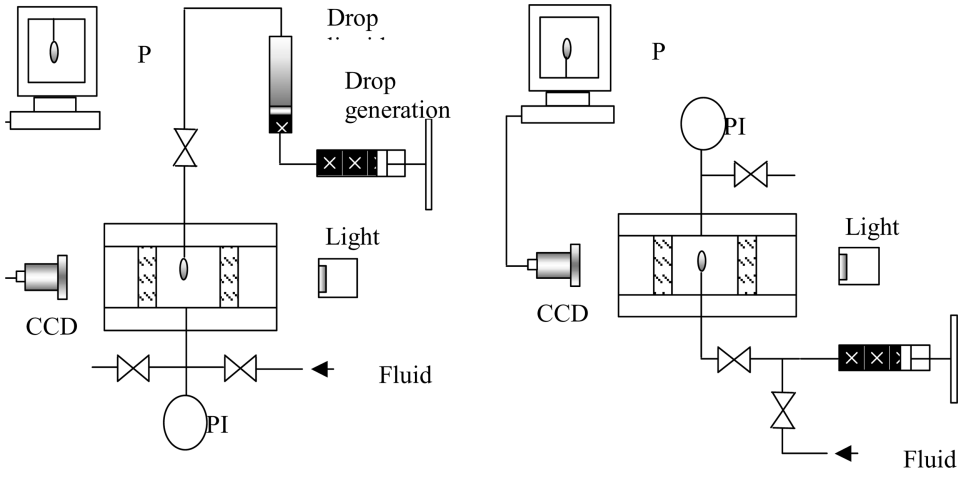

Fig. 2. Experimental set-up of the high - pressure pendant drop measurement.

Table 2
Materials for investigation by the high pressure pendant drop technique.

Drop Phase	Surrounding Phase
• Water	• Carbon dioxide
• Aqueous solutions	• Nitrogen
• Vegetative oils	• Inert gases
• High viscous resins	• Transparent liquids, e.g.
• Silicone oils	• Hydrocarbons
• Crude oils, refinery products	• Aqueous solutions
• Hydrocarbons, organic solvents	• Volatiles
• Rubber solutions	
• Polymer-melt	
• Liquid metals	
• Molten salts	
• Lubricants	

In this way also sessile drops on solid substrates may be evaluated with respect to wetting by detecting the three phase contact angle. Possible materials for investigation are listed in Table 2.

Fig. 3 and 4 show experimental data on interfacial tension in supercritical fluid atmosphere at elevated pressure. In general interfacial tension decreases as the pressure in raised due to enhanced density of the supercritical phase and following dissolution within the liquid phase.

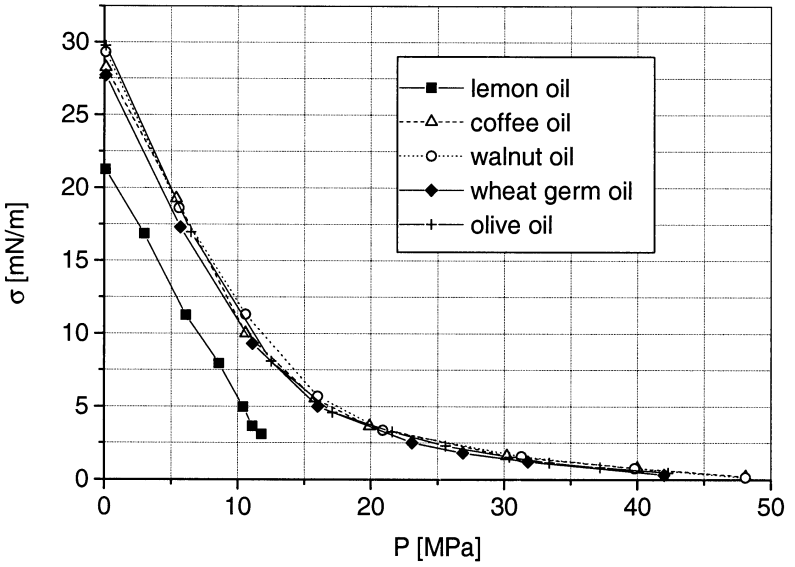

Fig. 3. Interfacial Tension of different triglyceride oils in carbon dioxide, 80° C.

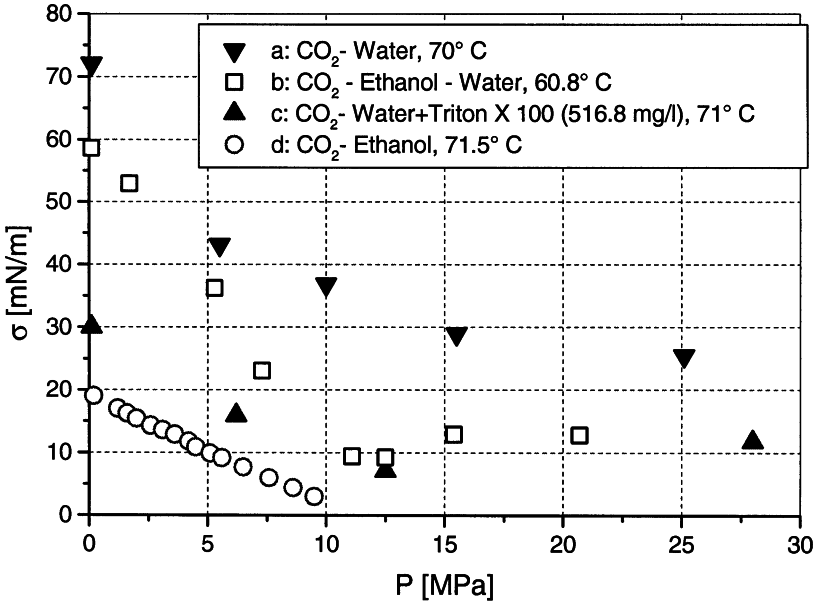

Fig. 4. Interfacial Tension of different aqueous systems in carbon dioxide.

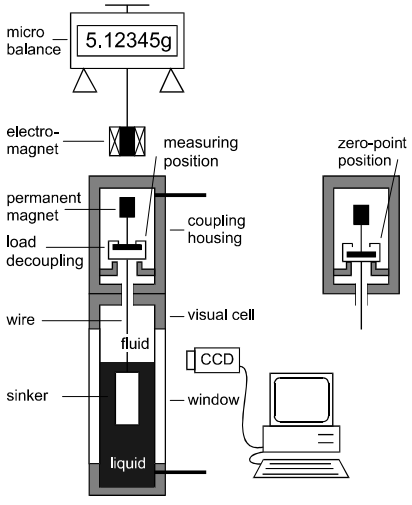

Fig. 5. Schematic of a magnetic coupled balance.

Table 3
Density of gases and gas saturated liquids.

Substance	Temperature	Density [kg/m^3] at a pressure of 0.1 MPa	15 MPa	30 MPa
N_2	40° C	1.1	165	282
	80 °C	1.0	136	248
CO_2	40° C	1.7	770	909
	80 °C	1.5	439	746
Water saturated with CO_2	40° C	992	1024	1036
	81 °C	971	1003	1017
Veg. Oil saturated with CO_2	40° C	906	926	944
	80 °C	880	893	913

Next to the interfacial tension densities of the adjacent fluid phases and their respective dynamic viscosities play an important role especially concerning droplet breakup, residence time of droplets and flooding of columns. The density of both contacting phases is preferably measured by a magnetic coupled balance provided by Rubotherm, Bochum [3]. The principle setup of such a balance is shown in Fig. 5. Table 3 gives some values of density at different pressures for comparison.

Similar to interfacial tension and density in supercritical fluid atmosphere also the dynamic viscosity of liquids is strongly affected by dissolution of the fluid phase. Fig. 6 shows the dynamic viscosity of corn oil measured with a rolling ball viscosimeter. The dissolved carbon dioxide molecules are positioned between the long chains of fatty acids. Consequently, inner frictional forces of the liquid are reduced lowering the viscosity.

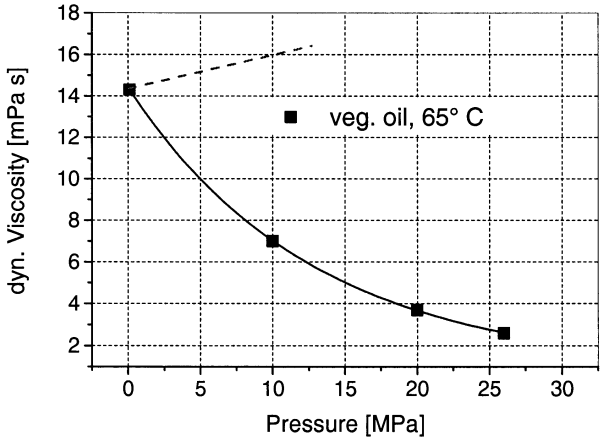

Fig. 6. Dynamic viscosity of corn oil in CO_2-atmosphere as function of pressure.

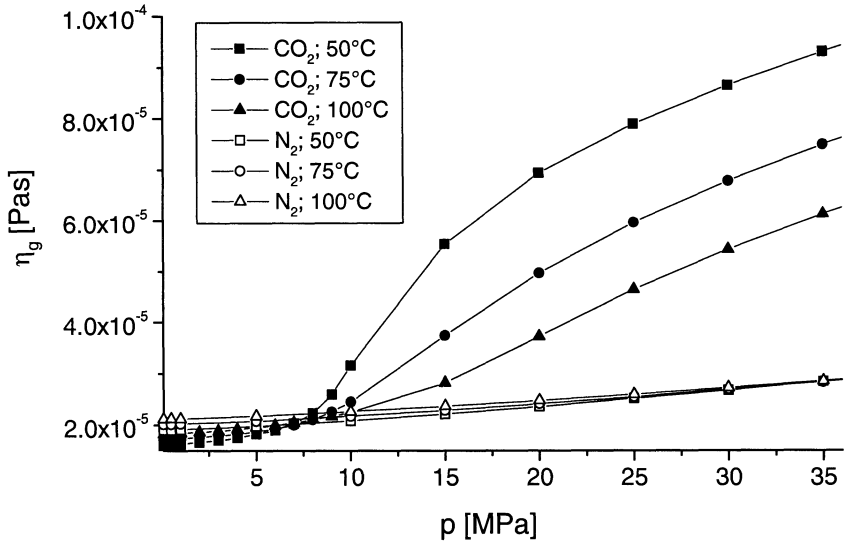

Fig. 7. Viscosity of CO_2 and N_2 as function of pressure.

On the other hand supercritical fluid viscosity is enhanced at increased pressure but remains significantly below viscosity of liquid solvents such as alcohol or water (Fig. 7).

3. COUNTERCURRENT EXTRACTION IN PACKED COLUMNS

Separation efficiency of packed columns that are usually operated in a countercurrent fashion, is strongly influenced by wetting of the packing surface. According to the wetting behavior, the liquid either spreads on the solid surfaces or gathers together forming single drops. Fig. 8 shows a schematic flow diagram of a supercritical fluid – liquid counter-current process using a high pressure packed column.

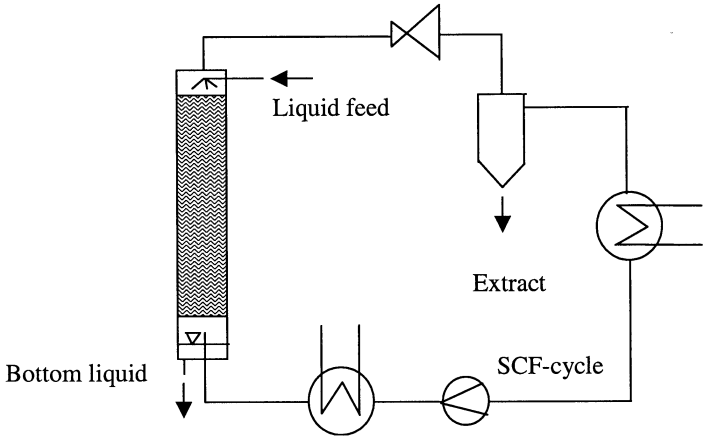

Fig. 8. Schematic diagram of a high-pressure packed column extraction.

The wetting behaviour is described by the so-called contact angle that on its turn depends not only on the drop liquid and the solid material, but also on the ambient liquid or gas and the structure of the solid surface. From thermodynamics a relationship between drop and ambient liquid, the contact angle and the interfacial energies of the solid surface in contact with the respective liquids may be deduced, called the Young's equation:

$$\sigma_{solid,fl} = \sigma_{liq,fl} \cos\theta + \sigma_{solid,liq} \tag{4}$$

This relationship may also be interpreted as a balance of forces in horizontal direction between the interfacial tension, $\sigma_{liq,fl}$, the solid – (drop) liquid interfacial energy, $\sigma_{solid,liq}$ and the solid – (surrounding) fluid interfacial energy, $\sigma_{solid,fl}$. From surface tension and contact angle the surface energy of solids in ambient air atmosphere can be deduced by applying Young's law to a

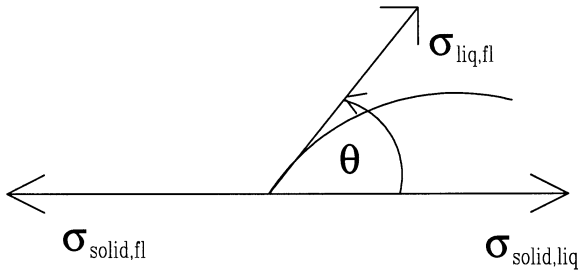

Fig. 9. Contact angle and interfacial energies acting at the three phase contact.

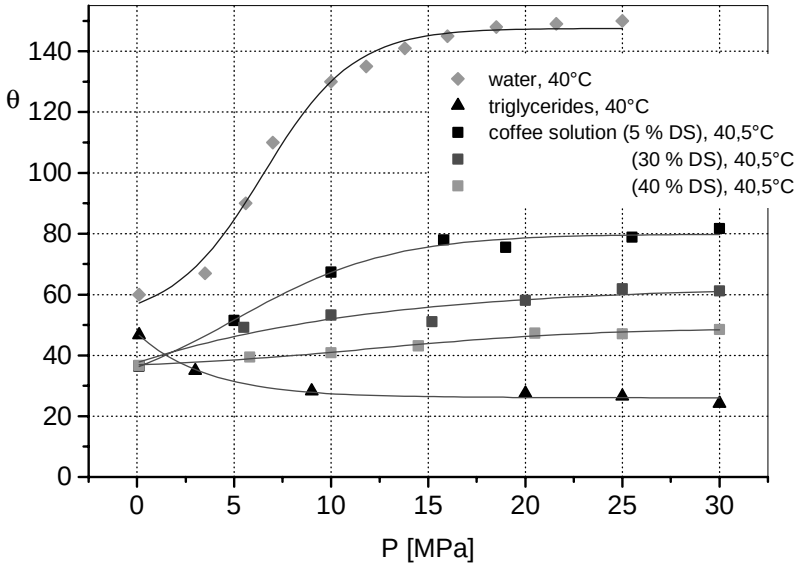

Fig. 10. Contact angel of various liquids on stainless steel at elevated pressure.

series of experimentally determined values of contact angle and surface tension and using adequate regression procedures [4]. In condensed gas atmosphere first attempts exist for obtaining the respective data of solid – fluid interfacial energies [5].

Tendentially, reduced interfacial tension leads to enhanced wetting following Young´s equation. Fig. 10 shows the contact angle of various liquids on packing material (stainless steel) as a function of pressure in CO_2 – atmosphere, measured by the mentioned sessile drop technique.

Reduced contact angle at elevated pressures leads to an enhanced wetted portion of the packing surface in case of triglyceride oils as indicated in Table 4 [6].

Table 4
Falling film characteristics deduced from experimental data, corn oil, Sulzer BX – packing, ϑ = 65° C.

P [MPa]	σ [mN/m]	θ [deg]	Re_{film}	Thickness [mm]	Wetted portion
10	9.5	25°	0.15	0.16	27 %
20	2.3	23.7°	0.22	0.17	37 %
23	1.9	23.6°	0.21	0.16	42 %
26	1.7	23.6°	0.20	0.15	48 %

In general, wetting of aqueous solutions becomes worse at elevated pressure which takes influence on the mass transfer area. Nevertheless, slightly better wetting of those solutions containing dry matter like proteins is compensated by enhanced mass transfer resistance and unfavorable partition coefficients resulting in lower separation efficiencies as shown in Fig. 11.

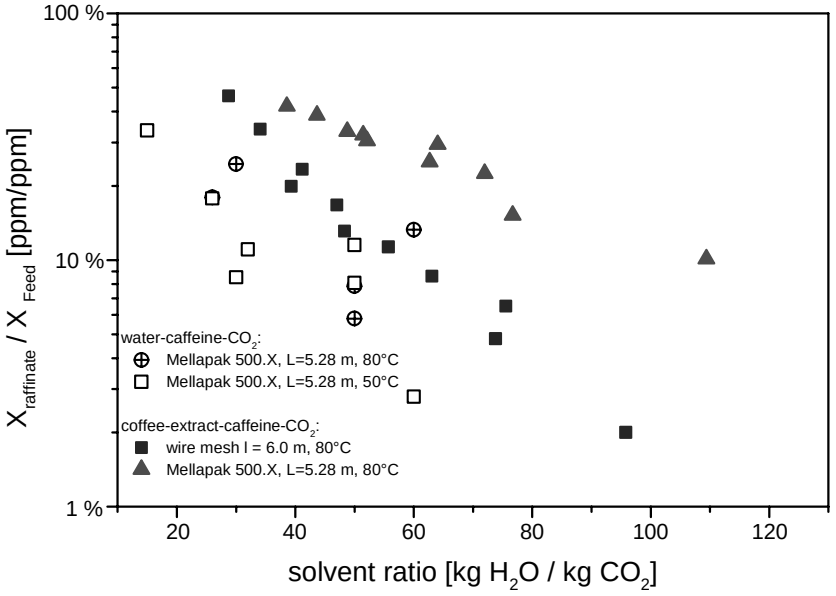

Fig. 11. Efficiency of decaffeination of different caffeine containing solutions, 28 MPa.

4. SUPERCRITICAL SPRAY PROCESSING

Various spray processes are known using supercritical fluids. Fig. 12 gives a classification of these processes according to the apparent interfacial phenomena.

The desired result of spray processing depends on the formation of fine droplets or particles because heat and mass transfer directly correspond to the surface area. Furthermore, the distribution of drop sizes has to be as homogeneous as possible. In principle, the Weber number of the gas phase is relevant for jet disintegration. The Weber number consists of the ratio of the disruptive fluid dynamic forces and the shape maintaining interfacial forces:

$$We = \frac{u_l^{\,2} \rho_l d}{\sigma} \tag{5}$$

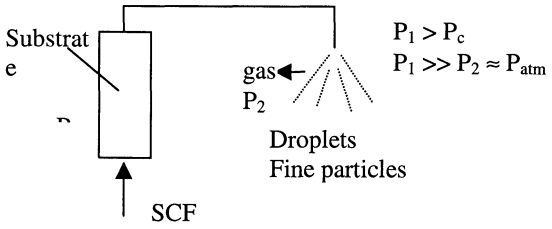

Rapid Expansion of Supercritical Solutions (RESS) [7]

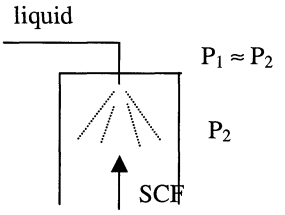

Counter-current Spray Extraction [8]

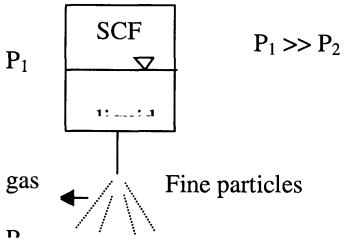

Particles from Gas Saturated Solutions (PGSS) [9]

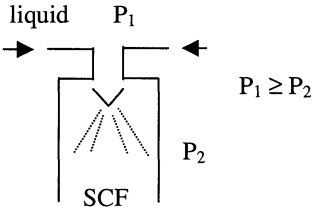

Two Phase Spray Extraction [10]

Fig. 12. Principles of supercritical spray processing.

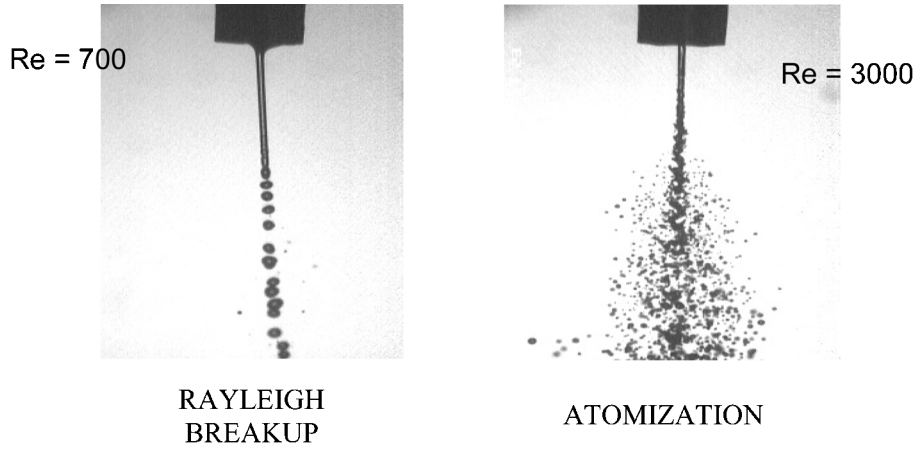

Fig. 13. Different regimes of jet disintegration.

Jet disintegration may be divided into different regimes depending on the We and the Re-number [11]. Fig. 13 illustrates these different regimes: Rayleigh breakup, sinuous breakup and atomization.

When spraying a liquid into a supercritical fluid like in high pressure spray extraction (Fig. 12) conditions influencing the behavior of the phase boundaries change dramatically. First of all the ambient fluid takes a liquid-like density. Thus, the shear stress at the interface of the flying droplets is no longer negligible and the density of the ambient supercritical gas has to be taken into account. Further, mass transfer effects between droplet and supercritical fluid appears in both directions based on the phase equilibrium. Due to concentration gradients in tangential direction of the boundary layer, a local distribution of interfacial tension occurs followed by surface convection and deformation of the droplet. Anyway, surface activity of common surfactants differs in condensed gas atmosphere but principle effects on colloidal behavior remain. In the first place, drop falling velocity depends on the density difference varying with pressure (Fig. 14).

Nevertheless, compared to solid spheres of the same density, the droplets are slightly faster due to the mobile phase boundary [12]. The velocity on its turn determines the residence time for extraction to take place. On the other hand drop velocity depends on the drag coefficient which is influenced by interfacial properties. Fig. 15 shows the drop drag coefficient compared to the drag coefficient of solid spheres.

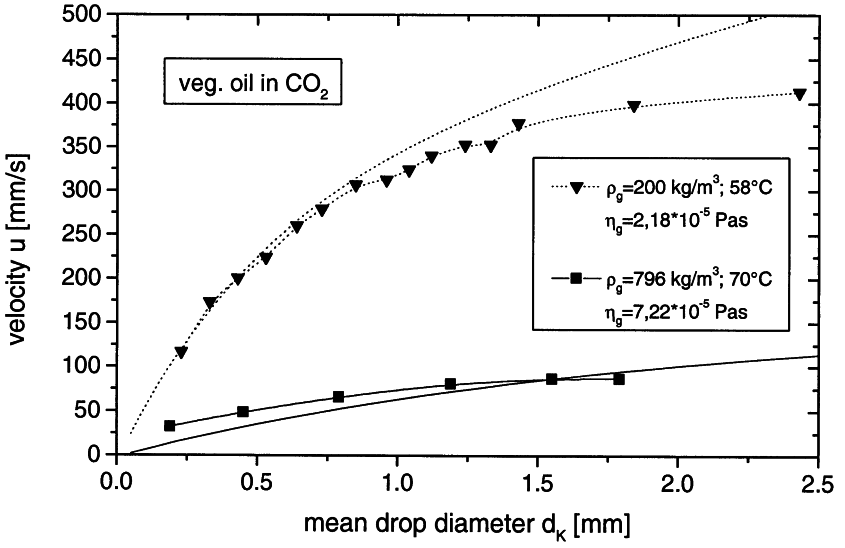

Fig. 14. Drop velocity compared to solid spheres.

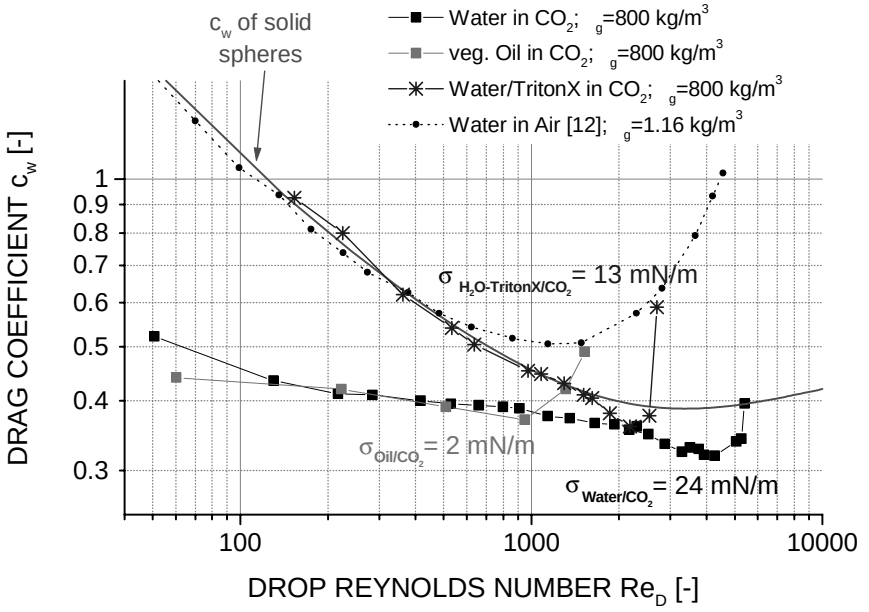

Fig. 15. Drag coefficients as a function of the Re-number.

It becomes clear that the mobile interface of a pure water drop lets this one fall much faster than a hard sphere. Unpurified triglyceride oil has a similar behavior because there are no components present that are active at the oil – CO_2 interface. Anyway reduced interfacial tension lets the drop deform earlier compared to water. Adding a little amount of triton immobilizes the interface and slows down the drop velocity.

Summarizing all aspects the disintegration of the droplets will be favoured by the reduced interfacial tension, σ, and the increased gas viscosity but damped by lowered friction forces of the liquid according to decreased η_l. The increased gas phase density, ρ_g, and viscosity, η_g, are not represented in relationships describing disintegration so far. The dominant impact is the high shear stress at the phase boundary leading to disintegration but conversely the jet velocity slows down hindering further droplet break-up. Density and viscosity of the supercritical gas were considered by dimensionless analysis [13] based on earlier publications [11] obtaining a congruent picture of the different spray regimes under supercritical fluid conditions. The resulting extended regime of atomisation enables broad application of supercritical spray processing. Besides the facilitated disintegration of droplets, the supercritical spray extraction proves to be advantageous because steady state velocity of free falling droplets decreases within dense gases enhancing the residence time especially in counter-current separation processes.

5. CONCLUSIONS

Interfacial phenomena affect supercritical processing to a high extent by determining the required energy input for creating mass transfer area, convection at the interfacial region, formation of colloids and taking influence on the residence time via drop falling or bubble rising velocity. This chapter shows methods for quantifying interfacial phenomena at elevated pressure in view of their interpretation with respect to the process. Mainly, decreasing interfacial tension at elevated pressure favours creation of new interface enhancing the efficiency of the liquid - supercritical process. In case solid packing is used, contact angle determines whether a falling film covers the solid surface or drops are just hindered from freely falling. In general, triglyceride oils cause little problems when being processed in columns using supercritical CO_2. In spite of the decreased interfacial tension impurities like mono- and diglycerides or phospholipids do not affect interfacial behavior, so colloidal stability is low. Interfacial tension of water – CO_2 is still relatively high which has a direct impact on wetting. Intending to lower the interfacial tension by adding surfactants helps wetting but increases colloidal stability and mass transfer resistance at the same time.

SYMBOLS

A	surface area	[m2]
Δc	concentration gradient	[kg/m3]
K	mass transfer coefficient	[m/s]
$\dot{M}$	mass flux	[kg/s]
R_1, R_2	radii of curvature	[m]
T	temperature	[K, °C]
P	pressure	[MPa]
d	drop diameter	[mm]
u	velocity	[m/s]
ρ_g, ρ_l	gas/liquid phase density	[kg/m3]
η_g, η_l	gas/liquid phase viscosity	[mPas]
σ, $\sigma_{liq,fl}$,	interfacial tension	[mN/m]
$\sigma_{solid,liq}$	solid – liquid interfacial energy	[mN/m]
$\sigma_{solid,fl}$.	solid – fluid interfacial energy	[mN/m]
θ	contact angle	

REFERENCES

[1] J.M. Andreas, E.A. Hauser, W.B. Tucker, J. Phys. Chem., 42 (1938), 1001.
[2] B. Song and J. Springer, J. Coll. Interface Sci., 184 (1996), 64.
[3] A. Tegetmeier, D. Dittmar, A. Fredenhagen, R. Eggers, Chem. Eng. Proc. 39 (2000), 399.
[4] F.M. Fowkes, Ind. Eng. Chem., 56 (1964) 12, 40.
[5] D. Klante, R. Eggers, C. Holzknecht, S. Kabelac, Forschung im Ingenieurwesen, 67 (2002), 56.
[6] Ph.T. Jaeger, R. Eggers, CHISA, 27.-31.8. 2000, Praha, Czech Rep.
[7] P.G. Debenedetti, J.W. Tom, X. Kwank, S.D. Yeo, Fluid Phase Equilibria 82 (1993), 311.
[8] H. Marckmann, R. Eggers, CHISA, 25.-29.8. 2002, Praha, Czech Rep.
[9] R. Eggers, H. Wagner, P. Jaeger, High Pressure Chem. Eng. (1996) Elsevier, 247.
[10] H. Wagner, R. Eggers, AIChE Journal, 42 (1996) 7, 1901.
[11] W.v. Ohnesorge, Zeitschrift angew. Math. u. Mech. 16 (1936), 6.
[12] Ph.T. Jaeger, J.J.M. Janssen, F. Groeneweg, W.G.M. Agterof, Coll. Surf., 85 (1994) A, 255.
[13] N. Czerwonatis, R. Eggers, Chem. Eng. Technol. 24 (2001), 619.

Supercritical Fluids as Solvents and Reaction Media
G. Brunner (editor)

Chapter 3.1.

Synthesis of silica aerogels and their application as drug delivery system.

I. Smirnova and W. Arlt

Technische Universität Berlin, Institut für Verfahrenstechnik, Sekr. TK 7,
Fachgebiet Thermodynamik und Thermische Verfahrenstechnik,
Straße des 17. Juni 135, D-10623 Berlin, Germany

1. INTRODUCTION

An aerogel is one of the most fascinating solid materials existing. It is a very light and highly transparent polymer material, which is often called "frozen smoke", because of its hazy blue appearance. An aerogel is a special porous material with extreme microporosity on a micron scale. It is composed of individual particles only a few nanometers in size, which are linked in a three - dimensional structure. Aerogels can be synthesized from silicon oxide (silica aerogels), and also from different organic and inorganic substances, for example titanium oxide, aluminium oxide, carbon etc. [1]

This novel material has many unusual properties, such as a low thermal conductivity, refractive index, sound speed, along with a high surface area and thermal stability. An aerogel can be made with a density only three times larger than that of air. Due to their unusual properties aerogels have many applications in different fields of science and industry [2, 3]. One of the most fascinating applications is the insulation of space shuttles with aerogels, practiced by NASA (USA). Many scientific groups are currently working with aerogels, which is evident by the International Symposia on Aerogels, taking place every three years. Both synthesis and innovative applications of aerogels are of great interest at the present time. In this work we will focus on silica aerogels.

The structure and properties of silica aerogels depend strongly on the synthesis conditions (e.g. amount of water, catalyst nature and concentration, solvent, temperature etc.). An important factor of the low density aerogels synthesis is the gelation time. In the one-step process the gelation of the sample with the density 0.02 g/cm^3 requires as long as 14 days. In the two-step process the gelation time of such samples can be as short as 72 hours, but this process includes

several tedious steps like special purification of the reagents and distillation of the alcohol after the first step.

Different types of catalysts were used in order to accelerate the gelation. In this work it is suggested to use CO_2 to enhance the gelation process. CO_2 was used for the supercritical drying of aerogels already since several years, but its influence on the gelation process itself was never reported. We studied the gelation process in presence of CO_2. A special attention was given to the influence of different factors (temperature, component ratio, solvent nature) on this process.

Our further purpose was to investigate the possibility to apply silica aerogels as drug delivery system. Silica aerogels have an advantage of being environmentally friendly and non-toxic and are also used in the pharmaceutical industry [4]. Since aerogels have an extremely large surface area, we could expect, that its use as a carrier can improve the dissolution and adsorption of drugs.

Two different mechanism of the release from aerogels are possible:

- Hydrophilic aerogels collapse in the aqueous media and so promote the dissolving of the target compound. The pharmaceuticals are adsorbed on the aerogels surface (eventually as a monolayer) and so the fast release is expected.
- Hydrophobic aerogels are more stable and the release is controlled by the diffusion of the substance from aerogels pores. In this case the slow release is expected.

By the choice of a suitable hydrophilic or hydrophobic aerogel, the pharmaceutical adsorbed on the aerogel can be released in accelerated or delayed form.

The kind of the loading plays also an important role. Liquids wet the hydrophilic aerogel structure and partly destroy it. If adsorption from the liquid solution (as suggested by Schwertfeger et al. [4]) is used to load an aerogel with a drug, the product which could be yielded by such process losses the characteristic properties of the aerogels to some extent. That is why this process does not seem to be optimal, especially for the hydrophilic silica aerogels.

The purpose of the present work is to find the procedure, which allows to load the hydrophilic aerogels with drugs without changing of aerogel`s structure. It should be also proved, whether the drug-aerogel formulations are suitable as a drug delivery system. To reach that it was essential to investigate the release of the corresponding drug from the aerogels. Special attention was given to those substances, whose immediate release is desired. In this case hydrophilic aerogels seem to be well suited as a carrier, because they collapse in water, resulting in a fast release of the pharmaceuticals.

2. SYNTHESIS OF SILICA AEROGELS: STATE OF THE ART

2.1. Process based on sodium silicate

The first report on the preparation of silica aerogels was published by Kistler in 1931 [5]. He tried to remove the liquid from a gel and to replace it by air, so that the structure of the gel does not shrink. That is why the final product was called an "aerogel".

The conventional drying of the gel in air resulted in considerable shrinkage. This phenomenon can be explained by the formation of liquid-vapour interfaces within the gel network. This resulted in an enormous surface tension, which causes a partial collapse of the network. The product of this drying method was hard glassy masses (xerogels), which were still porous, but the porosity did not exceed 50% [6].

Kistler`s idea to avoid any collapse based on the replacement of the liquid with air under supercritical conditions. The first experiments were done with silica gels filled with water.

To synthesize a silica gel Kistler used the reaction of sodium silicate (water glass) with hydrochloric acid [5]:

$$Na_2SiO_3 + 2\ HCl \rightarrow [SiO_2 \cdot x\ H_2O] + 2\ NaCl \quad (1)$$

The gels were dried by putting them into an autoclave and raising the temperature until the pressure exceeded the critical pressure of water and then slowly venting the vapors from the autoclave. The main problem of this process was its high temperatures and pressures (T^{cr}_{water} = 374°C, P^{cr}_{water} = 221 bar). Also the corrosiveness of the supercritical water causes some technical problems. To avoid these problems, Kistler extracted water with ethanol. In this way milder process conditions (T^{cr}_{MeOH} = 243°C, P^{cr}_{MeOH} = 63.8 bar) could be achieved. The aerogels obtained in this manner ranged from transparent to highly opalescent. The density of the aerogel was changed by varying the concentration of silica in the solution. Silica aerogels with densities between 0.02 and 0.1 g/cm^3 were produced in this manner [7].

This method was first extended to other inorganic gels and then to organic materials. Kistler described the formation of aerogels of alumina, ferric oxide, stannic oxide, nickel oxide, cellulose, gelatin etc. [5].

2.2. Processes based on tetraalkylorthosilicate

2.2.1. The one-step process

The next reported description of the preparation of an aerogel was given in 1966 [8]. Tetraethylorthosilicate (TEOS) was hydrolyzed in ethanol in presence of hydrochloric acid. This reaction can be summarized as follows:

$$Si(OCH_2CH_3)_4 + 2H_2O \xrightarrow[Cat.]{} SiO_2 + 4\,HOCH_2CH_3 \qquad (2)$$

Gel obtained by this reaction was altered in water, then water was replaced by methanol and the gel was dried supercritically.

This method was further developed and silicate gels were synthesized by using different tetrafunctional siliconalkoxide precursors, whose general chemical structure is written as $Si(OR)_4$, where R denotes an alkyl group ($R=C_nH_{2n+1}$, n=1,2,3....) [9, 10].

The hydrolysis reaction (3) replaces alkoxide groups (OR) with hydroxyl groups (OH).

$$\equiv Si - OR + H_2O \underset{\text{Esterification}}{\overset{\text{Hydrolysis}}{\leftrightarrow}} \equiv Si - OH + ROH \qquad (3)$$

Water and alkoxysilane are poorly miscible, so the additional solvent is needed to homogenize the mixture. A variety of solvents are used for this purpose: alcohols, acetone, dioxane, tetrahydrofurane etc. In the case of alcohols, it should be noted that in spite of being a solvent, alcohol can participate in an esterification reaction and thus reduce the hydrolysis rate.

Simultaneously with the hydrolysis (Eq. (3)) the condensation reaction, (Eq. (4, 5)) takes place. The product of the hydrolysis, silicidic acid (substituted to different extent), is dehydrated and polymerized through siloxane linkages (Si-O-Si). Polymerization occurs either by an alcohol-producing condensation reaction (4) or a water-producing condensation reaction (Eq. (5)).

$$\equiv Si - OR + HO - Si \overset{\text{Alcohol condensation}}{\leftrightarrow} \equiv Si - O - Si \equiv + ROH \qquad (4)$$

$$\equiv Si - OR + HO - Si \underset{\text{hydrolysis}}{\overset{\text{water condensation}}{\leftrightarrow}} \equiv Si - O - Si \equiv + H_2O \qquad (5)$$

One of the advantages of the method based on tetraethylorthosilicate is the fact that no impurities, like salts, are formed by the reaction of alcoxisilicates. The tedious washing of the alcogel essential in Kistler's method is no longer necessary.

According to this method, the reaction takes place in one step. The initial solvent is alcohol, so no substitution of the solvent is needed. Silica gels are dried at the supercritical conditions of the corresponding solvent. By this method, silica aerogels can be prepared in just a couple of days instead of weeks, needed for Kistler`s procedure [9-11].

Since then a lot of publications has been devoted to aerogel production. Sol-gel processes of silica were studied in detail and some were used to produce silica aerogels in industrial scale [12].

2.2.2. The two-step process

The fundamental study of sol-gel processes in a silicate system was done by the group of Brinker (Sandia National Laboratories, Albuquerque). They studied the influence of the rate of hydrolysis and gelation step on the structure of the silica gels [13]. It was shown, that although the hydrolysis and condensation takes place concurrently, it is possible to regulate the rate of both of them by changing the water amount and pH value of the solution. This conclusion lead to the formulation of the two-step sol-gel process.

In the **first step,** TEOS is mixed with a substoichiometric amount of water, solvent and acid catalysts, in particular hydrochloric acid (HCl). It was shown, that at this condition hydrolysis proceeds very rapidly and all added water is consumed in the first few minutes of the reaction to produce a distribution of hydrolyzed monomers. Subsequent condensation results in the formation of polymers, i.e. dimers and chain-like or cyclic species. It was supposed, that after that step water is fully consumed and the resulting polymers are fully esterified.

During the **second step** hydrolysis is completed by the addition of water under basic or acidic conditions. The hydrolyzed species undergo the polymerization reaction and finally form a gel.

2.2.3. Further modification of the two-step process

A modified two-step process was described, in which the **partly condensed silica intermediate** is formed [14]. This intermediate is dissolved with a non-alcoholic solvent so that the re-esterification reaction could be prevented to some extent. This process allows to produce aerogels of extremely low densities (up to $\rho = 0.003$ g/cm^3) within a reasonable time. The gelation time depends on the target density of the aerogel, but even in case of the most diluted samples it does not exceed 72 hours. The aerogels produced in this way are transparent and show the microstructure characteristic of polymeric gels [15].

2.3. Drying methods

Wet gel is a three-dimensional porous structure filled with the pore fluid. If one wants to remove the liquid from such structure by simple evaporation, then great attention should be paid to the capillary forces. Capillary pressure in the cylindrical capillary can be expressed as:

$$P_{cap} = \gamma_{LV} k \tag{6}$$

where k is the curvature of the meniscus formed in the capillary, γ_{LV} is the specific energy of the liquid-vapour interface (surface tension).

The importance of the capillary pressure to the drying of the gels is however not its effect on the vapour pressure, but its effect on the solid phase. The gel contracts as the liquid evaporates from its pores, because of the enormous stresses generated by the menisci in the tiny pores. These stresses can exceed the strength of the network by a considerable margin.

2.3.1. Supercritical drying

Since shrinkage and cracking are produced by capillary forces, those problems could be avoided by removing the liquid from the pores above the critical temperature (T^{cr}) and critical pressure (P^{cr}) of the liquid. At this point there is no longer any distinction between the liquid and vapour phases, the densities become equal, there is no liquid-vapour interface and no capillary pressure [16]. This process is called supercritical drying (SCD).

2.3.2. High temperature supercritical drying

There are two different ways of supercritical drying: high temperature supercritical drying and low temperature supercritical drying. High temperature SCD process can be schematically presented as shown in Fig. 1.

The wet gel, together with a sufficient amount of solvent (e.g. methanol) is placed in an autoclave. After the autoclave is closed, the temperature is slowly raised resulting in a pressure increase (step 1 in Fig. 1). Both the temperature and pressure are adjusted to values above the critical point of the corresponding solvent and kept there for a certain period of time. The fluid is then slowly vented out at constant temperature, which results in a pressure drop (step 2). When ambient pressure is reached, the vessel is cooled to room temperature (step 3). Thus, the phase boundary between liquid and gas has not been crossed during drying.

This process is widely used for silica aerogel production. However, problems arise due to the combination of high temperatures and high pressures as well as the flammability of the solvents.

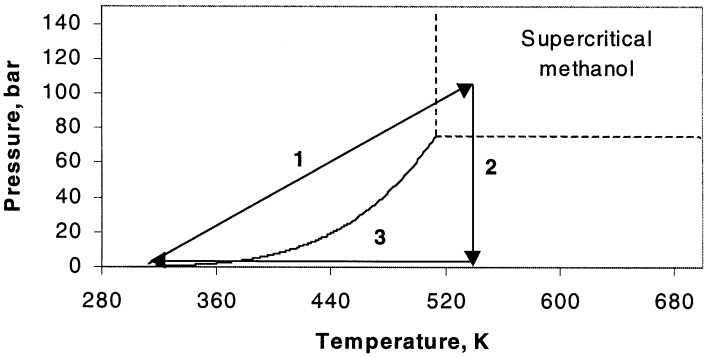

Fig. 1. High temperature supercritical drying.

2.3.3. Low temperature supercritical drying

An alternative method for aerogel drying was suggested [6]. The solvent present in the gel before the drying (mostly alcohol) is replaced by a liquid with a critical point near ambient temperatures. Liquid CO_2 was found to be the most practical choice. Low temperature SCD has the advantage of being executed by low temperature (< 40°C) and at a moderate pressure (< 80 bar). First the organic solvent (ex. CH_3OH) is extracted from the gel by liquid CO_2. When the solvent is completely removed by CO_2, the process is carried out similar to high temperature SCD. The temperature is raised to 40°C (which is above the critical temperature of CO_2, T^c = 31°C). Once 40°C is achieved, which guarantees the transition of CO_2 into the supercritical state, the system is slowly depressurized under natural flow. When the ambient pressure is reached, the system is cooled down to room temperature. Aerogels obtained by this method are hydrophilic.

Later the method was modified by using not liquid, but supercritical CO_2 [17]. In this case, the heating and cooling steps can be eliminated. A continuous process of aerogel production including recycling of CO_2 was also suggested.

In spite of the differences in the high temperature and low temperature SCD, the both procedures remain very expensive because high pressures are used. For this reason there is a great interest in sub-critical or ambient pressure drying. Ambient pressure methods for preparing aerogels are just emerging. These approaches offer great promise to lower aerogel production costs and thus represent an important consideration for the future development of these materials. The details of different methods can be found in [18-21]. Direct formation of silica aerogel powders in supercritical CO_2 and acetone was reported by [22]. All sub-critical drying processes result in aerogels with densities no lower than 0.1 g/cm^3. Up to the present time there is no way to produce low density aerogels other than using supercritical drying.

3. EXPERIMENTAL

3.1. Equipment and experimental procedure

A high pressure autoclave was constructed for the aerogels synthesis. This autoclave was used for both production of aerogels and drug loading. The principle schema of the autoclave is shown in Fig. 2.

The autoclave consists of a stainless steel (V4A) cylinder, 2 viewing glass windows (stainless steel 1.4462 and borosilicate glass DIN 7080), and 2 flanges, which are sealed with teflon rings. The maximal working pressure of the autoclave is 200 bar, maximal working temperature is 100 °C. For the extraction of the solvent the autoclave has 3 inlets and 2 outlets for CO_2. During the extraction of the solvent from the gel the optimal mixing between the gas and the solvent in the pores of the gel should be achieved. To reach this purpose the number and position of the inlets and outlets were simulated using "Fluent/3D" in order to get the optimal mixing of gas and solvent inside the gel.

The volume of the autoclave is 249.5 ml. The diameter of each inlet and outlet is 1 mm. For better mixing in the liquid phase, the autoclave can be rocked with constant velocity. The temperature is regulated by means of a heating jacket and temperature controller with an accuracy of ± 1°C. The temperature is measured with a Pt100 thermometer. The peripheral pipe lines were constructed to enable the gas support of the system. The flow sheet of the apparatus is shown in Fig. 2. For the main part of the experiments CO_2 support was needed. The gas comes from the tank (1), is compressed in the gas pump (3) (membrane compressor) and heated up to the target temperature in the heat exchanger (5).

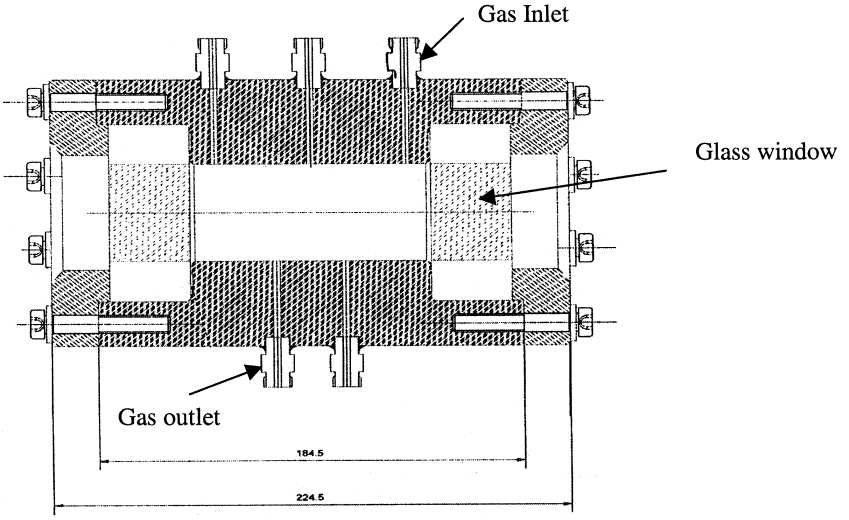

Fig. 2. Autoclave for the aerogel production.

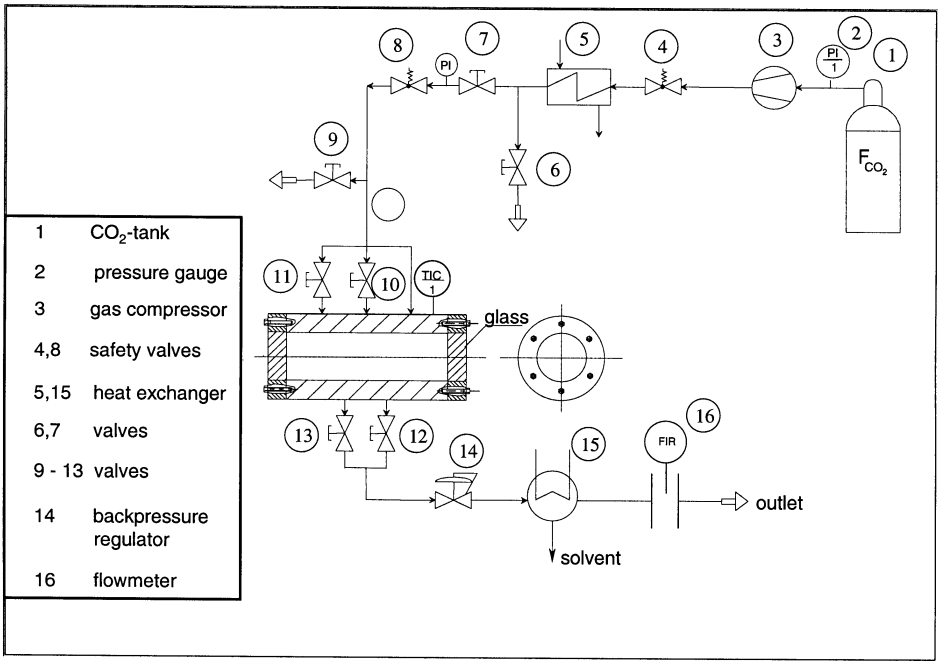

Fig. 3. Flow sheet of the apparatus for aerogel production and adsorption measurements.

The pump provides a constant flow rate, which can be regulated additionally by the back pressure regulator (14). A solvent, eventually present in an outlet gas stream can be condensed in a heat exchanger at 0°C (15). The flow rate of CO_2 is measured by the flow meter (16), calibrated using the air stream.

3.1.1. Selection of the synthesis method

It was our purpose to enhance the gelation and to reduce the gelation time. As mentioned above, the two-step process provides shorter gelation times as the one-step process. But the two-step process, as described in [14] includes several time consuming steps, like special purification of the reagents and distillation of the alcohol. The distillation of alcohol can be eliminated if aerogels of the densities not lower than 0.01 g/cm^3 are required, as it was done in [23]. We used the same approach. The principle scheme of the 2-step method and the component ratio recommended in [14] was kept. Hydrochloric acid and ammonium carbonate were chosen as catalysts following the common 2-step procedure. The concentration of both catalysts was varied in order to find the optimal conditions. But no distillation of alcohol or purification of the reagents as suggested in [14] was made. It was our aim to get the reaction enhancement, which would provide the same short gelation time as in the conventional two-step method, even after the elimination of these time consuming procedures.

3.1.2. Synthesis of a silica aerogel by the two-step method

Silica aerogels were made following the modified two-step. In the first step TMOS was mixed with water, methanol, and hydrochloric acid. The molar ratio of the components during the hydrolysis was as follows:

1 mol TMOS : 2.4 mol MeOH : 1.3 mol H_2O : 10^{-5} mol HCl.

All components were stirred for 30 minutes. No distillation of alcohol was made after the first step.

In the second step water, ammonia solution and acetonitrile were added to the mixture. The amount of acetonitrile was calculated to get the desirable concentration of TMOS (or target density). The target density of the gel is defined as:

$$\rho_{\text{target}} = \frac{m_{SiO_2}}{V_{sol}} \tag{7}$$

where m_{SiO2} is a amount of SiO_2 in the mixture, calculated from the amount of TMOS; V_{sol} is the sum of the volume of all compounds of the final mixture.

The final molar ratio of the components after the second step was as follows:

1 mol TMOS : 2.4 mol MeOH : 4 mol H_2O : 10^{-5} mol HCl : 10^{-n} mol NH_4OH; $1<n<4$.

The resulting mixture was poured directly in the autoclave. The volume of the solution was between 80 and 150 ml. The autoclave was heated up to the reaction temperature (25°C < T < 70°C). A part of the initial solution (~5 ml) was poured into a glass vial and stored separately at the same temperature (control sample). Its gelation time was determined by visual observation.

The autoclave was rocked to get better heat transfer. After the target temperature was reached, the CO_2, preheated to the reaction temperature (20-70°C) by means of the heat exchanger (Pos. 5, Fig. 5), was added to the solution in small portions. CO_2 was first pumped in a small gas vessel, this vessel was weighed and then CO_2 was added into the autoclave. The amount of CO_2 added to the system was determined by weighing of the gas vessel before and after such gas addition. Typically 2-3 g of CO_2 were added at once. The autoclave was rocked during this procedure. After the addition of each portion of gas, the pressure increased quickly and then decreased slowly due to the dissolving of CO_2 into the mixture. The mixture stayed colourless and transparent, no liquid-liquid phase separation was observed. CO_2 was further added to such a solution.

The viscosity of the liquid phase increased continuously with increasing CO_2 concentration. After a certain concentration of CO_2 was reached, the solution lost its fluidity and gelified. In this state, the gel did not move if the autoclave was rocked. At this point, no more CO_2 was added. The final pressure over the solution was between 30 and 50 bar. The resulting gel was aged in the autoclave during 1 - 72 hours. Then, supercritical drying was carried out following the principles of low temperature SCD, as described previously. CO_2 was preheated to the target temperature (20-70°C) and slowly introduced into the autoclave, so that the gel was not damaged by the sudden pressure change. The pressure was slowly increased up to 100 bar. Then, the outlet valve was opened and the CO_2 flowed through the gel. During this process some cracks could be seen in the gel body resulting from the gas flow. The flow rate was kept constant (100 NL/h). The outgoing stream then passed through pure water, which was analyzed by GC every hour. If any traces of acetonitrile were found, the water was changed and the extraction was continued. The extraction process was continued as long as no solvent (acetonitrile or TMOS) was found in the outgoing stream. For the given gel volume and flow rate the optimum extraction time was determined and used in the following experiments, so that the GC analysis was no longer necessary. After the extraction was completed, CO_2 was slowly vented out from the autoclave (flow rate being equal to 80 NL/h). The autoclave was cooled down to room temperature. At this moment the drying was finished and the aerogel could be removed from the autoclave.

3.1.3. Characterization of the aerogel properties

The bulk density of an aerogel was determined by weighing of a sample of a known volume. It was rather difficult to cut the aerogels in order to get the regular geometric shape. That is why special cutting cylinder were used for this purpose. Accurate cylindrical pieces with the volume of 1.8 ml could be produced by this way. The volume could be calculated by measuring of the length and diameter of the cylinder. Aerogel was then weighed. The density was determined as a mean value of at least 3 measurements.

Pore size and surface area were measured by nitrogen adsorption/desorption. The adsorption isotherm shows a hysteresis loop, typical for the mesoporous materials, having the pores within a diameter of 2-50 nm diameter. The reason of the hysteresis is the difference between the evaporation from the pore and the condensation within it. The measurements were carried out at the Institut für Technische Chemie, Technische Universität Berlin.

Optical properties of aerogels as well as their chemical composition were investigated by IR spectroscopy. For the spectroscopic measurements aerogels were powdered and pressed with KBr. The adsorption spectra were measured in the region from 600 to 4000 cm^{-1}. An IR Spectrometer Magna System 750 was

used for this measurements. The measurements were carried out at the Institut für Anorganische Chemie, Technische Universität Berlin.

3.1.4. Loading of silica aerogels with drugs

To load silica aerogels with organic substances, the same autoclave was used as for the aerogel production. Aerogels with a density of 0.03 g/m^3 and a BET surface area of 450-500 m^2/g were used for these experiments, if not otherwise specified.

First, the solubility of every drug in supercritical CO_2 was determined. To do that a specific amount of the drug was filled in a metal cage, weighed and placed on the bottom of the autoclave. The autoclave was closed and heated up to a fixed temperature (20-70°C). Then CO_2 was pumped into the autoclave up to the target pressure (140-180 bar) was reached. The system was stored under stirring for 10 hours to 3 days. The optimal dissolution time was determined experimentally for every chemical. After the equilibrium was reached, CO_2 was vented out with a constant flow rate (~100 N L/h) and then the autoclave was cooled to room temperature. The metal cage with the rest of the drug was weighed and the amount of the dissolved drug was calculated. The amount of CO_2 in the autoclave was calculated from the known volume and corresponding CO_2 density. The values of CO_2 density were taken from NIST data base [24]. The solubility of the drug was calculated and compared with the data from the literature (if existed).

Then the aerogel samples were loaded with the drug. A weighed amount of the drug together with two aerogel samples were placed into the autoclave. Thin pieces of aerogels (0.05 – 0.1 g) were used. The aerogel samples were wrapped in a filter paper in order to prevent the direct contact of both substances in the solid state. The autoclave was closed and heated up to a fixed temperature (40-70°C), then CO_2 was added. After the target pressure (140 – 180 bar) was reached, the system was stored at these conditions under continuous stirring at least 10 hours. In some cases, the dissolution process was very fast and it could be visually observed. Then CO_2 was vented out with a constant flow rate (~100 NL/h). After the ambient pressure was reached, the aerogel samples were weighed. The weight increase of the aerogel samples indicated the adsorption of the drug in the aerogel and its concentration could be roughly estimated.

To determine its concentration the aerogel exactly, the loaded aerogel sample was grounded into a powder and dispersed in a suitable solvent. The solvent which provides a good solubility of the corresponding drug at room temperature was chosen. The solution was stirred at least 30 min. The concentration of the drug in this solution was determined using gas chromatography or UV

Table 1
Methods of the determination of the drug concentration

Compound name	Solvent used	Analysis method used
Naphthalene	Toluene	GC
Ketoprofen	Acetonitrile	HPLC, UV–VIS Spectrometer
Griseofulvin	Acetonitrile	UV-VIS Spectrometer
Miconasol	Acetonitrile	UV-VIS Spectrometer

spectrometry. Based on these measurements the amount of the drug in the loaded aerogel was calculated. The corresponding solvents and method of analysis for every drug are summarized in Table 1.

A UV spectrometer (Specord 200 (2 beams), Analytic Jena) was used to determine the concentration of the drugs both for the adsorption and for drug release measurements. A quartz cuvette with a path length of 10 mm was used for the measurements. The absorbance was measured at the maximum value for all substances. The corresponding wave lengths are listed in Table 2.

3.1.5. Drug release measurements

A special apparatus was constructed for the drug release measurements. The scheme of the apparatus is presented in Fig. 4. Drug release measurements were carried out following the recommendations of the United States Pharmacopoeia (USP XXI). Due to these recommendations, the assembly consists of the following parts: a covered vessel made of glass, a motor, a metallic drive shaft, and a stirrer. The vessel is partially immersed in a water bath. The water bath permits holding the temperature inside the vessel within ± 0.3°C All measurements were carried out at 37°C in 0.1 N HCl at 100 min^{-1}. At the beginning of the experiment the substance (aerogel loaded with the corresponding compound) was introduced into the vessel, filled with 900 ml 0.1 N HCl, the motor was turned on and the time was registered from this moment. The amount of the target substance was calculated in order to get 10% of its saturation concentration (sink conditions). A 2 ml sample of the resulting solution was taken every 2-5 minutes. Every sample was filtered using a nylon filter with a pore diameter of 0.45 μm to ensure that no aerogel particles remained in the sample vessel.

Table 2
Wave length used for the UV measurements.

Substance	Wave length in 0.1 N HCl, nm	Wave length in acetonitrile, nm
Ketoprofen	258	252
Griseofulvin	293	293
Miconazol	280	280

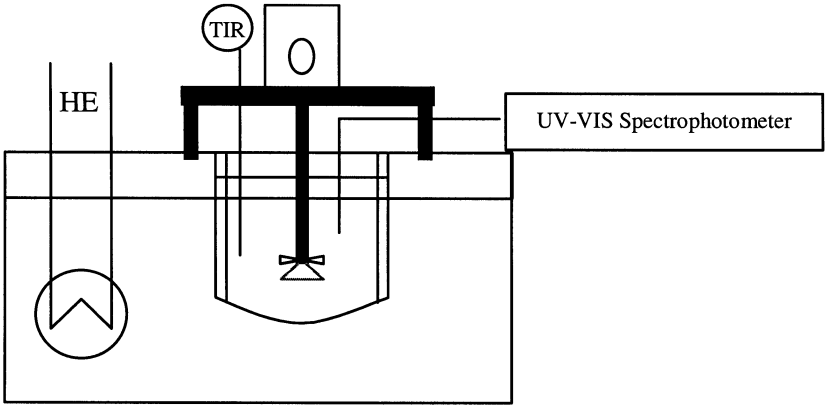

Fig. 4. Scheme of the release apparatus constructed at TUB, HE is a heating element, TIR - PT 100 thermometer.

The samples were stored in a water bath at 37 °C and after the release was finished, the concentration of the target compound in every sample was determined by means of UV absorption. The concentration in the vessel at the time when the sample was taken, was calculated. The release curves were presented as the dependence on the concentration of the drug in the vessel against time.

3.2. Influence of CO_2 on the gelation process: experimental results

The influence of CO_2 on the gelation time of the gels prepared according to the experimental procedure described above was investigated. In order to characterize this effect, gelation times were measured for the samples prepared by CO_2 addition and for the control samples, gelified by the same conditions but without CO_2 addition. The gelation time ($t_{gel}^{CO_2}$) was determined as a time interval from the moment of the CO_2 addition to the moment when the solution looses its fluidity. In these experiments the weighted amount of CO_2 was added to the liquid at once. The gelation time of the control sample (t_{gel}) was determined as the time interval between the moment when the target temperature was reached to the moment when the solution was completely gelified. The results for the solution with a target density 0.03 g/cm^{3}are presented in Table 3.

One can see that the gelation time decreases upon CO_2 addition. For example, the gelation time at 25°C is 161 hour for the conventional sol. By means of the addition of CO_2 this gelation time can be reduced to 60 minutes. At higher temperature the difference in gelation times is not so large, but still significant (21 hours compared to 53 minutes). This fact was never reported in the literature.

Table 3
Gelation times at 25 and 40°C. Component molar ratio:
1 mol TMOS : 2.4 mol MeOH : 4 mol H_2O : 10^{-5} mol HCl: 10^{-2} mol NH_4OH.

t_{gel} , 25°C	t_{gel}, 40°C	$t_{gel}^{CO_2}$, 25°C	$t_{gel}^{CO_2}$, 40°C
161 h	21 h	60 min	53 min

It is supposed that the gelation time depends strongly on the CO_2 concentration. So the gelation time was measured as a function of the CO_2 content in the system. The experimental results are presented in Fig. 5. The solid line represents the trend line fitted to the experimental data. The trend parameters are given in the legend.

It can be seen that the gelation time decreases rapidly with the increasing of the CO_2 content in the system and approaches a constant value if the total CO_2 concentration reaches 20 wt %. Further addition of CO_2 does not enhance the reaction significantly.

As CO_2 was added to the solution, it dissolved partly therein. Just after the CO_2 addition the pressure increased and than decreased rapidly because of the dissolution of CO_2 in the liquid phase. Usually the equilibrium was reached in 15-30 min and the pressure over the solution did not change any more. This value was taken for the evaluation. The final pressure over the system determines so far the CO_2 solubility.

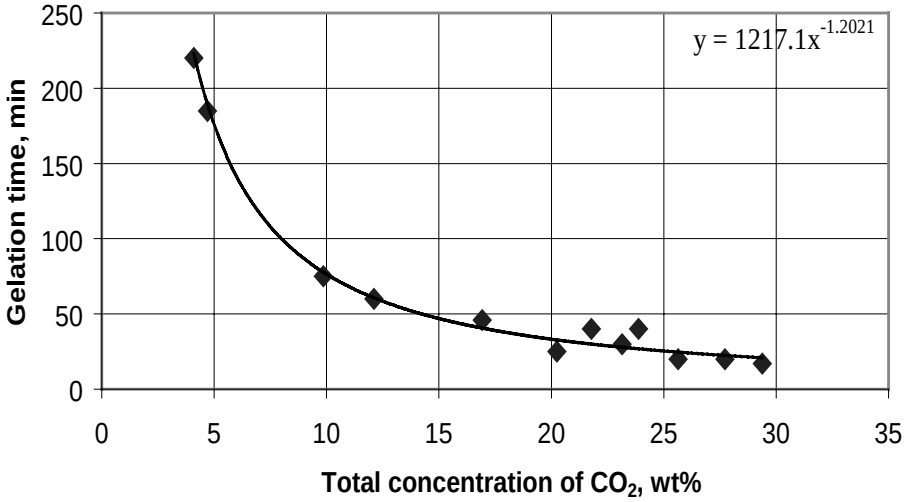

Fig. 5. Dependence of the gelation time on the amount of CO_2 added to the system at 40°C. Component ratio: 1 mol TMOS : 2.4 mol MeOH : 4 mol H_2O : 10^{-5} mol HCl: $2X10^{-3}$ mol NH_4OH. Solvent – acetonitrile; $\rho_{target} = 0.04$ g/cm^3

Taking into account that the reaction takes place in the liquid phase, we can expect that the reaction rate depends on the concentration of CO_2 in the liquid phase rather than on total CO_2 concentration in the system. It is difficult to estimate the concentration of CO_2 in such a reacting system directly, because the composition of the liquid phase changes continuously. In the case of slow reactions several methods which allow the measurements of the liquid phase concentration are known. In our case the addition of CO_2 leads to the acceleration of the reaction, so that the whole process can be completed in several minutes. So we could not reliably determine the concentration of CO_2 in the liquid phase during the reaction. However, it is possible to estimate this value from our experimental results using some assumptions. The initial solution consists of several components, including TMOS monomer, water, catalysts and a solvent, the main component being the solvent - acetonitrile. If the reaction is already proceeding, the solution contains also the reaction products such as partly hydrolyzed TMOS, methanol and a variety of polymer chains. But at the very beginning of the reaction (reaction time = 0) we can assume, that the volume of the mixture is a sum of the volume of all components (under neglection of the excess volume). In this case the volume of acetonitrile is proportional to the target density (Eq. (8).

$$V_{acetonitrile} = \frac{m_{SiO_2} - \rho_{\text{target}} V_{sol}}{\rho_{\text{target}}} \tag{8}$$

Knowing the volume of the mixture and the target density of the solution, acetonitrile concentration can be calculated. As soon as the most part of the experiments was made for the solutions of the target densities less than 0.04 g/cm^3, the concentration of acetonitrile was always greater than 75 wt%. So we deal with very dilute solutions, and in this case we can expect that the solubility of the CO_2 in our reacting mixture is close to the solubility of CO_2 in acetonitrile.

The vapor-liquid phase equilibrium of the acetonitrile - CO_2 mixtures is known [25, 26]. The concentration of acetonitrile in the vapor phase was found to be very low (mole fraction of CO_2 is close to unit) [25]. So we can neglect it and assume that the concentration of CO_2 in the gas phase is 100%. Using this assumption it is possible to estimate the concentration of CO_2 in the solutions studied. The estimation procedure is based on an iteration method and contains the following steps:

a) The volume of the liquid phase is calculated using the experimentally determined mass of the solution in the autoclave and the density of the liquid phase. The densities of the corresponding solutions were measured using a pycnometer with an accuracy ±1%. The results are summarized in Table 4.
b) The volume of the vapor phase is calculated as the difference between the total volume of the autoclave and the volume of the liquid phase.

c) The CO_2 mass in the gas phase is determined using its density under the experimental conditions. The pressure for every composition was determined experimentally. Fluid properties of CO_2 were taken from [23].
d) The amount of CO_2 in the liquid phase was calculated by subtracting of the CO_2 amount calculated in the step (c) from the total CO_2 amount added to the system.
e) A new liquid phase volume was calculated under the assumption, that the density of the liquid phase does not change significantly.

The iteration procedure was repeated up to the concentration of CO_2 in the liquid phase did not change significantly during the iteration.

Using this method the CO_2 concentration in the liquid phase was calculated for all experiments. The results for the system sol – CO_2 is presented in Fig. 6 in comparison with the experimental data of Kordikowski et al. [26] for the binary system CO_2 – acetonitrile.

One can see, that the solubility of CO_2 in our mixture is very close to that of acetonitrile, as expected. So the data of CO_2 solubility in acetonitrile can be used to make the first rough estimation of the CO_2 content in the liquid sol phase, if it can not be measured directly.

Using the procedure described above, we can also calculate the CO_2 concentration in the liquid phase for the experimental data shown in Fig. 5.

The results are presented in Fig. 7. The solid line represents the trend line fitted to the experimental data. It can be seen, that this dependence has the similar trend as that presented in Fig. 5. It shows, that even the total concentration of CO_2 in the system is a suitable parameter for the characterization of this phenomenon.

Table 4
Densities of the mixtures studied

ρ_{target}, g/cm^3	$\rho_{solution}$, g/cm^3 (23 °C)	$\rho_{solution}$, g/cm^3 (33 °C)
0.03	0.8079	0.7934
0.04	0.8184	0.8086
0.05	0.8267	0.8174

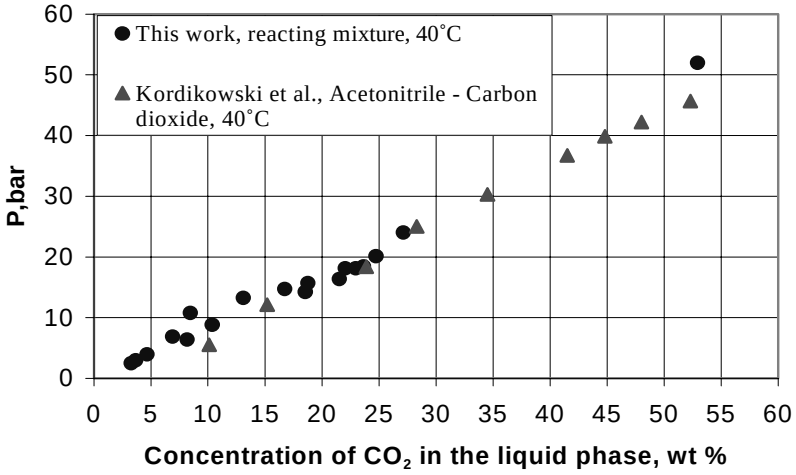

Fig. 6. Solubility of CO_2 in the reacting mixture at 40°C. Component ratio : 1 mol TMOS : 2.4 mol MeOH : 4 mol H_2O : 10^{-5} mol HCl: $2 \bullet 10^{-3}$ mol NH_4OH. Solvent-acetonitrile; ρ_{target} = 0.04 g/cm^3.

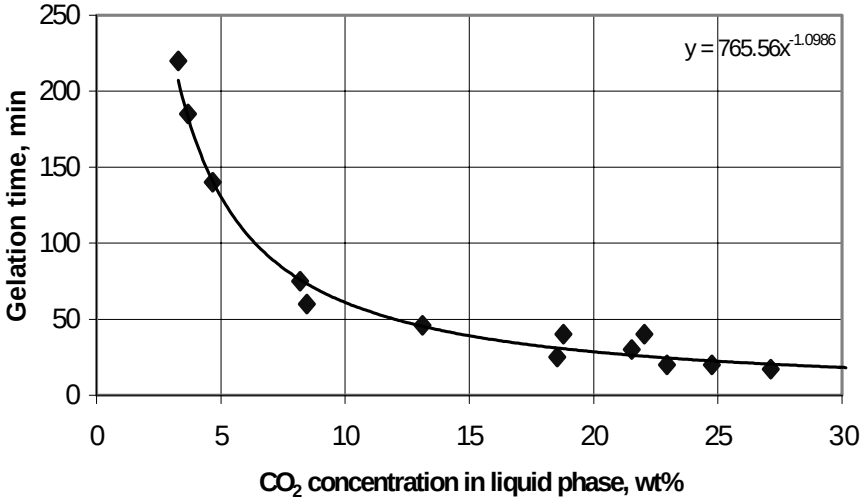

Fig. 7. Dependence of the gelation time on the CO_2 concentration in the liquid phase.

3.2.1. Determining of the optimal CO_2 concentration needed for the gelation

It was shown, that the addition of CO_2 always leads to a faster gelation. However, the gelation time depends on the CO_2 concentration in the solution. It was important to find an optimal concentration, which should be reached in the solution for the fast gelation. This was made following the procedure described previously. CO_2 was added to the solution in little portions every 5 minutes up to the gelation took place. The concentration reached in the liquid phase at this moment ($C_{CO_2}^{opt.}$) was considered to be an optimal value. Further CO_2 addition leads to the formation of a second liquid phase on the gel surface. The optimal concentration in the liquid phase ($C_{CO_2}^{opt.}$) was determined experimentally for every solution. Once determined, this value can be used for further experiments. In this case the corresponding amount of CO_2 can be added to the solution at once, instead of be added in little portions, to safe time. If the optimal concentration is exceeded by more than 10%, gelation also takes place, but precipitation of colloid particles may happen during aging. It was found out, that the aerogels, obtained in this case are less transparent, or completely opaque. So if a transparent aerogel is required, $C_{CO_2}^{opt.}$ should be determined experimentally for every specific case.

3.2.1.1. Influence of the aerogel`s target density

It was found, that $C_{CO_2}^{opt.}$ is a constant value for the solution of given concentration, but it varies with the TMOS concentration (or target density) of the solution. This effect was studied for the solution of different target densities. All other parameters were kept constant (component ratio: 1 mol TMOS : 4 mol H_2O : 10^{-5} mol HCl: 10^{-3} mol NH_4OH; t = 25°C). The dependence of $C_{CO_2}^{opt.}$ on the target density of the aerogel is shown in Fig. 8.

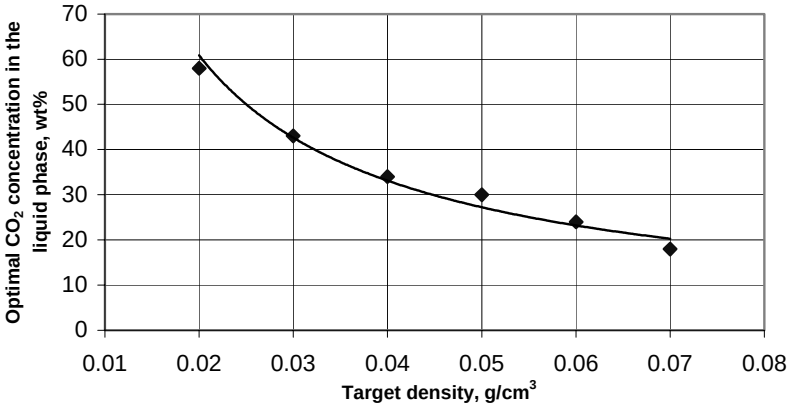

Fig. 8. The CO_2 concentration in the liquid phase needed for the given target density at 25°C.

One can see, that with the increasing target density $C_{CO_2}^{opt.}$ decreases. The larger target density means the larger initial concentration of TMOS in the solution (see the definition of the target density, Eq. (7)). The larger initial concentration of TMOS leads to a faster gelation and to denser gel. In this case the solution is simply more concentrated and so more monomers participate in the condensation reaction. That is why less CO_2 is needed to complete the gelation in the case of larger TMOS concentration (or larger target density).

3.2.1.2. Influence of the temperature

It is well known, that the gelation time depends on the temperature of the process [16]. Independent of the component ratio, gelation time decreases with increasing temperature. We studied the influence of the temperature on the optimal CO_2 amount needed for the gelation. It can be expected, that at higher temperature less CO_2 is needed for the gelation to be completed. The temperature dependence of the $C_{CO_2}^{opt.}$ was measured for different target densities. The results for different temperatures and target densities are summarized in Fig. 9. Solid lines represent the trend lines fitted to the experimental data. One can see, that for the solutions of all target densities $C_{CO_2}^{opt}$ decreases with increasing temperature. Both hydrolysis and condensation take place faster at higher temperature, so that less CO_2 is needed for the reaction enhancement. Target densities of the solutions studied were chosen following several criteria: in the case of relative high target densities ($\rho_{target} > 0.1$ g/cm^3) gelation time achieved by common

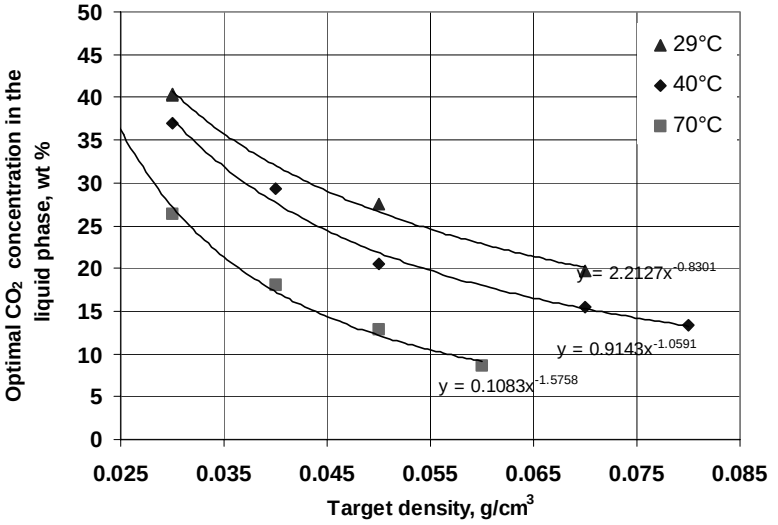

Fig. 9. Dependence of $C_{CO_2}^{opt}$ in the liquid phase on the target density of the aerogel at different temperatures.

processes is already low (< 1 hour), so in this case no additional reaction enhancement is needed; samples of low densities require longer gelation time, so the method suggested in this work can be useful. In the case of very low density ($\rho_{target} < 0.01$ g/cm^3) a very large amount of CO_2 would be needed (see Fig. 8). In this case it is useful to increase the amount of the basic catalyst before the CO_2 is added to the system. So for every given component ratio a specific target density region was chosen.

3.2.1.3. Combination of CO_2 with other catalysts

Catalysts play a decisive role in the gelation process. A number of different catalysts as well as their combinations were used for the aerogel synthesis. The fact that CO_2 leads to a faster gelation let us conclude that it acts in some way as a catalyst. In order to prove this fact different catalysts were used in combination with CO_2 and their influence on the gelation was studied. At first, all possible combinations of both catalysts commonly used for the gel synthesis NH_4OH and HCl with CO_2 were studied. All experiments were carried out at 25°C for the following component ratio:

1 mol TMOS : 2.4 mol MeOH : 4 mol H_2O : a mol HCl: b mol NH_4OH

Acetonitrile was used as a solvent in order to reach the target density 0.03 g/cm^3. Corresponding concentration of the catalysts as well as an appearance of the final solution are summarized in Table 5.

Table 5
Dependence of the gelation with CO_2 addition on the combination of catalysts used

Sample number	Catalyst used (mol catalyst per mol TMOS)		CO_2 mol ratio (mol CO_2 : mol TMOS)	Appearance of the final solution
	HCl (a)	NH_4OH (b)		
A1	10^{-5}	$2*10^{-2}$	0	Slow gelation resulted in a transparent gel
A2	10^{-5}	$2*10^{-2}$	16.72	Fast gelation resulted in a transparent gel
A3	0	0	0.1	Precipitation of colloid particles
A4	10^{-5}	0	0.1	Precipitation of colloid particles
A5	0	$2*10^{-2}$	16.72	Gelation resulted in slightly opaque gel

Sample **A1** was made by the common procedure using both HCl and NH_4OH at the first and second step correspondingly. This solution gelified after 23 hours giving a transparent gel phase.

Sample **A2** was made using the same procedure, but CO_2 was added to the solution. CO_2 amount was chosen so that $C_{CO_2}^{opt}$ determined for this conditions as described previously was achieved. It resulted in fast gelation (t_{gel} = 30 min) in agreement with our previous experiments. Transparent gel was obtained.

Sample **A3** was made without using any catalysts in the first and second step. In the first step TMOS, H_2O and methanol were stirred 30 min. After that additional water was added to reach the final component ratio 1 mol TMOS : 4 mol H_2O and the system was dissolved with acetonitrile to get the target density 0.03 g/cm^3. After that the mixture was filled in the autoclave and heated up to 40°C. CO_2 was slowly added to the system. Immediately after the addition of 5 wt% of CO_2 a precipitate appeared in the autoclave. CO_2 addition was stopped, solution was filtered and a white powder could be collected.

Sample **A4** was prepared similar to the sample A3, but HCl was added at the first step. CO_2 addition resulted in forming of white precipitate in the system. Sample **A5** was made analog to the sample A4, but NH_4OH was used as the catalyst. In contrast to the previous case, gelation took place within 30 minutes. The resulting gel was slightly opaque. The gel was dried at ambient pressure at 60°C.

The gels formed by the samples A1, A2 and A5 as well as the powders obtained from the samples A3 and A4 were dried at ambient pressure at 60°C. The resulting samples were analyzed by IR spectroscopy (see Fig. 10).

The spectra of all samples are very similar. This spectra were compared with the spectrum of silica aerogel and the major peaks were assigned as shown in Table 6.

Comparing the corresponding peaks we can see, that all samples consist predominantly of silicon oxide. The characteristic absorption at 1090 cm^{-1} and 806 cm^{-1} (SiO_2) is very strong. Some unreacted TMOS (2856 cm^{-1}) and water (3429, 1655 cm^{-1}) were also identified in the samples A2-A5, although it is difficult to say whether the corresponding peak represents the free unreacted water or water adsorbed on the gel surface, as in case of silica aerogel. It may be due to the uncompleted drying at 60°C. It should be stressed here, that this kind of IR spectra can give just a qualitative information about the sample, that is why we can not say anything about the concentration of the corresponding compounds.

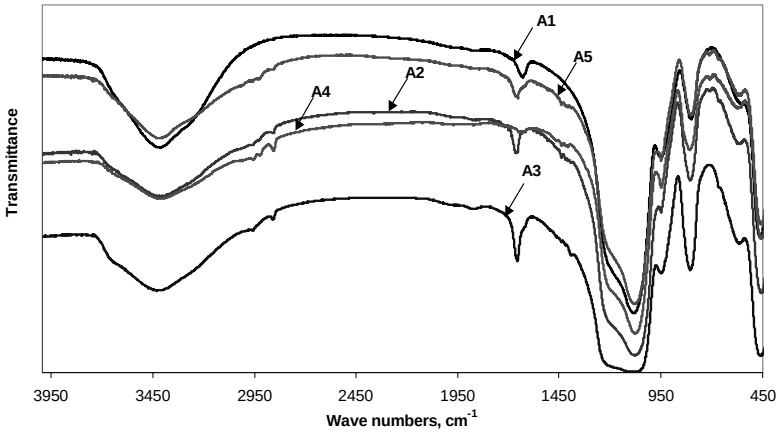

Fig. 10. IR spectrum of the samples A1-A5.

Table 6
IR Absorption bands and its attribution for silica aerogel

Wave number, cm^{-1}	Chemical Bond, [27], [28], [29]
3500-3400	Absorbed molecular water
3750	Free Si-OH on the surface of the gel
3665, 3540	Silanol groups linked to molecular water through hydrogen bonds, internal Si-OH
2958	Si-O-CH_3 symmetric stretching, C-H stretching
2856	C-H second stretching (methanol and unhydrolized TMOS)
1868, 806	(Si-O-Si); vibration of SiO_2 network
1655	H-O-H, absorbed molecular water
1456, 1412	C-H, ≡ Si -O-CH_3 (unhydrolized TMOS)
1090	≡ Si -O, vibration of silica network
806	Si-O-Si vibrational mode
948, 460	Si-O-Si deformation

Table 7
Effect of CO_2 addition in the system with NaOH at 40°C.

Base catalyst concentration	CO_2 concentration	$t_{gel}^{CO_2}$	t_{gel} (control sample)
1 mol TMOS: 0.002 mol NaOH	33,8 wt%	20 min	20 hours

Based on the spectra we can conclude, that precipitates obtained from the samples A3 and A4 consist mostly of silicon oxide and, thus, should be the result of the same chemical reaction as the gels A1, A2 and A5. It means that after CO_2 addition to samples A3 and A4, hydrolysis and condensation reactions also take place very rapidly, but lead to the formation of the colloid particles and not to a monolithic gel. So the effect of the reaction enhancement also takes place, just leading to another product.

As we can see CO_2 addition to the sol, in the case if no additional catalysts was used (sample A3), leads to a rapid precipitation of colloid particles. Obviously, CO_2 is not suitable as a single catalyst for the gel formation.

Also the combination of CO_2 and acid catalyst used in the first step (sample A4) shows the same effect. On the contrary, combination of CO_2 with the only basic catalyst (NH_4OH) leads to the rapid gelation (sample A5). The resulting gel is slightly opaque. As already discussed, an acid catalyst mostly accelerates the hydrolysis, and a basic one – condensation. Since CO_2 addition without HCl results in the gelation we can suppose, that CO_2 acts as an acid catalyst to some extend. A transparent gel can only be obtained, if both HCl and ammonia are used.

Potassium hydroxide (KOH) and sodium hydroxide (NaOH) instead of ammonia in the second step. The purpose of this experiments was to prove, whether the gelation enhancement by CO_2 is influenced by the nature of the base catalyst.

The starting solution was prepared in the same way, as described above. Acetonitrile was used as the solvent to reach the target density 0.03 g/cm^3. Both NaOH and KOH were used instead of ammonia in the second step. The component ratio was as follows: 1 mol TMOS : 2.4 mol MeOH : 4 mol H_2O :

10^{-5} mol HCl: $2 \cdot 10^{-3}$ mol NaOH (or KOH). CO_2 was added to the solution in small portions at 40°C. The same effect of the fast gelation was observed, as in the case of ammonia. Solutions gelatinated within 20 min, whereas the gelation time of the corresponding control samples was much longer. The results are illustrated in Table 7.

So we can conclude, that the gelation enhancement by CO_2 does not depend on the catalyst nature. The fast gelation took place, independent of the base catalyst used in the second step.

3.2.1.4. Influence of the solvent

Solvents play an important role in hydrolysis and condensation processes. Interactions between the solvent and reaction products (dimers, oligomers etc.) present in the solution have a strong influence on the process itself and in particular on the gelation time. It is supposed, that the effect of the gelation acceleration by CO_2 depends on the solvent used for the reaction. That is why it was essential to study this effect in different solvents. Seven solvents were chosen

for this experiment: methanol (MeOH), ethanol (EtOH), acetone, acetonitrile, formamide, dimethylformamide (DMF), dimethylsulfoxide (DMSO). These solvents belong to two different types: protic polar solvents and aprotic polar solvents, as shown in Table . Solubility of CO_2 in these solvents should be taken into account. The vapour-liquid equilibrium data for the system solvent - CO_2 can be found in the literature [30, 31]. For all systems the concentration of CO_2 in the vapour phase is close to 100 wt%, as it was already mentioned for the system CO_2 – acetonitrile. This fact is important, because in the following experiments, as in the case with acetonitrile, it was very difficult to determine the concentration of CO_2 in the liquid phase by direct measurements. This value was estimated using the iteration procedure described above. The densities of the solutions, which are needed for the calculation were measured at 40°C, using a pycnometer. The values are presented in the Table 10 in comparison with that of the corresponding solvent.

It can be seen, that the densities of the mixtures are similar to that of the corresponding solvents.

The experiments were carried out at 40°C. Solvents described above were used in order to get the target density 0.03 g/cm^3. Both in the first and in the second step the same solvent was used. Control samples were stored for gelation at the same temperature. All experiments were repeated at least twice. The results are summarized in Table 10.

Table 8
Classification of the solvents used for the synthesis

Protic polar solvent		Aprotic polar solvent	
CH_3OH	Methanol	C_2H_6OS	Dimethylsulfoxide
C_2H_5OH	Ethanol	C_3H_7NO	Dimethylformamide
CH_3NO	Formamide	CH_3CN	Acetonitrile
		C_3H_6O	Acetone

Table 9
Densities of the reacting mixtures at 40°C

Solvent used for the reaction	Density of the pure solvent, 20°C	Density of the solution just after the second step, 40°C
Methanol	0.791	0.801
Ethanol	0.789	0.789
DMF	0.949	0.939
Acetone	0.790	0.810
Acetonitrile	0.782	0.789
DMSO	1.101	1.06

Table 10
Effect of the CO_2 addition on the gelation process with different solvents

Solvent	P, bar	Total CO_2 concentration, wt%	C_{co_2} in the liquid phase, wt%	Appearance of the solution after CO_2 addition
Methanol	73.6	64.9	36.09	Precipitation of colloid particles
Ethanol	75.5	46.8	30-34 %	Precipitation of colloid particles
DMF	57.4	47.8	31.54	Gelation
Acetone	57.9	49.7	36.42	Gelation
Acetonitrile	32.1	37.2	28.08	Gelation
DMSO	65.2	38.9	21.82	LLE

It was observed, that CO_2 addition to the solution, made with DMF, acetonitrile and acetone leads to a gel formation. It should be noted, that the gelation in acetone and DMF solutions was not that complete as in the case of acetonitrile. Gels obtained in these systems were not so uniform and more opaque as in the case with acetonitrile. Anyway it was found, that the gelation basically took place. We suppose, that the quality of such gels can be improved by the optimization of the reaction conditions, like catalysts concentration and temperature.

In the case of methanol and ethanol no gelation could be achieved. After a certain concentration of CO_2 was reached in the solution (see Table 10), precipitation of colloid particles was observed. This effect was similar to the gelation process with CO_2 in the case, when no other catalysts are used.

In order to prove the chemical nature of these particles, the precipitate was collected, dried at 60°C and analyzed by IR spectroscopy. The corresponding spectra are presented in Table 11.

The spectra of the colloid particles obtained in this experiments are similar to those of silica aerogel, presented in Fig. 10. So in the case of ethanol and methanol the reaction enhancement also takes place, but leads to the precipitation of the colloid particles and not to the gel formation.

From these results we can conclude, that the gelation enhancement by the CO_2 addition takes place preferably in polar aprotic solvents (DMF, acetone, acetonitrile). Polar aprotic solvents dissolve both organic and inorganic reactants, but they are not able to hydrogen bonding with them. They are more inert than the protic solvents.

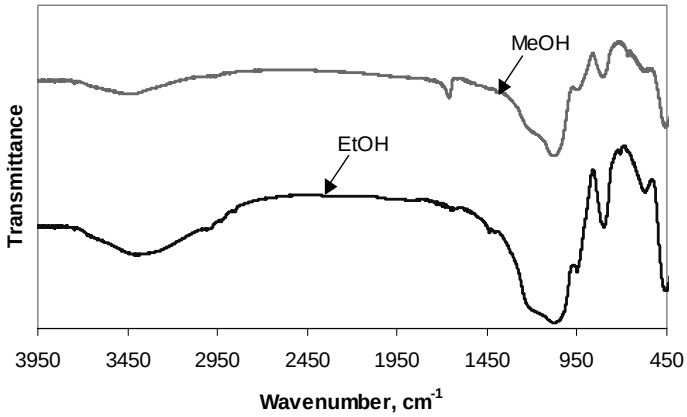

Fig. 11. IR Spectra of the colloid particles obtained in the from EtOH and MeOH solutions after CO_2 addition.

Table 11
Gelation times for different solvents without CO_2 addition. Component ratio: 1 mol TMOS : 2.4 mol MeOH : 4 mol H_2O : $2X10^{-3}$ mol NH_4OH. Target density = 0.03 g/cm^3

Solvent	Gelation time, hours
Methanol	1.7
Ethanol	1.8
Formamide	0.3
DMF	24.7
Acetone	54
Acetonitrile	40
DMSO	37

It is known, that the gelation time in a one-step process in aprotic solvents is longer as in polar protic solvents. In polar protic solvents the condensation rate is higher resulting in highly condensed particles [31]. It was proved whether the gelation times for the two-step process used in the present work, have the same tendency as shown by [31]. Gelation times without CO_2 addition were studied for all solvents used in the experiments with CO_2 enhanced gelation. The results are presented in Table 11.

One can see that the gelation time in the case of polar aprotic solvents (ACN, acetone, DMF, DMSO) is rather longer as that in polar protic solvents (methanol, ethanol). It agrees with the results for the one-step reaction [31].

Gelation time in the case of protic solvents is very short and the additional enhancement of the reaction by CO_2 might make the reaction so fast, that rather

colloid particles are formed as big clusters, leading to the gel phase. In the case of aprotic polar solvent the gelation time without the CO_2 addition is longer. CO_2 enhances the reaction also in this case, but the reaction is still slow enough to allow the formation of the uniform cluster (gel phase). This suggestion would explain the results presented in Table , showing that the gelation takes place preferably in the polar aprotic solvents.

3.2.2. Further experiments for the clarification of the gelation enhancement by CO_2

Although the effect of the gelation enhancement by CO_2 addition was studied at many different experimental conditions, its nature could not be fully understood from these studies. That is why we have carried out some other experiments in order to clear up the nature of the discovered effect.

It is known that the addition of strong acids during the second step can decrease the gelation time. This effect bases on the change of the pH value and shifting of the isoelectric point of the solution [32]. In our case CO_2 dissolves in the mixture and reacts partially with water, present in the system, to carbonic acid. Nevertheless, H_2CO_3 is a weak acid and in our case the pH of the solution changes only slightly with the CO_2 addition (pH=8 before the CO_2 addition, pH=7 after that). The pH values were measured by pH paper directly in the autoclave. Based on the assumption, that the gelation enhancement is caused by carbonic acid, we tried to replace CO_2 by some other acids. If this assumption is true, the addition of the weak acid instead of CO_2 at the same conditions would also lead to the fast gelation. Formic acid was used in these experiments. The starting mixtures were prepared by the same method, as in the case of CO_2 addition.

Formic acid solutions having different concentrations (0.01 %, 0.1 %, 1 %, 10 %) were added to 80 ml of the reacting mixture in small portions (1 ml). After the addition of every portion of the formic acid the system was stirred for 4-5 minutes and pH value was controlled. Formic acid was added up to the pH = 3 was reached. No gelation was observed during these experiments. The final solutions were let for gelation and gelified in 2-3 days.

We supposed that the carbonic acid resulting from the CO_2 addition might react with other components, present in the solution. One possibility can be that H_2CO_3 reacts with NH_4OH, as can be seen in eq. (7).

$$CO_2 + H_2O \leftrightarrow H_2CO_3$$

$$2\,NH_4OH + H_2CO_3 \leftrightarrow (NH_4)HCO_3 + 2H_2O \qquad (7)$$

This system is known to be a buffer solution, which can provide a preferable background for the condensation reaction. In order to model this effect and prove our suggestions, the influence of carbonate buffer solution (Na_2CO_3 + $NaHCO_3$) has been studied.

Similar experiments as in the case with formic acid were carried out with the carbonate buffer. Carbonate buffer having the pH value 10.1 was added to the 80 ml of the reacting mixture in 1 ml portions under constant stirring up to pH = 9 was reached. No gelation enhancement was observed as in the case of formic acid. Control samples gelified in 3 days.

Also the effect of ammonia hydrocarbonate ($NH_4 HCO_3$) itself was studied. The experiments were carried out similar as in the case of formic acid. Aqueous ammonia hydrocarbonate solutions having different concentrations (0.5 %, 2.5 %, 5%) were added to 20 ml of the reacting mixture in small portions (1 ml) at 20 °C. After the addition of every portion of ammonia hydrocarbonate, the system was stirred for 4-5 minutes. No gelation was observed during the experiments. The final solutions were let for the gelation and gelified in 2-3 days. The results of this experiment are summarized in Table 12.

If relatively large concentration of ammonia hydrocarbonate were used (B1, B2), precipitation of colloid particles took place. This effect was also observed with other base catalysts. If a certain catalyst concentration is exceeded, the precipitation takes place. That is why it is impossible to increase the catalyst concentration more than up to a certain level, if a gel formation is required.

In the case of lower ammonia hydrocarbonate concentration (B3), a normal slow gelation took place, as in the case of a common two-step procedure. No gelation enhancement was observed. Based on the experiments done, we can conclude that the enhancement of the reaction by CO_2 is not a simple effect of the change of pH value or the nature of ammonia carbonate. Both carbonate buffer and ammonia hydrocarbonate solution are not able to replace CO_2 with the same effect of the gelation enhancement.

Table 12
Influence of ammonia hydrocarbonate on the gelation

Sample number	$NH_4 HCO_3$ concentration of the initial solution, wt%	Final $NH_4 HCO_3$ concentration in sol, wt%	t_{gel}	Appearance of the final solution
B1	5	0.43	-	Precipitation of colloid particles
B2	2.5	0.123	-	Precipitation of colloid particles
B3	0.5	0.0043	4 days	Slow gelation resulted in a transparent gel

It was also supposed, that the pressure increase resulting from the CO_2 addition may also influence the reaction and lead to the faster gelation. Also reactions in the liquid phase are not much influenced by pressure, the addition of other gases (nitrogen and trifluoromethane) instead of CO_2 was studied at the same conditions in order to prove this idea. Both substances are in the supercritical state at the conditions used. R23 was chosen because its critical data are close to those of CO_2. The gases were added to the mixture after the second step in small portions at 40°C. In both cases the precipitation of colloid particles takes place just after the first portions of gases were added. No enhancement of the gelation was detected. So we can exclude the pressure as a factor, favorable for the gelation.

3.2.3. Gelation enhancement by CO_2 : suggestion to the process nature

The nature of the gelation enhancement by CO_2 was not fully cleared up in this work. Further investigation are needed to understand this effect. However, we summarize here our results and make some suggestions to the nature of this process.

It has been found, that the addition of supercritical CO_2 during the sol-gel process enhances the gel formation. The enhancement of the reaction, determined as the gelation times ratio ($t_{gel} / t_{gel}^{CO_2}$) depends on the target density of the solution and varies between 5 and 100. The CO_2 concentration in the liquid phase usually reached at the gel point is around 30 wt%. It was demonstrated, that increasing temperature and target density lead to the decrease of the optimal CO_2 concentration needed for the gelation. It was also shown that the reaction enhancement by CO_2 takes place only if CO_2 is combined with both catalysts used in common two-step process. If one or both catalysts are not used, CO_2 addition leads to the fast precipitation of colloid particles. It let us conclude, that the reaction enhancement by CO_2 addition always takes place, but in some cases it results not in gelation, but in particle's formation.

The same effect was observed if other solvents as acetonitrile were used for the reaction. It was found, that the fast gel formation enhanced by CO_2 takes place preferably in polar aprotic solvents (acetonitrile, dimethylformamide), whereas polar protic solvents (methanol, ethanol) promote the formation of the particles. At the same time this effect is not sensible to the nature of catalyst. The reaction enhancement was also observed, if other catalysts as hydrochloric acid and ammonia were used for the process.

The replacement of CO_2 with the other substances, which could appear in the mixture due to the chemical reactions (NH_4CO_3) did not result in the reaction enhancement. The addition of other gases, like nitrogen or trifluoromethane leads not to the gelation, but to the precipitation of SiO_2 particles. It means, that nature of CO_2 plays an important role for the gelation process.

As soon as CO_2 acts successfully only in combination with other catalysts, we can conclude, that CO_2 acts not (or not only) as a catalyst itself, but provides some optimal conditions for the condensation reaction, being accelerated by normal base catalysts (NH_4OH or NaOH). Also the strong dependence of this effect on the solvent nature let us conclude, that some interaction between CO_2 and the solvent might take place, as it shown by [33]. This suggestion might be proved by the spectroscopic measurements and will be the topic of our future work.

3.2.4. Optimization of the process parameter

A number of silica aerogels were produced from the gels, obtained by the two-step method modified by CO_2 addition. The drying procedure was already described in chapter 2. Anyway the process parameter were varied in order to find the optimal values, giving the transparent monolithic aerogels.

- Aging time was varied between 0 and 72 hours. It was observed, that an extremely short aging period (0-5 hours) results in weak aerogels, having a lot of cracks over the whole volume. Also the optical properties of aerogels were influenced by the aging time. Opaque, white aerogels were obtained after a short aging period. It is well known, that a certain aging period is needed for the stabilization and strengthening of the gel structure. 15 hours was found to be a suitable aging time. Practically, gels were left in the autoclave overnight for aging.
- Extraction temperature was varied from 4°C to 70 °C. We have found, that the low extraction temperatures (4-25°C) result in opaque aerogels and even lead to the particle formation in the gel body. The extraction temperatures being higher as 35°C lead to transparent aerogels. As soon as CO_2 turns to the supercritical fluid at 31°C, we can conclude that the supercritical CO_2 is a better extraction media for this process than liquid CO_2. Further increase of the extraction temperature (up 70°C) did not influence the properties of the aerogels. The most practical way is to run the extraction at the same temperature as the gelation and aging procedure. The temperature change can result in small cracks in the gel body, which lead to shrinkage during the extraction. We found 40°C to be the optimal value for the gelation, aging and extraction procedure.
- Extraction time depends strongly on the size of a gel, being controlled by the diffusion of the CO_2 through the pores of the aerogels. Binary diffusion coefficient were measured for several mixtures CO_2 – organic solvent [34] and can be used for the modeling of the drying procedure. Several models were applied for this purpose [35]. It was shown, that the extraction time needed to complete the solvent exchange depends mostly on the thickness of the gel sample. If the gelation is carried out directly in the autoclave, like in the present work, the gel has the same form as the autoclave, so it was diffi-

cult to vary the thickness of a gel. Anyway we have also found, that for samples having the volume 50 cm^3 3-4 hours extraction is needed, whereas a 120 cm^3 sample requires at least 24 hours solvent exchange. So the size and shape of the apparatus should be optimized to reach the minimum extraction time.

- Flow rate during the extraction plays also an important role in drying procedure. Too high flow rates can lead to the rises and inhomogeneity in the aerogel, whereas extremely low flow rates result in a very long extraction time. We have found 10-20 NL/h to be an optimal flow rate for the extraction procedure.

3.2.5. Physical properties of the aerogels obtained by CO_2 addition

A number of gels obtained by the CO_2 addition were dried to get an aerogel. In each case the control sample, gelified without CO_2 addition, was also dried and the properties of both samples were compared. We have found, that CO_2 amount used for the gelation ($C_{CO_2}^{opt.}$) is very important. It should be determined experimentally for every specific solution. As it was already mentioned, if this amount is exceeded, the transparency of the final aerogel is very low. On the contrary the sample made with the CO_2 concentration equal to $C_{CO_2}^{opt.}$ was completely transparent. For all aerogels discussed further the CO_2 amount used for the gelation was kept equal to the $C_{CO_2}^{opt.}$ values determined experimentally.

We produced aerogels with the densities $0.02 < \rho < 0.1$ g/cm^3, having BET surface areas of 500-700 m^2/g. The aerogels with lower densities can be also synthesized by the method with CO_2 addition, but such samples are very unstable, so longer aging is required. It was not our purpose to synthesize the aerogels with the ultra-low densities, so we did not find the optimal parameters for such samples. In order to compare both methods we present here the properties of two aerogel samples having the target density 0.03 g/cm^3 obtained from the same start solution. Sample C1 was obtained from the gel, synthesized with CO_2 addition. Sample C2 was prepared without CO_2 addition. Their physical properties are compared in Table 13.

One can see, that the properties of both samples are quite similar. Aerogel obtained using the CO_2 addition has a smaller pore diameter and slightly lower surface area than the sample prepared by the conventional method. The difference is very small, so it can also attribute to the experiment uncertainty.

Table 13
Comparing of the physical properties of aerogels, obtained by different methods

Sample number	Density, g/cm^3	Average pore diameter, nm	BET surface area
C1	0.0306	18.6	687 m^2/g
C2	0.031	21.2	700 m^2/g

4. SILICA AEROGELS AS A DRUG RELEASE SYSTEM: EXPERIMENTAL RESULTS

There are two general processes to load aerogels with chemicals:

a) through the chemical reaction during the sol-gel process or
b) by the post-treatment of dried aerogels.

Both processes in principle can be used for the loading of aerogel with a drug. If the process (a) is used, the drug should be added to the solution during sol-gel process. After that the gel containing the drug should be dried supercritically. In the case of high temperature SCD the corresponding substance should be exposed to high temperature and high pressure. It can cause undesirable chemical reactions, leading to changes in chemical structure of the drug. In the case of low temperature SCD this is not the case, however a lot of pharmaceuticals are soluble in CO_2 to some extent. In this case it is highly possible, that the drug will be extracted from the gel by supercritical CO_2. So this process is reasonable only for the substances having extremely low solubility in CO_2 at given conditions.

Process (b) can be realized in many different ways. Normally an adsorption process is used. Both adsorption from the liquid and vapour (gas) phase can be used. Adsorption from the liquid phase is widely used in pharmaceutical industry [33]. Anyway some problems can arise from using organic solvents in this process. The elimination of solvents by evaporation can cause a degradation of thermosensitive drugs; also some residual traces of solvent can be present in the product and influence its therapeutic properties [37]. Additionally, a contact with a liquid destroys the structure of the hydrophilic aerogel to some extent.
In the present work it was suggested to use adsorption from the supercritical gas phase.

Two different processes of the adsorption from the gas/vapor phase exist:

- Exposing of an aerogel to the vapour of a drug. In this case the vapour pressure of this substance should be high enough to get a reasonable loading of an aerogel.
- Dissolving of the drug in the supercritical gas phase followed with the adsorption of this compound by aerogel from the resulting solution. In this case the target compound should be soluble in the corresponding gas.

Supercritical CO_2 was chosen as a solvent for this process. The target substance was dissolved in supercritical CO_2 and remained in contact with an aerogel for the time long enough to get an equilibrium. The open pore structure of the aerogels allows the chemicals to diffuse through the aerogel body and to be adsorbed on the aerogel surface. Supercritical CO_2 was chosen for this process because of several reasons:

- CO_2 is non-toxic.
- Elimination of CO_2 from the medium can be easily achieved by lowering the pressure.
- Supercritical CO_2 is one of the most well studied media among the supercritical fluids. Solubilities of many organic substances inclusive pharmaceuticals have been reported [38-40].
- Supercritical CO_2 has been already used to load porous support materials, different from aerogels, with pharmaceuticals [37, 41].
- CO_2 is generally used for the production of silica aerogels as described above.

4.1. Manufacture of aerogel - drug formulations: experimental result

4.1.1. Experiments with a test substance

Loading of silica aerogels with chemicals by the adsorption from supercritical CO_2 solution was first conducted using a test substance in order to optimize the process parameters.

The experimental procedure is described in detailed in section 3.1.4. Naphthalene was chosen as a test substance because its solubility in CO_2 has been well studied and found to be rather high [38, 42]. Adsorption isotherms were measured at 40°C and 70°C. The theoretical maximal naphthalene concentration which can be used for the loading is limited by the solubility of naphthalene in CO_2. Solubility data [42] are given in Table 14.

Although in all experiments the concentration of naphthalene was below the saturation, it was difficult to handle the solutions having the concentration $C_{\text{naphthalene}} > 0.5$ wt%. In this case crystallization of naphthalene in the autoclave took place during the pressure release. Crystallization inside the aerogel was also observed. A picture of such sample is shown in Fig. 12.

Naphthalene crystals are spread in the aerogel. Black background allows to recognize them in the transparent aerogel sample. This effect is undesirable for the adsorption measurement, so the experiments were carried out only for those concentrations, where the crystallization did not take place. Due to this effect naphthalene concentration used for the adsorption measurements does not exceed 0.5 wt%. In the cases, when the lower concentration was used, aerogel samples stayed transparent after the loading. No naphthalene crystals could be detected by visual inspection and by both optical and electron microscopes.

Table 14
Solubility of naphthalene in CO_2 at 40 °C

P, bar	100	120	153	200
$X_{\text{naphthalene}}$	0.0069	0.01438	0.01969	0.02438
$C_{\text{naphthalene}}$, wt%	0.23795	0.4983	0.6848	0.8506

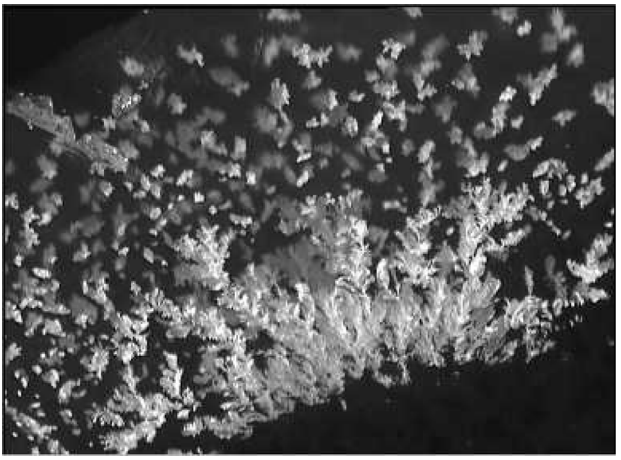

Fig. 12. Picture of the aerogel sample having naphthalene crystals inside.

The adsorption isotherms are presented in Fig. 13. It can be seen that the load of the aerogel with naphthalene increases with an increasing concentration of naphthalene in CO_2. It is expected, that saturation will be achieved and the loading comes to a constant value with increasing naphthalene concentration, although these concentrations could not be used because of the crystallization, described above.

The adsorption isotherm at 70°C was fitted using the Langmuir equation for the monolayer adsorption:

$$q_a = \frac{q_m bC}{1 + bC} \tag{10}$$

where q_a is a weight adsorbed per unit weight of adsorbent, q_m is a maximum load, C is a concentration of the absorbate in the bulk phase, b is a constant. Following parameters could be determined by fitting of experimental data: q_m = 0.079, b = 196.

It can be seen that the loading of silica aerogel with naphthalene which can be achieved by the proposed method is not very high (4%). Also it is known, that the benzoid ring system acts as an electron donor interacting with silanol groups, so the hydrophobic nature of naphthalene does not provide high adsorption values on the hydrophilic aerogel surface.

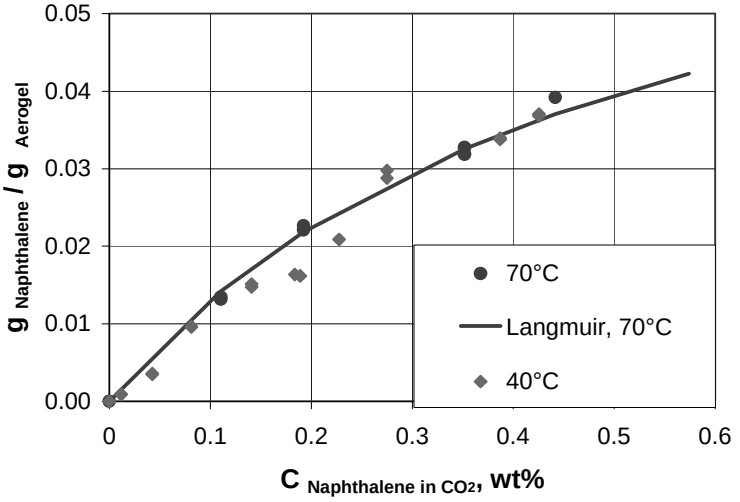

Fig. 13. Adsorption of naphthalene on silica aerogel at 40°C and 70°C.

It should also be mentioned, that adsorption of CO_2 molecules takes place simultaneously with the adsorption of naphthalene. Competition of both processes might take place. We did not study the CO_2 adsorption in detail, but it is known, that CO_2 density at the conditions used is relative high, so the contribution of the CO_2 adsorption is not negligible. Anyway the standard procedure includes the depressurization of the autoclave, what results in a desorption of CO_2 so that only traces of CO_2 stay in the aerogel at ambient pressure.

4.2. Loading of aerogels with drugs.

Experiments with naphthalene show that the process proposed in this work is suitable for the loading of silica aerogels with chemicals. After the process parameter were set up with the model substance, the experiments with drugs were carried out.

Following criteria were used to choose these substances:

- The drug should be soluble in CO_2.
- It should be stable at the process conditions used.
- Immediate release should be desirable for this drug, because we expect its faster release from the aerogel.

Three drugs, which fulfil this requirements were chosen for our experiments: *ketoprofen*, *griseofulvin* and *miconazol*.

4.2.1. Ketoprofen ((RS)-2-(3-benzoylphenyl) propionic acid)

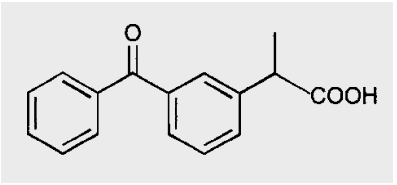

CAS number: 22071-15-4

M_w = 254.29 g/mol

Melting point = 94 °C

Fig. 14. Structural formula of *ketoprofen*

Ketoprofen (Fig. 14) is widely used as nonsteroidal anti-inflammatory drug for the relief of acute and chronic rheumatoid arthritis and osteoarthritis, as well as for other connective tissue disorders and pains. Both immediate release form and sustained release form exists depending on the specific application. Solubility of *ketoprofen* in CO_2 has been reported [43].

Experiments have been carried out at 70°C. The experimental procedure is described in details in chapter 3.1.4. During the impregnation of *ketoprofen* in the aerogel, no crystallization occurred in the pores of the aerogel as proved by simple inspection and by electron microscope. The adsorption isotherm of *ketoprofen* is presented in Fig. 15. The adsorption isotherm was fitted using the Langmuir equation. The following parameters were determined by fitting of the experimental data: $q_m = 0.303$, $b = 1249$.

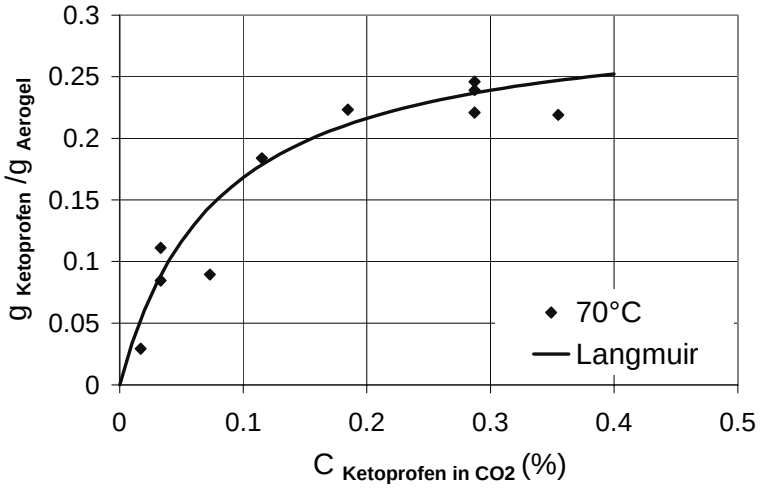

Fig. 15. Adsorption of *ketoprofen* on silica aerogel 70°C.

The results obtained in the experiments confirm that the aerogels can adsorb a relatively large amount of *ketoprofen* (up to 0.25 gram *ketoprofen* per gram aerogel). Better adsorption of *ketoprofen* compared to that of naphthalene might be explained by the hydrogen bonding between the OH groups of *ketoprofen* and silanol groups of silica aerogel.

Ketoprofen dosage in the pharmaceuticlas formulation used at present is rather low. Common *ketoprofen* pellets (e.g. Actron pellets from Bayer company, license 1-20705) contain 12,5 mg *ketoprofen* per pellet. In the case of 25 % loading 0.05 gram aerogel is needed in order to get this dosage. If aerogel with the density $\rho = 0.08$ g/cm^3 is used, the volume of the aerogel would have 0.63 cm^3. It is a quite realistic dosage for the pellets or capsule. Aerogel sample loaded with *ketoprofen* can be also pulverized and pressed to get a pellet or to be filled in a capsule.

4.2.2. Griseofulvin (7-Chloro-2',4,6-trimethoxy-6'b-methylspiro-[benzofuran-2(3H),1'-(2)-cyclohexene]-3,4'-dione)

Solubility of *griseofulvin* in CO_2 is not available, that is why it was determined experimentally. Solubility of *griseofulvin* in supercritical CO_2 at 40°C and 180 bar was found to be 0.03 wt%.

Adsorption of *griseofulvin* on silica aerogels was studied under the same conditions. The experimental results are presented in Fig. 17.

The maximum loading, which could be reached with *griseofulvin* is 8 %. This value is much lower as that of *ketoprofen*. It is difficult to explain this fact. We can only suppose, that there are no groups in *griseofulvin*, which can interact with silanol or other groups in silica aerogel. It is also possible, that it results from extremely low solubility of *griseofulvin* in CO_2 at the experimental conditions used.

We suppose, that the loading can be increased by the increase of the *griseofulvin* solubility in CO_2. There are several methods, allowing to reach that. Higher pressure can be used for the experiments in order to reach higher CO_2 density and so better solubility. Also entrainers, like ethanol or acetone can be applied. It is known, that even very little amount of entrainer (2-5 wt%) can improve the solubility of the organic compounds in CO_2 in several orders of magnitude.

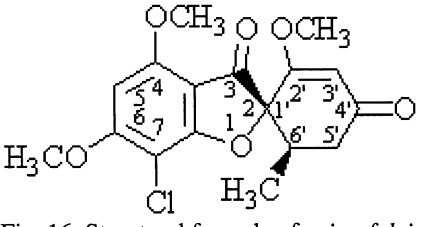

Fig. 16. Structural formula of *griseofulvin.*

CAS number: 126-07-8

$M_w = 352.8$ g/mol

Melting point = 222 °C

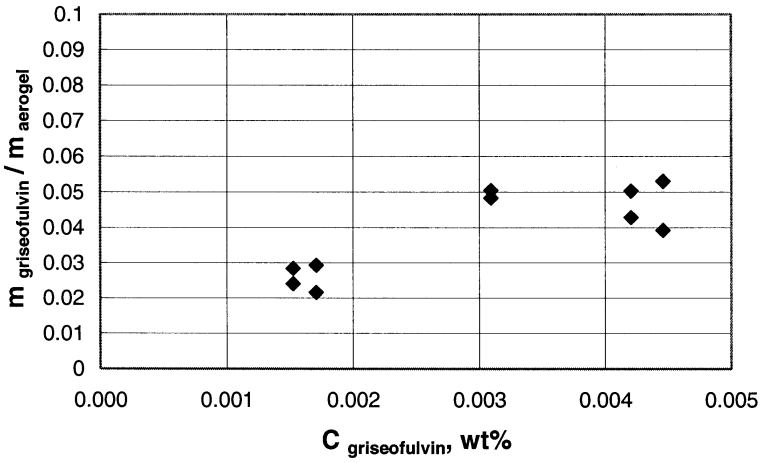

Fig. 17. Adsorption of *griseofulvin* on silica aerogel at 40°C.

4.2.3. Miconazol (1-[2-(2,4-dichlorophenyl)-2-[(2,4-dichloro-phenyl)-methoxy]-ethyl]-1H-imidazole

Solubility of *miconazol*e in supercritical CO_2 was not available, so it was determined experimentally. It was found that at 40°C and 180 bar the solubility of *miconazol*e is close to 0.2 wt%. The concentration range below the saturation was used for the adsorption experiments. All experiments were carried out at 40°C and 175 bar, like in the case of *griseofulvin*. The experimental results are presented in Fig. 19.

The loading of an aerogel with *miconazol*e is pretty high (up to 50%). The solubility of *miconazol*e in CO_2 is also much better, than that of *griseofulvin*. In this case we supppose, that aerogel can be used as a carrier material for *miconazol*e. As already mentioned aerogel can improve the reological properties of powders. In this case aerogel loaded with *miconazol*e can be used simultaneously as a carrier material and as an free flow agent.

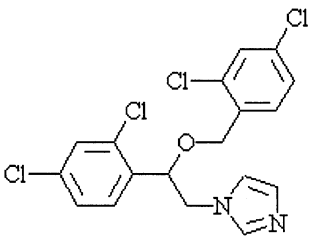

CAS number: 22916-47-8

M_w = 479.15 g/mol

Melting point = 184.5 °C

Fig. 18. Structural formula of *Miconazol.*

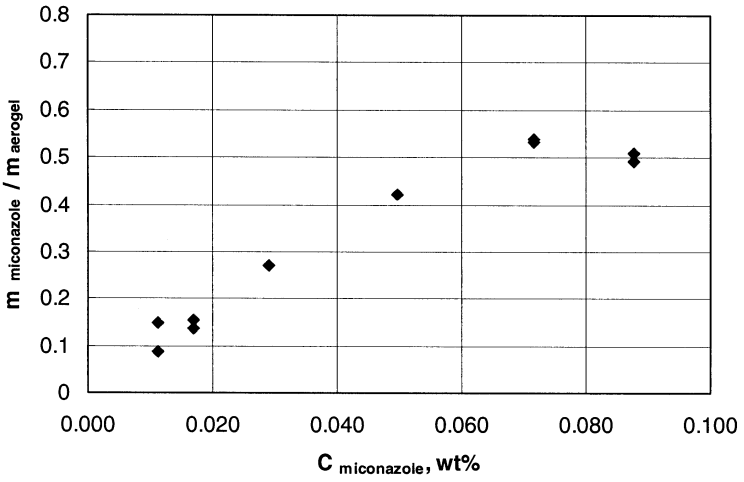

Fig. 19. Adsorption isotherm of *miconazole* on silica aerogel at 40°C, 175 bar.

4.2.4. Influence of the loading procedure on the chemical structure of drugs

Taking into consideration, that the pharmaceuticals were dissolved in supercritical CO_2 at high pressure and then adsorbed on silica aerogel, it was essential to prove, whether the chemical nature of a drug has been changed during this process. UV spectra of all drugs used in this work were taken before and after the loading procedure and compared with each other.

For the measurement of absorption in UV-VIS region the aerogel-drug formulations were dispersed in 0.1 N hydrochloric acid (standard dissolution medium). The position of the characteristic band was compared with those available in the literature. This method is one of the identification tests, recommended in German Pharmacopoeia [44]. Corresponding results are shown in Table 15. Characteristic peaks were detected on the same position in both pure drug solutions and aerogel formulation. Deviations ± 1nm are supposed to be an instrumental error.

Table 15
Specific UV absorption bands of different drug formulations

Substance	Maximal absorption, nm		
	Literature [44]	Pure drug dissolved in 0.1 N HCl	Formulation aerogel-drug dispersed in 0.1 N HCl
Ketoprofen	260	259	259
Griseofulvin	292	292.5	293
Miconazol	280	280	280

So we can conclude, that the loading procedure proposed in this work does not influence the chemical nature of the drugs used for our experiments.
Another question is the aggregate state of the drug in aerogel. As already mentioned, no crystalline structures have been found in the formulation aerogel-drug. Pure silica aerogels have an amorphous structure. We suppose, that drugs molecules are adsorbed on the surface of silica aerogel as a kind of a monomolecular layer. This fact also favour the fast release of the pharmaceuticals adsorbed on the aerogel. In the case of the crystalline drugs, even having a very small particle size, crystalline structure should be destroyed before the drug can be really dissolved. In the case of aerogel-drug formulations this step is eliminated.

4.3. Release of drugs from drug – aerogel formulations

Release of a drug from the specific formulation is the most important characteristic of this formulation. It was demonstrated, that at least three pharmaceuticals can be adsorbed on silica aerogel. Anyway, also the reverse process – desorption has to be studied. We investigated the release kinetics of all aerogel formulations, obtained by the adsorption from supercritical CO_2 as described in the previous chapter.

Solution of the hydrochloric acid has been chosen as a dissolution media following the recommendations of the German Pharmacopoeia [44]. The final concentration reached in the solution was equal to 10 % of the solubility of the corresponding drug in 0.1 N HCl at 37 C. Pure drug powders, used for the loading have been used as a standard. In every case the dissolution profile of the formulation "drug-aerogel" was compared with that of the pure substance.

4.3.1. Release of ketoprofen

In the case of *ketoprofen* both immediate release and sustained release are desirable, depending on every specific therapeutic effect.

Release of *ketoprofen* –aerogel formulation was determined experimentally and is shown below in comparison with that of crystalline *ketoprofen*. It can be seen, that the dissolution of *ketoprofen* from the aerogel-*ketoprofen* formulation, prepared by the adsorption from supercritical CO_2 solution is much faster as the dissolution of crystalline *ketoprofen*. Around 80 % of *ketoprofen* is dissolved already in 25 min if the aerogel formulation is used, whereas in the case of crystalline drug, 80 % is dissolved only in 200 min. This effect was expected and can be explained by both increase of specific surface area of the *ketoprofen* adsorbed on the aerogel and its non-crystalline structure in this formulation. Several approaches to describe the release profile exist [36]. The choice of the fitting model depends on the kind of dissolution.

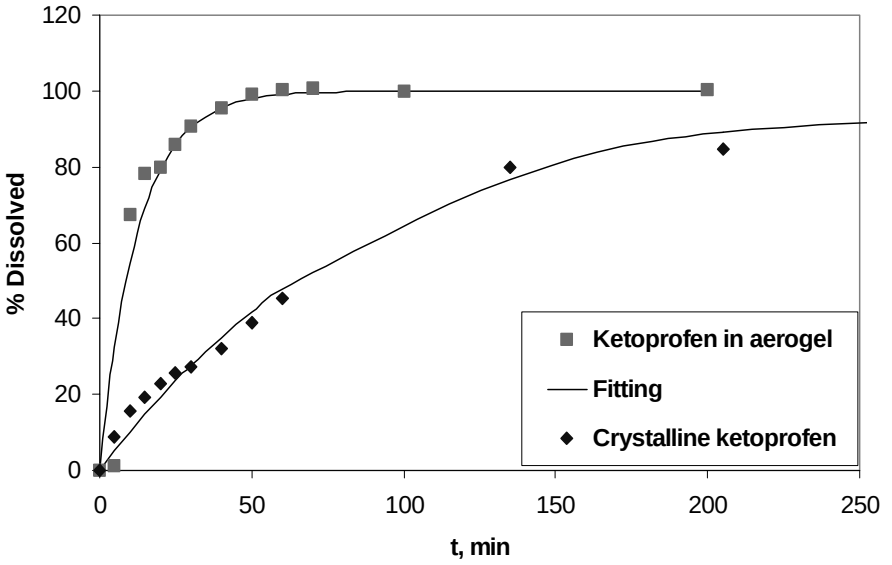

Fig. 20. Dissolution profiles of crystalline *ketoprofen* and aerogel-*ketoprofen* formulation, 37°C, 100 min^{-1}.

For the description of the fast release a so called "first order release model" [45] can be used:

$$C_{drug}(t) = 100\,(1 - e^{-kt}) \tag{11}$$

Equation (11) was used for fitting of the *ketoprofen* dissolution profiles (Fig. 20). Both dissolution of crystalline *ketoprofen* and aerogel-*ketoprofen* formulation could be fitted quite good with this approach.

4.3.2. Release of griseofulvin

Release of *griseofulvin* from the *griseofulvin* –aerogel formulation is presented in comparison with that of crystalline drug. Similar to *ketoprofen*, the dissolution of griseofulvin from the aerogel-griseofulvin formulation is faster than that of crystalline drug. Also the loading of aerogel with *griseofulvin* was not very high (see Fig. 17). Faster release can be obtained from this formulation. As much as 80 % of drug can be released in 30 min, what is 4 times faster, than the release of crystalline *griseofulvin* and twice faster as that of the micronized formulations [46]. If the loading of an aerogel with *griseofulvin* could be improved (for example by use of an entrainer during the dissolution in supercritical CO_2),

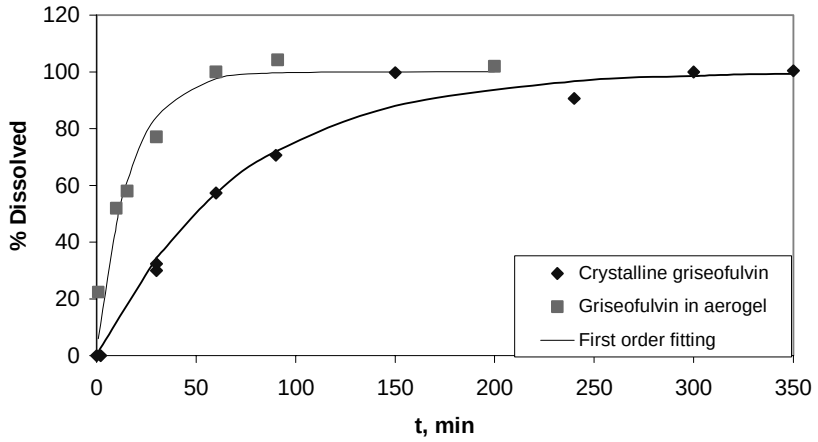

Fig. 21.Dissolution profiles of crystalline *griseofulvin* and aerogel-*griseofulvin* formulation.

aerogel-*griseofulvin* formulations with higher *griseofulvin* concentration could be used instead of a common micronized drug. The experimental results were fitted with the first order model (Eq.(11)).

4.3.3. Release of miconazol

Also the release profiles of *miconazol* were studied experimentally. The results are shown below. The experimental results were fitted with the first order model (11).

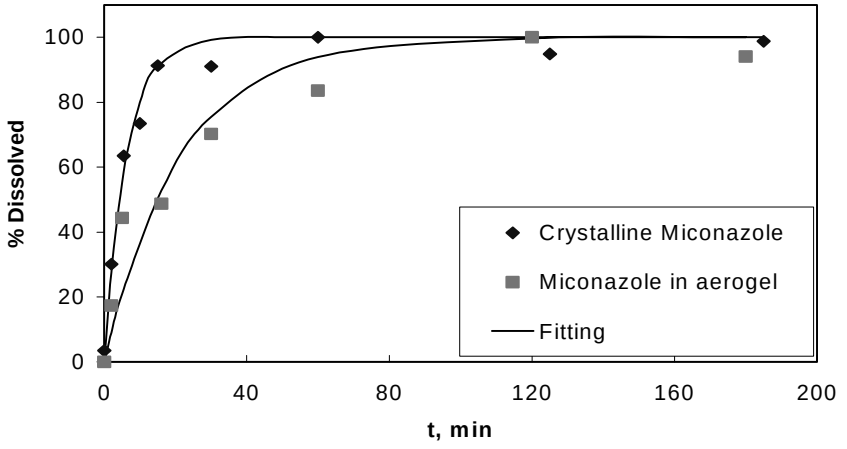

Fig. 22. Release profile of crystalline *miconazol* and aerogel-*miconazol* formulation.

partly hydrolyzed TMOS and thus, to some extent, inhibits t condensation. CO_2 may build an ionic complex with acetonitrile and compensating the solvation effect to some extent.

The nature of the gelation enhancement by CO_2 has not been fully explained through this work. Further investigations are required to fully understand this phenomenon.

A number of silica aerogels were synthesized by the modified two-step method described here. It was demonstrated that the gelation enhancement by CO_2 addition does not greatly influence the aerogel properties, the aerogel surface area, pore size and light absorbance have the same values as the corresponding samples prepared without CO_2 addition. Thus, CO_2 can be regarded as an alternative catalyst for the gelation process. The process suggested in the present work allows for relatively short gelation times. Also, the extraction time is reduced to some extent, because the gel phase contains around 30% CO_2 at the beginning of extraction. Summarizing all these facts one may conclude that the method proposed in the present work may be successfully employed in the production of aerogels, especially in the case of low density aerogels.

Silica aerogels produced by this method were tested as potential carrier materials for pharmaceuticals. An alternative method of loading of the aerogel with the corresponding compound was studied. This method is based on the adsorption of the organic compound onto the aerogel from their solutions in supercritical CO_2.

It was demonstrated that, in the case of the 3 investigated drugs this process allows for a high loading of the aerogel. The chemical structure of the investigated drugs is not influenced by the loading method. The aerogel-drug formulations produced by this method are therefore suggested as potential drug delivery systems in pharmaceutical applications.

The release profiles of such formulations were measured using a standard method, recommended in German Pharmacopoeia. It was found that the release of 2 drugs (*ketoprofen* and *griseofulvin)* from the aerogel-drug formulation is faster than that of the crystalline drugs and commonly used formulations. This effect can be explained by both the increase in the specific surface area of the drug adsorbed on the aerogel and its non-crystalline structure in this formulation. In the case of the other investigated drug (*miconazol*), no release acceleration was observed using the aerogel-drug formulation. This indicates that the release characteristics of aerogel-drug formulations must be tested for every individual drug.

As a result of these facts, one may conclude that the aerogel-drug formulations may be effectively used as drug delivery systems for drugs whose immediate release is desirable. Such formulations are especially favoured for those pharmaceuticals that have a long dissolution time because the release of such compounds can be significantly improved by adsorption on silica aerogels. This

It can be seen, that in the case of *miconazol* the release from the aerogel-*miconazol* formulation is even slower, as that of crystalline *miconazol*. It is difficult to explain this result. The fact, that the release of crystalline *miconazol* itself is pretty fast (80 % of *miconazol* are released just in 20 min), makes obvious, that the proposed procedure is not efficient in the case of *miconazol*. The crystalline form of this drug commonly used shows the release, which is fast enough for the therapeutic purposes. It shows, that the procedure, proposed in this work, should be tested for every drug independently in order to prove its efficiency in each individual case. In our case the release of two drugs (*ketoprofen* and *griseofulvin*) of three drugs investigated could be improved by using aerogel-drug formulation.

5. CONCLUSIONS

The present work was mainly concerned with the synthesis of silica aerogels and the conditions required to enhance the gelation process. The common two-step procedure was modified by the addition of supercritical carbon dioxide (CO_2) during the second step. CO_2 is commonly used in aerogel production for the solvent extraction, but its influence on the gelation process itself has not yet been reported.

It has been found that the addition of supercritical CO_2 during the sol-gel process enhances gel formation. The enhancement factor depends on the aerogel target density and varies between 5 and 100. The CO_2 concentration in the liquid phase generally reaches 30 wt% at the gel point.

It was evident that the amount of CO_2 required to realize such a rapid gelation process strongly depends on the experimental conditions. The reaction enhancement takes place only if CO_2 is combined with both catalysts used in the common two-step process; if one or both catalysts are not used, CO_2 addition leads to the rapid precipitation of colloidal particles.

Studies showed that the fast gel formation takes place preferably in polar aprotic solvents (acetonitrile, dimethylformamide), whereas CO_2 addition to the systems with polar protic solvents (methanol, ethanol) promotes particle formation.

It was demonstrated that CO_2 can be used successfully only in combination with other catalysts, used during the first and second steps. This allows one to conclude that CO_2 acts not (or not only) as a catalyst itself, but gives rise to some form of optimal conditions for the condensation reaction, being accelerated by normal base catalysts (specifically NH_4OH). Furthermore, the dependence of this effect on the solvent nature suggests that some interaction between CO_2 and the solvent might be taking place i.e. CO_2 may be participating in the solvation process. At the beginning of the reaction, acetonitrile solvates the

method can be used as an alternative to the micronization procedure, used for these purposes at present time.

REFERENCES

[1] N. Hüsing, Dissertation, Würzburg, 1997.
[2] F. Schwertfeger, D.Frank, M. Schmidt, J.Non-Cryst.Sloids, 225, 1989,18.
[3] D.R.Rolison, B.Dunn, J.Mat.Chem. 11, 2001, 963.
[4] F. Schwertfeger, A. Zimmermann, H. Krempel, US Patent 6,280,744, issued 28.08.2001.
[5] S.S Kistler, Nature 127, 1931, 741.
[6] Aerogels, ed. J. Fricke, Springer, Berlin, 1986.
[7] S.S Kistler, US Patent 2,093,454; US Patent 2,188,007; US Patent 2,249,767.
[8] J.B. Peri, J.Phys.Chem. 70, 1966, 2937.
[9] G. Nicolaon, Ph.D thesis, University of Lyon, 1968.
[10] G. Nicolaon, S. Teichner, Bull.Soc.Chim.Fr., 8, 1968, 3107; ibid. 9, 1968, 3555; ibid. 1968, 11, 4343.
[10] US Patent 3,672,833.
[11] S. Henning, L. Svenson, Phys. Scr. 23, 1981, 697; US Patent 4,327,065.
[12] C.J. Brinker, K.D. Keefer, D.W. Schaefer, C.S. Achley, J.Non-Cryst.Solids 48, 1982, 47.
[13] T.M. Tillotson, L.W. Hrubesh, J.Non-Cryst.Solids 145, 1992, 44.
[14] T.M. Tillotson, J.F. Poco, L.W. Hrubesh, I.M. Thomas US Patent 5,409,683, Issued 15.04.1995.
[15] C.J. Brinker, G.W. Sherer, "The physics and chemistry of sol-gel processing", Acad. Press, New York, 1990.
[16] M. J.van Bommel, A.B. de Haan, J.Non-Cryst.Solids 186, 1995, 78.
[17] R. Deshpande, D.W. Hua, D.M. Smith, C.J. Brinker J. Non-Cryst. Solids 144, 1992, 32.
[18] F. Schwertfeger, D. Frank, M. Schmidt , J.Non-Cryst.Solids 225, 1989, 18.
[19] F. Schwertfeger, A. Zimmermann, H. Krempel, WO 96/25850, issued 1996.
[20] D.A. Loy, E.M. Russick, S.A. Yamanaka, B.M. Baugher, Chem. Nature. 9, 1997, 2264.
[21] M. Moner-Girona, A. Roig, E. Molins, J. Llibre, Materials of ISA6, Albuquerque, N.M., USA October 8-11, 2000.
[22] Kun-Hong Lee, Sun-Youg Kim, Ki-Pung Yoo, J.Non-Cryst.Solids, 186, 1995, 307.
[23] NIST Chemistry WebBook, NIST Standard Reference Database Number 69, Eds. P.J. Linstrom and W.G. Mallard, July 2001, National Institute of Standards and Technology, Gaithersburg MD, 20899 (http://webbook.nist.gov).
[24] P.G. Bendale, R.M. Enick, Fluid Phase Equilibria 94, 1994, 227.
[25] A. Kordikowski, A.P. Schenk, R.M. Van Nielen, C.J. Peters, J.Supercritical Fluids 8, 1995, 205.
[26] S. Yoda, S. Ohshima, J.Non-Cryst.Solids 248, 1999, 224.
[27] Hüsing, Dissertation , Würzburg 1997.
[28] G. Orcel, J. Phalippou, L.L. Hench, J Non-Cryst.Solids 86, 1986, 114-130.
[29] C. Chiehming, C.Kou-Lung, D. Chang-Yih, J. Supercritical Fluids 12, 1998, 223.
[30] I. Artaki, T. Zeda J. Jonas, J.Non-Cryst.Solids 81, 1986, 381.
[31] W.L. Huang, K.M. Liang, S.R.Gu, J. of Non-Cryst. Solids 1258, 1999, 234.
[32] R.A. Ferrieri, I. Garcia, J.S. Fowler, A.P. Wolf, Nuc.Drug&Med., 26, 1999, 443.
[33] Z. Novak, Z. Knez, J. Non-Cryst. Solids 221, 1997, 163.

[34] A.Orlovic, S.petrovic, D.Radivojevic, D.Skala, Chem. Ind. 55, 2001, 244.
[35] H. Stricker, Physikalische Pharmazie, 3.rd edition, Wissenschaftliche Verlagsgesellschaft mbH Stuttgart, 1998.
[36] C. Magnan, C. Bazan, F. Charbit, J. Joachim, G. Charbit, in High Pressure Chemical Engineering, ed. Ph. Rudolph, Ch. Trepp, Elsevier, 1996.
[37] K.D. Bartle, A.A. Clifford, S.A. Jafar, and G.F. Shilstone, J. Phys. Chem. 20, 1991, 713.
[38] A. Vetere, Fluid Phase Equilibria 148, 1998, 83.
[39] V. Vandana, A.S. Teja, Fluid Phase Equilibria 135, 1997, 83.
[40] C. Domingo, J. Garcia-Carmona, M.A. Fanovich, J. Llibre, R. Rodriguez-Clemente, J. Supercrit. Fluids 21, 2001, 147.
[41] McHugh, M.E. Paulaitis, J.Chem.Eng.Data 25, 1980, 326.
[42] S.J. Macnaughton, I. Kikic, N.R. Foster, P. Alessi, A. Cortesi, I. Colombo, J. Chem. Eng. Data 41 1996 1083.
[43] Deutsches Arzneibuch, Wiss. Verlag Stuttgart, 1997.
[44] M.V. Shah, M.D. de Gennaro, H. Suryakasuma, J. Microencapsul. 4, 1987, 223.
[45] Food and Drug Administration, HHS, § 436.317, 21 CFR Ch.1 1998.

Supercritical Fluids as Solvents and Reaction Media
G. Brunner (editor)

Chapter 3.2.

Investigation and Modelling of the Gas-Antisolvent Process

A. Weber[a], R. Kümmel[a] and T. Kraska[b]

[a]Fraunhofer Institute for Environmental, Safety and Energy Technology, Osterfelder Strasse 3, D-46047 Oberhausen, Germany

[b]Department of Physical Chemistry, University Cologne, Luxemburger Str. 116, D-50939 Köln, Germany

1 INTRODUCTION

The gas-antisolvent precipitation process (GAS) has been suggested by Gallagher and Krukonis [1] more than a decade ago. The basic idea resembles a salting-out crysallization where the phase separation is initiated by adding an antisolvent to a binary solution causing a decrease of the solubility of the solute. In case of the gas-antisolvent process a compressed gas such as supercritical carbon dioxide is utilised as antisolvent. The process has gained rising interest, mainly from the pharmaceutical and fine chemical industries, since it allows a practically good control of shape and properties of the materials to be precipitated. During the past decade, many experimental results have been published showing promising opportunities to yield solid products according to various current demands [2-4]. Possible applications include the preparation of drug-delivery systems (e.g. for inhalation purposes), controlled-release materials, high-performance ceramics, nanoparticles, just to give a few examples. The number of examples published in the literature is still limited and so is the principal understanding of the process. A few approaches to model different aspects have been undertaken. Aaltonen et al. [5] studied the influence of the initial droplet size on the particle size of the finally formed solid products. Werling and Debenedetti [6,7] calculated the mass transfer between a toluene droplet and a carbon dioxide phase at near-critical and supercritical conditions. Bristow and Shekunov [8] analysed a supercritical precipitation process based on turbulent mixing and straightforward assumptions on nucleation and growth.

A general molecular background of the antisolvent phase separation in fluids is discussed in terms of quasi-binary global phase diagrams elsewhere [9]. Here we are trying to focus on specific ternary model systems consisting of carbon dioxide as antisolvent (component 1), a primary solvent, e.g. an alcohol or ketone (component 2), and a low volatile solute (component 3). The particle

formation in the primary solution droplets as the result of antisolvent diffusion into the droplet is considered. The combined phenomena of mass transport and phase formation have been studied by a continuous simulation model based on the conservation of mass and energy.

2 THE GAS-ANTISOLVENT PROCESS

2.1 Technical realization

There are, in general, two different ways to bring the primary solution in contact with the antisolvent. The first method is to fill an autoclave with the saturated primary solution and to pressurise the solution with carbon dioxide. As depicted in Fig. 1, this formation route can be easily performed and offers a number of benefits, for example, the recycling of the solvent and the subsequent drying of the solid products after crystallization to very low residual solvent levels. Finally, while operating in a closed system and generating practically no by-products, the gas-antisolvent process can be considered an environmentally benign technology.

On the other hand, this process variant is limited by several constraints. As a batch process, it is not really economically attractive. In this context it would only be useful for the re-crystallization of relatively small amounts of high-quality and expensive substances. However, it can be useful for specific lab-scale applications. Furthermore, the interface between the primary solution and the antisolvent is relatively small and hence the time the antisolvent needs to penetrate the solution is large.

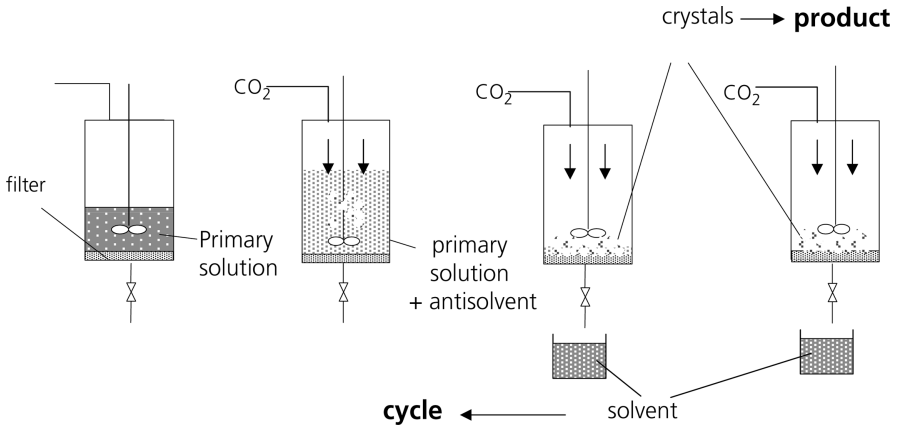

Fig. 1. Batch gas-anti-solvent crystallization.

This drawback could be improved by stirring, however, in such case one has to make sure that the stirrer does not influence the crystallization process in a negative way, for example, by heterogeneous nucleation or mechanical particle breaking. The fact that the diffusion of the antisolvent into the primary solution is slow leads to a relatively low degree of supersaturation which moves only slowly through the primary solution. A low supersaturation level causes a low nucleation rate yielding only few nuclei which have access to a large excess of dissolved solute molecules for their growth. As a result, relatively large particles with heterogeneous particle size distribution must be expected.

A more effective way of bringing the primary solution in contact with the antisolvent is to spray the primary solution through a nozzle into an atmosphere of highly compressed antisolvent. While the apparatus for such a process is somewhat similar to that of the rapid expansion from supercritical solution (RESS) process [10], the mode of operation is quite different. In RESS a high supersaturation is achieved by an expansion of the compressed supercritical fluid used as solvent through a nozzle, while here a liquid solution is injected into a vessel containing a supercritical fluid at high pressures. For the investigated variants of this technique several different acronyms have been established in recent years. The most prominent are PCA (Precipitation by Compressed Antisolvents) [11], SAS (Supercritical Antisolvent crystallization) [12], ASES (Aerosol Solvent Extraction System) [4], SEDS (Solution Enhanced dispersion by Supercritical Fluid) [13] or continuous GAS [14-15]. In the following sections we would like to go on referring to GAS for any of the discussed processes, since it is the most general expression.

A possible set-up is depicted in Fig. 2: in contrast to the batch process, the solution can be fed and withdrawn continuously until the crystallizer A1 is filled up with the solid product. The primary solvent is separated in S1 and can be recycled in the process. The antisolvent is recompressed after separation and led into the crystallizer again. In the GAS process the relatively incompressible

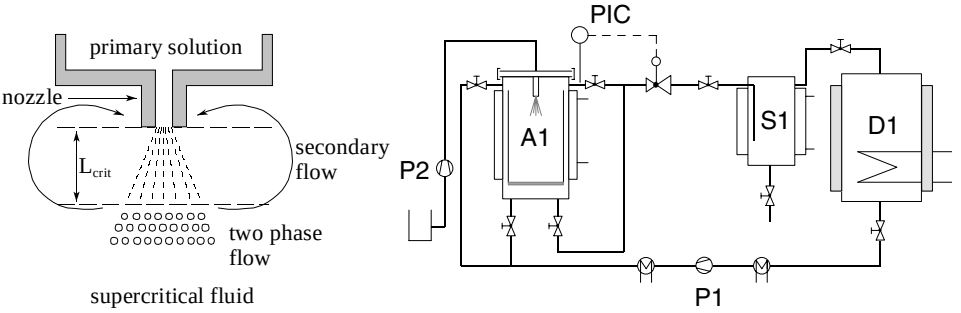

Fig. 2. Crystallization in a dispersed phase within the gas-antisolvent-process. A1: crystallizer, A2: separator, D: nozzle system, V: CO_2 storage tank, P1, P2: high pressure pumps.

primary solution is not much affected by fluid-mechanical effects in the nozzle. The nozzle is primarily aimed at dissipating the primary solution into many tiny droplets with a large surface/bulk ratio. In this case the diffusion of the antisolvent into the primary solution is much faster leading to higher supersaturations and higher nucleation rates which result in smaller particles with narrower size distribution.

2.2. A single-droplet model of the GAS process

The ternary system under study can be depicted as a dispersed liquid phase surrounded by a continuous antisolvent phase. The smallest units of the system are single droplets of the dispersed phase in which the crystallization takes place (Fig. 3). Factors influencing the crystallization are mainly the phase equilibria between solvent and antisolvent, the solid solubility at the actual antisolvent concentration, and the nucleation and growth rates of the particles.

The model used in this work consists of different parts governing diffusion processes, changes of the liquid phase volume and solute concentration, supersaturation and crystal growth.

2.2.1. Phase equilibria

The driving forces for the dissolution of the antisolvent in the droplet followed by the formation of the solid phase are gradients of the chemical potentials in the system at given external conditions. In order to combine these gradients, for example, with the degree of supersaturation, the phase equilibria have to be known. In case of the RESS process [10] the solubility of the solute in the pure supercritical fluid is required. Such solubility data can be modelled based on an accurate equation of state for the pure supercritical solvent [16]. In case of GAS the phase equilibria of the solvent/antisolvent system have to be taken into account.

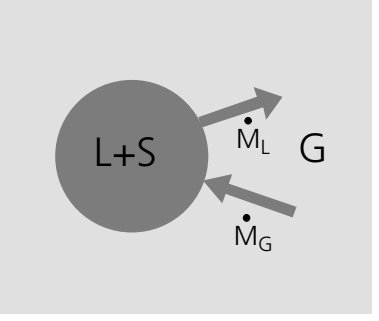

Fig. 3. Single droplet as the smallest unit of the GAS-process. L: primary solvent, S: solute, G: antisolvent.

Such phase equilibria are usually modelled by equations of state. Most popular are the cubic equations of state mainly due to their mathematical simplicity and wide-spread use. Alternatively molecular-based equation of state models are employed. The advantages, disadvantages and overlaps of these two approaches are discussed elsewhere in this book [9]. It could be shown that the influence of the solid component on the solvent/antisolvent gas-liquid phase equilibrium can be neglected since its concentration is two orders of magnitude lower compared with those of the solvent components. Measurements on different solids (ascorbic acid, paracetamol, salicylic acid) gave evidence that the difference in the liquid densities of mixtures with and without solid compounds is small. The nature of different solids is considered by measured liquid-solid equilibrium data.

2.2.2. Mass transfer

The mass transfer of the antisolvent into the droplet can be described by Fick's second law:

$$\frac{\partial c_1}{\partial t} = -\nabla \cdot \dot{n}_1 \tag{1}$$

The change in the antisolvent concentration c_1 with time equals the spatial gradient in the molar flux $\dot{n}_1$. It can be determined by different mass transfer models for multi-component systems using either effective diffusivities or Stefan-Maxwell correlations. In these investigations, $\dot{n}_1$ was calculated using fixed, effective diffusion coefficients:

$$\dot{n}_i = -c_{tot} \cdot D_{i,eff} \cdot \nabla x_i + x_i \cdot \sum_i n_i \tag{2}$$

At the beginning, there are only solute and solvent present in the droplet. It is assumed that equilibrium between the gaseous and the liquid phase is reached immediately at the phase boundary (first order boundary condition) because of the huge excess of the surrounding anti-solvent phase.

Due to non-equivalent diffusion into and out of the droplet the model has to take care of the subsidiary change of the droplet volume. This can be achieved balancing the median concentration $\bar{c}_{tot}$ of all components in the droplet, with the molar fluxes $\dot{n}_i$ entering and leaving the droplet via the phase boundary. In Eq. (3) and (4) R is the actual droplet radius, c_i denotes the concentration of the component i at the radial co-ordinate r.

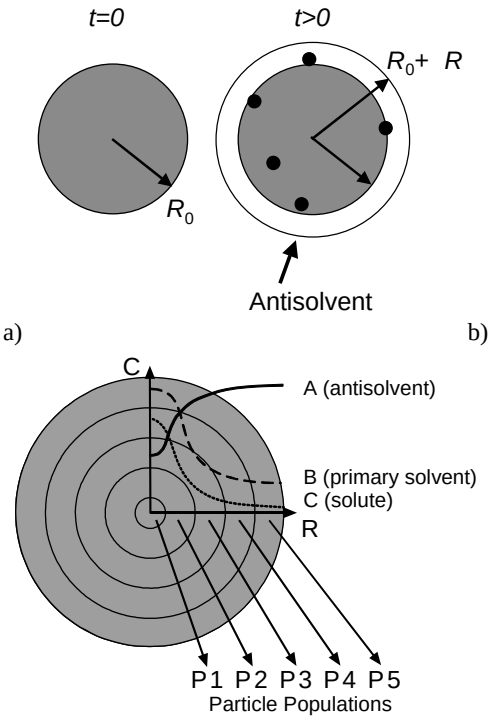

Fig. 4. Effects during crysallization in a droplet. a) Droplet before (*t=0*) and after (*t>0*) contact with the antisolvent. Here R_0 is the initial radius of the droplet and ΔR the increase of the balance space after a certain time. b) Sketch of the shell model with five shells. The diagram shows schematically the concentration of the three components from the core shell to the outer shell of the balance space.The concentrations and the population density of the crystals is derived for all shells at specified residence times.

$$\bar{c}_{tot} \cdot \frac{\partial V}{\partial t} + V \cdot \frac{\partial \bar{c}_{tot}}{\partial t} = -4\pi R^2 \cdot \sum_i \dot{n}_i \tag{3}$$

$$\bar{c}_{tot} = \frac{1}{\frac{4}{3}\pi R^3} \cdot \int_{r=0}^{r=R} 4\pi r^2 \sum_i c_i dr \tag{4}$$

The set of equations can be solved considering the following boundary conditions: By solving the set of coupled differential equations, considering the boundary conditions (3) and (4), the time-dependent concentration of all

components can be derived for any co-ordinate of the droplet. This information is used to calculate the local crystallization kinetics.

$$c_i\big|_{(t=0)} = c_{i,0} \qquad \text{with } i = 1, 2, 3 \tag{5}$$

$$\left.\frac{\partial c_i}{\partial r}\right|_{r=0} = 0 \qquad \text{with } i = 1, 2, 3. \tag{6}$$

2.1.1 Nucleation and particle growth

The formation of a particle in a droplet includes several consecutive steps. The first step is the nucleation yielding particles of the critical size sufficient for subsequent growth. Once clusters of critical size are formed, the particle growth can be governed by different processes. These processes are the accumulation of solute molecules at the surface of a particle, the agglomeration or breaking of particles or the structural reorganisation of particles. The relative significance of these different processes for the actual growth depends on experimental conditions like temperature, pressure and the degree of supersaturation. The degree of supersaturation as the driving force for the crystallization process can be expressed mathematically in different ways. Here we use the difference between actual *(c)* and equilibrium *(c*)* (saturation) concentrations:

$$S = c - c^* \tag{7}$$

For $S > 0$ the system is not stable and concentration fluctuations can lead to the nucleation of the solute.

The nucleation rate J is one important property for modelling the particle growth. Widely used is the classical nucleation theory by Becker and Döring [17] and Volmer and Weber [18] which treats the nucleation as an activated process. The activation energy of nucleation barrier of this process is the maximum difference of the Gibbs free energy of N single molecules and a cluster with N molecules. With the critical work of cluster formation ΔW^* one can calculate the nucleation rate for a pure substance:

$$J = K \cdot exp\left(-\frac{\Delta W^*}{k_B T}\right) \tag{8}$$

Here k_B is the Boltzmann constant and K a kinetic pre-factor. In the literature of mass crystallization an empirical approach is usually employed

which is given by a power law, which is quite similar to Eq. (8) with respect to its mathematical structure.

$$B = K_B \cdot S^n \tag{9}$$

Here B is the nucleation rate of a given substance and K_B and n are adjustable parameters. The particle growth rate G as the result of the accumulation of solute molecules at the surface of a cluster is usually modelled by a power equation similar to Eq. (9).

$$G = K_G \cdot S^g \tag{10}$$

According to the Burton-Cabrera-Frank (BCF) surface diffusion theory [19] the controlling step of the growth rate is the diffusion on the surface of the crystal. Assuming a screw-dislocation the theory predicts a power law with an exponent $g=2$ for the crystal growth rate which is independent of the crystal size. Based on the thermodynamic driving force given as the difference in the chemical potential $\Delta\mu^*$, the growth rate G can be described as:

$$G = k_g \left(\frac{\Delta\mu^*}{RT} \right)^2 = K_g \left[ln\left(\frac{a}{a^*} \right) \right]^2 \tag{11}$$

Here, k_g is the linear growth rate coefficient, a and a^* are the actual and the equilibrium activity of the solute respectively. In Eq. (11) R exceptionally denotes the gas constant, instead of the droplet radius. For systems without available activity coefficient data the equation reduces to Eq. (12) which is somewhat similar to Eq. (10), however using c/c^* as an alternative expression for the supersaturation.

$$G = k_g \cdot ln\left(\frac{c}{c^*} \right)^2 \tag{12}$$

Although the simple expression has only one parameter, it adequately fits measured data for many different substances and solvents published in literature [20-21]. The kinetic parameters used in this work were taken from [22]. The initially unknown nucleation rate constants were used to optimise the calculated particle size distribution.

2.2.4. Population balance

The solid phase under consideration consists of a population of individual particles. Therefore the balance equation is called population balance. For a system of an isolated droplet in a continuous gas phase the expression for the population balance can be as simple as

$$\frac{\partial N}{\partial t} + \frac{\partial (G N)}{\partial L} + D_L - B_L + N\frac{dV}{Vdt} = 0 \tag{13}$$

The number density N is the number of particles per unit volume V within the crystal size interval dL. Within the system, N is influenced by the nucleation rate B and the growth rate G of the crystals. The external co-ordinates can be substituted by the volume change dV with time. The population balance is also influenced by attrition and breakage of particles belonging to individual crystal classes. For this purpose, different kinds of birth and death terms (B_L, D_L) are to be included. In a system which is not much affected by considerable mechanical forces to the crystals, the terms for birth and death can be neglected. The birth rate due to nucleation only is taken care of by the boundary condition Eq. (14b).

$$N_{t=0} = 0 \quad , \quad N_{L=\infty} = 0 \tag{14a}$$

$$N_{L=L_0} = \frac{B_0}{G} \tag{14b}$$

The fluid-phase concentration of the solute also decreases with nucleation and growth of the crystals. In Eq. (15) ρ is the density of the pure solid phase; the particle shape is assumed to be spherical.

$$\frac{\partial c}{\partial t} = -\frac{\pi}{6}\rho B L_0^3 - G \int_{L=L_0}^{\infty} \pi \rho \, NL^2 dL \tag{15}$$

Based on the considerations for mass transfer, nucleation and crystal growth predictive calculations can be carried out. In order to model all the involved physical phenomena (diffusion, crystallization, mass balance etc.), the derived set of expressions containing a coupled system of parabolic and hyperbolic partial differential equations have to be solved simultaneously. Numerical solution routines were described previously [23-24]. The resulting information are the time resolved concentration profiles, change of the droplet size and crystal formation at predefined co-ordinates.

3. RESULTS

3.1. Determination of solid solubilities

One crucial prerequisite for modelling the solid formation is the availability of data on the solubility of the solid phase in the mixed solvent-antisolvent system. For this purpose measurements were carried out in the apparatus depicted in Fig. 5.

An empty column for preparative HPLC with a volume of 58 ml was filled with a mixture of the investigated solid substance and closed with sinter metal frits at both of its ends. The column was maintained at constant temperature in an air-bath and flushed with a mixture of carbon dioxide and primary solvent provided by two HPLC pumps (Kipp Analytica; 400 bar, 0-10 ml/min) at constant pressure and composition. After equilibrating in the column the fluid

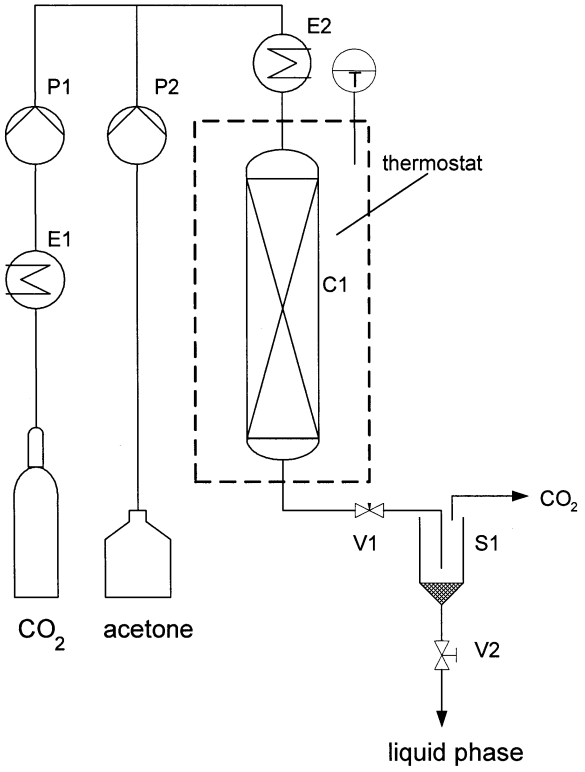

Fig. 5. Set-up for measuring solid solubilities. The two high pressure pumps P1 and P2 provide solvent (acetone) and antisolvent (CO_2) at constant pressure and constant flow rates to column C1, which is filled with a mixture of the solute (paracetamol) on glass beads and kept at constant temperature in an air bath. The equilibrated solute-solvent-antisolvent-stream is depressurised via V1 into the separator S1. The degassed solution from S1 is analysed for its solid content.

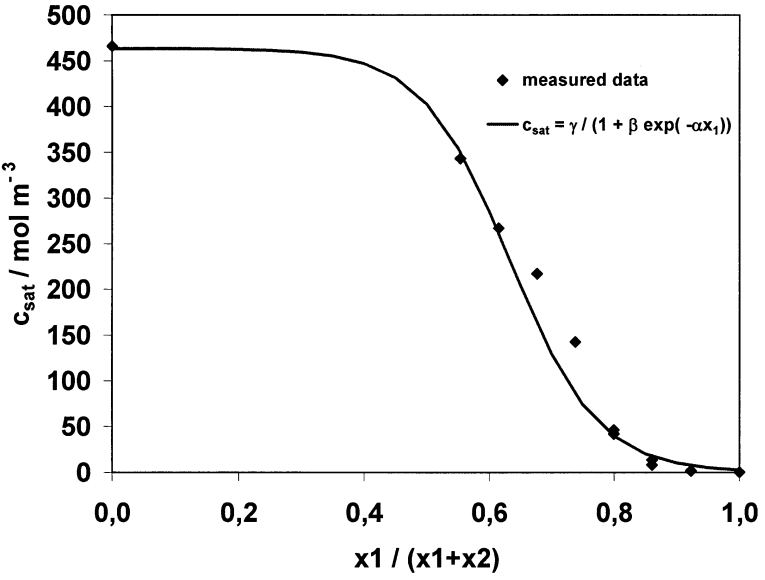

Fig. 6. Solubility of paracetamol in acetone at 40 °C dependent on the mole fraction of the antisolvent on a solute-free basis. The antisolvent mole fraction depends on the system pressure.

stream was released through a needle valve. The liquid was collected and analysed for its solid content by gravimetric or spectroscopic methods. Though it is also possible to fit the equilibrium data by equations of state [25-26], this leads to a mathematical expression, which is too unhandy to apply in the model. For a faster access the received data was simply fitted to an empirical function as shown in Fig. 6. In the following, experimental studies performed in the ternary system carbon dioxide (1) – acetone (2) – paracetamol (3) are discussed as an example for the systems of interest.

3.2. Model calculations

For the model calculations, a set of input parameters given in Table 1 was used. The initial radius of the droplet was assumed to be 50 μm which is about twice the size as predicted by jet-breakup models [5, 27] to take care of probable coagulation effects. Up to 100 concentric spherical shells were defined to illustrate the radial concentration profiles. The demonstrated calculations were carried out for a residence time of two seconds, in which the crystal size practically reached its ultimate value.

The simulation of typical process conditions (8.0 MPa, 40 °C) shows that the antisolvent rapidly dissolves in the droplet within fractions of a second (Fig. 7). The resulting equilibrium concentration rapidly reaches a very low

value and remains practically constant over the droplet radius after 0.1 seconds (Fig. 8a). This leads to a high supersaturation of the solution and immediate nucleation and growth of crystals. For 7.0 MPa this state is reached after 0.5 seconds only (Fig. 8b). The subsequent decay of the solute concentration near the core of the droplet is slower than near its boundary. It is also remarkable that a successful crystallization is more probable near the core than near the boundary of the droplet (Fig. 9). Near the core the particles reach a size of up to 5 μm in this calculations (Fig. 9a), further outside in the 50th of 100 shells the largest particles are about 0.15 μm (Fig. 9b), and in the 70th of 100 shells the particle size is about 0.08 μm (Fig. 9c).

This can be caused by the fact that the particle growth and the nucleation rate are balanced in the deeper shells while in the outer shells the solute is depleted rapidly just by nucleation leaving no material for subsequent growth of the nuclei. Regarding the mole fraction of the solute over the droplet radius in Figure 7c, it shows that the solute concentration runs down much faster in the outer shells of the droplet than in the core. In the 50th shell equilibrium conditions are reached after 0.2 seconds, in the 70th shell just after 0.01 seconds. This kinetically limits the amount and size of the crystals in the outer shells.

At lower pressures the maximum attainable supersaturation is reduced. This leads to a slight increase of the particle size near the core of the droplet while the probability of building crystals in the outer shells is vastly reduced (Fig. 10). In the case of 7.5 MPa, 40°C, the population balance near the core (5th shell) does not differ significantly from the result found for 8.0 MPa. For 7.0 MPa the effect is visible more clearly in the population balance near the core. For the outer shells the differences in the population balance is already visible for the pressure change from 8 MPa to 7.5 MPa. The development of the equilibrium solute solubility is markedly slower (Fig. 8b).

Table 1
Parameters used in the calculations

parameter	value	units
k_b	$1.0 \cdot 10^7$	$mol^{-n}m^{3n-3}s^{-1}$
n_b	3.0	
k_g	$3.0\ 10^{-8}$	$mol^{-g}m^{3g+1}s^{-1}$
n_g	1.0	
D_{AB}	$1.7\ 10^{-8}$	m^2s^{-1}
D_{AC}	$2.0\ 10^{-8}$	m^2s^{-1}
D_{BC}	$2.5\ 10^{-9}$	m^2s^{-1}
R_0	50	10^{-6} m

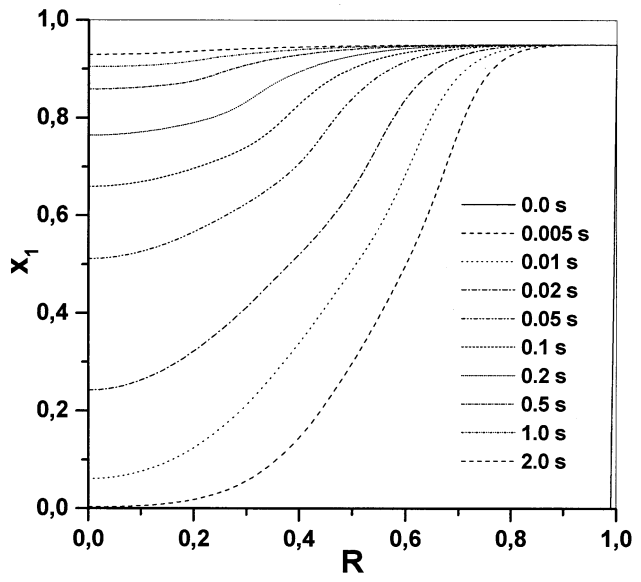
1,0
0,8
0,6
0,4
0,2
0,0
X_1
0,0
0,2
0,4
0,6
0,8
1,0
R
0.0 s
0.005 s
0.01 s
0.02 s
0.05 s
0.1 s
0.2 s
0.5 s
1.0 s
2.0 s

Fig. 7a

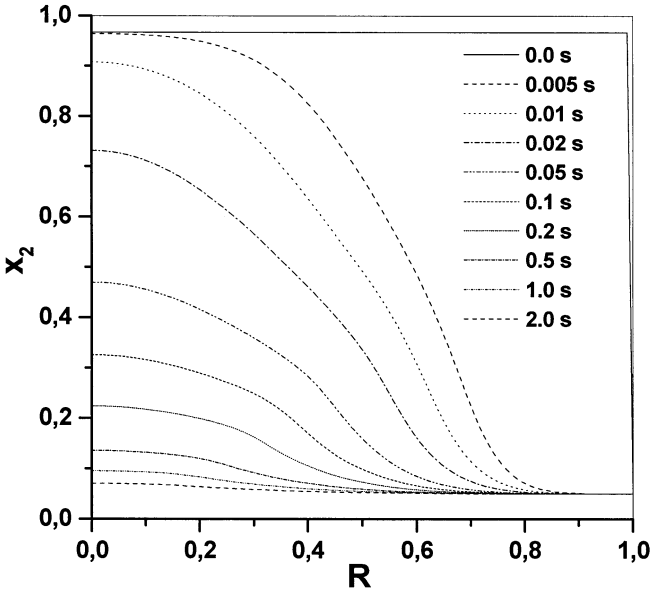
1,0
0,8
0,6
0,4
0,2
0,0
X_2
0,0
0,2
0,4
0,6
0,8
1,0
R
0.0 s
0.005 s
0.01 s
0.02 s
0.05 s
0.1 s
0.2 s
0.5 s
1.0 s
2.0 s

Fig. 7b

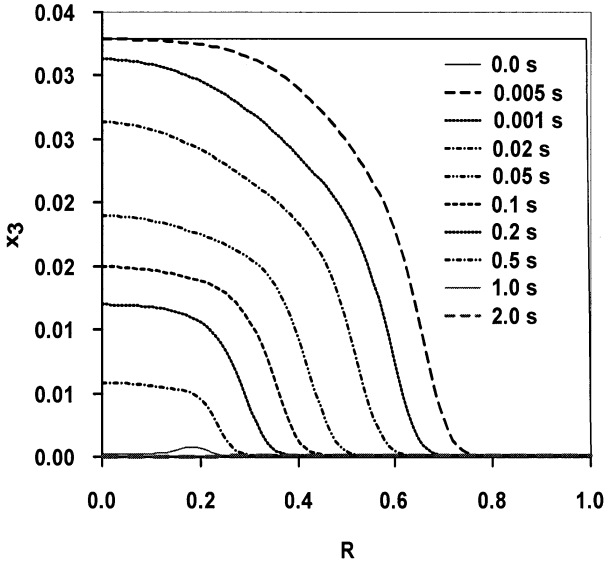

Fig. 7c

Fig. 7. Time resolved mole fraction of the antisolvent (1), the solvent (2) and the solute (3) in the droplet at 8.0 MPa and 40 °C. The concentration of the primary solvent (2) is counter currently depleted to the rising concentration of (1). *R* is the dimensionless radius of the droplet.

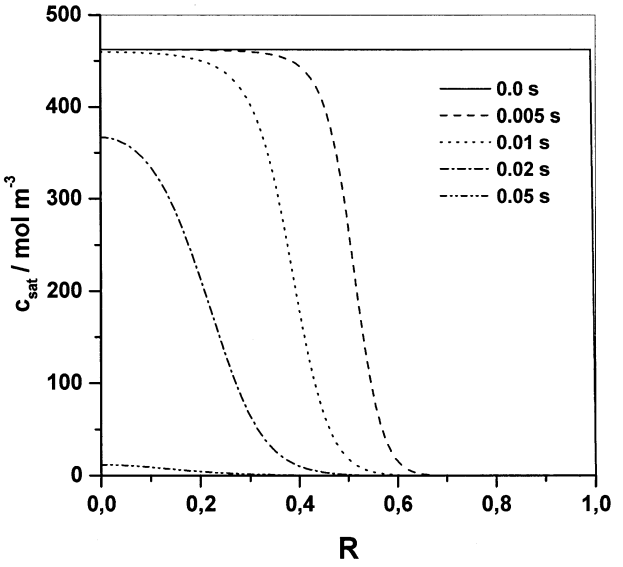

Fig. 8a

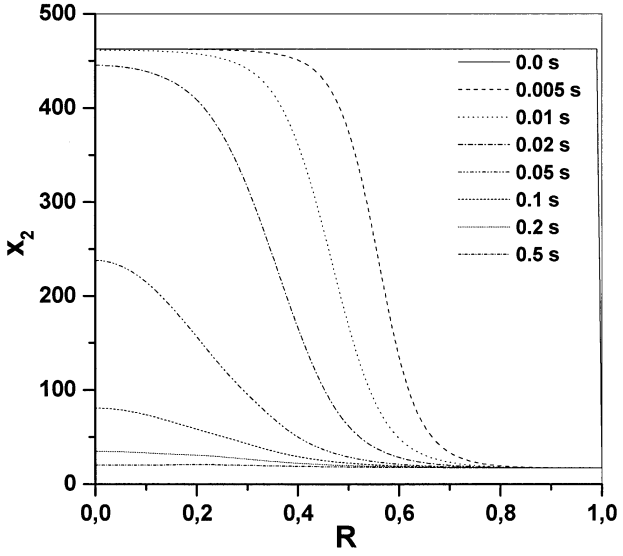

Fig. 8b

Fig. 8. Time resolved equilibrium concentration of the solute at 8.0 MPa (a) and 7.0 MPa (b). After 0.1 seconds for 8.0 MPa and 0.5 seconds for 7.0 MPa the solute equilibrium concentration almost vanishes yielding the highest possible supersaturation throughout the droplet.

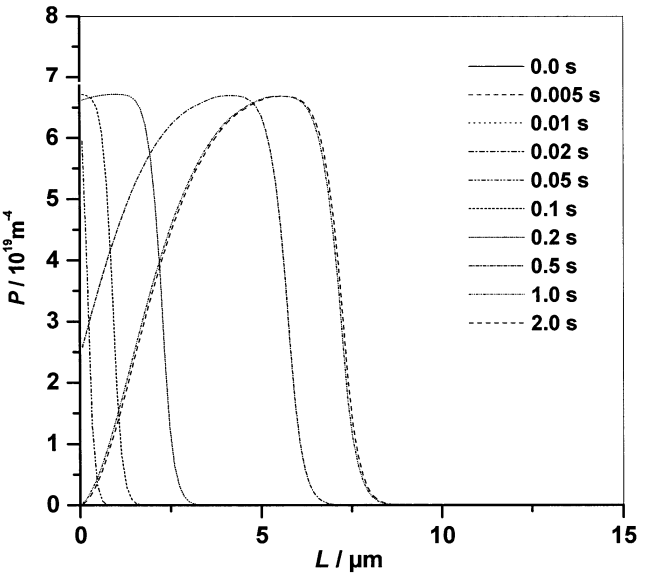

Fig. 9a

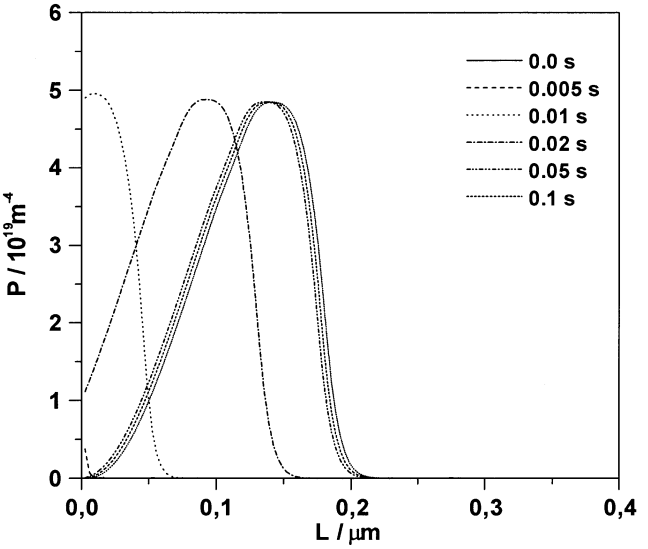

Fig. 9b

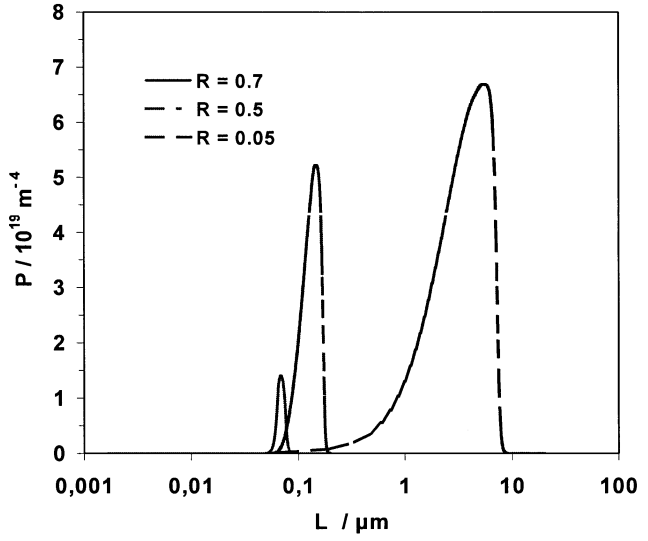

Fig. 9c

Fig. 9. Particle population near the core of the droplet (a) and in the 50th (b) shell of 100 shells at 8.0 MPa and 40 °C. Figure (c) shows the comparison of the distributions after 2 seconds at different positions in the droplet.

Also the maximum attainable supersaturation is smaller. The particle population in the 5th shell decreases and in the outer shells there is no population left. The development of the population balance with time shows that the crysallization is also slower. In addition, the results of calculations for 6.0 MPa showed just a weak population density near the core within a residence time of 2 seconds.

For comparison, Fig. 11 shows a measured particle size distribution for the system CO_2 – acetone – paracetamol at 8.0 MPa and 40 °C. In the particle size distribution two modes are visible at 20 µm and about 150 µm which relate to different stages of agglomeration. The mode with the smallest median particle size at 5.6 µm shows the crystal size of the product, which is near to the calculated value. Other crystallization experiments at pressures between 7.0 and 8.0 MPa yielded mean crystal diameters of 1.0 µm (8.0 MPa, 40 °C), 1.0 µm (7.5 MPa, 40 °C) and 13 µm (7.0 MPa, 40 °C).

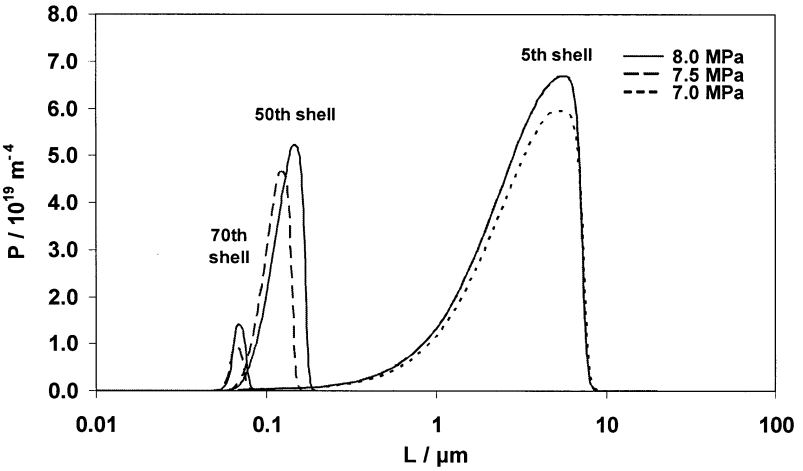

Fig. 10. Comparison of the distributions after 2 seconds at different positions in the droplet and different pressures.

4. CONCLUSIONS

Gas-antisolvent micronization procedures seem to offer new and prospective chances for a more detailed and successful particle design. Despite a variety of published results, a lot of work is still required to transfer laboratory work into an industrial scale. Mathematical models can be expected to simplify scale-up efforts and to define the most reliable parameters for large-scale processes.

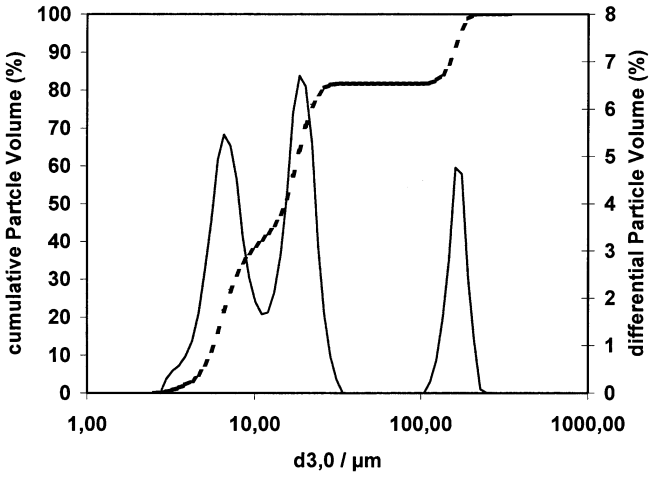

Fig. 11. Particle size distribution of paracetamol crysallized from acetone at 8.0 MPa and 40 °C. The mode at the smallest particle size refers the crystal size, both other modes represent different stages of agglomeration.

The present study was aimed at investigating the influence that process parameters take on the mechanisms of particle growth and the resulting particle size distributions. Based on a simplified single-droplet model, statistical population densities could be derived which describe the behaviour of an ensemble of droplets present in the real process and are in reasonable agreement with experimental results obtained from gas-antisolvent crystallization investigations. Since the model does not consider effects like particle agglomeration, the agreement cannot be expected to be very accurate.The gas-antisolvent process is characterised by high amounts of supersaturation and, therefore, by high concentrations of primary nuclei and narrow particle size distributions due to a rather low tendency to agglomeration steps. As could be shown by detailed model calculations based on phase equilibria, mass transport equations and population balances, the supersaturation required for the crystal formation process can be achieved within fractions of seconds and does not significantly differ across the radial coordinate of the solution droplet. In practice, the entire crystallization process can be finished within two seconds. As a result of these uniform operating conditions of particle formation, the driving forces observed at the outer surface of the droplet are quite similar to those that can be expected at the centre of the reacting system which is a most important presumption to the narrow particle size distribution obtained in

practically all experimental investigations. In addition, the results of the computations confirm previous findings that nucleation and particle growth and, therefore, the expected product properties are mostly determined by the antisolvent pressure and by the initial solute concentration. Temperature effects seem to exhibit a rather minor influence on the particle design, as could be shown by preliminary investigations [28].

First studies have shown that in quaternary systems, consisting of solvent, antisolvent and two solutes S_1 and S_2, fractional crystallization and solid-solid separations can be performed using the different course of solubility lines depending on pressure and temperature.

5. ACKNOWLEDGEMENTS

We would like to acknowledge the support of this work by the German Research Council (DFG) under grant Kr1598/11-1 and Ku873/4-1 and by the Fonds of German Chemical Industry (FCI).

REFERENCES

[1] P. M. Gallagher, M. P. Coffy, V. J. Krukonis, N. Klasutis, In: Supercritical Fluid Science and Technology Amer. Chem. Soc. Symp. Ser. 406 (1989) 334.
[2] B.Yu. Shekunov, P. York, J. Crystal Growth 211 (2000) 122.
[3] E. Reverchon, I. De Marco, G. Della Porta, J. Supercritical Fluids 23 (2002) 81.
[4] R. Thiering, F. Dehghani, N.R. Foster, J. Supercritical Fluids, 21 (2001) 159.
[5] M. Rantakylä, M. Jäntti, O. Aaltonen, M. Hurme, J. Supercritical Fluids 24 (2002) 251.
[6] J. O. Werling, P. G. Debenedetti, J. Supercritical Fluids, 18 (2000) 11.
[7] J. O. Werling, P. G. Debenedetti, J. Supercritical Fluids, 16 (1999) 167.
[8] S. Bristow, T. Shekunov, B.Yu. Shekunov, P. J. York, Supercritical Fluids 21 (2001) 257.
[9] L. V. Yelash, T. Kraska, this book.
[10] M. Türk, B. Helfgen, P. Hils, R. Lietzow, K. Schaber, this book.
[11] D. J. Dixon, K. P. Johnston, AIChE Journal 39 (1993) 127.
[12] E. Reverchon, G. Della Porta, A. Ditrolio, S. Pace, Ind. Eng. Chem. Res. 37 (3) (1998) 952.
[13] M. H. Hanna, P. York, D. Rudd, S. Beach, Pharm. Res. 12 (1995) S141.
[14] E.M. Berends, O. S. L.. Bruinsma, J. De Graauw, G. M. Van Rosmalen, AIChE J. 42 (1996) 431.
[15] F.E. Wubbolts, C. Kersch, G. M. van Rosmalen, In: Proccedings from 5th I.S.A.S.F, Nice, 1998, 249.
[16] T. Kraska, K. O. Leonhard, J. Jurtzik, D. Tuma, G. M. Schneider, this book.
[17] R. Becker, W. Döring, Ann. Phys. 24, (1935) 719.
[18] M. Volmer, A. Weber, Z. Phys. Chem. (Leipzig) 119 (1926) 277.
[18] A. Randolph, M. Larson, Theory of particulate processes, Academic Press (1988).
[20] R. Mohan, A. S. Myerson, Chem. Eng. Sci. 57 (2002) 4277.
[21] R. A. Granberg, D. G. Bloch, Å. C. Rasmuson, J. Crystal Growth 198/199 (1999) 1287.
[22] A. M. Zikic, R. I. Ristic, J. N. Sherwood, J. Crystal Growth 158 (1996) 560.

[23] C. Weiss, Modellierung und Simulation der Kristallisation in dispersen Systemen, Dissertation, Universität Dortmund 2001.
[24] C. Weiss, T. Hennig, R. Kümmel, J. Tschernjaew, Chem. Eng. Technol. 23 (2000) 485.
[25] J. C. de la Fuente Badilla, C. J. Peters, J. de Swaan Arons, J. Supercritical Fluids 17 (2000) 13.
[26] A. Shariati, C. J. Peters, J. Supercritical Fluids 23 (2002) 195.
[27] H.Wagner, Extraktion hochviskoser Medien in einer turbulenten Zweiphasenströmung unter erhöhten Drücken am Beispiel der Entölung von Sojalecithin, Fortschrittberichte VDI Reihe 3 Nr. 423, Düsseldorf, VDI-Verlag 1996.
[28] A. Weber, M. Beutin, J. Tschernjaew, R. Kümmel, In: Proc. 4th Int. Workshop on Crystal Growth of Organic Materials, Bremen, September 1997, 214.

Supercritical Fluids as Solvents and Reaction Media
G. Brunner (editor)

Chapter 3.3.

Formation of nanoscale drugs by Rapid Expansion of Supercritical Solutions (RESS): – Experimental and theoretical investigations –

M. Türk[a], B. Helfgen[b], P. Hils[a], R. Lietzow[a] and K. Schaber[a]

[a]Institut für Technische Thermodynamik und Kältetechnik, Universität Karlsruhe (TH), Engler-Bunte-Ring 21, D-76128 Karlsruhe (mail: tuerk@ttk.uka.de)

[b]Degussa AG, VT-P, Rodenbacher Chaussee 4, D-63457 Hanau-Wolfgang

1. INTRODUCTION

An increasing number of newly developed pharmaceutical substances are poorly soluble in both aqueous and organic media. Thus, the application of oral or injectable drugs is often limited by its insolubility, and the bioavailability of the drug is low compared to the initial dose and its toxicity threshold is close to the therapeutic dosage. The low bioavailability of such drugs can be improved by reducing the size of these particles [1]. In the pharmaceutical industry, several conventional techniques (e.g. milling and grinding, spray-drying, freeze-drying) have been utilized for particle size reduction. The disadvantages of using these techniques are thermal and chemical degradation of the product and broad particle size distributions [2, 3].

Until now, there are several methods for the formation of small low volatile organic substances. The primary techniques for particle formation involving supercritical fluids are: RESS (Rapid Expansion of Supercritical Solutions), PGSS (Particle Generation from Gas Saturated Solution), and GAS (Gas Anti-Solvent). Based on minor variations of the GAS-process, different techniques, including Aerosol Supercritical Extraction System (ASES), Precipitation with a Compressed Anti-solvent (PCA), Supercritical Anti-Solvent (SAS) and Solution Enhanced-Dispersion by Supercritical fluids (SEDS), are now in use. It has been shown in various publications that the RESS-process enables the micronization of thermally labile materials and the formation of particles of less than 500 nm in diameter [4-11]. The RESS-process utilizes the high solvating power of supercritical fluids. After loading the supercritical fluid with the solute, a very

rapid phase change from the supercritical to the gas-like state takes place during the expansion in the supersonic free jet. This leads to a very high supersaturation and subsequently to particle formation. Since the solvent is a dilute gas after expansion, the RESS-process offers a solvent free final product [12, 13].

First of all, the goal of our investigations was to explore the process conditions for the formation of nanoscale drugs by RESS. Secondly, based on these experiences, stable suspensions of poorly soluble drugs were produced by rapid expansion of a supercritical mixture through a capillary nozzle into aqueous solutions. In order to complete our experimental investigations and to improve process control, a comprehensive model of the RESS-process was developed. The model includes the expansion process inside the capillary nozzle, the supersonic free jet, the mach shock, and the expansion unit. The modelling of particle growth takes into account nucleation, condensation, and coagulation along the expansion device up to and including the expansion chamber [14, 15].

The paper is organized as follows: in section 2 the RESS-apparatus and typical results of our RESS experiments are presented. In section 3 the mathematical model is presented and some essential modelling results are discussed. In section 4 the feasibility to produce stable suspensions of nanoscale poorly soluble drugs is demonstrated. The main conclusions are summarized in section 5.

2. APPARATUS AND EXPERIMENTAL RESULTS

Fig. 1 shows schematically the apparatus used for the RESS-experiments. This apparatus enables experiments in the temperature range from 300 to 600 K and pressures up to 60 MPa [16, 18]. In all experiments, the gaseous CO_2 is cleaned, condensed, subcooled, and pressurized to the desired pressure with a diaphragm pump. To minimize the unsteadiness of the flow and to accelerate thermal equilibrium, pure CO_2 flows through the thermostated bypass section into the thermostated high-pressure vessel and through the heatable capillary nozzle into the expansion chamber. After equilibrium, the bypass section is closed and the supercritical CO_2 flows through an extraction column, which is packed with the solute. Then the saturated supercritical solution flows through a heated tube into a thermostated high-pressure vessel where the pre-expansion temperature and the pre-expansion pressure is measured. The supercritical solution is expanded through a heatable capillary nozzle with an inner diameter of 50 μm and a length of 50 μm always down to atmospheric conditions (300 K, 0.1 MPa). The precipitated particles are measured in the expansion chamber ($V = 22$ dm^3) online and in situ with the 3-Wavelength-Extinction Measurement technique (3-WEM). Samples for SEM-pictures (Scanning Electron Microscopy) can be taken at a distance of 300 mm to the nozzle exit. More details about the

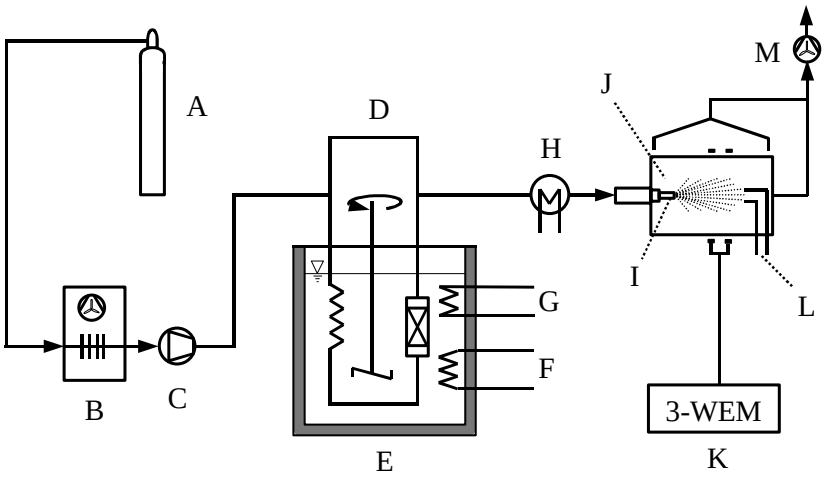

Fig. 1. **A**, solvent; **B**, cooling device; **C**, pump; **D**, bypass; **E**, extractor unit; **F**, cooling; **G**, heating; **H**, pre-heater; **I**, capillary nozzle; **J**, expansion chamber; **K**, 3-WEM; **L**, sample for SEM; **M**, vent.

apparatus, the experiments, and the measurement technique can be found elsewhere [16-18].

The results of the RESS experiments are summarized in Table 1. Fig. 2A shows the effect of pre-expansion conditions upon the particle size of naphthalene.

Table 1

Particle size of various solutes obtained from RESS-experiments. The nozzle temperature was ≈ 10 K above the respective pre-expansion temperature.

Solute	Pre-expansion conditions		Solvent	Particle size
naphthalene	353 – 373 K	13 – 20 MPa	CO_2	1.5 – 2.5 μm
benzoic acid	353 – 413 K	13 – 20 MPa	CHF_3	400 – 900 nm
benzoic acid	348 – 418 K	20 – 30 MPa	CO_2	208 – 461 nm
cholesterol	348 – 423 K	20 – 30 MPa	CO_2	192 – 253 nm
β-sitosterol	348 – 423 K	20 – 30 MPa	CO_2	166 – 219 nm
ibuprofen	308 – 318 K	10 – 20 MPa	CO_2	183 – 326 nm
griseofulvin	348 – 418 K	20 – 30 MPa	CHF_3	193 – 323 nm

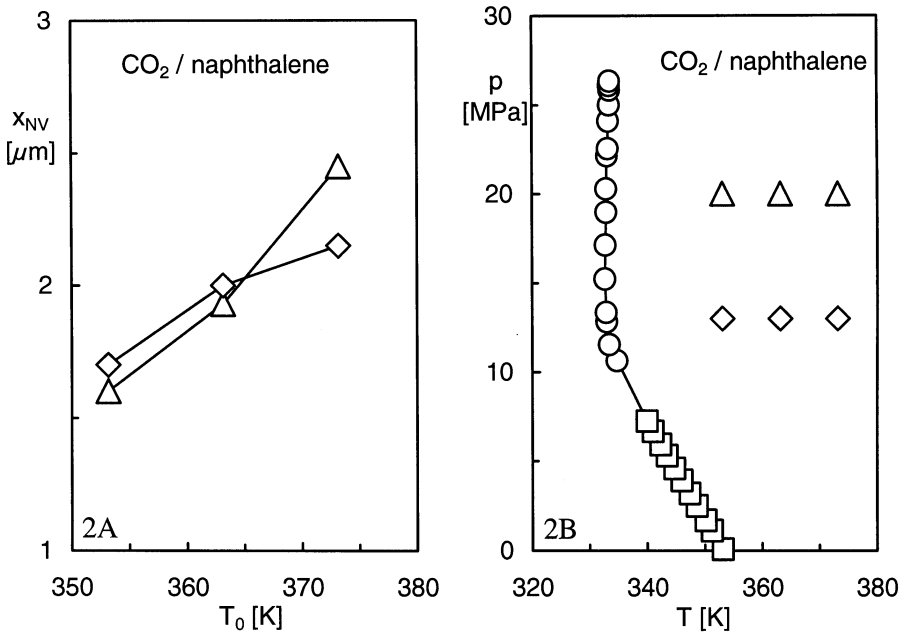

Fig. 2. Particle size of naphthalene obtained from different pre-expansion conditions. (Fig. 2A: ◇ 13 MPa, △ 20 MPa) Naphthalene melting points under CO_2 pressures. (Fig. 2B: ○ [19, 20], □ [21] ◇, △, pre-expansion conditions).

Within the range of process conditions investigated here, increasing the pre-expansion temperature from 353 K to 373 K increases the particle sizes from 1.5 μm to 2.5 μm. It is clarified in Fig. 2B that these relatively large naphthalene particles are mainly caused by the underlying phase behaviour of this system.

From Fig. 2B follows, that these experiments were performed at temperatures higher than the melting temperature of naphthalene. At these temperatures, a vapour-liquid equilibrium exists and the formation of liquid droplets can already occur prior to expansion. Thus large coalesced particles are formed which are principally formed from or via the liquid phase [7, 19, 20].

The particle size of benzoic acid varies from 200 to 900 nm depending on solvent and pre-expansion conditions. In general, the experiments performed with CO_2 lead to markedly smaller particles. For both naphthalene and benzoic acid holds, that increasing the pre-expansion pressure and lowering the pre-expansion temperature results in smaller particles [7, 9]. As shown in Fig. 3, the experiments performed with β-sitosterol, griseofulvin, and ibuprofen result in particle sizes in the range of 160 - 320 nm. In opposite to naphthalene and benzoic acid discussed above, no explicit dependency on the pre-expansion conditions on the particle size of the various drugs was observed.

The improvement of the bioavailability of the RESS-produced griseofulvin has been verified by dissolution experiments according to the Stricker model. The dissolution rate of griseofulvin produced by RESS is about two-fold higher than the common micronized material [8, 9].

It follows from modelling results (see section 3) that for the pre-expansion conditions as well as for all the systems investigated the residence time in the supersonic free jet is less than $\leq 10^{-7}$ sec. This leads to a calculated particle size of less than 10 nm and a high particle concentration ($\approx 10^{14}$ particles/m^3) at the end of the supersonic free jet [7, 14]. From these values it follows that particle growth is not finished in the supersonic free jet. Hence, the particles grow inside the expansion chamber to their final size and the post-expansion conditions are one key factor to control particle size. To confirm this, additional experiments with the mixture CO_2/benzoic acid under varying post-expansion conditions were carried out. Thereto pre-expansion conditions of 418 K and 20 MPa were chosen to vary the flow rate of air for purging the windows of the 3-WEM-measurement device in the expansion chamber. As discussed in more detail in literature, increasing the airflow rate from 0.75 to 2.4 m^3/h leads to a decrease in particle size from 528 to 280 nm [6]. Also, these experiments clarify the influence of two important process parameters on particle size. Both, a shorter residence time and hence less time available for particle growth as well as a higher dilution of the particles in the expansion chamber result in smaller particles. In addition, this explains the dependency of the particle size on the pre-expansion conditions discussed above.

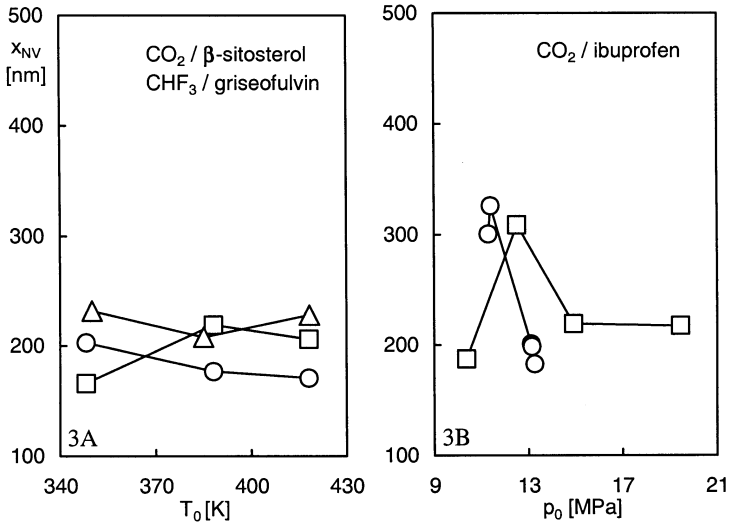

Fig. 3. Measured particle size of RESS-processed β-sitosterol, griseofulvin, and ibuprofen [6, 9]. Fig. 3A: β-sitosterol, □ 20 MPa, ○ 30 MPa, and griseofulvin △ 20 MPa. Fig. 3B: □ 308 K, ○ 318 K.

For the pre-expansion conditions investigated, the measured mass flow rate increase from 6.2 g CO_2/min at 418 K and 20 MPa to 13 g CO_2/min at 353 K and 30 MPa. In accordance with the experimental results, a higher mass flow rate means shorter residence time in the expansion chamber, which results in smaller particles [7, 9, 14, 15, 22]. The noticeable difference in the particle size of the pharmaceutical substances on the one hand and benzoic acid on the other hand results mainly from the difference in solubility of the solute in the supercritical solvent [7]. For example, at typical operating conditions in the extraction unit, (323 K and 20 MPa) the solubility of benzoic acid in CO_2 is about an order of magnitude higher than the solubility of β-sitosterol in CO_2 as well as of griseofulvin in CHF_3 [9]. From this it follows that, in accordance to the classical nucleation theory, the lower solubility leads to noticeable lower number concentrations and therefore smaller particles [7, 22]. As mentioned

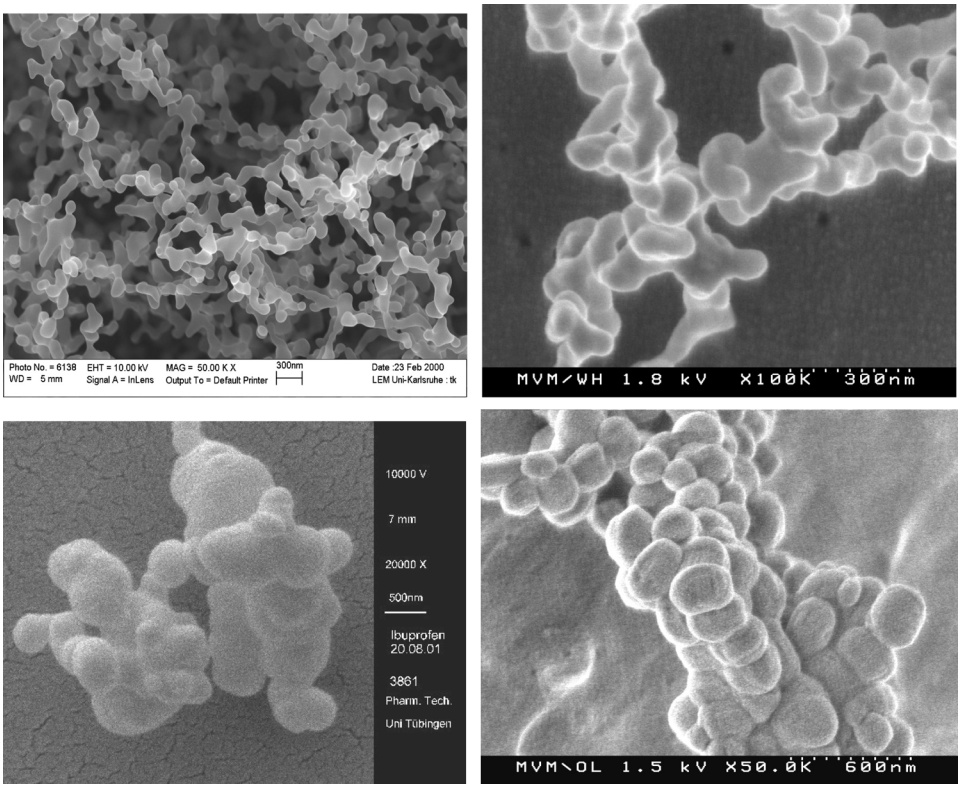

Fig. 4. Griseofulvin (above left), β-sitosterol (above right), ibuprofen (below left), and coenzyme Q_{10} (below right) particles produced by RESS.

above, SEM-probes can be taken out of the expansion chamber. Fig. 4 shows typical examples of particles obtained from RESS-experiments. Typically, these agglomerated particles show a spongy structure with a high surface area and consist of primary particles with a particle size between 50 nm and 150 nm.

3. MATHEMATICAL MODEL

The rapid expansion of a binary mixture of a supercritical solvent and a solute is modelled numerically considering the five parts: inlet of the capillary - capillary - free jet - mach shock - expansion chamber. The extended generalized Bender Equation of State (egB-EoS):

$$p = p(\rho, T) \tag{1}$$

was chosen to describe the thermodynamic properties of the pure solvent [23]. For the pure supercritical solvent, the one-dimensional flow calculation is based on mass, momentum and energy balances:

$$\rho \cdot A \cdot (dw/dx) + w \cdot A \cdot (d\rho/dx) = -\rho \cdot w \cdot (dA/dx) \tag{2}$$

$$\rho \cdot w \cdot (dw/dx) + (dp/dx) = -2 \cdot f \cdot w^2 \cdot \rho / D \tag{3}$$

$$w \cdot (dw/dx) + (dh/dx) = dq/dx \tag{4}$$

where ρ is the fluid density, A $(= D^2 \cdot \pi / 4)$ the flow area, w the velocity, x the distance along the expansion device, p the pressure, f the friction factor, h the enthalpy and q the heat. The model includes non-isentropic flow in the capillary inlet area, heat-exchange and friction in the capillary and particle growth in the expansion chamber. Based on the calculated pressure, temperature, and density profiles, the supersaturation, S, of the real solute-solvent mixture was calculated by means of a modified Peng-Robinson Equation of State [24].

$$S = [\phi(T, p, y_E) \cdot y_E(T_E, p_E)] / [\phi(T, p, y) \cdot y(T, p)] \tag{5}$$

In Eq. (5) ϕ is the solute fugacity coefficient in the dilute mixture, y_E the equilibrium mole fraction of the solute in the solvent at extraction conditions and y the equilibrium mole fraction at prevailing expansion conditions. The following expression for the nucleation rate J:

$$J = \theta \cdot Z \cdot \alpha_C \cdot n^2 \cdot \pi \cdot r^{*2} \cdot c \cdot exp(-\Delta G^* / k / T) \tag{6}$$

was used to describe the kinetics of particle formation. In Eq. (6) θ is the non-isothermal factor (= 1 for the systems investigated), Z the non-equilibrium factor, α_C the condensation coefficient, n the number of condensable molecules (= $\rho_M \cdot y_E \cdot N_A$), r^* the critical nucleus size (= $2 \cdot \sigma \cdot v_S / (k \cdot T \cdot \ln S)$) corresponding to the maximum value of the Gibbs energy of critical nucleus formation ΔG^* (= $4/3 \cdot \pi \cdot \sigma \cdot r^{*2}$), c the mean thermal velocity (= $(8 \cdot k \cdot T/(\pi \cdot m))^{0.5}$), k the Boltzmann´s constant, and m the mass of the solute. For the systems investigated, solvent dissolution in the incompressible solid was neglected and a value of 0.02 N/m for the solid-fluid interfacial tension σ was assumed. The particulate phase is described by the general dynamic equation (GDE) for simultaneous nucleation, condensation, and coagulation [14, 25-27]:

$$\partial n/\partial t = J(v^*) \cdot \delta(v - v^*) - \partial(G \cdot n)/\partial v + 0.5 \int_0^v (v - v^+, v^+) \cdot (v - v^+, t) \cdot n(v^+, t) dv^+ - n(v,t) \int_0^\infty \beta(v, v^+) \cdot n(v^+, t) dv^+ \quad (7)$$

The change of the particle concentration n within the limit of particle volume v to $v+dv$ is represented by the term on the left-hand side in Eq. (7). The first term on the right-hand side of Eq. (7) considers the nucleation of particles at a given nucleation rate J. The following expression takes into account the variation of the particle volume by condensation through the condensation rate G. Particle growth due to coagulation is described by the last two terms. A more detailed description of the hydrodynamic and aerosol modelling and of the influence of thermodynamic behaviour and solute properties on homogeneous nucleation in supercritical solutions is given in literature [14, 15, 22, 25].

In Table 2, the experimentally obtained particle sizes are compared with the modelling results [10, 14].

Table 2

Comparison between measured, a), and calculated, b), particle sizes.

Solute	Solvent	Particle size[a)]	Particle size[b)]
naphthalene	CO_2	1.5 – 2.5 μm	1.3 – 2.3 μm
benzoic acid	CHF_3	400 – 900 nm	450 – 550 nm
benzoic acid	CO_2	208 – 461 nm	740 – 800 nm
β-sitosterol	CO_2	166 – 219 nm	525 – 575 nm
griseofulvin	CHF_3	193 – 323 nm	325 – 355 nm

In general, with exception of CO_2/naphthalene and of CHF_3/benzoic acid, the measured particle sizes are about the two- to four-fold smaller than the calculated ones. It was mentioned above in the experimental section that the particle size of benzoic acid decreases with lowering the pre-expansion temperature and increasing the pre-expansion pressure. In contrast to these experimental results, the model predicts for all substances investigated only a weak dependence on both the pre-expansion temperature and pressure.

However, in case of griseofulvin an obviously satisfactory agreement between the measured und calculated particle size could be observed. Both, the calculated und the measured particle size are in the range from 200 to 350 nm, whereas the calculated particle sizes are slightly higher than the measured ones. Neither for the experimental nor for the calculated particle sizes no explicit dependency from the pre-expansion condition was found.

In summary, the comparison between experimental and calculated results shows a good agreement in the general trends but does not match exactly the measured mean particle sizes. Until now, these discrepancies in both particle size and dependence on the pre-expansion conditions could not be explained in detail and the clarification of these differences is part of our ongoing work.

4. STABILIZATION OF NANOPARTICLES

It was shown in the experimental section that a higher dilution of the particles in the expansion chamber inhibits post-expansion particle growth [6-9]. In addition, the modelling results suggest, that it should be possible to form particles smaller than 50 nm in diameter [14, 15]. The difficulty to achieve these small particle sizes is most likely due to growth and agglomeration during collisions in the subsonic free jet. However, some few investigations show that a promising method to prevent particle growth is to spray the supercritical solution directly into an aqueous surfactant solution [3, 7, 9, 11]. To investigate the feasibility of the RESS-process to produce stable suspensions of nanoscale particles the RESS-apparatus shown in Fig. 5 was used. In these experiments, the supercritical CO_2 mixture is now expanded through a thermostated capillary nozzle with an inner diameter of 35 μm and a length of 50 μm directly into the aqueous surfactant solution. At first, in order to minimize the unsteadiness of the flow and to accelerate thermal equilibrium, pure CO_2 flows through the thermostated bypass section into the thermostated high-pressure vessel and through the capillary nozzle into the aqueous solution. A thermocouple is used to measure the temperature of the surfactant solution. After thermal equilibrium was reached, the bypass section was closed and the experiments where conducted as described before in case of the RESS into air experiments.

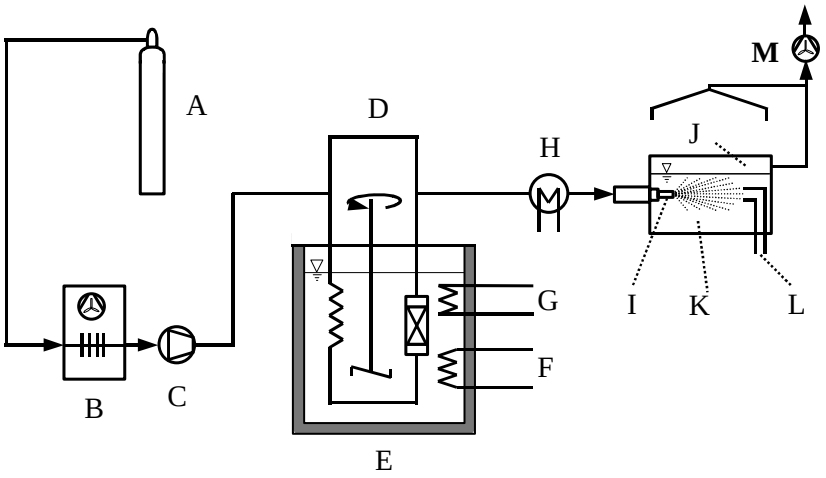

Fig. 5. **A**, solvent; **B**, cooling device; **C**, pump; **D**, bypass; **E**, extractor unit; **F**, cooling; **G**, heating; **H**, pre-heater; **I**, capillary nozzle; **J**, expansion chamber; **K**, solution; **L**, sampling for DLS; **M**, vent.

The nozzle is submerged approximately 3 cm below the surface of the aqueous surfactant solution to ensure a rapid contact of the expanded solution, and therewith the particles being formed, with the surrounding area. The anionic surfactant sodiumdodecylsulfate (SDS) as well as polyoxyethylene sorbitan monooleate (Tween-80), a non-ionic surfactant, were used to impede growth and agglomeration of β-sitosterol particles. Both surfactants are approved for use as an excipient in delivery formulation. To determine the size of the stabilized particles in terms of number-weighted and mass-weighted size distributions Dynamic Light Scattering measurements (DLS) were conducted.

All experiments were performed at a pre-expansion temperature of 388 K, a pre-expansion pressure of 20 MPa and an aqueous solution temperature of 303 K. First of all, as the base case, the supercritical CO_2/β-sitosterol mixture was sprayed into pure water. In these experiments, the aqueous surfactant solution became slightly turbid and large particles were observed visually which were too large for DLS measurements.

In the experiments performed with SDS, the aqueous solutions contain 0.22% or 1.1% (w/w) surfactant. Both concentrations are higher than the critical micelle concentration of SDS. Therefore, before spraying the CO_2/β-sitosterol mixture into the clear aqueous surfactant solution, these solutions were analysed by DLS. At both SDS concentrations investigated, the micelles were to small to scatter light and were not measurable by DLS. In case of Tween-80, the aqueous solutions contain 1.0% or 5.0% (w/w) surfactant. Again, both concentrations are higher than the critical micelle concentration and the aqueous Tween-80 solution

was analysed by DLS. In contrast to SDS, micelles with a size of 7 to 14 nm in diameter were measured in both Tween-80 solutions.

The results of spraying a supercritical CO_2/β-sitosterol mixture into different aqueous surfactant solutions are summarized in Table 3 [10, 11]. At all operating conditions investigated, very small β-sitosterol particles were obtained even though with different particle sizes. For all surfactants investigated, the lower concentrated solution leads to a slightly broader size distribution in comparison to the higher concentrated solution. Also, an increase in surfactant concentration results in a decrease in the particle size for both surfactants. The comparison between SDS and Tween-80 shows that the former surfactant leads to relatively smaller particles. In case of SDS, the smaller particles range from 30 to 75 nm and the larger particles are in the range from 80 to 300 nm. A similar result was obtained for Tween-80, the smallest particles range from 7 to 35 nm, however larger particles in the range of 80 to 130 nm and of 280 to 1100 nm were also determined. Nevertheless, the small particle sizes obtained in these experiments demonstrate impressively that the initially formed particles with very small particle size can be stabilized within the expanding jet without excessive particle growth due to agglomeration. Furthermore, these investigations show that the Rapid Expansion of Supercritical Solutions into an Aqueous Solution (RESSAS) is a promising method for the production stable aqueous formulations of water-insoluble drugs.

Fig. 6 shows a typical result for the size distribution of β-sitosterol particles stabilized in either a 0.22% or a 1.1% (w/w) aqueous SDS solution.

Table 3
Effect of surfactant concentration on measured particle size distribution of the stabilized β-Sitosterol particles.

Surfactant concentration (w/w)	Particle size distribution [nm]		
0.22 % SDS	40 - 75	110 - 300	
1.1 % SDS	30 - 55	80 - 200	
1.0 % Tween-80	20 - 35	80 - 130	390 - 1100
5.0 % Tween-80	7 - 20	85 - 110	280 - 800

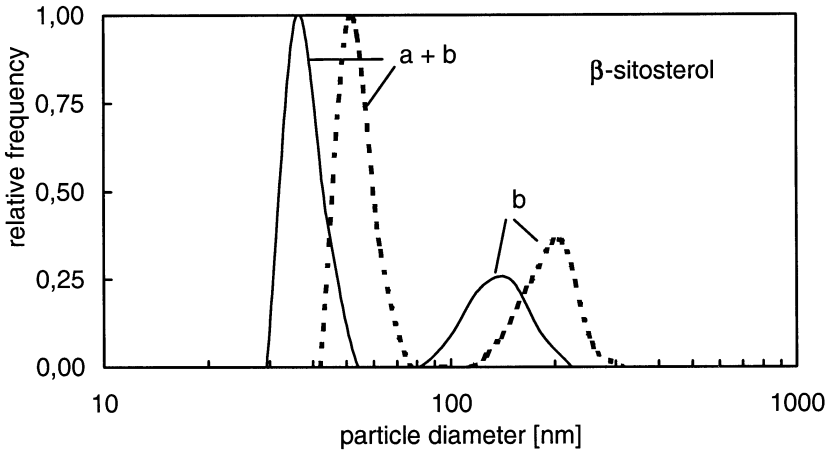

Fig. 6. Particle size distribution of β-sitosterol particles stabilized in either a 0.22 wt-% (dotted line) or a 1.1 (full line) wt-% aqueous SDS solution. Curve a) represents the number-weighted size distribution and curve b) represents the mass-weighted size distribution.

5. CONCLUSION

The experimental results demonstrate the applicability of the RESS-process to produce particles smaller than 500 nm. The particle size of the pharmaceutical substances β-sitosterol, griseofulvin, and ibuprofen precipitated by RESS was in the range from 160 to 320 nm. The improvement of the bioavailability of the RESS-produced griseofulvin has been verified by dissolution experiments according to the Stricker model. As a first step towards intravenous application of poorly soluble drugs, stable suspensions of nanoscale particles of β-sitosterol were produced. In these experiments, the supercritical mixture was sprayed directly into an aqueous surfactant solution. The particle sizes of β-sitosterol in the aqueous solution were smaller or equal to those produced by RESS into air. Thus, these experiments show that the RESS-technique is a promising method for the formulation of water-insoluble drugs. The modelling results show that particle growth is not completed in the supersonic free jet and the post-expansion conditions are an important factor to control particles size. The comparison between experimental and calculated particle size shows a good agreement in the general trends but does not match exactly the measured mean particle sizes. Nevertheless, a useful tool for the understanding and optimization of the RESS-process has been created. In addition, the importance of the knowledge of the SLG-line and of the phase behaviour of the systems involved for the production of nanoscale particles is clarified.

6. ACKNOWLEDGEMENTS

We gratefully acknowledge the support of this investigation by various grants of the Deutsche Forschungsgemeinschaft (Scha 524 / 5-1, 5-2, 5-3, 5-4 and Tu 93 / 2-1, -2, -3).

7. SYMBOLS AND ABBREVIATIONS

A	m^2	flow area, Eq. (2)
c	$m\ s^{-1}$	mean thermal velocity, Eq. (6)
D	m	diameter of the capillary nozzle
f		Fanning friction factor, Eq. (3)
G	$m^{-3}\ s^{-1}$	condensation rate, Eq. (7)
ΔG^*	[J]	Gibbs energy of critical nucleus formation, Eq. (6)
h	$[J\ kg^{-1}]$	enthalpy, Eq. (4)
J	$[m^{-3}\ s^{-1}]$	nucleation rate, Eq. (6)
k	$[Nm\ K^{-1}]$	Boltzmann´s constant: 1.38×10^{-23}, Eq. (6)
M	$[kg\ kmol^{-1}]$	molecular weight
m	[kg]	mass of the solute
N_A	$[mol^{-1}]$	Avogadro´s number: 6.023×10^{23}
n	$[m^{-3}]$	number of condensable molecules, Eq. (6)
p	[MPa]	pressure
q	$[J\ kg^{-1}]$	heat, Eq. (4)
r^*	[m]	radius of nucleus of critical size, Eq. (6)
S		supersaturation, Eq. (5)
T	[K]	temperature
V	$[dm^3]$	volume of the expansion chamber
v	$[m^3]$	particle volume, Eq. (7)
v_S	$[m^3]$	solute molecular volume in the solid phase
w	$[m\ s^{-1}]$	velocity, Eq. (2 - 4)
x	[m]	actual position, Eq. (2 - 4)
y		solute mole fraction in the fluid phase
y_E		solute mole fraction at extraction conditions
Z		Zeldovich nonequilibrium factor, Eq. (6)
α_C		condensation coefficient, Eq. (6)
β	$[m^3\ s^{-1}]$	coagulation coefficient, Eq. (7)
δ	$[m^{-3}]$	delta function, Eq. (7)
ϕ		fugacity coefficient of the solute, Eq. (5)
θ		nonisothermal factor, Eq. (6)
ρ	$[mol\ dm^{-3}]$	density of the fluid, Eq. (2, 3)

ρ_M [mol dm^{-3}] density of the mixture
σ [N m^{-1}] interfacial tension of the solute

REFERENCES

[1] R.H. Müller, B.H.L. Böhm, M.J. Grau, Pharm. Ind., 61 (1999) 74, 175.
[2] B. Subramaniam, R.A. Rajewski, K. Snavely, J. Pharm. Sci., 86, 8, (1997) 885.
[3] T.J. Young, S. Mawson, K.P. Johnston, I.B. Hendriksen, G.W. Pace, A.K. Mishra, Biotechnol. Prog., 16 (2000) 402.
[4] M. Türk, J. Supercrit. Fluids, 15, 1, (1999) 79.
[5] B. Helfgen, M. Türk, K. Schaber, J. Powder Techn., 110 (2000) 22.
[6] P. Hils, B. Helfgen, M. Türk, K. Schaber, H.-J. Martin, P.C. Schmidt, M.A Wahl, Proceedings of the 7th Meeting on Supercritical Fluids, Antibes, France, Tome 1 (2000) 27.
[7] M. Türk, professorial dissertation, Universität Karlsruhe (TH) (2001).
[8] M. Türk, P. Hils, B. Helfgen, K. Schaber, H.-J. Martin, M. A. Wahl, Proceedings of the 2nd International Meeting on High Pressure Chemical Engineering, Hamburg-Harburg, (2001).
[9] M. Türk, P. Hils, B. Helfgen, K. Schaber, H.-J. Martin, M. A. Wahl, J. Supercrit. Fluids, 22, 1, (2002) 75.
[10] M. Türk, P. Hils, B. Helfgen, R. Lietzow, K. Schaber, Part. Syst. Charact., 19 (2002) 327.
[11] M. Türk, R. Lietzow, P. Hils, K. Schaber, Chemical Engineering Transactions, Vol. 2 (2002) 621. Edited by Alberto Bertucco, ISBN 88-900775-1-4.
[12] P.G. Debenedetti, AIChE J., 36 (1990) 1289.
[13] J.W. Tom and P.G. Debenedetti, J. Aerosol Sci., 22 (1991) 555.
[14] B. Helfgen, doctoral thesis, Universität Karlsruhe (TH) (2001).
[15] B. Helfgen, M. Türk, K. Schaber, J. Supercrit. Fluids, in press.
[16] S. Cihlar, doctoral thesis, Universität Karlsruhe (TH) (2000).
[17] J. Meyer, M. Katzer, E. Schmidt, S. Cihlar, M. Türk, Proceedings of the World Congress on Particle Technology 3, Brighton, UK, (1998) 31.
[18] S. Cihlar, M. Türk, K. Schaber, Proceedings of the World Congress on Particle Technology 3, Brighton, UK, (1998) 380.
[19] A. Diefenbacher, doctoral thesis, Universität Karlsruhe (TH) (2001).
[20] A. Diefenbacher and M. Türk, J. Supercrit. Fluids, 22, 3, (2002) 175.
[21] S.-P. Hong and K.D. Luks, Fluid Phase Equilib., 74 (1992) 133.
[22] M. Türk, J. Supercrit. Fluids, 18, 3, (2000) 169.
[23] B. Platzer, G. Maurer, Fluid Phase Equilib., 10 (1989) 223.
[24] W.J. Schmitt and R.C. Reid, Chem. Eng. Data, 31 (1986) 204.
[25] B. Helfgen, P. Hils, Ch. Holzknecht, M. Türk, K. Schaber, J. Aerosol Sci., 32, 3, (2001) 1.
[26] S.K Friedlander, Smoke, Dust, and Haze, Fundamentals of Aerosol Behavior, John Wiley and Sons, New York, London, Sydney, Toronto, (1977).
[27] S.E. Pratsinis, J. Colloid Interf. Sci., 128 (1988) 416.

Supercritical Fluids as Solvents and Reaction Media
G. Brunner (editor)

Chapter 4.1.

Separation efficiency and axial mixing in packed high pressure extraction columns

O. Becker[a] and G. Heydrich[b]

[a] AllessaChemie GmbH, Alt Fechenheim 34, 60386 Frankfurt
[b] BASF, Ludwigshafen
both earlier Universität Erlangen, Lehrstuhl für Technische Chemie II.

1. INTRODUCTION

Typically high pressure counter current extraction processes are operated in separation columns. Because influence parameters like substance properties, extraction conditions, flow regime (drops or film), column load, and occurring back mixing effects are complex, the design procedure is often based on empirical considerations [1].

Liquid-liquid extraction processes under ambient pressure are very similar. Because of the higher industrial importance of this unit operation it has been investigated more systematic and in more detail than the corresponding high pressure extraction processes [2,3]. To make use of this experience it is required to check what part of the knowledge of conventional liquid/liquid extraction processes can be transferred to high pressure extraction processes.

After obtaining substance data (phase equilibria, physical data like density, viscosity, diffusivity) and selecting a suitable type of apparatus the usual proceeding in the design of extraction processes is to run laboratory scale extractions. Subsequently pilot plant experiments are often required as intermediate step to scale up these results to industrial throughputs [4].

It would be desirable to be able to make design calculations based on a few characteristic data. One possibility is the utilization of process simulation programs. Another method is to calculate the required column height based on theoretically derived mass transfer equations.

The disadvantage of these design methods is that typical fluid dynamic processes in separation columns like longitudinal mixing effects which lead to a reduction of concentration driving force along the column are not taken into

account. These effects mainly depend on the installed column packing in connection with the fluid dynamic properties of the phases flowing opposite to each other. The corresponding decrease in separation efficiency of liquid/liquid extraction columns has been discussed by several authors on a variety of column insertions. (*Miyauchi et al.*, 1960 [5], *Stemerding et al.*, 1963 [6], *Marr et al.*, 1978 [7])

Extraction with compressed gases under high pressure results in substantial deviation of physical properties like density or viscosity from usual conditions in liquid/liquid extraction. Extracting oleic acid glycerid mixtures with propane/carbon dioxide gas mixtures Czech found connections between separation efficiency and axial dispersion in a counter current high pressure extraction column filled with various insertions [8]. Unfortunately the experiments were all conducted without counter flow of dispersed raffinate phase.

The documented experimental data gained during this project consist mainly of residence time distribution measurements with counter flow of droplets. They shall contribute to clarify fluid dynamic dispersion effects and their relation to column insertions and substance systems. The findings obtained may be used as basis for the design of high pressure extraction columns for technical separation problems.

2. EXPERIMENTAL UNIT AND MEASURING TECHNIQUES

A detailed flow scheme of the high pressure extraction unit is given in [9]. Its main components are an extraction column of 7.5 m height and 6.7 cm diameter followed by two precipitation columns (3.8 m and 3 m) of the same diameter connected in series. Heat exchanger subsequent to the expansion valves allow to evaporate liquid fractions of the solvent as well as to adjust the chosen temperature to precipitate the extracted compounds. The extraction column and the first precipitator are equipped with double walled heating jackets allowing for a constant temperature. Particularly close to critical conditions only small changes in temperature may lead to large density fluctuations which may result in unwanted convective flows.

After leaving the second precipitator the extraction medium is cooled to increase its density. In the most favourable case (i.e. with a low cooling water temperature) it can be liquefied before it is recompressed to extraction pressure by a diaphragm pump. Before recirculating back to the extraction column the extraction solvent passes heat exchangers that allow to adjust extraction conditions by either heating or cooling depending on liquid or vapour phase recompression.

One possible method to regenerate the solvent with regard to the applied substance system ethanol/water is to apply a rectification column [10,11] to

separate the extract. To achieve a sufficient regeneration simply by a decrease in pressure it would have been necessary to expand the solvent to almost ambient pressure. Because the diaphragm compressor could only produce a satisfactory mass flow (up to 100 kg/h) at a pressure difference lower than 40 bar the circulating solvent was regenerated by pressure reduction down to 60 bar and subsequent scrubbing with water in the second precipitator. The mass flow of the solvent was determined by a coriolis mass flow meter.

To determine the disperse phase hold up it was possible to stop the flow of all entering and leaving streams quickly and to measure exactly the rising liquid level in the bottom vessel of the column by using capacitive level sensors. Sight glasses in the column walls allowed to film droplets with a video camera and to determine drop sizes for a statistic evaluation.

Special tracer dosing systems were developed to measure the residence time distribution. It was possible to reproducibly inject about 0.5 ml of solvent saturated tracer into the solvent stream before it entered the column. o-xylene was applied as tracer for the solvent phase. It is fully soluble in CO_2 and propane and almost insoluble in the water phase [12,13]. This way it could be ensured that the tracer signals were not distorted by additional mass transfer steps.

The o-xylene concentration was measured continuously by two identical UV-detectors fed by small side streams through short capillaries from the column center. The distance between the side stream outlets was 3.13 m. Because of a well detectable adsorbance band at 210 nm, o-xylene as a tracer can even be detected at high dilutions. Care was taken to use capillaries of exactly the same length and throughput (10 ml/min gaseous CO_2) to avoid distortion of the signals by different retention times. Moreover the capillaries and the measuring cells of the detectors were held on the same temperature as the column because otherwise condensing effects would have resulted in large fluctuations in the flow.

The drop phase residence time distribution was also measured. Analogous to the procedure in the continuous phase app. 1 ml of a 1 molar NaCl-solution was injected into the disperse phase inlet. During separate experiments specially designed conductivity probes were inserted into the column which enabled to measure a signal that was linear proportional to the tracer concentration in the drop phase.

In both cases the measured signals were recorded every 1-3 seconds. The main parameters for the measurement of the residence time distribution are given in Table 1.

Table 1
Compilation of relevant parameters for residence time distribution measurements

	Water Phase	Continuous Phase
Distance of detectors	3,13 m	3,13 m
Tracer substance	NaCl-Solution (1 mol/l)	o-xylene (saturated with solvent)
Amount of tracer	1 ml	0,5 ml
Tracer inlet	1,6 m above the first detector	1,6 m below the first UV-detector
Analysis method	Conductivity	UV-Detection (210 nm)

To determine the separation efficiency raffinate and extract phase samples were taken by expanding them to ambient pressure with volumetric detection of the solvent content. The remaining liquid was weighed and analysed by gaschromatography. It turned out that with this substance system particular care had to be taken during sampling and that additional cooling was required because otherwise the analytic results were irreproducible by reason of uncontrolled desorption of ethanol from the liquid water phase.

3. SUBSTANCE SYSTEM AND INVESTIGATED COLUMN PACKINGS

A mixture of 25 wt% ethanol and water was extracted by supercritical carbon dioxide. In some cases residence time distributions were also run with propane under high pressure. The extraction conditions with CO_2 were 100 bar at a temperature of 40°C. When propane was used the pressure was set to 50 bar at 60°C where the gas was subcritical with respect to pressure and therefore had to be considered as moderately compressible liquid.

Phase equilibria for the system ethanol/water/CO_2 available from the literature were compiled by Bjola [14]. As an example Fig. 1 shows the phase equilibrium with carbon dioxide at five different pressures. Care had to be taken to avoid regions below 48°C and 91 bar because a third phase may be formed [19]. Because ethanol as transferred component would have significantly increased the solubility of the o-xylene tracer all RTD-experiments were run without ethanol.

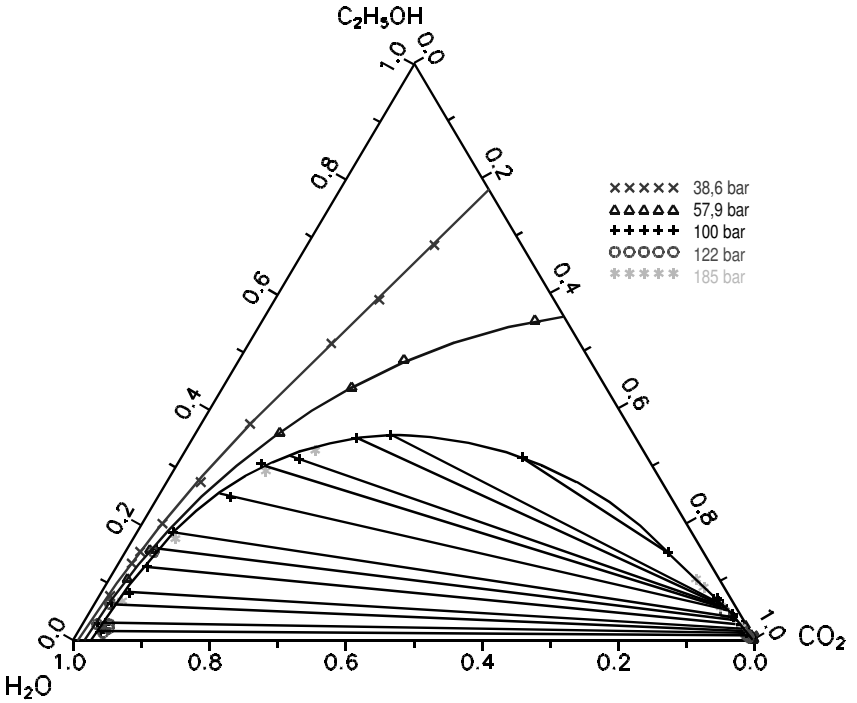

Fig. 1. Phase equilibrium of the system ethanol/water/CO_2 at pressures from 38 to 185 bar and 40°C

Table 2
Experimental conditions and physical properties of the pure supercritical and pure (ethanol free) water phase

	Carbon dioxide/Water		Propane/Water	
Critical data of extraction solvent	p_c=73,8 bar T_c=31,1°C		p_c=42,5 bar T_c=96,7°C	
Pressure	100 bar		50 bar	
Temperature	40°C		60°C	
Surface tension without transferred compound [15,16]	29 mN/m		54 mN/m	
	Extract phase	Raffinate phase	Extract phase	Raffinate phase
State of phase	supercritical	liquid	liquid	liquid
Density	640 kg/m³	1007,6 kg/m³	445 kg/m³	987 kg/m³
Viscosity [17,18]	$5 \cdot 10^{-5}$ kg/(ms)	$6{,}9 \cdot 10^{-4}$ kg/(ms)	$7{,}3 \cdot 10^{-5}$ kg/(ms)	$4{,}6 \cdot 10^{-4}$ kg/(ms)

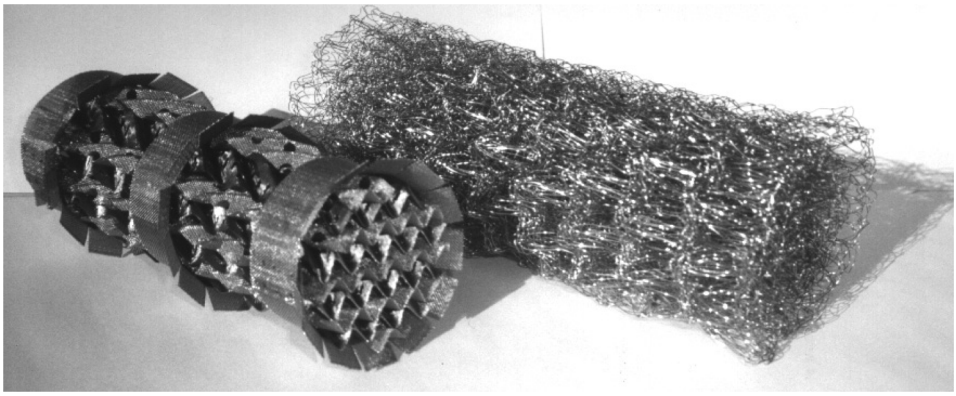

Fig. 2. Packings applied in high pressure extraction

Experimental conditions and calculated physical properties of the pure water phase and the pure solvent phase are put together in Table 2. Ethanol as transferred compound during the mass transfer experiments decreases the surface tension and the density difference. Correlations to take these effects into account can be found at *Heydrich* [15]

Separation efficiency and hydrodynamics of a Sulzer wiregauze packing (type BX, Fa. Sulzer Chemtech AG, Winterthur, Switzerland) and a prototype of a wiremesh packing (Fa. Rhodius GmbH, Weißenburg, Germany) were investigated. As shown in Fig. 2 the structure differs strongly between the two packings. The Sulzer BX is made of wiregauze and has the classic cross channel structure. The wiremesh packing is in contrast made of crimped and rolled up wiremesh mats. Due to the structure of the knitted wire mats the packing shows a cascaded substructure with was considered to be advantageous regarding its efficiency. Table 3 sums up the main geometrical parameters of both packings installed.

Table 3
Geometrical data of the packings

	Sulzer BX	Wiremesh Packing
Element height	165 mm	210 mm
Void fraction	88 %	88 %
Specific surface area	500 m^2/m^3	296 m^2/m^3

4. RESULTS

The main goal of determining the hydrodynamic parameters and the separation efficiency of two structural different packings in a high pressure column was to identify the combined influence of substance system and packing geometry and to verify weather the observed effects can be described using the well known methods of liquid/liquid extraction.

The separation efficiency of both packings was tested with an active height of 3 m. This allowed the concentrations of raffinate and extract phase to be in a well analysable range and the obtained raffinate concentration was not limited by the residual content in the solvent after regeneration.

The obtained number of separation stages was evaluated according to two different methods. In the beginning the calculation in Jänecke-Coordinates was preferred because a certain mutual solubility of extract and raffinate phase could be expected according to the equilibrium diagram. The results of this method were compared with those obtained by the Cremser-Brown-Souders equation [20]. The latter assumes that equilibrium and balance line are straight and that raffinate and extract phase are not miscible in each other. Related to the extract phase concentration its notation is:

$$n_{th} = \frac{\ln\left[\left(\frac{w_{x\alpha} - w_{y\alpha}/m'_{yx}}{w_{x\omega} - w_{y\alpha}/m'_{yx}}\right)\left(1-\frac{1}{\lambda}\right)+\frac{1}{\lambda}\right]}{\log\lambda} \qquad (1)$$

λ is the extraction factor and m'_{yx} is the slope of the equilibrium curve in the equilibrium plot where the weight fraction of the solute in the solvent was chosen as ordinate. Both methods were compared by *Heydrich* [15]. The findings show that the results in the considered loading interval were almost identical with a similar scattering. The extraction factor varied between 0.5 and 1.5 during the experiments.

4.1. Separation efficiency

The obtained stage heights for the Sulzer BX packing are displayed in Fig. 3 and Fig. 4. The curves are plotted with constant solvent ratio at changing total load and vice versa.

The plotted heights are in a typical range with regard to extraction columns. Taking into account that the solvent ratios were always considerably higher than unity it is obvious that changes in the total crossectional load are mainly caused by variation of the supercritical phase throughput. The decrease in stage height respectively the better separation efficiency with rising column load is a result of the following effects:

- Increased interfacial area caused by a higher hold up with rising disperse phase load.
- Lower dispersion heights because of higher phase velocities respectively reduced back mixing.
- Increased slip velocity between droplets and continuous phase and hence an increased mass transfer coefficient.

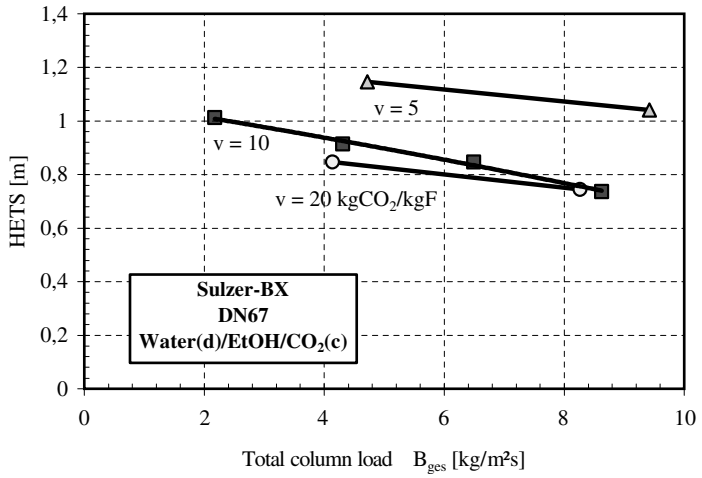

Fig. 3. Height of a separation stage of the Sulzer BX packing as function of column load

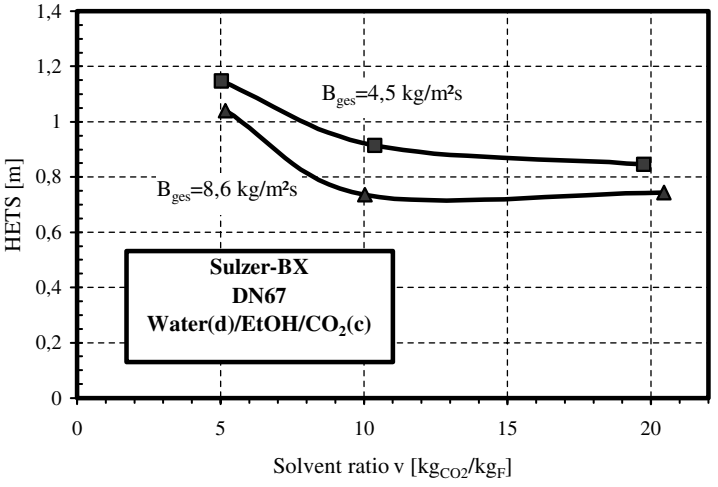

Fig. 4. Height of a separation stage of the Sulzer BX packing as function of solvent ratio

Similar stage heights were determined by Bernad et al. with the same substance system and a Sulzer BX packing in a column of 54 mm diameter and 1.4 m height [21].

The stage heights found for the wiremesh packing at identical column loads, solvent ratios and hence the same extraction factors were almost double in comparison to the BX packing (see Fig. 5 and Fig. 6). Despite this fact the curve

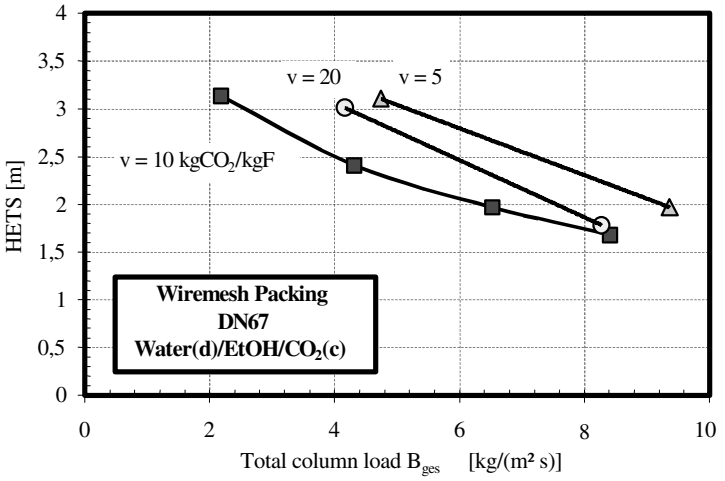

Fig. 5. Height of a separation stage of the wiremesh packing as function of column load.

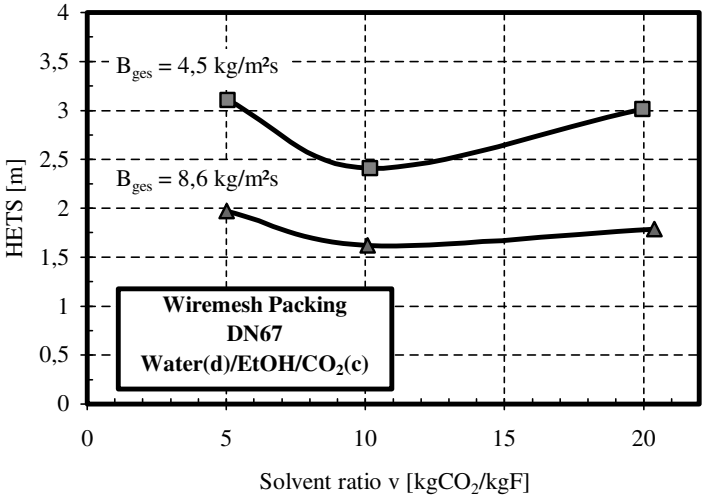

Fig. 6. Height of a separation stage of the wiremesh packing as function of solvent ratio.

traces follow the same trends. In both cases the stage heights at a solvent ratio of five are maximum and decrease with extract phase throughput. In contrast to the packing with cross channel structure the wiremesh packing shows a lower separation efficiency when the solvent ratio is increased to 20.

Gamse et al. have extracted wine in a column of 2 m height and 34 mm diameter filled with pall rings (10x10mm) and found stage heights between 2.5 and 6 meters with increasing efficiency at rising solvent ratio [11].

The stage heights of the two packings evaluated according to the described methods are considerably different. This primarily confirms that the structure of the applied packing is of significant influence upon the separation efficiency also in high pressure extraction. The fact that droplet flow could be observed in both packings verifies as well that the geometric surface area of the packing elements is of secondary influence and has no direct impact on interfacial area. In distillation and absorption processes where the packing surface is wetted by a liquid film the specific surface of the packing elements is of major importance.

4.2. Drop sizes

To be able to analyse the hydrodynamic parameters it was required to determine average drop sizes. This was done by evaluation of pictures taken with a video camera through sight glasses in the column wall. At least 300 drops were measured in all cases in order to get a certain statistic background for the measured drop diameters.

The ethanol content of the raffinate phase causes a strong decrease of surface tension along with a diminishing drop size. As an example Fig. 7 shows experimentally determined histograms for each of the tested packings

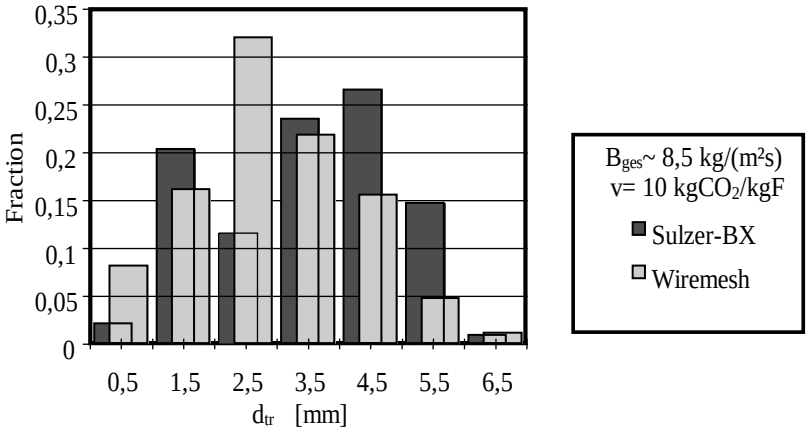

Fig. 7. Comparison of measured drop sizes in the Sulzer BX and the wiremesh packing.

Caused by the mass transfer out of the droplets one has to reckon with enhanced coalescence and therefore with a minor fraction of very small droplets. It is shown that the fraction of droplets in a size interval between 0 and 1 mm is larger for the wiremesh packing. The Sulzer packing showed in all cases a bimodal drop size distribution with one maximum at small sizes and one at larger diameters. In contrast the wiremesh packing usually caused a monomodal distribution.

4.3. Hold up

Apart from the disperse phase load the operating hold up of an extraction column depends mainly on three system parameters. These are the free falling or rising velocity of droplets, the mutual hindrance of the droplets, and the packing geometry disturbing the free falling path of the droplets and thus leading to an increased hold up.

The hold up for each packing determined by applying the quick shut method is compared in Fig. 8. As expected, the disperse phase hold up increases with the liquid load. The hold up of the wiremesh packing with its rolled up structure is 0.25 to 0.5% lower than that of the wiregauze packing with the cross channel structure. This is remarkable because the average ethanol content of the droplets in the wiremesh packing is higher caused by the lower separation efficiency which in turn causes smaller droplets having a lower falling velocity.

The measured drop size can be reproduced with Eq. (2). Depending on the packing an individual prefactor η is required to take into account the strong tendency of the droplets to coalesce.

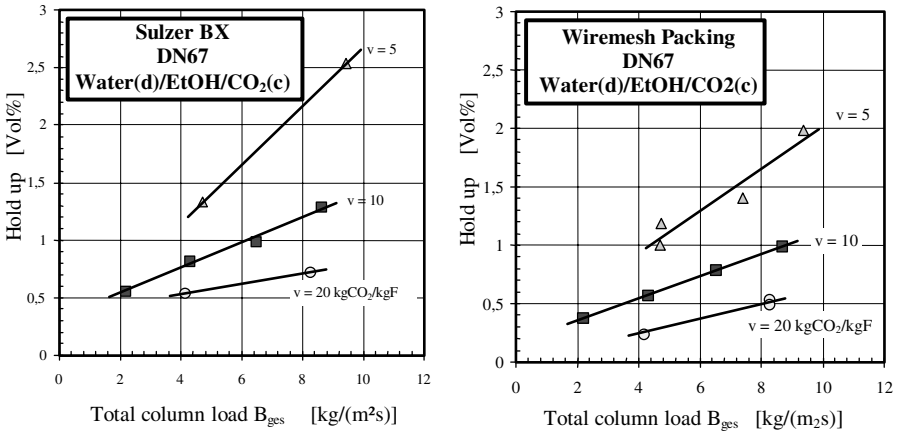

Fig. 8. Experimentally determined hold up for both packings.

$$d_{32} = 1{,}15 \cdot \sqrt{\frac{\sigma}{\Delta\rho\, g}} \tag{2}$$

It was necessary to introduce prefactors above the value of η=1,4 suggested by Seibert [22]. Obviously the tendency of drop coalescence is more expressed with this supercritical substance system as with conventional solvents under ambient pressure. The parity plot represented in Fig. 9 shows that experimental and calculated drop diameters comply sufficiently well.

Proceeding with the model proposed by Seibert, it was possible to reproduce the measured hold up using Eq. (2) and the implicit Eq. (3):

$$\phi_d = \frac{U_d \cos^{-2}\left(\frac{\pi\zeta}{4}\right)}{\varepsilon\left(U_{so}\, e^{\frac{6\phi_d}{\pi}} - \frac{U_c}{\varepsilon(1-\phi_d)}\right)} \tag{3}$$

Therein the free falling drop velocity U_{so} was calculated according to the method of Grace et al. [23] which bases on about 1500 experimental data points. ζ represents the tortuosity factor and ε is the void fraction of the packing. A more detailed explanation is also given in [9].

As Fig. 10 shows, the disperse phase hold up could be calculated for both column insertions with sufficient accuracy. A trend toward the prediction of a lower hold up than the actually measured in the range of very low droplet flow can be observed.

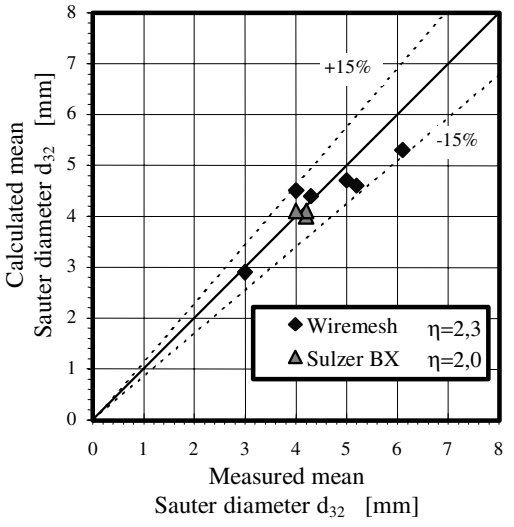

Fig. 9. Parity plot for the calculation of the mean sauter diameter according to Eq. (2)

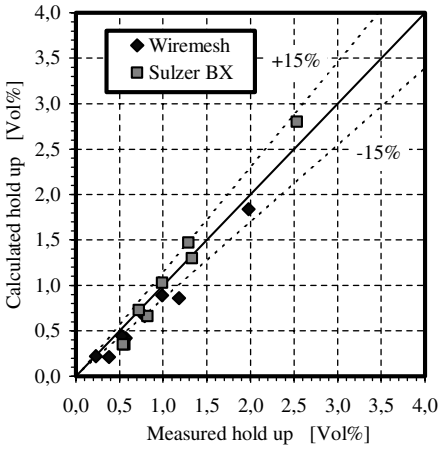

Fig. 10. Parity plot for the calculation of the disperse phase fraction in the investigated column packings.

4.4. Residence time distribution of the continuous phase

Up to now the presented data like drop size distribution, drop size, hold up and interfacial area do not indicate a strongly differing hydrodynamic behaviour of the two packings. Measurements of the residence time distribution in the continuous phase allow interpretations because the applied evaluation method of the time domain analysis reveals information about the average phase velocity inside the column and the axial dispersion coefficient at the same time. Based upon the phase velocity results one is able to identify considerably different flow patterns of the continuous phase.

4.4.1. Wiremesh packing

Fig. 11 compares the experimentally determined continuous phase velocity with the calculable interstitial velocity. Provided that the free crossectional area of the column is reduced by 4 % by the volume fraction of the packing and the disperse phase hold up it is surprising to find phase velocities that are almost two times higher than the interstitial velocity. This phenomenon seems to be particularly expressed at low supercritical phase throughput and low disperse phase loads. At higher throughputs and decreasing solvent ratio (corresponding to a higher liquid load) the measured phase velocities tend toward the expected values of the interstitial velocity.

The measured high phase velocities suggest the idea that the rolled up structure of the wiremesh packing guides the flow to the core. The packing density along the center is lower than in the outer region which restricts the flow of the supercritical phase to the middle region. Induced by a higher drop density in the center of the packing at higher liquid loads, the velocity profile is changed

so that the outer regions of the packing are more and more included into the flow. Fig. 12 schematically illustrates this idea.

It is obvious that steep velocity gradients of the continuous phase are of negative influence upon the detectable axial dispersion coefficient. This is the more expressed as the velocity differs between the flow in the centre of the packing and close to the column walls.

The experimental results obtained for the axial dispersion coefficient displayed in Fig. 13 confirm this. In the region of low throughput the velocity difference between center and boundary is not yet large and hence the dispersion coefficient shows moderate values. With increasing supercritical phase throughput and less equilibrating influence of the liquid phase the gradient rises. Therefore the highest values of the dispersion coefficients are measured when the boundary regions of the packing are not sufficiently well included into the supercritical phase flow and the liquid phase load is low.

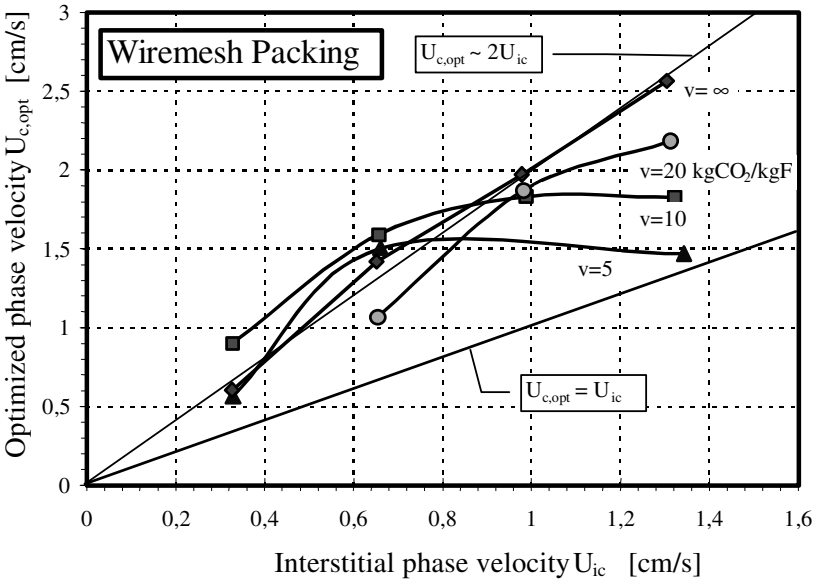

Fig. 11. Average flow velocity in the continuous phase of the wiremesh packing from RTD-exeriments as function of the interstitial phase velocity.

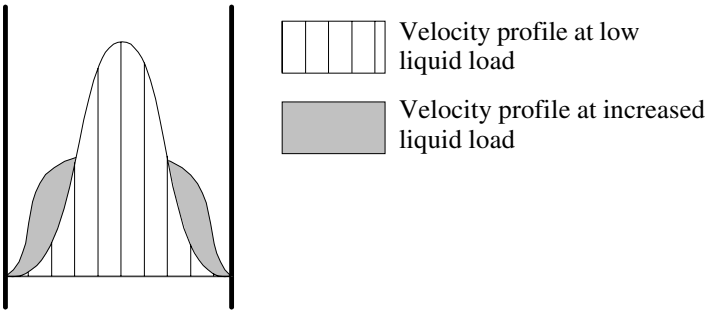

Fig. 12. Schematic sketch of the continuous phase velocity profile in the wiremesh packing at varying liquid load.

4.4.2. Sulzer BX packing

The results for the Sulzer BX packing look different. Caused by the cross channel structure one can assume a fairly equilibrated velocity profile close to plug flow conditions. The results of the phase velocity obtained by RTD experiments shown in Fig. 14 confirm this assumption. They comply well with the calculable interstitial velocities. It has to be taken into account that the void fraction of the Sulzer packing is merely 88 vol% and the hold up is in most cases below 2 vol%.

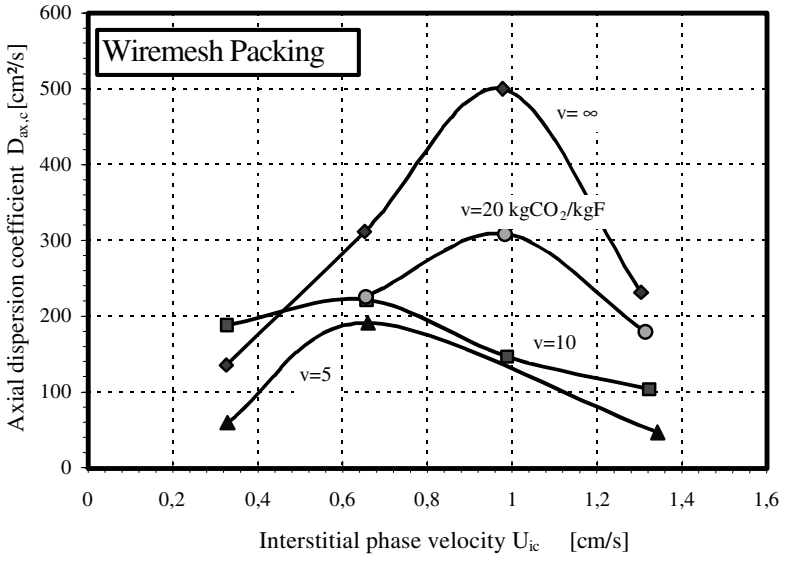

Fig. 13. Measured axial dispersion coefficient in the supercritical continuous phase with the wiremesh packing.

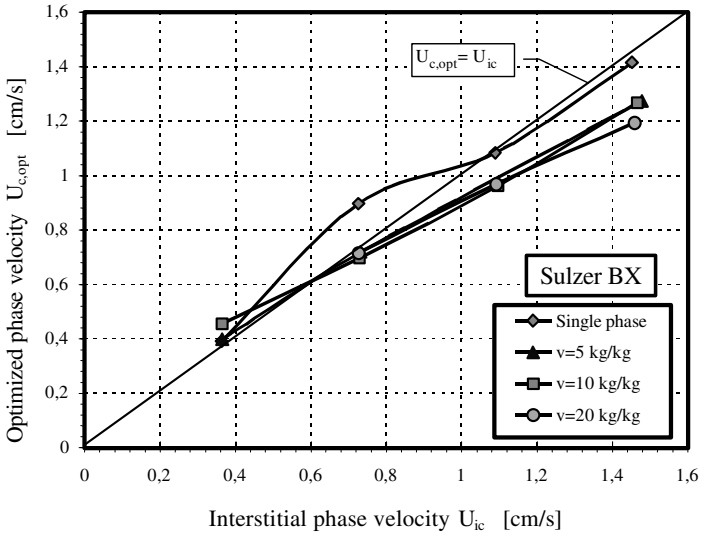

Fig. 14. Average flow velocity in the continuous phase of the Sulzer BX packing from RTD-exeriments vs. interstitial phase velocity.

One can observe that the solvent phase velocity gradually decreases below the theoretical interstitial velocity U_{ic}. It can be assumed that this effect can be attributed to the formation of a bypass flow between packing and column wall. This effect becomes only visible as with higher supercritical phase throughput and increased liquid phase load a systematic deviation occurs being larger than the experimental scattering.

With respect to the phase velocity the BX packing behaves fairly ideal. Looking at the results of the dispersion coefficient a deviation from the expected results was found. It could be shown that the dispersion coefficient without counter flow of liquid is on a significantly higher level than with dispersed phase flow as depicted in Fig. 15. Obviously the dispersed phase flow rate seems to play a minor role.

The presence of the liquid phase in the wiregauze packing seems to reduce axial backmixing in the continuous phase. Because the measured phase velocities are close to ideal, large bypass flows as a reason are not likely. One can rather assume that the wiregauze of the packing in dry state is directly penetrated by the supercritical carbon dioxide phase particularly because the individual sheets are perforated with holes in a regular pattern. In case of counter flow of a dispersed phase these holes are blocked by droplets and the solvent flow has to follow mainly the channels. Thus application of a dispersed phase leads to significant reduction of axial dispersion in this packing.

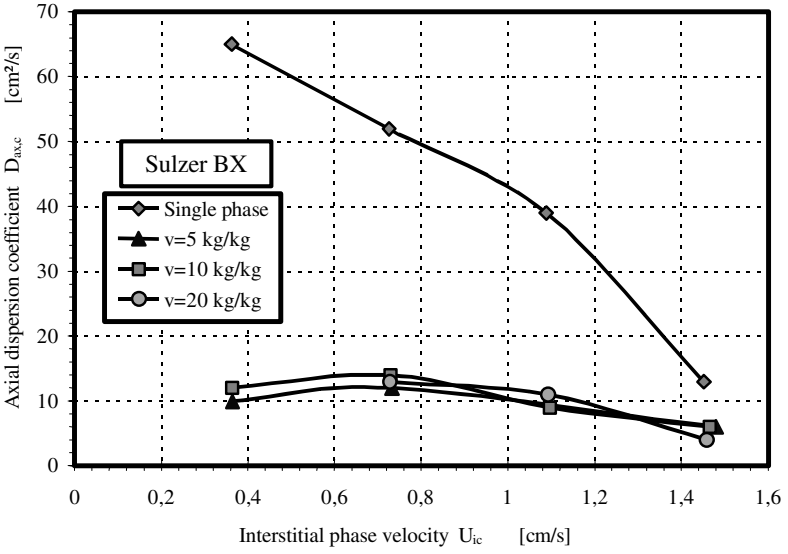

Fig. 15. Experimental results of the axial dispersion coefficient in the supercritical phase of a Sulzer BX packing

Apart form this observation it can be stated that the absolute values of the dispersion coefficient are about one order of magnitude lower than in the respective experiments with the wiremesh packing.

4.5. Residence time distribution of the disperse phase

Measurements of the residence time distribution in the disperse phase are discussed controversial. This is mainly because the information obtained by these experiments may not be overestimated [24].

The drop phase is not a continuum in the intention of the dispersion model. Droplets of different sizes may flow past each other with their inherent rising or falling velocity and there is usually no transport against the main flow direction. In this case it is often referred to the forward mixing model [25]. Coalescence events between individual droplets can be estimated as seldom compared to pulsed or stirred columns and hence a mass exchange between droplets is not likely. The following basic statements concerning the drop phase residence time distribution are to be taken into account:

- Evaluations of axial dispersion coefficients in the disperse phase are only meaningful and transferable if frequent coalescence and breakage of droplets takes place and small velocity differences between droplets are

likely (synonymous to a narrow drop size distribution). In these cases the drop phase behaves similar to a continuum. [26]

- If the above prerequisites are not fulfilled, only measurements of a specific application (with a fixed distance between the probes) can be compared with each other. The absolute values of the dispersion coefficients are not transferable to other configurations.
- Interpreting the dispersion coefficient merely as an adaptable parameter, the time domain analysis allows to calculate average drop phase velocities.

The following Fig. 16 compares the drop phase velocities in the two tested packings obtained by evaluation of tracer signals. In both cases the drop velocity rises nearly linear with increasing liquid load. It also becomes obvious that the cross channel structure of the BX packing is more suitable to reduce the falling velocity of the droplets and hence to create a larger hold up which in turn produces a larger interfacial area.

Based on the statements above, measurements of the dispersion coefficients in the drop phase can only be compared with each other.

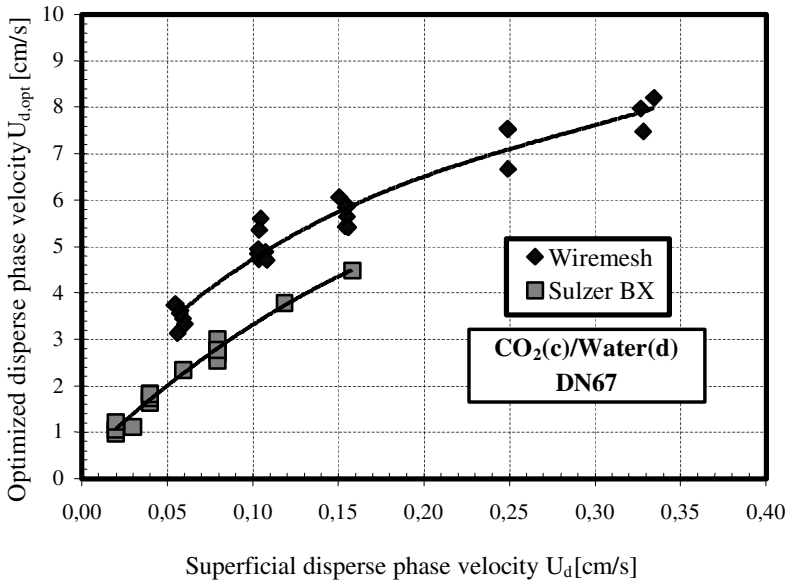

Fig. 16. Drop phase velocity from tracer experiments.

As depicted in the plots of Fig. 17 the scattering of the obtained data is expectedly high. The trends of both packings are similar. At low drop phase load the base of the tracer signal stays comparatively narrow indicating a narrow drop size distribution. At higher throughput the tracer signals become wider (corresponding to an increase of the axial dispersion coefficient) indicating that the drop sizes are not as uniform as they were before. The slightly higher values of the wiremesh packing may be attributed to a wider drop size distribution caused by the different structure. The differences are too small for a safe interpretation.

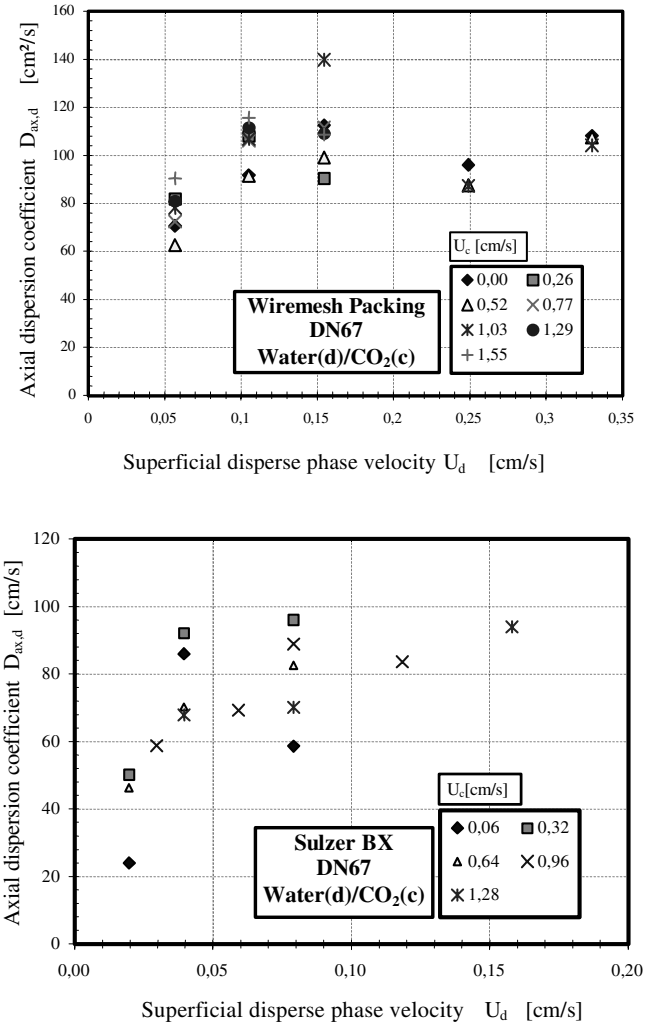

Fig. 17. Measured values of dispersion coefficients in the drop phase for both packings.

4.6. RTD experiments with propane

The question whether the supercritical state of the continuous phase has a particular impact upon backmixing and may influence the separation efficiency was investigated with propane as continuous phase. The pressure was set to 50 bars and the temperature to 60°C. At these conditions the state of the solvent is supercritical with respect to pressure but is below the critical point regarding the temperature and can therefore be considered as a moderately compressible liquid. Its viscosity is similar to that of supercritical carbon dioxide (see Table 2).

The tracer experiments using propane were run identical to those with carbon dioxide. The tracer substances were the same and the Sulzer BX packing was installed.

The measured velocities of the propane phase were similar to that of carbon dioxide. A detailed evaluation of absolute values was unfortunately not possible because of a defective sensor circuit which caused an almost constant but afterwards not correctable deviation.

As shown in the following Fig. 18 the experimentally found values of the axial dispersion coefficient were in the same range as with carbon dioxide but over all slightly lower. It seems that the disperse phase load has a stronger impact but a clear trend is not given.

One possible reason for the observed higher dispersion coefficients in the supercritical carbon dioxide could be the proximity of the operating conditions

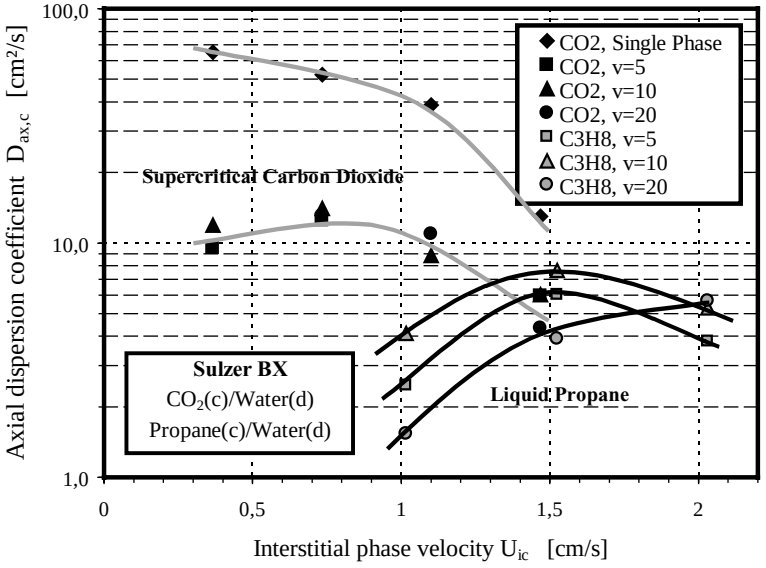

Fig. 18. Comparison of dispersion coefficients with supercritical CO_2 and liquid propane as solvent phase in the Sulzer BX packing.

to its critical point. Already minute temperature differences may lead to unwanted density convections which particularly at low continuous phase velocities result in increased axial mixing. With liquid propane the density changes with temperature are significantly lower hence superimposed convectional flows are rather unlikely.
The tracer experiment results in the drop phase are practically identical to those with carbon dioxide as continuous phase. The density difference between propane and water is about 165 kg/m³ higher but this does not lead to measureable differences in the average drop phase velocity. A comparison with the values of carbon dioxide in Fig. 19 shows that the differences are in the range of the experimental data scattering. The geometry of the channels in conjunction with the falling droplets seems to be of major influence notably because the drop diameters are in the same range as with carbon dioxide.

5. SUMMARY

To extract water phases with compressed gases large solvent ratios are usually required and high density differences are present. The viscosity of the super- or nearcritical continuous phase is about one order of magnitude lower as in conventional liquids, which intensifies the adverse impact of unfavourable flow patterns caused by the missing viscous damping effect.

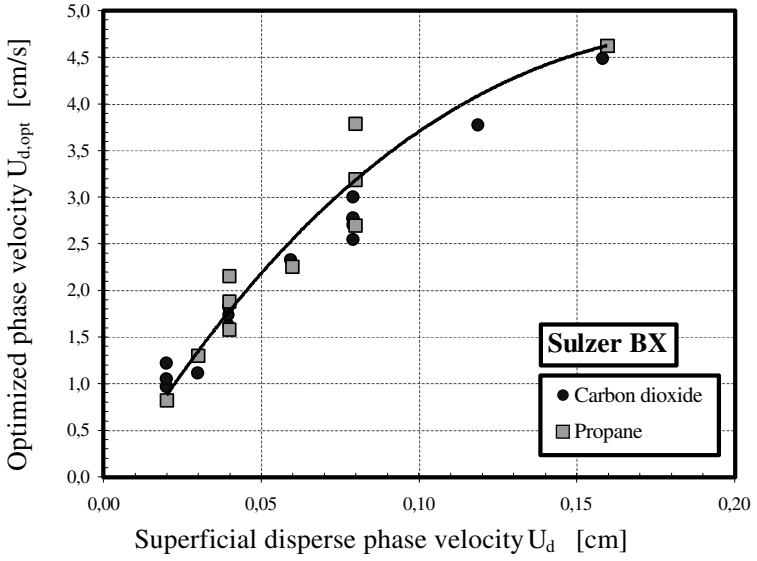

Fig. 19. Comparison of measured drop phase velocities with liquid propane and carbon dioxide as continuous phase.

The lower separation efficiency of the wiremesh packing compared to the Sulzer BX packing can mainly be attributed to two reasons:

One is the smaller interfacial area determined on the basis of drop size and hold up measurements. This is also supported by the fact that the drop phase velocities in the cross channel structure were smaller than in the wiremesh packing. In addition the comparison of results with carbon dioxide and propane indicate that the drop phase velocity is apparently far more determined by the structure of the packing as by the density difference between the phases.

The second reason for the lower separation efficiency of the wiremesh packing was found by evaluation of the residence time distribution in the continuous phase. It turned out that the geometry of the wiremesh packing produces a strongly increased continuous phase flow velocity in the center of the packing whereas the flow in the boundary regions close to the wall stays low. The radial velocity gradient caused by this flow pattern was the reason for increased axial dispersion effects which in turn diminished the separation efficiency.

The impact of the presence of the drop phase upon back mixing is positive in both tested packings. In the wiremesh packing with its rolled up structure, a higher dispersed phase load leads to an equilibration of the continuous phase velocity profile because the flow resistance in the packing center is increased. In the BX packing the drop phase blocks the flow path of the continuous phase in a way that it can't penetrate the wiregauze directly. This leads to a strongly reduced backmixing compared to single phase flow. The amount of disperse phase present in the column is obviously of minor importance with this packing.

Going from supercritical to liquid state as done by applying carbon dioxide at 100 bar and 40°C and then propane at 50 bar and 60°C showed that the backmixing behaviour was slightly different. Propane as continuous phase showed visibly lower axial dispersion coefficients as carbon dioxide. It can be assumed, that in the vicinity of the critical point of a solvent, superimposed density convections may contribute to an increased axial mixing particularly because the viscous damping effect is much lower than with conventional liquids.

In addition to the experiments with the high pressure column a further experimental program was conducted with conventional liquid/liquid extraction column measurements in laboratory and industrial size [9,27]. Based on these results a model was set up in order to allow the calculation of axial dispersion coefficients in liquid/liquid and supercritical extraction columns. It turned out that the results of the wiremesh packing did not follow the general trend probably because the deviations caused by the irregular flow pattern were too large.

6. NOTATION

a_p	[m²/m³]	Specific packing surface area
B_{ges}	[kg/m²s]	Total column load
d_{32}	[m]	Sauter diameter of droplets
$D_{ax,i}$	[m²/s]	Axial dispersion coefficient in phase i
HDU	[m]	Dispersion height [= $(D_{ax,i}/U_i)$]
m'_{yx}	[-]	Slope of equilibrium line in distribution diagram (dw_y/dw_x)
m_{yx}	[-]	Slope of equilibrium line in concentration diagram (dc_y/dc_x)
n_{th}	[-]	Number of theoretical stages
U_i	[m/s]	Superficial velocity of phase i
U_{ic}	[m/s]	Interstitial velocity of the continuous phase $[= U_c/(\varepsilon(1-\phi_d))]$
$U_{i,opt}$	[m/s]	Velocity of phase i obtained from time domain fit
U_{so}	[m/s]	Free falling drop velocity
v	[kg/kg]	Solvent ratio
w_i	[kg/kg]	Weight fraction of transferred compound in phase I

Greek Symbols

ε	[m³/m³]	Packing void fraction
ϕ_d	[m³/m³]	Fraction of dispersed phase in free column volume
η	[-]	Prefactor
λ	[-]	Extraction factor [$=m_{yx}U_y/U_x$]
$\Delta\rho$	[kg/m³]	Density difference
σ	[N/m]	Surface tension
ζ	[-]	Tortuosity factor [$=a_p d_{32}/2$]

Indices

c	Continuous phase
d	Disperse phase
x	Raffinate phase
y	Extract phase
α	Entering flow
ω	Exiting flow

REFERENCES

[1] Blaha-Schnabel, A., Peter, S., Weidner, E. et al.: Influence of interfacial tension and viscosity on the bahavior of a packed column in near-critical fluid extraction; Chem. Eng. Com. 146 (1996), S.13.

[2] Rauscher, H.: Untersuchungen einer pulsierten Siebboden-Extraktionskolonne bei extremen Phasenverhältnissen; Dissertation, TU München, 1992.

[3] Rauber J.: Untersuchungen zum Trennverhalten von strukturierten Packungen bei der Flüssig/flüssig-Extraktion mit hohen Phasenverhältnissen; Dissertation, Universität Erlangen, 1996.

[4] Brunner, G.: Industrial process development countercurrent multistage gas extraction (SFE) processes; J. Supercrit. Fluids 13 (1998), S.283.

[5] Miyauchi, T., Mc Mullen, A. K., Vermeulen, T.: Longitudinal dispersion in two-phase continuous flow operations: Calculation methods; U. S. Atomic energy comission, Report No. UCRL-3911 Rev., 1960.

[6] Stemerding, S., Zuiderweg, F. J.: Axial mixing and its influence on extraction efficiency: A simplified approximation method for design calculations; The Chem. Eng. (1963) 5, S.CE156.
[7] Marr, R., Moser, F.: Vermischungseffekte in Flüssig/Flüssig-Extraktionskolonnen; Chem.-Ing.-Tech. 50 (1978) 2, S.90.
[8] Czech, B.: Das Betriebsverhalten einer Gegenstromkolonne bei der Erzeugung von Diglyceriden mit Hilfe der nahekritischen Extraktion; Dissertation, Universität Erlangen, 1991.
[9] Becker O.: Axiale Vermischung und Maßstabsvergrößerung bei statischen Kolonnen für die Extraktion von Flüssigkeiten; Fortschr.-Ber. VDI Reihe 3 Nr. 750, VDI Verlag: Düsseldorf 2002.
[10] N. Ikawa, Y. Nagase, T. Tada et al.: Separation process of ethanol from aqueous solutions using supercritical carbon dioxide; Fluid Phase Equil. 83 (1993), S.167.
[11] T. Gamse, I. Rogler, R. Marr: Supercritical CO_2 extraction for utilisation of excess wine of poor quality; J. Supercrit. Fluids 14 (1999), S.123.
[12] J. A. Riddick, W.B. Bunger, T. K. Sakano: Organic solvents, 4. Ed., John Wiley: New York 1986.
[13] D. Walther: Messung und Korrelation von Hochdruck-Dampf-Flüssigkeits-Gleichgewichten in binären Mischungen aus Kohlendioxid und Benzolderivaten bei Temperaturen von 313 K bis 393 K und Drücken bis 22 MPa; Dissertation, Universität Kaiserslautern 1992.
[14] B. Bjola: DFG Final Report 1997
[15] G. Heydrich: Untersuchungen zum Trennverhalten von strukturierten Packungen bei der Extraktion mit verdichtetem Kohlendioxid; Dissertation Universität Erlangen 1999
[16] VDI Wärmeatlas; Springer Verlag: Berlin 1997.
[17] S. Hirohama, T. Takazuka, S. Miyamoto et al.: Measurement and correlation of phase equilibria for the carbon dioxide-ethanol-water system; J. Chem. Engng. Jap. 26 (1993) 4, S.408.
[18] Fa. Tega: Personal Communication.
[19] A.V. Shvarts, G. D. Efremova: High-order critical phenomena in the system ethanol-water-carbon dioxide; Rus. J. Phys. Chem. 44 (1970) 4, S.614.
[20] R. E. Treybal: Liquid Extraction; 2. Ed., McGraw Hill: New York 1963.
[21] L. Bernad, A. Keller, D. Barth et al.: Separation of ethanol from aqueous solutions by supercritical carbon dioxide – comparison between simulation and experiments; J. Supercrit. Fluids 6 (1993), S.9.
[22] A. F. Seibert, J. R. Fair: Hydrodynamics and mass transfer in spray and packed liquid-liquid extraction columns; Ind. Eng. Chem. Res. 27 (1988) 3, S.470.
[23] J. R. Grace, T. Wairegi, T. H. Nguyen: Shapes and velocities of single drops and bubbles moving freely through immiscible liquids; Trans. IChemE 54 (1976) 1, S.167.
[24] O. Levenspiel, T. J. Fitzgerald: A warning on the misuse of the dispersion model; Chem. Eng. Sci. 38 (1983) 3, S.489.
[25] V. Rod: Calculating mass transfer with longitudinal mixing; Brit. Chem. Eng. 2 (1966) 6, S.483.
[26] W. J. Korchinsky: Liquid-liquid extraction column modelling: Is the forward mixing influence necessary?; Trans. IChemE 70 (1992) Part A, S.333.
[27] O. Becker: Axial mixing and scale up in static packed liquid extraction columns; Chem. Eng. Technol. 26 (2003) 1, S.35.

Supercritical Fluids as Solvents and Reaction Media
G. Brunner (editor)

Chapter 4.2.

Separation of organic compounds from aqueous solutions by means of supercritical carbon dioxide.

G. Brunner[a], M. Budich[b]

[a]Technische Universität Hamburg-Harburg, Eissendorfer Str. 38, D-21073 Hamburg, Germany

[b]BASF AG, D-67056 Ludwigshafen, Germany

SUMMARY

Supercritical fluid extraction (SFE) was applied to separate multicomponent liquid mixtures by means of countercurrent SFE, in particular concentrating volatile (non-electrolyte) organic components from aqueous solutions using supercritical carbon dioxide (CO_2). Experiments were carried out with mixtures of CO_2+ethanol+water because a variety of mixtures includes ethanol and water, e.g. alcoholic beverages, aqueous-ethanolic plant extracts, and fruit juices. Therefore, distribution coefficients of several volatile components such as acetaldehyde, ethyl acetate, ethyl butyrate, hexanal, and linalool were measured as a function of the percentage of ethanol in the liquid mixture. Selectivity of volatile organic components was strongly influenced by the percentage of ethanol in the liquid phase. The experimental technique of VLE measurements was improved by taking sample into a flask cooled with liquid nitrogen and separating CO_2 and condensate afterwards. Countercurrent extraction of ethanol-water mixtures was improved by refluxing liquid CO_2 to the top of a separation tower. The height of one theoretical stage was found to be a function of the ethanol content of the liquid phase. During flooding point measurements, a low cross-section capacity was observed for the close-meshed EX packing for liquid mixtures of high water content. This phenomenon was not observed for another type of structured packing with larger spacing (Sulzer CY packing). Therefore, the limited cross-section capacity for aqueous solutions is explained by the large surface tension between water and the packing material.

1. INTRODUCTION

In the juice processing countries, significant parts of the juice are concentrated to ca. 15% of its initial mass by a cascade of evaporators. The concentrated juice is stored at temperatures around 255 K in stainless steel tanks [1]. Condensate from the first evaporator is distilled in an aroma recovery unit (Fig. 1) in order to prevent loss of volatile flavor components During evaporation, a small quantity of oil which is present in the juice sacs is partly removed. A two-phase mixture is formed in the aroma recovery unit due to the low solubility of oil components in water. The oily fraction is called essence oil. The aqueous aroma phase is called orange aroma, essence, water-phase essence or just water-phase. Essence oil and water-phase are added to juice concentrate to adjust original flavor.

A simplified mass flow diagram (Fig. 2) for citrus processing shows that the available quantity of cold-pressed peel oil and d-limonene predominates that of essence oil and water-phase. Multiplication of quantities by the amount of processed oranges gives the possible world production of raw flavoring material:

- orange peel oil: 71200 metric tons per year,
- essence oil: 1780 metric tons per year,
- water-phase: 8900 metric tons per year.

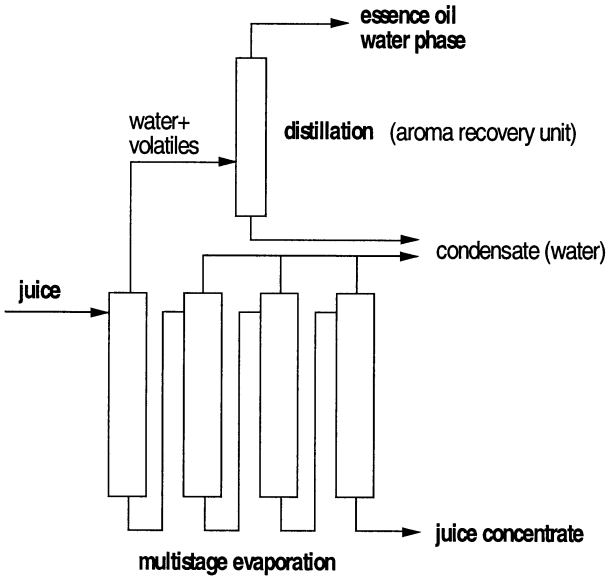

Fig. 1. Juice evaporation and aroma recovery.

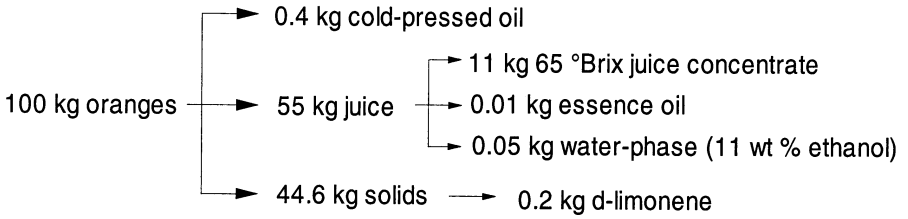

Fig. 2. Mass flow diagram for citrus products [2].

The above calculated annual world production is in good agreement with literature data of Moshonas and Shaw [3]. Aqueous flavor concentrates, which are recovered after juice evaporation, contain the most volatile fraction of flavor components. Due to very low thresholds of around a few ppb, these volatile components contribute significantly to the flavor of the juice. Water-phase that is available on the market is usually concentrated by distillation. The composition of a water-phase is a function of the operating conditions of the process and the quality of the original juice. Special attention has to be paid on avoiding the loss of high-volatile components with non condensable gases.

Extraction with supercritical carbon dioxide (SFE)could probably be used effectively to recover and concentrate the valuable organic compounds. The investigation of citrus oil flavor compounds serves as an example for treating non-electrolyte volatile organic compounds dissolved in water-ethanol systems. Ethanol is the major volatile organic component in orange juice (maximum 0.3 wt %; [4]). Therefore, it is collected in the aroma recovery unit, and it is common to refer to the ethanol content of a water-phase. Aroma recovery units in citrus industry are adjusted to produce water-phase with an ethanol content of 15 vol % (equal to 12.2 wt %) or less to avoid taxes due to larger ethanol concentrations. According to Shaw [5], most producers of aqueous fruit essences adjust the ethanol level to 13 vol % (10.6 wt %) because customers are used to this quality, although the production of high-proof concentrates would reduce storage and transportation costs.

Characteristic organic components of orange water-phase are illustrated in Table 1. Acetaldehyde, ethyl acetate, and ethyl butyrate belong to the topnote fraction that adds a fresh character to the juice. With an increase in molecular weight, solubility in water becomes less due to a decrease in polarity. Water-phase with around 11 wt % of ethanol and essence oil form a two-phase mixture in phase equilibrium. Aroma components dissolved in the water-phase are significantly polar and of low molecular weight, as e.g. acetaldehyde, ethyl acetate, ethyl butyrate, and different groups of C6-aldehydes. Nonpolar terpenes and oxygenated terpene-derivatives represent the essence oil phase and are of minor importance for water-phase composition.

Table 1
Organic components in orange water-phase of 11 wt % ethanol

Name, formula, molecular weight [g/mol], boiling point [6], [K]	**Group**	**Structure**	**Quantity** [1], **[ppm], solubility in water** [7] **at 293 K [wt %]**
acetaldehyde, C_2H_4O 44.05; 293.35	aldehyde		603 completely miscible
methanol, CH_4O 32.04; 337.85	alcohol	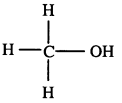	5000 [8] completely miscible
ethyl acetate, $C_4H_8O_2$ 88.1; 350.25	ester	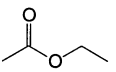	50 ca. 8.5
ethyl butyrate, $C_6H_{12}O_2$ 116.16; 394.15	ester	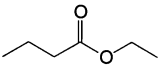	11 ca. 0.68
hexanal, $C_6H_{12}O$ 114.18; 401.18 [9]	aldehyde	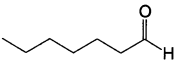	28 0.6 [9]
trans-2-hexenal, $C_6H_{10}O$ 112.17; 419.65 [10]	aldehyde	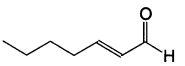	10 v.sl.s.
linalool, $C_{10}H_{18}O$ 154.24; 471.15	alcohol	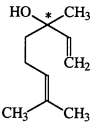	37 v.sl.s.

(v.sl.s. = very slightly soluble).

When applying vacuum distillation to produce a concentrated water-phase, an effective cooling system is required to recover volatile components, but some parts of the volatile fraction are always lost together with the non-condensable inert gases and removed by the vacuum pump. Detailed explanations on the recovery of volatiles from evaporator condensates are given elsewhere [11]. Dealcoholization plants for beverages use wash towers for the recovery of volatiles [12], and parts of the wash water are added to the dealcoholized product.

The removal of high-boiling aroma components from water is favored by the presence of ethanol that acts as an entrainer and improves the yield. Furthermore, the low water solubility of some high-molecular weight components results in a large enrichment in the vapor phase regardless of pure component's boiling points [13]. Whenever vacuum or atmospheric distillation are applied to a further fractionation of a fruit juice water-phase, topnote fractions of high commercial value can be produced, but high quantities of ethanol affect the selectivity of the separation process.

Conventional fractionation processes of aqueous phases may include solvent extraction, gas stripping, and reverse osmosis. Suitable solvents for extraction could be isopentane and diethyl ether, but are of low importance due to food safety standards. Separating orange water-phase by reverse osmosis is not carried out in large scale. Laboratory tests showed a decreasing yield with increased ethanol content linked with a loss in acetaldehyde due to its small molecular weight [14]. Liquid or supercritical carbon dioxide have been proposed three decades ago as solvents [15]. We will report on the results of our investigation below.

2. SUPERCRITICAL FLUID EXTRACTION OF AQUEOUS SOLUTIONS

2.1. Literature review

Separation of organic components from aqueous solutions by SFE was proposed for a variety of applications. To distinguish different objectives, three main research topics can be defined and are illustrated with some examples:

- production of valuable organic fractions:
  - separation of azeotropic mixtures,
  - recovery of (volatile) flavor fractions,
  - purification and fractionation of plant extracts.
- removal of undesirable or waste organic components:
  - dealcoholization of beverages,
  - separation of impurities from fermentation processes,
  - industrial waste water treatment,
- enrichment procedures for analysis of aqueous samples.

Analytical procedures cover preconcentration methods to detect trace components in aqueous samples and to fractionate complex mixtures. Although CO_2 favors nonpolar or lipophilic components, polar or high-molecular weight components can also be extracted from aqueous solutions due to low solubility of high-molecular weight components in water. This is easily demonstrated with caffeine [16].

One application that was never realized commercially is dehydration of aqueous coffee extract combined with decaffeination in spray columns using supercritical CO_2. This process was proposed in a patent by Zosel [17]. No significant change in flavor was reported when producing caffeine-free instant coffee. While the formation of foam must be taken into account for countercurrent treatment of aqueous coffee extracts, solutions of pure caffeine in water do not show any foaming due to the absence of surfactants [18]. Foaming may be minimized by enforcing the formation of a thin film of liquid rather than bubbling

bling CO_2 through a liquid phase [17]. The tendency of natural aqueous solutions to form stable foam limits the use of countercurrent processes where foam causes flooding.

The treatment of industrial waste water was studied for some phenols in analytical scale [19], and small quantities of polycyclic aromatic hydrocarbons were successfully detected combining SFE and SFC [20]. Metal ions were removed from aqueous solutions by forming less polar complexes with ligands that have a good solubility in supercritical CO_2 [21].

Another application is the separation of carbohydrates from aqueous solutions [22]. The solubility of carbohydrates in the vapor phase was enhanced by adding an entrainer, either 2-propanol or ethanol. However, separation factors remained too small for an economic fractionation. Further measurements were carried out with the objective to form two liquid phases and to study partitioning of different carbohydrates between an aqueous and an organic phase for the system CO_2+acetone+water [23]. It was found that some carbohydrates decompose in the ternary mixture. Therefore, this process cannot be applied for the production of high-grade carbohydrates. However, the formation of a second liquid phase in supercritical gas+organic solvent+water systems is an interesting phenomenon and is in analogy to the salting-out effect of solids in the presence of a third component [24]. This enables the recovery of many organic solvents from aqueous solutions. Details about the complex phase behavior of ternary systems comprising CO_2, water, and an organic solvent are reported by Adrian [25].

Dealcoholization of beverages by supercritical fluids was investigated for wine and beer to improve the recovery of volatile aroma components by Perrut [26]. So far, the demand of the market is rather low. Naturally, it is almost impossible to reduce the amount of ethanol without losing the character of a product. However, the steady development of improved membrane processes and aroma recovery units resulted in various industrial dealcoholization processes [12]. Research groups from all parts of the world studied the system CO_2+ethanol+water or carried out extraction of fermented aqueous solutions with liquid or supercritical gases, especially CO_2 and propane. All conventional methods to separate ethanol and water include disadvantages like a high energy demand for heating that increases with the desired purity of ethanol. The use of additives requires additional separation processes. Membrane processes show limits in yield and throughput. Therefore, the use of supercritical solvents has been studied for decades. Results of our own investigation have been published separately [27, 28]

Besides alcoholic beverages, other liquid mixtures comprising ethanol and water are involved in separation processes. Complex aqueous mixtures like distilled flavor concentrates from fruit juices are characterized by a high percentage of natural ethanol compared to the quantity of other organic components. There-

fore, phase equilibria of such an aqueous organic mixture and a supercritical gas are influenced by the behavior of the mixture ethanol+water.

Many pharmaceutical standard procedures use mixtures of ethanol and water to extract plant material [29]. If unwanted components from the plant are also dissolved, extracts require further purification. For some applications, an ethanol-water extract is already the final product, but usually distillation is applied to concentrate the valuable part of a diluted mixture. It might also be necessary to fractionate hydrophilic and lipophilic components or polar and nonpolar fractions, respectively. Preparative chromatography can be applied to obtain products very rich in a certain component.

2.2. Removal of impurities from ethanol+water mixtures.

Fukuzato et al. [30] studied the removal of impurities from a fermentation broth in a pilot plant of 14 m total height and 230 mm ID. It was proposed to remove impurities from a diluted feed by supercritical CO_2 prior to atmospheric ethanol distillation. The combination of SFE with conventional distillation was reported to be more economic than a two-step SFE process. Experiments on the pilot plant were performed as follows. Methanol, isoamyl alcohol, and n-propanol were added at infinite dilution to aqueous mixtures of ethanol. VLE measurements were carried out with liquid CO_2 at 298 K and 7.1 MPa and with supercritical CO_2 at 313 K and 10.1 MPa. The results are illustrated in Fig. 3 and compared to data of Hirohama et al. [31].

CO_2 is more selective for ethanol than for methanol, and separation factors remain almost constant at different operating conditions but change with increasing ethanol concentration of the aqueous phase. At low ethanol concentrations, the separation factor of a certain alcohol to ethanol is mainly a function of the polarity of this component or its water solubility, respectively. Therefore, the separation factor of a component of very low water solubility like isoamyl alco hol is around 100 with respect to ethanol in diluted aqueous solutions. For all components that were investigated by Fukuzato et al. [30] and Hirohama et al. [31], separation factors approach unity at high ethanol concentrations.

This is due to the increasing solubility of all components in the aqueous phase. Moreover, at most conditions, except 334 K and 10 MPa, the ternary mixture CO_2+ethanol+water is of type I, and separation of impurities from ethanol is limited by solubility. Fukuzato et al. [30] concluded that supercritical fluid extraction of impurities from fermentation broths should be carried out prior to the separation of ethanol from water. To minimize the loss of ethanol during purification, it was suggested to supply water to the top of the purification column to reduce the loss of ethanol. The feed used for pilot plant experiments contained 90 wt % of ethanol. Purification was carried out with liquid CO_2 at 298 K and 7.5 MPa, and the product was almost free of impurities at a solvent-to-feed ratio of only 2. Some ppm of acetaldehyde and methanol remained in the raffinate.

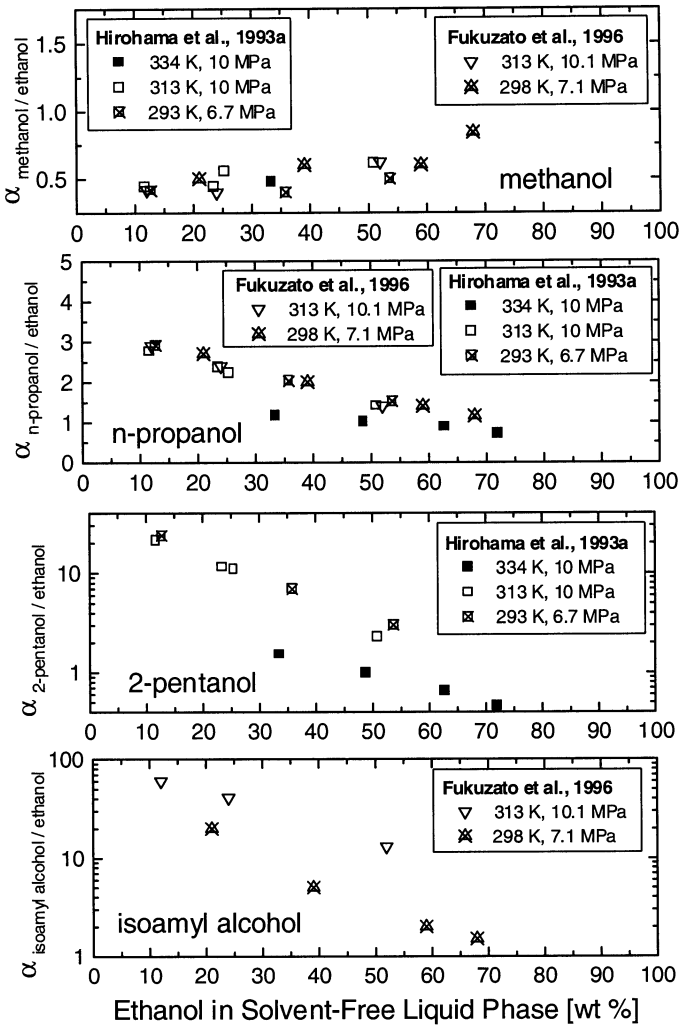

Fig. 3. Separation factors of alcohols to ethanol.

Pilot plant capacity was not fully exploited with an absolute solvent flow rate of 210 kg/h, equal to a cross-section capacity of 5054 kg/(m²h). The pilot plant was disassembled after the project was finished [32] because the number of plants that are allowed to produce ethanol in Japan is limited.

Hirohama et al. [32] studied the separation of acetaldehyde, methanol, n-propanol, ethyl acetate, and 2-pentanol from aqueous ethanol solutions at different temperatures and pressures, see Fig. 4. Separation factors were lowest at 334 K and 10 MPa, when the ternary mixture CO_2+ethanol+water is of type II. No data are available for separation factors in pure ethanol, but it can be assumed

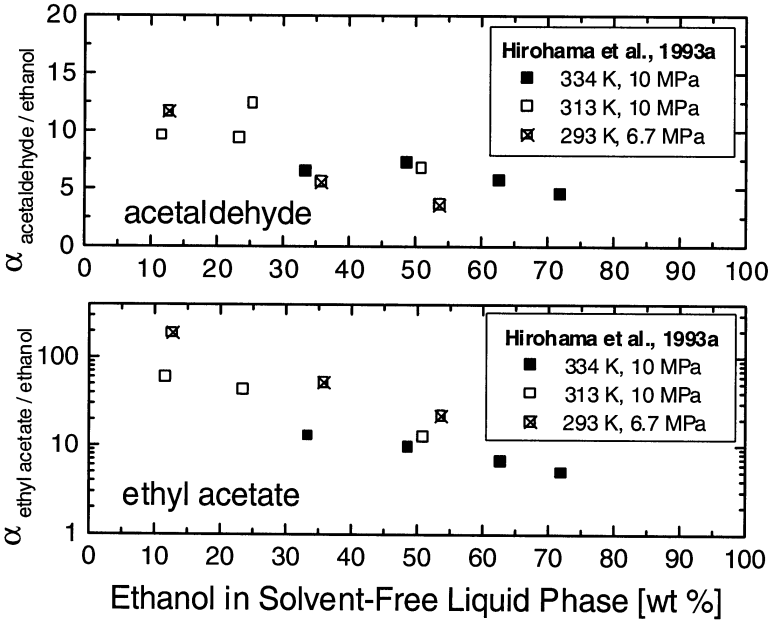

Fig. 4. Separation factors of volatile organic components to ethanol.

that selectivity of CO_2 will only be influenced by vapor pressures. Therefore,separation factors of alcohols of higher boiling point to ethanol like n-propanol and 2-pentanol will be less than 1 at higher ethanol concentrations of the liquid phase.

After observing best separation of impurities with liquid CO_2 at near-critical conditions, Hirohama et al. [33] investigated countercurrent extraction combined with an ethanol recovery unit. To reduce loss of ethanol during the extraction of impurities, CO_2 was fed to the bottom of a second column charged with water from the top. The water-to-solvent ratio was adjusted to recover most of the ethanol. Impurities were separated from the solvent in a third column. Internal reflux of liquid CO_2 was proposed to improve separation of volatile components from the solvent. Hirohama et al. [33] did not direct attention towards the production of anhydrous ethanol. An additional countercurrent column would be required to separate ethanol and water after removing impurities from the feed.

2.3. Production of aqueous flavor concentrates.

One of the first studies on volatile flavor concentrates from fermented beverages was reported by Jolly [34] who worked with liquid CO_2 to extract wine aroma. It was suggested to use this aroma concentrate to improve flavor character of wine that is poor in quality. Prior to extraction, suspended particles were

removed by a centrifuge or filter to avoid contamination of packing material with solids and to reduce the tendency of the natural product to foam. Further research on wine aroma was reported in different patents (Wiesenberger et al. [35]; Seidlitz et al., 1990 [36]) and scientific papers (Fernandes et al. [37], Gamse et al. [38]), but according to Perrut [26], industrial acceptance is still very small. However, as long as large quantities of poor quality wine are used for ethanol production each year, flavor concentrates could be exploited as valuable byproducts of this process.

Seidlitz et al. [36] proposed the removal of organic components from alcoholic beverages by vacuum distillation followed by separation of flavor components from the distillate by using near-critical CO_2. Advantages of this technique include the avoidance of foam formation, reduction of process costs due to lower volume of product that is treated under high pressure. As known from other papers, e.g. Gamse et al. [38], contacting gaseous CO_2 with liquid CO_2 in the separator was reported to improve the recovery of organic components from the solvent.

Perrut [26] evaluated several papers in this field and added results of own experiments. White wine was treated with CO_2 in a countercurrent column and separated by two-step decompression. The first extract was rich in water and ethanol but also had some wine flavor, whereas extract withdrawn from the second separator was less in quantity but rich in volatile flavor. Aroma recovery was greatly enhanced by using a packed column instead of a cyclone separator for the second separation step. Although there is no further explanation in the paper, this effect seems to be due to the realization of liquid CO_2 reflux.

For aroma recovery from fruit juices, Randall et al. [39] first intended to extract a flavor fraction directly from fruit juices. After observing the formation of foam, the authors suggested to work with aqueous flavor distillates from fruit juices or essential oil instead. The good quality of CO_2 extracts obtained from aqueous apple essence was reported earlier by Schultz et al. [15]. Distribution coefficients of flavor components were derived from experiments in a continuously operated single-stage apparatus [39]. After sampling and analyzing the aqueous phase which had been in equilibrium with liquid CO_2, distribution coefficients were calculated from the difference between composition of feed and sample. Results are illustrated in Fig. 5, including linear and branched molecules. Liquid CO_2 showed a higher selectivity for esters than for alcohols. This is due to the lower polarity of esters equal to a lower solubility in the aqueous phase. Distribution coefficients of components of homologous series increased exponentially with a linear increase of the number of carbon atoms. Very similar results were obtained by Fukuzato et al. [30] and Hirohama et al. [30].

A countercurrent apparatus was constructed by Schultz et al. [40] consisting of a Scheibel column of about 3 m total height and 40 mm ID. Recovery of organic components was below 50 wt %, because regeneration of the solvent

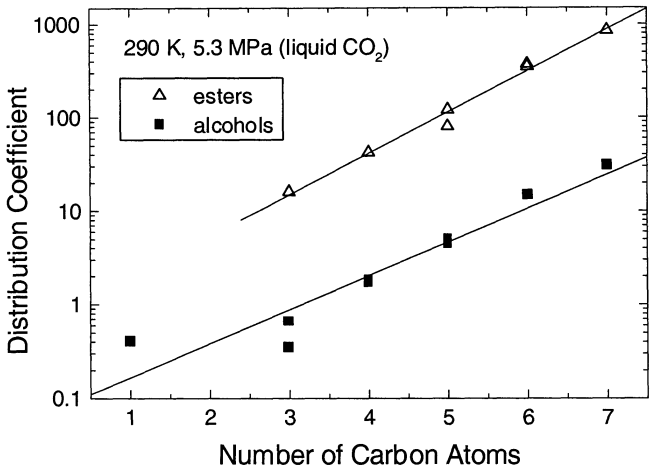

Fig. 5. Influence of the carbon number on distribution coefficients.

was incomplete. Therefore, volatile components like ethyl acetate and isoamyl alcohol were recirculated in higher concentration with the solvent than low volatile components like α-terpineol or carvone.

A new technique combining the use of membranes with SFE was proposed by Sims et al. (1996) [41] and applied to aqueous solutions of volatile flavor components from fruit juices. Liquid CO_2 is passed on one side of the membrane, the fruit juice on the other. Selective removal of flavor compounds from the liquid feed mixture is caused by concentration gradients across the membrane. It is reported that intra-membrane resistance is minimized by the high diffusivity of near-critical CO_2. Recovery of many characteristic flavor components was above 95 % at 297 K, 10 MPa, and a solvent-to-feed ratio of 2, while methanol and most of the ethanol remained in the raffinate.

2.4. Conclusions and perspectives for further research.

The variety of publications that cover VLE data of aqueous solutions with sub- and supercritical gases is a good basis to investigate several applications, especially for aqueous mixtures that include ethanol. VLE data of different groups for the ternary mixture CO_2+ethanol+water are still not in agreement and imply that experiments with volatile components are difficult to perform.

Supercritical CO_2 is very selective for volatile organic components that are almost insoluble in water. If ethanol is present in the mixture, the separation of flavor or other organic components from the extract is difficult to achieve. Information about the separation of volatile organic components from pure ethanol

is scarce, because most work was carried out at conditions where ethanol was completely miscible with CO_2.

Most available data sets cover measurements with model mixtures. Thus, several problems with natural aqueous solutions are still unresolved, since some phenomena observed and mentioned in literature were not further investigated. This includes foam formation as well as recirculation of volatile components after solvent regeneration and reactive behavior of concentrated fractions in presence of CO_2.

3. OWN INVESTIGATION OF AQUEOUS ORGANIC SOLUTIONS.

3.1. Orange Water-Phase

Commercial Brazilian orange water-phase with 11 wt % ethanol (provided by Eckes-Granini, Nieder-Olm, Germany) was used to investigate the separation of volatile organic components from aqueous solutions. The orange water-phase was stored at 278 K under inert gas (N_2) headspace. After the short storage period of a few weeks, no change in feed composition was observed by repeated GC analysis. For longer storage, it is recommended to keep water-phase at around 255 K to preserve quality [11].

Table 2 lists some key components of orange water-phase. The composition is given in wt % or ppm (mg/kg) and is based on GC analysis using response factors. For the purpose of comparison, the results of three references are shown, of which two are from literature [3, 8] and one of the same feed material carried out by a specialized laboratory (Eckes-Granini, Nieder-Olm, Germany). According to GC analysis, the feed material contained 88.5 wt % water, 11 wt % ethanol, and around 0.5 wt % other organic volatiles. Literature data show the variety of composition for different products. Differences between the analysis carried out in this work and additional analysis by the specialized laboratory may be due to problems with co-eluting peaks or inaccurate response factors.

The reliability of the GC method of this work was confirmed frequently by analyzing model solutions of known composition. Methanol is present in significant quantities of 0.36 wt %, followed by acetaldehyde with about 700 ppm. Most components with a major impact on flavor character are present in some ppm. Linalool is part of the carbonyl fraction that is almost insoluble in water. Components listed in Table 2 can be also found in many other fruit juices [3] and fermentation broth [31].

Table 2
Composition of natural orange water-phase.

Component	This work	Comparable analysis [1]	Literature A [8]	Literature B [3]
acetaldehyde	720 ppm	603	600	193
ethyl acetate	17 ppm	50	100	-
methanol	0.36 wt %	-	0.5	0.29
ethanol	ca. 11 wt %	-	13	12.22
ethyl butyrate	11 ppm	11	50	10
hexanal	14 ppm	28	-	5
trans-2-hexenal	22 ppm	10	-	11
linalool	58 ppm	37	-	84
water	ca. 88.5 wt %	-	85	87.3

3.2. Analytical procedures for aqueous samples

The GC column used for the analysis of organic components in aqueous solutions had a polar layer to enable the separation of volatile components. It had the following specification:

- name: Stabilwax (Restek, Bad Soden, Germany)
- type: polar; polyethylene glycol (PEG) layer
- dimensions: 60 m, 0.25 mm ID, 0.25 μm df.

GC capillary columns are known to be sensitive to aqueous samples. To prevent column damage, a guard column (Hydroguard FS, 5 m, 0.25 mm IS, Restek) was installed before the Stabilwax column by using a "press-tight" connector (Restek). With this set-up, all sample components entered the column with the carrier gas, but condensing and reboiling took place in the guard column.

For sample preparation an internal standard solution was prepared from butyl acetate (IS) diluted in ethanol. A small quantity of this solution was added to each aqueous sample to obtain an overall IS concentration between 0.1 and 0.2 wt %. Whenever sample size was very small, ethanol was added to enable Karl Fischer Titration and GC analysis. Moreover, for very concentrated samples, peak separation was improved by ethanol dilution. GC data were referred to the original sample.

GC Method: Due to very close retention times of some components in natural orange water-phase, the following GC method was developed that enabled a good peak separation. Split ratio, injected volume, and liner were changed to get the desired resolution of sample components.
Injector: 513 K, Detector: 523 K,
Temperature program: 303 K, constant for 5 min,

3 K/min to 353 K,
5 K/min to 513 K,
15 min constant at 513 K

Split ratio: 1:50 (ca. 0.8 mL:40 mL), (carrier gas pressure: 200 kPa)
Liner: "Baffle Splitter" with glass wool (Restek)
Injected sample: 0.5 µl

Samples from experiments with a model mixture did not show problems of coeluting peaks. To analyze ethanol in methanol, it was sufficient to maintain 313 K isothermally for 15 min. For all other samples, the following temperature program was applied:

Modified temperature program: 333 K, constant for 7 min,
5 K/min to 513 K,
10 min constant at 513 K.

Response Factors: The composition of a sample can only be analyzed quantitatively if peak areas are corrected by means of response factors with respect to a suitable internal standard component. The percentage of a component i can be calculated from the percentage of internal standard by Eq. (1).

$$\text{wt \% i} = \text{wt \% IS} \frac{\text{Peak Area i}}{\text{Peak Area IS}} \text{RF}_\text{i} \tag{1}$$

RF_i is the response factor of component i with respect to the internal standard and accounts for the sensitivity of the detector for different molecular fragments. If the same peak area is calculated for samples of equal concentration of i and IS, the response factor would be 1. Response factors were determined with mixtures of model substances of known composition and found independent of water or ethanol content. Besides the sensitivity of the detector, RF_i also compensates for sample handling including injection technique, evaporation effects in the split liner and other methodical errors. Therefore, it is difficult to transfer RF_i values to another GC method. Whenever a small peak elutes right after a large peak, the area of co-elution may cover a large percentage of the small peak. In this case, RF_i is a function of the concentration of component i. This behavior was found for ethanol diluted in methanol. Because the concentration of IS was kept at a constant level, it is equivalent to represent RF_i as a function of the peak area ratio (PAR_i). For all other components, RF_i was almost constant within the PAR_i range from 0.01 to 10. RF_i values are shown in Table 3. The same results were obtained for components dissolved in methanol. Note that RF_i of ethyl butyrate is almost 1, because its chemical structure is very similar to that of butyl acetate. There is a clear decrease of RF_i with retention time.

The decrease of RF_i at higher retention times can be explained by the change of molecular structure. Compared to small molecules like acetaldehyde,

Table 3
Response factors of flavor components in aqueous solutions.

Component	Retention time	Response factor *with respect to butyl acetate*
acetaldehyde	4.98	1.71
ethyl acetate	6.22	1.30
ethyl butyrate	9.18	1.02
hexanal	10.51	0.90
trans-2-hexenal	15.26	0.88
linalool	25.57	0.72

the number of molecular fragments increases for long-chain molecules or components of high boiling point. The clear relationship between retention time and RF_i enables to estimate RF_i for components of a natural water-phase that elute between the components of a model mixture.

The water content of aqueous samples was determined by Karl-Fischer titration (KFT) using a semiautomatic dead-stop titration unit (type TR 152, Schott, Mainz, Germany). The principle of this technique is to measure a solution's conductivity. Hydranal Solvent (No. 34800, Riedel-de Haën, Seelze, Germany) was used as the receiving solvent, and Hydranal Titrant 5 (No. 34801, Riedel-de Haën) as a titrator. Titre was determined both by pure deionized water and by a calibration standard ("Eichstandard 5,00", No. 34813, Riedel-de Haën). While working with a constant quality of chemicals, the value of titre did not change.

Parameters of the titration unit were set to a stop value of 10 μA, a titration rate between 5 and 20 (depending on the amount of water in the sample), and 10 s delay after the stop value was reached. Titre is expressed by Eq. (2). A typical value was 4.88 mg/mL. The water content of a sample is calculated by Eq. (3) with $V_{T,sample}$ as the volume of titrator that is added to compensate the quantity of water in the sample.

$$\text{Titre} = \frac{m_{H_2O}}{V_T} \tag{2}$$

$$wt\ \%\ H_2O = \frac{Titre\, V_{T,sample}}{m_{sample}} \times 100 \tag{3}$$

3.3. Sampling procedure for aqueous systems

Vapor-Phase Sampling: Compared to high-boiling citrus oil components, the measurement of phase equilibria for volatile organic components in aqueous mixtures required additional attention. On the one hand, solubility of extract in

supercritical CO_2 was very low. On the other hand, changes in sample composition due to evaporation of volatile components needed to be minimized.

Liquid nitrogen was used to solidify the entire content of the vapor-phase autoclave. A 250-mL flask was equipped with a top part comprising a capillary

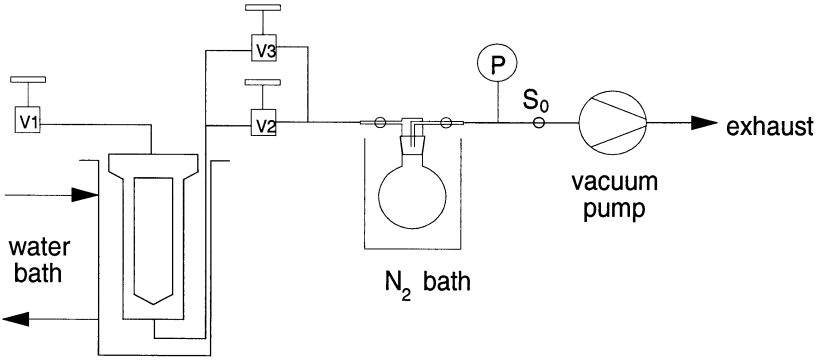

Fig. 8. Sampling procedure for VLE measurements of aqueous solutions.

and two stopcocks, very similar to the upper part of the cold traps. The conical joint was lubricated with silicon grease. The principle set-up is shown in Fig. 8. Special attention was given to the method to transfer the contents of the flask into sample tubes (Fig. 9). A detailed description of the procedure is presented by Budich [42].

Liquid-Phase Sampling: The procedure of sampling into a nitrogen-cooled flask was also applied to liquid-phase samples when a high CO_2 solubility in the liquid phase was observed, e.g. for the binary system CO_2+ethanol. For those mixtures, results were more accurate than those carried out by the capillary method. The amount of liquid phase was limited by the chosen definition of a maximum pressure drop of 0.2 MPa. Sampling of the liquid phase took less than two minutes. Thus, liquid-phase composition was not affected by pressure drop.

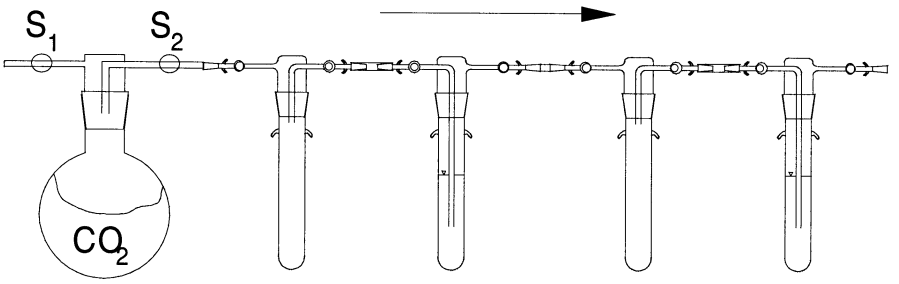

Fig. 9.Set-up for sublimation of solid CO_2.

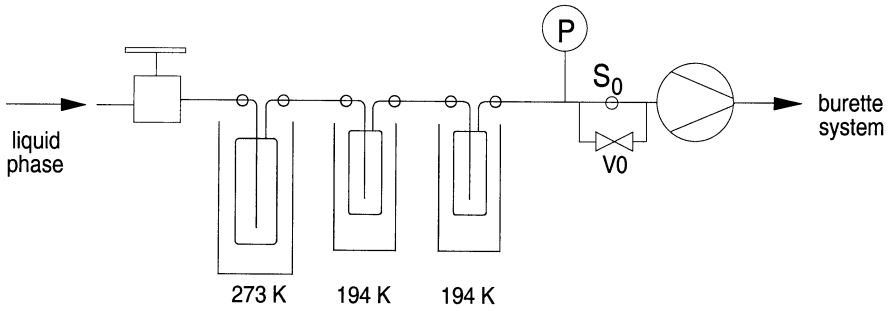

Fig. 10.Liquid-phase sampling for volatile components.

However, for most experiments with aqueous solutions, solubility of CO_2 in the liquid phase was low, and the liquid phase was sampled by the capillary method (Fig. 10). A large cold trap was connected to two regular cold traps cooled by an acetone-dry ice mixture. To enable a better condensation of volatile components, stopcock S_0 was closed after evacuating the cold trap system. While the liquid phase entered the cold traps, the increase in pressure was controlled by a vacuumeter to avoid exceeding 80 kPa absolute pressure. After 30 s of conditioning, S_0 was opened carefully to remove gaseous CO_2 from the cold traps until 0.5 kPa was reached. Then it was closed to avoid removal of the most volatile component acetaldehyde that has a boiling pressure of 0.18 kPa at 194 K [6]. The amount of CO_2 was determined by the burette method.

This discontinuous sampling procedure was repeated until enough condensate (about 2 mL) accumulated in the first cold trap where most of condensable part of the sample remained. The small part of sample that condensed in the second and third trap was not neglectable due to a very different composition. However, it would have been impossible to analyze small drops of volatile condensate from a cold trap after weighing. Therefore, the condensate was transferred from the second and third cold trap to the first in the following way. The contents of the Dewar vessels were changed after sampling. The large trap was cooled by liquid nitrogen, whereas the second and third were heated to 333 K using hot water. The vacuum pump was connected to the large trap, and the final stopper of the regular traps was closed before evacuation. Within a few minutes, every drop of condensate was removed from the regular traps by vacuum and solidified in the large trap. Due to the location of the glass tube, the amount of condensate was limited to a maximum of 5 mL.

After collecting condensate in the large cold trap, liquid-phase samples were stored inside a refrigerator at T_R of around 273.15 K for the same period of time as the vapor-phase sampling flask (~4 hours). Before weighing, stoppers were opened while the cold traps were still inside the refrigerator. After some minutes, conditions inside the trap were supposed to be ambient pressure and T_R. Stoppers were closed before transferring the cold traps to the weighing

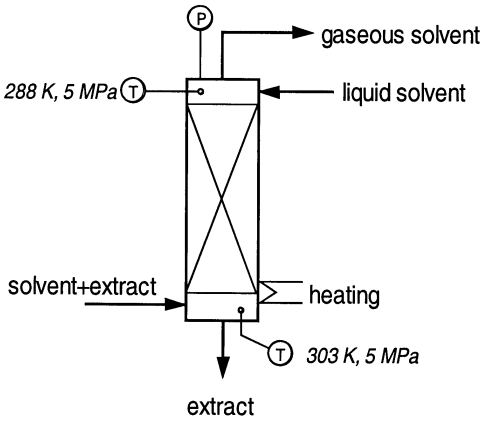

Fig. 11. Improved solvent regeneration.

room. An empty test trap was weighed during several experiments to check the influence of condensing humidity on the surface of the cold trap. Due to fast conditioning of the glass surface and repeated removal of condensed humidity, experimental error was negligible.

3.4. Improvements in solvent regeneration

For aqueous mixtures of organic components a modification of the separation unit that was realized (Fig. 11) if the residual loading of the solvent was still significant after pressure reduction. To reduce the content of the extract compounds in the solvent to a much lower level, liquid solvent obtained from the condenser was pumped to the top of the separation tower. This reflux induced a multistage regeneration of the solvent. The upper part of the separation tower was cooled by the boiling solvent. The bottom heater was set to completely evaporate liquid solvent near the extract inlet. By this technique, the loss of solvent with the extract was minimized. The effect of solvent purification depends on the number of theoretical stages in the separation tower and the reflux ratio of solvent.

4. VLE MEASUREMENTS

Vapor-liquid equilibria of CO_2+ethanol+water mixtures were investigated at 333 K and 10.0 MPa. These conditions were chosen after observing promising results from a paper of Ikawa et al. [43]. the ternary mixture CO_2+ethanol+water was investigated again due to the disagreement of literature data in order to find more accurate data and to develop a reliable sampling technique for volatile components. Measurements were carried out by the conventional sampling method using cold traps cooled with acetone+dry ice and by an improved

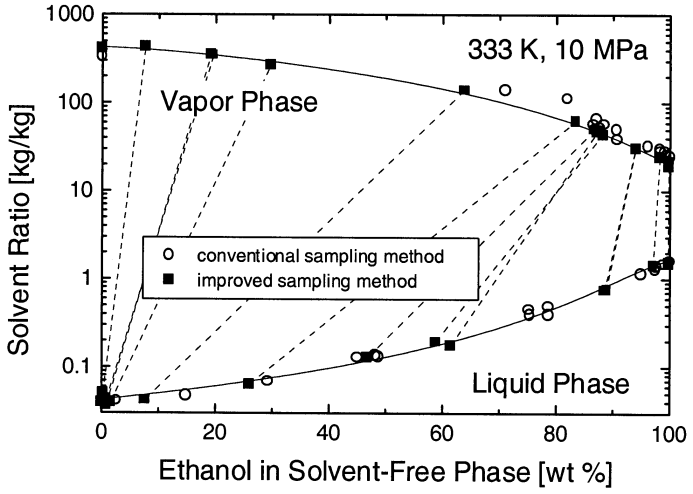

Fig. 12. VLE data of CO_2+ethanol+water at 333 K and 10 MPa.

method using liquid nitrogen (see above). Fig. 12 illustrates VLE data in the Jänecke diagram. Liquid-phase sampling by either the conventional or improved technique yielded similar results. A smaller solubility of extract in the vapor phase was detected by the conventional method, because condensation of sample was incomplete in the acetone+dry ice cooled cold traps.

After observing VLE data of the ternary mixture CO_2+ethanol+water, small quantities of volatile aroma components were added to investigate selectivity of CO_2 for organic components in high dilution. Additional VLE measurements were carried out with a natural orange water-phase. Usually, the percentage of ethanol dominates the percentage of other organic components. Therefore, the behavior of the mixture CO_2+ethanol+water is relevant for many separation problems. Characteristic components in orange juice water-phase were chosen to understand the influence of pure component properties on selectivity. Components of good water solubility included acetaldehyde (completely miscible) and ethyl acetate (8.5 wt %). Ethyl butyrate (0.68 wt %), hexanal (0.6 wt %), trans-2-hexenal, and linalool were chosen to represent components of low water solubility. In fermentation broth, alcoholic beverages, or fruit juices the quantity of these and other flavor components usually ranges from 1 to 100 ppm.

To enable a reliable detection of aroma components by GC, relatively large quantities of aroma components were added to different mixtures of ethanol and water. The concentration of aroma components was set between 150 ppm and 1.5 wt % for each component. Components of high water solubility were added in larger quantities than others. The following diagrams illustrate results of experiments obtained with both the conventional and improved sampling method

that are compared to correlations for the mixture CO_2+ethanol+water. Measurements with the conventional method were performed with orange water-phase and a model mixture, both with an initial ethanol content of 10-11 wt %, whereas a large range in ethanol percentage was investigated with the improved method by using different model mixtures.

Fig. 13 demonstrates the agreement of vapor-phase density of ternary and multicomponent mixtures comprising CO_2, ethanol, and water. Only a few data points at low loading conditions are out of range. In Fig. 14, the Jänecke diagram is shown for the multicomponent mixture in comparison to correlations for the CO_2+ethanol+water mixture. Good agreement was observed when the entire organic fraction of the solvent-free sample was used as parameter instead of the ethanol content. Most vapor-phase data that were obtained by the conventional method show a lower solubility of extract in the vapor phase.

During measurements with the conventional method, two experiments with the mixture CO_2+orange water-phase were performed. After the first experiment, the liquid phase remained in the equilibrium vessel to be used for a second experiment. By this technique, the percentage of organic components in the liquid phase decreased.

Compared to data for the ternary mixture CO_2+ethanol+water, a much lower ethanol content of the vapor-phase condensate was observed for both measurements with original orange water-phase, whereas sample composition for the proceeding experiment was in agreement to results of the ternary mixture. This behavior was not observed during measurements with the improved sampling method.

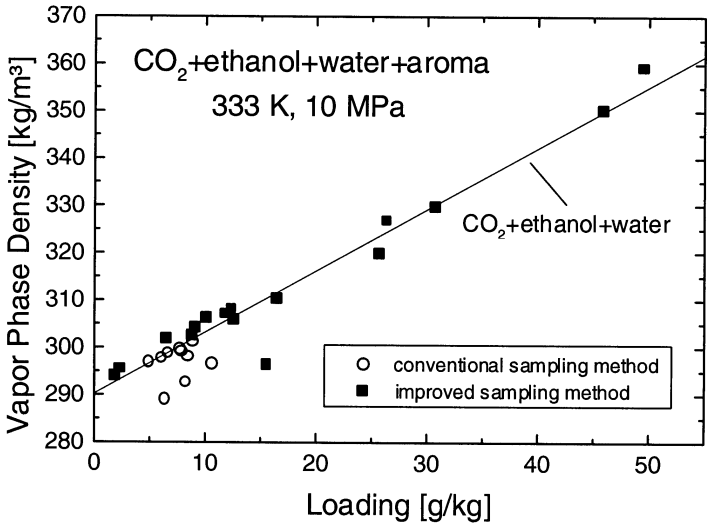

Fig. 13. Density of the vapor phase for multicomponent aqueous mixtures.

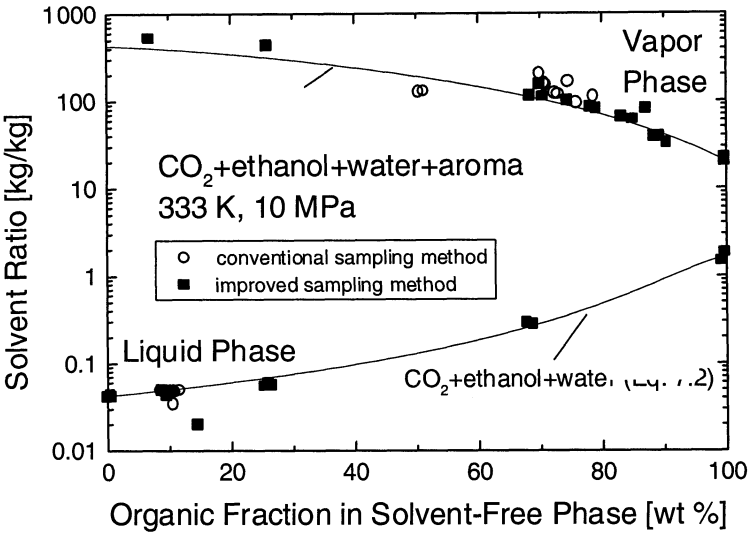

Fig. 14. Comparison of mutual solubility.

Separation factors of ethanol to water are compared in Fig. 15. No significant influence of the initial flavor concentration on VLE data was observed. However, selectivity of CO_2 for aroma components was quite large. The major part of the organic fraction dissolved in the vapor phase. During measurements with the conventional sampling method, parts of flavor components were lost

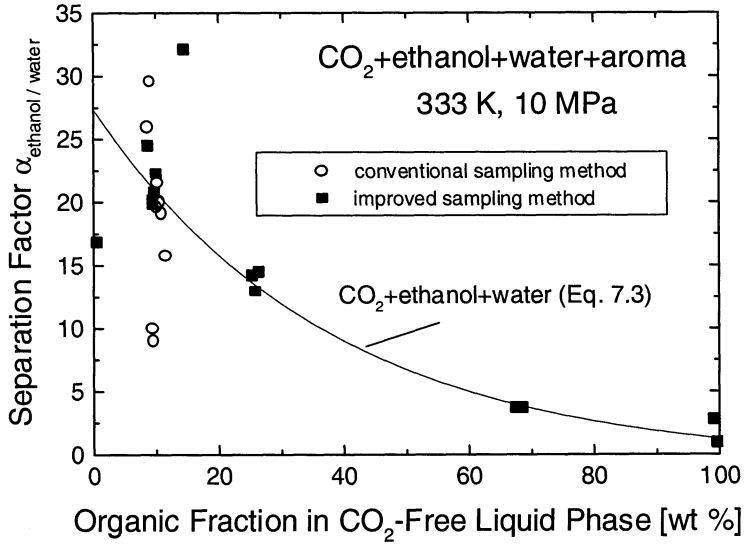

Fig. 15.Comparison of separation factors of ethanol to water.

with gaseous CO_2. Only data from the improved sampling method are presented in the following diagrams. Fig. 15 illustrates that distribution coefficients of volatile organic components decrease with increasing ethanol content of the solvent-free liquid phase. Similar results were reported by Hirohama et al. [31] and Fukuzato et al. [30]. At low ethanol concentrations in the liquid phase, a better enrichment in the vapor phase was found for those components that are characterized by a low solubility in water. Moreover, distribution coefficients of components of the same class are increasing with rising carbon number as shown for ethyl acetate and ethyl butyrate. This effect was presented earlier by Randall et al. [39] for alcohols and esters by using liquid CO_2.

Relatively low distribution coefficients were found for acetaldehyde when dissolved in pure water, whereas at high ethanol concentrations distribution coefficients were larger than those of other components. This is due to the influence of vapor pressures and the fact that all components are completely miscible with ethanol. Therefore, the distribution coefficient of a relatively low volatile component like linalool becomes less than 1 in almost pure ethanol.

The lines in Fig. 16 and the following diagrams visualize the trend of data and have no theoretical background. Scattering of data is due to the different initial concentration of aroma components. The influence of actual aroma content of the solvent-free liquid phase on distribution coefficients is demonstrated in Fig. 17.

The comparison of data for acetaldehyde and ethyl acetate demonstrates that distribution coefficients decrease with an increasing percentage of aroma in the liquid phase. Note that the accuracy of GC data is not guaranteed below a

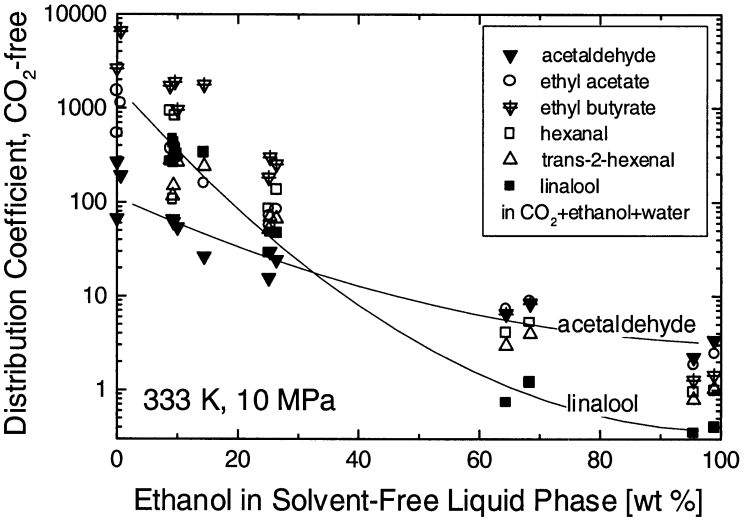

Fig. 16. Distribution coefficients of volatile flavor components.

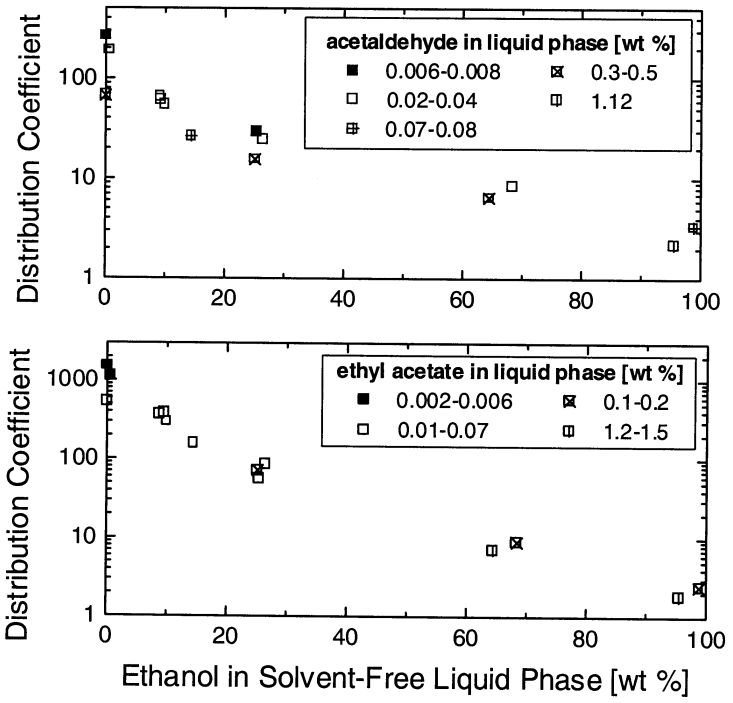

Fig. 17. Influence of concentration on distribution coefficients.

weight fraction of 150 ppm (= 0.015 wt %). However, data of Fig. 17 follow a clear trend, even if the difference is rather low.

The selectivity of CO_2 for flavor components with respect to ethanol is better observed from separation factors. In Fig. 18, separation factors of acetaldehyde and ethyl acetate with respect to ethanol are compared to literature data. Separation factors of ethyl butyrate to ethanol are included to demonstrate the effect of the chain length on selectivity.

The comparison reveals that measurements of this study are in good agreement to literature data of Hirohama et al. [31] at 334 K and 10 MPa. When separated from almost pure water, separation factors of ethyl butyrate to ethanol are much larger than those of ethyl acetate to ethanol. This is due to the lower solubility of ethyl butyrate in water. When separated from almost pure ethanol, the lower vapor pressure of ethyl butyrate induces a lower separation factor with respect to ethanol compared to ethyl acetate. However, separation factors with respect to ethanol are still above 1 for ethyl butyrate, although its vapor pressure is below that of ethanol (see Table 4). This demonstrates the higher affinity of supercritical CO_2 to nonpolar components if vapor pressures are in the same range.

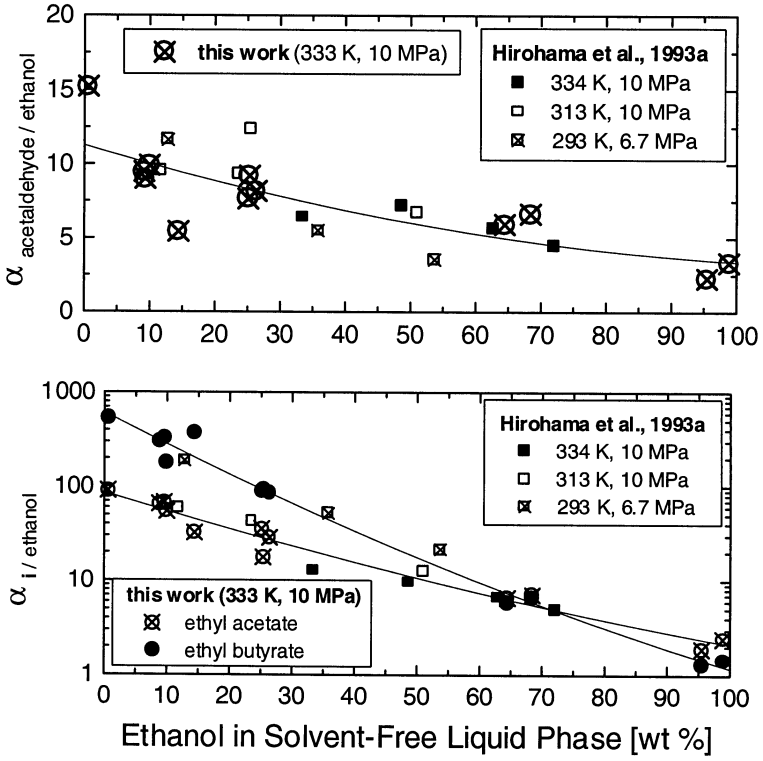

Fig. 18. Influence of ethanol on distribution coefficients.

Separation factors of the comparatively low volatile components hexanal, trans-2-hexenal, and linalool with respect to ethanol are illustrated in Fig. 19. At a constant ethanol content of the liquid phase, separation factors decrease according to the component's vapor pressures. Note that this is not a general characteristic as demonstrated for ethyl acetate and ethyl butyrate. Separation factors are influenced by polarity, volatility, and the affinity of CO_2 to certain functional groups.

Data points for hexanal and trans-2-hexenal that belong to measurements with natural orange water-phase are different to those of the model mixture. This might be due to minor components that co-elute with the component of interest. Separation of either hexanal or trans-2-hexenal from ethanol seems nearly impossible. In analogy to its distribution coefficient, the separation factor of linalool to ethanol remains below 1.0 at an ethanol content above 60 wt %.

The observation of changing selectivities is important for multistage separation processes when dealing with complex mixtures like aqueous-organic solutions. A nonpolar component of low vapor pressure like linalool will be easily

removed from an aqueous feed mixture by supercritical CO_2. If any volatile-component, e.g. ethanol, which is selectively dissolved by CO_2, is present in major quantities, refluxing extract into a multistage column will further in quantity of this volatile component in the extract. At the same time, the quantity of the said nonpolar component, e.g. linalool, is decreasing in the extract. Thus, this component accumulates inside the column. A side stream will be required to remove a fraction rich in this component. crease the ?

Table 4:
Comparison of pure component vapor pressures at 333 K.

Component	Vapor pressure	Antoine parameters lnP[kPa]=A+B/T [K]		Reference
		A	B	
Acetaldehyde	5.1×10^5 Pa *	17.33	−3697.47	[7]
Methanol	8.6×10^4 Pa	18.62	−4719.79	[7]
Ethyl acetate	5.7×10^4 Pa	17.44	−4461.04	[7]
Ethanol	4.6×10^4 Pa	19.29	−5149.55	[7]
Water	2.0×10^4 Pa	Wagner equation		[44]
Ethyl butyrate	1.2×10^4 Pa	16.95	−4817.88	[7]
Hexanal	8.0×10^3 Pa	17.08	−4998.65	[45]
trans-2-Hexenal	4.2×10^3 Pa	16.85	−5131.13	[46], [10]
Linalool	4.5×10^2 Pa	17.85	−6208.82	[6]

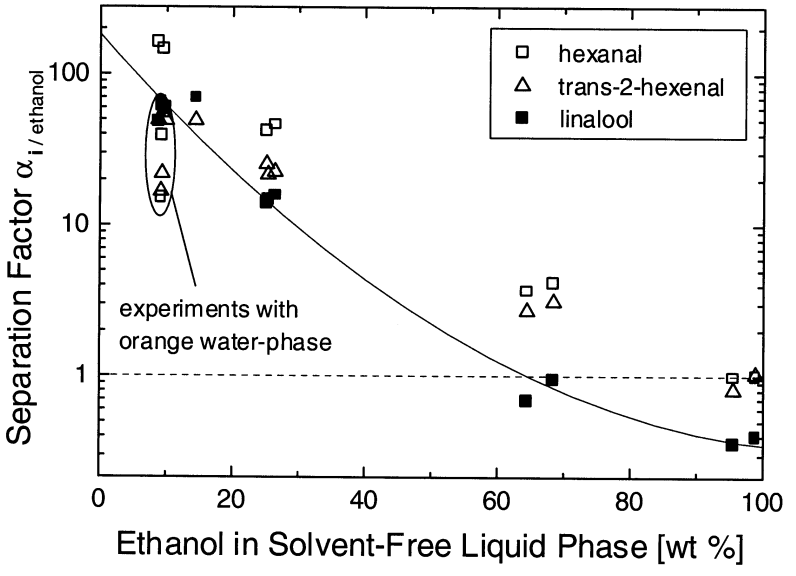

Fig. 19. Separation factors for different low-volatile aroma components.

5. COUNTERCURRENT EXPERIMENTS

To confirm the suitability of the predictions by the stage calculation model [42], countercurrent experiments with aqueous mixtures of ethanol were carried out with feed mixtures with an ethanol content between 10 and 94 wt %. Pressure and temperature in the extraction tower were set constant to 10 MPa and 333.15 K. Pressure and temperature at the bottom of the separation tower were set constant to 5 MPa and 303.15 K. Ethanol and water were mixed prior to each experiment. Denaturated ethanol was used for most experiments to reduce experimental costs. By using pure ethanol during some runs it was confirmed that the influence of the additive methyl ethyl ketone was negligible for overall process evaluation and the selectivity of ethanol to water.

Additional countercurrent column experiments were performed with natural orange water-phase and a model mixture of aroma components. This model mixture had a similar composition like the natural water-phase. The results of all experiments with aqueous solutions are illustrated here to demonstrate the similar behavior of ethanol+water mixtures and aqueous solutions that comprise major quantities of ethanol. Flooding occurred several times during experiments with aqueous solutions, mainly caused by an increasing raffinate-phase level above the location of the solvent inlet. When flooding started, the raffinate flow rate decreased rapidly. It was not possible to restart an experiment after some minutes, because any remaining liquid inside the packing had to be withdrawn to avoid new flooding.

5.1. Extract purity

During experiments with ethanol+water mixtures, several parameters were changed to understand the behavior of the process. It was confirmed that it is possible to produce an extract of 99 wt % ethanol from a feed mixture of 45 wt % ethanol. First experience was gained with the mixture ethanol+water by establishing total reflux. Extracts from a feed mixture with 35 wt % ethanol had a purity between 96 and 98 wt %. Experiments with ethanol of almost azeotropic composition yielded an extract with a remaining water content of just 0.5 wt %.

5.2. HETS evaluation

To evaluate the quality of the multistage fractionation, HETS values were calculated by the above-mentioned stage calculation model of Ponchon-Savarit. HETS values within the 2-m enriching section of the column are always discrete numbers, because the computer program did not calculate fractions of one stage. Fig. 20 demonstrates the influence of extract purity on HETS in both the enriching and stripping section of the column.

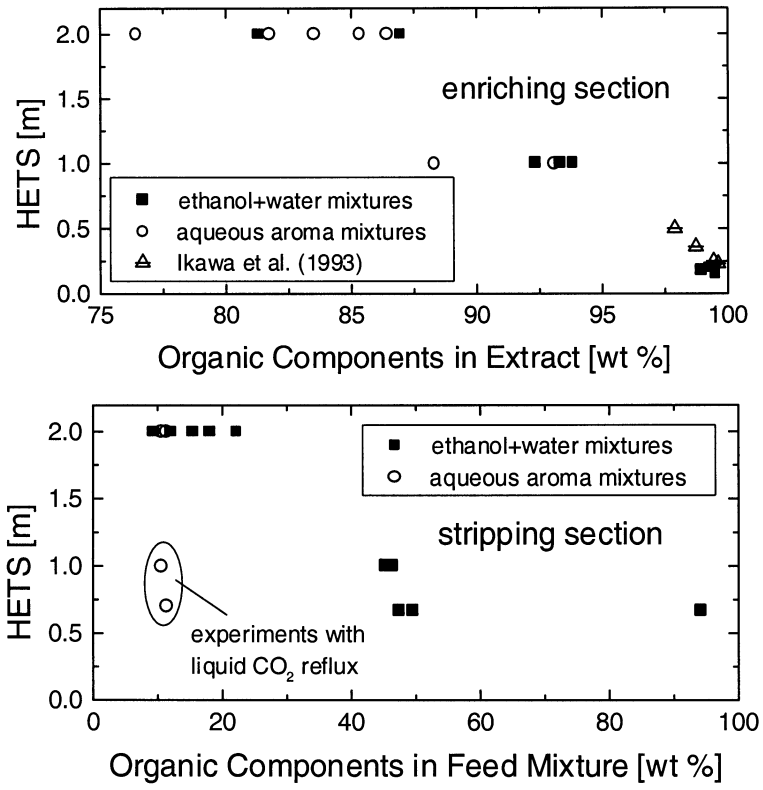

Fig. 20. HETS for aqueous mixtures.

For all experiments, a characteristic decrease of HETS was calculated with an increasing ethanol content of the extract. In principle, the decrease of HETS can be due to an inaccurate representation of separation factors at high ethanol concentrations. However, Ikawa et al. [44] reported the same trend of HETS with a different stage calculation method and larger separation factors. Therefore, a change in the mixture's properties like mutual solubility is believed to cause the change of HETS.

Within the stripping section of the column only one or two stages were realized due to an incomplete separation of ethanol and CO_2 in the separation tower. Any residual loading of the solvent caused a decrease in the possible number of theoretical stages. The influence of an improved solvent regeneration is demonstrated in Fig. 20 for the stripping section of the column. This effect is further explained below. Note that the required number of stages to reduce the ethanol content of the raffinate is rather low in the stripping section because of large separation factors. However, with increasing ethanol content of the feed mixture, HETS decreased. This is easily explained by the lower influence of re-

circulated ethanol at larger feed concentrations. Moreover, the influence of any transport property on HETS is also likely in the stripping section.

5.3. Solvent regeneration

For most experiments with aqueous solutions, conditions in the separator were set to 303 K and 5 MPa. At these conditions, residual load of CO_2 after regeneration is around 0.5 wt % with respect to pure ethanol (Fig. 21). At lower temperatures and pressures, a decreased residual loading would have been observed, but separating conditions were limited by two process characteristics. Although residual loading becomes minimum near the vapor pressure of pure CO_2, solubility of CO_2 in the liquid phase increases dramatically at the same time, thus inducing a high loss of solvent with the extract. Therefore, conditions should be set far from the one-phase region of the mixture solvent+extract.

Moreover, the formation of gas hydrate is a limiting factor for the minimum temperature of CO_2 in its liquid state. Gas hydrate crystals are formed from water and CO_2 molecules at low temperatures. According to Gmelin [48], a gas hydrate may exist in both liquid and gaseous CO_2 at temperatures below 283 K. The probability of formation of the gas hydrate is low at this temperature when a steady flow is enforced. However, due to subcooling of liquid CO_2 in the condensers, a separating pressure of 5 MPa (condensation at 287.4 K) was set as a limit for experiments with aqueous solutions. During first experiments, the valves of the recirculation pump were blocked when liquid CO_2 was subcooled below 278 K at 5 MPa. Therefore, the cooler was set to a higher minimum temperature.

Due to recirculation of ethanol with the solvent, the ethanol content of the raffinate phase was higher than expected. For most experiments, the residual ethanol content of the raffinate remained almost unchanged between 5 and 10 wt %. Raffinate composition is demonstrated in Fig. 21. Actual and calculated raffinate composition are compared with respect to the mass balance for organic components.

Some loss of product that was observed during each experiment. This loss was caused by incomplete condensation of ethanol when gaseous solvent left the extract receiver. This was proven by adding two cold traps, cooled with acetone+dry ice. Condensate from these cold traps was about 2 g/h in total and increased at a higher absolute extract flow rate. Another explanation for loss of product is the slow adjustment of a constant hold-up of the packing.

The loss was added to the extract flow to calculate actual reflux ratio and loading. Whenever this assumption was wrong, the mass balance for organic components must reveal a lower calculated percentage of organic components in the raffinate compared to the actual value, because the loss flow should have a smaller percentage of aroma components like the liquid phase in the stripping section of the column.

For most aqueous mixtures of aroma components, calculated raffinate compositions were in good agreement to actual product composition. This agreement confirms the suitability of adding loss and extract flow. For ethanol+water mixtures, calculated values were larger than actual raffinate composition. This indicates a steady formation of hold-up.

After establishing the technique of refluxing liquid CO_2 to the separation tower (Fig. 12), the lowest content of organic components in the raffinate was 0.4 wt %. This was obtained with a reflux flow of 5 kg CO_2/h. At a lower CO_2 reflux, e.g. 1.5 kg/h, the remaining content of organic components in the raffinate was still 5 wt %. No further evaluation of an optimum CO_2 reflux ratio was performed because of missing information on VLE data at these conditions.

Fig. 22 demonstrates that the quantity of extract that was removed from the separation tower was up to 5 g/kg lower than the value that was calculated from VLE data as represented by the line. According to Feng et al. [48], this is in perfect agreement to the residual solubility of ethanol at 303 K and 5 MPa (Fig. 23). Except of one data point, this was also observed during experiments with liquid CO_2 reflux, although the use of liquid CO_2 reflux affected the composition of raffinate.

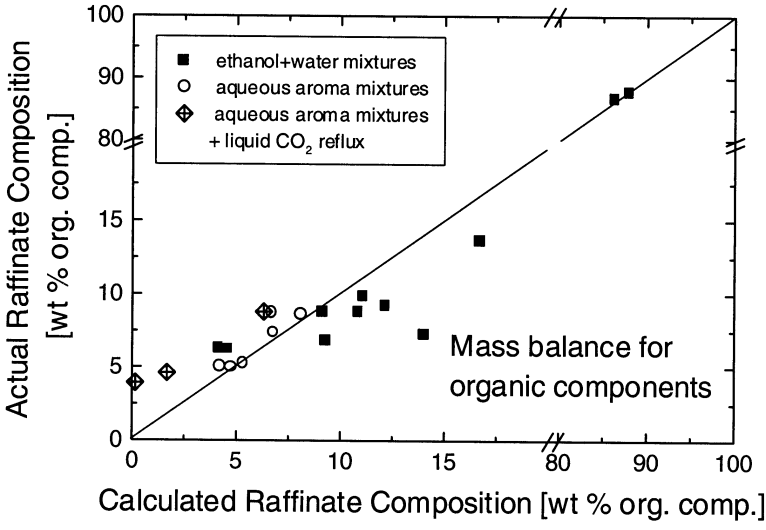

Fig. 21. Mass balance for countercurrent column experiments.

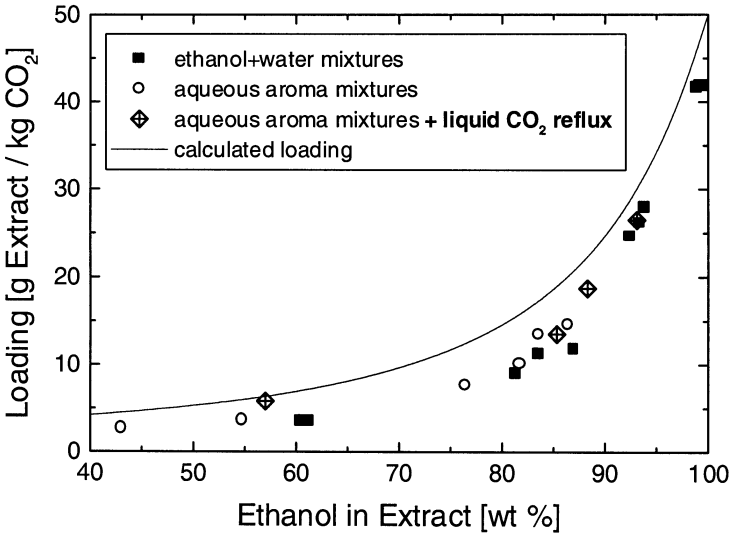

Fig. 22. Comparison of calculated and actual loading.

5.4. Enrichment of flavor components

According to VLE measurements, most aroma components are enriched in the vapor phase and some are difficult to separate from the solvent. Fig. 23 presents the concentration ratio in each phase to visualize the behavior of the process. Supercritical CO_2 had the lowest affinity to methanol due to its polarity and complete miscibility with water. As shown in Fig. 23, separation factors of methanol to ethanol are less than one. Nevertheless, it is possible to enrich methanol and most others components in the vapor phase. Acetaldehyde showed a lower enrichment in the vapor phase than ethanol. Largest enrichment was observed for ethyl acetate and all less volatile components, that were not detected in the raffinate. Accumulation of low-volatile components inside the enriching section of the separation column was not observed.

Liquid CO_2 reflux was only carried out during experiments 6, 7, 8, and 10. For run No. 8, a much lower reflux flow of 1.5 kg/h was chosen to investigate the appropriate flow rate of liquid CO_2 to the separation tower. This low reflux flow was not sufficient to reduce the residual amount of volatile components.

Experiment No. 10 was performed at a reflux ratio of CO_2 of 0.5. This is equal to 5 kg /h CO_2 reflux and 10 kg/h solvent flow into the extraction tower. The residual loading of CO_2 after regeneration was not taken into account by the stage calculation model. In case of volatile products, the residual loading reduces the efficiency of the countercurrent process. When ethanol enters the column with the solvent, it is not possible to obtain a raffinate free of ethanol.

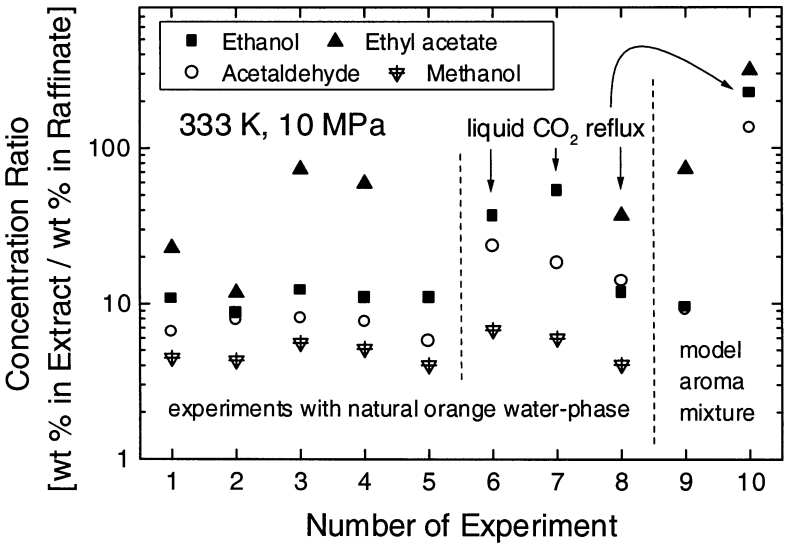

Fig. 23. Enrichment of aroma components in supercritical CO_2.

6. CONCLUSIONS

Similar to the refining of essential oil mixtures, the fractionation of aqueous solutions that include volatile and other organic components has a high potential as long as it deals with products of high market value. Observations of this study with ethanol+water mixtures included the increase of HETS with an increasing percentage of water in the liquid phase. Moreover, flooding behavior was affected by the water content of the liquid phase. From the available data it can be concluded that separation of organic components from water by means of supercritical carbon dioxide is easily achieved as long as these components are characterized by high vapor pressures or low solubility in the aqueous phase. If ethanol is present in the feed mixture, a highly concentrated aroma fraction also comprises ethanol if no further separation step is established. Experiments with aqueous solutions demonstrated the improvement of product quality after establishing liquid carbon dioxide reflux to the separation tower . This technique can be applied easily to any SFE process that deals with volatile components. Due to high distribution coefficients for many low-volatile hydrocarbons, supercritical carbon dioxide is a suitable solvent to remove trace components from aqueous solutions. Complex solubility effects may occur when one organic component like ethanol is present in major quantities.

REFERENCES

[1] A.M. Popken, Personal communication. Eckes-Granini GmbH, Nieder-Olm, Germany, 1997.
[2] R.J. Braddock, By-Products of Citrus Fruit. Food Technol, 49 (9) 1995, 74-77.
[3] M.G. Moshonas and P.E. Shaw, Flavor Evaluation of Concentrated Aqueous Orange Essences. J Agric Food Chem, 38, 1990, 2181-2184.
[4] E.W. Bott and P. Schöttler, Separatoren, Dekanter und Prozeßlinien für die Citrus-Verarbeitung. Technisch-wissenschaftliche Dokumentation Nr. 14, 1989. Westfalia Separator AG, Oelde, Germany.
[5] P.E. Shaw, Private communication, 1998. U.S. Department of Agriculture, South Atlantic Area Citrus & Subtropical Products Laboratory, Florida.
[6] R.C. Weast, M.J. Astle and W.H. Beyer, CRC Handbook of Chemistry and Physics. 68th edition, 1987, CRC Press, Boca Raton, Florida.
[7] R.H. Perry, D.W. Green and J.O. Maloney, Chemical Engineers' Handbook. 6th edition, 1984, McGraw-Hill, New York.
[8] J.D. Johnson and J.D. Vora, Natural Citrus Essences. Food Technol, 37 (12) 1983, pp 92, 93, 97.
[9] R. Kühn and K. Birett, Merkblätter Gefährliche Arbeitsstoffe. Ecomed Verlagsgesellschaft, 1979, Landsberg, Germany.
[10] Römpp, Lexikon Chemie. 10th edition, 1996, Georg Thieme Verlag, Stuttgart, Germany.
[11] M. Pala and H.J. Bielig, Industrielle Konzentrierung und Aromagewinnung von flüssigen Lebensmiteln. Fortschritte der Lebensmittelwirtschaft, 5, 1978, TU Berlin, Germany.
[12] L. Narziß, W. Back and S. Stich, Versuche mit einer Gegenstromdestillationsanlage mit Rektifikation zur Entalkoholisierung von Bier. Brauwelt, 133, 1993,1806-1820.
[13] U. Hochberg, Fortschritte bei der Aromagewinnung. Flüssiges Obst, 54 (3), 1987, 124-133.
[14] R.J. Braddock, G.D. Sadler and C.S. Chen, Reverse Osmosis Concentration of Aqueous-Phase Citrus Juice Essence. J Food Sci, 56, 1991,1027-1029.
[15] T.H. Schultz, R.A. Flath, D.R. Black, D.G. Guadagni, W.G. Schultz and R. Teranishi, Volatiles from Delicious Apple Essence – Extraction Methods. J Food Sci, 32, 1967, 279-283.
[16] A. Birtigh, Regeneration der Fluidphase bei der Gasextraktion. Dissertation, TU Hamburg-Harburg, 1995, Germany.
[17] K. Zosel, Process for the Direct Decaffeination of Aqueous Coffee Extract Solutions. U.S. Patent 4,348,422, 1982.
[18] G. Brunner, Gas Extraction. Steinkopff, Darmstadt, 1994,Germany.
[19] A. Akgerman, R.K. Roop, R.K. Hess and S.D. Yeo, Supercritical Extraction in Environmental Control. In: Reviews in Modern Theory and Applications, Bruno TJ, Ely JF, Eds, 1991, 479-509.
[20] C.P. Ong, H.H. Lee and S.F.Y. Li, Direct Coupling of Supercritical Fluid Extraction-Supercritical Fluid Chromatography for the Determination of Selected Polycyclic Aromatic Hydrocarbons in Aqueous Environmental Samples. Environmental Monitoring & Assessment, 19, 1991, 63-71.
[21] F. Dehghani, T. Wells, N.J. Cotton and N.R. Foster, The Use of Dense Gases for the Extraction of Metal Compounds. In: Value Adding Through Solvent Extraction, Shallcross DC, Paimin R, Prvcic LM, Eds, The University of Melbourne, Australia, 2, 1996, 967-971.

[22] A.P. Bünz, Hochdruckphasengleichgewichte in Mehrkomponentensystemen aus Kohlenhydraten, Wasser, Alkoholen und Kohlendioxid. Dissertation, TU Hamburg-Harburg, Germany. VDI-Fortschrittbericht 3/406, 1995, VDI-Verlag, Düsseldorf, Germany.

[23] O. Pfohl, J. Timm, R. Dohrn and G. Brunner, Measurement and Correlation of Vapor-Liquid-Liquid Equilibria in the Glucose+Acetone+Water+ Carbon Dioxide System. Fluid Phase Equilibria, 124, 1996, 221-233.

[24] D.M.T. Newsham and O.P. Stigset, Separation Processes Involving Supercritical Gases. Paper presented at the Symposium "Alternatives to Distillation", Manchester, Great Britain, Inst Chem Eng Symp Ser No. 54, 1978.

[25] T. Adrian, Hochdruck-Mehrphasengleichgewichte in Gemischen aus Kohlendioxid, Wasser, einem wasserlöslichen organischen Lösungsmittel und einem Naturstoff. Dissertation, Universität Kaiserslautern, 1997, Germany.

[26] M. Perrut, Aromas from Fermented and Distilled Beverages by Liquid-Fluid Fractionation. Proc 4th Int Symp Supercrit Fluids, Sendai, Japan, C, 1997, 845-852.

[27] M. Budich and G. Brunner: Supercritical fluid extraction of ethanol from aqueous solutions. J. of Supercritical Fluids 25 (2003) 45 – 55.

[28] M. Budich and G. Brunner: Supercritical fluid extraction of volatile components from aqueous solutions. 2nd International Meeting on High Pressure Chemical Engineering March 7-9, 2001, Hamburg, Germany.

[29] R. Voigt, Pharmazeutische Technologie für Studium und Beruf. 7th edition, Ullstein Mosby, Berlin, 1993, Germany.

[30] R. Fukuzato, N. Ikawa, Y. Nagase, Development of New Processes for Purification and Concentration of Ethanol Solution Using Supercritical Carbon Dioxide. In: Value Adding Through Solvent Extraction, Shallcross DC, Paimin R, Prvcic LM, Eds, The University of Melbourne, Australia, 2, 1996, 1011-1016.

[31] S. Hirohama, T. Takatsuka, S. Miyamoto and T. Muto, Phase Equilibria for the Carbon Dioxide-Ethanol-Water System with Trace Amounts of Organic Components. J Chem Eng Japan, 26, 1993, 247-253.

[32] R. Fukuzato, Private communication. 1997, Kobe Steel Ltd., Japan.

[33] S. Hirohama, T. Takatsuka, S. Miyamoto and T. Muto, A Study of Mass-Transfer in the Extraction of Impurities from Ethanol Aqueous Solution by Carbon Dioxide as a Solvent. J Chem Eng Japan, 27, 1994, 107-113.

[34] D.R.P. Jolly, Wine Flavour Extraction With Liquid Carbon Dioxide. Process Biochemistry, 16, 1981, 36-40.

[35] A. Wiesenberger, R. Marr, J.A. Schildmann and R. Weisrock, Process for Producing Alcohol-Reduced or Alcohol-Free Beverages Made by Natural Fermentation. US Patent No. 4,867,997, 1989.

[36] H. Seidlitz, E. Lack and F. Lackner, Verfahren zur Verminderung des Alkoholgehaltes alkoholischer Getränke. Austrian Patent No. 391 875, 1990.

[37] S. Fernandes, J.A. Lopes, A.S. Reis Machado, M. Nunes da Ponte and J.C. Reves, Supercritical CO_2 Extraction from Wine Fermentation Broths. Proc 3rd Int Symp Supercrit Fluids, Strassbourg, France, 2, 1994, 491-495.

[38] T. Gamse, I. Rogler and R. Marr, Supercritical CO_2-Extraction for Utilization of Excess Wine of Poor Quality. Proc 4th Italian Conference on Supercritical Fluids, Capri, Italy, 1997, 191-196.

[39] J.M. Randall, W.G. Schulz and A.I. Morgan, Extraction of Fruit Juices and Concentrated Essences with Liquid Carbon Dioxide. Confructa, 16, 1971, 10-19.

[40] W.G. Schultz, T.H. Schultz, R.A. Carlson and J.S. Hudson, Pilot-Plant Extraction with Liquid CO_2. Food Technol, 28 (6), 1974, pp 32-36, 88.

[41] M. Sims, J.R. Robinson and A.J. Dennis, . Porocritical Fluid Extraction: A New Technique for Continuous Extraction of Liquids with Near-Critical Fluids. In High Pressure Chemical Engineering, P.R. von Rohr, C. Trepp, Eds, Elsevier Science, New York, 1996, 205-209.

[42] M. Budich, Countercurrent Extraction of Citrus Aroma From Aqueous and Nonaqueous Solutions Using Supercritical Carbon Dioxide. Dissertation, Hamburg 1999. Fortschrittberichte VDI, Ser. 3, No. 606.

[43] N. Ikawa, Y. Nagase, T. Tada, S. Furuta and R. Fukuzato, Separation Process of Ethanol from Aqueous Solution Using Supercritical Carbon Dioxide. Fluid Phase Equilibria, 83 (1993) 167 – 174.

[44] R.G. Reid, J.M. Prausnitz and B.E. Poling, The Properties of Gases and Liquids, 4th ed., McGraw Hill, New York, 1987.

[45] C.L. Yaws, Handbook of Vapor Pressures, Vol. 2, Gulf Publishing Company, Houston, 1994.

[46] J. D´Ans and E. Lax, Taschenbuch für Chemiker und Physiker, Band I, 3rd ed., Springer, Berlin, 1967.

[47] Gmelin, Handbuch Kohlenstoff, Vol. C3, Verlag Chemie, Weinheim, 1973.

[48] Y.S. Feng, X.Y. Du, C.F. Liu and Y.J. Hou, An Apparatus for Determining High Pressure Fluid Phase Equilibria and its Application to Supercritical Carbon Dioxide Mixtures. Proc. 1st. Int. Symp. On Supercritical Fluids, Nice, France, 1988, 75 – 84.

Supercritical Fluids as Solvents and Reaction Media
G. Brunner (editor)

Chapter 4.3.

Supercritical SO_2 for preparation of sulfur dioxide complexes and for recovery of precious metals from used catalysts

D.K. Breitinger, A. Bogner, M. Lauter and R. Loos

Institute of Inorganic Chemistry, University of Erlangen-Nürnberg, Egerlandstrasse 1, D-91058 Erlangen, Germany

1. SUMMARY

Since no experiences at all have been available for handling of supercritical sulfur dioxide in autoclaves first of all tests of the resistance of material and accessories against this fluid have had to be performed. The autoclaves used resist to the pure fluid under supercritical conditions; copper is appropriate as material for washers, teflon is useless. In the presence of oxidants like sulfur trioxide or sulfuryl chloride silver has to be used as material for washers. Under these conditions glass insets provide limited protection of the autoclaves to corrosion.

In attempts to introduce further sulfur-dioxide ligands into sulfur-dioxide complexes like $[RuX(SO_2)(NH_3)_4]X$ (X = Cl, Br, I) or $[Ru(OH_2)(SO_2)(NH_3)_4](BF_4)_2$ by means of supercritical SO_2 the educts remain unchanged against the expectations. Reaction of the bis(hydrogensulfito) complex $[Ru(SO_3H)_2(NH_3)_4]$ with anhydrous sulfuric acid (molar ratio 1:2) in supercritical SO_2 yielded the bis(sulfur-dioxide) complex $[Ru(SO_2)_2(NH_3)_4](HSO_4)_2$, as shown by analytical data and IR spectra. A similar reaction with molar ratio 1:1 seemingly yielded the compounds $[Ru(SO_3H)(SO_2)(NH_3)_4](HSO_4)$ and $[Ru(SO_3H)(SO_2)(NH_3)_4]_2SO_4$ as a mixture; these results have to be confirmed further. As a result a way is opened to prepare oligosulfur-dioxide complexes from oligosulfito complexes of *eg* platinum-group metals *via* elimination of H_2O from hydrogensulfito complexes obtained by protonation with strong acids like HBF_4, HPF_6, H_2SiF_6, or the like.

Treatment of used catalytic converters with supercritical sulfur dioxide, also in presence of oxidants like SO_3 or SO_2Cl_2 and with prolonged reaction time, does not improve the extractability of the catalytically active metals

platinum and rhodium. Thus, this procedure is not appropriate for processing of used catalysts and recovery of the precious metals.

2. PROCEDURES AND RESULTS

2.1. Experimental

The working conditions for the use of sulfur dioxide as a supercritical fluid are determined by the crital data T_k = 157.2 °C = 430.4 K and p_k = 78.7 bar.

The experiments have been performed in stainless-steel high-pressure autoclaves (C. Roth, Karlsruhe) with volumes of 100 and 250 ml, respectively. The manufacturer of this equipment, as well as other manufacturers, did not have practical experience with the resistance of the material towards SO_2 under supercritical conditions. Thus, experience had to be gained for the behaviour of the material under working conditions. Sulfur dioxide has been condensed into and frozen in the autoclaves purged with nitrogen gas and cooled with liquid nitrogen; even so, the presence of small amounts of water and/or sulfur trioxide SO_3 cannot completely excluded. The filled and closed autoclaves have then been heated to and kept at working temperature for a given time.

The initially used teflon seals turned out not to be sufficiently resistant at the working temperatures; they started to soften at about 150 °C, a finding which has been confirmed afterwards by the manufacturer upon request. Satisfactory results have been obtained with commercially available silver seals in the connections of the autoclave head to the accessories (valves, pressure-gauges) and with less expensive copper seals between head and beaker of the autoclave. Since not commercially available, these copper washers had to be punched from appropriate copper sheet and machined for this particular purpose. The autoclaves fitted out in this manner proved to be resistant against pure SO_2 up to 180 °C and 100 bar.

In the presence of oxidants, such as sulfur trioxide SO_3 or sulfuryl chloride SO_2Cl_2, these copper seals have been attacked, and silver seals between autoclave head and beaker had to be used. Finally, in experiments with more than 3 h duration under these conditions the autoclave showed signs of corrosion. In order to avoid this corrosion and also attack by the noble-metal compounds to be used later on glass insets have been used because of the insufficient thermal stability of teflon.

2.2. Sulfur-dioxide ruthenium complexes

2.2.1. Reactions and characterization of the reaction products

The reactions in supercritical SO_2 aimed at preparing not yet known purely inorganic oligo-sulfur-dioxide complexes, especially of ruthenium, as solely oli-

go-SO_2 complexes with organometal fragments of low-valent transition metals are known up to now.

Some sulfur-dioxide ruthenium compounds have been prepared on a conventional route [1, 2] in order to use them as potential educts in substitution reactions with supercritical sulfur dioxide at 160 °C. The intended reactions, depending on the educts used, are as follows:

$$[RuX(SO_2)(NH_3)_4]X + SO_2 \longrightarrow [Ru(SO_2)_2(NH_3)_4]X_2 \ (X = Cl, Br, I) \quad (1)$$

$$[Ru(OH_2)(SO_2)(NH_3)_4](BF_4)_2] + SO_2 \longrightarrow [Ru(SO_2)_2(NH_3)_4](BF_4)_2 + H_2O \quad (2)$$

In these experiments merely the unchanged educts could be isolated. At reaction temperatures above 200 °C the compounds started to decompose yielding a mixture of various degradation products, but only metallic ruthenium could be identified by X-ray powder diffractometry. Higher temperatures were avoided since attempts to treat used catalytic converters with SO_2 at 250 °C and ambient pressure revealed a tendency to disproportionation along the following equation:

$$3\ SO_2 \longrightarrow S + 2\ SO_3 \quad (3)$$

Therefore, the most appropriate temperature range 158-165 °C was kept, *ie* just above the critical temperature.

Another route was tried with an elimination reaction on a bis(hydrogensulfito) ruthenium(II) complex $[Ru(SO_3H)_2(NH_3)_4]$ (**1**) [3] already known in a similar form [1, 2], with two possible ratios of the educts:

$$[Ru(SO_3H)_2(NH_3)_4] + 2\ H_2SO_4 \longrightarrow [Ru(SO_2)_2(NH_3)_4](HSO_4)_2 + 2\ H_2O \quad (4)$$

$$[Ru(SO_3H)_2(NH_3)_4] + H_2SO_4 \longrightarrow [Ru(SO_2)_2(NH_3)_4]SO_4 + 2H_2O \quad (5)$$

Although sulfuric acid as elimination reagent makes the rapid analysis by IR spectrometry more difficult due to overlap of the absorption bands of coordinated hydrogensulfite and sulfur dioxide and of extracomplex hydrogensulfate and sulfate, respectively, it was nevertheless used for experimental reasons. It is anhydrous, stable under the reaction conditions chosen, sufficiently acidic to protonate the ligands SO_3H of **1**, and able to split off and to bind water. Also, sulfur trioxide present in sulfur dioxide due to the way of its production, is suitable for the intended reaction, irrespective of the imposed difficulties to dose the reactants in the exactly stoichiometric ratio.

A series of reactions with a 1:2 ratio of the educts (equation (4)) always yielded a red solid. Analyses for nitrogen and sulfur on the average gave a ratio

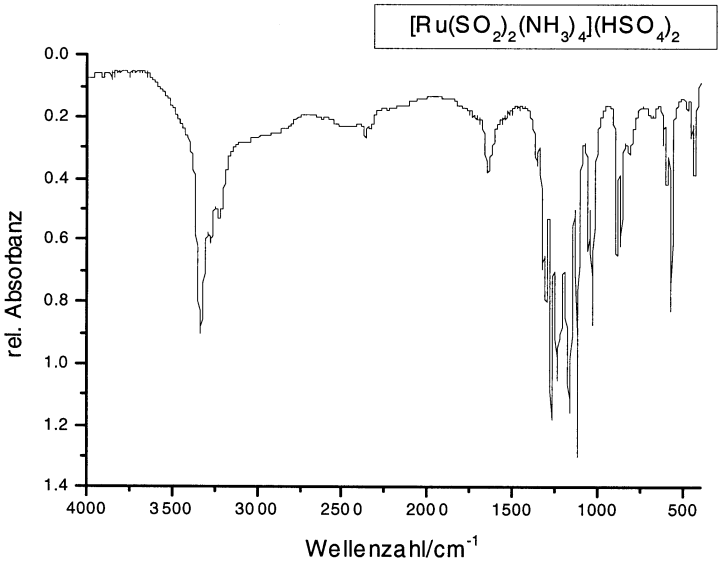

Fig. 1. IR spectrum of $[Ru(SO_2)_2(NH_3)_4](HSO_4)_2$, formed after equation (4).

N:S = 1:1, consistent with equation (4). IR spectra (Fig. 1) show the absorption bands characteristic for the SO_3H ligands of **1** (*cf* [2, 4]), especially ν(S-OH) at 750 cm^{-1}, to disappear and vibrations of SO_2 ligands [2, 5-7] to appear, together with bands of the HSO_4^- anions. In spite of the complications due to overlap of ν(SO) vibrations in both educts and products of reaction (4) the IR spectra indicate the formation of the bis(sulfur-dioxide) complex $[Ru(SO_2)_2(NH_3)_4](HSO_4)_2$ (**2**). Additional problems with the interpretation of the IR spectra arose if the elimination reagent was overdosed, since the excess stubbornly adhered and withstood attempts to remove it by liquid SO_2 and by other inert solvents, like dichloromethane CH_2Cl_2. An attempt to remove an excess of H_2SO_4 with water under fading of the colour not surprisingly led to a new product, which could not be identified yet.

In order to avoid an excess of sulfuric acid a series of reactions with molar ratio H_2SO_4 : $[Ru(SO_3H)_2(NH_3)_4]$ = 1:1 has been performed according to equation (5). Under these circumstances the hydrogensulfate anion proved not to be sufficiently acidic to split off water completely after equation (5). Analyses of the reaction products on the average gave a ratio N:S = 1.47 (theory: 1.33). Consequently, the reaction ran partly after:

$$[Ru(SO_3H)_2(NH_3)_4] + H_2SO_4 \longrightarrow [Ru(SO_3H)(SO_2)(NH_3)_4](HSO_4) + H_2O, \quad (6)$$

ie consuming one proton of H_2SO_4 for the elimination of H_2O, and partly after:

$$2\ [Ru(SO_3H)_2(NH_3)_4] + H_2SO_4 \longrightarrow [Ru(SO_3H)(SO_2)(NH_3)_4]_2SO_4 + 2\ H_2O \quad (7)$$

The conclusion is that hydrogensulfate is able to protonate the neutral bis-(hydrogensulfito) complex, but no more the cation $[Ru(SO_3H)(SO_2)(NH_3)_4]^+$ formed in the first step of protonation and elimination of water. In addition to the analytical data also details in the IR spectra of the reaction products support this interpretation: These spectra show the characteristic bands of sulfur-dioxide ligands, combined with a weakening of the absorptions typical for the hydrogen-sulfito ligands of **1** and for its hydrogen-bond system [4], and the appearance of the bands of the HSO_4^- anion.

2.2.2. Thermal degradation of the reaction products

For further characterization a series of thermogravimetric analyses (TGA) of known compounds and of reaction products (equation (4), H_2SO_4 slightly overdosed) have been performed.

The hygroscopic sample experienced a continuous mass loss up to about 200 °C, indicating transformation and removal of still adhering hydrates of sulfuric acid. With respect to the presence of hydrogensulfate, which releases the oxidant sulfur trioxide during thermal decay, the TGA was run with the sample in an air flow. This procedure should yield ruthenium dioxide as the final degradation product, however, the X-ray powder diffractogram also showed metallic ruthenium to be present in the residue of the thermal degradation.

Some spectrometrically and structurally well characterized sulfur-dioxide ruthenium(II) compounds were studied by TGA in order to detect possible intermediates in the thermal degradation. The objects of these studies were the already presented ruthenium(II) compounds $[RuX(SO_2)(NH_3)_4]X$ (X = Cl, Br, I), $[Ru(OH_2)(SO_2)(NH_3)_4](BF_4)_2$, and for comparison the ruthenium(III) compound $[RuCl(NH_3)_5]Cl_2$. For $[RuX(SO_2)(NH_3)_4]X$ (X = Cl, Br) TG-MS spectra* have been measured, some ones alternatively with air and nitrogen flow, respectively. In case of indications for a possible intermediate the samples were kept at the respective temperature under protective gas flow for removal of gaseous reaction products, and the residues characterized by elemental analyses and powder diffractometry.

For the compound $[RuBr(SO_2)(NH_3)_4]Br$ the trace of differential thermogravimetry (dTG) (Fig. 2) shows two minima around 300 °C and 420 °C. The solid residue obtained after 1 h at 300 °C under protective gas obviously is amorphous (no reflections in the powder diffractogram). In the IR spectrum the

* TG-MS: Simultaneous thermogravimetry and mass spectrometry; cooperation with Prof Dr J Kristof, Department of Analytical Chemistry, University of Veszprém, Hungary.

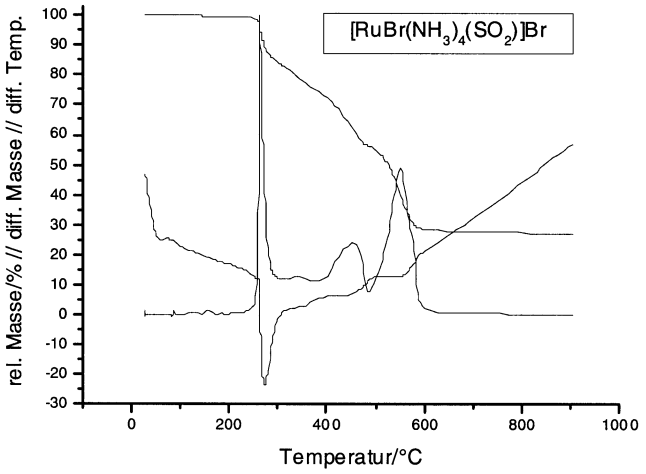

Fig. 2. Thermal degradation (TGA, dTG, DTA) of $[RuBr(SO_2)(NH_3)_4]Br$

bands of the sulfur-dioxide ligands have lost intensity, and new bands have appeared. Elemental analysis indicates a lowering of the nitrogen content, corresponding to a loss of ammonia. Further heating at 420 °C leaves a black solid still containing 11% of sulfur, but no more nitrogen. The powder diffractogram displays the reflections of ruthenium metal and RuS_2. The reaction gases condensed to a white solid containing both sulfur and nitrogen.

The TG-MS measurements reveal that there is a loss of sulfur dioxide in all phases of degradation. Therefore, simple interpretations of the TG diagrams are not possible and isolation and characterization of well defined intermediates not promising.

The kind of the final product of the TG depends on the gas flow: Under air flow the residue is ruthenium dioxide RuO_2 in all cases, under an inert gas flow the ruthenium metal remains.

2.3 Treatment of used catalytic converters

2.3.1. Used catalysts under study

An available used catalytic converter (Ford) contained two slightly sooted monoliths, about 340 g each. Three samples of this material were coarsely crushed; after treatment with chlorine or *aqua regia* the contents of platinum (1614(19) ppm) and rhodium (321(7) ppm) were determined by ICP-AES.

2.3.2. Process and findings

Based on the experiences reported on in section 2.1 samples of catalysts, either untreated or oxidized in air or impregnated with KCl (from aqueous solution), were placed in an open teflon inset in the autoclave, then SO_2 was condensed and frozen under nitrogen with external cooling; the SO_2 used contained small amounts of H_2O and SO_3. The closed autoclave was heated to supercritical temperature ($T \leq 250$ °C, $p \leq 90$ bar) and kept under these conditions for 6, 12 and 24 h, respectively.

The thus treated samples of catalysts were extracted first with water, then with dilute and half-concentrated aqueous HCl, respectively; the extracts were reduced to 100 ml and the metal content determined by means of ICP-AES. None of these variants provided an improved extractability of platinum and rhodium (metal contents in the extracts below 0.25 mg/l).

Also, addition of sulfuric acid, hydrogen peroxide H_2O_2 or sulfuryl chloride SO_2Cl_2, even with prolonged reaction times, did not improve the extractability (again metal contents below 0.25 mg/l). These findings and beginning corrosion of the autoclave under these conditions was the reason for abandoning these tests. An attempt with a teflon inset closed with a teflon lid as a separate reaction vessel within the autoclave was not successful due to the already mentioned softening of the material under the chosen reaction conditions.

Disproportionation of SO_2 with formation of elemental sulfur (*cf* section 2.2.1., equation (3)) was not observed under the conditions described above.

Comparative tests with platinum mohr in place of the catalyst did not modify the sample significantly.

In contrast to the chlorination of used catalytic converters applying several variants to produce hexachlorometallates of platinum(IV) and rhodium(III) [8-10] action of supercritical sulfur dioxide, even in the presence of oxidants, does not effect practically useful extractability of the platinum-group metals.

ACKNOWLEDGEMENTS

Support by the Deutsche Forschungsgemeinschaft (grant Br 422/24-(1+2) is gratefully acknowledged.- Thanks are also due to Prof Dr R G Schwab, Institute of Geology and Mineralogy, University of Erlangen-Nürnberg, for performing thermal analyses.

REFERENCES

[1] L.H. Vogt, J.L. Katz, S.E. Wiberley, Inorg. Chem., 4 (1965) 1157.
[2] R. Breiter, Dissertation, University of Erlangen, 1993.
[3] D.K. Breitinger, R. Breiter, Z. Naturforsch., 45b (1990) 1651, and references therein.
[4] D.K. Breitinger, G. Bauer, M. Raidel, R. Breiter, J. Tomkinson, J. Mol. Struct. 267 (1992) 55.
[5] D.K. Breitinger, R. Breiter, J. Mol. Struct. 349 (1995) 45.

[6] M. Lauter, D.K. Breitinger, R. Breiter, J. Mink, E. Bencze, in S.-L. Zhang and B.-F. Zhu (eds.), ICORS 2000, Proc. XVIIth Intern. Conf. on Raman Spectrosc., Beijing, China, August 20-25, 2000, Wiley, Chichester-New York, 2000, 114.
[7] M. Lauter, D.K. Breitinger, R. Breiter, J. Mink, E. Bencze, J. Mol. Struct. 563-564 (2001) 383.
[8] O. Bähr, Diploma Work, University of Erlangen, 1994.
[9] R. Loos, Diploma Work, University of Erlangen, 1994.
[10] A. van Dreuten, Diploma Work, University of Erlangen, 1995.

Supercritical Fluids as Solvents and Reaction Media
G. Brunner (editor)

Chapter5.1.

Polymerization in supercritical carbon dioxide: surfactants, micelle formation, and heterophase polymerization

W. Steffen[a]*, U. Scherf[b], L. Berger[a], J. Kadam[b], A. Schlewing[a], and R. Güntner[b]

[a] Max Planck Institute for Polymer Research, Ackermannweg 10, 55128 Mainz, Germany
[b] Bergische Universität Wuppertal, Fachbereich Chemie, Makromolekulare Chemie, Gaußstr. 20, 42097 Wuppertal, Germany
* corresponding author; electronic mail: steffen@mpip-mainz.mpg.de

1. INTRODUCTION

Due to their unique physical and chemical properties supercritical fluids are in the center of interest for processing of materials [1], plasticizing of polymers, in extraction processes, as well as solvent in polymerization reactions [2-4]. The latter is at the center of interest of our work. We concentrated on the polymerization of poly(vinylpyrrolidone) (PVP) as a model compound in an heterogeneous polymerization process. Poly(vinylpyrrolidone) as a polymer is a vital ingredient in food, pharmaceutical and medical applications. The production of clean polymers, free of solvent and in many cases free of water is adamant for many applications. In chain transfer reactions supercritical carbon dioxide (sc-CO_2) does not take part [5] as well as it is not expected to form complexes with monomer, macroradical or polymer in the reaction.
Sc-CO_2 can be used to study the influence of solvent quality. Varying pressure and/or temperature one can change the solvation properties of this solvent. It is known, that sc-CO_2 is a poor solvent for most polymers as e.g. poly(styrenes), poly(methacrylates) and poly(acrylates) [3].

In order to arrive at our goal we had to characterize and study the behavior of the diblock colpolymers we used in our model heterogeneous polymerization of PVP as stabilizer. The block copolymer chosen was poly(styrene-b-dimethylsiloxane) (PS-b-PDMS). PS serves here as the CO_2-phobic and PDMS

as a CO_2-philic part. The expected amphiphilic behavior should lead to micelle formation given the proper pressure and temperature range.

As the method of choice we used dynamic light scattering to monitor the aggregation behavior of this stabilizer in sc-CO_2. For this purpose we newly designed a light scattering cell to be able to do static and dynamic light scattering under varying angle and thus varying scattering vector. Several other light scattering systems have been developed in the past [6-8]. To study thermodynamic properties of polymer solutions as function of composition, pressure and temperature and at the same time to have an inexpensive design for multipurpose use we designed our own optical flow-through high pressure cell for light scattering [9].

The structure of this article is as follows: a) we will discuss the basic theoretical foundation of our scattering experiment, b) the experimental setup as well as the polymerization procedures used are described, c) discussion of the results of light scattering on the homopolymer PDMS as a test system and the stabilizer PS-b-PDMS, and last d) results from the heterogeneous polymerization of PVP.

2. THEORY

2.1. Light scattering

We do not want to repeat the general theory of scattering and in particular light scattering but refer the reader to the excellent books of Berne and Pecora [10], Chu [11], Kerker [12], and others. Here we repeat only the formulae necessary to understand our results and the analysis of our dynamic light scattering experiments.

The result of scattering in general is obtained in reciprocal space and the scattering geometry explained in terms of the scattering vector which is defined as:

$$q = |\vec{q}| = \frac{4\pi n}{\lambda_0} \sin\left(\frac{\Theta}{2}\right) \tag{1}$$

with n refractive index of the medium, λ_0 wavelength of the incident light and Θ the angle between incident and scattered radiation. The corresponding length scale in real space is obtained by $d = 2\pi/q$.

In dynamic light scattering, using the method of photon correlation spectroscopy (PCS), scattered light at times t, $t+\Delta t$ is collected and computed to obtain the correlation between the scattering processes at different times.

$$G^{(1)}(\vec{q},t)=\left\langle E^{*}(\vec{q},0)E(\vec{q},t)\right\rangle_{t} \tag{2}$$

is the autocorrelation function of the scattered electric field $E(\vec{q},t)$ and

$$g^{(1)}(\vec{q},t)=\frac{G^{(1)}(\vec{q},t)}{\left\langle E(\vec{q},0)\right\rangle^{2}} \tag{3}$$

its normalized counterpart. Since in the experiment we do not detect electric fields but light intensities (square of the amplitude of $E(\vec{q},t)$) the measured quantity is

$$g^{(2)}(\vec{q},t)=1+f\left(g^{(1)}(\vec{q},t)\right)^{2} \tag{4}$$

the normalized intensity autocorrelation function being connected to the normalized field autocorrelation function by the Siegert relation (Eq. (4)) above. The parameter f is the contrast factor taking the experimental circumstances into account. In an ideal light scattering experiment $f=1$. In the real experiment nowadays values of f close to one can be achieved by introducing single mode fiber optics in the detection system as

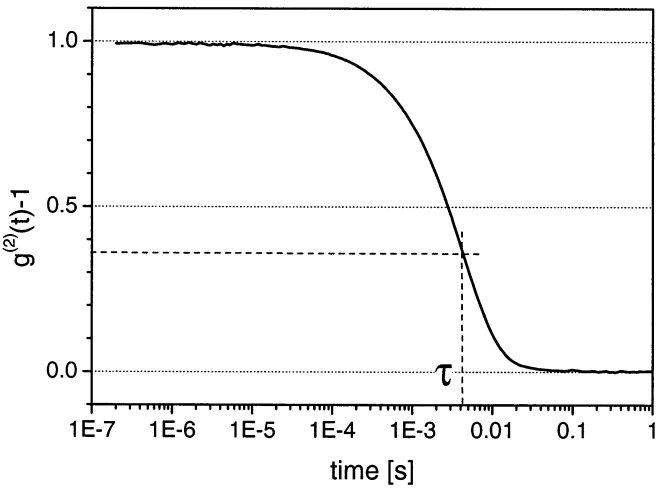

Fig. 2. Correlation function of 1 vol% polystyrene latex in water at room temperature, angle = 35°. τ is the characteristic time of the relaxation process observed.

we did. $g^{(2)}(\vec{q},t)$ is obtained in the homodyne light scattering experiment in which only light scattered by the sample is detected. A typical experimental curve of polystyrene latex as a 1 vol% solution in water at a scattering angle of 35° is depicted in Fig. 1. The opposite experiment would be the heterodyne light scattering one experiences when a local oscillator producing elastically scattered light is introduced. In fully heterodyne conditions the characteristic time measured for the dynamical feature looked at differs by a factor of two since in the heterodyne experiment $g^{(1)}(\vec{q},t)$ is measured directly.

A possible local oscillator could be stray light from cell walls etc. Great care has to be taken to avoid this contribution. Since a further result of heterodyning is the reduction of the contrast factor f the state, homodyne or heterodyne, one is measuring can be controlled by measuring the contrast of a known sample as e.g. latex particles of polystyrene highly diluted in a water suspension. One of the angles of our test of our setup is shown in Fig.1. Since the contrast is almost one and the form of the observed correlation function is close to be single exponential, we are sure to work in homodyne condition.

All theories and models explain the scattering behavior in terms of the field autocorrelation function. This has to be taken into account in the analysis of the light scattering curves by fitting the square of $g^{(1)}(\vec{q},t)$ to the experimentally obtained $g^{(2)}(\vec{q},t)-1$.

For the analysis of light scattering curves from PCS several methods can be used. Besides the well known CONTIN algorithm [13], a inverse Laplace-method to obtain the distribution of relaxation times, and the methods of the Cumulants (see e.g. [14]), the easier to handle Kohlrausch-Williams-Watts function(KWW) [15, 16].

$$g^{(1)}(t)=\exp\left\{-\left(\frac{t}{\tau}\right)^{\beta}\right\} \tag{5}$$

can be a method of choice. The advantage of the KWW function is that the theory predicts a value for the parameter β describing the width of the distribution of relaxation times to be $\beta=1$, which is a single exponential decay, in the case of a diffusion of monodisperse particles. Such a case is depicted in Fig. 1. The particles are not really monodisperse, but the polydispersity M_w/M_n of this polystyrene latex standard (Polyscience) is 1.05 and the mean diameter is 115 nm. To illustrate the measured quantity τ is plotted on the graph, positioned at $1/e$ for a single exponential decay as is here the case. A fit with Eq. (5) led to a value of $\beta=0.98$. A measurement like this can be used to obtain the maximum possible contrast f (comp. Eq. (4)) in the real experiment. As one can observe our setup is close to be ideal in terms of contrast. If in another experiment in the

same setup contrast factors of less then $f = 1$ are obtained the reason has to be found in not resolved, usually faster relaxation processes [17] outside of the measurement window of PCS. With the help of other experimental techniques as e.g. Fabry-Perot interferometry these faster processes might be explored.

In the further analysis not the fitting parameter τ but its mean value

$$\langle \tau \rangle = \frac{1}{\beta} \Gamma\left(\frac{1}{\beta}\right) \tau, \tag{6}$$

where Γ is the Gamma function, has to be used.

Hydrodynamic theory in the case of the diffusion of a particle in the limit of infinite dilution and scattering vector $q \to 0$ delivers for the relaxation rate $<\Gamma>$:

$$\langle \Gamma \rangle = \frac{1}{\langle \tau \rangle} = \langle D \rangle q^2 \tag{7}$$

with D the diffusion coefficient. Stokes and Einstein connected D to the radius of a sphere of radius R moving in a medium of viscosity η

$$\langle D \rangle = \frac{k_B T}{6\pi\eta \langle R_H \rangle} \tag{8}$$

k_B is here the Boltzmann constant and T the temperature in Kelvin. R_H is the so called hydrodynamic radius, the radius of an equivalent sphere moving through a homogeneous medium. This hydrodynamic radius and the real dimension of the particle in question is subject of influences or better interaction between the medium and the particle. One distinguishes here between slip and stick modus as extreme cases where in the former there is no attraction or even repulsion between solvent molecules and particle and in the latter at least one layer of solvent molecules 'sticks' to the surface of the particle. This leads to an apparent radius which in the first case is smaller then the real radius and in the second case is larger than the radius of the particle studied. In the case of CO_2 because of the lacking dipole moment we expect besides the van der Waals interaction no other relevant influence of the apparent radius by stick or slip. The radius obtained by the light scattering experiment thus should be close to the real radius of the particles.

2.2. Polymerization

Reaction under heterogeneous reaction conditions are widely used in industry and academia for the formulation of polymer latices. Heterogeneous reaction conditions can be macro, micro, or mini-emulsion with or without stabilizer. A recent survey and comparison can be found in [18] or in the textbook [19]. To transport the principles to reactions in supercritical CO_2 we decided to look for thermodynamically stable emulsions. In order to achieve this we had to decide for a stabilizing agent which we found in the form of PS-b-PDMS and part of this work was to find the thermodynamic stable region in the phase diagram of the multi component system.

The principle of stabilization is depicted in Fig. 2. A CO_2-philic part, here the PDMS chain, and a CO_2-phobic part, here the PS-chain, aggregate under certain pressure, temperature and concentration conditions eventually to a micellar structure. Adding monomer, e.g. styrene or vinylpyrrolidone, and choosing the inner, CO_2-phobic part right, the monomer will concentrate and fill these micelles. Adding a CO_2 insoluble starter molecule like AIBN will result in a nano-reactor initially a few nanometer in diameter. The initiator is activated by reaching a certain temperature and the polymerization of the product starts in the monomer swollen micelles with stabilizer in. Other micelles without starter act as monomer reservoirs. This type of hetero-phase nucleation for polymerization in a micro-emulsion leads to a broad distribution of molecular weight as we have observed in the formulation of PVP as shown in later chapters.

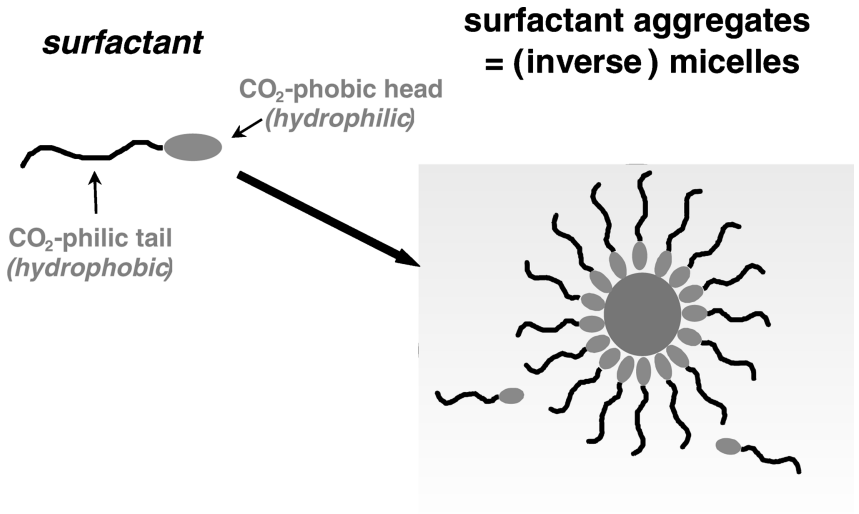

Fig. 2. Sketch of aggregation of amphiphilic molecules to form a micelle. The inner part is e.g. an in sc-CO_2 insoluble molecule.

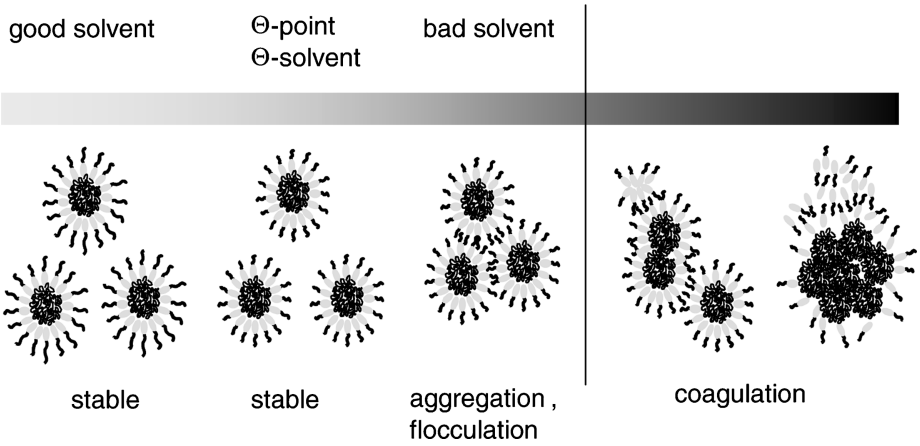

Fig. 3. Generalized picture of the influence of the solvent quality to the micellization behavior of amphiphilic molecules.

But before looking further into the process until complete polymerization of all monomer in the ideal case, a few words about the stability of such micellar structures. The main mechanisms for destabilization in an emulsion are molecular diffusion degradation (Ostwald ripening) and coalescence by collisions. Ostwald ripening can be suppressed by addition of small amounts of highly monomer soluble and here CO_2-insoluble compounds.

In Fig. 3 the aggregation behavior of micelles in dependence of the solvent quality is depicted. In our system using CO_2 as solvent the solvent quality is influenced not only by temperature but by pressure as well. In micro-emulsions in regular solvents as e.g. water the whole process can only exist above the critical micelle concentration (cmc) of the surfactant used. In sc-CO_2 as in other pressurized systems a critical micelle pressure (cmp) exists as well as shown by [20] for the systems poly(1,1-dihydroperfluorooctylacrylate) and poly(vinylacetate).

3. EXPERIMENTAL

In the course of heterogeneous polymerization in sc-CO_2 theoretical predictions about the behavior of the quaternary system sc-CO_2 as solvent, monomer, stabilizer, and initiator is difficult. Especially the aggregation behavior of the stabilizer, in our case the block-copolymer PS-PDMS, depending on pressure, temperature and relative amount of the as co-solvent acting monomer has to be studied in situ to decide for the best route for the later polymerization reaction. Three methods are available: small angle neutron scattering, small angle x-ray scattering and light scattering of which we choose the last because of its easy availability.

3.1. Materials and sample preparation

In all experiments and polymerization reactions we used CO_2 of grade 4.5 from Linde company (Germany). It was used without further purification but was dried over molecular sieve (4 Å). Vinylpyrrolidone (VP) as the monomer was purchased from Aldrich (purity 99%+). It was de-inhibited using an activated basic alumina column. The starter or initiator for the polymeric reaction was 2,2´-azobis(isobutyronitrile) (AIBN) purchased from Fluka and was re-crystallized from methanol and dried under vacuum before usage in the polymerization reaction. In our light scattering experiments involving monomers we added 0.01 vol% of 4-methoxyphenol (FLUKA) as inhibitor of thermal polymerization reactions.

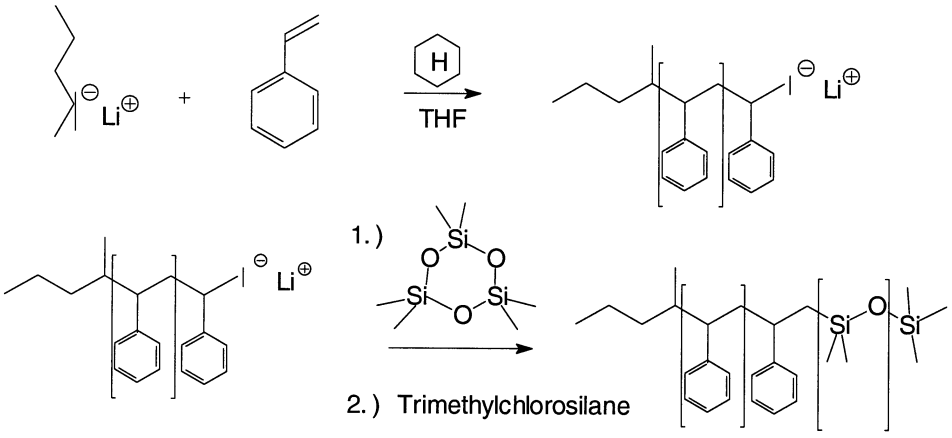

Fig. 4. Scheme of polymerization route to obtain the block copolymer PS-b-PDMS. First step: polymerization of styrene to PS; second step adding PDMS to the PS chains by polymerization of D3 trimethylchlorosilane.

Table 1:
Physical properties of the stabilizer molecules PS-b-PDMS prepared in our laboratory

identifier	M_w(PS)	M_w/M_n (PS-b-PDMS)	M_w (PDMS)
PSPDMS1 (4/14)	3800	1.05	14400
PSPDMS2 (4/36)	4400	1.06	36200
PSPDMS3 (5/25)	5300	1.09	24500
PSPDMS5 (6/7)	5700	1.09	6900
PSPDMS6 (6/20)	6100	1.06	19500
PSPDMS7 (7/37)	7200	1.07	37400
PSPDMS8 (9/10)	9400	1.06	10000
PSPDMS9 (14/58)	14300	1.05	57500
PSPDMS10 (11/127)	10500	1.06	127000
PSPDMS11 (15/18)	15400	1.06	18100
PSPDMS12 (17/50)	16800	1.10	49900
PSPDMS13 (23/105)	23100	1.10	104900

The studied homo-polymer PDMS was anionically polymerized in our laboratory according to ref. [21]. The molecular weight M_w = 113000 g/mol and the polydispersity of 1.21 was determined by Gel-Permeation Chromatography (GPC). To clean and to remove dust the polymer was dissolved in toluene, the solution filtered through an 0.22 μm Teflon filter (Millipore) into a dust free vial. Subsequent evaporation of the solvent under high vacuum at 320 K insured complete removal of the solvent.

The diblock copolymer PS-b-PDMS used as a stabilizer in our polymerization experiments was synthesized by living anionic polymerization following literature procedures [22]. The principle is shown in Fig. 4. In the course of this procedure first the PS chain is polymerized and after completion of this first reaction step a small part is taken out of the otherwise hermetically sealed reaction vessel for the analysis of the block to obtain the molecular weight of the intermediate stage of the PS chain. In a second step the cyclic dimethylsiloxane trimer D3 is added. The PDMS block is formed starting from the "living" PS macro-anion by ring opening anionic polymerization. Finally trimethylchlorosilane is added for the formation of trimethylsilyl (TMS) endcaps.

After forming the block-copolymer we determined the ratio of M_n(PS) to M_n(PDMS) monomers by ^{1}H nuclear magnetic resonance thus obtaining the overall molecular weight and the molecular weight of the PDMS block using the known molecular weight of the PDMS segments. The polydispersity of the so

obtained diblock copolymers determined by GPC was in all cases $M_w/M_n < 1.1$. In order to study the influence of composition and molecular weight of the stabilizer on the polymerization we produced a range of block copolymers as listed in Table 1.

When used in light scattering experiments all substances have to be dust free. To ensure this we dissolved the polymers in toluene (Fluka, 99%+), filtered the solution through 0.22 μm Millipore filters into dust free vials. The solvent was carefully evaporated at 323 K for at least one week.

To prepare light scattering samples containing PDMS we placed 15 mg into the made dust free high pressure cell and flushed with CO_2 for one hour. Then the cell was heated to the temperature of the experiment and subsequently pressurized with CO_2 to the pressure of this experiment. This solution know was stirred with the help of a magnetic stirring bar placed in the high pressure cell to assure complete mixing within one hour. Before starting the light scattering experiment we let the solution equilibrate for one further hour. This was necessary since directly after the mixing presumably strong compositional fluctuations led to extra relaxation processes in the light scattering data.

The same preparation procedure applied for the PS-b-PDMS light scattering samples. In addition we added monomer to the solution to mimic the starting point of a polymerization reaction as it normally takes place in a high pressure autoclave. In a polymerization reaction additionally starter as e.g. AIBN would be added. Since we do not want to start a polymerization at all during our light scattering experiment we added the inhibitor 4-methoxyphenol. The relative concentration of either initiator AIBN or inhibitor 4-methoxyphenol (0.01 vol%) is to small to expect changes in the aggregation behavior of the stabilizer.

All polymerization reactions took place in a 60 ml stirred autoclave(Medimex, 1.4980 steel alloy). In these autoclaves typically 4 g of monomer were placed as well as 50 mg AIBN plus the desired amount of stabilizer. We degassed this mixture three times by freezing, applying vacuum and subsequent flushing with CO_2. This procedure proved to be necessary to remove oxygen and water from the mixture which otherwise produce unwanted side effects during the polymerization.

3.2. High pressure environment

In both the light scattering experiments and in the polymerization of PVP we use similar high pressure equipment for the pressurization. Namely HPLC pumps HP880 (Jasco, Japan) are used to pressurize the CO_2 from the cylinder. To monitor and vary pressure and temperature a purpose build controller was used in combination with resistance cartridge heaters and Pt100 resistance temperature sensors. In most cases two Pt100 were used to monitor the temperature in the sample itself as well as in the pressure container. This proved

to give better results in terms of temperature stability which never exceeded a precision of ±0.1 K. The inner temperature sensors are HP-Pt100 (PTG company, Germany). The pressure sensors used are from WIKA company (Germany).

Light scattering: The high pressure optical flow through cell we designed for our light scattering experiment had to fulfill several requirements. Its design should allow for easy cleaning since in light scattering impurities like dust can make the experiment impossible. Hence we designed it to be a flow through cell so we can clean the interior with a stream of supercritical CO_2. Another requirement was the accessibility to the scattered light from as many as possible angles. For further applications in particle sizing we wanted the design to be robust, not too expensive to manufacture and easy to handle.

Our high pressure light scattering cell is depicted in Fig. 5 and 6. The outer container, best visible as a ring in Fig. 6 is made from stainless steel alloy 1.4701. During the production one has to take great care not to magnetize the material since later a magnetic stirring bar in the sample chamber can only

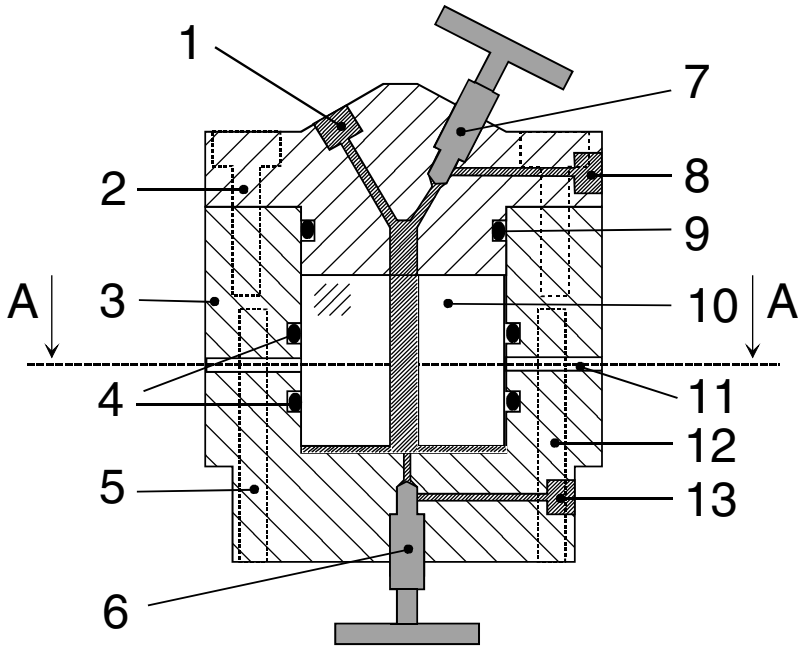

Fig. 5. Vertical cross section of the high pressure light scattering cell.

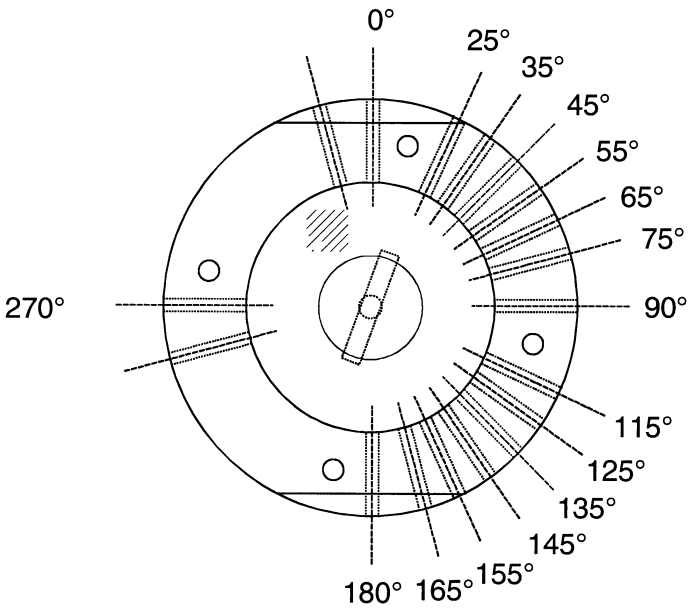

Fig. 6. Horizontal cross section A→A from Figure 5. Position of the bores for scattered and incident (0° →180°) light.

be driven by an outside magnet when the cell itself is not paramagnetic. I.e. no polishing is allowed since this changes the magnetic properties of this stainless steel. The actual pressurized chamber is a cylinder of fused quartz (Hellma company, Mühlheim, Germany), highly polished with an outer diameter of 60 mm, height 40 mm and an inner cylindrical bore of 15 mm. This cylinder now allows us to have in principle a 360° window, only the stainless steel container with its discrete bores is limiting the accessible angles. We used quartz instead of sapphire – another possible choice as window material – since sapphire is known to become bi-refringent under pressure thus limiting the experimental possibilities since a distinction between polarized and depolarized components of the scattered light is not possible any more. Fused quartz has no problem in this direction but one has to pay for this advantage with less pressure resistance of the material. It is known that fused quartz becomes brittle under high pressure. Because of this reason we designed our cell in a way to minimize pressure gradients of the quartz cylinder. The pressure medium is around the cell apart from a small ring at and around the bores for the incident and the scattered light. There O-rings (EPDM 80, Parker, USA) as sealing material were used. Within the usual safety margins the maximum pressure was calculated and tested to be 60 MPa at a temperature of 373 K. Below the quartz cylinder a removable stainless steel plate is placed for easy removal of the cylinder from

the stainless steel container. The steel container is fitted with an inlet in the bottom sealed with a valve.

The sample in the sample chamber can be stirred by a Teflon coated magnetic stirring bar driven by an external rotating magnet under the bottom of the steel mantle integrated into the holder of the cell. Integrated into the steel mantle are four cartridge heaters and a holder for a Pt100 temperature sensor. The cover of the cell is stainless steel sealed by O-rings against the steel mantle. This cover contains three G1/4 connectors for inner temperature sensor, pressure sensor and backpressure regulator (Nupro, USA). A fourth connector in the cover is the upper inlet for CO_2 sealed with a valve.

The whole construction had to fulfill one more requirement which proved to be vital for light scattering experiments. After filling and closing no solution or sample has to be outside the temperature regulated space. Otherwise convectional flows could occur leading to strong correlated signal and hence additional correlation functions in the experiment making the experiment difficult if not impossible to perform.

The leakage rate of our design was experimentally determined to be less than 0.2 MPa/h, small enough to neglect the resulting change of density (since preferably solvent will escape) in the sample during the usual light scattering experiment.

As can be seen from Eq. (1) and (8) we need for a successful analysis of the light scattering data the numerical values of the refractive index n and the viscosity η of the mixture/solutions. Values for CO_2 below and above the critical point are available from Ref. 17. Unfortunately the data stops below the experimental range we were about to explore so we set out to complete this set of data.

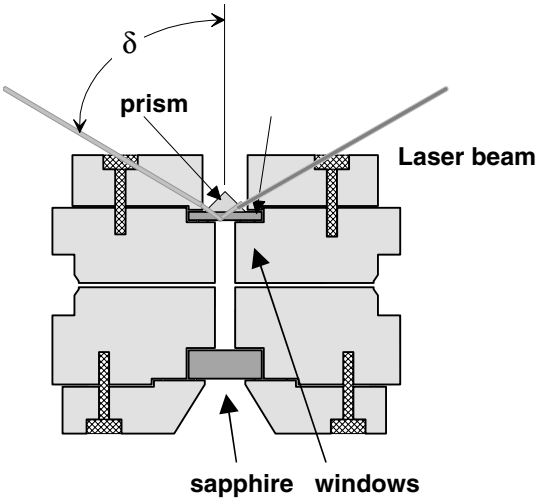

Fig. 7. High pressure cell used for refractive index experiment.

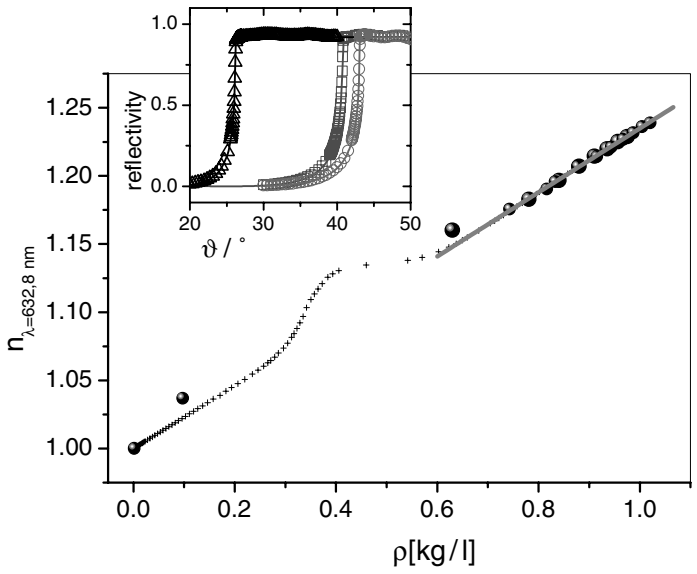

Fig. 8. Refractive index of CO_2 depending on its density. Small crosses: literature values by Obriot et.al. [17]. The inset shows typical curves from the reflection experiment.

Therefore the refractive index was obtained experimentally using the method of reflection at a a surface. The high pressure apparatus used was developed by G. Kleideiter [23, 24] and used in a Kretschmann configuration [25] . The cell we used is depicted in Fig. 7 and the values of n obtained at an incident wavelength of 632 nm are shown in Fig. 8 together with literature values for *n* by Obriot [17]. The inset of Fig. 8 displays typical experimental curves at 308 K from the refractive index experiment together with fits using a transfer-matrix method [24]. Our light scattering experiments take place at 532 nm incident wavelength. To accommodate the different wavelength we recalculated the refractive index using a Cauchy relation after Howell [26]:

$$n(\lambda)-1=4{,}375\times10^{-4}+2{,}58\times10^{-18}m^2/\lambda^2+2{,}3\times10^{-28}m^4/\lambda^4 \qquad (9)$$

As discussed before, we need the viscosity η of the solutions. In a first step we calculated the viscosity of sc-CO_2 at a given set of temperature and pressure

using the algorithm of Ely [27]. To obtain η we used the mixing rule by Lucas [28].

Polymerization: The autoclaves used for the polymerization reaction (Medimex, 1.4980 steel alloy) were combined with a stirrer to mix the solution during the chemical reaction to ensure homogeneous distribution of AIBN. This is necessary to obtain not to polydisperse products.

3.3. Light scattering setup

The method of light scattering utilized in our experiment is the so called photon correlation spectroscopy (PCS) or quasi-elastic or dynamic light scattering. The basic scheme of our setup is depicted in Fig. 9. The single line, single mode laser used is either a frequency doubled continuous wave Nd:YAG-Laser (Adlas DPY 425 II, Germany) or a Nd:YVO_4 (Verdi V2, Coherent) both at 532 nm wavelength. The incident power on the sample in the cell was, depending on the system, between 5 and 100 mW.

Our high pressure cell is mounted on a goniometer to allow easy access to all angles possible. The accuracy of scattering angle we achieved in our experiment was ± 0.1°. The detection of the scattered light was achieved via a

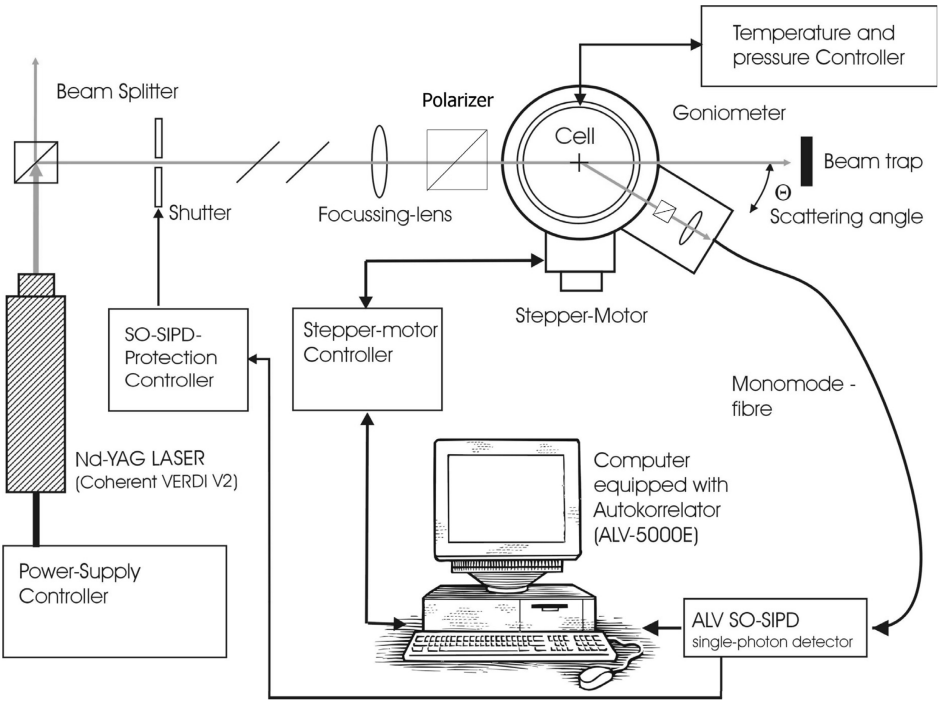

Fig. 9. Light scattering setup for photon correlation spectroscopy.

single mode optical fiber and a single photon detector (SO-SIPD, ALV, Langen, Germany). This detector setup is based on a two photo-multiplier (PM) tube and a beam-splitter to feed each PM 50% of the detected light. This setup ensures in combination with a pseudo cross correlation done in the hardware correlator (ALV5000/E, ALV) the signal to be free from artificial data at short correlation times.

With the help of the focussing lens the incident laser light is concentrated into the scattering volume in the cell. The polarizer, a Glan prism (Halle, Berlin), extinction coefficient 10^6, selected only the vertically polarized component of the laser light and the analyzer, a Glan-Thompson prism (Halle), extinction coefficient 10^7, again selects the vertical part. In this so called VV polarization configuration only density fluctuations are detected, e.g. diffusional motion.

3.4. Polymerization of poly(vinylpyrrolidone)

We obtained carbon dioxide (grade 4.5) from Linde company. It was used after drying over molecular sieve (4 Å).

For the heterogeneous polymerization we used as stabilizer a diblock copolymer with a CO-philic and a CO-phobic block. The solubility of PDMS is known from literature and we combined this with the known relative insolubility in sc-CO_2 of PS. The diblock copolymer was synthesized in our laboratory via living anionic polymerization according to literature procedures [22].

Typically 4 g of monomer were placed in a 60 ml stirred autoclave (Medimex) plus 50 mg of AIBN and the desired amount of stabilizer. To start the reaction, the autoclave was heated to 353 K, CO_2 was then added slowly until the temperature and pressure for a given experiment were reached. The reaction, schematically drawn in Fig. 10, was allowed to take place over 8 hours. Then the autoclave was cooled to room temperature at a rate of smaller than 5 K/min and subsequently the pressure was reduced at a rate smaller than 2 bar/min. The reactant were characterized without further treatment.

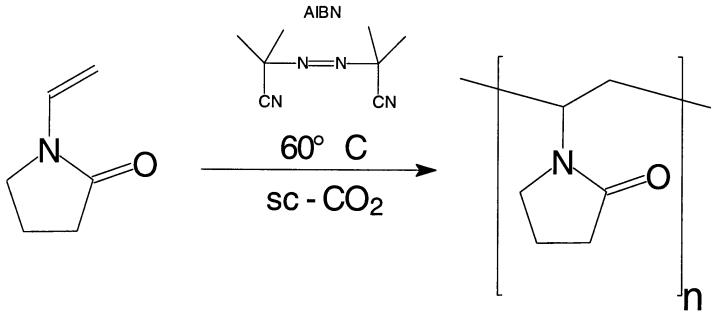

Fig. 10. General polymerization route for poly-vinylpyrrolidone with the help of the starter molecule AIBN.

For the characterization of our polymers the standard method of GPC to obtain the molecular weight M_w and M_n as well as the size distribution polydispersity M_w/M_n was used utilizing a Waters 590 GPC with a styrene-divinylbenzene (SDV) column of dimension 500 mm x 8 mm, paricle size 10 μm, pore sizes of 500, 10^5, and 10^6 Å. As solvent we used water at 20° C. The eluted polymer was detected by a UV-Soma/RI-ERC system. To calculate the molecular weights we used narrowly distributed poly(ethylene oxide) (PEO) standards. For further analysis we used a Bruker 300 MHz instrument to obtain NMR data. All scanning electron micrographs (SEM) pictures were done with a LEO EM912 (1 kV, InLens).

4. RESULTS

A main aspect of our work was the development of a high pressure light scattering cell as described in a previous chapter. With the help of this cell we want to explore the possibilities of structure formation of stabilizers in sc-CO_2 namely the formation of micelles. These micelles are wanted as micro- or nano-reactors in a later heterogeneous polymerization reaction to produce in a controlled way latex particles. As discussed before, most polymers apart from fluorinated polymers and some siloxane polymers do not dissolve in sc-CO_2 and the only route to obtain polymers with control over their microstructure and morphology is to stabilize the educts and products during the chemical reaction.

In a first step after completing our high pressure cell we performed experiments on poly-dimethylsiloxane (PDMS). It is know, that PDMS can be dissolved in sc-CO_2 to a certain degree. Our experiment on PDMS in sc-CO_2 thus serves two purposes. First we use it as a test to compare the in the experiment obtained radii with literature values from neutron scattering and second the solvation behavior of the PDMS part of the block copolymers later on used can be estimated.

The second part of the light scattering study involves the study of the aggregation behavior of a mimicked system for the actual polymerization with the only difference of adding inhibitor 4-methoxyphenol instead of the starter molecule AIBN for polymerization. The obtained result can later be used to optimize the requirements for a successful polymerization.

4.1. Dynamic light scattering on PDMS

In Fig. 11 a set of correlation functions of 1 vol% PDMS in sc-CO_2 at 40.3 MPa and 316 K is depicted. Fits to this data lead to the relaxation rate of this polymer in sc-CO_2 shown in the inset of Fig. 11. From this with the help of Eq. (4), (7), (8) we obtain the diffusion coefficient $D = 2.6*10^{-10}$ m^2/s and the hydrodynamic radius R_H = 8nm.

This parameter R_H can now be compared with the radius of gyration R_g of a polymer coil. Following Haug and Meyerhoff [29] we can calculate $R_g = 0.0027\ M_w^{0.5}$ under Θ-conditions. This results for our PDMS of M_w=113800 g/mol to R_g=9.1 nm. Kirkwood and Riseman [30] postulate a ratio between R_g and R_H to be a specific constant of a polymer species in solution to be described as a Gaussian coil. Experimental results for PDMS led to a ratio of 1.21 [31] and for polystyrene to 1.27 [32]. With this correction we expect as hydrodynamic radius R_H = 7.5 nm. The question if we are in Θ-conditions for the quality of the solvent sc-CO_2 at our temperature and pressure has been answered by Melnichenko et.al. [33]. They studied PDMS in sc-CO_2 with the technique small angle neutron scattering and found the radius of gyration to be independent of pressure and temperature up to 52 MPa and 338 K and moreover they found it to be equal to the radius under Θ-conditions.

Our value of R_H = 8nm is within the experimental uncertainties equal to what is expected from theory since we did not take into account solvent effects, e.g. draining effects as well as errors in the data used for refractive index and for the shear viscosity, both needed in the previous computation.

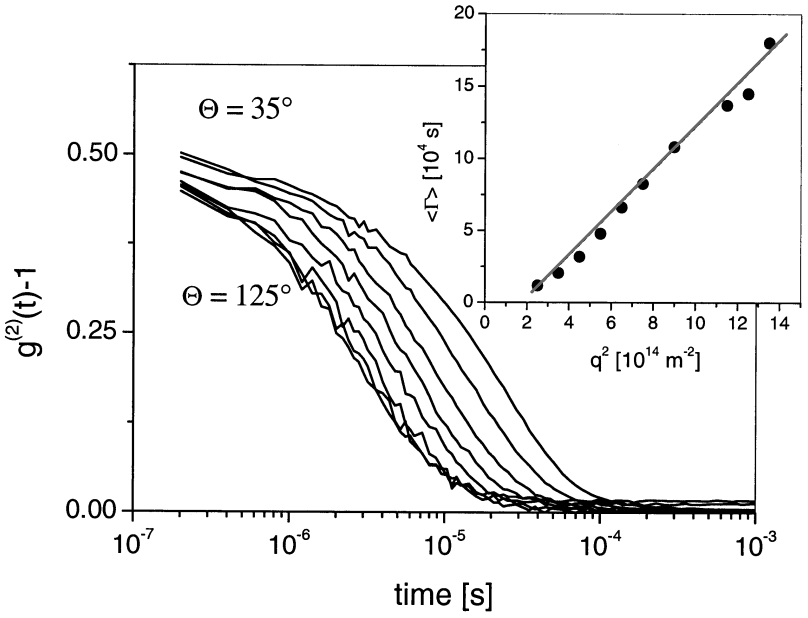

Fig. 11. Correlation functions $g^{(2)}(t)$-1 of PDMS as measured in the angular range from 35° to 125° at T = 316 K and p = 40.3 MPa. The inset shows the inverse relaxation time or relaxation rate $<\Gamma>$ vs. square of the scattering vector, q^2. The linear fit leads to the diffusion coefficient D as slope of the function.

A look at Fig. 11 reveals that the contrast of the correlation functions is not close to one as expected from the test measurement of PS latex particles (see Fig. 1). The experiment on PS rules out heterodyne scattering which would lead to a contrast of smaller than one since we use the same experimental surroundings and setup. This discrepancy is due to relaxation modes outside of the time window of the PCS experiment. From test we know there are no substantial slow components and the conclusion has to be sought at shorter times.

A possible explanation could be the existence of fluctuations in the solvent sc-CO_2. We are far away from the critical parameters T_c=304.2 K and p_c=7.8 MPa and critical fluctuations, if those had set in they would be expected to have very small correlation length and thus fast relaxation times.

Another explanation could be density fluctuations as manifestation of clustering of CO_2 molecules in the supercritical state. Indication for the existence of such structures was given through small angle x-ray scattering studies [34], x-ray diffraction [35] and neutron diffraction [36] experiments. The correlation length found in these studies where around 1 nm. Such small fluctuations lead to fast relaxation motions as observed here. This feature was observed in all our light scattering experiment in sc-CO_2 and will be discussed further in the next chapters.

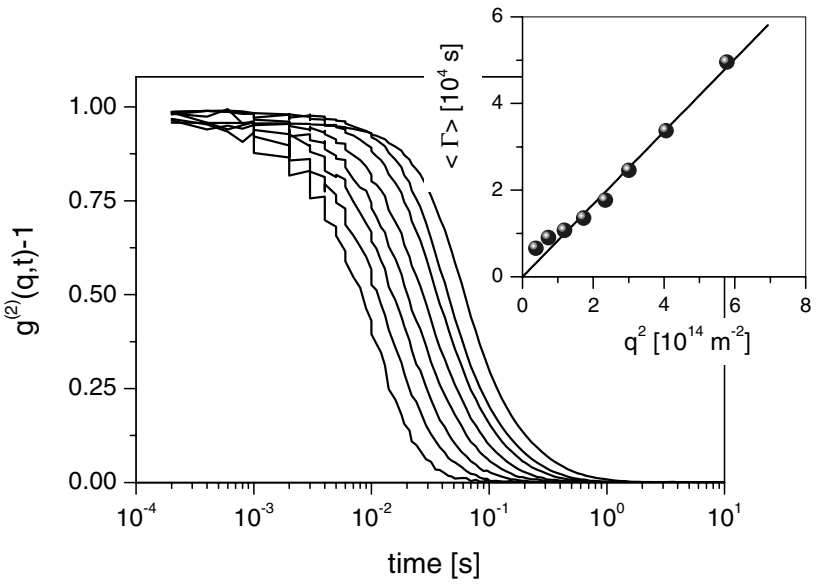

Fig. 12. Correlation function of PS-b-PDMS plus styrene in CO_2 at 338 K and 40.4 MPa. The inset depicts the diffusion constant as the slope of $<\Gamma>$ vs. q_2.

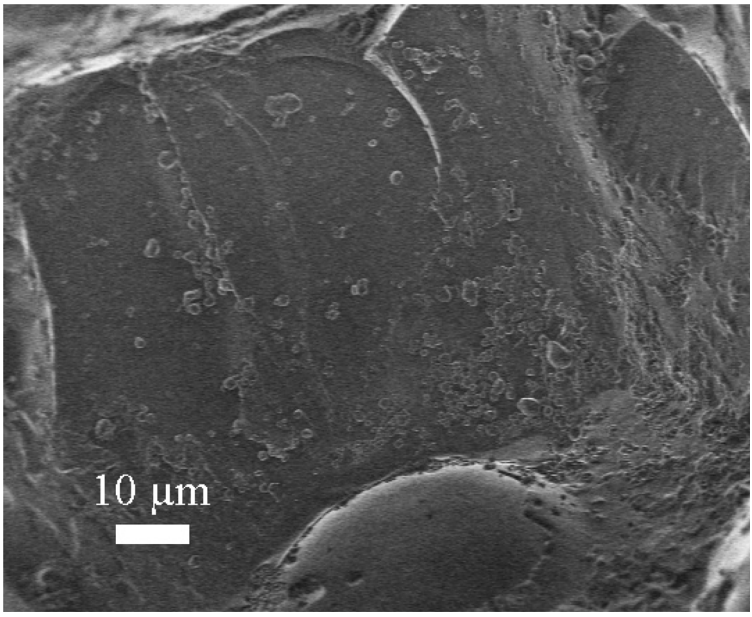

Fig. 13. PVP synthesized in a precipitation polymerization without the aid of a stabilizer. The picture was taken on milled product with scanning electron microscopy.

4.2. Dynamic light scattering on PS-b-PDMS

As an example in Fig. 12 we show the intensity correlation function of the amphiphile PS-b-PDMS, block length ratio 9/27, in sc-CO_2 plus styrene and the inhibitor 4-methoxyphenol. In contrast to the result from pure PDMS in CO_2 we measure a contrast of almost equal to one and the fits showed a β_{KWW} close to one as well. Only in the plot of $<I>$ vs. q^2 we see a difference. For a diffusional motion the data should go through the origin. In all samples we measured we found this upturn at small q respectively small angles. A possible explanation could be a precipitation of micelles after coagulation as depicted in Fig. 2.

Calculating the hydrodynamic radius R_H following Eq. (4), (7), (8) we obtain 31 nm as the radius of the micelle. This is much smaller as the particles we generate later in our polymerization experiment.

4.3. Polymerization of PVP

A usual question raised in discussing polymerization in sc-CO_2 is why this is advantageous compared with other polymerization techniques as e.g. precipitation polymerization in a standard solvent or if it comes to heterogeneous polymerization if this cannot be done as well in aqueous systems not requiring high pressure setups.

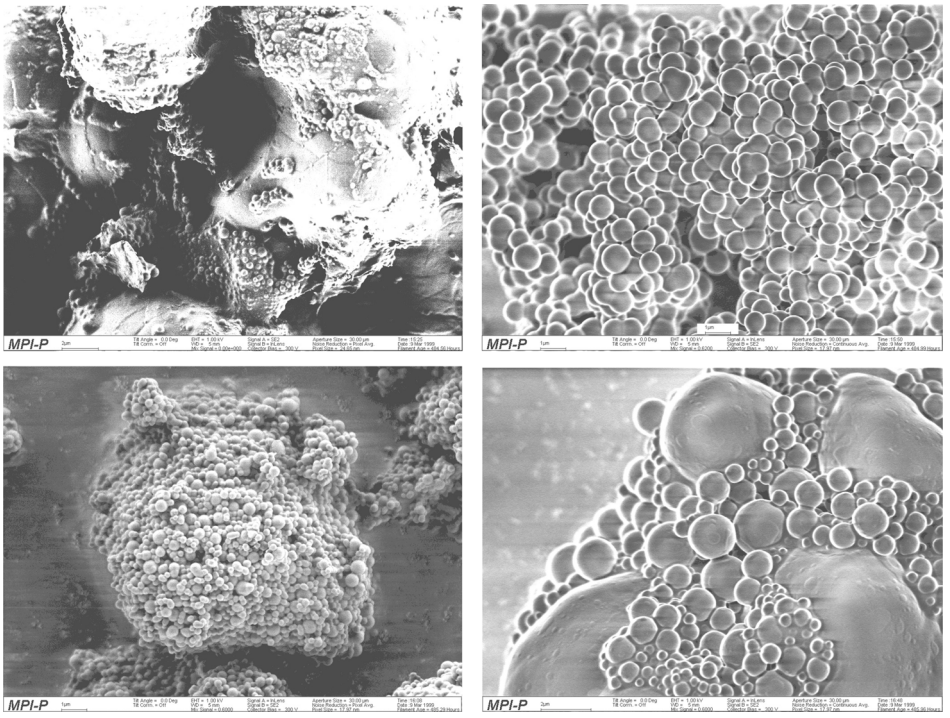

Fig. 14. Morphology of the obtained PVP-latex particles depending on the block length/block length ratio of the stabilizer PS-b-PDMS. Concentration 5 vol%, block length ratios PS/PDMS: 4/36, 5/25, 6/7, and 6/20 from left to right; polymerization at 350 K and 38 MPa.

The first part is answered easily, since in those cases where one wants to obtain a pure product a polymerization in organic solvent always poses the risk of not complete removal of the solvent - in life sciences and in pharmacy often a hindering factor for the usability. Processability can be an argument as well to speak for a reaction in heterogeneous surroundings. The second part has to be answered from system to system. In many cases the complete absence of H_2O is a predicament for further use or the reaction cannot be done as an aqueous heterogeneous system.

The polymer poly(vinylpyrrolidone) (PVP) we set out to produce is difficult to obtain in a conventional dispersion or emulsion polymerization in aqueous reaction. Polymerization of PVP without stabilizer results in white or slightly yellow, glassy material. The result of a test in sc-CO_2 at 353 K, 39 MPa, 8h reaction time is shown in Fig. 13 as a scanning electron micrograph of a

particle milled from the precipitation in the reactor. PVP has, depending on the molecular weight, a glass transition temperature of 410 to 448 K. This high glass transition temperature leads to problems in the further processing of the material if produced in this way.

The addition of a small percentage of stabilizer, in our case PS-b-PDMS, changes the physical properties of the product completely. We have explored different molecular weight of the stabilizer and changed the percentage used of the more successful. The product in most cases was a powdery PVP material which was easily recovered from the reaction vessel.

We used in a polymerization at 350 K, 38 MPa, 8h reaction time, stabilizer changing the block length ratio as indicated in Table 1. Fig. 14 is a selection of these experiments namely at a concentration of 5 wt% and block length ratios of 4/36, 5/25, 6/7, and 6/20 from left to right. Fig. 15 is a representation of changing the concentration. The stabilizer used here is the type 6/20 with a range of concentration of 10, 5, 2, and 1 wt% in a polymerization reaction at 350 K, 38 MPa, and 8h reaction time. Our result was that a concentration of only 1 wt% and a block length ratio of app. 1/3 and an overall molecular weight of close to 30000 g/mol of the stabilizer gave the best results. For these parameters we obtained uniform particles with a narrow size distribution approximately 1 μm in diameter. The molecular weight of the PVP polymers constituting the latices is around 240000 g/mol in all cases but with a broad distribution in molecular weight as expected from the course of polymerization.

The SEM picture show in all cases aggregation of the latex particles and in some cases even coagulation. The aggregation behavior of the spheres can be understood. At ambient temperature and pressure the PDMS part of the blockcopolymer is above its glass transition temperature. We expect the PDMS to be on the outside of the spheres since these where in a micelle or in a stabilized reaction as the CO_2-philic part immersed in the solvent while the PS-part as the CO_2-phopbic part is expected to be in the inside. Thus due to the mobility of the PDMS chains these can "stick" together and act as a glue for the agglomeration. In a magnification of Fig. 15, lower left corner, one observes in Figure 16 the parts where the latex spheres break the agglomeration. Only a thin layer of the sphere takes part in the separation, the PS-part incorporated in the sphere had to be taken off as well in the break since the chemical bond between PS and PDMS hinders a separation of the block copolymer in its constituents.

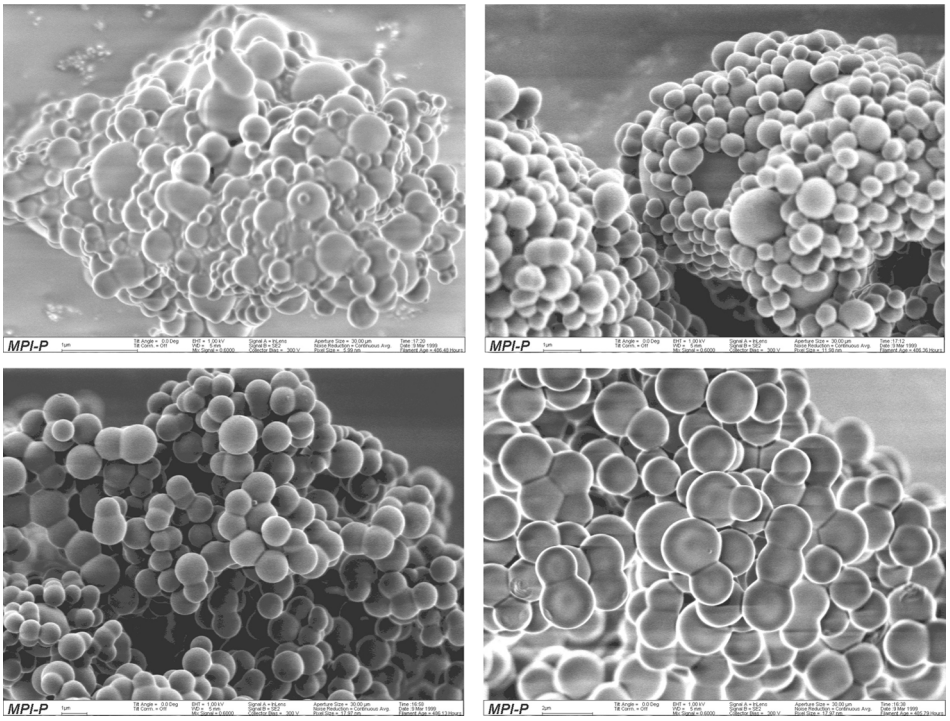

Fig. 15. Morphology of the obtained PVP-latex particles depending on the concentration of the stabilizer PS-b-PDMS of block length ratio6/20. Concentration 10, 5, 2, 1 vol%; polymerization at 350 K and 38 MPa.

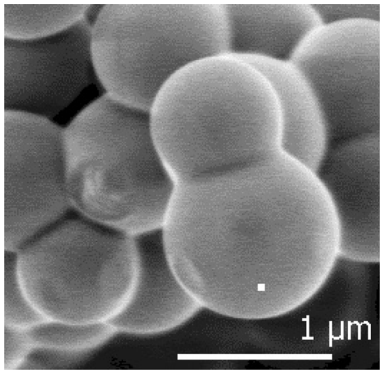

Fig. 16. Enlarged part of picture in lower right corner of Fig. 15.

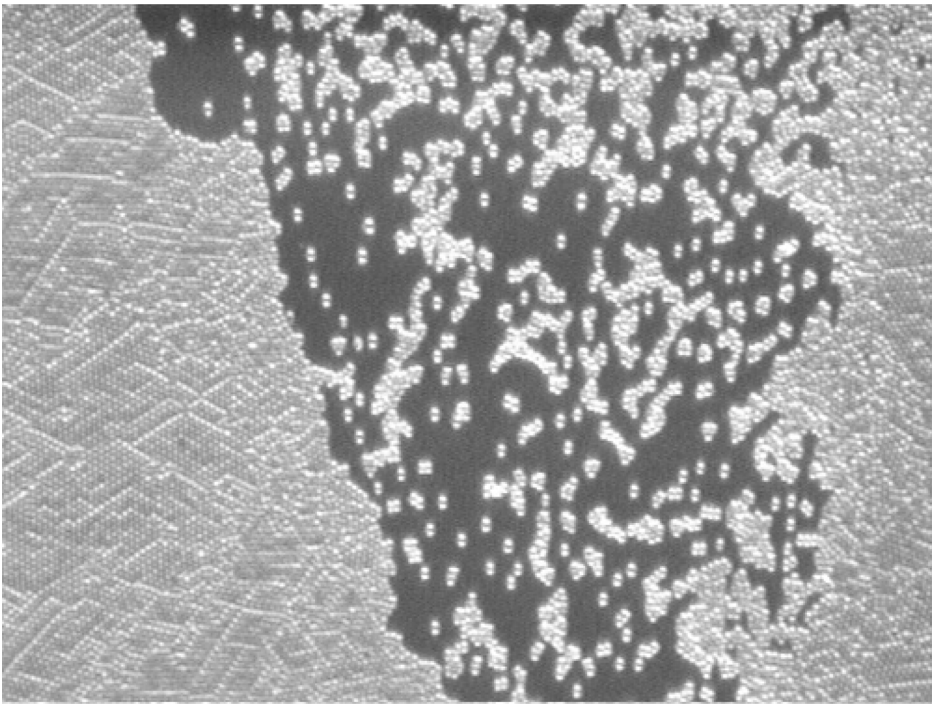

Fig. 17. PVP latex particles form a monolayer with a partially 2d crystalline domains on a glass substrate demonstrating the high degree of monodispersity of the particle size.

After redispersing the product with the 6/20 and 1 wt% parameters in a non-solvent for PVP – otherwise the spheres would be destroyed – we created by solution casting a monolayer of spheres on a glass substrate. As can be seen from Fig. 17 the PVP latex particles partly form a 2d crystal on the surface of the glass substrate as has been made visible by a light microscope. The crystalline domains formed are a further proof for the high monodisperse size distribution of the spheres.

5. CONCLUSION

In the course of our experiments we were able to produce well defined latex particles of poly-vinylpyrrolidone of about 1 μm diameter with a small size distribution. From this size we have to conclude that the particles were created in a stabilized reaction through the in sc-CO_2 amphiphilic block copolymer PS-b-PDMS. As determined by light scattering experiments the size of the micelles these amphiphilic molecules form at about the same experimental conditions is only 60 nm in diameter, much smaller than the product in the polymerization.

ACKNOWLEDGEMENT

We thank the German Science foundation (DFG) for financial support through the Schwerpunktprogramm SP 1019 „Überkritische Fluide".

REFERENCES

[1] M.A. McHugh, V.J. Krukonis, Supercritical Fluids Extraction: Principles and Practice, 2nd ed., Butterworth-Heineman: Stoneham, MA, 1993.
[2] J.M. DeSimone, Z. Guan, and C.S. Elsbernd, Science 257, 945 (1992).
[3] J.L. Kendall, D.A. Canelas, J.L. Young, J.M. DeSimone, Chem. Rev. 99, 543 (1999).
[4] K.A. Shaffer, T.A. Jones, D.A. Canelas, J.M. Desimone, S.P. Wilkinson, Macromolecules 29, 2704 (1996).
[5] T.J. Romack, E.E. Maury, J.M. DeSimone, Macromolecules 28 (1995) 912.
[6] J.P. Blitz, J.L. Fulton, and R.D. Smith, J. Phys. Chem. 92, 2707 (1988).
[7] J. Kojima, Y. Nakayama, M. Takenaka, and T. Hashimoto, Rev. Sci. Instrum. 66, 4066 (1995).
[8] S. Zhou, B. Chu, and H.S. Dhadwal, Rev. Sci. Instrum. 65, 1955 (1998).
[9] T. Berger, W. Steffen, Rev. Sci. Inst., 71 (2000) 2467.
[10] B.J. Berne and R. Pecora, Dynamic Light Scattering (Wiley, New York, 1976).
[11] B. Chu, "Laser Light Scattering", 2nd Ed., Academic Press, New York (1991).
[12] M. Kerker, "The Scattering of Light and other Electromagnetic Radiation", Academic Press Inc., New York (1969).
[13] S.W. Provencher, Comput. Phys. Commun. 27, 229 (1982).
[14] W. Brown, "Dynamic Light Scattering", Clarendon Press, Oxford (1993).
[15] R. Kohlrausch, Ann. Phys. 12, 393 (1847).
[16] G. Williams, D.C. Watts, Trans. Faraday 66, 80 (1970).
[17] J. Obriot, J. Ge, T.K. Bose, J.-M. St.-Arnaud, Fluid Phase Equilibr. 86, 315 (1993).
[18] K. Landfester, Macromol. Rapid Commun., 22, 896 (2001).
[19] H.-D. Doerfler, "Grenzflächen – und Kolloidchemie", VCH, Weinheim (1994).
[20] S. Zhou, B. Chu, Macromolecules, 31, 5300 (1998); ibid 31, 7746 (1998).
[21] U. Maschke, T. Wagner, X. Coqueret, Macromol. Chem. 193, 2453 (1992)
[22] Zilliox, J.G.; Roovers, J.E.L.; Bywaters, S. Macromolecules, 1975, 8, 573.
[23] W. Knoll, Ann. Rev. Phys. Chem 49, 569 (1998).
[24] G. Kleideiter, Dissertation, Osnabrück (1999).
[25] W. Karthe, R. Müller, „Integrierte Optik", Akademische Verlagsgesellschaft, Leipzig (1991).
[26] J.T. Howell, Phys. Rev. 6, 81 (1915).
[27] J.F. Ely, CO2PAC: „A Computer Program to Calculate Physical Properties of Pure CO_2", National Institute of Standard and Technology, Washington DC (1986).
[28] K. Lucas, Chem. Ing. Tech. 53, 959 (1981).
[29] A. Haug, G. Meyerhoff, Macromol. Chem. 53, 91 (1962).
[30] J.G. Kirkwood, J. Riseman, J. Chem. Phys. 16, 565 (1948).
[31] C.J.C. Edwards, R.F.T. Stepto, and J.A. Semylen, Polymer 23, 865 (1982).
[32] H.-U. ter Meer, W. Burchard, Colloid Poly. Sci. 258, 675 (1980).
[33] Y.B. Melnichenko, E. Kiran, G.D. Wignall, K.D. Heath, S. Salaniwal, H.D. Cochran, M. Stamm, Macromolecules 32, 5344 (1999).

[34] K. Nishikawa, I. Tanaka, Y. Amemiya, J. Phys. Chem., 100 (1996) 418.
[35] T. Morita, K. Nishikawa, M. Takematsu, H. Iida, S. Furutaka, J. Chem. Phys., 101 (1997) 7158.
[36] R. Iishi, S. Okazaki, I. Okada, M. Furusaka, N. Watanabe, M. Misawa, T. Fukunaka, J. Chem. Phys., 105 (1996) 701.
[37] T. Berger, B. McGhee, U. Scherf, W. Steffen, Macromolecules, 33 (2000) 3505.

Supercritical Fluids as Solvents and Reaction Media
G. Brunner (editor)

Chapter 5.2.

The kinetics of the early stage of dispersion polymerization in supercritical CO_2

U. Fehrenbacher[a] and M. Ballauff[b]

[a]Fraunhofer-Institut für Chemische Technologie, Joseph-von-Fraunhofer-Str. 7, 76327 Pfinztal
[b]Polymer-Institut, Universität Karlsruhe, Kaiserstr.12, 76128 Karlsruhe

1. INTRODUCTION

Typical vinyl-polymers are only scarcely soluble in supercritical carbon dioxide (sc-CO_2) whereas vinyl monomers mix easily with this solvent [1] Hence, the polymerization of vinylmonomers e.g. methylmethacrylate (MMA) in sc-CO_2 proceeds via a dispersion polymerization. Recent work has demonstrated that the dispersion polymerization of MMA in sc-CO_2 leads to well-defined particles with narrow size distribution if suitable surfactants or macro-monomers are added [2-5]. This allows to generate polymer particles in an environmentally-friendly solvent for a wide range of applications. A systematic application of dispersion polymerization of vinyl monomers in sc-CO_2, however, requires an advanced understanding of the kinetics of this process and its dependence on a large number of variables as e.g. the concentrations of the monomer, of the initiator, and of the surfactant.

A central problem is the very early stage of dispersion polymerization in which the formation of particles takes place. To date, the mechanism of particle formation in dispersion polymerization is less well-understood than in emulsion polymerization [6]. According to the model proposed by Paine some years ago, dispersion polymerization proceeds through two stages: 1. A very short nucleation stage in which the primary particles are formed through coagulation, and 2. a growth phase in which the number of particles per volume N/V stays constant [7]. In the latter stage, the surfactant covers the particles so that sufficient steric stabilization [5] prevents further coagulation.

The experimental test of the predictions of Paine [7] is faced with considerable difficulties because the first stage of dispersion polymerization is very short. Moreover, the resulting N/V expected to be small. In principle, turbidimetry is the method of choice to follow the growth of particles out of a homoge-

neous medium [3-5]. If the total scattering cross-section of the sample is measured at several wavelengths, the particle diameter σ and the number density N/V can be determined simultaneously by application of Mie's theory [8]. The practical implementation of this method to the problem at hand, however, is faced with two major difficulties: i) the refractive indices of the particles, of the surrounding medium and its dependence on the wavelength must be known with good accuracy, and ii) the measured turbidity yields the "turbidity-average"-diameter that depends sensitively on the size distribution of the particles [9, 10]. Problem i) is aggravated by the fact that usual vinyl-polymers are swollen by sc-CO_2 and by monomer considerably which must be taken into account.

In recent papers we have reported on investigations of the dispersion polymerization of methyl methacrylate (MMA) in presence of the macromonomer poly(dimethylsiloxane)-monomethylacrylate (PDMS-MA) [11, 12]. This system has already been studied by Johnston and coworkers [3-5]. We could show that N/V and the diameter σ of the growing particles can be measured on-line by time-resolved measurements. Moreover, the degree of swelling of the resulting poly(methyl methacrylate) (PMMA) by sc-CO_2 and the refractive index of the swollen PMMA can be determined by wave-guide spectroscopy [13]. Hence, all problems of the turbidimetric experiment could be solved. Here we wish to review these experiments and discuss the main results.

2. ANALYSIS OF PARTICLE FORMATION BY TURBIDIMETRY

The turbidity τ is the attenuation of the beam of light according to $\tau=(1/l)\ln(I_0/I)$ where l is the length of the optical path, I_0 and I are the intensities of the incident and the transmitted light, respectively [8]. If absorption can be excluded the turbidity is solely due to the scattering of the light by the particles. We have shown that the measured turbidity τ can be factorized into integrated form part $Q(\sigma,\lambda^2,m)$ and an integrated structure factor $Z(\lambda^2,\lambda,m)$ where λ is the wavelength of the light in the suspending medium [10]. Hence, for particles of diameter σ it follows that

$$\tau = \frac{2\pi}{3} \cdot \frac{N}{V} \cdot \left(\frac{n_o \pi}{\lambda_o} \right)^4 \cdot \left(\frac{m^2 - 1}{m^2 + 2} \right)^2 \cdot \sigma^6 \cdot Q(\sigma, \lambda^2, m) \cdot Z(\lambda^2, \phi, m) \qquad (1)$$

where $m=n_p/n_o$ is the relative refractive index of the particles, n_o is the refractive index of the medium, n_p the refractive index of the particles, and N/V denotes the number of particles per unit volume. The volume fraction ϕ of the particles in the system follows as by $\phi = (N/V)(\pi/6)\sigma^3$. For the small volume fractions under

consideration $Z(\lambda^2,\lambda,m)$ is unity in excellent approximation. For a system of polydisperse, non-interacting spheres eq. (1) can be extended to [10-12]

$$\tau_0 = \frac{2\pi}{3} \cdot \frac{N_{av}}{V} \cdot \left(\frac{n_o \pi}{\lambda_o} \right)^4 \cdot \left(\frac{m^2 - 1}{m^2 + 2} \right)^2 \cdot \sigma_\tau^{\,6} \cdot Q_M(\sigma_\tau, \lambda^2, m) \tag{2}$$

where the measured normalized cross section $Q_M(\sigma_\tau,\lambda^2,m)$ is defined through [10]

$$Q_M(\sigma_\tau, \lambda^2, m) = \sum_i^p \frac{N_i}{V} \sigma_i^{\,6} \cdot Q_i(\sigma_i, \lambda^2, m) / \sum_i^p \frac{N_i}{V} \sigma_i^{\,6} \tag{3}$$

and the turbidity-average diameter σ_τ by

$$\sigma_\tau^{\,3} = \frac{\sum_i^p \frac{N_i}{V} \sigma_i^{\,6}}{\sum_i^p \frac{N_i}{V} \sigma_i^{\,3}} \tag{4}$$

Given these definitions, the average number density N_{av}/V determined by the turbidimetric analysis follows as [11, 12]:

$$\frac{N_{av}}{V} = \frac{\tau_0}{\frac{2\pi}{3} \cdot \left(\frac{n_o \pi}{\lambda_o} \right)^4 \cdot \left(\frac{m^2 - 1}{m^2 + 2} \right)^2 \cdot \sigma_\tau^{\,6} \cdot Q_M(\sigma_\tau, \lambda^2, m)} \tag{5}$$

$Q(\sigma,\lambda^2,m)$ depends strongly on λ if σ_τ is not too small. So both N_{av}/V and σ_τ can be obtained if τ is measured at several wavelengths. The measurements must therefore be done simultaneously at several wavelengths. If the relative refractive index m is known with sufficient accuracy, both N_{av}/V and σ_τ can be determined. For a known size distribution $Q_M(\sigma,\lambda^2,m)$ is calculated from Mie's theory. In all cases the size distribution has been taken from the analysis of the particles by scanning electron microscopy (SEM). For the details of the calculations the reader is deferred to reference [12].

3. EXPERIMENTAL PROCEDURE

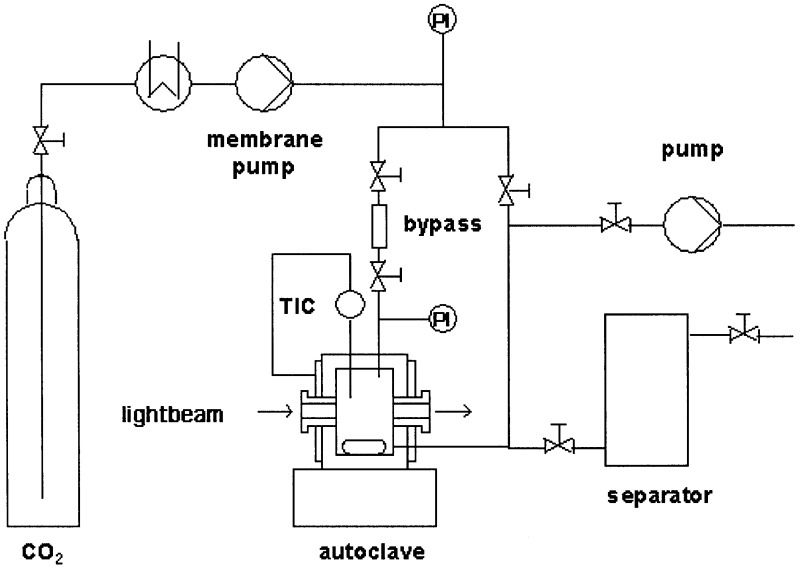

Fig. 1 Scheme of the apparatus used for the study of the dispersion polymerization of MMA in sc-CO_2. The polymerization in the autoclave is directly monitored through the measurement of the turbidity. The initiator AIBN is injected through a bypass which starts the reaction. The reaction can be quenched through injection into the separator under pressure. The separator is filled with n-octane containing a small amount of methylhydroquinone to stop the radical polymerization. The autoclave is thermostated to ± 1 degrees. Taken from ref. [11,12].

Fig. 1 displays the scheme of the experimental set-up used in these experiments [11, 12]. The main component is the autoclave (100mL) with two sapphire windows. The content of the autoclave can be stirred by a magnetic stirring bar which lies underneath the optical path. The turbidity can be measured directly through these windows (length of the optical path: 4.97cm) by connecting the cell with light guides to a Zeiss MCS 522 UV/VIS/NIR diode array spectrometer in a spectral range of 400 to 950nm. The content of the autoclave can be transferred under a pressure into a separator filled with organic solvents (n-octane). Thus, the reaction can be quenched and the particles analyzed by electron microscopy [11, 12].

The autoclave is thermostated with the temperature control being better than ± 1°C. Carbon dioxide can be filled into the autoclave under pressure by use of a membrane pump (Lewa, Leonberg, Germany). The apparatus can be evacuated by a vacuum pump to remove Oxygen and a bypass allows to inject small amounts of initiator into the pressurized autoclave.

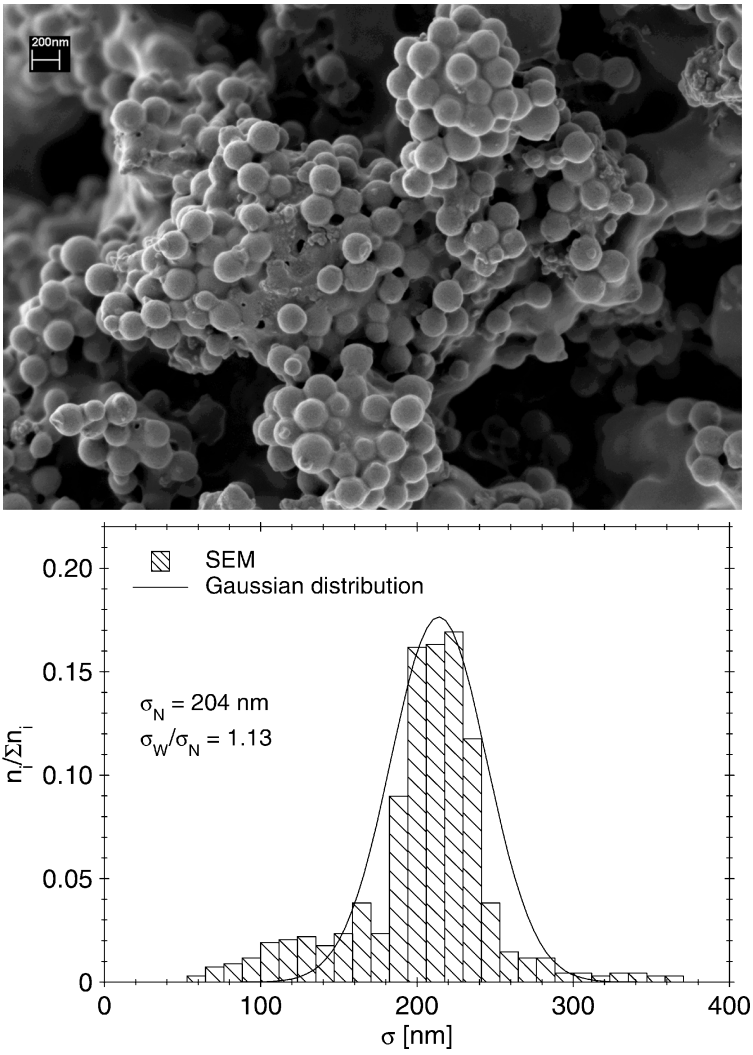

Fig. 2 Analysis of the size distribution by electron microscopy. The upper part displays the micrograph obtained by scanning electron microscopy taken after 340s whereas the lower part shows the number distribution that resulted from counting 680 particles. The line gives the best fit of the distribution by a Gaussian. See Ref. 12.

The polymerization was done by charging the reaction with the monomer MMA and the respective amount of PDMS-MA under an atmosphere of CO_2. The initiator AIBN was injected into the reactor by CO_2 under elevated pressure in order to start the polymerization. The extinction was measured simultaneously in the entire spectral range of the spectrometer (400 – 950nm). Quenching

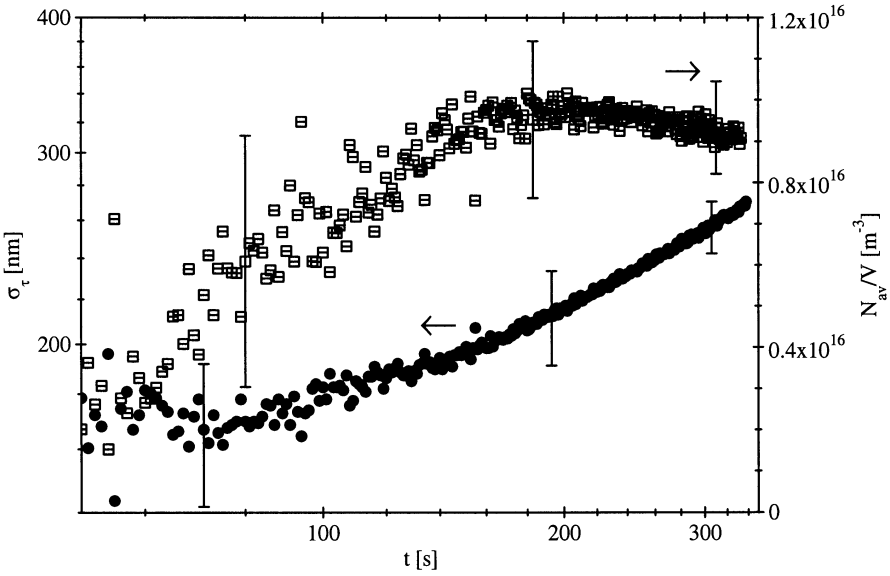

Fig. 3 Turbidity-average diameter σ_τ and average number density N_{av}/V of the particles as function of time. (monomer concentration: 0.95Mol/L; concentration of PDMS-MA: 6.5wt.% relative to MMA; amount of AIBN: 49.9mg (0.003Mol/l); temperature: 60^{0}C) together with the respective error bars. The calculation of the data has been done using the experimental particle distribution (cf. the discussion of fig. 2). The larger error at shorter times is due to the smaller size of the particles that is followed by $Q_M(\sigma_\tau\lambda^2,m)\approx 1$ and a less secure evaluation of the data. Taken from ref. [12]

of the polymerization could be done by transferring the entire content into the separator filled with n-octane under pressure (see fig. 1). To stop the radical polymerization immediately, 0.2wt.% methylhydroquinone had been added to the n-octane. The particles resulting from the polymerization in the autoclave were washed carefully with n-octane and collected by centrifugation. Thus, the size of the particles could be determined by SEM and the resulting radii coincided with the results obtained from turbidimetry [12].

An important improvement of the turbidimetric analysis could be achieved through introduction of precise optical data and swelling rates of the particles that have been determined independently by waveguide spectroscopy [13]. Moreover, the refractive index of a PMMA-film that had been swollen by an appropriate mixture of MMA and CO_2 could be measured directly. Typical degrees of swelling of the particles are between 27 (pure CO_2, 330bar) and 40 vol.% (1.5M MMA, CO_2, 330bar). The details of the method are given in reference [13].

4. RESULTS AND DISCUSSION

4.1. Analysis of τ and size distribution

The data reported herein derive from the study of the dispersion polymerization of MMA in presence of PDMS-MA [11, 12]. In order to achieve a kinetic analysis of this polymerization, the monomer concentration (0.65 to 2.2 Mol/L), the amount of initiator AIBN (25 – to 180mg in 100mL), of the macromonomer concentration 6.5wt.% (based to the amount of MMA) and of the temperature (55 - 70^{0}C) was varied. Given the moderate solubility of the stabilizer PDMS-MA, a pressure of 330bar was maintained throughout all experiments reported here. A smaller pressure resulted in flocculation at low conversion and poor reproducibility [12].

The polymerization was started through injection of AIBN (cf. fig. 1). The onset of particle formation could be seen by a yellowish and then a reddish color. Full conversion is reached only after ca. 500min but the analysis done here is restricted to 300s at the most. The much larger particles formed after longer reaction time are difficult to measure because of their strong forward scattering that would render the obtained turbidities less accurate. Hence, the present analysis is restricted to very small conversions.

The analysis of the turbidity τ between λ = 500 - 800nm for σ_τ and N_{av}/V rests on the accurate determination of the size distribution that has been derived from electron microscopy. Fig. 2 displays typical results from such an analysis obtained by quenching after 340s [12]. At least 680 particles from several micrographs were thus used for the determination of the size distribution. Moreover, data obtained by SEM served for the check of the turbidimetric determination of σ_τ.

Evidently, the experimental distribution cannot be well described by a Gaussian but is skewed towards smaller particles. The polydispersity is rather small, however, and the electron micrograph demonstrates directly the fact that well-defined particles are obtained under the experimental condition applied here [12].

Fig. 3 presents the main result of the turbidimetric analysis, namely the turbidity-average diameter σ_τ (see equ.(4)) and the turbidity-average particle density N_{av}/V (see eq.(5)) [12]. The experimental error is largest at small conversion. This is due to the small particle radii which renders the dependence of the measured normalized scattering cross section defined by eq.(3) small. It must be kept in mind that the size distribution enters into the calculation of both quantities. A possible onset of coagulation may therefore increase the experimental error at higher conversion and lead to a slight decrease of N_{av}/V. Fig. 3 demonstrates, however, that the formation and growth of polymer particles can directly be observed in situ by the present method as function of time. In the following

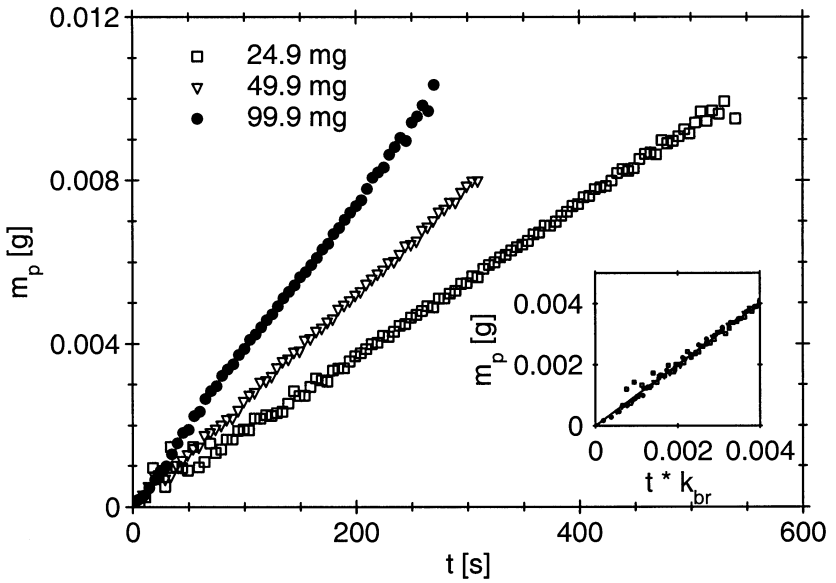

Fig. 4. Mass m_p of PMMA as a function of reaction time t. Parameter of the different curves is the amount of added initiator AIBN indicated in the graph. The concentration of MMA was 0.95Mol/L, the concentration of PDMS-MA 6.5wt.% relative to MMA, and the temperature was 60^{0}C. The inset shows the same data but as function of t scaled by the rate constant k_{br} that has been take from the slope of the curves [12].

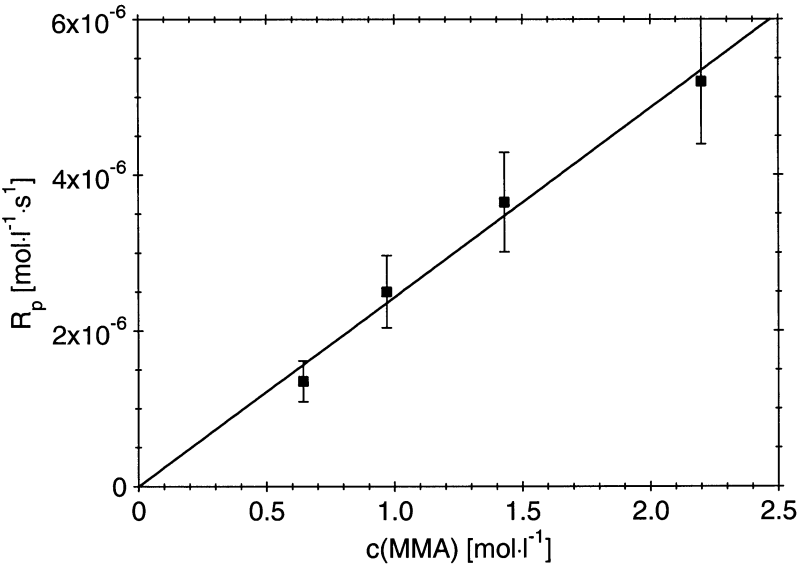

Fig. 5. Analysis of the overall kinetics of the dispersion polymerization. The rate R_p of polymerization as function of monomer concentration. The concentration of AIBN was 0.003Mol/L, the concentration of PDMS-MA 6.5wt.% relative to MMA, and the temperature was 60^{0}C. Taken from ref. [12].

we shall show that these data may be used for a complete kinetic analysis of the dispersion polymerization in sc-CO_2.

Fig. 3 demonstrates that the dispersion polymerization of the present systems proceeds through two stages: The average number of particles first increases markedly (stage I) and stays practically constant in a second stage (t >150s). At the same time the average diameter σ_τ of the particles is at first virtually constant but increases in a monotonous fashion at longer times. This finding is of central importance for the subsequent modeling of the dispersion polymerization [12].

4.2. Kinetics of polymerization

The product of σ_τ^3 and N_{av}/V thus determined then may be used to calculate the total amount m_p of polymer formed at time t [11,12] The degree of swelling of the particles by the mixture of CO_2 and MMA determined in ref. [13] has been used for this calculation. In this way turbidimetry serves as a microbalance that allows to weight minute amounts of polymer and hence to perform a conventional kinetic analysis. Fig. 4 displays a set of data obtained at different initiator concentrations. Parameter of the different curves is the amount of added initiator AIBN. The strictly linear increase of m_p as function of t is directly evident and the slope of these curves may be converted to the respective rate constants k_{br}. The inset of fig. 4 proves the consistency of this procedure. All data collapse to a single master curve if t is scaled by the slope k_{br} of the curves [12]. There a short induction period of 10 – 50s which has been subtracted from t in all data to be discussed here. It must be noted that this short induction time is only obtained if the autoclave is carefully heated under CO_2 prior to the experiments, otherwise much longer induction periods result. Small amounts of impurities sticking to the wall of the container that might disturb the polymerization must hence be removed [11,12].

The mass of polymer formed per unit time may subsequently converted to the rate R_p of polymerization and analyzed as usually done in the case of bulk polymerizations [14]:

$$R_p = k_{app}[M][AIBN]^{0.5} \tag{6}$$

Fig. 5 gives a typical example of this analysis by showing the dependence of R_p on the monomer concentration *[M]*. Good linearity is seen and a similar analysis of the dependence of R_p on the concentration of initiator shows that equ.(6) provides an excellent description of the kinetics of polymerization. Moreover, the dependence on temperature can be deduced [12].

All data clearly demonstrate that the continuous phase is the locus of polymerization [11]. As an alternative, the particles may be taken as the locus of

polymerization similar to the well-studied case of emulsion polymerization. This can be argued from the much lower number density N_{av}/V of the particles. Taking these densities and assuming the case 2 of the Smith-Ewart theory [14], a R_p lower by three order of magnitude would result which clearly can be ruled out. We therefore arrive at the conclusion that the early stage of the dispersion polymerization proceeds as a conventional bulk polymerization. Polymerization within the particles plays no role. In a later stage that is not considered here, however, polymerization may also take place within the particles [15].

4.3. Formation of particles

With the kinetics of polymerization being clarified, the formation of particles will be discussed next in terms of N_{av}/V and σ_τ. It is expedient to discuss first the dependence of these quantities on the concentration of initiator. The concentration of the initiator only changes the rate of polymerization but no other variable of the system. The discussion of fig. 3 had already demonstrated that the dispersion polymerization studied here proceeds through two stages: At first N_{av}/V grows approximately linear to reach a critical value $(N_{av}/V)_{crit}$ but stays virtually constant in the second stage. If a distinct mechanism of particle formation is present, the evolution of N_{av}/V and $(N_{av}/V)_{crit}$ should only depend on the amount of polymer formed in the continuous phase. Fig. 6 shows that all data obtained for a given monomer concentration but different initiator concentrations collapse approximately on a master curve if t is scaled with the respective rate constants k_{br} [12]. The number density N_{av}/V as function of time increases to reach a final value $(N_{av}/V)_{crit}$ that only depends on the amount of polymer formed so far. Moreover, the data demonstrate that in the first stage in which the particles are formed is restricted to conversions lower than 0.1%.

Hence, there is an extremely short time in which the particles are formed but a much longer period in which growth takes places. This is followed by a narrow size distribution of the particles as analyzed by electron microscopy (see the discussion of fig. 2). The subsequent analysis shows that a minimum particle size $(\sigma_\tau)_{crit}$ can be deduced from the data which is critical size of the particle just after formation. The analysis leads to $(\sigma_\tau)_{crit}$ between 150 and 170nm [12].

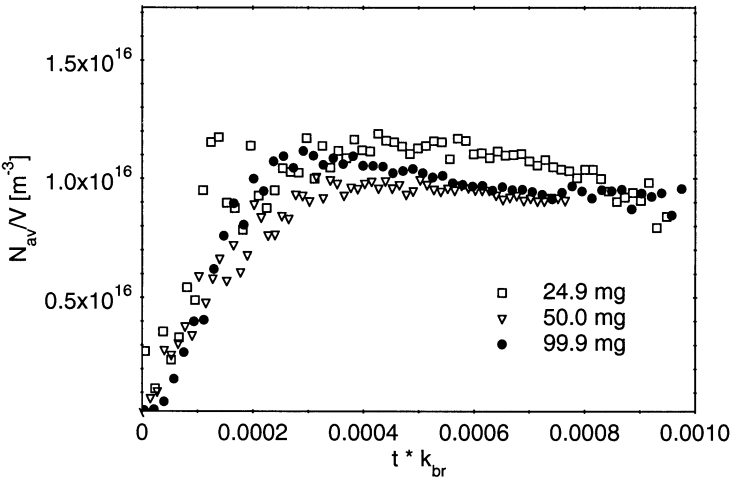

Fig. 6. Analysis of the particle formation in the course of dispersion polymerization. The average number of particles per volume N_{av}/V is plotted against the reduced reaction time t^*k_{br}. The concentration of MMA was 0.95Mol/L, the concentration of PDMS-MA 6.5wt.% relative to MMA, and the temperature was 60^0C. The amount of the initiator AIBN used in each run is indicated in the graph. The induction period of 10 – 50s was subtracted from t in all curves [12].

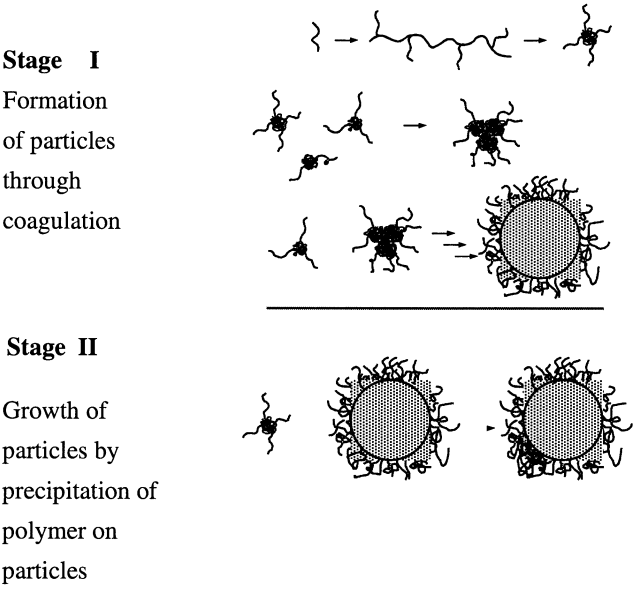

Fig. 7. Scheme of the modeling of dispersion polymerization by a two-stage mechanism: The polymer is formed in the homogeneous phase. In stage I the particles are formed through coagulation of polymer and N_{av}/V increases with time until a critical value $(N_{av}/V)_{crit}$ is reached. In stage II the number of particles N_{av}/V remains constant. All newly formed polymer is precipitated onto the surface of the particles and the diameter σ_τ grows as $t^{1/3}$. Taken from ref. [12].

4.4. Modeling of the dispersion polymerization

The model proposed for the formation of particles is displayed in fig. 6 [12]. It follows in essence the suggestion of Paine [7]. In stage I particles are formed through coagulation of single polymer chains and instable small particles. The size of these primary particles is rather large (ca. 150 – 170nm) and stability is only achieved if the entire surface is covered by PDMS-chains. An estimate of $(\sigma_v)_{crit}$ may be calculated from Paine's model [7] to be ca. 150nm which agrees with the present findings. Paine's model also allows to calculate the final diameter σ_f of the particles and the number density $(N/V)_{crit}$. With the kinetic data discussed above $(N/V)_{crit}$ is predicted to be of the order of 10^{15} to 10^{16} particles per m^3 which is found indeed. Given the various sources of error in these estimates the agreement of theory and experiment can be regarded as satisfactory [12].

5. CONCLUSION

The early stage of dispersion polymerization of MMA in sc-CO_2 has been studied by turbidimetry [11, 12]. The average number of particle N_{av}/V, the turbidity-average diameter σ_v, and the mass of polymer m_p as a function of time have been derived from these data for conversions lower than 0.1%. The analysis leads to the following conclusions

i) In the early stage investigated here the polymerization takes solely place in the homogeneous phase. This can be concluded from the kinetic analysis of the reaction rates and from a comparison of the experimental rates with theoretical estimates.

ii) The dispersion polymerization proceeds through two stages: In stage I the polymer forms new particles with a critical diameter $(\sigma_v)_{crit}$ of 150 - 170nm. After this very short period of particle formation all polymer precipitates on the particles. In this second stage N_{av}/V remains constant. The rate of polymerization, however, remains constant in all stages. The experimental data derived from this analysis are in semi-quantitative agreement with the model proposed by Paine. This demonstrates that the steric stabilization by the macromonomer PDMS-MA is the decisive factor that determines the critical diameter $(\sigma_v)_{crit}$ of the particles and hence their final size.

ACKNOWLEDGEMENT

Financial support by the Deutsche Forschungsgemeinschaft, Schwerpunkt "Überkritische Fluide", is gratefully acknowledged. The authors are indebted to Th. Hirth, Fraunhofer Institut für Chemische Technologie, Pfinztal-Berghausen, Germany, for helpful discussions and technical support.

REFERENCES

[1] C. F. Kirby, M. A. McHugh, Chem. Rev. 99 (1999) 565.
[2] J. L. Kendall, D. A. Canelas, J. L. Young, J. M. DeSimone, Chem. Rev. 99 (1999) 543.
[3] M. L. O´Neill, M. Z. Yates, K. P. Johnston, C. D. Smith, S. P. Wilkinson, Macromolecules 31 (1998) 2838.
[4] M. L. O´Neill, M. Z. Yates, K.P. Johnston, C. D. Smith, S. P. Wilkinson, Macromolecules 31 (1998) 2848.
[5] K. P. Johnston, Curr. Opinion Colloid Polym. Sci. 5 (2000) 351.
[6] M. D. Croucher, M. A. Winnik, in: F. Candau, R. H. Ottewill, (eds.), Polymer Colloids, Kluwer Academic Press, Dordrecht, 1990.
[7] A. J. Paine, Macromolecules 23 (1990) 3109.
[8] M. Kerker, The Scattering of Light and Other Electromagnetic Radiation, Academic Press: New York, 1969.
[9] M. H. G. M. Penders, A. Vrij, J. Chem. Phys. 93 (1990) 3704.
[10] U. Apfel, K. D. Hörner, M. Ballauff, Langmuir 11 (1995) 3401.
[11] U. Fehrenbacher, O. Muth, Th. Hirth, M. Ballauff, Macromol. Chem. Phys.201 (2000) 1532.
[12] U. Fehrenbacher, M. Ballauff, Macromolecules 35 (2002) 3653.
[13] U. Fehrenbacher, Th. Jakob, T. Berger, W. Knoll, M. Ballauff, Fluid Phase Equ. 200 (2002) 147.
[14] G. Odian, Principles of Polymerization, 3rd edition, Wiley, New York 1991.
[15] C. Lepilleur, E. J. Beckmann, Macromolecules 30 (1997) 745.

Supercritical Fluids as Solvents and Reaction Media
G. Brunner (editor)

Chapter 5.3.

Rate coefficients of free-radical polymerization in homogeneous fluid mixtures with carbon dioxide

S. Beuermann* and M. Buback

Institut für Physikalische Chemie, Georg-August-Universität Göttingen, Tammannstraße 6, 37077 Göttingen, Germany

1. INTRODUCTION

Supercritical CO_2 ($scCO_2$) has emerged as an attractive alternative for low volatile organic solvents. Besides being environmentally benign, CO_2 offers further benefits for carrying out chemical processes. With respect to polymerizations, the reduced viscosity of CO_2-containing reaction mixtures and the easy separation of CO_2 from the polymeric product are of particular interest. Polymer melts containing CO_2 are well suited for spraying processes to yield polymer particles of well defined morphology. Thus polymer synthesis and particle generation, both in CO_2, may be combined into an integrated process. A major concern has been that polymerizations of monomers such as styrene or (meth)acrylates may not be carried out in homogeneous CO_2-containing phase because of the poor solubility of these polymers in CO_2 [1]. We could show that this needs not to be the case. The degree of monomer conversion accessible in homogeneous fluid phase may be significant and strongly depends on CO_2-content, on pressure, and on the molecular weight of the polymer [2]. Particularly important is the cosolvent action of the monomer, which, e.g., allows for styrene polymerizations up to 40 % monomer conversion in homogeneous fluid phase containing 20 wt.% CO_2. For monomers such as glycidyl methacrylate almost complete monomer conversion may be reached in homogeneous phase containing 20 wt.% CO_2 [3].

In technical polymerizations, optimization of processes conditions including safety assessment, requires modeling of the polymerization kinetics which crucially depends on the availability of accurate rate coefficients for all relevant individual reaction steps.

In addition to the requirement of knowing the kinetic data for the modeling, polymerization rate coefficients in CO_2 are of appreciable mechanistic interest, which is associated with the unique properties of this solvent medium. The low viscosity of CO_2 is particularly attractive with respect to studying the diffusion-controlled termination reaction. The poor solvation power of CO_2, on the other hand, provides insight into solvent effects on propagation rate.

The present contribution deals with the effect of a CO_2 environment on rate coefficients of free-radical polymerization. In Section 2, results for propagation rate coefficients, k_p, and in Section 3 for termination rate coefficients, k_t, will be presented and discussed. As restricting polymer molecular weight is often an important issue for polymerizations carried out in CO_2, Section 4 addresses the influence of CO_2 on chain-transfer rate coefficients. In Section 5, reactivity ratios for copolymerizations in CO_2 will be presented.

2. PROPAGATION REACTION

2.1. Measurement of propagation rate coefficients

The propagation rate coefficient, k_p, for a large number of monomers has been derived via the PLP-SEC technique, which combines pulsed laser initiated polymerization (PLP) with subsequent measurement of the polymer molecular weight distribution (MWD) by size-exclusion chromatography (SEC). An evenly spaced sequence of laser pulses is applied onto the monomer/photoinitiator system until a small initial monomer conversion, typically of two per cent, is reached. The almost instantaneous production of free radicals by each laser pulse causes an enhanced termination probability for radicals generated by preceding pulses. This situation gives rise to a characteristic structure of the MWD. As an example, the full line in Fig. 1 shows an MWD from PLP, with a laser pulse repetition rate of 25 Hz, of cyclohexyl methacrylate at 40 °C and 300 bar in 40 wt.% of CO_2.

As has been detailed in the original literature [4], k_p is calculated from Eq. (1).

$$L = k_p \cdot c_M \cdot t \tag{1}$$

where c_M is the monomer concentration, t the time between two subsequent laser pulses and L the number of propagation steps between two laser pulses. L is given by the position of the inflection point of the MWD. This inflection point corresponds to the maximum of the first derivative curve of the MWD, which curve is given by the dashed line in Fig. 1.

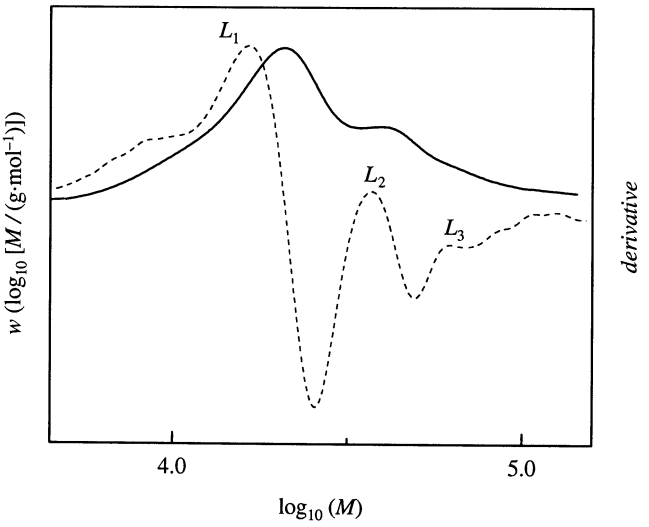

Fig. 1. Molecular weight distribution for poly(cyclohexyl methacrylate) (full line) and the associated first derivative curve (dashed line) obtained from a polymerization at 40°C and 300 bar in 40 wt.% CO_2 at a laser pulse repetition rate of 25 Hz.

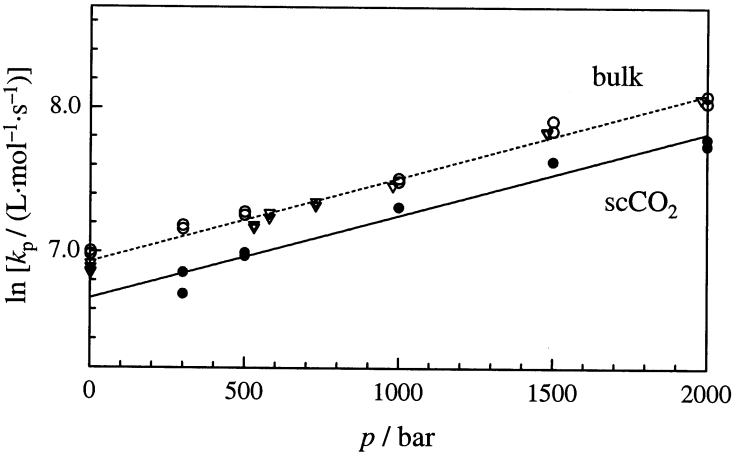

Fig. 2: Pressure dependence of k_p for cyclohexyl methacrylate polymerizations at 40 °C in bulk and in 40 wt.% CO_2; literature data (triangles) are taken from Ref. 5. The full line represents the linear fit of k_p for polymerizations in CO_2. The entire set of k_p data for bulk polymerizations is fit by a single straight line (dashed line).

The influence of CO_2 on k_p for methacrylates, acrylates, styrene, and vinyl acetate has been studied. As an example, Fig. 2 gives the pressure dependence of k_p for cyclohexyl methacrylate (CHMA) at 40 °C. It is clearly seen that k_p values in the presence of CO_2 are below the corresponding bulk data. The straight lines in Fig. 2 represent fits to the entire set of k_p data for polymerizations in bulk (dashed line) and to the data measured in CO_2 (full line). The slopes of these lines are almost identical. The following activation volumes, $\Delta V^{\#}(k_p)$, are calculated according to the relation:
$\partial(\ln k_p)/\partial p = -\Delta V^{\#}/(R \cdot T)$:

$\Delta V^{\#} = -(15.2 \pm 0.4)\ cm^3 \cdot mol^{-1}$ (bulk)

$\Delta V^{\#} = -(14.9 \pm 1.1)\ cm^3 \cdot mol^{-1}$ (40 wt.% CO_2)

The findings for CHMA are typical for the monomers studied so far: The activation volumes (and also the activation energies) of k_p, within experimental accuracy, are not affected by CO_2 whereas for several monomers, in particular for acrylates and methacrylates, a clear reduction of k_p (as deduced from Eq. 1) is seen in solution with CO_2 [6]. The extent of this reduction depends on the type of ester group. Table 1 summarizes some of the results. $k_{p,CO2}/k_{p,bulk}$ is the ratio of k_p (from Eq. 1) for polymerization in 40 wt.% CO_2, $k_{p,CO2}$, to k_p for bulk polymerization, $k_{p,bulk}$, with both rate coefficients referring to identical temperature and pressure.

Table 1
The ratio of $k_p/k_{p,bulk}$ with k_p referring to polymerizations in 40 wt.% CO_2. For further details see text.

monomer		$k_{p,CO2}/k_{p,bulk}$
methyl acrylate	MA	0.55
butyl acrylate	BA	0.60
dodecyl acrylate	DA	0.75
methyl methacrylate	MMA	0.60
butyl methacrylate	BMA	0.75
dodecyl methacrylate	DMA	0.75
glycidyl methacrylate	GMA	0.80
cyclohexyl methacrylate	CHMA	0.75
iso-bornyl methacrylate	iBoMA	0.60

The data in Table 1 indicate that for acrylates and methacrylates with linear alkyl ester groups, the reduction in k_p in the presence of 40 wt.% CO_2 is strongest for MA and MMA. With cyclic ester groups, as seen for GMA, CHMA, and iBoMA (Scheme 1), the opposite trend is observed: iBoMA with its bulky ester group shows the strongest CO_2 effect, whereas for the small glycidyl group only a modest reduction in $k_{p,CO2}$, by 20 %, is seen. As the activation parameters are not changed by the addition of CO_2 , the effect on k_p is assumed not to be just a kinetic one [6]. Inspection of Eq. (1), which is used to derive k_p, tells, that the experimental quantities are L, deduced from SEC, and t derived from the pre-selected time interval between two successive laser pulses. Strictly speaking, the experiment thus allows only for the determination of the product $k_p \cdot c_M = L \cdot t^{-1}$.

The estimate of the k_p data presented so far, e.g. in Table 1, thus rests on the assumption that c_M at the free-radical site is identical to overall c_M. The alternative assumption would be that $k_{p,CO2}$ is identical to $k_{p,bulk}$ and that the local monomer concentration at the free-radical site, $c_{M,loc}$, differs from overall c_M. The agreement of activation energy and of activation volume of k_p, in bulk and in solution containing 40 wt.% CO_2, appears to be in favor of this second assumption [6].

The occurrence of local monomer concentrations may be explained by the poor solvent quality of CO_2 for the particular polymers with polar acrylate and methacrylate segments. Because of unfavorable interactions between these segments and CO_2, interactions between polar segments within polymeric (and thus macroradical) are more important as compared to the situation in bulk polymerization. Such intersegmental interactions of polar groups may result in a smaller monomer concentration at the site of the propagating chain end. For monomers with long flexible alkyl ester groups, the alkyl moiety may provide some shielding of the polar segments. Thus $c_{M,loc}$ is closer to c_M and the apparent reduction in k_p (see Scheme 1) is less pronounced. This explanation applies to *n*-alkyl methacrylates and *n*-alkyl acrylates.

Scheme 1

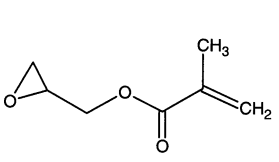

GMA

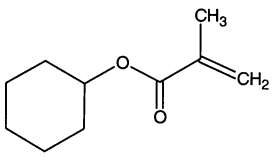

CHMA

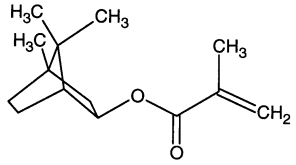

iBoMA

The above arguments on the influence of CO_2 on k_p made for *n*-alkyl (meth)acrylates obviously may not be transferred to monomers with cyclic ester groups, where with GMA and CHMA a smaller CO_2-induced reduction of k_p is seen than with iBoMA. The reason for the strong CO_2 influence in case of iBoMA is suggested to be due to the rigid structure of the bridged cyclic ester group. In contrast to the highly flexible dodecyl ester group, the *iso*-bornyl group is less effective in shielding the polar segments from each other. The cyclohexyl group in CHMA is less rigid than the *iso*-bornyl group. The reduction of k_p in CO_2 thus is closer to the one observed for DMA. The smaller CO_2-induced reduction in k_p with GMA may, at least partly, be due to the appreciable solubility of poly(glycidyl methacrylate) in $scCO_2$ [3]. GMA homopolymerizations and copolymerizations with significant amounts of GMA may be carried out up to fairly high degrees of monomer conversion in fluid phases containing high weight fractions of CO_2. This finding suggests favorable interactions between CO_2 and GMA segments. As a consequence, the monomer concentration at the GMA macroradical site should be closer to overall c_M than in *n*-alkyl methacrylate systems of similar ester size.

Based on the preceding discussion one might expect that with monomers carrying a polar group on the alkyl chain, e.g. a hydroxyl group, a particularly strong CO_2-induced reduction of k_p will occur. No difference between $k_{p,CO2}$ and $k_{p,bulk}$ was, however, seen for hydroxypropyl methacrylate (HPMA) [7]. This observation may be understood by assuming strong intra-segmental H-bonds between the OH- and carbonyl groups. As a consequence, inter-segmental interactions of polar groups within a macroradical will be diminished and local monomer concentration should not differ significantly from overall monomer concentration. Thus $k_{p,CO2}$ should be close to $k_{p,bulk}$ [7].
In addition to the (meth)acrylates discussed so far, $k_{p,CO2}$ for styrene and vinyl acetate (VAc) polymerizations has been studied. Although polystyrene is poorly soluble in $scCO_2$ [8], no effect of CO_2 on k_p is seen [9]. This finding again is understood as resulting from the absence of polar inter-segmental interactions within the macroradical. Thus local styrene concentration at the site of the radical chain end should not significantly differ from analytical styrene concentration.

Scheme 2

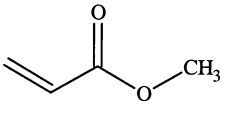

MA

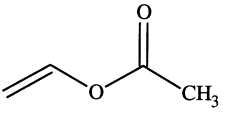

VAc

Investigations into $k_{p,CO2}$ of VAc were of interest in order to see whether this monomer, which is isomeric to methyl acrylate (MA), see Scheme 2, exhibits a similar CO_2 influence on the propagation rate as MA does. k_p of VAc, however, turns out to be invariant toward CO_2 concentration [10]. The finding is assigned to the remarkably good solubility of poly(vinyl acetate) (PVAc) in CO_2 as compared to poly(methyl acrylate) (PMA) [8]. Thus, PVAc segments appear to favorably interact with CO_2 and $c_{M,loc}$ should be the same as overall VAc concentration. In order to check, whether the solvation by CO_2 is different from the situation in bulk polymerization, Monte Carlo simulations have been carried out which are described in the subsequent section.

2.2. Modeling of the solvation in CO_2 for PMA and PVAc

The Monte Carlo simulation techniques used for studying the solvation of PVAc and PMA by either the associated monomer or by CO_2 were applied in a cooperation with Dr. M. Drache (Clausthal) who developed these methods. The simulations were extended to situations in which two polymer molecules were interacting in an environment of either monomer molecules or CO_2. Polymer molecules were represented by 9-mers of PVAc and PMA. The generation of a 9-mer is performed as follows (for details see Ref. 11): Using the program Cerius 2.0 [12] the monomer structure is generated and nine monomer repeat units are linked together. By applying 500 iteration steps, the geometries are optimized in a force field. Since many conformations may exist in liquid phase, a set of 1000 conformers was generated by stochastic variation of the torsional angle and by subsequent geometry optimization. For each conformer the charge distribution was calculated by the charge-equilibration method (QEQ) and the structures are finally optimized applying an MM3 force field. These optimizations are carried out using the program package TINKER [13].

The resulting PMA and PVAc aggregates are modeled with the program EVOCAP (excluded volume constraint assembly packing [14]), which is based on atomistic Monte Carlo simulations. Considering excluded volume contributions, solvent molecules (either monomer or CO_2) are positioned into the vicinity of the aggregates, thus forming aggregate–solvent clusters. After the addition of each solvent molecule, at fixed aggregate conformation, an optimization with respect to the rotational and translational degrees of freedom of the solvent molecule is performed. Further solvent molecules are added to the cluster until no additional aggregate–solvent interactions can be produced. The structure of the aggregate with its solvent shell (cluster) is then optimized using the program TINKER and a more closely packed solvent shell is obtained. After that, the solvent shell is filled with additional solvent molecules and another TINKER optimization is carried out.

From the cluster energy, $E_{cluster}$, composed of the 9-mer ($E_{9\text{-mer}}$) and of the solvent shell (E_{shell}) energies, the interaction or cohesion energy ($E_{cohesion}$) is obtained [11]:

$$E_{cohesion} = E_{cluster} - E_{9\text{-mer}} - E_{shell}.$$

Cohesion energies of PMA and PVAc in a solvent shell of the associated monomer or of CO_2 are estimated from at least 1000 clusters for each particular solute–solvent situation. The $E_{cohesion}$ data allow for comparison of interaction energies of a given 9-mer in the two solvent environments. Fig. 3 gives the distribution of the cohesion energies of PMA in a solvent shell of either MA or CO_2. The $E_{cohesion}$ energies may be fit by a Gaussian distribution for each solvent.

Fig. 3 indicates a weaker cohesion energy for PMA in CO_2 than for PMA in MA, which is in agreement with the fact that MA is a better solvent for PMA than is CO_2. The difference in cohesion energies is estimated to be 113.6 kJ·mol^{-1}. For PVAc in solution of CO_2 and in VAc a smaller difference in cohesion energies, 83.2 kJ·mol^{-1}, is found. The two cohesion energies being closer together suggests that solvation of PVAc by either the monomer or CO_2 is not that different as in the case of PMA. This result agrees with the expectations based on the k_p studies.

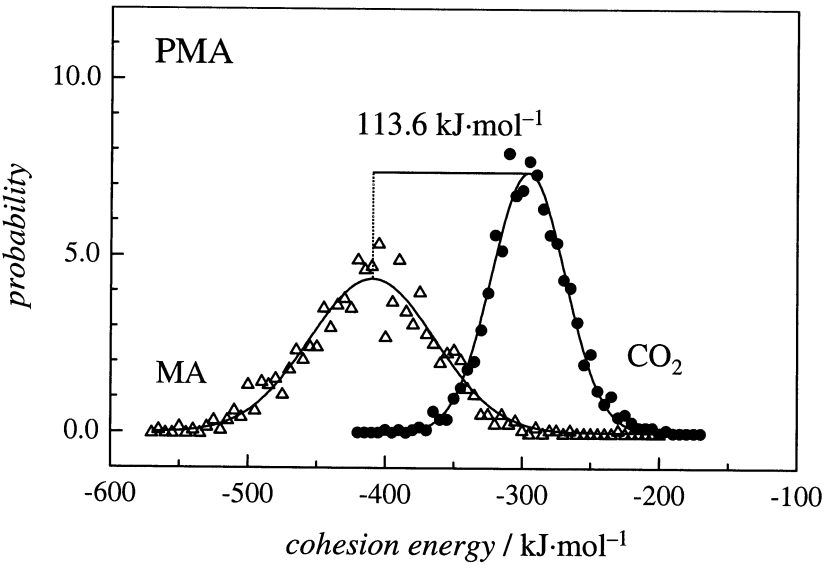

Fig. 3. Gaussian distributions of the cohesion energy for aggregates of PMA in a solvent shell of either MA or CO_2.

The estimates so far were carried out for a comparably small single 9-mer. Thus, contributions to solvation from the coiling of a polymer molecule and from intra- and intermolecular interactions of polymeric segments are not included. In order to account for part of these effects, interactions of pairs of 9-mers in a solvent shell of either the monomer or of CO_2 were modeled. In each case, at least 500 clusters of the two 9-mers embedded in their solvent environment were calculated. The interaction energy between the two 9-mers, $E_{\text{interaction}}$, is estimated according to the following relation [11]:

$$E_{\text{interaction}} = E_{\text{polymer pair}} - E_{\text{polymer 1}} - E_{\text{polymer 2}}.$$

The 9-mer interaction energies in CO_2 for both systems are presented in Fig. 4. On the l.h.s., results for PVAc and on the r.h.s. for PMA are shown. The distribution of interaction energies within PVAc-PVAc pairs in CO_2 is adequately represented by a Gaussian distribution. In contrast, a Gaussian fit to the distribution of $E_{\text{interaction}}$ for clustered PMA-PMA pairs (gray line) provides only a rather poor representation of the simulated data. Therefore the PMA-PMA data were fit by two Gaussian distributions (dashed lines in Fig. 4). The superposition of these individual Gaussians leads to an adequate representation (bold line in Fig. 4) of the simulated $E_{\text{interaction}}$ distribution. The requirement of using two Gaussians for fitting $E_{\text{interaction}}$ in the case of PMA dimers is indicative of specific interactions between the PMA molecules.

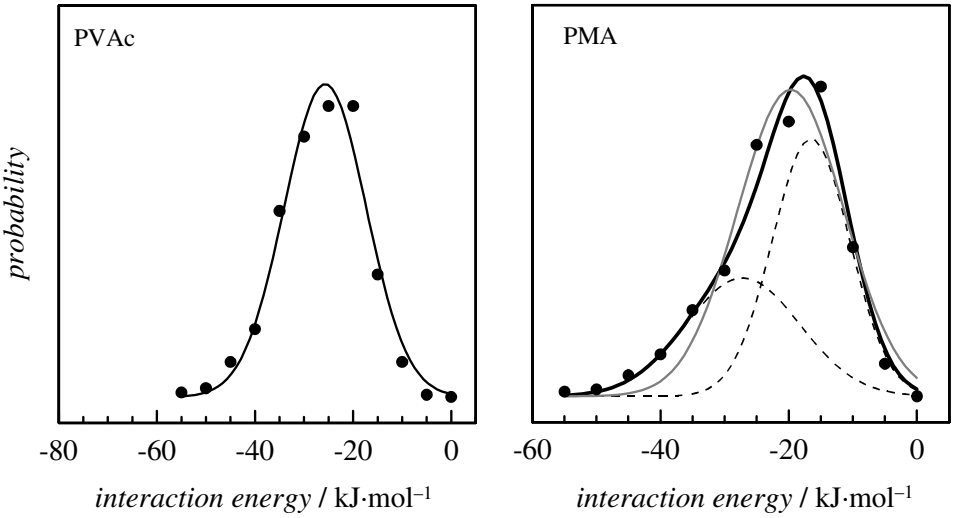

Fig. 4. Interaction energies between PVAc-PVAc (l.h.s) and PMA-PMA-pairs (r.h.s.) solvated by CO_2. For details see text.

The simulation results indicate that (a) the difference in solvation energy of PVAc by either monomer or CO_2 is smaller than the corresponding difference for PMA solvation and (b) specific interactions between PMA oligomers occur in the presence of CO_2, whereas the Monte Carlo simulations are not indicative of any such specific interactions for the PVAc system. These findings are fully consistent with the arguments put forward to explain the influence of CO_2 on the propagation kinetics of MA- and VAc-homopolymerizations.

3. TERMINATION REACTION

A major effect of adding CO_2 to a free-radical polymerization system consists in a significant reduction of the viscosity of the reaction medium. This change may largely affect termination rate. We will now discuss termination rate coefficients, k_t, for acrylates and methacrylates in the initial monomer conversion range where k_t has been found to be constant over fairly large ranges, up to about 15% with the methyl ester monomers and up to at least 60% with the dodecyl ester members of the two monomer families. These plateau regions are assigned to termination rate control by segmental diffusion (SD) [15]. SD refers to the mechanism in which diffusion of the radical sites of two overlapping macroradicals controls termination rate. The k_t data discussed here are chain-length averaged values.

3.1. Acrylate polymerizations

The termination reaction for acrylate polymerizations has been investigated in detail for methyl, butyl, and dodecyl acrylate applying the single-pulse (SP)–PLP technique. A laser single pulse is applied to a monomer/photoinitiator mixture. The monomer conversion induced by one laser pulse is measured via time-resolved NIR spectroscopy with a time resolution of microseconds. For a detailed description of the technique the reader is referred to Ref. 16 and 17. Fitting the measured monomer concentration vs. time trace yields the coupled parameter k_t/k_p. With k_p being known from independent PLP–SEC studies, chain-length averaged k_t is immediately obtained from the SP–PLP experiment. By successive SP–PLP experiments, the conversion dependence of k_t may be mapped out. Further details are given, e.g., in Ref. 18.

Fig. 5 depicts the conversion dependence of k_t for methyl acrylate and dodecyl acrylate at 40 °C and 1000 bar. The filled data points refer to k_t data in the presence of CO_2, the open points to k_t for bulk polymerizations. The latter data are taken from Ref. 18. As may be expected from the significant lowering in viscosity associated with the addition of CO_2, Fig. 5 shows a significant

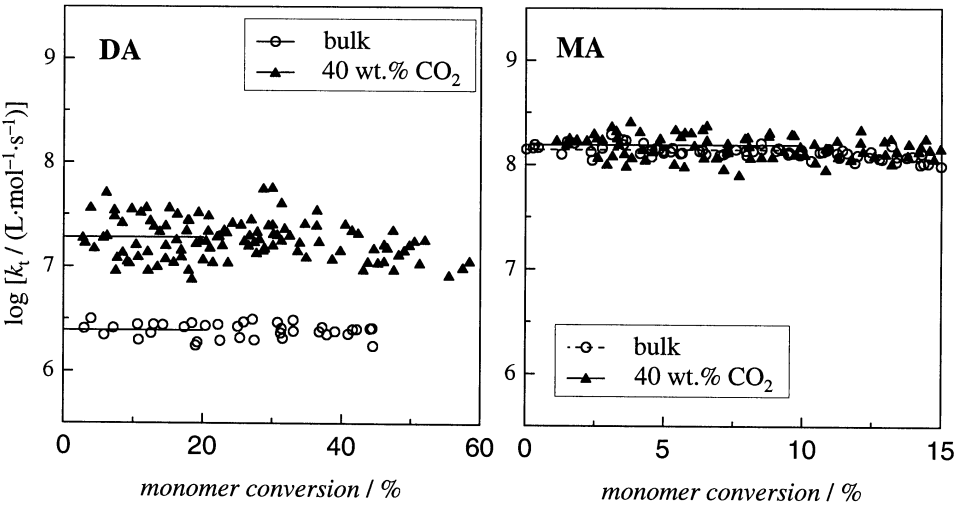

Fig. 5. Conversion dependence of k_t for MA and DA homopolymerizations in the presence of 40 wt.% $scCO_2$ and in bulk from SP-PLP experiments at 40°C and 1000 bar.

increase, by about a factor of eight, in k_t for DA in the presence of 40 wt.% CO_2. The DA data in $scCO_2$ are given for monomer conversions up to about 60 %. Since the SP–PLP technique is only applicable to homogeneous systems, the data in Figure 5 also illustrates, that polyDA is reasonably well soluble in $scCO_2$ with some DA monomer being present.

In contrast to DA, no CO_2 influence on k_t is seen with MA, as is shown on the right hand side of Fig. 5.

The experimental findings for k_t in the plateau region under SD control may be understood as follows: The microviscosity in the interior of two overlapping macroradical coils is significantly reduced by the adding CO_2 to the system. In DA homopolymerization the long alkyl ester chains provide a strong shielding of the radical sites. Thus, even two radical functionalities which are fairly close to each other do not necessarily terminate. As a consequence of such unsuccessful approaches, the macroradical coils may get separated before they undergo termination. With MA polymerization, the small methyl group will not effectively shield radicals from each other and once two radical sites get into close proximity they will terminate. This smaller shielding efficiency, at least partly, explains the higher bulk k_t value of MA compared to DA. With CO_2 being present, the mobility of polymer segments is largely enhanced as is the frequency of forming close contacts of the radical sites within overlapping macroradicals. As a consequence, the k_t values for DA increase upon the addition of CO_2. For MA, overlap of two macroradicals mostly results in termination. An increase in segment mobility due to $scCO_2$

thus will not markedly enhance k_t. The variation with CO_2 of k_t for both MA and DA strongly supports the view of segmental diffusion being operative at low and moderate degrees of monomer conversion.

3.2. Methacrylate polymerizations

k_t data for methacrylate polymerizations in $scCO_2$ could not be determined via the SP–PLP technique because of insufficient signal-to-noise quality. Termination rate has thus been deduced from chemically initiated polymerizations carried out with in-line detection of monomer conversion via FT–NIR spectroscopy. Kinetic analysis at known initiation rate yields the parameter $k_p/k_t^{0.5}$ as a function of monomer conversion. With k_p being known from PLP–SEC, k_t is immediately obtained for the experimental conversion range. Details of the experiment and procedure are given elsewhere [2, 11]. The conversion dependence of k_t for methyl and dodecyl methacrylate homopolymerizations in solution of 40 wt.% CO_2 and in bulk at 80°C and 300 bar is shown in Fig. 6. For both monomers, k_t for polymerization in $scCO_2$ is higher than in bulk.

Fig. 6 demonstrates that, contrary to what has been seen for acrylate polymerizations, the impact of CO_2 on k_t is similar for the two monomers that largely differ in the size of the alkyl ester group. k_t for both MMA and DMA is increased by about a factor of 4.5. This observation suggests, that the effect of CO_2 is primarily on segmental mobility which is controlled by the α–CH_3 groups at the polymer chain. The strong impact of the CH_3-substituent on k_t is also indicated by the bulk k_t values. As seen in Fig. 5, k_t for DA is about a factor of 50 smaller than for MA, whereas a reduction in k_t by only a factor of 5 occurs in going from MMA to DMA.

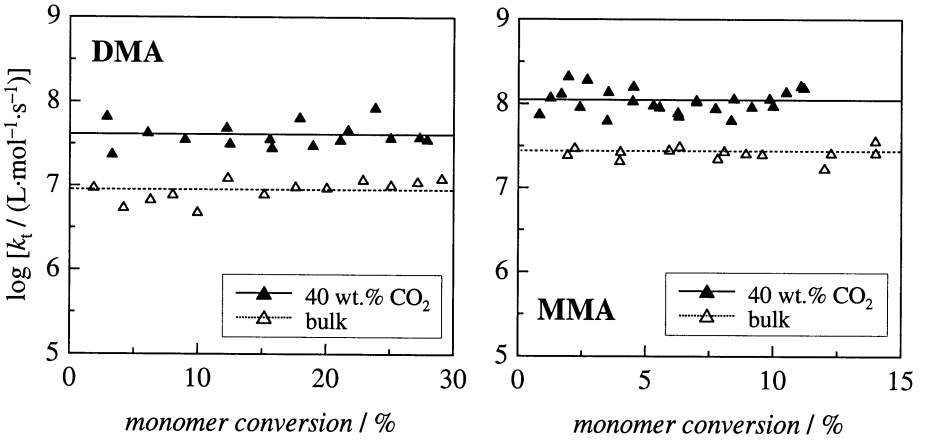

Fig. 6. Conversion dependence of k_t for DMA and MMA homopolymerizations at 80°C and 300 bar in bulk and in solution of 40 wt.% of CO_2.

4. CHAIN-TRANSFER REACTION

Chain transfer is of particular relevance for free-radical polymerizations in $scCO_2$, because the homogeneity of the polymerizing mixture strongly depends on the molecular weight of the produced polymer. Low molecular weight material is obtained by adding chain-transfer agents (CTAs). Both conventional CTAs, such as mercaptans, and catalytic chain-transfer agents (CCTA) may be applied. As CCTAs mostly Co-complexes are used. They are associated with very high chain-transfer rate coefficients, k_{tr}, that are almost as large as termination rate coefficients [23]. The impact of CO_2 on chain-transfer to *n*-dodecyl mercaptan (DDM) and to a Co(II)-complex (*bis*(methanol) complex of *bis*(difluoroboryl) diphenylglyoximato cobalt (II), CoPhBF) in MMA polymerizations has been investigated. The structure of the latter is given in Scheme 3.

Scheme 3

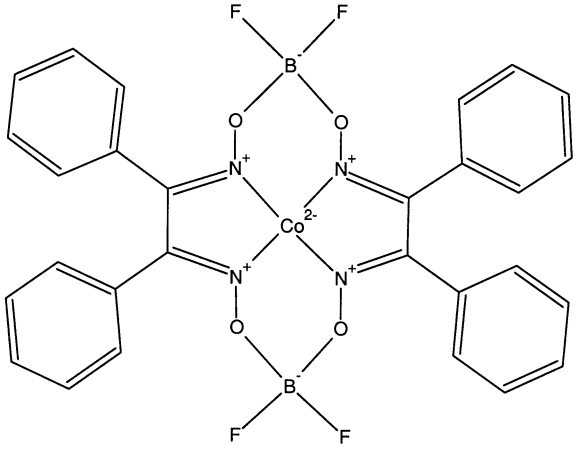

The *bis*(methanol) Co(II)-complex was prepared as detailed in Ref. [19]. The polymerizations were carried out in bulk and in 40 wt.% of CO_2. In the experiments with CoPhBF special care was taken to minimize contact with oxygen. Details are given elsewhere [20].Polymerizations with either DDM or CoPhBF were initiated applying excimer laser pulses with a repetition rate of 1 Hz and using low initiator concentrations of around 0.2 mmol·L^{-1} of 2,2-dimethoxy-2-phenylacetophenone. The resulting polymer was analyzed by SEC. Applying the procedure described by Clay and Gilbert [21], chain-transfer constants, $C_T = k_{tr}/k_p$, were calculated from number molecular weight distributions. With k_p being known, k_{tr} is directly available.

4.1. DDM as chain-transfer agent

The k_{tr} values for DDM in MMA polymerizations are presented as a function of pressure in Fig. 7. k_{tr} is calculated from C_T via the associated k_p values determined for polymerizations in bulk and in $scCO_2$, respectively [20]. The k_{tr} data for polymerizations in $scCO_2$ are by at most 10 % higher than in bulk. This difference is not considered to be significant within experimental uncertainty. From studies into k_p for MMA polymerizations in CO_2 it is known, that for polymerization to low molecular weight material the reduction in propagation rate induced by CO_2 is minor and $k_{p,CO2}$ is close to $k_{p,bulk}$ [22]. This size effect introduces some additional, but small uncertainty into the estimate of k_{tr} from C_T.

In Fig. 7, the lines representing linear fits to the experimental data show only slightly different slopes, indicating that the activation volumes of k_{tr} are almost the same for polymerizations in bulk and in CO_2. The following values were derived:

$\Delta V^{\#}(k_{tr}) = -(5.3\pm3.7)$ cm^3·mol^{-1} (bulk)

$\Delta V^{\#}(k_{tr}) = -(4.4\pm2.9)$ cm^3·mol^{-1} ($scCO_2$)

4.2. CoPhBF as catalytic chain-transfer agent

In contrast to the situation with conventional chain-transfer agents, only very small amounts of Co(II) complex are required to obtain low molecular weight polymer. Given in Fig. 8 are MWDs for MMA polymerizations at 80 °C and 300 bar in 40 wt.% of CO_2. The ratios of the concentration of Co(II) complex

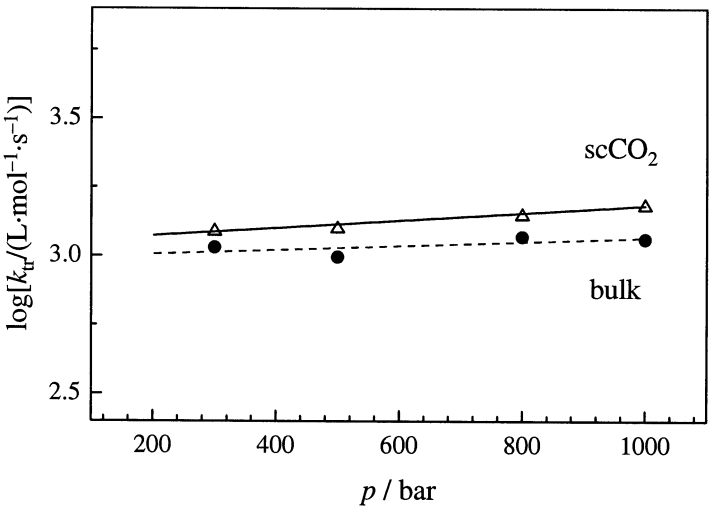

Fig. 7. Pressure dependence of k_{tr} for DDM in MMA polymerizations at 60°C in bulk and in solution of 40 wt.% $scCO_2$.

to monomer concentration, ([CoPhBF]/[MMA]), are given in the figure. A mole ratio of only $3.5 \cdot 10^{-7}$ results in a decrease of molecular weight by around 2 orders of magnitude: e.g. from 10^4 to 10^6 g·mol^{-1} for the MWD peak maxima.

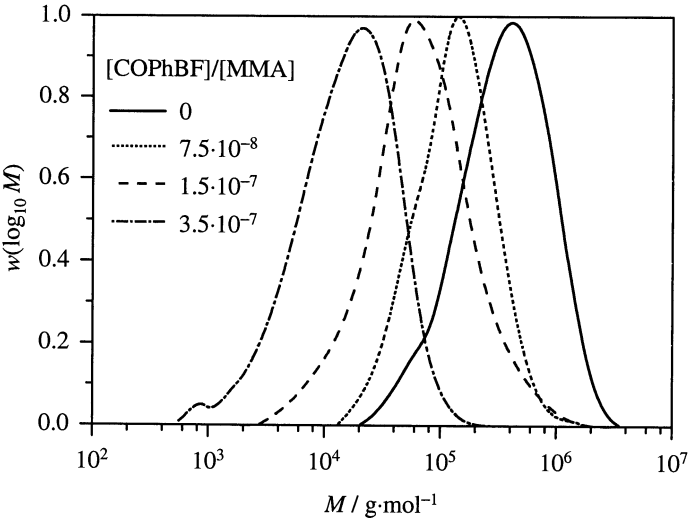

Fig. 8. Molecular weight distributions for PMMA obtained from polymerizations in the presence of CoPhBF at 60 °C and 300 bar in 40 wt.% $scCO_2$. For details see text.

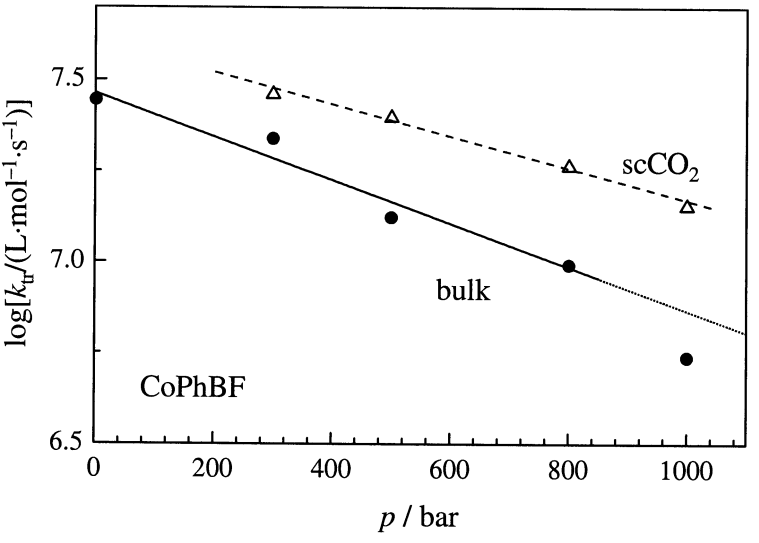

Fig. 9. Pressure dependence of k_{tr} for CoPhBF in MMA polymerizations at 60°C in bulk and in solution of 40 wt.% $scCO_2$.

The chain-transfer rate coefficients, k_{tr}, are 10^7 to 10^8 L·mol^{-1}·s^{-1} [23]. These numbers are close to termination rate coefficients [24]. The pressure dependence of k_{tr} for MMA polymerizations at 80°C in bulk and in 40 wt.% CO_2 is shown in Fig. 9. The data for k_{tr} are higher for reactions in CO_2. At 800 bar, k_{tr} is increased by a factor of 2 in the presence of CO_2. Figure 9 also shows that k_{tr} decreases with pressure and that the slopes of the linear fits to the experimental data are slightly different. For fitting the bulk polymerization data, the data point for 1000 bar has not been considered, because this polymerization experiment proceeded very quickly and gel-effect conditions may have been reached [25]. Under gel-effect conditions, molecular weight may be influenced by effects other than the action of the CTA.

k_{tr} for polymerizations in $scCO_2$ is associated with an activation volume of $\Delta V^{\#}(k_{tr})$ = (31.5±7.3) cm^3·mol^{-1}, which is almost identical to the activation volume observed for k_t in MMA bulk polymerization [25].

5. REACTIVITY RATIOS

The studies into propagation rate, in Section 2, revealed clear effects of CO_2 for some of the methacrylates and acrylates, but no such effect for styrene and for vinyl acetate. The question needs to be asked whether and to which extent this data has implications for propagation in copolymerizations and for reactivity ratios, which latter quantities are defined as the ratio of homo- to crosspropagation rate coefficients. In the following scheme, the four propagation reactions are listed, which need to be considered for a binary copolymerization within the frame of the terminal model. The reactivity of the macroradical, within this model, is exclusively determined by the terminal unit.

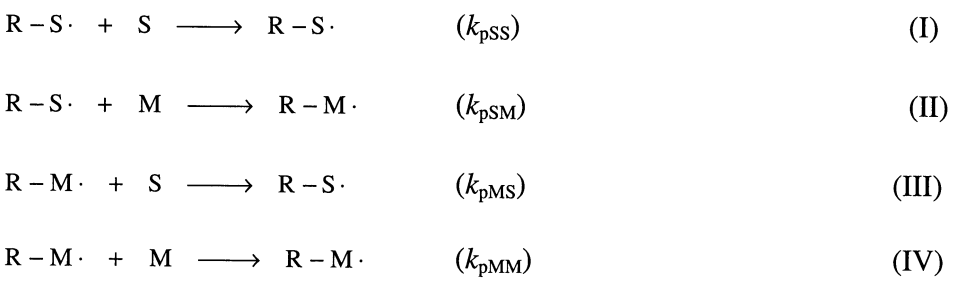

Reactions I and IV are the homopropagation reactions of monomer S (styrene) and M (acrylate or methacrylate), respectively.

The reactivity ratios, e.g. $r_S = k_{pSM}/k_{pSS}$ for styrene, were determined for binary copolymerizations in the presence of 40 wt.% CO_2. For comparison, also polymerizations in bulk and in solution of toluene were carried out. The

composition of copolymer from reaction to small degrees of monomer conversion was determined by 300 MHz ^{1}H–NMR spectroscopy. Details of the copolymerization experiments and of spectroscopic analysis are given elsewhere [26].

Copolymer composition data for styrene–BA copolymerizations at 80°C are given in a Lewis–Mayo plot in Fig. 10. The filled triangles refer to polymerizations in the presence of 40 wt.% CO_2, the circles and open triangles to polymerizations in toluene and in bulk, respectively. It is clearly seen, that the reaction medium has no significant influence on copolymer composition. A fit of the entire data set to the Lewis–Mayo equation yields as reactivity ratios: $r_S = 0.84 \pm 0.08$ and $r_{BA} = 0.23 \pm 0.02$ [26]. Copolymerizations of styrene and alkyl methacrylates as well as of styrene and glycidyl methacrylate also provide no indication of any CO_2 effect on the reactivity ratios [3, 22, 26]. The same result is obtained for the copolymerization of dodecyl acrylate and methyl acrylate [22].

The finding that reactivity ratios are not influenced by the presence of CO_2 although the associated homopropagation rate coefficients are affected to rather different extents is easily understood in terms of the assumption, put forward in Section 2, that CO_2 affects local monomer concentration in the interior of the macroradical coil, but leaves the propagation rate coefficient unchanged. According to this argument, properties of the radical may be modified by the addition of a solvent. The reactivity ratio which characterizes

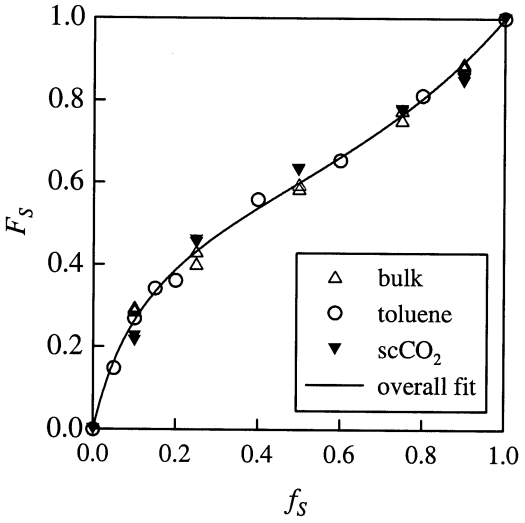

Fig. 10. Lewis–Mayo plot for styrene–BA copolymerizations at 80°C and 300 bar in scCO$_2$ and in bulk. Experiments in toluene were carried out at ambient pressure. The line represents a fit to the entire data set [26].

relative propagation rate of two monomers adding to a one and the same type of macroradical must not, at least not markedly, be affected, as the ratioing procedure eliminates the effects of the solvent on the (same) macroradical. A similar argument explains why in copolymerizations with strong penultimate effects, i.e. where the penultimate unit at the free-radical terminus influences propagation rate, reactivity ratios based on the terminal model provide an adequate and reasonable representation of copolymer composition [27].

Copolymerization rate will certainly reflect the effects of CO_2 seen with the homopolymerizations. This is easily understood as the homopolymerizations constitute limiting situations of the copolymerization systems. It depends on the extent of the CO_2 influence on homo k_p of the particular system under consideration whether the variation of copolymerization k_p with CO_2 needs to be taken into account.

6. CONCLUSIONS

Free-radical polymerizations of common monomers such as styrene and (meth)acrylates may be carried out in homogeneous CO_2-containing fluid phase. The propagation reaction is moderately influenced by CO_2. k_p is diminished by up to 45 % below the bulk polymerization k_p value. This effect is explained by changes in local environment, in particular of local monomer concentration at the free-radical site. This explanation is supported by Monte Carlo simulations of solvation of oligomeric species by either the associated monomer or by CO_2. The observed invariance of reactivity ratios toward CO_2 concentration is also in favor of this explanation. The rate coefficient for the chain-transfer reaction to a Co(II) complex is enhanced by a factor of two in the presence of 40 wt.% CO_2 as compared to bulk polymerization. The diffusion controlled termination reaction may be strongly varied by the addition of CO_2. The largest such effect is seen with DA polymerization where 40 wt.% CO_2 give rise to an enhancement in chain-length averaged k_t (at low and moderate degrees of monomer conversion) by a factor of eight.

ACKNOWLEDGEMENTS

Financial support of this study by the *Deutsche Forschungsgemeinschaft* (Schwerpunktprogramm: „Überkritische Fluide als Lösungs- und Reaktionsmittel“), by the *Bundesministerium für Forschung und Bildung* (BMBF), by the *EU* (TMR network "Superclean Chemistry 2"), and by the *Fonds der Chemischen Industrie* is gratefully acknowledged. We are very grateful to Dr. Marco Drache (Technical University Clausthal) for advising us how to use his Monte Carlo simulation tools and for his cooperation and

support in performing the simulations. The important contributions of Dr. Dorit Nelke, who carried out a significant number of the experiments underlying the present contribution are also gratefully acknowledged.

REFERENCES

[1] J. L. Kendall, D. A. Canelas, J. L. Young, J. M. DeSimone, *Chem. Rev.*, 99 (1999) 54.
[2] S. Beuermann, M. Buback, C. Isemer, A. Wahl, Macromol. Rapid Commun., 20 (1999) 26.
[3] M. Jürgens, PhD. thesis, Göttingen, 2002.
[4] O. F. Olaj, I. Bitai, F. Hinkelmann, Makromol. Chem., 188 (1987) 1689.
[5] M. Buback, C.H. Kurz, Macromol. Chem. Phys., 199 (1998) 2301.
[6] S. Beuermann, M. Buback, F.-D. Kuchta, C. Schmaltz, Macromol. Chem. Phys., 199, (1998) 1209; S. Beuermann, M. Buback, C. Schmaltz, Macromolecules, 31 (1998) 8069.
[7] S. Beuermann, D. Nelke, Macromol. Chem. Phys., submitted for publication
[8] F. Rindfleisch, T. P. DiNoia, M. A. McHugh, J. Phys. Chem., 100 (1996) 15581.
[9] S. Beuermann, M. Buback, C. Isemer, I. Lacík, A. Wahl, Macromolecules, 35 (2002) 3866.
[10] S. Beuermann, M. Buback, D. Nelke, Macromolecules, 34 (2001) 6637.
[11] D. Nelke, PhD. thesis, Göttingen, 2002.
[12] *Cerius*^{2} Simulation Tools, Release 4.0; Biosym/Molecular Simulation Inc., 1998.
[13] J. W. Ponder, F. M. Richards, J. Comput. Chem., 8 (1987) 1016.
[14] M. Drache, PhD. thesis, Clausthal, 1994.
[15] M. Buback, Makromol. Chem., 191 (1990) 1575.
[16] S. Beuermann, M. Buback, C. Schmaltz, Ind. Eng. Chem. Res., 38 (1999) 3338.
[17] M. Buback, H. Hippler, J. Schweer, H.-P. Vögele, Makromol. Chem., Rapid Commun., 7 (1986) 261.
[18] M. Buback, A. Kuelpmann, C. Kurz, Macromol. Chem. Phys., 203 (2002) 1065.
[19] A. Bakac, M. E. Brynildson, J. H. Espenson, Inorg. Chem., 25 (1986) 4108.
[20] V. El Rezzi, PhD. thesis, Göttingen 2001.
[21] P. A. Clay, R. G. Gilbert, Macromolecules, 28 (1995) 552.
[22] C. Isemer, PhD. thesis, Göttingen, 2000.
[23] A. A. Gridnev, S. D. Ittel, Chem. Rev., 101 (2001) 3611; J. P. A. Heuts, G. E. Roberts, J. D. Biasutti, Aust. J. Chem., 55 (2002) 381.
[24] S. Beuermann, M. Buback, Prog. Polym. Sci., 27 (2002) 191.
[25] S. Beuermann, PhD. thesis, Göttingen, 1993.
[26] A. Wahl, PhD. thesis, Göttingen, 1999.
[27] M. Buback, A. Feldermann, C. Barner-Kowollik, I. Lacík, Macromolecules, 34 (2001) 5439

Supercritical Fluids as Solvents and Reaction Media
G. Brunner (editor)

Chapter 5.4.

Ammonia as reagent or reaction medium for polymers

W. Mormann*, H. Jung and D. Spitzer

Universität Siegen, FB8, Laboratorium für Makromolekulare Chemie, D-57068 Siegen, Germany (mormann@chemie.uni-siegen.de)

1. INTRODUCTION

Supercritical fluids as reaction media have gained increasing interest during the past twenty years. Carbon dioxide is by far the most frequently used solvent for supercritical extraction and chemical reactions [1]. Use of carbon dioxide in polymerisation has been spurred by the work of deSimone and his group [2]. Ammonia - also a gas under normal conditions - has been used by far less. A literature search for the last decade gave 2563 articles on supercritical carbon dioxide and 61 for supercritical ammonia (source Science Citation Index).

The overwhelming preference for carbon dioxide has several reasons: Easy handling in terms of environmental impact as it is taken from the air and consequently may be released into the air. It is inert towards most organic and bio molecules. It reacts only with carbanions that are not likely to be present in extraction procedures, which excludes, however, anionic polymerisations in carbon dioxide. The rather low critical temperature (see Table 1) and the relatively high density at the critical point are further advantages.

Ammonia is more expensive, cannot be released into the air and is more toxic than carbon dioxide. Use as reaction medium or as solvent for extractions is limited due to the high reactivity of ammonia towards a number of functional groups present in organic and bio molecules. It can participate in many nucleophilic displacement and acid -vourable for its use as solvent in liquid or supercritical extraction.

Representative properties of ammonia and of several common solvents are given in Table 1. The dipole moment of ammonia is only slightly lower than that of water or methanol, while carbon dioxide has no dipole moment. The dielectric constant of ammonia is only one fifth that of water and even lower than that of ethanol. Like water ammonia can act as hydrogen bond acceptor and donor. These properties may be the reason why ammonia can dissolve a number of inorganic salts (halides, cyanides, thiocyanates, nitrates or nitrites) and also

Table 1
Physical constants of selected solvents [4]

Solvent	T_{crit} [5] /°C	P_{crit} [5] /bar	ρ_{crit} [5] /g cm^{-3}	ε /25 °C	μ /Debye	p K_a [6]
Water	374,4	226,8		78,5	1,8	14,0
Methanol	240,5	78,9		32,6	1,65	16,7
Ammonia	132,4	112,8	0,235	16,9	1,47	29,8 [7]
n-Hexane	234,2	29,6		1,9	0	-
Carbon dioxide	31,3	76,3		1,0	0	-

water as well as polar organic compounds (alcohols, amines, esters) and, on the non polar end, hydrocarbons like cyclohexane. This allows running reactions under homogeneous conditions which is impossible in other solvents [3].

The higher critical temperature of ammonia with respect to carbon dioxide includes the option to work in liquid ammonia up to 130 °C, which may be convenient in terms of equipment as the vapour pressure at 20 °C is only 8,6 bar and at 100 °C 62,5 bar.

There are few examples where liquid ammonia has been used as solvent in polymer chemistry. Anionic polymerisation of styrene is one early example [8] another is silylation of cellulose with chlorotrimethylsilane [9]. Ammonia is known to activate cellulose by intercalation in the crystal lattice thus breaking intra- and intermolecular hydrogen bonds, which are mainly responsible of the low reactivity of non-activated cellulose [10].

Ammonolytic reactions of polycarbonate and poly(ethylene terephthalate with ammonia, mainly in aqueous solution, have been reported [11 - 13]. Ammonolytic cleavage of polyurethanes in supercritical ammonia has been reported [14]. Buback and Rindfleisch described the reaction of poly(ethylene-co-methyl acrylate) in supercritical ammonia; they converted the ester functions to amide and nitrile groups [15].

Chemical recycling of polymers with carboxylic acid derived functional groups by ammonolysis results in formation of acid amide moieties as compared to carboxylic acid groups from hydrolysis. The former cannot be used directly for the re-synthesis of polymers. Ammonolysis of polymers with functional groups of carbonic acid in the main chain will result in the formation of urea as "acid amide", a compound which among others can be used as fertilizer.

In this article we report on our work in the field of ammonolysis of step growth polymers i.e. polyesters, polyamides, polycarbonates using ammonia as reaction medium and reagent. The second part of the paper deals with trimethylsilylation of starch in ammonia as reaction medium.

2. MATERIALS, EQUIPMENT, TECHNIQUES

Poly(butylene terephthalate) (PBT) molar mass 6600 g/mol was synthesised according to [36].

Poly(ethylene terephthalate) (PET) bottle grade (5x5x0,1 mm).

Vectra® A 950 RX: LC-Polyester 73 mol% 4-hydroxybenzoic and 27 mol% 6-hydroxy-2-naphthoic acid units [55]; Hoechst AG, Frankfurt (cylindrical granules with 2 mm diameter and 3 mm length).

Makrolon® 2400: Bisphenol-A-polycarbonate; Bayer AG, Leverkusen (cylindrical granules with 2 mm diameter and 3 mm length).

Poly(hexamethylene carbonate); Bayer AG, Leverkusen (flakes).

Starch dried at 80 °C (0,05 mbar, 12 h).

Hexamethyldisilazane was purified by fractional distillation.

Saccharin dried at 50 °C and 10 mbar.

The work reported in the present paper was performed in stainless steel autoclaves (Werkstoff 1,4571) or in a tubular reactor with continuous flow of ammonia. The autoclaves used o-rings from perbunan up to 120 °C and from teflon up to 200 °C as seals and flanges to close the cylindrical vessels. They were equipped with thermocouple, pressure gauge, valve for filling and sampling. Heating was made either with an electric heating jacket or with a fluid pumped through the heating jacket. The autoclaves had glass windows for visual observation of the contents. Mixing of components was achieved either with a mechanical stirrer powered by an electro motor (autoclave in Fig.1), with a magnetic stirring bar or with steel balls (autoclave in Fig. 2).

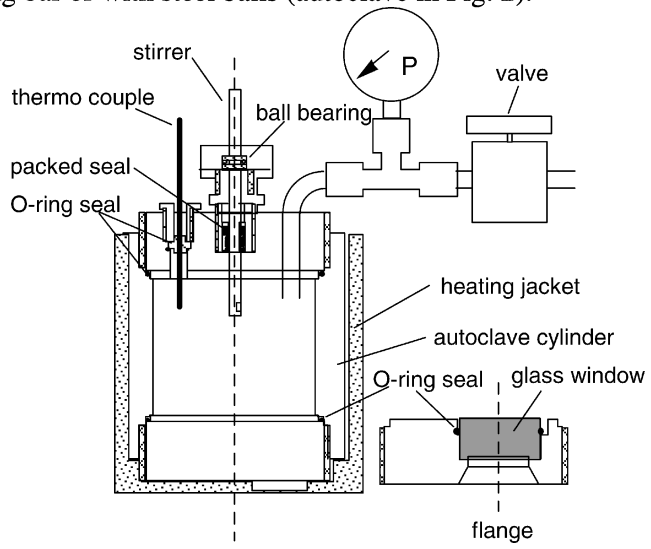

Fig. 1. Autoclave with mechanical stirrer and glass window (150 or 880 mL).

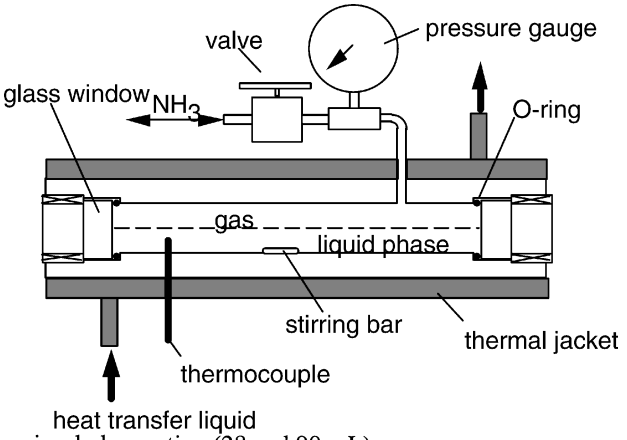

Fig. 2. Autoclave for visual observation (28 and 90 mL).

The continuous flow reactor consisted of a pressure vessel for ammonia which was heated to 35 °C to ensure sufficient pressure for the delivery of ammonia to the pump. The pump was an HPLC-pump with flow-rates from 0,01 to 9,99 mL/min. The reactor tubes had sintered metal filters at both ends, a diameter of 7,6 mm and variable length to provide volumes between 3,6 and 13,6 mL. Temperature was controlled and monitored with thermo couples at both ends of the reactor tube and at the outlet, pressure was controlled at the pump and monitored with a high pressure transmitter after the reactor. The whole set up after the pump was contained in a temperature controlled oven.

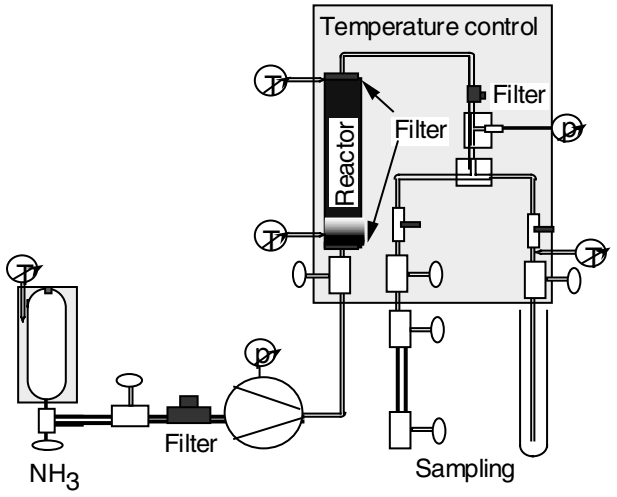

Fig. 3. Tube reactor (extractor) with continuous flow of ammonia.

Samples can be taken with pressure vessels or with (semi)continuous flow of material which is enabled with a constant position of a needle valve or by intermittent opening and closing. This procedure is accompanied by a pressure drop but pressure is all the time far above the vapour pressure of ammonia.

Solubility of polymers and ammonolysis products was determined in the autoclave for visual observation. Saturated solutions were prepared at a given temperature; samples were taken from the fluid phase. Ammonia was removed, the sample dried, weighed and characterised.

Table 2
Solubility of polymers and ammonolysis products of polyesters and polyamides

Compound	T °C	p bar	Solubility wt.%	Solubility g/100ml
PBT	100	170-200	1,1	0,5
(M_n 6600 g/mol)	180	200	(reaction)	(reaction)
PET	100	140-145	(reaction)	(reaction)
Vectra	120	150-250	(reaction)	(reaction)
Bisphenol-A-PC	30	12	(reaction)	(reaction)
Poly(hexamethylen-	30	12	5,0	3,1
carbonate)	60	26	9,9	6,3
	100	63	19,5	11,1
Bisphenol-A	18	8	48	107
	90	51	> 92	-
Urea	31	12	58,1	-
	66	30	80,7	
	109	74	91,5	
1,2-Ethandiol	> -33	> 0	∞	∞
1,4-Butanediol	20	9	∞	∞
	100	75	∞	∞
Terephthalamide	50	150-200		0,85
	100	170-200		0,82
	150	320-350		0,54
	180	195-200		0,18
Adipic acid amide	25	10	0,26	1,16
	80	41	2,3	1,28
Hexamethylene diamine	25	10	45,3	50,5
	65	30	∞	∞

Solubility could also be determined in the continuous extraction apparatus. The tube reactor was charged with the material under investigation, filled with ammonia, heated to the desired temperature, a volume corresponding to the volume of the reactor was collected at low flow rate and analysed. Values obtained from the different methods differed by less than 5 %. Solubilities are given in Table 2 or in the corresponding chapters.

3. SOLVOLYTIC REACTIONS OF POLYMERS WITH AMMONIA

Ammonolysis of polyesters and polyamides has been investigated. When possible solubility of polymers was studied first then reaction conditions were optimised mainly with respect to temperature and catalysis. Reactions were complete when no oligomeric or polymeric materials were left (formation of a clear solution, size exclusion chromatography). Products were separated by extraction with a specific solvent and identified by comparison with authentic material.

3.1. Ammonolysis of Polyesters

Ammonolysis of polyesters gives the diols and the amides of the diacids used as reaction products in case of AA BB type polymers and hydroxyacid amides for AB monomers (cf. Scheme 1). Polyesters studied were polyethylene terephthalate, polybutylene terephthalate and (Vectra), a liquid crystalline polyester composed of p-hydroxybenzoic acid and 6-hydroxy-2-naphthoic acid.
Ammonolysis of PET and PBT was studied in an autoclave. Reactions were complete when a homogeneous mixture had formed. Ammonia was evaporated and the solid was stirred with water or with tetrahydrofuran (THF).

Reaction of PET was complete in 2 h at 120 °C, with ammonia containing 22 percent water it took 2,5 h, products were in all cases terephthalamide and ethyleneglycol. PBT required more severe reaction conditions even at 160 °C it took 11 h until reaction was complete. Therefore several catalysts were studied to elucidate their efficiency. With titanium(IV)-ethanolat, ammonium chloride

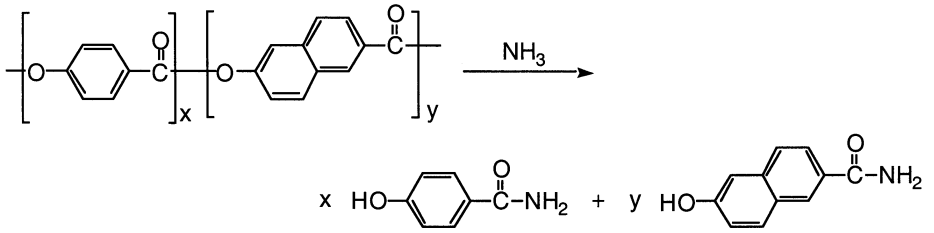

Scheme 1. Ammonolysis of alkylene terephthalates and Vectra.

Table 3
Ammonolysis of PET and PBT

No.	Polyester /wt.%	catalyst /mol %	T /°C	t /h
PET	11,5	-	120	2
	2,2	water (22 wt)	120	2,5
PBT	4,0	-	160	11
	3,7	NH_4Cl (5,0)	160	5
	4,1	DABCO (5,0)	160	5
	4,7	$Ti(OEt)_4$ (5,6)	160	5
	3,9	$Cu(OAc)_2$ (0,4)	160	2,5
	3,9	DBTDL (4,0)	160	2,5
Vectra	15,3	-	120	2
	18,1	water (2,7wt)	120	2

and 1,4-diazabicyclo[2.2.2]octane (DABCO) reaction time could be reduced to 5 h, an increase in reactivity by a factor of two. With copper(II)-acetate monohydrate and dibutyltin dilaurate ammonolysis was complete after 2,5 h, an increase by a factor of more than four.

Vectra® a fully aromatic liquid crystalline polyester is hardly soluble in common solvents. Mixtures of chlorohydrocarbons and phenols or fluorinated alcohols have to be used. Ammonolysis was studied under the conditions used for PET and in addition with 1,1 and 2,7 % water. Again formation of a clear solution indicated complete reaction as both amides are soluble in ammonia under the reaction conditions which took two hours.

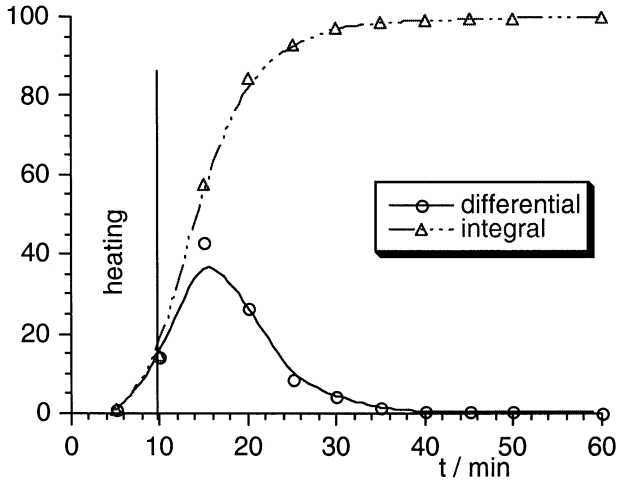

Fig. 4. Ammonolysis of Vectra with continuous flow of ammonia.

Ammonolysis combined with extraction of solubles at 120 °C was made in the continuous reactor. Samples were collected over 10 minutes and ammonia was evaporated. In Figure 4 the total percentage extracted after a given time and the percentage of each fraction are plotted against the duration of extraction. From Figure 4 can be seen that it takes only 60 minutes including time for heating to completely degrade the polyester to the corresponding hydroxyacid amides. Within 20 minutes more than 90 percent were degraded and extracted. Oligomeric or polymeric fractions could not be detected with size exclusion chromatography (SEC). The acid amides were separated and quantified with high performance liquid chromatography (HPLC) using the pure amides as reference materials.

The surprisingly fast reaction is due to some swelling of the polymer in ammonia followed by fast ammonolysis which is favoured by the phenolic leaving group.

3.2. Polycarbonates

Polycarbonates, the esters of carbonic acid and diols or bisphenols, will be discussed in a separate chapter because ammonolysis not only is of academic or analytical interest. It can have practical use because in this case the products formed are the diol (bisphenol) and urea. The former can directly be used for the synthesis of new polycarbonates, urea also for the synthesis of polymers or as fertiliser.

3.2.1. Poly(hexamethylene carbonate)

Poly(hexamethylene carbonate) in terms of structure is an extension in the series from fully aromatic, aromatic-aliphatic to aliphatic polyesters. Solubility of this polymer could be determined since the reactivity is rather low in liquid ammonia. In addition to determination of solubility in the liquid phase in an autoclave continuous extraction was used in order to determine molar mass of the fractions. Samples were collected in the intermittent mode over 10 minutes and studied by SEC after evaporation of ammonia. Results from extraction are by 1 mass percent lower than those from the autoclave as shown in Figure 5.

Analysis of extracts with SEC revealed that fractionation occurs. This is demonstrated with the molecular weight distribution curves from SEC for different fractions extracted at 35 and 100 °C. From Figures 6 and 7 can be seen that separation takes place according to molar mass and also that higher homologues become soluble with increasing temperature. Oligomers are extracted first and molar mass of extracts increases with time.

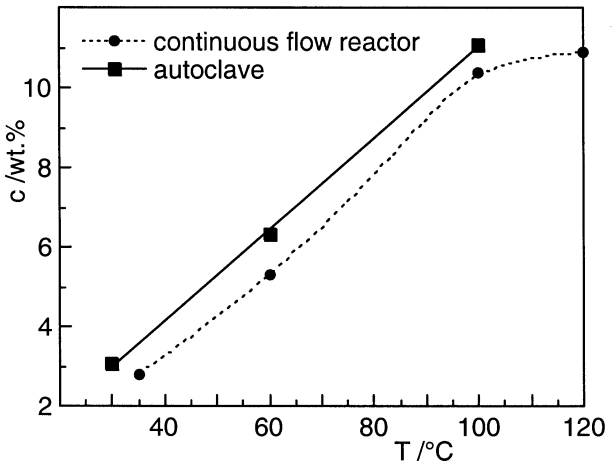

Fig 5. Solubility of poly(hexamethylene carbonate).

A systematic study of solubility as a function of time and temperature was made with poly(hexamethylene carbonate). The continuous reactor was charged with a sample of polycarbonate at a given temperature, ammonia was pumped through and fractions were collected in the intermittent mode. All fractions were analysed by size exclusion chromatography. In Figure 8 a series of curves of the extracted mass after different times are plotted for temperatures from 35 to 180 °C. From 35 to 100 °C the extracted fraction increases from 25 to more than 90 percent and decreases with further increase of temperature. This indicates lower critical solution behaviour. Under supercritical conditions solubility fur-

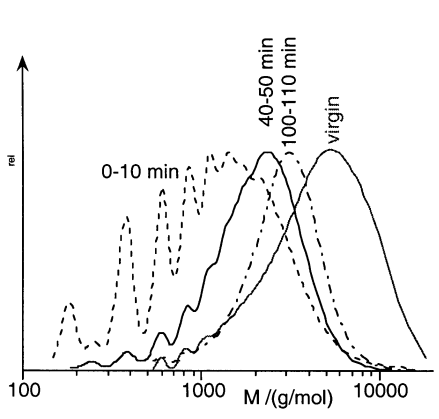

Fig. 6. Extraction at 35 °C.

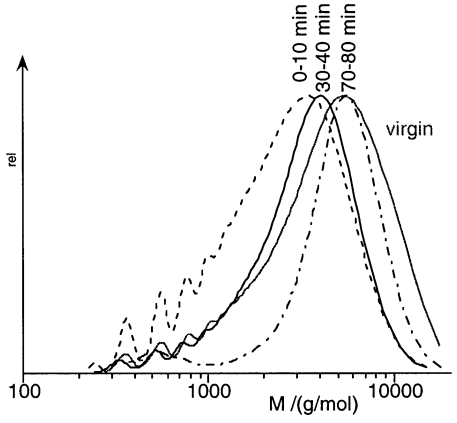

Fig. 7. Extraction at 100 °C.

Molecular weights of extracts of poly(hexamethylene carbonate) with ammonia.

ther decreases and the shape of the curves changes in the sense that solubility increases with time. This is due to ammonolytic degradation of the polymer.

In Figures 9 and 10 molar masses of the extracted fractions at different temperatures of Figure 8 are plotted versus time. Up to 120 °C molar mass of fractions increases with time, solubility, however, decreases above 100 °C. Under supercritical conditions above 150 °C molecular weight of extracts is practically constant with time for a given temperature. Hence, poly(hexamethylene carbonate) can be degraded in a controlled fashion.

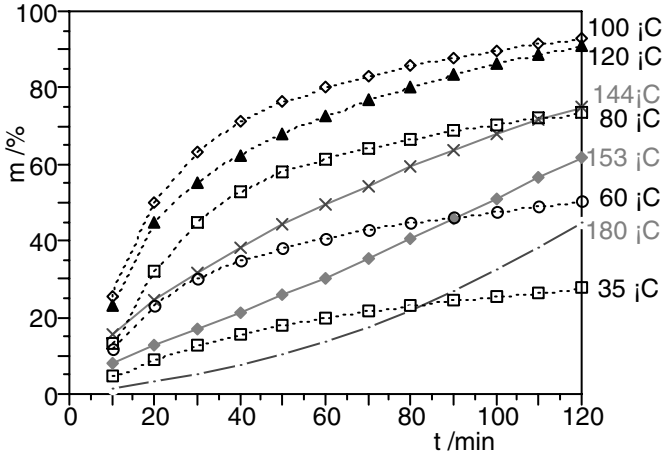

Fig. 8. Extracts from poly(hexamethylene carbonate) at different temperatures.

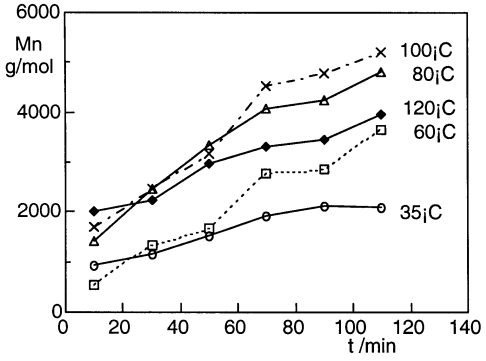

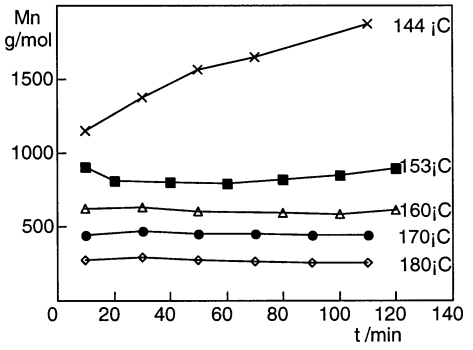

Molecular weights of extracts of poly(hexamethylene carbonate).

Fig. 9. Extraction with liquid ammonia.

Fig. 10. Extr. with supercritical ammonia.

Table 4
Molecular weight distribution (SEC) and polydispersity (D) of residues from extraction of poly(hexamethylene carbonate) at different temperatures.

	T /°C	D
Virgin	-	2,56
Residues of extraction	35	1,42
	60	1,35
	100	1,32
	120	1,31
	150	1,70
	180	1,80

Molecular weights of residues of extraction support these results. They increase up to 100 °C. With further increase of temperature molar mass of residues decreases due to ammonolytic degradation. Up to 100 °C polydispersity of the residues decreases due to fractionation, it increases above 120 °C caused by random cleavage of the polymer chains (cf. Table 4).

To study complete ammonolysis of poly(hexamethylene carbonate) a 20 percent mixture in ammonia was reacted at 200 °C and 1000 bar for 2h in an autoclave. Samples were taken after the times given in Fig. 12. A shift to lower molecular weight with time is observed and the amount of hexanediol increases. After 2 h only hexanediol can be found in the SEC-chromatogram.

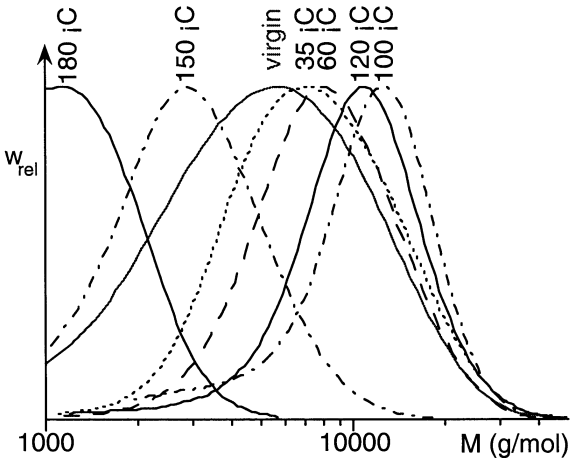

Fig. 11. Molecular weight distribution (SEC).

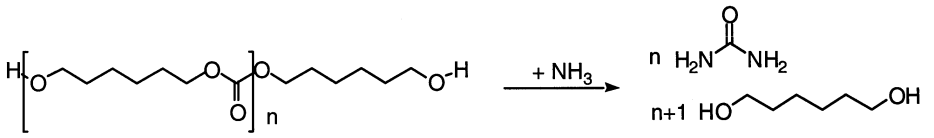

Equation 1. Ammonolysis of poly(hexamethylene carbonate).

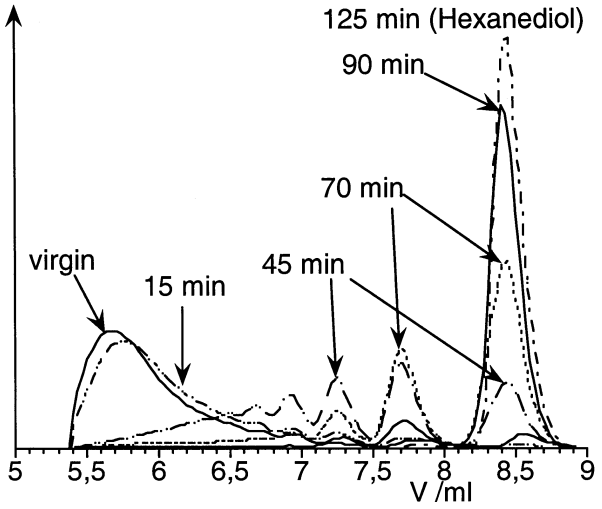

Fig. 12. SEC curves of ammonolysis of poly(hexamethylene carbonate); 200°C, 1000 bar.

3.2.2. Ammonolysis of Bisphenol-A-Polycarbonate

Based on the results of ammonolysis of bisphenol-A-polycarbonate in organic solvents [11] experiments in ammonia were made at room temperature in an autoclave and at the boiling temperature of liquid ammonia (- 33 °C). Experiments to determine solubility of the polymer had shown that it dissolves upon degradation. Again formation of a clear solution indicated that the reaction was complete. After removal of excess ammonia the white solids were triturated either with water or with tetrahydrofuran. Bisphenol-A is insoluble in cold water and soluble in THF, while urea is easily soluble in water but insoluble in THF. It turned out that urea was found only upon triturating of the solid with water; dissolution of bisphenol-A in THF left a residue consisting mostly of ammonium cyanate and traces of urea.

THF-soluble or water insoluble fractions were analysed by HPLC and IR-spectroscopy. Samples from incomplete reactions had carbonyl bands at 1724 cm^{-1} and two peaks in the HPLC in accordance with bisphenol-A and a carbamate. Oligomers or polymers could not be detected with size exclusion chromatography. Reaction conditions and results of ammonolysis of bisphenol-A-polycarbonate are collected in Table 5.

Table 5
Conditions and results of bisphenol-A-polycarbonate ammonolysis.

No.	m(PC) /g	$m(NH_3)$ /g	T /°C	p /bar	t /min	Products
3.3.1	18,2	51,1	20	8,6	5[a]	bisphenol-A, urea, carbamate
					15	bisphenol-A, urea
3.3.2	10,0	26,62	20	8,6	15	bisphenol-A, NH_4NCO
3.4	18,2	100	-33		15 300	bisphenol-A, NH_4NCO

a: Sample from supernatant solution of PC pellets

Ammonolysis proceeded rather slowly at -33 °C. After 5 h bisphenol-A and ammonium cyanate were obtained in 18,7 % yield. Unreacted polycarbonate was unchanged in terms of shape and identical with virgin material according to the IR-spectrum (formation of OH-absorption). These findings suggest that ammonolysis starts from the surface directly or after some swelling. In liquid ammonia at 20 °C ammonolysis was complete after 15 minutes. A sample taken after 5 minutes contained small amounts of carbamate but no polymer. Temperatures above 60 °C led to a brownish discoloration of bisphenol-A.

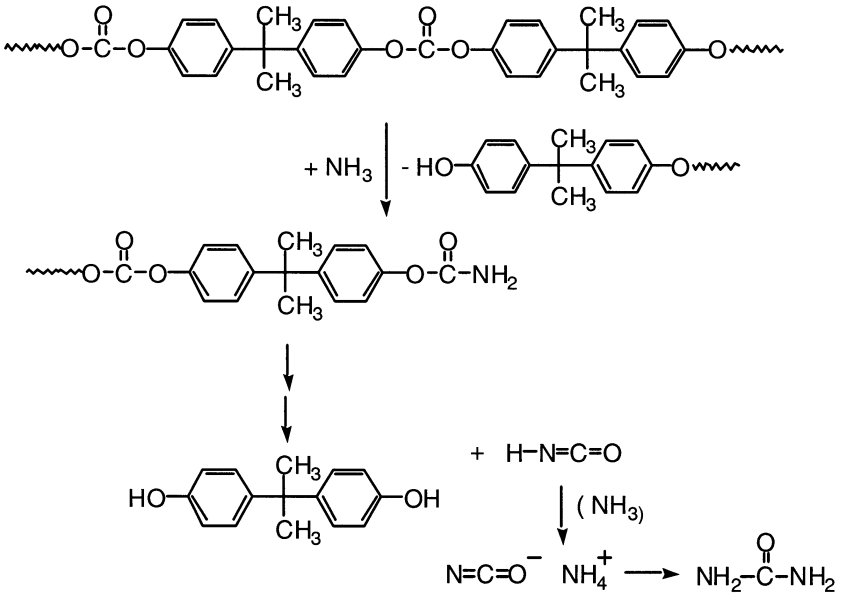

Scheme 2. Ammonolysis of bisphenol-A-polycarbonate.

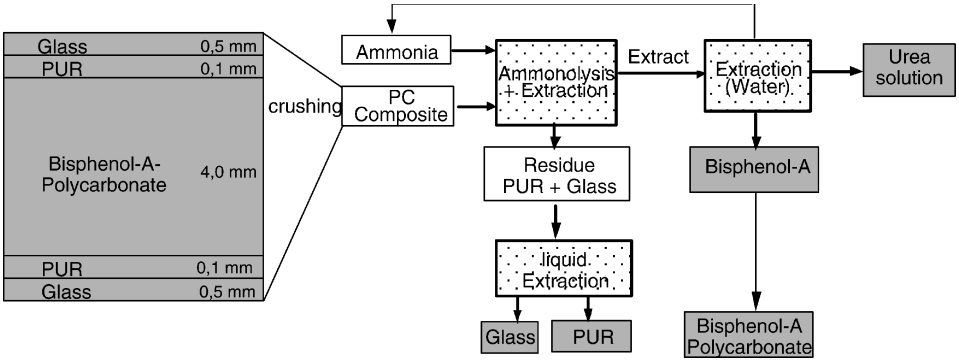

Fig. 13. Recycling of car windows (schematic flow diagram)

Experimental results suggest a mechanism as outlined in Scheme 2. First step is the addition of ammonia followed by elimination of phenol under formation of a carbamate. The second step can be either a new addition elimination sequence leading to urea and phenol or elimination of cyanic acid followed by neutralisation with ammonia. During solubility studies of urea no ammonium cyanate had been detected, hence cyanic acid must have been cleaved off the carbamate. This also explains why aromatic polycarbonates cannot be obtained from bisphenols and urea [16].

The ease of ammonolytic cleavage of bisphenol-A-polycarbonate can be used for selective degradation and chemical recycling of blends and composite materials containing BPA-polycarbonate, e.g. compact disks having an aluminum layer on one side and a protective coating on the other. Car windows made from a polycarbonate inner layer to which thin glass layers are attached with a polyurethane adhesive that are under development can also be recycled with liquid ammonia.

The materials are crushed to increase the surface where ammonia can attack. Reaction with ammonia leaves aluminum and the coating in case of compact disks, while the glass and the polyurethane adhesive are the residue of the car window. Work-up of the ammonia soluble polycarbonate constituents is done as described above. The polyurethane (PUR) can be recycled by ammonolysis under more severe conditions [14] or separated for re-use by dissolution in a suitable solvent. A schematic flow diagram of such a process is shown in Figure 13.

3.3 Polyamides

Polyamides should be more stable towards solvolytic cleavage than polyesters as the amide moiety is by far less reactive. The electron releasing amino groups decrease the electrophilicity of the carbon, hence stronger nucleophiles

and or more drastic conditions are required for solvolytic cleavage. Studies in this paper were made with poly(hexamethylene adipamide) (PA 66). Complete ammonolysis will result in formation of hexamethyenediamine and adipic acid diamide.

Ammonolysis was made with 15 to 25 weight percent of polyamide 6,6 in ammonia. Experiments made to find suitable reaction conditions showed that without catalyst 200 °C were necessary to achieve some conversion. A number of potential catalysts (ammonium chloride, DABCO, titanium(IV)-ethanolate, copper(II)-acetate and dibutyltin dilaurate) were studied at 200 °C and 70 h reaction time, some also at lower temperature.

Work-up was done by evaporation of ammonia and triturating of the solid residue with methanol. IR-spectra of the methanol soluble fraction showed N-H valence vibrations of secondary amides at 3310 cm^{-1}, of primary amides at 3380 and 3190 cm^{-1} and the amide carbonyl vibration at 1640 cm^{-1}. Hence oligomers were extracted with methanol which was also proven by molecular weight from viscometry in 85 % formic acid solutions. Hexamethylenediamine was identified by gas chromatography. The insoluble fractions were polyamide that had practically not changed. Reaction conditions methanol soluble fraction and its molecular weight are summarised in Table 5. Based on these results no complete ammonolysis, only statistic cleavage to oligomers occurred which is represented by equation 2.

Table 6
Ammonolysis of PA 66.

No.	Catalyst[a] /mol %	T /°C	t /h	p /bar	MeOH-sol /%	M_W [b] /g mol^{-1}
1	--	115	24	93	0	6790
2	--	200	70	330	54,5	1263
3	H_2O (2000)	200	70	1000	44,8	2096
4	NH_4Cl (41)	150	70	280	92,3	1070
5	NH_4Cl (25)	200	70	600	87,2	1028
6	DABCO (50)	160	65	600	32,9	2201
7	DABCO (26)	200	70	280	61,1	1130
8	$Ti(OC_2H_5)_4$ (12)	200	70	280	55,0	2358
9	$Cu(OAc)_2$ (0,5)	200	70	1400	10,0	3497
10	DBTDL (5)	200	113	450	36,4	2489

a: related to amide groups; b: from viscometry in 85 % formic acid;
starting material had PA 66 molecular weight 26600;

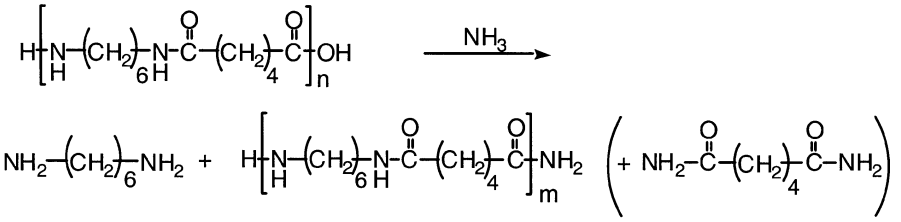

Equation 2. Ammonolysis of PA 66.

Taking the experiment at 200 °C without catalyst (55 % solubles with a molecular weight of 1250) as reference only ammonium chloride and to a small extent DABCO had a catalytic effect. With the former ninety percent solubles with a molecular weight below 1100 were obtained. With this catalyst 160 °C are sufficient to obtain the same results. DABCO gave 61 % solubles with molecular weight 1130 which is only slightly better than the non catalysed reaction.

With water, titanium(IV)-ethanolate, and DBTDL no catalytic effect could be observed. Solubles are in the range from 35 to 55 %, less or equal to the non catalysed reactions, molecular weight of solubles is in the range from 2100 to 2500, hence significantly higher than in the non catalysed reaction. Copper(II)-acetate seems to have an anticatalytic effect as the amount of methanol soluble material was significantly less and the molecular weight significantly higher than in the non-catalysed reaction.

The results from Table 6 suggest that complete ammonolysis is not possible under the conditions used. Equilibrium is reached despite of the huge molar excess of ammonia.

4. AMMONIA AS REACTION MEDIUM FOR SILYLATION REACTIONS

Use of ammonia as reaction medium is limited due to its high reactivity. Silylation, a reaction in which active hydrogen mostly of hydroxy, thio and amino groups is replaced by an organosilicon moiety, has the aim to impart volatility and organophilicity to hydrophilic organic compounds. It is one of the few reactions where ammonia does not compete or interfere with the substrate.

In the field of polymers, silylation of poly(vinyl alcohol) [3, 17], cellulose and starch has been reported [9]. The big difference in polarity requires special solvents for the reaction e.g. pyridine [9,18], dimethylacetamide [19], or formamide [20]. Furthermore reactive silylating agents like N,O-bis(trimethylsilyl)acetamide [18] or chlorotrimethylsilane [9, 18, 21] are needed. Tedious purification of the polymer is necessary to remove residual silylating agent, salts and solvent.

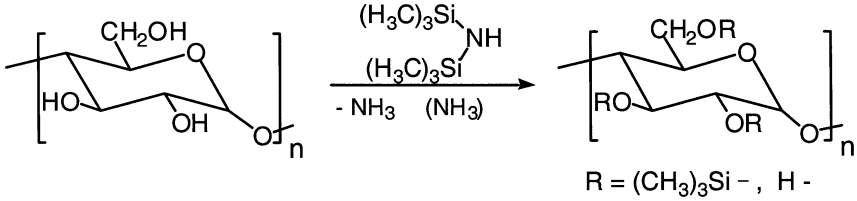

Equation 3. Silylation of starch with hexamethyldisilazane in ammonia.

Silylation with hexamethyldisilazane (HMDS) in ammonia has the advantage that ammonia is left upon reaction of HMDS, hence only ammonia is present in the reaction medium, which can easily be removed by evaporation (cf. equation 3). We were able to show that this reaction proceeds at elevated temperature and performed silylation of poly(vinyl alcohol) in ammonia, a reaction that proceeds under homogeneous conditions [3]. Silylation of cellulose could also be performed but as a heterogeneous reaction. [22].

4.1. Trimethylsilylation of starch

Starch is a poly(α-D-glucopyranoside) with 1,4- and 1,6 linkage of glucose units. Depending on its origin it consists of linear amylose with 1,4–linked glucose units and hyperbranched amylopectin (see Fig. 14) which in addition has 1,6-linked units. Both constituents of starch are non-melting solids due to a network of inter and intramolecular hydrogen bonds. This is why activation is required to allow reactions like etherification or esterification to proceed in reasonable time.

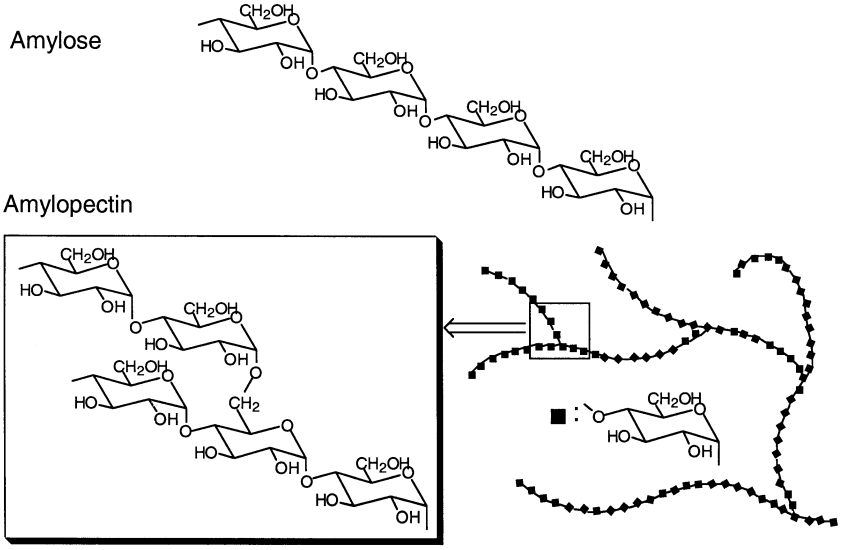

Fig. 14. Constituents of starch.

Like cellulose starch can be activated with ammonia [23 - 25]. Inter- and intramolecular hydrogen bonds are broken with ammonia which reduces steric hindrance and improves accessability of hydroxy groups. To learn about the behaviour of starch in ammonia, solubility of amylose and amylopectin in ammonia was investigated and also the amount of ammonia absorbed by starch at ambient pressure. Amylose is slightly soluble in ammonia (cf. Fig. 16) while amylopectin (waxy corn starch is swollen only). The ammonia uptake does not significantly depend on the type of starch as shown in Figure 15. At room temperature approximately 10 percent ammonia are absorbed which corresponds almost exactly to 1 mol ammonia per mol anhydroglucose unit. This amount decreases to less than 1 percent at 130 °C which indicates that there is no stoichiometric complex only a temperature dependent equilibrium.

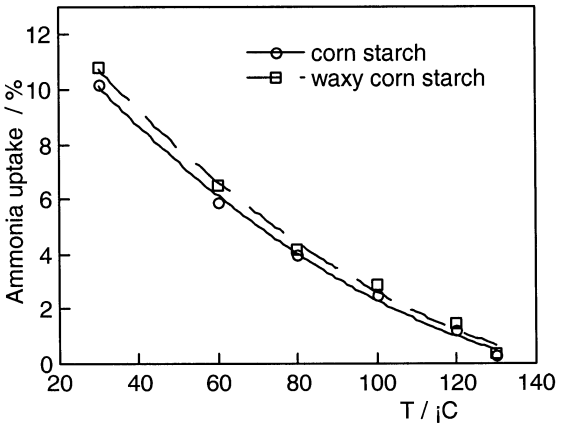

Fig. 15. Ammonia uptake of starch.

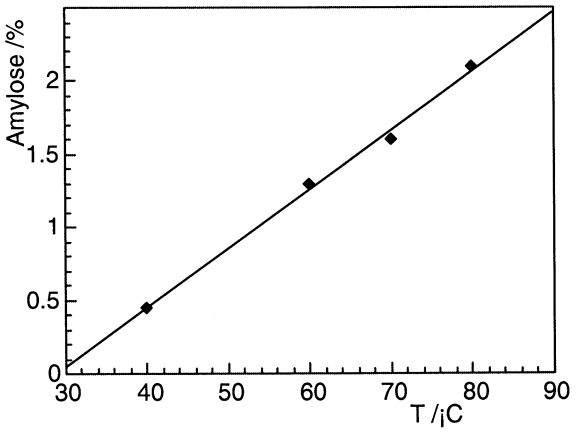

Fig. 16. Solubility of amylose in ammonia.

Table 7
Properties of starches used for silylation

Starch	Amylose content /%	Mn /g mol^{-1}	Mw /g mol^{-1}	D
Amylose	100	337100	912300	2,7
Potato (Cerestar)	25	205800	557700	2,7
Potato (Fluka)	27	10310	24290	2,4
Corn	24	-	-	-
Waxy mais	<1	-	-	-
Degraded	-	3240	28800	8,9

Silylation of starch was studied with the aim to achieve complete and controlled partial silylation. Starch types used were amylose, amylopectin (waxy mais starch), potato starch and a degraded starch. They were dried to constant weight at 80 °C and 15 mbar. In Table 7 starches used are listed with their amylose content, molar mass and polydispersity index D. Data have been obtained from trimethylsilylated starches.

A number of experiments was made to find out conditions for complete silylation and also to study the influence of the main reaction parameters. Experimental data and results are collected in Table 8. Data in Table 8 show that the type of starch has a strong influence on the degree of silylation. Supercritical conditions have no advantage. The activating effect of ammonia, which is based on the cleavage of hydrogen bonds in starch is practically absent, hence hydroxy groups are not accessible to silylation.

Table 8
Influence of reaction parameters on silylation of starches

No.	Starch type	n(AGE:$SiMe_3$:NH_3:Sacc)	t /h	T /°C	DS
1	Potato	1,0 : 18,6 : 38,1 : 0,0	15	80	1,9
2	(Cerestar)	1,0 : 18,6 : 37,5 : 0,129	15	80	3,0
3	"	1,0 : 15,2 : 35,5 : 0,129	4	80	2,9
4	"	1,0 : 6,0 : 38,9 : 0,021	15	80	2,8
5	Potato (Fluka)	1,0 : 8,0 : 8,3 : 0,021	15	80	3,0
6	Mais	1,0 : 15,0 : 37,3 : 0,129	15	80	3,0
7	Amylose	1,0 : 6,0 : 37,8 : 0,021	15	80	3,0
8	Amylopectin	1,0 : 15,0 : 37,3 : 0,129	15	80	2,7
9	"	1,0 : 15,0 : 37,8 : 0,129	15	140	1,9
10	"	1,0 : 10,5 : 6,0 : 0,015	24	80	3,0
11	"	1,0 : 6,0 : 6,0 : 0,015	15	80	2,9
12	Degraded	1,0 : 8,1 : 3,6 : 0,021	15	40	2,9

Table 9
Controlled stoichiometric silylation of starches

No.	Starch type	n(AGE:$SiMe_3$:NH_3:Sacc)	t/h	T/°C	DS
24	Amylose	1,0 : 2,23 : 39,1 : 0,014	7	80	2,17
25		1,0 : 2,26 : 37,3 : 0,014	15	80	2,10
26	Potato	1,0 : 1,80 : 37,0 : 0,014	15	80	1,69
27		1,0 : 2,20 : 37,7 : 0,014	15	80	2,10
28		1,0 : 2,00 : 37,8 : 0	15	140	1,03
29		1,0 : 2,00 : 37,8 : 0,014	15	140	0,71
30	Degraded	1,0 : 2,25 : 8,00 : 0,014	21	40	2,2

80 °C proved to be the optimum temperature. With soluble material like degraded starch the reaction also proceeds near room temperature (entry 12 Table 8). Reaction time depends on the starch type. 15 h are sufficient for amylose rich starches while up to 24 h are required for amylopectin. Silylation without catalyst proceeds only to medium degrees of silylation (entry 1 Table 8). For higher degrees of substitution use of saccharin as catalyst has shown to be necessary and quite efficient [26]. The ratio of silylating agent to hydroxy groups is not important as long as the Si/OH ratio is two or more.

Complete silylation of amylopectin was not possible under the conditions suited for amylose rich starch. Decrease of both ammonia and HMDS concentration relative to that of starch enabled complete silylation. Obviously the ratio of HMDS to ammonia is more important than that of ammonia or HMDS to hydroxy groups. It seems that both components have to be present in sufficient amounts at the reacting sites. Excess of one hinders the action of the other.

Controlled partial silylation of starch has not been possible to date. It requires that the silylating agent be completely used. Reactions were made with amylose containing starches using the normal procedure except that the amount of ammonia was increased to ensure sufficient wetting of starch and mixing of components. Reaction conditions and results are summarised in Table 9.

Data of Table 9 show that controlled partial silylation of starch with stoichiometric amounts of silylating agent is possible. Calculated and experimental degrees of silylation are in close agreement. Experimental values are slightly lower than theoretical most likely because of some humidity present which consumes HMDS. Without catalyst and at higher temperature controlled partial silylation is not possible.

Kinetics of silylation were studied despite the fact that silylation of starch in ammonia is a heterogeneous reaction. Amylose and amylopectin were selected for these experiments. Each data point required one experiment. In this series the autoclave was charged with ammonia, catalyst and starch, sealed, heated to 60 °C and HMDS was added with a spindle press. Reactions were

Table 10
Kinetics of silylation of amylose with HMDS in ammonia (60 °C).

No.	n(AGE:$SiMe_3$:NH_3)	t /h	DS_{Si}	THF soluble DS	THF soluble %	THF insoluble DS	THF insoluble %
35	1,0 : 2,16 : 41,3	0,5	0,73	1,9	10	0,60	90
36	1,0 : 2,21 : 42,1	1	1,20	2,0	22	0,92	78
37	1,0 : 2,16 : 41,3	2,5	1,56	2,0	25	1,33	75
38	1,0 : 2,16 : 38,9	5	1,94	2,1	37	1,68	63
24	1,0 : 2,23 : 39,1	7	2,17	2,1	45	1,65	55
25	1,0 : 2,26 : 38,6	15	2,10	2,2	80	1,88	20

stopped by cooling through rapid evaporation of ammonia under adiabatic conditions, the residue was extracted with THF, the degree of silylation of the total and of the soluble and insoluble fractions was determined

Kinetic analysis of the experiments resulted in first order kinetics for both amylose and amylopectin as shown in Fig. 17. First order kinetics had been found already in the homogeneous silylation of poly(vinyl alcohol). Since there are no pseudo first order conditions it is assumed that formation of the active silylating species is fast and completely on the product side. Another condition is that all hydroxy groups present in the system are accessible, which obviously is the result of the activation with ammonia. Rate constants of silylation were k_{80}: 0,49 h^{-1} for amylose and 0,21 h^{-1} for amylopectin which means that amylose reacts 2,3 times faster than amylopectin.

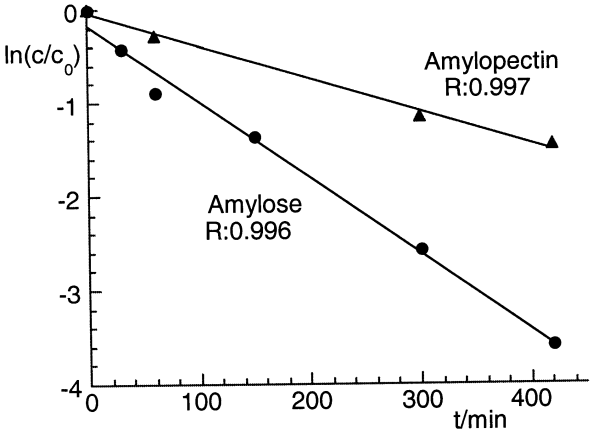

Fig. 17. First order plot of silylation of starch with hexamethyldisilazane in ammonia (60 °C).

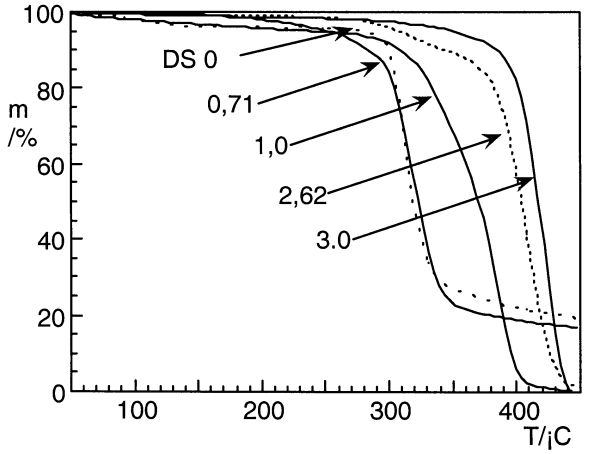

Fig. 18. Thermogravimetry curves of silylated potato starch.

Thermal properties and solubility of silylated starches have been studied. Thermal stability was measured by thermogravimetry. A series of curves from silylated potato starch is shown in Figure 18. Beginning with a DS of 1 thermal stability increases with DS. In addition, the mechanism of degradation changes as no char is formed which can be seen from the fact that weight loss goes to completion.

Thermal stability as measured by the temperature at which 50 percent weight loss has occurred was does not depend on the type of starch, it only depends on the degree of silylation. This is shown in Fig. 19.

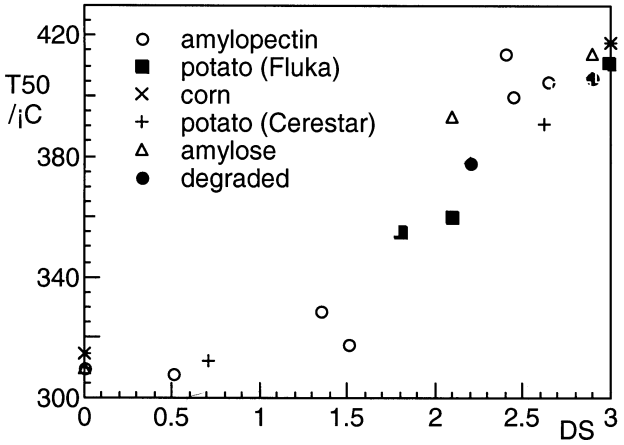

Fig. 19. Temperature of 50 % weight loss for different starch types and degrees of silylation.

Table 11
Solubility of silylated starch in organic solvents.

Starch	DS	THF w%	$CHCl_3$	Toluene
Amylose ($MgSO_4$)	3,0	100	-	-
Potato (Cerestar)	2,9	18	-	-
Potato (Fluka)	2,9	100	+	+
Amylopectin	2,9	3	-	-
Degraded (Cerestar 08381)	2,9	100	+	+
	2,2	100	+	+

Solubility of starches was studied quantitatively in THF and in a qualitatve manner in chloroform and toluene. For THF the soluble fraction was determined through extraction in a Soxhlet apparatus using teflon thimbles. Solubility strongly depends on the starch type and also on the degree of silylation and on molecular weight. Amylose with a DS above 2 is soluble in THF, potato starch (DS 2,9) with high molar mass only to 18 percent with lower molar mass to 100 percent. For less polar solvents molecular weight seems to have more influence than degree of substitution. No solvent was found for amylopectin.

5. CONCLUSIONS

Ammonia in the liquid or in the supercritical state can be favourably used as reactant and solvent for polymers if one takes into account the high reactivity. Ammonolysis of polyesters, polycarbonates and polyamides has been investigated. Stability of polyesters towards ammonolytic cleavage increases in the order fully aromatic, aromatic aliphatic, aliphatic. The surprisingly fast and complete degradation of Vectra, a liquid crystal polyester, recommends ammonolysis as a suitable analytical method.

Poly(hexamethylene carbonate) can be fractionated by extraction below 100 °C and degraded in a controlled manner under supercritical conditions. Aromatic bisphenol-A-polycarbonate is degraded to bisphenol-A and urea already at room temperature. This allows selective degradation of blends and composite materials like compact disks and car windows thus constituting a new method of chemical recycling.

Ammonia is the solvent (reaction medium) of choice for silylation of hydroxy group containing polymers especially cellulose and starch with hexamethyldisilazane. Complete silylation as well as controlled partial silylation with stoichiometric amounts of silylating agent has been achieved. An advantage of the new synthesis is that ammonia is the only by-product formed, which allows

simple work-up by evaporation of ammonia. Saccharin as catalyst is required for complete and controlled partial silylation.

ACKNOWLEDGEMENT

The work reported in the present paper has been supported by the Deutsche Forschungsgemeinschaft, Schwerpunktprogramm Überkritische Fluide als Lösungs- und Reaktionsmittel".

REFERENCES

[1] W. Leitner, Chemie in unserer Zeit, **37**, 32 (2003).
[2] Y-L Hsiao, E. E. Maury, J. M. DeSimone Polym. Prepr. (Am. Chem. Soc., Div. Polym. Chem., **36,1**, 190 (1995).
[3] W. Mormann and Th. Wagner, J. of Polymer Science: Part A: Polymer Chemistry, **33**, 1119 (1995).
[4] C. Reichardt, „Lösungsmittel-Effekte in der organischen Chemie", 2nd ed., Verlag Chemie, Heidelberg 1973, 162.
[5] G. Wilke, K. Zosel, P. Hubert, O. G. Vitzthum, G. M. Schneider, H. Lenz, U. Franck, E. Stahl, W. Schilz, E. Schütz, E. Willing, E. Klesper, S. Peter, G. Brunner, R. Eggers, Angew. Chem. **90**, 747 (1978).
[6] T. C. Waddington, „Nichtwässrige Lösungsmittel", Hüthig Verlag, Heidelberg 1973, 10.
[7] J. Jander, „Anorganische und allgemeine Chemie in flüssigem Ammoniak", in: Chemie in wasserfreiem flüssigem Ammoniak, Vol. 1 (1), John Wiley & Sons, Berlin 1966, 49.
[8] W. C. E. Higginson, N. S. Wooding, J. Chem. Soc. 760 (1952).
[9] H. A. Schuyten, J. W. Weaver, J. D. Reid and J. F. Jurgens, J. Am.Chem. Soc., **70**, 1919 (1948).
[10] K. Hess, C. Trogus, Ber. Dtsch. Chem. Ges. **68**, 1986 (1935).
[11] US 4,885,407 (1989), to Gereral Electric Company, invs. D. W. Fox, E. N. Edward, (Chem. Abstr. **112**, 200223, 1990).
[12] IN 154,774 (1984), to Nirlon Synthetics Fibers and Chemicals Ltd., (Chem. Abstr. **104**, 51243, 1986).
[13] JP 74,132,027 (1974), to Teigin Ltd., invs. Kawase, Shopi, et al., (Chem. Abstr. **83**, 44005, 1975).
[14] H. Lentz, W. Mormann, Makromol. Chem., Macromol. Symp. **57**, 305 (1992).
[15] M. Buback, F. Rindfleisch, Chemie-Ingenieur-Technik **67**, 591 (1995).
[16] W. Heitz, P. Ball, H. Füllmann Angw. Chem. **92**, 742 1980).
[17] K. Bredereck, K. Strunk, H. Menrad, Makromol. Chem. **126**, 139 (1969).
[18] J. F. Klebe and H. L. Finkbeiner, J. Polym. Sci. Part A-1, **7**, 1947 (1969).
[19] W. Schempp, T. Krause, U. Seifried, A. Koura, Papier **38**, 607 (1984).
[20] R. E. Harmon, K. K. De, S. K. Gupta, Stärke **25**, 429 (1973).
[21] G. Greber and O. Paschinger, Papier, **35**, 547 (1981).
[22] W. Mormann, T. Wagner, Macromol. Rapid Commun. **18**, 515 (1997).
[23] R. Taft, Journal of Physical Chemistry **34**, 2792-2800 (1930).
[24] J. E. Hodge, in Methods in Carbohydrate Chemistry, Vol. 4, 1st ed. Academic Press, New York, London, (1964) 279.
[25] I. A. Wolff, D. W. Olds, G. E. Hilbert, .l Amer. Chem. Soc. **73**, 346 (1951).
[26] C. A. Bruynes, T. K. Jurriens, J. Org. Chem. **47**, 3966 (1982).

Supercritical Fluids as Solvents and Reaction Media
G. Brunner (editor)

Chapter 5.5.

Inorganic materials (metals, ceramics, glasses) under the influence of reactants in supercritical aqueous solutions as well as Chemical reactions (partial oxidations, hydrolysis, dehydrations) under the influence of inorganic materials in supercritical aqueous solutions

H. Vogel, C. Kaul, Th. Richter, W. Henk and S. Hain

TU Darmstadt, Ernst-Berl-Institut für Technische und Makromolekulare Chemie, Technische Chemie I, Petersenstr. 20, D-64287 Darmstadt

1. INTRODUCTION

The trend towards using supercritical fluids in chemical practice only intensified at the beginning of the eighties. Technical processes using carbon dioxide as the supercritical medium were developed (decaffeination and hop extraction); initial approaches for this purpose were already in existence in the fifties. Furthermore, due primarily to the special solvent properties of supercritical fluids, supercritical fluid chromatography and the dissolution and subsequent precipitation of particles having adjustable particle size distributions (RESS, SAS) now form part of industrial practice.

Supercritical water (SCW) has been growing in importance as a medium for chemical reactions for about ten years. This is attributable primarily to relatively recent targets set in waste water treatment, that is to say the elimination of poorly biodegradable substances. It is possible to convert these substances into less toxic and more readily degradable compounds. During this time there has been a marked rise in general interest in the use of the special *pVT*-dependent physical properties of SCW. Further, it is only very recently that the potential for synthesis which SCW chemistry affords has caught the eye of chemists.

Many technically important syntheses are afflicted by the selectivity/conversion problem, i.e. starting from the reactants and products there are also reaction pathways which lead to unwanted by-products (reaction networks). Important items in the chemist's toolkit for optimizing these reaction

networks with respect to the desired product are usually catalysts, in addition to the classical process parameters of temperature, pressure and concentration. An additional fine-tuning knob is the choice of the reaction medium. However, for the industrial chemist a change in the solvent in the process development is associated with great expense since the entire work-up procedure has to be altered.

A key advantage of chemistry in SCW is the possibility of varying the properties of the reaction medium over a wide range solely by changing the pressure and temperature. The reaction can be optimized in this way without changing solvent. This can be seen particularly clearly in the variation of the relative static dielectric constant ε and the pK_W value as a function of temperature and pressure, two physical properties which have a decisive effect on polarity and acid/base-catalytic properties. Furthermore, the reaction kinetics can be strongly affected in the supercritical region by varying the pressure (kinetic pressure effect). In addition, many nonpolar organic substances (e.g. cyclohexane) and gases (e.g. oxygen) are highly soluble in SCW so that mass transfer restrictions due to phase boundaries do not apply.

The possibilities described are based in the final analysis on the molecular structure of water which can give rise to unique spatial structures through hydrogen bonding. Changes in these structures result in significant modifications in physicochemical properties.

Summarizing, SCW has great potential with regard to the optimization of chemical syntheses. There are, however, drawbacks arising from working at high pressures (high investment costs), the problem of corrosion (expensive materials) and the lack of kinetic and thermodynamic data. For these reasons applied research in the field of chemistry in SCW must not remain confined to synthetic chemistry, rather the issues concerning materials and thermodynamics must also be addressed in the research at the same time.

2. MOTIVATION

The aim of this project has been to run reactions under heterogeneous catalysis in SCW, which acts both as a solvent and as a reactant. The investigation of model reactions concerning selectivity and conversion ratio was carried out. Partial oxidations, hydrolysis and dehydrations were investigated first as reactions without and later with catalysts. An important research task has been the search for corrosion-resistant reactor materials (alloys), catalyst materials (metals) and catalyst carriers (ceramics). The stability of these materials was investigated in non-reacting systems (SCW – SCW/O_2 – SCW/AcOH). Furthermore the stability of educts and products in SCW and the phase behaviour were investigated.

3. EQUIPMENT

3.1. The continuously operating corrosion reactor

The experiments were carried out in a continuous high-pressure equipment with a 250 mL autoclave made of the nickel-based alloy Inconel 625 (wall thickness 25 mm, metallic sealing) as the central component. Inconel 625 has proved to be effective in SCW both under acidic as well as oxygenated conditions and has exhibited adequate stability. The aqueous solutions are conveyed via an electric preheater made of Inconel 625 and through the autoclave with the aid of a diaphragm pump. The material leaving the reactor is cooled and decompressed in two stages. Temperature both in the reactor and the preheater is controlled by eurotherm controllers. Pressure is controlled by a relief valve (Fig. 1).

3.2. The tubular reactor

The core of this high-pressure-plant is a changeable tubular reactor made of Inconel 625, which is one meter long and has an internal volume of 3,6 or 49,5 mL depending on the diameter of the tube used.

Water (or in the case of oxidations a hydrous solution of hydrogen peroxide) is pumped into the tubular reactor via a weight-controlled diaphragm pump and brought up to reaction temperature by a resistance heater. In the case of hydrogen peroxide the stream passes first a heated decomposer filled with silver particles to decompose the hydrogen peroxide into oxygen and water.

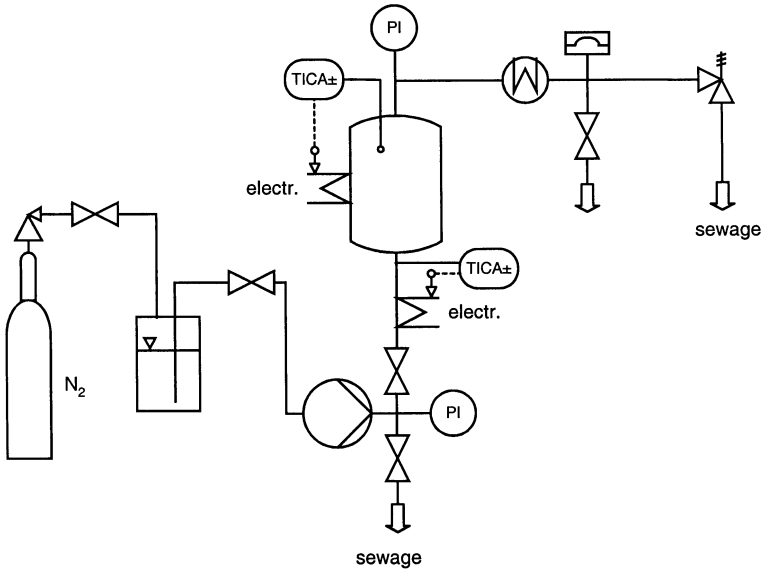

Fig. 1. Flow diagram of the continuously operating corrosion reactor.

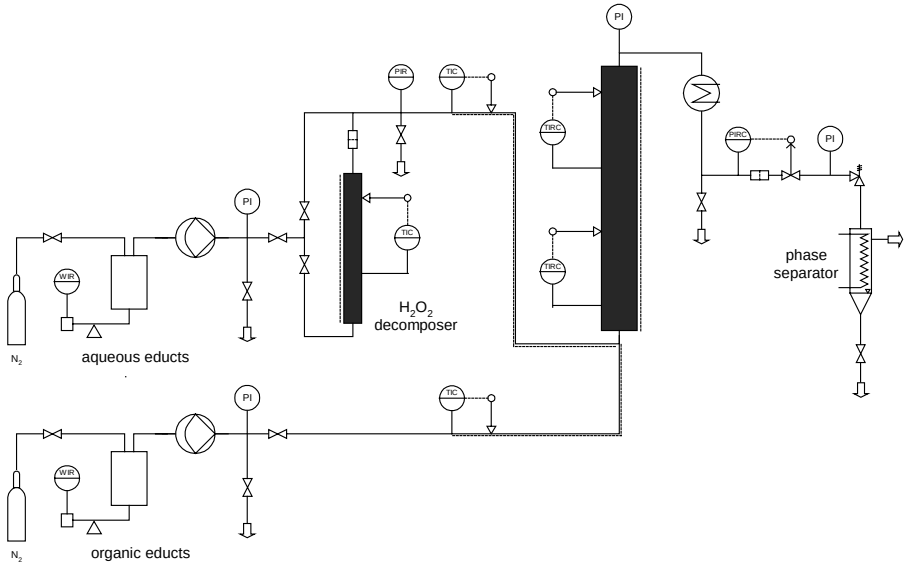

Fig. 2. Flow diagram for the tubular reactor.

The organic component is conveyed in the same manner via a second diaphragm pump. The streams are mixed in a T-piece and fed into the reactor, which is maintained at the required operating temperature by an electrically heated two-zone tubular furnace. The hot reactor discharge traverses a cooling section and is decompressed to ambient pressure by a control valve. The reaction-mixture is separated into liquid- and gas-phase in a cooled phase separator. The corresponding flow diagram is displayed in Fig. 2.

3.3. The jet loop reactor

The jet loop reactor is a differential reactor. It is fed by a high-pressure diaphragm pump. First the solution is preheated and then enters the reactor by a nozzle (0,5 mm). The low pressure around the nozzle causes a loop-shaped forced flow in the reactor. The reactor effluents are cooled and then decompressed in two stages. The gaseous and the liquid phase are separated. Mass flow, pressure and temperature in the preheater and the reactor are controlled by the software Visual Designer®. The flow diagram of the experimental setup is shown in Fig. 3.

3.4. The optical cell

The measurements concerning the phase behaviour and density are carried out in a 30 mL cylindrical optical cell made of Inconel 625 (Fig. 1). Two oppositely placed, graphite-sealed sapphire windows allow the visual obser-

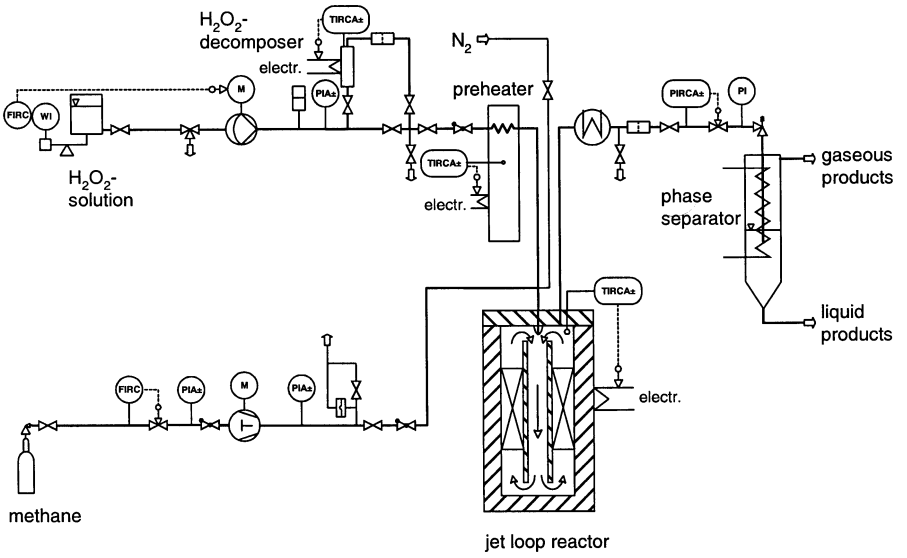

Fig. 3. Flow diagram for the jet loop setup.

-vation of the whole interior. To ensure thorough mixing a magnetic rod made of an aluminium-nickel-cobalt alloy, which is encased in Inconel 625 to protect it against corrosion, is used. A permanent magnet rotating outside the cell causes the magnetic rod to rotate. The temperature of the viewing cell is controlled by means of cartridge heaters distributed around the circumference. The temperature is measured by means of a thermocouple in the interior. Two screw presses serve to convey the components into the previously evacuated viewing cell and to generate pressure afterwards.

4. THE CORROSION OF METALS AND METAL OXIDES

4.1. Corrosion tests in pure water

The corrosion behaviour of metals in sub- and supercritical water as well as in 3 % (g g^{-1}) acetic acid solution and in oxygen containing water was investigated. Experiments were carried out in the continuously operating corrosion reactor characterized in chapter 3.1 with a reactor volume of 250 mL under varying residence times.

4.2. Summary

Studies of corrosion in SCW have shown that specifically in the transition region from subcritical to supercritical the highest specific rates of

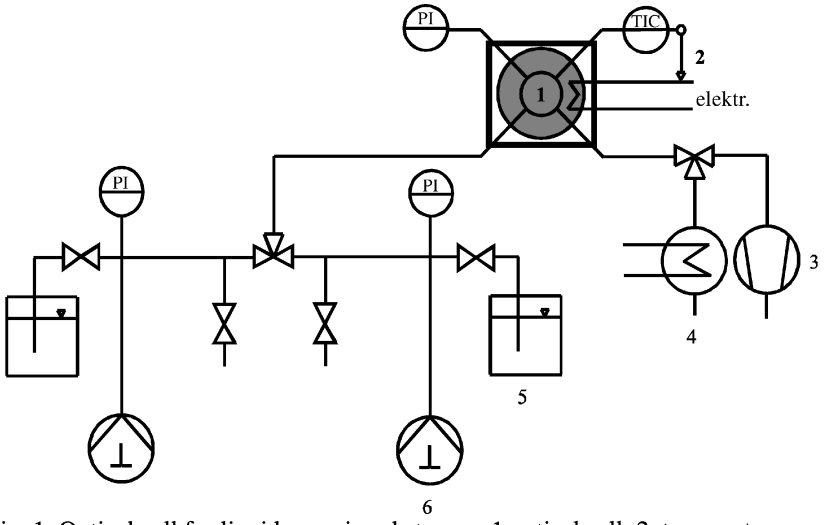

Fig. 1. Optical cell for liquid organic substances. 1 optical cell; 2 temperature control; 3 vacuum pump; 4 cooler and separator; 5 storage jar; 6 screw press.

change in mass occur, this being brought about by the sharp change in the dissociation of water. Thus the investigated materials except nickel (copper, silver, nickel, ruthenium, palladium and cobalt oxide) are stable in pure sub- and supercritical water.

In acetic solutions the materials Ag, Pd, Co_3O_4-CoO and Ru are applicable without high mass- or surface loss. When copper is used under higher acid concentrations and sub- or supercritical conditions at high densities a large loss of surface must be taken into account.

For oxygen containing solutions ruthenium is not a proper catalyst because of large mass loss. The materials Pd, Co_3O_4-CoO and Cu are applicable without large surface loss as catalysts. By inserting copper attention should be paid to not copper but copper oxide being the catalytic phase, because stable oxide layers form on the surface of copper. Silver corrodes in oxygen containing solutions especially under sub- and supercritical conditions at high densities. Silver in oxygen containing solutions is only a proper catalyst with low oxygen concentrations or if oxygen reacts faster with the reactant than with the catalyst.

Palladium can be inserted universally as a catalyst, since it is stable under all tested conditions. Iridium features outstanding stability in all corrosive (also chlorine and oxygen containing) solutions. Thus it is qualified as a lining material for SCWO-reactors. For this a nonporous application of the layers must be guaranteed. Another possible application for iridium is the manufacture of measuring electrodes, which are usable in situ under supercritical conditions.

5. THE CORROSION OF CERAMICS

5.1. Investigations on ceramics

The corrosion of ceramic materials in sub- and supercritical water as well as in sub- and supercritical 3 % (g g^{-1}) acetic acid solution was investigated [1]. Tests were carried out in the continuously operating corrosion reactor described in chapter 3.1 with residence times from 30 to 150 minutes. Ceramics of aluminium oxide and titanium oxide, aluminium titanate and common catalyst carriers were investigated.

One of the most common catalyst carriers is γ-Al_2O_3. This material was not investigated, because it is known to be unstable in supercritical water [2]. Promising is α-Al_2O_3, which has only a low surface. Investigated samples of porous α-Al_2O_3 are Alsint porös, Al 25 and Al_2O_3 by the Inocermic company.

In the main the titanium oxide ceramics are anatase. In some investigations titanium oxide is considered stable in supercritical water [3]. An advantage is the possibility of manufacturing titanium oxide of high purity with surfaces of 50 m^2 g^{-1}.

Besides pure TiO2 and Al_2O_3-ceramics also two aluminium titanate-ceramics by the Ceramtec company and zirconium oxide ceramics were tested.

Also carrier materials which are used in common processes were investigated. These were PdO on Al2O3 (Degussa), HP 661/4, carrier by Südchemie and activated carbon by Degussa.

Besides corrosion tests of Si_3N_4 by the Kyocera company, of two ZrO_2-ceramics by Kyocera and by the Vogt company and of one MgO-ceramic by the Sembach company were done. All of these ceramics were unstable.

5.2. Summary

Alsint porös by Haldenwanger, Al 23, Al 25 and F99,7 by Friatec, both aluminium titanate ceramics by Ceramtec, one Al_2O_3- and one TiO_2-ceramic by Inocermic and TiCatC and TiO_2-Pellet E3-588-191-002 by Sachtleben Chemie proved to be stable.

The investigated aluminium titanate ceramics are not suitable to be used as catalyst carriers, because they are not porous and have only low specific surfaces.

From the other stable and also porous materials TiCatC and TiO_2-Pellets E3-588-191-002 were chosen as potential carrier materials, because they have an appreciable surface of about 50 m^2/g.

6. INVESTIGATION OF THE CATALYTIC ACTIVITY OF INORGANIC MATERIALS ON MODEL REACTIONS IN SUPERCRITICAL AQUEOUS SOLUTIONS

6.1. Partial oxidations of methane and of cyclohexane (model substances for saturated hydrocarbons)

6.1.1. The Partial oxidation of methane in SCW

6.1.1.1. Motivation

Methanol is one of the most important intermediates of the chemical industry with an annual production of 29 million tons (*1996*). The direct production of methanol from natural gas in gas phase is hardly realisable because formed methanol is oxidated faster than methane. For this reason the production of methanol on the technical scale takes place indirectly via syngas. The motivation to oxidate methane directly to methanol in supercritical water is the stabilisation of the polar oxygenates (methanol, formaldehyde) by hydration. Hence the deceleration of further oxidation and thus higher selectivities are expected.

6.1.1.2. Summary

The partial oxidation of methane in supercritical water was investigated under the application of different heterogeneous catalysts and without any catalyst [4]. The analyses were carried out under the following reaction conditions: Feed concentration of methane from 0,1 to 4 % (mol mol^{-1}), feed concentration of oxygen from 0,1 to 2 % (mol mol^{-1}), temperatures of 375 to 500 °C, pressures of 22 to 35 MPa and a total feed mass flow from 25 to 100 g min^{-1} (residence times of 1 to 20 s).

Besides the influence of the reaction conditions on the conversion ratio and selectivity of the desired products methanol and formaldehyde the pseudo activation energies, activation volumina and the partial reaction orders of methane and oxygen were determined.

Total selectivities from 50 up to 80 % were obtained only at conversion ratios of less than 1 %. With increasing conversion ratio the selectivities of methanol and formaldehyde decrease rapidly. In return then the total oxidation products carbon monoxide and carbon dioxide become the main products.

The presence of heterogeneous catalysts in the methane oxidation had only little effect on the selectivity and conversion ratio. In liquid phase the reaction already takes place without the presence of a catalyst. This leads to the assumption that a radical reaction mechanism similar to the gas phase oxidation of methane occurs. The catalytical activity of the employed systems pushes the reaction towards the total oxidation products, so that maximum

yields of the desired products methanol and formaldehyde were obtained without any catalyst. Since catalytical activity of the reactor material was found, it is possible that the reaction on laboratory scale is always superposed by wall catalysis.

6.1.2. The partial oxidation of cyclohexane in SCW

6.1.2.1. Motivation

Approximately 63 % of the world's cyclohexanone/ol production occurs through homogeneous liquid phase oxidation of cyclohexane. Hence this reaction represents an important step on the way to producing polyamide fibres (over adipic acid to nylon 6.6, or over ε-caprolactam to nylon 6). Given that the valuable products are reactive intermediate products - they are easily overoxidized to carbon acids under ring-opening reactions and chain reduction - the reaction is carried out at a conversion of only 5 to 10 % to reach economic selectivities of about 80 to 85 % [5]. Attempts to increase the conversion rates with similar selectivity are for instance realised in the boric acid process. Despite all improvements, the technical preparation of cyclohexanone/ol is still an unsatisfactory process regarding the selectivity/conversion.

So far only the oxidation of cyclohexane in supercritical CO_2, but not in supercritical water, is described in literature [6]. Crittendon analysed a whole range of cyclohexane derivates in SCW with regard to dehydration or hydration as well as dehydrogenation or hydrogenation [7].

6.1.2.2. Summary and Outlook

The analyses were carried out under the following reaction conditions: Pressures of 25 and 30 MPa, temperatures of 350 to 420 °C, residence times of approximately 1 to 80 s, an initial concentration of cyclohexane of 5 % (g g^{-1}) and a ratio of O_2 to cyclohexane of 0,5/1 (mol mol^{-1}), i.e. stoichiometric relating to the formation of cyclohexanone/ol [8].

It turned out that cyclohexane can be transformed into cyclohexanol, cyclohexanone and cyclohexene in SCW. In all, 24 different products were identified and quantified. As main products, cyclohexene, cyclohexanol/one, carbon monoxide, carbon dioxide and carboxylic acids (mainly short-chain monocarbon acids) were found. In addition, various alcohols such as 1-propanol, 1-butanol or 1-pentanol were identified in the liquid phase. In the gaseous phase, saturated hydrocarbons such as methane or ethane, as well as unsaturated hydrocarbons (ethene, propene) were detected. Since the reaction is extraordinarily fast, no kinetic measurements were practicable in the region below one second. The conversion of oxygen was virtually 100 % for every residence time. The valuable products cyclohexanol, cyclohexanone and cyclohexene could be presented with a total selectivity of about 30 %. Cyclo-

hexanol dehydrates in SCW to cyclohexene. In contrast to the liquid phase oxidation, the oxidation to adipic acid only plays a minor role. Formic acid is the main product of all formed carboxylic acids in the subcritical area. In the supercritical area, however, formic acid decomposes quantitatively. Silver and platinum catalyze the total oxidation of cyclohexane.

With a total selectivity relating to the valuable products (EN/ONE/OL) of 30 % and a 100 % conversion of oxygen, the oxidation of cyclohexane in SCW is not feasible in technical dimensions. A remedy could be the reduction of the residence time in the area of milliseconds, as well as the discovery of a suitable catalyst which - due to the drastic conditions of SCW - not only must turn the reaction in the right direction, but also has to be sufficiently stable.

6.1.3. Oxidation of isobutene (model substance for unsaturated hydrocarbons)

6.1.3.1. Motivation

The oxidation of isobutene can take place by two different reaction pathways (Fig. 5).

1. Oxidation at the C1-Atom resulting in isobutanol (2), isobutyraldehyde (3) and isobutyric acid (4).
2. Oxidation at the C3-Atom resulting in methacrolein (5) as well as methacrylic acid (6).

On the technical scale the second route - the gas phase oxidation of isobutene with air to methacrolein in the presence of mixed-oxide catalysts - is well established. The technical production of isobutyraldehyde runs via the hydroformylation of propene in the presence of Co-, Rh- or Ru-complexes as catalysts. The question arises: What kind of reaction pathway takes place under supercritical water conditions without any catalysts?

6.1.3.2. Summary

The examinations were carried out under temperatures of 350 to 420 °C, pressures of 25 to 35 MPa, a feed concentration of 5 % (g g^{-1}) *tert*-butanol and a *tert*-butanol / O_2 ratio of 2/1(mol mol^{-1}). Isobutene is the only product of the uncatalyzed dehydration of *tert*-butanol in sub- and supercritical water (chap. 6.3.1). Thus *tert*-butanol is used as the reactant. The following oxidation of the in situ formed isobutene leads to isobutyraldehyde as the main product and isobutanol, carbon dioxide, carbon monoxide and methane as by-products. Under the examined reaction conditions an increase of temperature and pressure raises the selectivity relating to isobutyraldehyde. Isobutyraldehyde can be formed with a selectivity of 50 % relating to *tert*-butanol (conversion 80 %) at 420 °C and 35 MPa. Platinum catalyzes the total oxidation of *tert*-butanol. An addition of salt results in a negative effect relating to the selectivity of isobutyraldehyde.

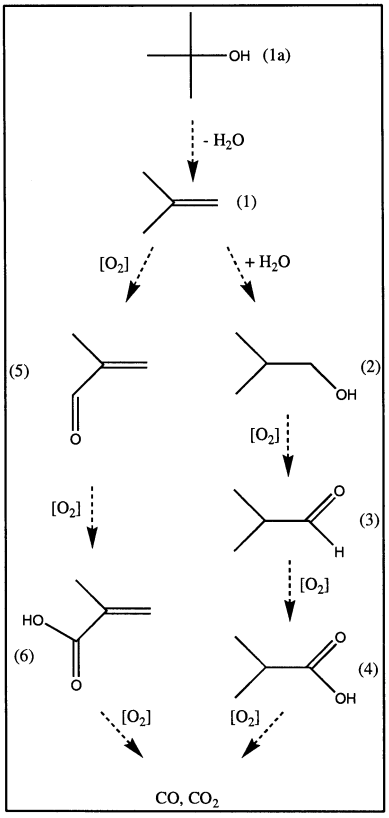

Fig. 5. Scheme of possible reaction pathways for the partial oxidation of *tert*- butanol.

6.1.4. Partial oxidation of m-*xylene (model substance for aromatic hydrocarbons)*

6.1.4.1. Motivation

The production of isophthalic acid by homogenic liquid phase oxidation of *m*-xylene takes place in 95 % acetic acid using an additional co-catalyst. Holliday et al. investigated the oxidation of alkylic aromats under subcritical conditions (300 – 355 °C, 24 MPa) in a batch reactor [9]. In experiments without a catalyst educts were regained unchanged. Adding manganese dibromide as a catalyst, at a residence time of 60 minutes and 352 °C as the highest temperature, a yield of 16 % isophthalic acid and 4 % *m*-toluic acid was obtained. At a reaction time of 30 minutes and a maximum temperature of 313 °C with manganese dibromide a yield of 20 % *m*-tolualdehyde and with manganese triacetate a yield of 10 % *m*-toluic acid was achieved.

6.1.4.2. Summary

Experiments were run in the continuous high pressure plant provided with a tubular reactor described in chapter 3.2. The investigations were made at temperatures of 350 to 420 °C, pressures of 23 to 30 MPa and a feed concentration of 5 % (g g^{-1}) *m*-xylene.

Oxidation of *m*-xylene with molecular oxygen is possible in SCW without a catalyst. The conversion ratio of *m*-xylene was about 60 %. As a result of the quantitative consumption of the inserted oxygen no higher conversion ratio of *m*-xylene could be obtained. The main product of the *m*-xylene oxidation is *m*-tolualdehyde reaching selectivities up to 55 %. Like in industrial scale the reaction stops in laboratory scale at the stage of aldehyde and acid. Further oxidation of *m*-tolualdehyde and *m*-toluic acid is inhibited by the deactivation of the aromatic system caused by the carbonyl- and carboxyl group. To accomplish oxidation to isophthalic acid catalyic activation is needed. The insertion of platinum supported TiCatC (TiO_2) as a heterogeneous catalyst did not increase the selectivity of aldehyde and acid, but of the total oxidation products.

6.1.5. Summary: Partial oxidations under heterogeneous catalysis

Within the scope of the investigated partial oxidations different heterogeneous catalysts were tested. In detail the following catalysts were chosen.
Oxidation of methane:

- Splinters of the reactor material Inconel 625 (0,4 mm – 2 mm)
- blank sheet pieces of copper (3 x 3 x 0,5 mm)
- blank sheet pieces of an eutectic silver-copper alloy (3 x 3 x 0,5 mm, 72 % (g g^{-1}) Ag)
- blank sheet pieces of silver (3 x 3 x 0,5 mm)
- blank sheet pieces of a gold-silver alloy (3 x 3 x 0,5 mm, 2,8 % (g g^{-1}) Ag)
- technical catalyst (Ag supported Al_2O_3).

Oxidation of cyclohexane:

- Sintered pressings of platinum, silver and copper.

Oxidation of isobutene:

- Platinum, 1 wt. % on alumina.

Oxidation of *m*-xylene:

- Platinum supported TiCatC (TiO_2).

The examined catalysts either promote above all the reaction paths towards the total oxidation products or have no influence on the reaction at all. Solely in the methane oxidation reactions did the selectivity of methanol increase under Ag or Inconel catalysis and mild reaction conditions.

6.2. Hydrolysis of ethyl acetate

6.2.1. Motivation

Carbonic esters react in SCW to the corresponding acids and alcohols. The ester cleavage of ethyl acetate (5 % g g^{-1}) in water at 25 MPa and various temperatures between 330 and 410 °C and the influence of salts on this reaction were investigated.

6.2.2. Summary

The conversion of ethyl acetate first begins to rise after the temperature is increased up to the critical region. Afterwards it declines and at even higher temperatures the conversion rises again. With increasing residence times the conversion is also on an increase.

The conversion without salt is at about 25 %. The additon of 0,1 % g g^{-1} Na_2SO_4 does not change the average conversion. The addition of 0,1 % g g^{-1} $ZnSO_4$ increases the conversion substantially up to about 95 %.

6.3. Dehydrations

6.3.1. Dehydration of tert-*butanol*

6.3.1.1. Motivation

Xu and Antal examined the dehydration of *tert*-butanol in "hot water", i.e. a temperature range of 225 to 320 °C [10, 11]. They found that hydronium ions formed by the ordinary dissociation of water are the primary catalytic agents for the dehydration reaction. In this work the temperature range is extended up to 420 °C. Investigations were made at temperatures of 350 to 420 °C, a pressure of 25 MPa and a feed concentration of 5 % (g g^{-1}) tert-butanol.

6.3.1.2. Summary

Isobutene is the only product of the uncatalyzed dehydration of *tert*-butanol in sub- and supercritical water. The conversion rate depends on the residence time at all investigated temperatures. Near the critical point we can find the highest conversion rate (up to 0.93) at 380 °C and in near- and supercritical water the equilibrium is reached very fast (after 10 s); in 'hot water' it takes much longer. There is a strong dependence of the conversion on the dissociation constant and the density of water.

6.3.2. Dehydration of 1,4-butanediol

6.3.2.1. Motivation

Many examinations about the dehydration of alcohols, e.g. ethanol, in supercritical water (SCW) can be found in literature. In most cases the reaction products are olefins. These examinations were usually carried out in small batch- or plug-flow reactors (volumes < 5 ml) where there was no exclusion of catalytic wall effects.

Today, the production of tetrahydrofuran (THF) via the dehydration of 1,4-butanediol (BTD) is carried out in liquid-phase at elevated temperatures in the presence of a dehydrating agent, e.g. sulfuric- or phosphorus acid, acidic salts or ion-exchangers. The disadvantages of using agents like mineral acids are mainly the waste disposal of the soiled acid and the high costs of a corrosion-resistant reactor.

6.3.2.2. Conclusion and outlook

The measurements of the dehydration of 1,4-butanediol were carried out in a plug-flow reactor described in chapter 3.2 with a flow-rate up to 4 kg/h, pressures from 23 to 35 MPa and temperatures of 300 to 400 °C [12].

The dehydration of 1,4-butanediol to tetrahydrofuran is a reaction that possesses disadvantages under conventional conditions caused by the use of mineral-acids and the corrosion problem interconnected with it. These disadvantages can be remedied by the use of pure supercritical water as the reaction medium, as well as catalyst. The selectivity of the reaction regarding THF is nearly 100 %. Only traces of CO_2 and CO were detected.

The ionic mechanism, which exists under conventional conditions, could be validated by the examinations of this present work not only in the sub- but also in the supercritical range. No hints of a change in the mechanism could be found. The activation energies range between 82 and 116 kJ mol^{-1} and are in typical areas for this type of reaction. The volumes of activation are positive in the subcritical range, which is also expected for unimolecular reactions, and negative in the supercritical area, which can be explained, for example, by the alteration of the structure of water and thereby the alteration of the surroundings of the activated complex.

6.4. Catalysis in supercritical water

6.4.1. Manufacturing of catalysts

Two proper ceramics (TiCatC and E3-588-191-002, chap. 5) were impregnated by hexachloroplatinic acid. The carriers were reduced after impregnation for one hour in a revolving tubular furnace in hydrogen flow at 500 °C. For technical reasons 5 % hydrogen in nitrogen was used.

For corrosion tests after the reduction the materials were exposed to supercritical water for 50 hours at 410 °C and 25 MPa.

Both materials show high loss of platinum. Overall the amount of abrasion is low, i. e. the materials are stable. Thus platinum is weakly bound to the surface. Nonetheless two catalysts are formed for application in supercritical water. Following investigations were made with these catalysts.

6.4.2. Hydrogenation of cyclohexene

The hydrogenation of cyclohexene was investigated. In doing so not cyclohexene and hydrogen, but cyclohexanol and formic acid were the reactants, because these can be brought in as an aqueous solution. That way the handling is considerably easier. In situ under reaction conditions hydrogen and cyclohexene were formed in high amounts.

In a previous work the stability of formic acid in SCW was investigated [13]. Formic acid reacts in SCW depending on the reaction conditions to carbon monoxide and water or to carbon dioxide and hydrogen.

$$CO + H_2O \longleftarrow HCOOH \longrightarrow CO_2 + H_2$$

With these results it can be ensured that formic acid decomposes to carbon dioxide and hydrogen under the chosen reaction conditions. By application of a formic acid excess, concerning the amount of hydrogen which is needed to hydrate the reactant, enough hydrogen is brought in.

The dehydration of cyclohexanol to cyclohexene was investigated in dependence on temperature (330 °C to 410 °C) and pressure (25 to 34 MPa). Also the formation of cyclohexane by addition of formic acid to the feed solution was investigated.

The conversion ratio of the uncatalyzed dehydration of cyclohexanol (3 % ($g\ g^{-1}$)) increases with increasing temperature up to 390 °C and then decreases. Below 390 °C values of 50 to 85 % were reached. With increasing pressure the conversion ratio increases little. By adding (2 % ($g\ g^{-1}$)) formic acid to the feed solution the conversion ratio of the dehydration, which is acid-catalyzed, increases to about 90 %. Cyclohexane is formed in low yields up to 1 % at low temperatures. At high temperatures cyclohexane was not detected.

The reaction described above was investigated under catalysis. TiO_2-carriers (E3-588-191-002) by Sachtlebenchemie, which were impregnated with hexachloroplatinic acid and reduced afterwards (see chapter 6.4.1), were inserted. As feed solution 3 % ($g\ g^{-1}$) cyclohexanol and 2 % ($g\ g^{-1}$) formic acid in water were used. This corresponds to a 45 % molar excess of formic

acid. The conversion ratio of cyclohexanol decreases with increasing temperature from 90 % to 68 %. The conversion ratio hardly rose with increasing residence time and with increasing pressure. Cyclohexane is detected, the desired product has formed. The yield of cyclohexane decreases from 9 % at 330 °C with rising temperature to 2 % at 410 °C. With rising residence time the yield of cyclohexane increases.

The attempt to synthesise a catalyst for application in supercritical water was successful. The desired product cyclohexane was detected, if only in small amounts.

7. CONCLUSION

Corrosion studies of metals showed that most investigated metals, e. g. copper, silver and palladium, were stable in pure SCW. For reactions in e. g. oxygen containing SCW palladium and copper appear to be suitable as catalysts. In corrosion tests of ceramic materials in SCW aluminium titanate, Al_2O_3- and TiO_2-ceramics proved to be stable. One TiO_2-ceramic was used as a platinum supported carrier in the partial oxidation of *m*-xylene and the hydrogenation of cyclohexene.

Chemical syntheses such as partial oxidation, hydrolysis, dehydration and hydrogenation can be carried out in SCW. Partial oxidations are possible in SCW, but show several problems. For example, the partial oxidation of methane to methanol has suitable selectvities regarding methanol and formaldehyde only at very low conversion rates. A solution may be the further reduction of the residence time. As an example for hydrolysis the ester cleavage of ethyl acetate was investigated; this reaction occurs even in "pure" SCW. By addition of $ZnSO_4$ the conversion increases. According to the investigated reactions SCW is a suitable medium for dehydration. The examined dehydration of 1,4-butanediol showed a selectivity regarding THF of nearly 100 % and was even possible without adding any acid. The hydrogenation of cyclohexene to cyclohexane by addition of formic acid, which decomposed to hydrogen and carbon dioxide, was successful. The cyclohexene was formed in situ by dehydration of cyclohexanol. In several reactions, esp. in partial oxidations, catalysts were examined, but they either promote above all the formation of the total oxidation products or have no influence on the reaction at all. One exception was Ag or Inconel catalysing the partial oxidation of methane to methanol under mild reaction conditions.

REFERENCES

[1] C. Kaul, H. Vogel, H.E. Exner, Mat.-wiss. u. Werkstofftech. 30 (1999) 326-331.
[2] M. Schacht, Dissertation Universität Heidelberg (1998).
[3] G.T. Hong, Patent WO 9616906 (1996).
[4] D. Bröll, A. Krämer, H. Vogel, Chem.-Ing.-Tech. 74(6) (2002) 795-800.
[5] F. Eschenröder, H. Vogel, Chem.-Ing.-Tech. 69 (1997) 976-980.
[6] M. Mukhopadhyay, P. Srinivas, Ind. Eng. Chem. Res. 33 (1994) 3118-3124; Ind. Eng. Chem. Res. 35 (1996) 4713-4717; Ind. Eng. Chem. Res. 36 (1997) 2066-2074.
[7] R.C. Crittendon, E.J. Parsons, Organometallics *15* (1994) 2587-2591.
[8] T. Richter, H. Vogel, Chem. Eng. Technol. 25(3) (2002) 265-268.
[9] R.L. Holliday, B.Y.M. Jong, J.W. Kolis, J. Supercrit. Fluids 12 (1998) 255-260.
[10] X. Xu, M.J. Antal Jr., AIChE J. 40(9) (1994) 1524-1531.
[11] X. Xu, M. J. Antal Jr., D.G.M. Anderson, Ind. Eng. Chem. Res. 36 (1997) 23-41.
[12] T. Richter, H. Vogel, Chem. Eng. Technol. 24 (2001) 340-343.
[13] T. Richter, Diplomarbeit TU Darmstadt (1998).

Index

acentric factor, 221
acetaldehyde, 489-519
acetic acid - carbon dioxide (hydrogen bonding), 354
acetic acid, 164-183
acetylacetone, 325
acrylate polymerization, 575, 583, 584
acrylic acid, 66
activation energies (diffusion), 360
activation volumes (diffusion), 360
adamantane, 245, 250- 253, 254, 255, 265
adsorption (of drugs on aerogels), 382, 389, 391-393, 414-425
aerogel - drug formulation, 314, 421, 424
aerogel, 381-427
aerogel properties, 391
aerosol supercritical extraction system (ASES), 148, 431,449
aggregation of amphiphilic molecules, 538
alkoxysilane, 384
alkyl acrylate, 65, 75, 76
alkylbenzenes, 21
alpha function, 18, 19, 23
ammonia – acetonitrile (diffusion coefficients), 356
ammonia – benzene (diffuson coefficients), 356
ammonia – methanol (diffusion coefficients), 357
ammonia as reaction medium, 593-616
ammonia, intradiffusion coefficient, 343
ammonia, self diffusion coefficient, 343
ammonolysis of bisphenol-A-polycarbonate, 604
ammonolysis of polyamides, 594, 597, 598, 609, 610
ammonolysis of polyesters, 594-600, 616
ammonolysis of polymers, 593, 594
ammonolytic cleavage of polyurethanes, 594
ammonolytic reactions, 594
anthracene, 16, 24
anthraquinone, 122-143, 250-252, 258, 260, 262, 264-266
anti-solvent, 43, 44, 47-51, 54-57, 60, 225, 229-231, 431-447
aqueous flavor concentrates, 497
aqueous salt solutions, 163
aqueous solutions, 489-522
aqueous solutions (wetting), 366, 372
aroma components, 491
aroma recovery, 490
arsenic, 326
As-chelate, 323
ascorbic acid, 433
Aspen Plus®, 283
associating compound, 295
asymmetric binary mixture, 148
attraction term, 211, 214-223
attractive interactions, 297
autoclave for visual observation, 595
axial dispersion coefficient, 465-486
axial mixing, 465, 485, 486
azeotrope, 180
back mixing, 465
Barker-Henderson perturbation theory, 221
batch gas-anti-solvent crystallization, 429
benzoic acid - carbon dioxide, 451-457
benzoic acid – trifluoromethane, 451
binary critical line, 124
binary interaction parameter, 283
binodal curve, 180
biphenyl, 155
BQ75 term, 222
1,4-bis-(alkylamino)-9,10-anthraquinone, 128
Carbamate, 317
carbon dioxide - β-carotene, 133
carbon dioxide – 2-propanol, 85-120
carbon dioxide - acetic acid, 167, 178
carbon dioxide – adamantane, 245, 250, 254
carbon dioxide – benzene (diffusion coefficient), 352
carbon dioxide – diphenylmethane, 24, 25
carbon dioxide – ethanol – water, 489-522
carbon dioxide – ethanol, 85-120
carbon dioxide – ethylbenzene, 21
carbon dioxide – hexadecane, 21, 22
carbon dioxide – hexylbenzene, 21
carbon dioxide – hydrogen (diffusion coefficients), 353
carbon dioxide - m-xylene, 26
carbon dioxide – naphthalene, 25, 152
carbon dioxide - n-heptane, 24
carbon dioxide - orange water-phase, 508
carbon dioxide – phenanthrene, 17
carbon dioxide – propylbenzene, 21
carbon dioxide - water - acetic acid - sodium acetate, 177

carbon dioxide - water - acetic acid - sodium chloride, 169
carbon dioxide - water - acetic acid, 163
carbon dioxide - water, 167, 169, 170, 178-183
carbon dioxide - β-carotene, 241-268
carbon dioxide + 1-decanol, 10, 12, 29, 32
carbon dioxide + dodecane, 6, 11, 13, 30, 31
carbon dioxide- benzene, 23
carbon dioxide, 42-44
carbon dioxide, intradiffusion coefficient, 343-362
carbon dioxide, self diffusion coefficient, 343
carbon dioxide-1-octanol, 21, 22
carbon dioxide-squalane, 78
Carnahan-Starling equation, 215
Carnahan-Starling-van der Waals EoS, 245
carotene (β-), 121-145, 241-268
catalysis in supercritical water, 630
catalytic activity of inorganic materials in supercritical aqueous solutions, 624
catalytic converters (used), 528
ceramics in supercritical aqueous solutions, 617
chain molecule solutions, 211
chain molecules, 299
chain-transfer agent, 586
chain-transfer rate coefficient, 574, 585, 588
chain-transfer reaction, 585, 590
chelate, 323
chelator, 324
CHF_3/naphthalene, 153
chlorotrifluoromethane ($CClF_3$), 128
cholesterol - carbon dioxide, 451
Chrastil method, 142, 244, 256, 259, 260
cloud-point, 39-55, 63, 61-84
cluster energy, 580
co-solvent, 225, 231
coexistence curve, 48
cohesion energy, 580
colloidal stability (interfacial tension), 376
column packing, 468-486
compressibility factor, 214, 215, 218, 220
construction materials for sulfur dioxide, 523
contact angle, 364, 366, 370, 371, 376
continuous GAS, 431
copolymer systems (PC SAFT), 319
copolymer, 43, 66, 73, 295, 306
copolymerization, 574, 578, 588-590
correlation of the solubility, 241-268
corresponding states principle, 221
corrosion of ceramic materials, 623
corrosion of metals and metal oxides (SCW), 621
corrosion reactor, 619
co-solvent (polymerization), 573
co-solvent, 26, 39, 46, 49, 54-57, 60, 64, 70, 82
countercurrent extraction processes, 465
countercurrent extraction, 369, 489-522
countercurrent processing, 363, 370
countercurrent SFE, 489-522
critical behaviour, 243, 244
critical compressibility factor, 219
critical curve, 147
critical exponent, 242, 243, 246
critical isotherm, 242, 247, 248
critical micelle concentration (cmc), 539
critical phenomena in polymer systems, 214
critical phenomena, 224
critical point, 124
critical temperature minimum (CTM), 234
critical volume fraction, 234
crystallization from supercritical solutions, 323
cubic equations of state, 151
cyclohexyl methacrylate, 576
Debye-Hückel, 174, 183
dehydrations in supercritical aqueous solutions, 617, 618, 626-633
density distribution function, 245, 246
density ratios for recompression, 300
density-dependent mixing rules, 185-209
deuterium, self diffusion coefficient, 343
dialkyldithiocarbamate, 325
diblock copolymer, 533, 541, 542, 548
dielectric constant, 175
diglycerides, (interfacial tension), 376
diketonate (β-), 325
dimerization, 164, 176, 178
dimethyl ether, 269-294
dipolar interaction, 295
Disperse Red 11 (1,4-diamino-2-methoxyanthraquinone), 128
Disperse Red 60 (1-amino-4-methoxy-2-phenoxy-9,10-anthraquinone), 128

dispersion, 298
dispersion dye, 250, 251
dispersion dyestuff, 122, 124, 128, 137
dispersion polymerization in carbon dioxide, 559-571
distribution coefficients, 490, 498, 499, 510-512, 520
Dortmund Data Bank, 17
drag coefficient, 376
drop shape analysis, 365
drug delivery, 381, 382, 425
drug release, 393, 413
dynamic light scattering, 458
dynamic light scattering, 534, 547, 549, 552
dynamic solubility investigation, 128
dynamic viscosities, 368
dynamic viscosities of coexisting phases, 269
electrolytes, 164, 169, 174, 176, 179
enriching section, 514
equations of state, EOS, 1, 16, 17, 22
equation of state for the critical region, 242
equilibrium cell, 5
equilibrium solubility, 124, 129, 136
essence oil, 490
ethane - 1-decanol, 5, 8, 28
ethane – decane, 6, 7, 28
ethane – dodecane, 12
ethane – octacosane, 23, 24
ethane, 42-45
ethanol - hydrogen - dimethyl ether, 276
ethanol - hydrogen – propane, 275
ethanol – water - carbon dioxide, 468-486
ethanol (EOH), 61, 64, 70, 71, 82
ethyl acetate, 61, 64, 69-71, 82, 83, 489-519
ethyl butyrate, 489-519
ethyl oleate, 274
ethylene - 1-decanol, 6, 11, 12, 30, 34
ethylene – dodecane, 31
ethylene – naphthalene, 25
ethylene – vinyl acetic acid, 85-120
ethylene + diphenylmethane, 23, 24
ethylene, 39, 44-47, 53, 55-60, 66, 67
ethylene/LDPE, 72
ethylene/PEA, 72
ethylene/poly(ethylene-co-acrylic acid) (EAA), 63-65, 83
ethylene/-poly(ethylene-co-vinyl acetate) (EVA), 63-65
ethylene/-polyethylene, 63, 64, 83
extractability (of chelates), 323-340
falling film, 371
fatty acid ester (hydrogenation), 281
fatty alcohols, 269
flavor concentrates, 497
flooding point, 489, 494, 514, 519
Flory-Huggins theory, 234
flow behavior of coexisting phases, 271
flow calorimeter, 3-7, 27
flow regime, 465
flow type apparatus (for equilibrium), 164
fluid-fluid phase diagram, 185-209
fluorinated dithiocarbamate, 343
fluoroform (CHF_3), 128
free-radical polymerization in carbon dioxide, 573-590
Free-Volume-Theory, 65
fugacity approach, 242, 245, 249
fugacity coefficient, 16
GAS (Gas Anti-Solvent), 148, 315, 429-447, 449
gas-gas equilibria, 185-209
gel permeation chromatography, 67
gel permeation chromatography, GPC, 42, 66
gelation, 381-426
g^E-mixing rules, 19
glass cell (high pressure), 344
glasses in supercritical aqueous solutions, 617
global phase diagram method, 213
griseofulvin – trifluoromethane, 451-460
griseofulvin, 393, 394, 317-425
group contribution equations of state, 18, 20
gyromagnetic ratio, 348
hard sphere model, 343, 345, 351, 361
hard-sphere fluid, 214, 295, 299
hard-sphere repulsion term, 214
helium, 42-45
Helmholtz energy, 277-299
Henry activity coefficient, 125
heterogeneous catalysis, 270, 281
heterogeneous polymerization of PVP, 534
heterophase (heterogeneous) polymerization, 533, 534, 540, 548, 549, 552
HETS evaluation, 514-516, 519
Hexanal, 489-519
hexene (1-), 42

high pressure cell used for refractive index, 545
high pressure extraction process, 465-486
high pressure light scattering cell, 543
high pressure NMR, 343
high-pressure phase equilibria correlation, 185-209
high-pressure solubility correlation, 242
hold up (column), 467, 472, 475-479, 486
homopolymer PDMS, 534
homopolymers, 295, 306, 322
hydrodynamics (column), 470-486
hydrogen bond formation, 355
hydrogen bonding, 347, 354
hydrogen, self diffusion coefficient, 343
hydrogenation of cyclohexene, 631
hydrogenation of fats in a supercritical fluid, 269-294
hydrogen-bonding, 295, 297, 321,
hydrolysis in supercritical aqueous solutions, 617, 618, 629-632
hydrolysis of ethyl acetate, 629
hydrolysis reaction, 384
hydrophilic aerogels, 382
hydrophobic aerogels, 382
hydroxyl proton chemical shift, 354
hydroxypropyl methacrylate (HPMA), 578
ibuprofen - carbon dioxide, 451-460
ibuprofen, 159, 160
inert gas, 43, 47-51, 55-57, 60
influence of inorganic materials in supercritical aqueous solutions, 617
inorganic materials in supercritical aqueous solutions, 617-632
interaction energy, 581
interaction parameter, 164, 173-183
interfacial phenomena, 363-376
intradiffusion coefficient, 343-361
ionic interaction parameters, 179, 180
ionic species, 164, 173, 174, 176, 183
isomerization, 122, 123, 132, 134, 136, 143
jet loop reactor, 620
ketoprofen, 393, 394, 416-425
kinetics of dispersion polymerization, 559, 567, 568
kinetics of silylation, 613
LCST, 236
Lennard-Jones fluid, 297
Linalool, 489-419
living anionic polymerization, 541
loading of silica aerogels, 392
low density polyethylene (LDPE), 66
lower critical endpoint (LCEP), 124, 147, 148
lower critical solution temperature, LCST, 52
low-volatile organic compounds, 241-244, 249-251, 265
magnetic coupled balance, 367
mapping approach, 213
Margules term, 175, 183
mass transfer (GAS), 433
mass transfer resistance (interfacial tension), 372, 376
Mathias-Copeman (alpha function), 18
MD-simulation, 343-351, 361
mean field equation of state, 243, 245
Melhem modification, 163, 172, 183
melting point, 148-160,
membranes for SFE, 499
metal chelates, 323-340
metal ions in carbon dioxide, 323-340
metals in supercritical aqueous solutions, 617
methacrylate polymerization, 573, 575, 584
methane, 42-44
methanol - carbon dioxide (diffusion coefficients), 355
methanol - carbon dioxide (hydrogen bonding), 354
methanol - hydrogen – dimethyl ether, 288
methanol - hydrogen – propane, 287
methyl acrylate, 62, 64, 72,
methyl oleate, 274
methylmethacrylate, MMA, 559 - 570
micelle formation, 533, 534, 538, 540, 549, 552, 554, 556
micellization of amphiphilic molecules, 539
Miconasol, 393, 394
micro-emulsion, 538, 539
micronization, 449
microporosity, 381
micro-sampler, 5
miscibility windows, 231
mixing rules, 19
mixing theories, 185-209
mixtures of non-associating components (PC SAFT), 301

mixtures with associating components (PC SAFT), 303
mixtures with multipolar components (PC SAFT), 305
modeling (RESS), 455
molality, 169
molecular based equations of state, 212
molecular fluids, 211
molecular mobility in supercritical fluids, 343-361
molecular perturbation theory, 212
molecular weight distribution, 52, 574, 575, 586, 587
monochlorotrifluoromethane - β-carotene, 254, 256, 257, 258, 259, 265
monoglycerides, (interfacial tension), 376
Monte-Carlo integration, 215
multicomponent liquid mixtures, 489-519
multicomponent phase equilibria, 180
multipolar compound, 295
nanoscale drugs, 449
naphthalene- carbon dioxide, 451
naphthalene, 153
n-butane, 42-46
near critical region, 213
neon-krypton, 185-209
nitrogen, 39, 41-43, 47-49, 51, 55, 60
nitrous oxide - β-carotene, 254, 255, 257, 258
nitrous oxide (N_2O), 128
nuclear magnetic resonance, NMR, 42
nucleation (GAS), 435
octadecyl (AQ18), 128
octanoic acid (OA), 61, 64, 70, 71, 82
optical cell (SCW), 630
orange peel oil, 490
orange water-phase, 500
organic solid solutes, 147
organo phosphorous compounds, 328
osmotic coefficient, 179, 180
Ostwald ripening, 539
packed column, 369
packed column, 465
packing fraction, 214-219, 300
palmitic acid methyl ester – carbon dioxide (diffusion coefficient), 352
Panagiotopoulos - Reid mixing rule, 153, 173-183
Paracetamol, 415, 420, 421, 427, 428
partial molar volume, 158, 160
partial oxidation in supercritical aqueous solutions, 617, 618, 624-632
particle formation, 147, 160, 560
particle growth (GAS), 435
particle size distribution, 431, 436, 445-449, 459, 461
particle size, 149, 159, 160,
Patel-Teja-EoS, 151
PBT, 595, 597, 599
PC-SAFT, 80
Pd-chelate, 315
pendant drop method, 364-366
Peng-Robinson (EOS), 17, 151-161, 163, 164, 171, 172, 178-183, 211, 218, 219, 220, 283
Peng-Robinson-attraction term, 218
pentane-2,4-dione, 317
perturbation term, 245-248
perturbation theory, 295-302, 321
perturbed-chain-SAFT EoS, 65, 295-322
PET, 595, 597, 599
PGSS (particle generation from gas saturated solution), 148, 149, 431
phase behaviour, 147, 149, 159-161
phase diagrams, 185-209, 225
phase equilibria, 1-340
phase equilibrium (in situ), 85-120
phase equilibrium criteria, 185-210
phospholipids, (interfacial tension), 376
Pitzer model, 174, 179,
PMMA - 3-octanone, 235
poly(butyl acrylate) (PBA), 65
poly(dimethylsiloxane)-monomethylacrylate, PDMS-MA, 559, 570
poly(ethylene terephthalate, 594
poly(ethylene-co-1-hexene), EH, 42, 43, 48
poly(ethylene-co-butyl acrylate) (EBA), 64
poly(ethylene-co-methyl acrylate) in ammonia, 594
poly(ethylene-co-vinyl acetate) copolymers (EVA), 39, 42, 43, 48
poly(glycidyl methacrylate), 578
poly(hexamethylene carbonate) (ammonolysis, solubility), 600, 601
poly(methyl acrylate) (PMA), 64,
poly(styrene-b-dimethylsiloxane) (PS-b-PDMS), 532
polyamide (ammonolysis), 594, 597, 598, 607-616

polybutylene terephthalate (ammonolysis), 598
polycarbonate, 594, 595, 600, 601, 604-606, 616
polydimethylsiloxane/polyhexylmethyl-siloxane (PDMS/PHMS), 233
polydispers blends, 231
polyester (ammonolysis), 594-600, 616
polyethylene terephthalate (ammonolysis), 598
polymer solutions, 225
polymer systems (PC SAFT), 316
polymeric compound, 295
polymerization in a micro-emulsion, 538
polymerization in homogeneous fluid mixtures, 573-590
polymerization in supercritical carbon dioxide, 533-556
polymerization of poly(vinylpyrrolidone) (PVP), 533, 548
polyoxyethylene sorbitan monooleate (Tween-80), 458
population balance, 437
power law (equation of state), 242, 243
Poynting-factor, 15, 16
precipitation by compressed antisolvents, PCA, 150, 431, 449
Predictive Soave-Redlich Kwong (PSRK), 6, 283
Prigogine's rule, 47, 60
propagation rate coefficient, 574, 589
propane + 1-decanol, 6, 29
propane + dodecane, 6, 9, 28
propane, 42-46
pulsed laser initiated polymerization (PLP), 574
quadrupolar interaction, 295
radial distribution function, 299
Raman spectroscopy, 85-120
rapid expansion of supercritical solutions (RESS), 449-460
rate coefficients of polymerization, 573-590
reaction rates in presence of SCF, 280
reactivity ratios for copolymerization, 574, 588-590
recovery of precious metals, 523-529
recycling of car windows, 606
Redlich-Kwong EoS, 211, 219-221
Redlich-Kwong term, 218
Redlich-Kwong-Aspen EoS, 283
Redlich-Kwong-Soave EoS, 17, 151-161, 211, 271
reference equations of state, 213, 298
removal of impurities from ethanol+water mixtures, 495
repulsion term, 211, 214-219
repulsive interactions, 297
residence time distribution (column), 477
response factors of flavor components, 503
RESS (rapid expansion of supercritical solutions), 148, 149, 159, 160, 323, 373, 432, 449-460
retrograde solubility, 127, 140
Rh-chelate, 323
SAFT EoS, 39, 55-57, 65, 285
SAFT-VR attraction term, 220
salicylic acid, 433
salting-out, 169
Schwarzentruber-Renon EoS, 283,
Scott equation, 216
selectivity of carbon dioxide for flavor components, 511
self diffusion coefficient, 343-361
separation efficiency, 465-486
separation factor, 494-518
separation factors of alcohols to ethanol, 496, 497
SFC-apparatus, 128
silica aerogel, 381-426
silicidic acid, 384
silylation of starch, 609
silylation reaction, 608
simple fluid mixtures, 185-209
simplified equation of state, 211
single-droplet model (GAS), 432
sitosterol (β-)- carbon dioxide, 451-460
size distribution, 565
size-exclusion chromatography, 574
sodium acetate, 163-171, 179-182
sodium chloride, 163-171, 177, 179-183
sodiumdodecylsulfate (SDS), 458
sol-gel process, 413
solid solubilities (GAS), 438
solid-fluid phase diagram, 185-209
solubility correlations, 249, 253, 260, 264
solubility isotherm, 127, 129, 139, 141, 143
solubility of ammonolysis products in ammonia, 597
solubility of chelates in carbon dioxide, 323-340

solubility of polymers in ammonia, 597
solubility of solids, 121, 122
solubility of solids, 15
solution enhanced dispersion by supercritical fluid, SEDS, 148, 431, 449
solvation for PMA and PVAc in CO_2, 579
solvatochromism, 122, 123, 132, 135, 143,
solvent power, 39
solvent regeneration, 506
soybean oil - hydrogen - carbon dioxide, 271-273, 278
soybean oil - hydrogen - dimethyl ether, 271, 276
soybean oil - hydrogen – propane, 271, 274-276
soybean oil, 271-279
spectrophotometric analysis, 128
spray extraction, 373
spray processin, 363, 373, 376
stabilization of nanoparticles, 457
standard fugacity, 16
static equilibrium apparatus, 149
static principle (for equilibrium measurement), 128
stripping section, 514
styrene, 573
sublimation, 127, 185-209
sulfur dioxide (supercritical), 523-529
sulfur dioxide preparation of complexes, 523-529
sulfur hexafluoride (SF_6), 128
sulfur-dioxide ruthenium complexes, 524
Sulzer BX packing, 470
Sulzer CY packing, 489, 490,
Sulzer EX packing, 489
supercritical anti-solvent (SAS), 148, 431, 449
supercritical aqueous solutions, 617-632
supercritical drying, 382, 386, 387, 391
supercritical fluid extraction (SFE), 489-519
supercritical fluid reaction, 323
supercritical water (SCW), 617-632
surface tension, 489
surfactant, 375, 376, 533
synthesis of silica aerogel, 390
termination rate coefficient, 574, 582, 585, 588
termination reaction, 574, 582, 590
terpenes, 491
tetraethylorthosilicate (TEOS), 384
tetrafunctional siliconalkoxide precursor, 384
textile colorant, 128
textile dyeing, 122
thermodynamic fundamentals of fluids and solids, 185-209
thermogravimetric analyses (TGA), 525
TMOS, 390, 425
topnote fraction, 491
TPT1 approach, 223
translational molecular mobility, 351
Trebble-Bishnoi-Salim-EoS, 151
Tributylphosphate, 326
triglyceride ester, 269
triglycerides, 269
trimethylsilylation of starch in ammonia, 594
triple point, 124
tubular reactor (SCW), 619
turbidimetry, 559, 560, 564, 567, 570
UCST, 236
upper critical endpoint (UCEP), 124, 147, 148
upper critical solution temperature, UCST, 52
used catalyst, 523
UV/VIS, 128
van der Waals EoS, 211-240
van der Waals mixing rules, 151
van der Waals repulsion term, 214
van Konynenburg and Scott types of phase diagrams, 225
vapor pressure of the solid phase, 15, 16
variable volume cell, 66
view cell, 40, 41, 152
vinyl acetate, 39, 42, 52-54, 59, 60, 63, 72
virial coefficient, 212-222
virial equation, 215
viscosity, 368, 369, 376
VLE measurements, 1-340
volatile (non-electrolyte) organic component, 489-519
volume translated Peng-Robinson, 17
volume translation, 217
water – carbon dioxide (interfacial tension), 366, 376, 377
water + acetic acid, 177
water-phase, 490
wetting behaviour, 364, 366, 370-372, 376
wiremesh packing, 470-486